

The University of Nottingham

School of Chemical, Environmental and Mining Engineering



**SWIRLING PIPEFLOW OF NON-
NEWTONIAN AND PARTICLE-LADEN
FLUIDS**

Ruth Julie Jane Tonkin, B.Eng (Hons)

Thesis submitted to the University of Nottingham

for the degree of Doctor of Philosophy.

September 2004

ABSTRACT

This thesis describes the application of novel swirl inducing pipe to various pipe configurations, when pumping a range of fluids and fluid / particle mixtures. An extensive experimental programme, incorporating particle image velocimetry and photography, was implemented using a pipe flow loop designed specifically for the purpose.

Experimental data was obtained on the effect of a 4-lobe near-optimal swirl pipe on coal-water, sand-water and magnetite-water slurries of various particle size. Results indicated that swirl induction produced greater benefit for denser slurries and higher concentrations, and that swirl induced into slurries containing larger and denser particles decayed more rapidly. At low velocity, experimental data highlighted a reduction in the total pressure drop experienced across a 3.0m horizontal pipe section, a downward sloping section and vertical pipe bends, when the swirl-inducing pipe was present.

PIV was used to measure the axial and tangential velocity of swirling flows downstream of a near-optimal swirl-inducing pipe. It was confirmed that a significant tangential velocity was generated when pumping water in the turbulent regime, however, when the fluid viscosity was increased, leading to laminar flow, no significant tangential velocity was detected.

ACKNOWLEDGEMENTS

Firstly, I would like to thank Prof. Nick Miles and Dr. Trevor Jones for providing supervision throughout this research. I especially appreciate the guidance, inspiration, encouragement and time generously given to me by Dr. Trevor Jones and the support and guidance on the overall vision of the project provided by Prof. Nick Miles. I gratefully acknowledge Dominic Rhodes at British Nuclear Fuels Limited and the University of Nottingham for supporting the project financially.

I particularly appreciate help received from Dr Jeyakumar Ganeshalingam throughout the project and the kind support offered by Chanchala Ariyaratne through the production of the swirl pipe and use of her CFD results.

General assistance provided by Dr. Doug Brown, Bill Cully, Guy Jones, Dr. Warren Jones, Prof. J. Mitchell, Dr George Rice, Steve Shingfield, Marion Smith, Dr Alan Thompson, Phil Windsor and Robert Wooton is also gratefully acknowledged, with particular thanks to Tony Gospel for regular technical help and advise. I would also like to thank Dr A Aroussi, Jake Roberts, Phil Rogers and Dr. Donald Giddings for their assistance in using particle image velocimetry and Ryan Stevenson for help with the use of the tomography system.

Finally, I offer sincere thanks to my parents, husband, sister and brother for their invaluable support.

CONTENTS

ABSTRACT..... i

ACKNOWLEDGEMENTSii

CONTENTS.....iii

LIST OF FIGURESvii

LIST OF TABLESxii

NOMENCLATURE..... i

Chapter 1 INTRODUCTION 1

1.1 Aim and objectives4

1.2 Structure of thesis5

Chapter 2 LITERATURE REVIEW 7

2.1 Flow of settling slurries7

2.1.1 Classification7

2.1.2 Pipeline design.....9

2.2 Flow of non-Newtonian fluids.....10

2.2.1 Classification10

2.2.2 Pipeline design.....12

2.3 Suspension rheology and transport of coarse particles.....17

2.4 Swirling pipe flow19

2.4.1 Swirl decay and tangential velocity distributions.....23

2.5 Flow in bends.....25

2.5.1 Particle-laden fluids.....25

2.5.2	Non-Newtonian fluids	30
2.6	Flow in inclined pipes.....	31
2.7	Summary	33

Chapter 3 SELECTION OF TEST MATERIALS..... 35

3.1	Identification of potential non-Newtonian fluids	35
3.2	Methodology	40
3.2.1	Dissolution.....	42
3.2.2	Rheology.....	43
3.3	Fluid selection.....	44
3.4	Fluid characterisation	46
3.4.1	Thixotropy	47
3.4.2	Storage	49
3.4.3	Changes in apparent viscosity with age.....	50
3.4.4	Effect of bacteria	52
3.4.5	Effect of evaporation	54
3.4.6	Temperature	56
3.4.7	Batch comparison	57
3.4.8	Effect of biocide concentration.....	58
3.4.9	Effect of salt concentration.....	59
3.4.10	Change in rheology over Days 1-2	63
3.4.11	Transient time tests	64
3.5	Choice of settling slurry	65
3.6	Summary / implications for the pipe flow loop.....	68

Chapter 4 DESIGN OF A STEEL PIPE FLOW LOOP..... 72

4.1	Design criteria.....	72
4.2	Layout.....	73
4.3	Structural alterations.....	75
4.4	Influence of operational procedure on design of test loop	76
4.5	Components	77
4.5.1	Pipework.....	77
4.5.2	Swirl pipe.....	80
4.5.3	Pump.....	84
4.5.4	Tank design.....	88
4.5.5	De-aerator	95
4.5.6	Valves	96
4.5.7	Weigh tank.....	97
4.5.8	Cooler	98
4.5.9	Measurement of flow parameters	98
4.6	Summary.....	104

Chapter 5	OPERATIONAL PROCEDURE AND	
EVALUATION OF THE PIPE FLOW LOOP	105	
5.1	Summary of major changes to pipe flow loop design	105
5.2	General operational procedure.....	108
5.3	Component evaluation	113
5.3.1	Pipework.....	113
5.3.2	Tank.....	114
5.3.3	De-aerator	116
5.3.4	Autex unit	116
5.3.5	Cooler	117
5.3.6	Splitter box	118
5.4	Calibration	119
5.5	Hysteresis.....	121
5.6	Negative pressure drop	128
5.7	Summary.....	129
Chapter 6	VISUALISATION OF SWIRLING FLOWS	130
6.1	Visualisation of swirling flows using particle image velocimetry	130
6.1.1	Introduction	130
6.1.2	General methodology	132
6.1.3	Measurement of axial velocity	134
6.1.4	Measurement of tangential velocity	147
6.2	Visualisation of swirling flows using a novel electrical resistance tomography system.....	155
6.2.1	Introduction and methodology.....	155
6.2.2	Results and discussion	157
6.3	Conclusions	162
Chapter 7	EFFECT OF SWIRL-INDUCTION BEFORE	
BENDS	164	
7.1	Introduction	164
7.2	Methodology specifics.....	165
7.3	Results and discussion	166
7.3.1	Biological and rheology tests results	166
7.3.2	Pressure drop over cylindrical pipe	167
7.3.3	Effect of bend radius on pressure drop over bend	168
7.3.4	Effect of swirl on pressure drop over bend.....	170
7.4	Conclusions	173

Chapter 8 EFFECT OF SWIRL ON SETTLING SLURRIES...
..... **175**

8.1 Introduction 175

8.2 Methodology specifics..... 176

8.3 Results and discussion 179

 8.3.1 Particle size..... 179

 8.3.2 Concentration..... 181

 8.3.3 Pressure drop 183

 8.3.4 Tangential velocity 195

8.4 Conclusions 206

Chapter 9 CONCLUSIONS AND RECOMMENDATIONS 209

9.1 Design of a steel pipe flow loop 209

9.2 Velocity distribution downstream of swirl inducing pipes..... 209

9.3 Electrical resistance tomography (ERT)..... 210

9.4 Effect of swirl induction before bends..... 210

9.5 Effect of swirl on settling slurries..... 211

9.6 Thesis contribution 214

9.7 Recommendations 215

REFERENCES..... 217

LIST OF FIGURES

Figure 2.1: Flow regimes and typical pressure drop curve	8
Figure 3.1: A graph to show the variation in thixotropy with solution age.	47
Figure 3.2: Rheology results for the samples stored in sealed pipe lengths	50
Figure 3.3: The variation of apparent viscosity with age at different shear rates.	51
Figure 3.4: Comparison of CMC types.....	57
Figure 3.5: Effect of biocide concentration on rheology	59
Figure 3.6: Effect of salt concentration.....	61
Figure 3.7: Comparison of the behaviour of Walocel solutions on the day of making (Day 1) and the next day (Day 2).....	63
Figure 3.8: Transient shear stress response for 2.0% w/w Walocel at a constant value shear rate of 461.00s^{-1}	65
Figure 4.1: Isometric view of the 3 flow loop design options.	74
Figure 4.2: Various views of the Autex unit in position. a) view of sieve, water meter and autex unit; b) view inside hopper; c) hopper feeding into mixing tank.	76
Figure 4.4: Special radius bends and inclined sections (dimensions in mm). ...	80
Figure 4.5: 3 and 4-lobe swirl pipes (drawn by Ariyaratne. 2002).....	81
Figure 4.6: Perspex flow loop (taken from Ganeshalingam, 2002).....	82
Figure 4.7: Pressure drop over bend for water only.....	83

Figure 4.8: Helix and Stator in a progressive cavity pump, adapted from Mono Pumps Ltd (2002).....	86
Figure 4.10: Photographs of the tank on the Perspex flow loop, operating with 0.7% v/v beads at varying speeds, with a long and short inlet pipe.....	92
Figure 4.11: Dimensions and photograph of the conical tank	94
Figure 4.12: Photograph and drawings showing the de-aerator.	95
Figure 4.13: Photograph and drawing of the valves used in the flow loop.	97
Figure 4.14: Photograph of the Cooler	98
Figure 4.15: Flow measurement equipment.....	100
Figure 5.1: Photographs of the Mono pump, the inverter and motor.	106
Figure 5.2: Photograph of the Warman pump.	107
Figure 5.3: Views of the side, top and inside the splitter box.....	108
Figure 5.4: Photograph of the inclined pipe section	113
Figure 5.5: Photographs of the tank on the steel flow loop while running with 1.4% v/v beads at varying speeds.	114
Figure 5.6: View of the top leg of the flow loop in the standard configuration.	119
Figure 5.7: Graphs showing the pressures recorded during PIV experiments.	122
Figure 5.8: Pressure hysteresis observed using the Mono pump with the de- aerator online.....	123
Figure 5.9: Pressure drop over the lower pipe section when pumping water with the Mono pump, with the de-aerator online.....	128

Figure 6.1: Classification of swirl types (redrawn from Steenbergen and Voskamp, 1998)	131
Figure 6.2: a: Laser trolley containing the lasers and controllers, processor and PC, b: lasers, c: camera and viewing screen.	133
Figure 6.3: Experimental set up for axial PIV tests.....	135
Figure 6.4: Rheological parameters and graph to show the change in apparent viscosity with age for axial PIV tests	136
Figure 6.5: Variation in axial velocity with cross section for water at a nominal velocity of 1.0m/s ($Re = 55\ 000$)	137
Figure 6.6: CFD predictions for the tangential velocity contours at exit of swirl pipe (Ariyaratne, 2004)	142
Figure 6.7: Variation in axial velocity with cross section for CMC at a nominal velocity of 1.0m/s ($Re_{MR} = 380$)	143
Figure 6.8: Viscosity patterns in pipe cross-sections ($P/D = 4$), Ariyaratne (2004).	146
Figure 6.9: Photograph of the tangential viewer and diagram of the pipe loop configuration used for these tests	147
Figure 6.10: Experimental set up for tangential PIV tests.	148
Figure 6.11: Rheological parameters and graph to show the change in apparent viscosity with age for tangential PIV tests	149
Figure 6.12: Processed PIV results for each condition at 1 velocity only.	150
Figure 6.13: Radial distribution of tangential velocity.	153
Figure 6.14: Recent CFD predictions of the radial distribution of tangential velocity.....	155

Figure 6.15a: ERT operating on the Perspex flow loop; b: Electrodes 156

Figure 6.16: Tomograms and photographs of the flow condition at various
velocities and downstream distances from the swirl pipe with a
sand concentration of 0.7% v/v 157

Figure 6.17: Tomograms and photographs of the flow condition at various
velocities and downstream distances from the swirl pipe with a
bead concentration of 1.4% v/v 158

Figure 6.18: Pressure drop characteristic and associated tomograms for 1.4%
v/v plastic beads without swirl induction (taken from
Ganeshalingam, 2002) 160

Figure 6.19: Pressure drop characteristic and associated tomograms for 1.4%
v/v plastic beads with swirl induction at a downstream distance
of 8D (taken from Ganeshalingam, 2002). 161

Figure 7.1: Rheological parameters and graph to show the change in
apparent viscosity with age for CMC bend tests..... 166

Figure 7.2: Comparison of the theoretical and measured pressure drop over
horizontal pipe for CMC..... 167

Figure 7.3: Pressure drop over various radii bends for the 2.7% v/v coarse
sand–water slurry, with no swirl induction. 168

Figure 7.4: Graph to show the effect of swirl before a bend 171

Figure 8.1: Diagram of the top leg of the flow loop for particle tests 177

Figure 8.2: Series of graphs to illustrate the degradation of solid particles..... 179

Figure 8.3: Pressure drop and cost over horizontal pipes for sand slurries of
various particle sizes. 185

Figure 8.4: Comparison of pressure loss over horizontal pipe, for slurries of various particle sizes, with no swirl-induction present (after Durand, 1953)	188
Figure 8.5: Pressure drop over horizontal pipes a bend for coal slurries of various particle sizes.	192
Figure 8.6: Comparison of pressure loss for slurries of various density (after Durand, 1953)	193
Figure 8.7: Diagram of the cross-section (LHS) and length (RHS) of pipe with particle track.....	196
Figure 8.8: Example analysis (1.4% v/v coarse sand, 1.7m/s)	197
Figure 8.9: Two photographs taken under the same conditions to illustrate the unsteady flow observed (2.7% v/v coarse sand, 1.1m/s).	198
Figure 8.10: An example of the results for 1.4% v/v coarse sand at an axial velocity of 1.7m/s.....	200
Figure 8.11: Series of graphs showing the tangential velocity and percentage decay verses the axial velocity, for sand slurries of various particle sizes, determined from the central lines.....	201
Figure 8.12: Flow downstream of an inclined section of pipe with and without swirl induction (1.4% v/v coarse sand, 1.7m/s).....	204
Figure 8.13: Comparison of PIV and photographic data	205

LIST OF TABLES

Table 2.1: Summary of size based flow classifications.....	9
Table 2.2: Time-independent fluid models. (Heywood <i>et al.</i> , 1998).....	12
Table 2.3: Equations describing laminar pipe flow of the primary time- independent fluids.....	14
Table 2.4: Parameters of the Metzner and Reed generalised approach (Govier and Aziz, 1972).....	16
Table 3.1: Comparison of information in literature on fluid characteristics.....	38
Table 3.2: Details of CMC used in the preliminary tests.....	41
Table 3.3: Comments and observations.....	45
Table 3.4: Fluid characterisation tests performed.....	46
Table 3.5: Thixotropy of the series 3 tests (Walocel).....	49
Table 3.6: Ranked mean percentage overnight weight losses of samples over 15 days.	56
Table 4.1: Summary of advantages and disadvantages of main pipe materials (adapted from Bain and Bonnington, 1970).....	78
Table 4.2: Comparison of the pressures measured in the top leg of the Perspex flow loop with a long or standard inlet pipe.....	93
Table 4.3: Valves used in the flow loop.	97
Table 4.4: Flowmeter positioning.....	99
Table 5.1: Result of consultation with Mono Pumps Ltd.....	126
Table 6.1: Time between laser pulses.....	135

Table 6.2: Reference codes for the tests performed.....150

Table 6.3: Maximum tangential velocities for W-Sw results.151

Table 6.4: Maximum tangential velocities for W-Sw and CFD results

 Ariyaratne (2003).....154

Table 8.1: Parameters of the solids used in the tests; $\% v/v = V_s/V_l \times 100$178

Table 8.2: Delivered solids concentrations.....181

NOMENCLATURE

A	Constant defined by $A = \frac{\omega}{u}$	
A	Area of pipe wall	m ²
C	Concentration	% v/v
C	Input volume fraction	v/v
dP	Pressure drop	Pa/m
D	Pipe diameter	m
d ₅₀	Particle diameter, such that 50% solid by weight are small than d ₅₀	μm
E	In situ volume fraction	v/v
<i>f</i>	Friction factor	
<i>f_l</i>	Alternative pseudoplastic friction factor	
g	Gravitational acceleration	m/s ²
H	Head above pump	m
H	Holdup ratio	
He	Hedstrom number	
He _{HB}	Hedstrom number for the Herschel-Buckley model	
<i>h_f</i>	Frictional head loss	
h	Height of cone	m
i	Pressure gradient of solid-liquid mixture	Pa/m
i _w	Pressure gradient for water alone	Pa/m
k	Fluid consistency index	Pas ⁿ

k'	Fluid consistency index for the Metzner and Reed generalised approach	Pa s^n
k	Resistance coefficient for fittings	
k	Factor given by Einstein to be 2.5.	
k/d	Relative roughness	
k	Thermal conductivity	$\text{W m}^{-1} \text{K}^{-1}$
L	Pipe length	m
L/D	Non-dimensional distance	
n	Flow behaviour index	
n'	Flow behaviour index for the Metzner and Reed generalised approach	
P_v	Vapour pressure of liquid	Pa
P_0	Pressure in tank	Pa
Q	Volumetric flowrate	m^3/s
r	Radius	m
R^2	Correlation co-efficient	
r/R	Non-dimensional radial distance	
R/D	Bend curvature radius to diameter ratio	
Re	Reynolds number	
Re_{MR}	Metzner and Reed Reynolds number	
Re_{PL}	Pseudoplastic Reynolds number	
Re_{PLI}	Alternative pseudoplastic Reynolds number	
Re_B	Bingham plastic Reynolds number	
S	Average slip velocity	m/s

s	Specific gravity of solid particles	
t	Thickness	mm
t	Time elapsed	s
U	Velocity in direction of x axis (PIV results)	m/s
u	Mean axial velocity	m/s
V	Flow Velocity	m/s
V	Velocity in direction of y axis (PIV results)	m/s
V	Volume	m ³
V _s	Superficial velocity	m/s
v	Tangential velocity in $v = r\omega$	m/s

Greek letters

α	Angle defined by diagram in Appendix D.11 Figure 3De	rad
η_p	Plastic viscosity – Bingham plastic model	Pas
η	Viscosity of the disperse system	Pas
η_o	Viscosity of the continuous phase	Pas
γ	Shear rate	s ⁻¹
μ	Viscosity	Pas
ΔP	Pressure drop	Pa
ρ	Density	kg/m ³
ρ_s	Slurry density	kg/m ³
τ	Shear stress	Pa

τ_y	Yield Stress - Herschel-Buckley and Bingham plastic model	Pa
τ_w	Wall shear stress	Pa
ρ	Density	kg/m
θ	Angle depicted in diagram B.20	°
θ	Angle defined by diagram in Appendix D.11 figure	rad
θ	Angle swept out by particle with tangential motion	rad
ν	Dynamic viscosity	m ² s ⁻¹
ω	Angular velocity	m/s

Subscripts

l	liquid
max	Maximum value of parameter
mean	Mean value of parameter
min	Minimum value of parameter
s	solids

Abbreviations

C	Carbopol
CCD	Charge-coupled device camera
CFD	Computational Fluid Dynamics
CMC	Sodium carboxymethyl cellulose

D.S.	Degree of substitution
ERT	Electrical resistance tomography
GG	Guar gum
H→V	Flow direction – horizontal to vertical
HPC	Hydroxypropylcellulose
F.S.	Full scale
Labview	Data acquisition software from National Instruments Corporate Headquarters, 11500 North Mopac Expressway, Austin, Texas 78759-3504, USA
L	Laponite
LBG	Locust bean gum
LHS	Left hand side
MC/HPMC	Methylcellulose / hydroxypropylmethylcellulose
N.B.	Nominal bore
Nd:YAG	A twin pulsed laser
NI-DAQ	Data acquisition software from National Instruments Corporate Headquarters, 11500 North Mopac Expressway, Austin, Texas 78759-3504, USA
NPSH	Net Positive Suction Head
PC	Personal computer
PIV	Particle image velocimetry
PVP	Polyvinylpyrrolidone
PVC	Polyvinyl chloride

PT9, PT15	Steel pressure transducers
P3, P4	Transducers from Perspex flow loop
RHS	Right hand side
V→H	Flow direction – vertical to horizontal
x-section	cross section
XG	Xantham gum

Used in keys / graphs:

sc 1.36	test condition: water carrying coarse sand at 1.4% v/v
sc 2.03	test condition: water carrying coarse sand at 2.0% v/v
sc 2.71	test condition: water carrying coarse sand at 2.7% v/v
sm 1.36	test condition: water carrying medium sand at 1.4% v/v
sm 2.03	test condition: water carrying medium sand at 2.0% v/v
sm 2.71	test condition: water carrying medium sand at 2.7% v/v
sf 2.71	test condition: water carrying fine sand at 2.7% v/v
c24 1.36	test condition: water carrying ultra-coarse coal at 1.4% v/v
c24 2.03	test condition: water carrying ultra-coarse coal at 2.0% v/v
c24 2.71	test condition: water carrying ultra-coarse coal at 2.7% v/v
cc 1.36	test condition: water carrying coarse coal at 1.4% v/v
cc 2.03	test condition: water carrying coarse coal at 2.0% v/v
cc 2.71	test condition: water carrying coarse coal at 2.7% v/v
beads 2.71	test condition: water carrying plastic beads at 2.7% v/v
mc 1.36	test condition: water carrying coarse magnetite at 1.4% v/v

CMC+s	test condition: CMC carrying coarse sand at 2.7% v/v
BO	test condition: open CMC sample containing Busan biocide
PO	test condition: open CMC sample containing Proxel biocide
CO1	test condition: open CMC control sample, series 1
CO2	test condition: open CMC control sample, series 2
NO	test condition: open CMC sample containing Nalco biocide
NS	test condition: sealed CMC sample containing Nalco biocide

Terminology

<i>Italics</i>	Used to show direct quotations
Slurry	Used loosely to refer to the solid-particle mixtures tested
Leg	Refers to a length of pipe, for example upper leg, lower leg
Standard pipe	316L, schedule 10 stainless steel pipe with circular cross section and 0.055m diameter
Perspex flow loop	The flow loop used by Raylor (1998) and Ganeshalingam (2002)

Chapter 1 INTRODUCTION

The flow of fluids through pipes has long been studied and is commonly encountered in everyday life. Newtonian and non-Newtonian fluids are of widespread importance in industry and a vast amount of research has been conducted into the behaviour and flow of these fluids. A similarly vast field of research addresses the behaviour and flow of particle-laden fluids, often termed slurries. Materials ranging from copper to strawberries can be pumped over long or short distances in cross country or process-plant pipelines.

Non-Newtonian flow is important in a range of industries, such as clay, oil and food. Clay slurries are used in ceramics, cement, drilling fluids, moulding sands, paints and paper (Johnson *et al.*, 1999). Non-Newtonian fluids are also used to carry coarse particles. In fact, Bain and Bonnington (1970) state that non-Newtonian carriers can lead to reduced pressure drop and Heywood *et al.* (1998) agree that “*shear thinning media are highly suitable for transporting coarse particles*”.

An important part of designing a pipeline is the choice of an operational velocity. Pumping of coarse particles in the homogenous regime results in unacceptably high abrasion and pumping power, whereas pumping in the stationary bed regime reduces throughput and increases the risk of pipe blockage and downtime. In industry, slurries are generally transported in the heterogeneous or sliding bed flow regimes, a little above the minimum pressure drop. In the heterogeneous regime

the particles are suspended through the turbulence generated in the liquid, however there is a vertical concentration gradient across the pipe. Operation in these regimes may lead to increased wear in the bottom half of the pipe and reduced system efficiency (Heywood *et al.*, 1998).

Over the past 100 years interest has developed in the use of swirling flow fields to address these problems. A swirling flow is a fluid motion with a tangential velocity component (Gupta *et al.*, 1984), primarily generated by:

- Tangential entry
- Guided vanes
- Pipe rotation
- Non-circular pipes

The application of swirl to solid-liquid pipeflow serves to provide a turbulent motion that keeps the particles in suspension at lower velocity. This can lead to a variety of benefits as documented in literature. For example Howard (1939, 1941) used riffled pipe in dredging the Mississippi and recorded an increased throughput of 45%. Similarly, Charles *et al.* (1971) used internal spiral ribs to generate swirl in settling slurries and found a reduction in power consumption, pressure gradient and critical velocity.

At the Nottingham Mining and Minerals Centre, research into an innovative method to generate swirl flow using helically formed pipes, has been ongoing since 1993, when the idea was first proposed by Jones (1997). Raylor (1998, 1999) and Ganeshalingam (2002) continued this work, using computational fluid dynamics (CFD) to optimise the design of the swirl flow pipe and investigate its application prior to vertical bends. It was found that the pressure drop over the bend was reduced when preceded by a swirl-inducing pipe and a near-optimal pipe design was specified. In addition a short project was undertaken using a steel flow loop and sand–water slurry to investigate the wear experienced by a bend when preceded by a 3-lobe swirl-inducing pipe. The rate of wear was found to be greater when the bend was preceded by swirl, however this was attributed to operating at too great a velocity.

These studies have produced valuable results, however, the majority of the experimental work was limited to smooth pipes, vertical bends and water-plastic bead slurries. To promote use of the swirl pipe in industry its wider application must first be demonstrated.

1.1 Aim and objectives

The aim of this research was to investigate experimentally the application of novel swirl inducing pipe to different pipe configurations, when pumping a range of fluids and fluid / particle mixtures. Various flow visualisation techniques were used to examine the flow patterns created. The objectives of the project were to:

- Design, commission and calibrate a steel pipe flow loop
- Select and characterise a suitable non-Newtonian fluid for use in the flow loop
- Investigate the effect of a swirl-inducing pipe positioned upstream of vertical and horizontal bends of various radii, on the pressure drop over the bend, for non-Newtonian and particle-laden fluids.
- Investigate the decay of tangential velocity downstream of a swirl-inducing pipe.
- Investigate the effect of swirl on the pressure drop in inclined pipes, considering different pipe angles and flow up and down.
- Investigate the performance of the swirl pipe when pumping slurries of varying particle size and density.

1.2 Structure of thesis

This thesis is split into 9 chapters including this one, which provides a brief introduction to the subject area and outlines the aims of the research and the structure of the thesis. A range of methodologies were used, including desktop experiments, operation of pipe flow loops and flow imaging techniques. The general operation of the pipe flow loop is given in Chapter 5 with other methodology described in detail in the appropriate chapter.

Chapter 2 introduces some of the theory relating to the flow of fluids through pipes, which is utilised in this research. Literature relevant to the current project is reviewed and an overview of the development of the use of swirl pipe flow is presented.

The following three chapters document preparatory work performed. Chapter 3 describes the selection of a range of materials for use in the pipe flow tests. Carboxymethyl cellulose was found to be a suitable non-Newtonian fluid and a study of the behaviour of this fluid in terms of a number of important factors was conducted. Following this, the procedure used to specify the type, size and concentration of solids to be pumped is presented. Chapter 4 then details the steps involved in the design of a new flow loop for the swirl pipe tests. The design requirements, layout options and operational factors were discussed, followed by a description of the components used in the flow loop. Chapter 5 outlines the

general methodology used in operating the flow loop, evaluates the design and documents some problems experienced with the performance of the system.

The next three chapters document and discuss the pipe flow experiments. Chapter 6 describes the use of particle image velocimetry to examine the distribution of axial and tangential velocity downstream of the swirl-inducing pipe. The experiments were performed in a similar way to those of Ganeshalingam (2002) to maintain some constancy with his work while advancing knowledge about the application of swirling pipe flows to industrial use. The application of a novel electrical resistance tomography technique to pipeline transport was also investigated. Chapter 7 examines the effect of bend radius and upstream swirl-induction on the pressure drop over the bend when pumping water, CMC and a sand-water slurry. The effect of swirl-induction before vertical bends and inclined pipes for a range of settling slurries is then presented in Chapter 8. The pressure drop was measured and tangential velocities estimated using a photographic technique.

The final chapter draws together the key findings and presents recommendations for future research.

Chapter 2 LITERATURE REVIEW

This section introduces some of the theory relating to the flow of fluids through pipes, which is utilised in this research. An overview of the development of the use of swirl pipe flow and a review of literature relevant to the current project is presented.

2.1 Flow of settling slurries

2.1.1 Classification

The behaviour of slurries is complex and affected by many factors. There are variables associated with the system, for example, velocity and temperature. Other factors relate to the pipe infrastructure, for example, length, roughness, bend radius and still others to the constituent particles, such as density, size, shape and particle size distribution. In addition, it is common for separate phases to travel at different velocities, leading to a phenomenon known as holdup.

The behaviour of settling slurries in pipes can be divided into a series of generally accepted flow patterns, which are mainly dependent on velocity, as shown in Figure 2.1.

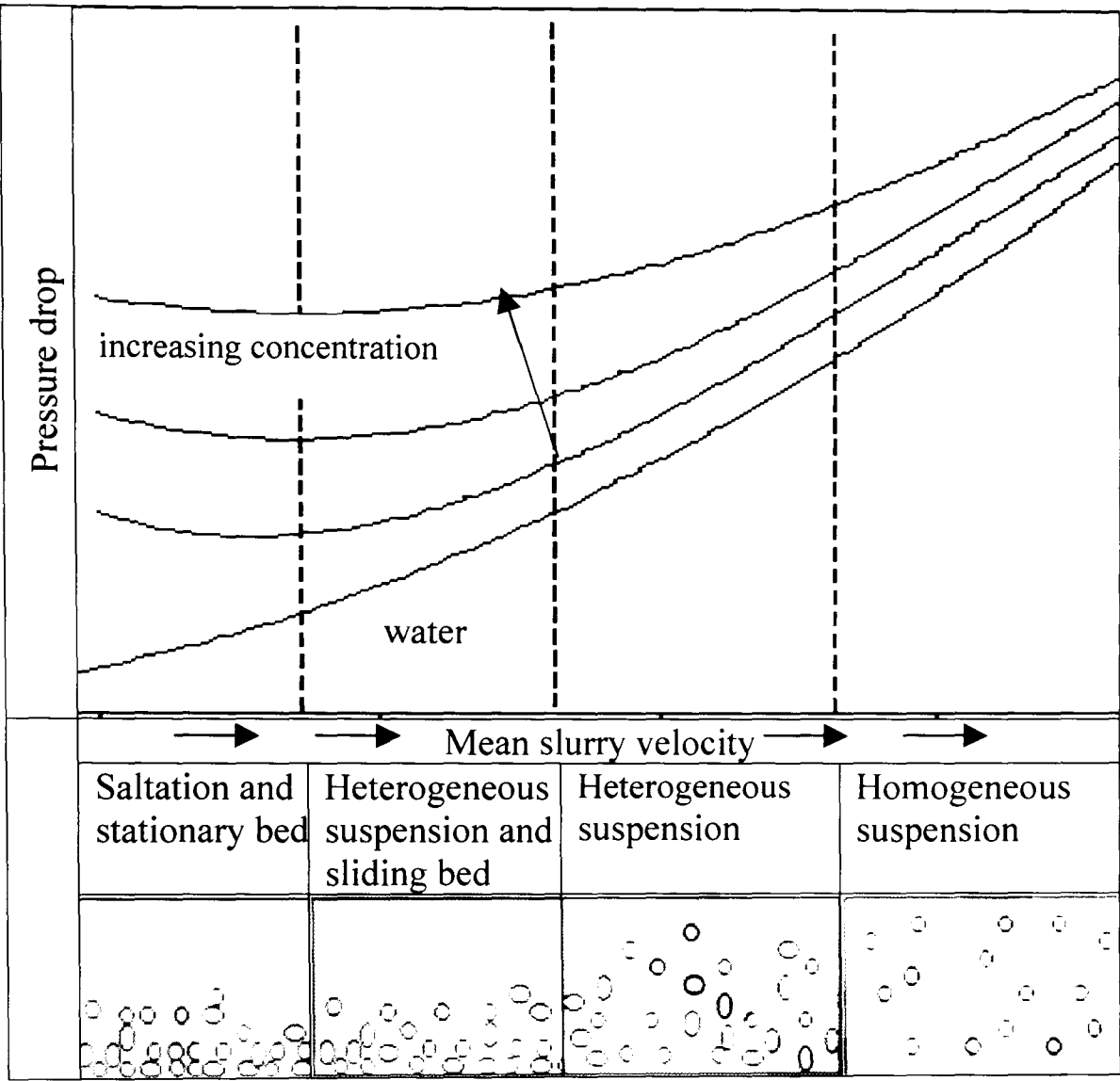


Figure 2.1: Flow regimes and typical pressure drop curve

Slurries are sometimes termed *settling* or *non-settling*. The first three categories in Figure 2.1 are settling slurries, since the particles readily settle out. The fourth category can be called non-settling, as all the particles remain in suspension. The distinction between these flow patterns has proved hard to define, leading some authors to define further transitional regimes. Some sources suggest that particle size alone is an adequate classification measure, but there is some disagreement over the cut off sizes (Table 2.1). Other sources used settling rate to define the flow regimes, however classification by size or settling rate does not take account of the effect of velocity on the flow regimes. Newitt *et al.* (1955) derived pressure

drop correlations and equated these to give equations for the velocity range of each regime, but these equations are limited by the range of data used in the correlation. To differentiate between settling and non-settling slurries Heywood *et al.* (1998) advise a comparison of particle settling time and slurry residence time. These considerations were important when selecting test materials (Chapter 3).

Table 2.1: Summary of size based flow classifications.

Classification	Size range	Researcher
Homogenous	<40 μ m	Hughmark (1961)
	<30 μ m	Stepanoff (1969)
	<40 μ m	Bain and Bonnington (1970)
	<20 or 30 μ m	Durand (1953)
Intermediate	25-50 μ m	Durand (1953)
Heterogeneous	>40 μ m	Bain and Bonnington (1970)
	>50 μ m	Durand (1953)
Heterogeneous - suspension	40 μ m – 2mm	Hughmark (1961)
	50 μ m - 0.2mm	Stepanoff (1969)
	50 μ m - 0.2mm	Durand (1953)
Transitional	0.2mm - 2mm	Durand (1953)
Heterogeneous - saltation	>2mm	Hughmark (1961)
	>2mm	Stepanoff (1969)
	>2mm	Durand (1953)

2.1.2 Pipeline design

Literature concerning the design of settling slurry pipelines is based on empirical and semi-empirical correlations. There are generally two types of correlation one based on pressure, the other on velocity. Many correlations exist for critical velocity, based upon several different critical velocity definitions, including Durand (1953), Spells (1955), Hughmark (1961), Roco and Shook (1985) and

Kökpınar and Göğüs (2001). Examples of correlations based on pressure are Newitt *et al.* (1955), Turian and Yuan (1977) and Maruyama *et al.* (1980).

Since the early 1970's, much research has focussed on validating and refining the two-layer mechanistic model derived by Wilson. This model is based on the division of the flow into two parts – a contact load, contributing to sliding friction in the base of the pipe and a suspended load in the upper portion of the pipe. Gillies *et al.* (1991) modified the model to take account of the presence of fines, while Pugh and Wilson (1999) analyse the effect of the interface between the two layers. Sundqvist *et al.* (1996b) attempted to validate one form of the model for coarse high density slurries and found that it underestimated the pressure loss. This illustrated the point made by Heywood *et al.* (1998) that even mechanistic analyses are unreliable outside the range of experimental data used.

2.2 Flow of non-Newtonian fluids

2.2.1 Classification

There are many types of non-Newtonian materials. Non-Newtonian fluids are generally divided into three categories consisting of time-dependent, time-independent and viscoelastic (Tanner, 1985). For a time-dependent fluid the relationship between shear stress and shear rate depends on the time the fluid has been sheared (Tanner, 1985). The main time-dependent fluids are thixotropic and

rheopectic. When thixotropic fluids are subject to constant rate shearing, a substantial lowering of the apparent viscosity with time results (Walters 1980).

Visco-elastic fluids display characteristics of solids and fluids. The deformation of such fluids varies with the time of application of stress (Ghannam and Esmail, 1997) and after deformation they exhibit partial elastic recovery (Tanner, 1985). Rosenberg (1997) describes viscoelasticity as the “*simultaneous existence of viscous and elastic properties in a material.*” Materials that exhibit this behaviour include polymer melts, polymers and soap solutions (Chhabra and Richardson, 1999).

The rate of shear of a time-independent fluid is a function of the shear stress and does not depend on the time the fluid has been sheared (Tanner, 1985). Time-independent fluids can be shear thinning or shear thickening. The apparent viscosity of a shear thinning fluid decreases with shear rate, while that of a shear thickening fluid increases. As described in Chapter 3, time-independent fluids were the focus of a section of this research.

A number of models are available to describe various types of time-independent fluids, of which three stand out as the most commonly employed (Table 2.2). Shear-thinning fluids or pseudoplastics are often modelled by a power law (sometimes called the Ostwald-de-Waele model). Examples of these materials are paints, paper pulp and polymers. The power law has also been used to model shear thickening or dilatant fluids (Chhabra and Richardson, 1999). Other fluids

follow the Herschel-Buckley model (or the generalised Bingham plastic model). described by a power law with a yield stress. The last category of time-independent fluids is the Bingham plastic. This is also known as a generalised Newtonian fluid and like a Newtonian fluid has a constant viscosity but in addition possesses a yield stress. Some examples of Bingham plastics are limestone slurries, sewage sludge and drilling mud (Bain and Bonnington, 1970). In reality, fluids display a complex combination of the behaviours described, however by identifying the principal characteristics of a fluid, the models can be used as a basis for further calculation (Chhabra and Richardson, 1999).

Table 2.2: Time-independent fluid models. (Heywood *et al.*, 1998)

Fluid	Model
Pseudoplastic	$\tau = k\dot{\gamma}^n$; k = fluid consistency index, n = flow behaviour index < 1
Herschel-Buckley	$\tau = \tau_y + k\dot{\gamma}^n$; τ_y = yield stress
Bingham plastic	$\tau = \tau_y + \eta_p \dot{\gamma}$; η_p = plastic viscosity
Dilatant	$\tau = k\dot{\gamma}^n$; k = fluid consistency index, n = flow behaviour index > 1

2.2.2 Pipeline design

The design of non-settling slurry pipelines is based on the rheological equation of the fluid to be pumped. Therefore, fluid studies to ascertain the fit of rheological equations are an important part of design. Much research has focused on transitional and turbulent flow of non-Newtonian fluids (Dodge and Metzner, 1959; Wilson and Thomas, 1985; Slatter and Van Sittert, 1999). This work was

not discussed further, since the current study concentrated on the laminar regime, in order to avoid unreasonable pumping costs.

For laminar flow, pipeline parameters (for example, volumetric flow rate) can be calculated from first principles. Equation 2.1 is part of what is known as the Rabionwitsch-Mooney relations. The derivation of this equation can be found in many texts, for example, Skelland (1967), Govier and Aziz (1972), Heywood *et al.* (1998) and Chhabra and Richardson (1999).

$$Q = \frac{\pi}{8} \left(\frac{D}{\tau_w} \right)^3 \int_0^{\tau_w} \tau^2 \gamma d\tau \quad \text{Equation 2.1}$$

$$\text{where } \tau_w = \frac{D\Delta P}{4L} \quad \text{Equation 2.2}$$

By substituting the constitutive equations (Table 2.2) into Equation 2.1 and performing the integration, formulas for the volumetric flow rate of each fluid type are obtained (Table 2.3, Equations a). These formulas can be rearranged to give τ_w , which is substituted into Equation 2.3 leading to the definition of a Reynolds number (Table 2.3, Equations b and c).

$$f = \frac{2\tau_w}{\rho V^2} \quad \text{Equation 2.3: Definition of the Fanning friction factor}$$

It can be seen from Table 2.3, Equation 1b, that the friction factor definition for a pseudoplastic (using Re_{PL}) takes the same form as the friction factor equation for laminar Newtonian flow. Chhabra and Richardson (1999) highlight that this definition of the friction factor allows the Newtonian friction factor chart to be

used for time-independent non-Newtonian fluids in the laminar regime. Govier and Aziz (1972) define a second power law Reynolds number (Table 2.3. 1c. Re_{PL1}) that they claim is preferable, as it does not force the data to be aligned with the Newtonian case as Re_{PL} does. However many texts following Govier and Aziz (1972) give no mention to this alternate definition.

Table 2.3: Equations describing laminar pipe flow of the primary time-independent fluids.

Fluid type	Equations
Power law	$1a) \frac{2V}{D} = \frac{8Q}{\pi D^3} = \left(\frac{n}{1+3n} \right) \left(\frac{\tau_w}{k} \right)^{\frac{1}{n}}$ $1b) f = \frac{16}{Re_{PL}}; \text{ alternatively } f_1 = \left(\frac{16}{Re_{PL1}} \right) \left(\frac{1}{8} \right) \left(\frac{2+6n}{n} \right)^n$ $1c) Re_{PL} = \frac{8D^n V^{2-n} \rho}{k} \left(\frac{n}{2+6n} \right)^n; Re_{PL1} = \frac{D^n V^{2-n} \rho}{k}$
Bingham Plastic	$2a) \frac{2V}{D} = \frac{8Q}{\pi D^3} = \frac{\tau_w}{4\eta_p} \left[1 - \frac{4}{3} \frac{\tau_y}{\tau_w} + \frac{1}{3} \left(\frac{\tau_y}{\tau_w} \right)^4 \right]$ $2b) f = \frac{16}{Re_B} \left(1 + \frac{He}{6Re_B} - \frac{He^4}{3f^3 Re_B^7} \right)$ $2c) Re_B = \frac{DV\rho}{\eta_p}; He = \frac{D^2 \tau_y \rho}{\eta_p^2}$
Herschel-Buckley	$3a) \frac{2V}{D} = \frac{8Q}{\pi D^3} = \frac{n}{\tau_w^2} \left(\frac{\tau_w}{k} \right)^{\frac{1}{n}} \left(1 - \frac{\tau_y}{\tau_w} \right)^{\frac{1+n}{n}} \left[\frac{(\tau_w - \tau_y)^2}{1+3n} + \frac{2\tau_y(\tau_w - \tau_y)}{1+2n} + \frac{\tau_y^2}{1+n} \right]$ $3b) f = \text{funct}(Re_{PL}, He, f)$ $3c) Re_{PL} = \frac{8D^n V^{2-n} \rho}{k} \left(\frac{n}{2+6n} \right)^n; He_{HB} = \frac{D^2 \rho}{\tau_y} \left(\frac{\tau_y}{k} \right)^{\frac{2}{n}}$

Metzner and Reed (1955) developed a calculation method based on the Rabinowitsch-Mooney equation that is applicable to any time-independent fluid, in the laminar flow regime. The derivation can be found in their paper and many other texts. They suggest that Equation 2.4 may be used to define the fluid behaviour and also define Equation 2.5.

$$\tau_w = k' \left(\frac{8V}{D} \right)^{n'} \quad \text{Equation 2.4}$$

$$\text{where: } n' = \frac{d \ln(D\Delta P / 4L)}{d \ln(8V / D)}$$

$$f = \frac{16}{\text{Re}_{ME}} \quad \text{Equation 2.5}$$

Combining Equations 2.3, 2.4 and 2.5 yields:

$$\text{Re}_{MR} = \frac{D^{n'} V^{2-n'} \rho}{\gamma} \quad \text{Equation 2.6}$$

where : $\gamma = k' 8^{n'-1}$ and the fluid consistency index (k') and flow behaviour index (n') for each fluid type are shown in Table 2.4.

Table 2.4: Parameters of the Metzner and Reed generalised approach (Govier and Aziz, 1972)

For Power law fluids:	For Bingham plastics:
$n' = n$	$n' = \left[1 - \frac{4}{3} \frac{\tau_y}{\tau_w} + \frac{1}{3} \left(\frac{\tau_y}{\tau_w} \right)^4 \right] \left[1 - \left(\frac{\tau_y}{\tau_w} \right)^4 \right]^{-1}$
$k' = k \left(\frac{1+3n}{4n} \right)^n$	$K' = \tau_w \left\langle \eta \left\{ \tau_w \left[1 - \frac{4}{3} \frac{\tau_y}{\tau_w} + \frac{1}{3} \left(\frac{\tau_y}{\tau_w} \right)^4 \right] \right\}^{-1} \right\rangle^{n'}$
$\gamma = k \left(\frac{1+3n}{4n} \right)^n 8^{n-1}$	$\gamma = 8^{n'-1} \tau_w \left\langle \eta \left\{ \tau_w \left[1 - \frac{4}{3} \frac{\tau_y}{\tau_w} + \frac{1}{3} \left(\frac{\tau_y}{\tau_w} \right)^4 \right] \right\}^{-1} \right\rangle^{n'}$

Metzner and Reed (1955) found that the laminar flow region extends to a friction factor value of about 0.008 or Re_{MR} of 2000-2500. The generalised approach is particularly useful for fluids that do not conform easily to one of the constitutive equations. For example, Perona (2003) applies this approach to model fruit purees whose degree of dilution substantially effects the magnitude of the yield stress and consistency index. The approach appears to be widely used as Pinho *et al.* (2003) state:

‘For pipe flow there is general agreement on the use of either the wall viscosity, especially under the turbulent regime, or an apparent viscosity based on the definition of the generalised Reynolds number of Metzner and Reed, 1955.’

Therefore, given the rheological parameters, the laminar flow of time-independent fluids may be easily modelled. However Heywood *et al.* (1998) warn that the

accuracy of the resulting formulae is limited by the accuracy of the data and the closeness of fit to the chosen constitutive equation.

2.3 Suspension rheology and transport of coarse particles

At the beginning of the last century the viscous behaviour of homogenous suspensions was noted. Einstein proposed the following equation (quoted in Rutgers, 1962):

$$\eta/\eta_0 = 1 + (k \times C) \quad \text{Equation 2.7}$$

η = viscosity of the disperse system

η_0 = viscosity of the continuous phase

k = factor, varies with the particle properties; Einstein gave $k = 2.5$.

C = concentration / v/v

Many people have since modified this semi-theoretical equation to fit empirical results. Rutgers (1962) and Jinescu (1974) have produced comprehensive reviews of work on the rheology of suspensions containing 280 and 133 references respectively. Recent work in this field was performed by Kawatra and Bakshi (1995), Slatter (1999), Shi and Napier-Munn (1996), and Richardson *et al.* (1999). Kawatra and Bakshi (1995) found that a high ash seam bituminous coal with 80% passing 34 μ m was pseudoplastic beyond 20% w/w solids. Shi and Napier-Munn (1996) tested milled ferrosilicon slurry, limestone slurries, ground gold slurry and

lead-zinc-copper slurry. They modelled these slurries as non-Newtonian liquids, specifically dilatant or pseudoplastic liquids with a yield. Slatter (1999) also claims that homogenous mineral slurries should be modelled using the yield pseudoplastic model. However, Richardson *et al.* (1999) modelled anthracite coal and kaolin suspensions using the power law model.

Slatter's work (1999) also documents the development of a new Reynolds number for yield-pseudoplastic fluids, in which he described the presence of an unsheared solid plug that inhibited turbulence. A similar effect was documented by other authors, who additionally described advantages of this structure for conveying coarse particles. Bain and Bonnington (1970) state that non-Newtonian carriers can lead to reduced pressure drop, while Heywood *et al.* (1998) describe the effect clearly:

"Shear thinning media are highly suitable for transporting coarse particles. In the low shear region near the centre of the pipe, the apparent viscosity is high and the settling velocity of the suspended coarse particles is either low, or zero if the medium has sufficiently large yield stress. Near the pipe wall, shear rates are high, apparent viscosities are low and in consequence pressure gradients in the pipeline are not excessively great."

Richardson *et al.* (1999) provide a useful overview of relevant literature, including studies that found a reduction in operational velocity, pressure gradient and power consumption when transporting coarse particles with power law or Bingham plastic suspensions rather than water.

2.4 Swirling pipe flow

Raylor (1998) and Ganeshalingam (2002) have produced a comprehensive review of the historical development of the use of swirl induction to improve solids transport. A summary of this is provided before their work is reviewed.

The interest in the application of swirling flows to solid-liquid pipe flow originated with Gordon and Gordon (1899) who patented the use of helical ribs in pipes or conduits. The main application of the patent was in the dredging industry, to prevent the deposition of sediment, however optimal dimensions for the ribs were not specified.

Robinson (1923) and Yuille (1928) obtained further patents for ribbed pipe designs. Robinson's patent, also for application in hydraulic dredging, aimed to reduce the likelihood of spoils becoming lodged in the delivery pipe to avoid the associated increase in power consumption and chance of blockage. Unlike the Gordons' design, this patent used continuous ribs along the length of the pipe. Robinson also suggested the use of several ribs, depending on the slurry type and pumping power available. Again to prevent slurries settling, Yuille's invention consisted of repeated ribbed pipe sections, which produced less friction than continuous ribs, leading to reduced power consumption.

The first use of non-circular pipes to generate swirl flow is attributed to Howard (1939, 1941), who performed extensive tests using 2 and 4 inch pipe

(approximately 50 and 100mm), a range of slurries and a range of riffle / rib configurations. Riffled pipe was also used in dredging the Mississippi and an increased throughput of 45% reported.

Wolfe (1967) investigated the use of helically ribbed pipe in slurry transport, for application in the mining industry. The main findings were that the optimum angle of helix was 45° , the system could be operated at lower velocities and stopped and restarted easily, and wear was reduced.

Charles *et al.* (1971) used a single spiral rib to generate swirl in sand slurries and found a reduction in power consumption, pressure gradient and critical velocity. In addition an optimum pitch to diameter ratio of 5 was suggested.

Schriek *et al.* (1974) found that sand–water slurries could be pumped through pipes containing three internal spiral ribs at a lower pressure drop than through smooth pipes. Tests were performed on 2 and 6 inch diameter pipe (approximately 50 and 150mm) and a shallow optimum pitch to diameter ratio (P/D) of 8 was determined. However, it was concluded that a P/D range of 5-11 showed no significant difference from the optimum. Singh and Charles (1976) also found an optimum pitch to diameter ratio of 8, as well as an optimum rib height of 15-20% of the pipe diameter.

At the Nottingham Mining and Minerals Centre, Raylor (1998) and Ganeshalingam (2002) have investigated an innovative technique to use helically formed pipes to induce swirl into solid-liquid flows. Raylor (1998) conducted experimental work, pumping water-plastic bead mixtures in a Perspex flow loop. It was found that the pressure drop over the bend was reduced when preceded by a swirl-inducing pipe. At the same time, a computational fluid dynamics investigation was performed to analyse the use of variable and fixed pitch pipe designs. This indicated that longer lengths of variable pitch pipe produced a greater tangential velocity, although a constant pitch pipe, with a pitch to diameter ratio of 8, resulted in the minimum pressure drop.

Ganeshalingam (2002) refined the pipe design by using CFD to investigate the effect of cross-sectional shape, pipe length and differing pitch. The greatest advantage (based on swirl intensity per normalised pressure loss) was obtained from a 4-lobe pipe with a pitch to diameter ratio (P/D) of 8 and a length of 0.4m. Experimental work was used to quantitatively validate the CFD predictions in terms of axial velocity and pressure, with good agreement obtained. The pressure drop across the swirl pipe was found to increase with velocity but was insensitive to changes in concentration, leading to the conclusion that the application of swirl was more useful at low velocity and high concentration. In addition, swirl induction was shown to suspended particles at lower flow rates than in cylindrical pipe only.

A small-scale internal project was undertaken using a steel flow loop and sand – water slurries to investigate the wear experienced by a bend, when preceded by a 3-lobe swirl-inducing pipe. The weight and thickness of the bend was recorded and the wear rates were found to be greater when the bend was preceded by swirl. However, since swirl was known to have greatest effect at low velocity, this result was attributed to the high operational velocity of 3.5m/s (Primavera, 2001).

The work of Raylor (1998) and Ganeshalingam (2002) was important to identify a near-optimum pipe design and gain insight into the potential benefits associated with the use of the swirl-inducing pipe. However, the bulk of the research was limited to coarse, low density, heterogeneous slurries, which constitutes only a fraction of fluid / slurry types. In addition, with the exception of the work of Primavera (2001), experiments were limited to turbulent smooth pipe flow.

No literature directly relating to the swirling pipeflow of non-Newtonian fluids was found, however information on the flow of these fluids through annuli with rotation of the inner cylinder was available. Although the similarities between the situations are limited it was considered worthy of note that Nouri and Whitelaw (1997) found that the eccentric rotation of the inner cylinder had a similar effect on Newtonian and power law fluids.

2.4.1 Swirl decay and tangential velocity distributions

As illustrated by Yuille's patent (1928), periodic application of swirl induction should maximise the benefits obtained from swirling flows, while minimising pressure loss. Therefore, the rate of decay of induced-swirl is important to its application in solids transport. Similarly the tangential velocity distribution downstream of the induced swirl was of particular interest to allow prediction of the optimum distance for reapplication of swirl-induction and further understand the flows produced. With the exception of research conducted at Nottingham, literature is only available for the decay of single-phase swirling flows and includes the following publications.

Krieth and Sonju (1965) considered the decay of tape-induced swirling flow in water. They found that within 50 diameters the swirl decayed to 10-20% of its initial intensity, with more rapid decay at lower velocities. The tangential velocity distribution was found to approximate to the initial distribution at downstream distances of less than 20 diameters. Further downstream, the profile took on a triangular shape with a maximum velocity at distance of approximately 80% of the pipe radius, from the centreline.

Murakami *et al.* (1976) investigated the effect of wall roughness on the rate of decay of free and forced vortex swirl flow. Swirl was observed to decay exponentially, with an exponential constant that was proportional to the friction

factor. As the flow decayed the tangential velocity pattern changed from an initial forced-free vortex type, through a transitional type to a forced vortex type.

Kitoh (1991) studied turbulent swirling flow in cylindrical pipe and confirmed that the swirl decayed exponentially, but found that the decay coefficients depended on swirl intensity. The tangential velocity distribution was also analysed and found to constitute three regions: core, annular and wall. The core and annular regions were characterised by free and forced vortices and the tangential velocity expressed as the sum of these motions.

More recently, Steenberg and Voskamp (1998) conducted experiments on swirling flows in cylindrical smooth pipes. The findings of previous authors that swirl decayed exponentially and the rate of decay decreased as velocity increased, were confirmed. They also derived an exponential co-efficient for smooth pipes and identified three swirl types according to the radial distribution of tangential velocity. These classifications included the “*concentrated-vortex (CV)*” pattern in which the rotation is concentrated near the pipe centre, the “*solid-body (SB)*” pattern with an almost uniform rotation and the “*wall-jet (WJ)*” with angular momentum distributed near the wall.

At Nottingham, Ganeshalingam (2002) found that following swirl induction, particle suspension endured in cylindrical pipe for a considerable length, dependant upon the velocity and solids concentration. Decay rates obtained from CFD showed good agreement with the exponential formula of Steenbergen and

Voskamp (1998). In addition, electrical resistance tomography was used to develop an innovative approach to predict the downstream decay of suspended particles, by calculating the centre of gravity of the particles. However, these results relate to smooth pipe flow and since Murakami *et al.* (1976) found that rate of decay of swirl was related to the pipe friction factor, significant differences may be observed in rough pipe flow. In addition, no experimental data on the tangential velocity generated by the swirl pipe was obtained.

2.5 Flow in bends

2.5.1 Particle-laden fluids

Bends are an important part of any pipeline and as such, the flow mechanisms and pressure drop across bends are of great interest to industry. Bends are susceptible to excessive wear, which leads to loss of time and money. An increased pressure drop is also associated with bends, which is complicated by many factors including solids concentration, pipe diameter, mean flow velocity, the radius of the bend, and the specific gravity and particle size distribution of the solids (Mukhtar *et al.*, 1995). However, although single-phase flow patterns within bends are reasonably well understood and many studies on pneumatic conveying through bends have been performed, the literature on the flow of slurries through bends is limited.

Ayukawa (1969), one of the earliest studies of hydraulic conveying around bends, derived a semi-empirical formula for the pressure drop over a bend in the vertical plane. The formula, which was in good agreement with empirical results presented, was based on the assumption that the loss factor consisted of two parts – one part due to pure fluid and an additional factor due to the solid particles. An equation for the optimum bend radius was presented and Ayukawa stated that in general bends with a large radius of curvature were most advantageous. Furthermore, it was noted that pressure drop depended greatly on the particle motion and that the region up and downstream of the bend was affected to same extent as with pure fluid.

Toda *et al.* (1972) followed on from Ayukawa (1969), by obtaining further insight into flow mechanisms. They investigated the effect of the radius of curvature of a bend on the pressure drop across it, examining a range of velocities and concentrations for vertical and horizontal bends and analysed flow patterns in the bends using photographs. Using hydraulically smooth pipe, they found that in a horizontal bend at low flow velocities the particles were particularly affected by secondary flows, which lifted them along the inside wall. However, at higher flow rates the secondary flows were overpowered by the centrifugal force. In bends with a small radius of curvature, a stationary bed was not formed, but at larger radii the same flow state as for straight pipe was observed. In vertical bends the effect of gravity was noticeable. At low flow some dispersion by secondary forces was observed at the bend outlet, however, at higher flow the centrifugal force was dominant, forcing most particles to the outside wall.

The pressure drop across the horizontal and vertical bend was also examined. For low-density particles (1.1g/cm^3) flowing through a horizontal bend, no increase in pressure drop with concentration was observed for the range tested, whereas with higher density particles (2.5g/cm^3), an additional pressure drop was measured, that remained fairly constant as flow rate increased. For a smaller radius of curvature, larger particles showed no increase in pressure drop with concentration, whereas smaller particles, for which the drag reduction was not so great, showed an increase in pressure drop with concentration. In vertical bends the effect of particles was found to be greater because of the effect of the gravitational force. For the denser particles the pressure drop increased with increasing concentration, even for bends with the smallest curvature. Again, the additional pressure drop due to the addition of particles was constant regardless of flow rate.

Nasr-El-Din and Shook (1987) aimed to assess the effect of particle size on the concentration distribution downstream of a vertical 90-degree bend of short and long radius, using sand. For the standard elbow, they found that fine (0.18mm) particles concentrated at the inner wall and medium (0.45mm) particles at the outer wall. This was attributed to the medium particles having larger inertia and thus not succumbing to the secondary flow as easily as the fine particles. For short radius bends, the concentration distribution was symmetrical about the pipe axis, and velocity profiles were flatter than that of water. Straightening vanes were employed to eliminate the effect of secondary flow but this was unsuccessful. For long radius bends the secondary flows were weaker and the concentration distribution was asymmetrical with two minima.

Mukhtar *et al.* (1993) investigated the concentration and particle size distribution in two planes of a horizontal bend, for a multi-sized slurry at various velocities and concentrations. It was found that the bend tended to increase the homogeneity of the concentration profile, although the coarser particles exhibited a more asymmetric profile than the finer particles. The coarse particles tended to be concentrated towards the outside of the bend and the concentration profile became more uniform as the input concentration and velocity increased.

Mukhtar *et al.* (1995) performed experiments on two multi-size slurries of different densities, with a horizontal bend of radius ratio 4. They found that the bend loss co-efficient was relatively independent of solids concentration and density, and independent of velocity at a flow velocity of greater than 0.5m/s plus the deposition velocity. It was also found that, at all concentrations tested, the value of the relative pressure (pressure drop in bend / pressure drop in straight pipe) was less than that for water. It was concluded that the presence of particles inhibited secondary flow and the particles were more homogenous in the bend than in the straight pipe. They found that close to the deposition velocity the relative pressure value fell below one. At this velocity a strongly asymmetric flow was found in the straight pipe, which increased the pressure drop, while in the bend the particles remained suspended by the secondary flows.

Some authors have attempted to reduce the excess pressure loss and wear experienced in pipe bends using novel pipe design. Horii *et al.* (1991) proposed the use of an altered bend to reduce erosion and blockage in pneumatic flows. The

design consisted of a diameter that increased fivefold over the inlet section, then decreased to the inlet value over the outlet section, to produce vortices in the expansion and contraction. Using flow visualisation they found that the outlet flow from the modified bend was concentrated near the pipe axis, whereas flow out of a conventional bend is concentrated in the outer wall region. The modified bend was found to last 100 times longer than a conventional bend of the same diameter, when subject to a flow of alumina and air. It was concluded that the critical erosion angles of 30-60° were avoided due to the changes in flow induced by the bend. The air velocity in the expanded section was below the expected blockage limit but no such problems occurred.

Similarly, Mishra *et al.* (1998) designed two modified bends and tested them along with a conventional bend. The area of cross-section of the bend was increased linearly from the inlet to the middle of the bend, then reduced by the same rate to the outlet, by modifying the radius of curvature of the outer wall. Using zinc tailings, it was found that the bend with the largest central cross-section (double that of the standard bend) showed the least wear, less even than the bottom of a straight pipe. For this bend, equal rates of wear were observed across three measuring points on the outer wall. A more uniform particle distribution was measured in the modified bends, than in the standard bend and this was attributed to the interaction of secondary and centrifugal forces. Finally, it was noted that despite the increased cross-section, deposition did not take place in the bends near the deposition velocity.

Raylor (1998) applied swirl induction prior to a bend and found a reduction in the pressure drop across it. Ganeshalingam (2002) followed on from this by testing a range of bend radii and reported a pressure loss reduction of 20-40% for small radius bends and 0-20% for large radius bends, when swirl-induction was applied upstream. The pressure loss reduction was more significant at low flow rate.

2.5.2 Non-Newtonian fluids

The literature available on the subject of non-Newtonian flow through bends and fittings was limited, with searches yielding few results. Edwards *et al.* (1985) measured the frictional head loss for Newtonian and non-Newtonian fluids through a range of fittings, including 90° elbows. They found that in the laminar regime the results for both Newtonian and non-Newtonian fluids followed the same Reynolds number - resistance coefficient correlation.

Das *et al.* (1991) investigated the flow of four concentrations of sodium carboxymethyl cellulose through 45°, 90°, 135° and 180° mild steel horizontal bends. The pressure drop over the bend was found to decrease as apparent viscosity decreased and a generalised correlation was developed.

Turian *et al.* (1998) published an extensive work on the flow of non-Newtonian fluids through bends, fittings, valves and venturi meters. An extensive range of experiments was performed to determine the loss coefficients for 90° bends of four

different radii of curvature when pumping water alone and four concentrations of laterite and gypsum. The resistance co-efficient was found to decrease with increasing flow rate in the laminar flow regime. In addition, the resistance coefficients for all the bends approached constant asymptotic values, which were the same as the corresponding coefficients for water.

However, Slatter and Pienaar (1999) highlighted problems associated with applying datasets and analyses relevant to specific fluids and fittings, available in the literature, for practical design purposes. It was noted that in the case of yield-pseudoplastics the increase in head loss associated with fittings was probably due to the energy consumed in breaking down the plug as it passed through the fitting. The use of a Reynolds number, which took account of the presence of a solid plug, was proposed to establish dynamic similarity for fittings.

2.6 Flow in inclined pipes

As in the case of pipe bends, the flow of slurries through inclined pipes is of great practical importance, since long distance pipelines by necessity contain inclined pipe sections.

Worster and Denny (1955) conducted a series of test on the pressure drop over pipes inclined at a range of upward and downwards sloping angles. The excess pressure drop attributable to the solids in the inclined section was found to be

equal to the sum of the excess pressure drops in the horizontal and vertical pipes that connected the same points.

Diniz and Coiado (1999) investigated pipe inclination using upward and downward sloping sections, at angles of 5.5° , 11.0° , 22.5° , 34.0° and 45.0° . Empirical equations were developed to fit the data obtained, however, a large difference was noted between the results and the equation of Worster and Denny (1955) for the downward sloping section. The results showed that head loss in the downward sloping pipe was always lower than in horizontal pipe and head loss in horizontal pipe always lower than head loss in upward sloping pipe. However, the Worster and Denny (1955) equation makes no distinction between upward and downward flow accounting for the variation. It was also found that in the upward sloping pipe, head loss increased as sand concentration and inclination angle increased. Whereas in the downward sloping pipe head loss decreased as sand concentration and inclination angle increased.

Doron *et al.* (1997) adapted a three-layer pipeflow model (including stationary bed, moving bed and heterogeneous mixture) to account for the effect of pipe inclination and gathered data on the flow of solid-liquid mixtures in upward and downward inclinations of up to 7° . As with horizontal pipe, a higher concentration resulted in a higher pressure drop and the characteristic shape of the pressure drop curve was retained. An upward inclination resulted in an increase in pressure drop and critical velocity, whereas a downward inclination led to a decrease in pressure

drop and critical velocity. Good agreement was obtained between the pressure model and experimental data, however the model over-predicted the deposit velocity for the downward inclination.

2.7 Summary

Classification systems and basic pipeline design methods for settling slurries and non-Newtonian fluids have been briefly presented. In addition, the use of rheological models to describe homogenous flows and the application of shear thinning fluids for the transport of coarse particle was introduced.

Literature has shown that the application of swirl induction to heterogeneous flow was advantageous in terms of increasing the homogeneity of the particle distribution at lower velocity and thereby reducing power consumption and wear. The application of helically formed pipes to solid-liquid flow is a new concept, documented predominantly by Raylor (1998) and Ganeshalingam (2002). However, no research investigating the application of swirl induction to non-Newtonian and homogenous particle slurries was identified.

Several sources in the literature have described the rate of decay of induced swirl in single-phase systems, using an exponential decay formula. Ganeshalingam (2002) was first to consider the decay of a two-phase particle system, however, these results relate to smooth pipe flow. Since Murakami *et al.* (1976) found that rate of decay of swirl was related to the pipe friction factor, the decay of swirl

experienced in rough pipe may vary considerably from that in smooth pipe. In addition, no experimental data on the tangential velocity generated by the swirl pipe has been obtained.

A number of studies of solid-liquid flow through bends have found that gravity has a significant effect on the flow conditions in a bend in the vertical plane, coarse particles travel at the outer wall of the bend and the homogeneity of particles within the bend was increased. In addition, the use of novel bend designs and changing the upstream flow conditions has resulted in improvements in the pressure drop and wear experienced over bends. Limited literature was available on the flow of non-Newtonian fluids through finite bends. Literature relating to inclined pipe configurations has also been briefly reviewed.

Chapter 3 SELECTION OF TEST MATERIALS

The aim of the study documented in the following chapter was to identify a range of materials that would be suitable for use in the pipe flow tests outlined in Chapter 1. Carboxymethyl cellulose was found to be a suitable non-Newtonian fluid. A study of the behaviour of this fluid in terms of a number of important factors was then conducted. Following this, the procedure used to specify the type, size and concentration of solids to be pumped was presented.

3.1 Identification of potential non-Newtonian fluids

The theory of rheology has been outlined in the Chapter 2. Here this knowledge is applied to highlight the desirable properties of a fluid for the pipe flow investigation.

The majority of non-Newtonian fluids used in pipe flow tests are cellulose-based polymers (for example, Sa Pereira and Pinho, 1994; Wang and Chukwu, 1996; Illicali and Engez, 1996). They are quite expensive and difficult and time consuming to dissolve on a large scale. To minimise these problems a fluid was sought that would display constant behaviour over several runs on consecutive days and thus reduce the number of batches of solution required. This meant that a time-dependent fluid could not be used because its apparent viscosity would decrease as the test progressed. Similarly, highly viscoelastic fluids, which display partial recovery after deformation, were avoided where possible.

Pure viscous flow and perfect elastic deformation are idealisations that are only realised under some conditions. Mashelkar and Decarajan (1976) described the difficulty in determining whether a fluid is purely viscous or viscoelastic and explain that under certain conditions water can show elastic effects. Furthermore, Tam and Tiu (1989) state:

'It is generally accepted that most polymer solutions, no matter how dilute exhibit not only shear-dependent viscosity but also elastic characteristics.'

Hence to find a time-independent, purely viscous material was perhaps an impossible task. The fact that the behaviour of a material depends so strongly on the context of the application has influenced the approach taken throughout this investigation. A comprehensive characterisation of the materials was not attempted, but an investigation to determine appropriate materials and knowledge required for this application was conducted.

Heywood *et al.* (1998) give little attention to shear thickening slurries and claimed that “*by far the most common industrial slurries*” were shear thinning. Given this widespread use in industry and the application to particle transport (Section 2.3), it was felt that a time-independent shear thinning fluid with minimal viscoelasticity was the best option for this investigation. The behaviour of such fluids is further complicated by the following factors:

- The apparent viscosity of some fluids tends to change with time when in storage under no or very low shear (such as gravity). Rosenberg, (1997)

found that the apparent viscosity of carboxymethyl cellulose changed significantly with storage.

- The temperature dependence of apparent viscosity and the tendency for the temperature of a re-circulating fluid to increase with time meant that the behaviour of the fluid would change over the course of a run.
- All water-soluble cellulose derivatives are susceptible to microbiological degradation, with the magnitude of degradation depending on several factors, including: contaminants present, temperature, pH, oxygen available and concentration (Stelzer and Klug, 1980).

Each of these factors, if uncontrolled would compromise the reuse of the fluid, so were also considered during the investigation.

The apparent viscosity range of a cellulose-based polymer is dictated by the concentration in solution. Therefore a target apparent viscosity range was needed to allow a suitable concentration to be determined. Pinho and Whitelaw (1990) used a solution with an apparent viscosity range of 30 - 180mPas (over 1000 - 0s⁻¹) to investigate the flow of shear thinning fluids in pipes, so this was accepted as a suitable target. In an ideal situation a range of concentrations would be tested in the pipe flow loop, however this was beyond the scope of this work.

Initially, literature was examined to discover fluids commonly used in pipe flow tests. Laponite (L), sodium carboxymethyl cellulose (CMC) and xanthan gum (XG), often used in flow studies (for example Escudier and Presti, 1996; Escudier *et al.*, 1999; Pinho and Whitelaw, 1990) were identified as possibilities. In addition, polyvinylpyrrolidone (PVP), methylcellulose / hydroxypropylmethylcellulose (MC / HPMC), hydroxypropylcellulose (HPC), locust bean gum, (LBG), guar gum (GG) and carbopol (C) were suggested by colleagues (Jones, 2000) for investigation. All the fluids have industrial uses, for example, in paints, cosmetics, ceramics, foods and oil drilling fluids and are compared to the application requirements and considerations in Table 3.1.

Table 3.1: Comparison of information in literature on fluid characteristics

Fluid	Model / thixotropy	Other factors
PVP	<i>“not especially thixotropic, rapid relaxation times”</i> (Blecher <i>et al.</i> , 1980).	Dissolves in cold water Low temperature sensitivity (Blecher <i>et al.</i> , 1980).
MC, HPMC	Pseudoplastic, non-thixotropic at 20°C and <5% w/w (Greminger and Krumel, 1980).	Dissolves in cold water, smooth clear, temperature dependent (Greminger and Krumel, 1980).
HPC	<i>“little or no... thixotropy... pseudoplastic at high shear rates... good resistance to shear degradation”</i> (Butler and Klug, 1980).	Temperature dependent (Butler and Klug, 1980).
LBG	Pseudoplastic, no yield, <i>“viscosity.. at any given rate of shear is independent of time and prior shear testing..provided shear rates not high enough for degradation.. eg in pumps”</i> (Seaman, 1980) .	Temperature dependent (Seaman, 1980).

L	Herschel-Buckley in laminar regime ($Re < 1500$) (Escudier and Presti, 1996) Thixotropic reconstruction (Rockwood Specialties, 2001)	Biocide used Viscosity increases with time – 30% over 7 days (Escudier and Presti, 1996). Cannot support microbial growth, temperature independent (Rockwood Specialties, 2001).
CMC	Ostwald-de-Waele 1-3% w/w time-independent, 4, 5% w/w thixotropic (Ghannam and Esmail, 1997). Some shear degradation (thixotropy) noted (Pinho and Whitelaw, 1990). Most with degree of substitution < 1 are thiotropic (Stelzer and Klug, 1980).	Mixed 4 hrs, settled 8hrs to ensure complete hydration, biocide used (Pinho and Whitelaw, 1990). Degradation with time significant (Rosenberg, 1997). Temperature dependent (Geldard, 2000).
XG	Pseudoplastic with yield (RT Vanderbilt Company, Inc, 2000).	Biocide needed (Cotrell <i>et al.</i> , 1980, Sutherland, 1984) Degradation with time negligible, Stable over broad temperature range (RT Vanderbilt Company, Inc, 2000)
C	Herschel-Buckley model (Recknagle and Shekarriz, 1998) Thixotropic - viscosity degradation with shear (Park and Irvine, 1997).	Temperature dependent (Park and Irvine, 1997)
GG	Pseudoplastic behaviour in solution. Excellent resistance to shear degradation (Maier <i>et al.</i> , 1993).	Pronounced temperature dependency (Maier <i>et al.</i> , 1993)

Material Key: PVP = polyvinylpyrrolidone, MC = methylcellulose, HPMC = hydroxypropylmethylcellulose, HPC = hydroxypropylcellulose, LBG = locust bean gum, L = Laponite, CMC = sodium carboxymethylcellulose, XG = Xanthan gum, C = Carbopol, GG = Guar gum

Attention initially focused on Laponite due to its reported temperature independence and resistance to biological degradation. However, the thixotropic behaviour and increase in apparent viscosity with time also reported led to it being disregarded. Carbopol was also eliminated based on its temperature dependence

and thixotropy. Locust bean gum was found to have a suitable rheology at low shear rate, but for this application would behave thixotropically so was not suitable.

For the remaining fluids shown in Table 3.1, key information was lacking, such as the time dependence / independence of xanthan gum. Similarly carboxymethyl cellulose (CMC), guar gum, polyvinylpyrrolidone, hydroxypropylmethylcellulose / methylcellulose and hydroxypropylcellulose appear to have suitable rheologies but no reference was found to age phenomena. Given this lack of information and the variation in behaviour due to material grade, concentration and testing procedures, a test series was undertaken to examine which of the six fluids not previously disregarded would be most suitable for use in the pipe flow loop.

3.2 Methodology

The selection and characterisation tests took place over an extended time period and as knowledge about the application grew, the test procedure evolved. The most significant changes were in the CMC supply that was used. These changes, listed in Table 3.2, were made based on cost considerations.

Table 3.2: Details of CMC used in the preliminary tests

Supplier, Product number	Details	Estimated conc. to achieve target behaviour	Estimated cost per batch
Sigma, C4888	400-800mPas (2% w/w in water) – D.S. = 0.7	2% w/w	£1490
Aldrich, 323063	3000-6000mPas (1% w/w in water) - D.S. = 0.83	0.07% w/w	£36
Univar, Walocel	900-1500mPas (2% w/w in water) - D.S. = 0.82-0.95	1% w/w	£44

The CMC used in the fluid selection tests (C4888), was available in small quantities at the time of the tests and at ‘medium viscosity’ it avoided weighing tiny masses. However, estimations later revealed the prohibitive cost of producing a batch of this product for the pipe flow tests. A higher viscosity product (323063) was identified as a possible alternative. With a higher degree of substitution, this product was expected to be less thixotropic than the initial CMC. However, when tested, it was found to produce a solution less viscous than the quoted value and more shear thinning than C4888 (Appendix A.1-A.2). This significantly increased the required concentration and the cost per batch. Finally, a bulk supply of CMC was found and tests revealed that it would meet the requirements of the pipe flow tests at a reasonable cost. An attempt was made to minimise the effect of these changes by comparing the fluids and checking that each fluid met the shear thinning and thixotropy requirements.

Standard methodology used for all the tests is described here with more specific details of the individual tests presented in Appendix A.3.

3.2.1 Dissolution

Dissolution methods were carefully selected, by referring to literature, in an attempt to ensure the concentrations of the fluids were reproducible. Several papers specific to xanthan gum, hydroxypropylmethylcellulose and carboxymethyl cellulose describe the use of a mixer to create a vortex to which the powder was slowly added (Appendix A.4). Since this was considered a feasible method of producing the fluid on a large scale, it was applied to the desktop experiments.

Escudier *et al.* (2001) found that the rheology of CMC is, in practical terms, insensitive to the use of tap water as a solvent. Therefore tap water was accepted as a solvent and appropriate masses of tap water and solute weighted. The solute was slowly added to the water in a continuous stream of powder whilst mixing with a Janke and Kunkel high-speed mixer (Appendix A.10). The entire speed range of the mixer (8,000-24,000 rpm) was used in making the solutions, increasing the rate as the apparent viscosity increased. In general, this was an effective means of dispersing the powders and avoiding lump formation.

To dissolve CMC, Pinho and Whitelaw (1990) allowed 8 hours for it to fully hydrate and noted an increase in apparent viscosity over the first 24 hours. Therefore, it was decided that all the samples would be made on Day 1 and left overnight to hydrate before the rheology tests (Day 2).

3.2.2 Rheology

The rheology of the solutions was measured using a Bohlin VOR Rheometer, which is a rotational controlled-rate instrument with a range of geometries (Appendix A.5-A.9). The sample cell consisted of a concentric cup and bob. The cup was rotated and the apparent viscosity of the fluid caused a retarding force on the bob. The torque on the bob was measured and together with the area of the bob, used by a computer programme to calculate the shear stress. The shear rate was also calculated from the angular velocity and dimensions of the cup by the programme. Chhabra and Richardson (1999) described the main errors associated with such measurement systems to be end effects, wall slip, inertia, secondary flows, viscous heating effects and eccentricities due to misalignment. However, a cooling circuit was added to the rheometer, which held the cup in a temperature bath at 25°C to reduce viscous heating effects. A disadvantage of concentric cylinder systems, highlighted by Bain and Bonnington (1970) was that they do not reflect the mode of shear in pipes and therefore rely on models more than capillary rheometers.

Cup and bobs of 14 and 25mm diameter (Appendix A.8-A.9) were used and samples transferred to the cup using a pipette. To obtain reliable readings the geometry and torsion elements were carefully selected to keep the torque range within 1.8 and 80%. The shear rate, shear stress, apparent viscosity, temperature and percentage torque at the time of measurement were recorded. The instrument was set to perform an up/down sweep, measuring at 1.16, 2.91, 7.31, 18.50, 46.00,

116.00, 291.00, 461.00, 731.00 and 1160.00s⁻¹ to give an up curve and 731.00s⁻¹ down in the same steps for the down curve. A thermal equilibrium time of 1 minute before measurements and an autozero time of 5s were employed. For each shear rate there was a delay before measurement of 5s and the recorded value was integrated over 15s. The gap was set to 0.18mm.

The up and down curve were measured to allow the thixotropy to be calculated, from the hysteresis area formed. Ghannam and Esmail (1997) used a shear rate range of 0.15 to 749s⁻¹ to test the thixotropy of CMC solutions. They employed several cycles (of 200, 100 and 60s) to ensure that the gel structure was destroyed, but established that one cycle was sufficient to achieve the total hysteresis area at concentrations similar to the target concentration of this work. Based on this evidence it was assumed that the test programme described above (a range of 1.16 to 1160s⁻¹ over 200s) destroyed the gel structure.

3.3 Fluid selection

The aim of these tests was to select a fluid for use in the pipe flow tests from among the six possibilities. The results are summarised in Table 3.3 and shown graphically in Appendix A.11. The tests performed are not in the least exhaustive and have many limitations and uncertainties associated with them. For example, the method of dissolution employed may not be viable for all the samples and may have affected the rheology. A more suitable dissolution method may eliminate the frothing effect observed with some samples. However, this method was employed

to represent the likely means of dissolving the solution for use in the pipe flow loop and if frothing was a problem in this case, it was also likely to be a problem in pumping, when the entrapment of air would affect the pressure drop. Therefore, the solutions that exhibited frothing (HPMC, HPC, PVP) can be eliminated.

Table 3.3: Comments and observations

Fluid Conc. / % w/w	Dissolution (mean mixing time/ minutes)	Thixotropy	Shear thinning	Apparent viscosity		
				Range /mPas	Comments at:	
					High shear	Low shear
3% HPC	Bubbles a lot when mixing (22)	Negligible	Minimal	4 – 14	Too low	
10% PVP	Fine bubbles under high shear – looks milky (31)	Negligible	Minimal	129 – 208	A little high	–
0.75% XG	Good fairly rapid (18)	Negligible	Highly	20 – 6260	On target	Very high
1.25% GG	Satisfactory (24)	Negligible	Highly	89 – 14800	A little high	Very high
2.5% CMC	Good fairly rapid (15)	Negligible	Evident	125 – 527	A little high	–
1.25% HPMC	Bubbles a lot when mixing (14)	Negligible	Evident	81 – 354	On target	–

Table 3.3 shows that xanthan gum (XG), guar gum (GG) and hydroxypropylcellulose (HPC) can be eliminated as a choice for the homogenous fluid, because they do not fit the shear thinning / apparent viscosity requirements (Section 3.1). While the use of a different grade of HPC may have produced a concentration closer to the target apparent viscosity, the frothing observed during dissolution was reason enough to disregard it. Similarly polyvinylpyrrolidone (PVP) and hydroxypropylmethylcellulose (HPMC) exhibited frothing, which left CMC as the best choice. Literature and previous experience with CMC indicated problems with temperature sensitivity and degradation with age. Bubbles also

occurred in CMC but to a lesser extent than in HPMC, PVP and HPC. Therefore, further tests were performed to quantify the temperature sensitivity and investigate the viscoelastic effects and degradation with age.

3.4 Fluid characterisation

To characterise the behaviour of relevant properties of the selected fluid, four test series were undertaken. A matrix outlining the tests performed, along with further details of the method is given in Appendix A.3, this is summarised in Table 3.4.

Table 3.4: Fluid characterisation tests performed

Test series	Variables investigated	CMC type used
1	Thixotropy, biocide type, storage, viscosity changes with age, effect of bacteria, effect of evaporation.	Sigma 3,23063
2	As above plus effect of temperature	Sigma 3,23063
3	CMC type, effect of salt, viscoelasticity, change in rheology over days 1-2.	Sigma 3,23063, Walocel
4	Effect of biocide concentration, repeatability of sample preparation.	Walocel

Test series 1 and 2 analyse the same variables but were performed in two series to allow enough time for the daily measurements to be taken within each working day. Three samples were tested in series 1, namely a control sample (no biocide) and samples containing Busan and Proxel biocides, with a Nalco biocide and a control sample tested in series 2.

3.4.1 Thixotropy

Results from series 1 and 2 were used to analyse the thixotropy of the CMC samples as follows. Power law equations, widely used to model pseudoplastic fluids, were fitted to the results and good fits with high r^2 values were obtained. As an alternative the Herschel-Buckley model was considered, however this consistently gave negative yield stresses so was dismissed.

The up curve and down curve were plotted separately to obtain two power law equations. The curves were then integrated, between the upper and lower shear rates that were within the torque range, usually $2.91 - 1160\text{s}^{-1}$, to find the thixotropy.



Figure 3.1: A graph to show the variation in thixotropy with solution age.

Figure 3.1 shows that all the majority of hysteresis areas were negative. Negative thixotropy values occur when the area under the down curve is larger than the area

under the up curve. Ghannam and Esmail (1997) also found negative thixotropy values (rheopectic) when testing CMC, they conclude

'This indicated that the sample was drying up during the test, and, consequently, the viscosity was increasing over the down curve.'

Concerning the numerical value of the results, Ghannam and Esmail (1997) considered that 8 – 12kPa/s constituted thixotropic behaviour. The majority of the present results lie between –0.5 and –1.5kPa/s, so were considered time-independent because of their low numerical value. The last four results for the Nalco samples were not within this band and although not fully rheopectic, should be viewed with caution. It was concluded that time-dependence was negligible over all 15 days for all except the Nalco samples, for which it was negligible for the first 11 days.

The calculations described above were also performed on the series 3 test results to check the thixotropy of Walocel. The results of the calculation are displayed in Table 3.5. Applying the reasoning above, the 0.8% and 1.0% w/w concentrations can be considered time-independent. As series 3 tests were only performed on one day, it was assumed that the pattern of thixotropy with age is similar to the series 2 results and that the sample can be used for up to 11 days.

Table 3.5: Thixotropy of the series 3 tests (Walocel)

Sample	0.8%t	0.8%d	1.0%t	1.5%t	1.7%t	1.7%d	2.0%t
Thixotropy /kPas	-0.78	-1.66	-1.23	-3.48	-3.75	-4.41	-33.20

Note: t indicates solutions prepared with tap water
d indicates solutions prepared with de-ionised water

3.4.2 Storage

Another aspect of series 1 and 2 experiments was to assess the possibility of leaving the CMC solution in the pipe loop overnight, by sealing a volume of solution in a 0.25m steel pipe (of the specification to be used on the pipe flow loop) by bolting a steel plate to each end of the pipe. The rheology of the samples was measured on Day 2, before sealing the sample in the pipes until Day 15, when the rheology was measured again. The pipes were inverted 20 times each day to agitate the fluid. During series 1, a Busan and a control sample were sealed in a pipe, whereas during series 2, a Nalco and a control sample were stored in a pipe.

It can be seen from Figure 3.2 that the rheology of all the solutions, except the one containing Nalco, changed appreciably whilst stored in the pipe. The biological tests revealed no bacteria present in the Busan or Nalco samples, but a bacterial presence was detected in the control sample for both series, before and after sealing in the pipe (Appendix A.12-A.15). Therefore it cannot be concluded that bacteria caused the degradation observed because the rheology of the Busan sample changed but no bacteria were detected. A visual inspection of the pipes on day 15 showed no biological growths or other adverse effects. This leads to the

conclusion that Nalco sample may be left stationary in the pipe flow loop overnight.

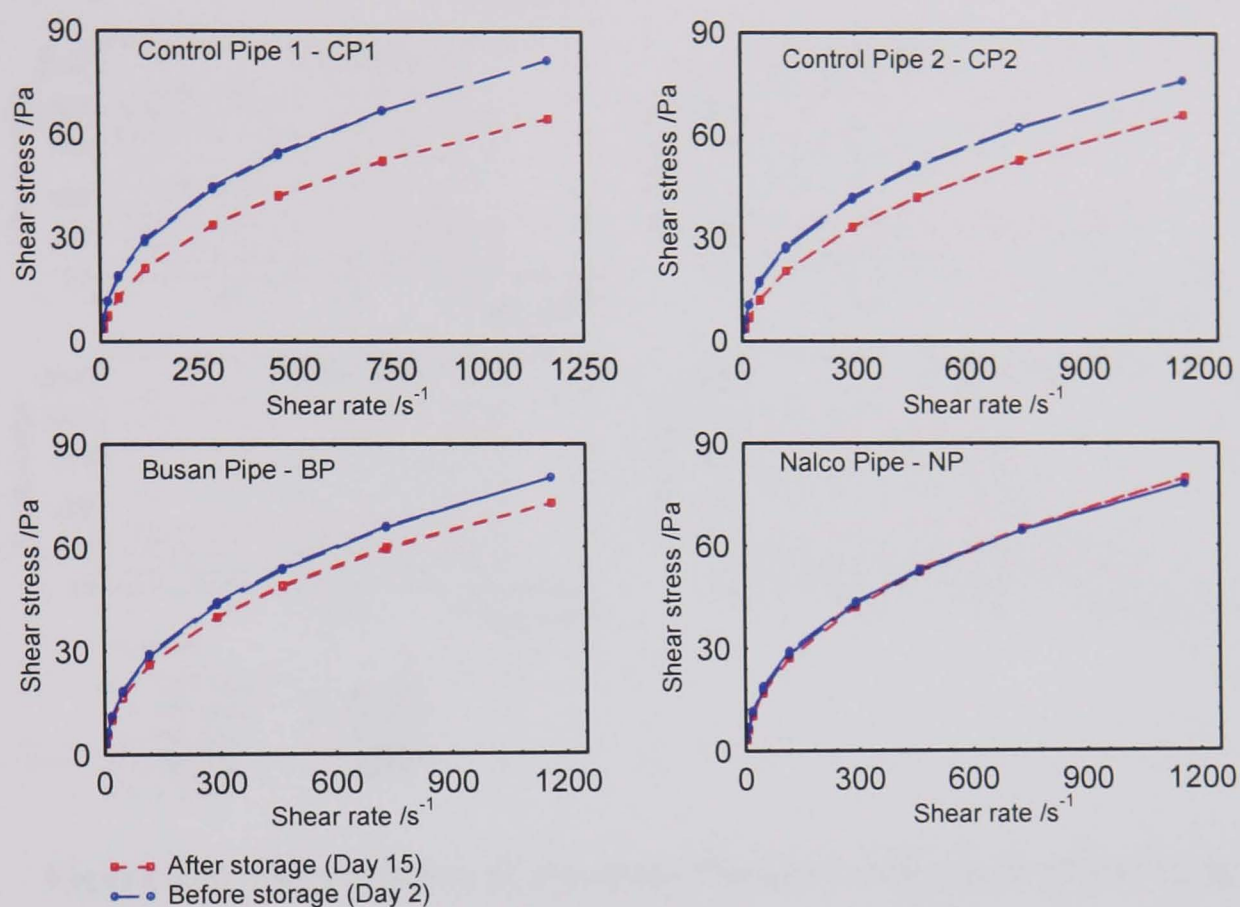


Figure 3.2: Rheology results for the samples stored in sealed pipe lengths

3.4.3 Changes in apparent viscosity with age

The series 1 and 2 results were plotted as shown in Figure 3.3 to highlight any degradation with age. It was important to avoid fluids that displayed this degradation to allow the fluid to be reused. A first glance suggested that there was little variation with age for the Busan, Proxel, sealed Nalco and series 1 control samples. The apparent viscosity of the open Nalco and series 2 control samples tended to increase gradually and decrease rapidly with age respectively.

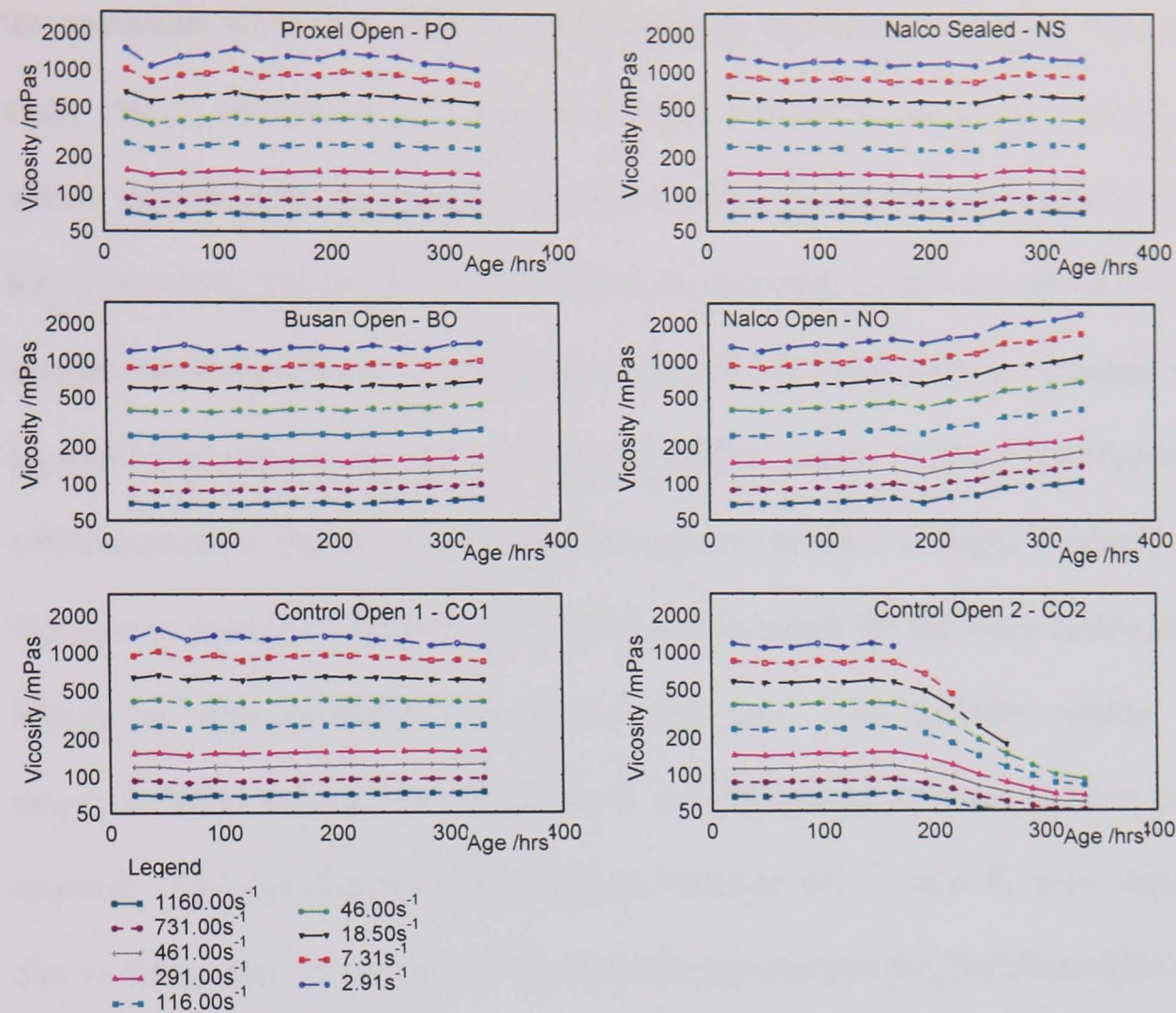


Figure 3.3: The variation of apparent viscosity with age at different shear rates.

LHS: Series 1; RHS: Series 2. Note: Each point (for one particular time at one particular rate), except for 1160s⁻¹, is the mean of three up curves and three down curves because thixotropy is assumed to be negligible. Measurements for 1160s⁻¹ were only taken three times as part of the up curve, so these points are the mean of three.

The graphs in Figure 3.3 usefully highlight the trends in the open Nalco and series 2 control samples, however it is difficult to assess the significance of the variation in the remaining samples from the graphs alone. For this reason, a 2-way analysis of variance (ANOVA) was performed on the results, using a computer package called Statistica. The independent variables were day number and sample, and the dependent variable was viscosity. Nine analyses were performed, one for each shear rate and appropriate steps were taken to ensure the assumptions underlying

the technique were met. The ANOVA showed significant variation for all nine shear rates. So post hoc comparisons were performed using the Scheffe test, which identified the homogenous groups shown in Appendix A.16. The Scheffe test showed that the trends observed from for the open Nalco and series 2 control samples were significant, as expected. Figure 3.3 indicates that the decrease in the apparent viscosity of the series 2 control sample begins at about 160 hours old, which equates to day 8. The Scheffe test shows the trend to begin on day 9. The increase in apparent viscosity observed from the graph for the open Nalco sample begins at approximately 216 hours, day 10. The Scheffe results show unquestionable homogeneity until day 6, and significant differences from day 11 onward. The significance of differences between days 7 and 10 were uncertain due to differences in variances. The Scheffe test showed that the viscosities of the Proxel, series 1 control and sealed Nalco samples were statistically constant over 2 weeks and these samples were statistically equal to each other. The same is true for the Busan sample until day 14 when some shear rates give significant or questionable results. The Proxel sample performs best with no significant or questionable results. Therefore, the ANOVA confirmed results observed from Figure 3.3.

3.4.4 Effect of bacteria

The effect of biological degradation on the fluid was investigated by monitoring the level of bacteria in the solutions throughout test series 1 and 2. A Sanicheck kit manufactured by Biosan laboratories was used to detect the presence of

bacteria in the solutions. The kit consists of indicator strips that were dipped into the solution for 10 seconds, sealed in a plastic envelope, then incubated for approximately 24 hours at 30°C and photographed. Unfortunately the supply of Sanicheck kits was limited and further kits could not be obtained for series 2, so the presence of bacteria was tested using agar plates. 1ml of the sample was extracted using a sterile pipette and spread on to the plate. The plates were incubated for 48 hours at 30°C.

The results of the series 1 biological tests are shown in Appendix A.12-A.14. It is seen that bacteria were present in the series 1 control sample from the outset, while the results for Proxel showed no indication of bacteria presence at any point in the test. The results for Busan indicate that bacteria appeared on the thirteenth day. The series 2 control sample showed a growth that covered the majority of the plate area on all days except day 12 when no growth was observed (Appendix A.15). This result is peculiar and no reason for it has been identified, except a possible mistake in the preparation of the plate. The samples that contained biocide showed much less growth, with no growth on some days and a small amount of growth on others. However, the days when growth was observed were interspersed with days of no growth and no overall pattern of increasing growth was observed.

Conflicting conclusions about the affect of bacteria on CMC may be drawn from these results. The biological test indicated that both control samples contained

bacteria, yet the apparent viscosity results for the series 1 sample show little variation while the apparent viscosity of the series 2 sample decreased rapidly after 160 hours (Section 3.4.3). Why the two samples behaved differently was unclear.

Possible reasons are:

- The bacteria colonies established in the solutions were of different types, leading to different viscosity responses.
- The salt concentration of the tap water used to prepare the solutions changed significantly between the two test series.

However, as two different biological test methods were used it is hard to compare the two series. The same method used throughout would have been a more reliable indicator. Therefore, due to conflicting results and different methods, the effect of bacteria on the apparent viscosity of a solution was inconclusive from these results, but the series 2 control sample and the two control samples that were sealed in a pipe indicate that there may be an effect.

3.4.5 Effect of evaporation

Rosenberg (1997) suggests that evaporation will cause an increase in concentration and hence apparent viscosity, so from day 4 of the series 1 tests and throughout the series 2 tests, the weight of each sample was recorded before and after the daily viscosity test to allow the overnight weight loss to be calculated. In test series 2 the apparent viscosity of the open Nalco sample increased with age while the

sealed Nalco sample remained relatively constant in comparison (Figure 3.3), perhaps indicating that evaporation was acting to concentrate the CMC. However in test series 1 all the solutions were open and none show the trend of increasing apparent viscosity seen in the open Nalco sample.

For the first 3 days of the series 1 tests, the air temperature of the storage area was recorded with a mercury thermometer before and after rheological testing. From the 5th day onward the temperature was recorded every half hour by a temperature sensor. A temperature sensor was also placed close to the tank on the pipe loop for the same period, so the difference in ambient conditions between the labs could be observed. However, no obvious correlation can be seen between the temperature and the overnight weight loss (Appendix A.17). When no correlation was found, an attempt was made to investigate the influence of humidity on evaporation, however, only records of the outdoor humidity were available and these showed no correlation to the weight loss (Appendix A.18).

The open Nalco sample had the second highest percentage weight loss (Table 3.6), but this was only 0.28% higher than the series 1 control sample, which showed no noticeable increase in apparent viscosity. As the evaporation in the test was minimal little can be read into these results. It was unclear if the increase in apparent viscosity was due to evaporation or not.

Table 3.6: Ranked mean percentage overnight weight losses of samples over 15 days.

Sample	Mean percentage weight loss	Standard deviation
Series 2 Control	1.36	0.27
Nalco Open	1.32	0.19
Series 1 Control	1.04	0.21
Busan Open	0.99	0.21
Proxel Open	0.76	0.13
Nalco Sealed	0.00	0.01

3.4.6 Temperature

In series 2, tests were performed to assess the temperature dependence of CMC. On Days 2, 8 and 15 rheological measurements for the control and Nalco open samples were performed over a range of temperatures. Appendix A.19 and A.20 show the results of these experiments. Contradicting the decrease in apparent viscosity with temperature expected (Geldard, 2000), the Day 2 and Day 8 results gave a low apparent viscosity at 25°C. It was hypothesised that this occurred because the 25°C sample was measured out of sequence, therefore the test procedure was changed for Day 15 as described in Appendix A.3. This resulted in a decrease in apparent viscosity with temperature as expected. However, the Day 15 results may have been distorted because the control sample had a much lower apparent viscosity and the Nalco sample at a slightly higher apparent viscosity than intended (Figure 3.3). Due to this aging effect, the magnitude of the temperature change cannot be reliably assessed. Unfortunately, the change in methodology also makes a comparison of the temperature response with age impossible.

Appendix A.23 shows a very large negative thixotropy for the 15 and 20°C Nalco results, thought to be due to a discontinuity in measurement. The increase in apparent viscosity with age and low temperature increased the torque out of the measurement range at high shear rate. Therefore readings were taken from 1.16s^{-1} – 731s^{-1} introducing a measurement gap. No clear pattern of changing thixotropy with age is observed.

3.4.7 Batch comparison

The results from series 2 and 3 are collated and compared in this section to investigate how closely the Walocel behaviour resembled the behaviour of the Sigma 3,23063 CMC. Each sample was prepared using tap water from the pipe loop laboratory and sealed overnight, before the rheology was measured on Day 2.

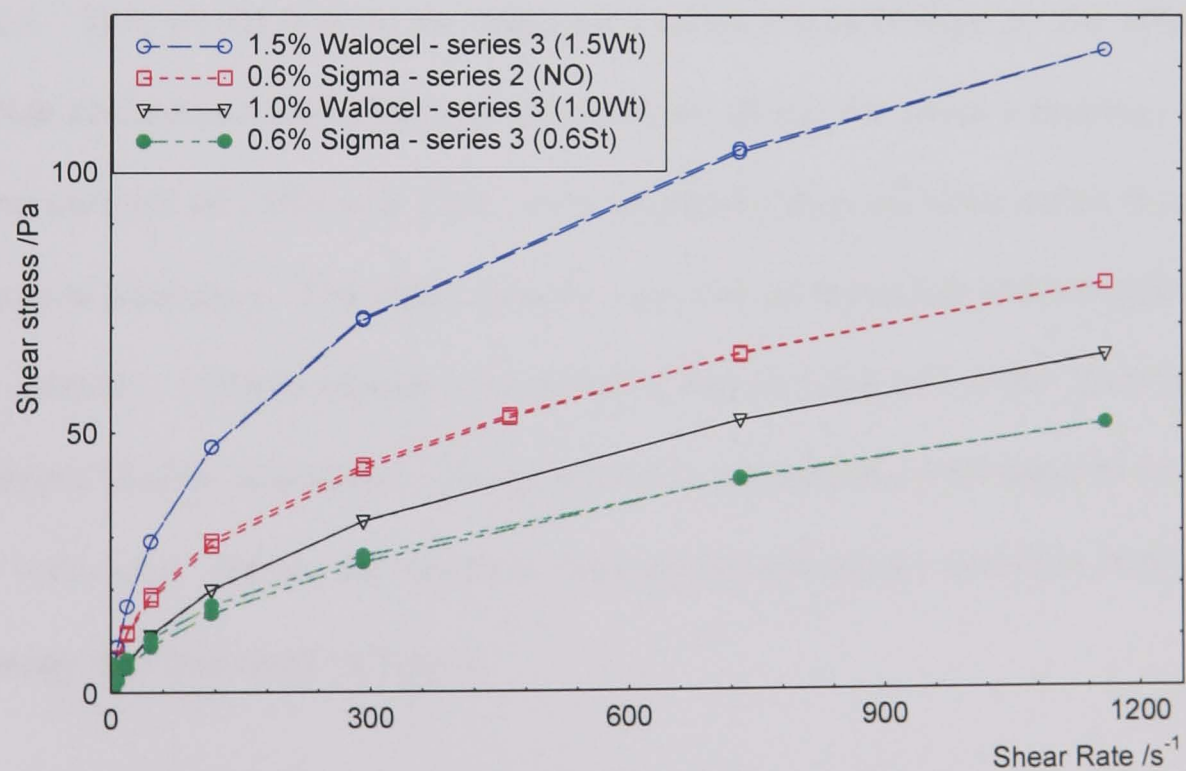


Figure 3.4: Comparison of CMC types.

Figure 3.4 shows that to attain similar fluid behaviour to that of the Sigma 3,23063 CMC (series 2) a concentration of Walocel of between 1.0 and 1.5% w/w must be used. Figure 3.4 also enables the comparison of two batches of Sigma CMC, performed with a time gap of 6 months between them. The large difference in the results may be due to different salt concentrations in the tap water used to prepare the solutions, degradation of the CMC powder or an undetected gross error. Despite the reduction in apparent viscosity a concentration of 1% w/w Walocel chosen for use in the pipe flow experiments.

3.4.8 Effect of biocide concentration

The possibility that the presence of bacteria could be detected part way through a series of pipe flow tests was considered. In this case, as a precautionary measure, to mitigate against possible degradation, an additional quantity of biocide could be added. This would lead to an unknown biocide concentration, so the effect of biocide concentration on rheology was assessed during the series 4 rheology tests. Three samples of 1.0% w/w CMC were prepared using tap water taken from the pipe flow laboratory. The repeat samples were mixed separately and not split from one solution. 100ppm biocide was added to two samples and to the final sample 1000ppm biocide was added. The process was repeated at concentrations of 1.4% and 1.8% w/w. Again, the solutions were sealed and stored overnight before the rheology was measured on Day 2.

The results of these tests, shown in Figure 3.5, indicate that a difference in biocide concentration by a factor of 10 has little effect on the rheology of the solution. Figure 3.5 also indicates that two solutions individually dissolved under the same conditions give similar results. This implies that the difference in behaviour observed between the 0.6% w/w Sigma CMC results in Section 3.4.7 were not due to large random errors in the dissolution.

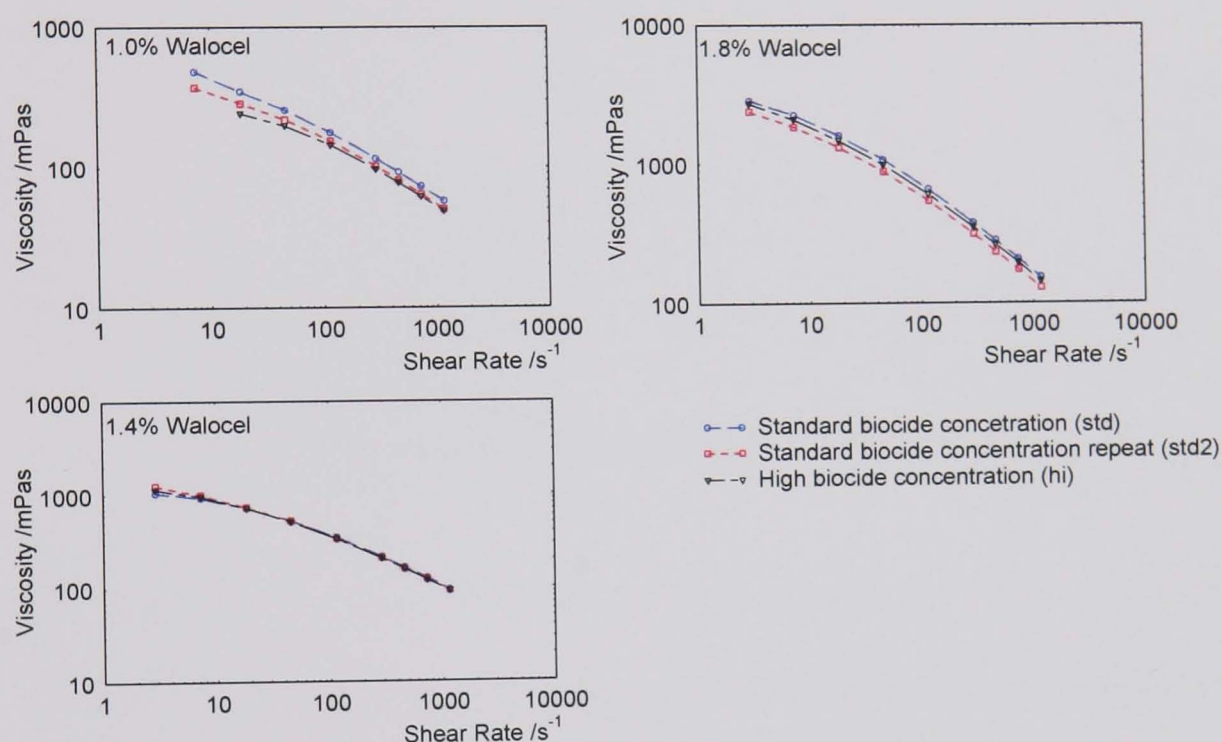


Figure 3.5: Effect of biocide concentration on rheology

3.4.9 Effect of salt concentration

The results of Section 3.4.4 highlighted the possibility of the solvent salt concentration affecting the rheology of the CMC. Therefore, during series 3, a test was conducted to assess the assertion of Escudier *et al.* (2001) that the rheology of CMC was insensitive to the use of tap water as a solvent. CMC samples made with tap water were compared to samples made with de-ionised water at three

concentrations. The tap water was taken from the pipe loop laboratory and de-ionised water from the Reverse Osmosis Plant (Section 5.2). The solutions were stored overnight in sealed glassware at room temperature, and the rheology measured on Day 2. This test provided a simple way to examine the effect of salt concentration, by utilising the relatively high salt concentration of tap water and the negligible salt concentration of de-ionised water. The results are presented as rheograms in Figure 3.6.

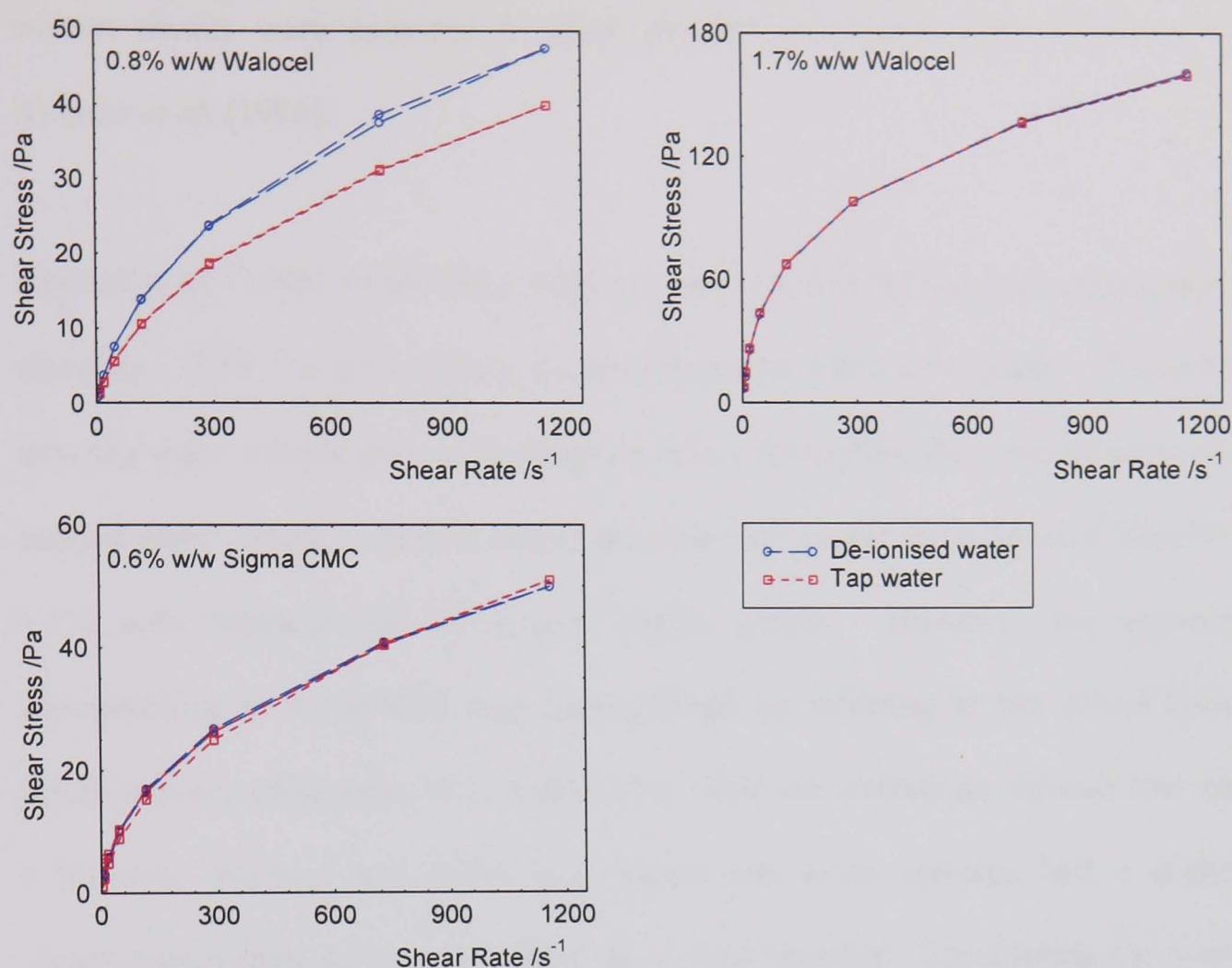


Figure 3.6: Effect of salt concentration

Little difference was observed between the 0.6% w/w Sigma CMC samples, with the tap water curve very slightly lower. At a concentration of 1.7% w/w the Walocel curves were almost identical, but at 0.8% w/w a large difference was seen between the solutions prepared with tap water and de-ionised water.

Kulicke *et al.* (1996) investigated the effect of salt concentration on CMC using de-ionised water and 0.01 and 1.0mol/l sodium chloride solutions as solvents, which equates to a sodium concentration of 23 and 2300mg/l. Severn Trent Water (2004) estimated the concentration of sodium in the water supplied to the laboratory to be 25mg/l. Although the tap water also contained further salts, the

current results were expected to show smaller differences those observed by Kulicke *et al.* (1996).

Kulicke *et al.* (1996) found that a high salt concentration led to a reduced apparent viscosity. This can immediately be seen from the 0.8% w/w graph. The 0.8% w/w tap water sample gave a significantly lower curve than the corresponding de-ionised water sample. At first glance this does not appear to be the case from the 1.7% w/w Walocel and 0.6% w/w Sigma graphs. However, the apparent inconsistency in the results may be explained by referring to the actual CMC concentrations (Appendix A.3, Table 2A). The concentrations showed that the 1.7% w/w Walocel and 0.6% w/w Sigma tap water samples had a higher concentration than the corresponding de-ionised samples. Considering the small differences expected, it is suggested that this could counter the reduction in apparent viscosity due to the presence of salt. In addition, Kulicke *et al.* (1996) found that the effect of salt was less marked at higher concentrations. Therefore, the effect of salt on the 1.7% w/w sample would be less than on the 0.8% w/w sample and the concentration difference would be more likely to align the curves. In a similar way, the CMC concentration of the 0.8% w/w de-ionised water solution was greater than the corresponding tap water solution, so this may have acted to increase the separation of the curves, magnifying the effect of the salt.

3.4.10 Change in rheology over Days 1-2

Geldard (2000) found the apparent viscosity of CMC to increase over the first 24 hours and attributed this result to hydration of the CMC. This information was integrated into the methodology of the current tests and checked during series 3, by measuring the rheology of three CMC concentrations (Walocel) made with tap water, which were sealed overnight.

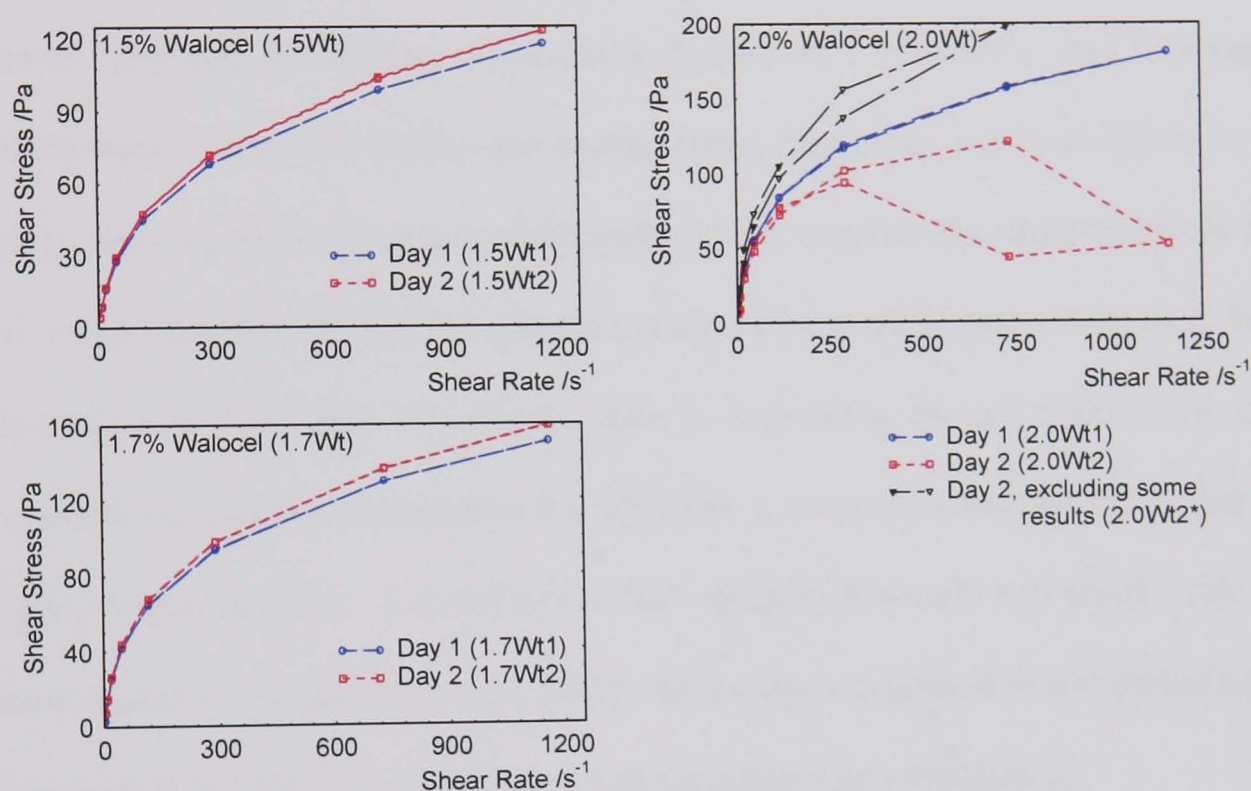


Figure 3.7: Comparison of the behaviour of Walocel solutions on the day of making (Day 1) and the next day (Day 2).

The 1.5 and 1.7% w/w tests showed a steeper rheogram on Day 2 than on Day 1, confirming previous results (Geldard, 2000). The results from the 2.0% w/w test were quite different to the other results. Each set of data was presented as the mean of three trials. The data from one of the 2.0% w/w trials was substantially different to the other two, so this anomalous trial was omitted from the mean

calculation and the results plotted. This gave a curve that follows the pattern for the 1.5 and 1.7% w/w tests displaying an increase in the apparent viscosity over the first night. The amended 2.0% w/w curve also shows significant thixotropy, which was be expected at high CMC concentrations (Ghannam and Esmail, 1997).

3.4.11 Transient time tests

Several sources in literature found that CMC concentrations comparable to the present case did not display viscoelastic properties. Mashelkar and Decarajan (1976) tested CMC and Kaolin for normal stress difference and found them to be purely viscous, while Ghannam and Esmail (1997) conducted a creep recovery test and concluded that the fluid displayed purely viscous behaviour. However, both these sources warn that viscoelastic data is dependent on test conditions, so a transient time test was undertaken during series 3, to confirm that the CMC did not display viscoelasticity. A 2.0% w/w CMC sample (Walocel) was made with tap water, sealed overnight and on the following day was subjected to a constant value shear rate of 461.00s^{-1} for 20 minutes and the shear stress measured.

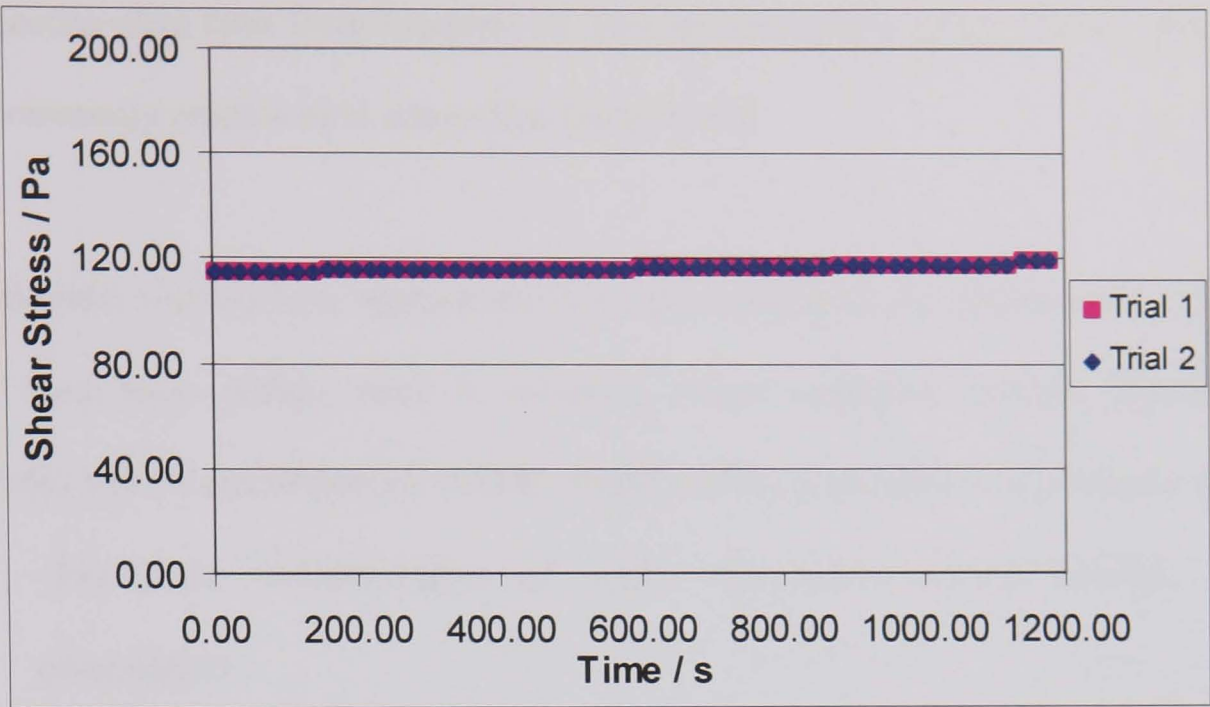


Figure 3.8: Transient shear stress response for 2.0% w/w Walocel at a constant value shear rate of 461.00s^{-1}

Over the course of the test the shear stress increased marginally. From this it is assumed that CMC concentrations of 2.0% w/w and less will display minimal viscoelastic effects in the pipeflow application.

3.5 Choice of settling slurry

Water was an obvious choice for a Newtonian carrier fluid. The availability and abundance of knowledge about this substance are advantageous, however, it does hold some disadvantages, such as the temperature dependency of its viscosity. Since the effects of this can be minimised by using a cooling system and logging temperature, water was accepted as a suitable transport medium.

As specified in the aim of this research, a predominant factor in the choice of suitable solids for the slurry, was the density of the solids. Sand, coal and

magnetite were seen from literature to have an appropriate range of densities and be commonly employed in slurry pipeline research.

Sand-water slurries have application in the dredging industry (Turian *et al.*, 1971) and have been widely used in research, recent examples include, Sundqvist (1996a) and Ni and Matousek (1999). Smith (1955) reported that sand slurry was

'free from complications of scale deposition, crystal growth, and coagulation'

which presented a major benefit for research purposes. Sand was also used in previous investigations of swirling flows, such as Charles *et al.* (1971) and Schriek *et al.* (1974) (Section 2.4) and has a density of approximately 2.65g/cm^3 and a Mohs hardness of approximately 7.

Coal-water slurries have also formed the basis of a number of flow studies from Worster and Denny (1955) to Logos and Nguyen (1996). Coal has played a major part in industry for many years and since any cleaning, upgrading and waste processing involves conveying coal-water slurries, pipeline transport is inevitably important. Hydraulic transport of coal has been used in mining operations with a number of advantages such as a reduction in personnel, costs, dust levels and the space required for transport equipment (Jeremic, 1982). The properties of coal vary between mines, with densities ranging from, for instance, 1.18g/cm^3 (Logos and Nguyen, 1996) to 1.48g/cm^3 (Roh, 1995).

A number of pipe flow studies, such as Arena *et al.* (1998), Sundqvist *et al.* (1996b) and Carlson and Ing (2003) involved the use of magnetite or magnetite ore. Within these studies the density of magnetite ranged from 4.46g/cm^3 to 5.20g/cm^3 . This naturally ferromagnetic material is one of the most important ores for the iron and steel industry.

Given that each material was readily available, coal, sand and magnetite were accepted as suitable particulate materials for use in this investigation. In addition, a number of experiments were performed with the plastic beads used by Raylor (1998) and Ganeshalingam (2002).

Sand was selected to produce materials of different particle sizes because it was the material with intermediate density. By necessity, the selection of particle size ranges was dominated by consideration of the size distribution of the raw material, although information from literature was also utilised. As described in Chapter 2, pipeline flow patterns were often classified in terms of particle size. Initially it was hoped to test slurries with particle sizes corresponding to the heterogeneous saltation, heterogeneous suspension and homogeneous flow regimes shown in Table 2.1. However, producing the extreme particle sizes posed a problem in that sufficient quantities of material $> 2000\mu\text{m}$ and $< 40\mu\text{m}$ could not be obtained from the sand available. Therefore, target size ranges chosen were by considering the classification of particle sizes with heterogeneous behaviour into 3 categories (Durand, 1953) of fine ($200\text{-}50\mu\text{m}$), intermediate ($2000\text{-}200\mu\text{m}$) and coarse

(>2000 μm) in combination with the size of screens and quantity of material. This led to the production of particle size ranges of 106-75, 1000-500 and 2000-1000 μm . In addition, it was found that the coal contained a significant proportion of material above 2000 μm , so an ultra-coarse size fraction of 4000-2000 μm was produced for this material.

Since this work is building on that of Raylor (1998) and Ganeshalingam (2002), it was viewed advantageous to maintain some similarities with their work. For this reason, target concentrations of 1.4, 2.7, 5.4 % v/v were chosen from within the range used by Ganeshalingam (2002).

3.6 Summary / implications for the pipe flow loop

Tests were performed to select a fluid for use in investigating the effect of swirl on non-Newtonian liquids. CMC was selected from 6 other fluids for its shear thinning, non-thixotropic properties at the grade and concentration used. It complied with the required apparent viscosity and showed minimal frothing in comparison to the other fluids. An investigation was then conducted into the affect of bacteria, age, temperature, evaporation, salt and biocide concentration on the behaviour of CMC and a check of the viscoelastic properties of the material was performed. The following points summarise the results and recommendations arising from this investigation:

- The viscosities of the series 1 open control, the open Proxel and sealed Nalco samples were found to be most consistent over 14 days. The

consistency of the open Busan sample dropped off a little towards the end of the test. Overall the Proxel sample performed best.

- The hypothesis that the presence of bacteria in the solutions will result in a decrease in apparent viscosity was neither proved nor disproved due to the conflicting evidence discussed. However, inconsistency between the control samples and insensitivity of the rheology to biocide concentration formed a good case for biocide addition. The suppliers recommended that Busan be disposed of by decreasing the pH to pH 5-6 and storing for 2 days until it decomposed, before draining. Proxel must be neutralised by adding a solution of sodium meta-bisulphite, whereas at these concentrations Nalco can merely be poured down the drain with plenty of water. For this reason Nalco was selected for use in the pipe flow tests, despite the slightly better performance of Proxel.
- The thixotropy results showed that the series 1 control, open Busan and open Proxel samples showed negligible thixotropy over the two-week test period, whereas the Nalco samples showed negligible thixotropy over the first 11 days. Thus, the CMC solution containing 100ppm Nalco 2593 biocide is suitable for use in swirl pipe tests for up to 11 days.
- The hypothesis that evaporation will concentrate the solutions and increase the apparent viscosity with time was neither proved nor disproved due to

the conflicting evidence discussed. In addition, rough calculations (using surface area to volume ratios) indicated that evaporation from the open tank would be less significant than from glassware in the desktop tests and the generally lower temperature in the pipe flow loop laboratory favours less evaporation. However, an open tank would introduce uncertainty over evaporation into the tests, so a lid was recommended. Use of a lid will also avoid contamination of the CMC by deposition from the atmosphere.

- No adverse effects on the pipes were observed after control and biocide solutions were stored in them for 2 weeks, allowing the solution to be stored the pipe loop.
- The apparent viscosity of CMC was confirmed to decrease with temperature, so it was recommended that the temperature of the CMC be monitored when pumping and a cooler added to the pipe flow loop.
- The effect of salt on the rheology of CMC was clear at 0.8% w/w Walocel. Therefore, to ensure that the water has a low salt concentration, which is consistent for each batch, it was decided to use Reverse Osmosis water to make the large-scale CMC batches.

- The rheological behaviour of the CMC was found to be insensitive to biocide concentration, allowing biocide to be added if biological tests indicated a need.
- The viscoelasticity of CMC at these concentrations was confirmed to be minimal.

The tests have not rigorously characterised the behaviour of CMC, but have achieved their aim of allowing well-informed decisions to be made on the design of the pipe flow loop and methodology for the pipe flow tests.

Throughout the tests the CMC has been modelled as a pseudoplastic and the fluid consistency index (k) and flow behaviour index (n) have been determined. The series 2 test results gave a mean k and n value of 2.96 and 0.46 respectively. These values were used in the design of the steel pipe flow loop to estimate the minimum and maximum pressure drops expected and check that sufficient head was maintained over the pump (Chapter 4).

The choice of settling slurries was considered and water was selected as a carrier fluid. Coal (2000-1000 and 4000-2000 μm), sand (106-75, 1000-500 and 2000-1000 μm) and magnetite (2000-1000 μm) particles were chosen for addition to the water, to assess the effect of swirling flows on slurries with varying particle size and density. Target concentrations of 1.4, 2.7, 5.4 % v/v were set.

Chapter 4 DESIGN OF A STEEL PIPE FLOW LOOP

This chapter details the steps involved in the design of a new flow loop for the swirl pipe tests. The requirements for the new loop and a number of layout options were initially considered. Operational factors that influence the design were then discussed, followed by a description of the design of components used in the flow loop.

4.1 Design criteria

A vertical rectangular design, based on the pipe loop used by Raylor (1998) and Ganeshalingam (2002) (referred to as Perspex flow loop) was envisioned. The current design aimed to incorporate the following features of the Perspex flow loop:

- Pressure and volumetric flow rate measurements
- Minimised aeration of the slurry
- Flow loop layout to accommodate the exchange of pipe sections and different radius bends. (Flexibility was important to allow the design to cope with unexpected ideas and problems that arose as research progressed).
- Variable pump flow rate.
- Provision for draining the flow loop.
- Addition and removal of solids.

To achieve the aims of the work, the following additional requirements for the pipe flow loop design were derived:

- The loop should be constructed of a more durable material so abrasive slurries can be transported.
- In addition to pressure and flow rate measurements, it should be possible to measure the temperature and solids concentration in the loop.
- Maximum length should be obtained from the space allowed. Throughout literature long test sections are used, for example, Simkhis *et al.* (1999) used a test section 200 pipe diameters long. Toda *et al.* (1972) measured pressure drop over a length of 166 pipe diameters. A long measurement section is needed in order to get a reliable pressure drop and a long distance prior to the test section is important to ensure flow is fully developed. Das *et al.* (1991) employed a length greater than 50 pipe diameters and Mukhtar *et al.* (1995) used a length of approximately 150 pipe diameters to limit disturbance from other components.
- If possible provision should be made for horizontal bends and inclined pipes.

4.2 Layout

The steel structure around which the flow loop was constructed consisted of two platforms accessed from ground level and the laboratory balcony (Appendix B.10, B.11). The structure supports a pipe loop with reservoir tank for another project around which the new pipe loop was built. Limited space was available at each

end of the structure for expansion. The design of the flow loop was carried out in consultation with outside companies and internal technicians.

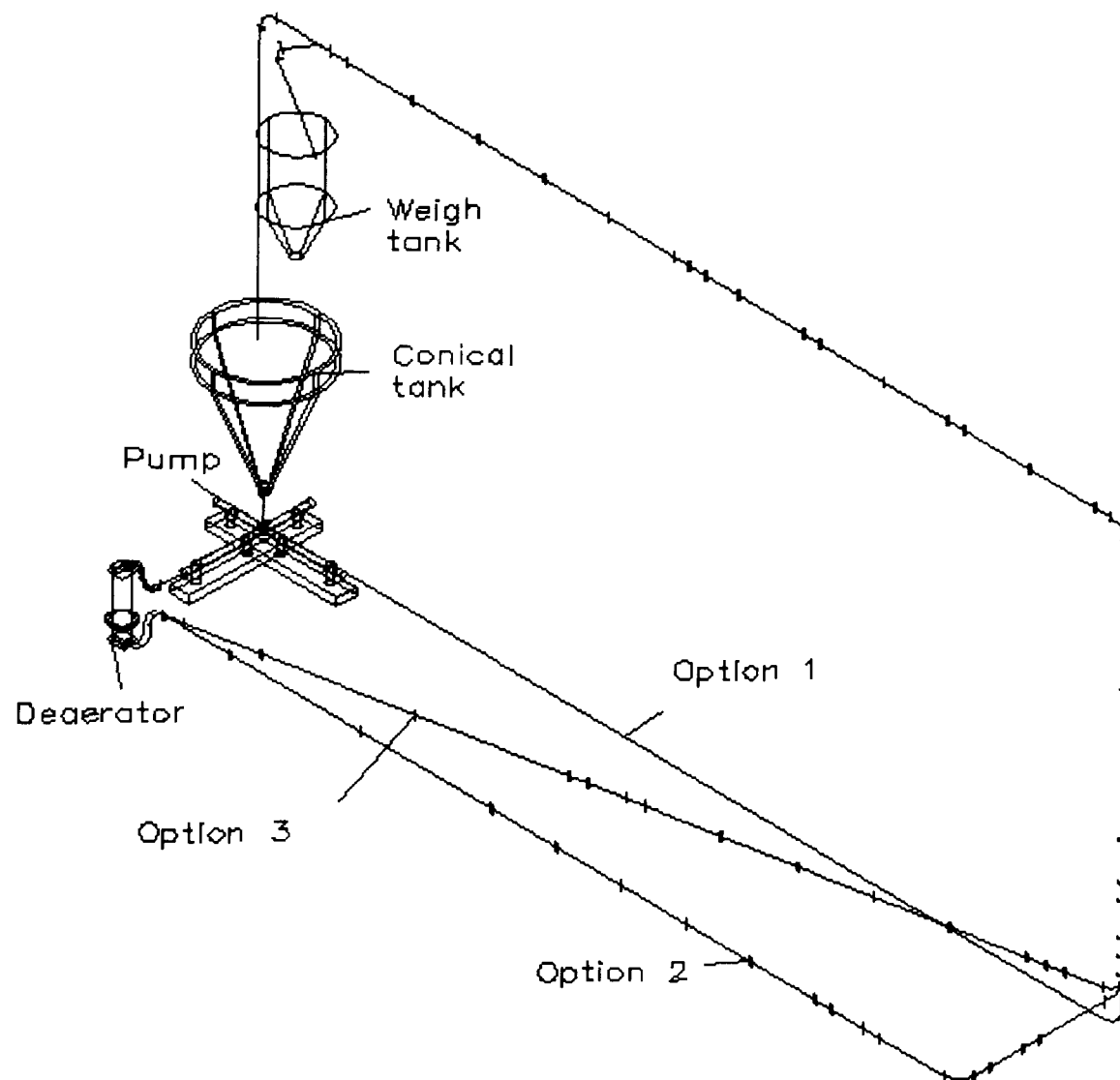


Figure 4.1: Isometric view of the 3 flow loop design options.

Lengths are omitted to aid clarity.

Referring to plans of the existing structure, three layout options were formulated. Provision was made for an inclined section in each (positioning of inclined section illustrated in Appendix B.6-B.7) and a horizontal bend in one. Option 1 is a vertical loop and options 2 and 3 are extensions on this idea and are illustrated in Figure 4.1. The components needed for each option were analysed and little difference was found in the lengths of pipe required (Option 1: 33.4m, Option 2:

37.7m, Option 3: 35.8m). In terms of the overall cost of the flow loop these differences were insignificant. The main problem associated with option 1 was that two bends of non-standard radii were required to divert the pipes around an obstruction. This diversion would unsettle the flow and was located approximately 4m before the position of the inclined section, when in use. A longer horizontal length, to allow flow stabilisation before the inclined section, was preferred. Options 2 and 3 provided this. An advantage of option 2 was the inclusion of a horizontal bend with a long straight before it. However, the length of the straight before the vertical bend was severely limited and was expected to be too short for stabilisation of the flow, making studies of the vertical bend difficult. Another problem with this design occurred in the inclined configuration, when the whole of the leg preceding the vertical bend, a length of 2.6 metres would have to be raised and suspended (see Section 4.5.1). Option 3 eliminated these problems but did not include a horizontal bend.

In light of this assessment, it was decided to construct option 3. However, enough components were purchased to enable the flow loop to be modified to option 2 for experiments on horizontal bends, if time allowed.

4.3 Structural alterations

To accommodate the chosen design initial structural alterations were required. The second storey balcony was extended to allow access to the bend at the top of the vertical leg and an additional structure was required to support the conical

tank, which was positioned outside the original structure (Appendix B.10 and B.11). The weigh tank was moved along and down to make room for the inclined section on the top leg. Birtley Process Equipment Limited, Chesterfield, performed these modifications.

4.4 Influence of operational procedure on design of test loop

During the design of the test loop, the mixing and transfer of the viscous liquid (CMC) and the insertion and removal procedures for the solid particles were considered in an effort to achieve problem free operation.

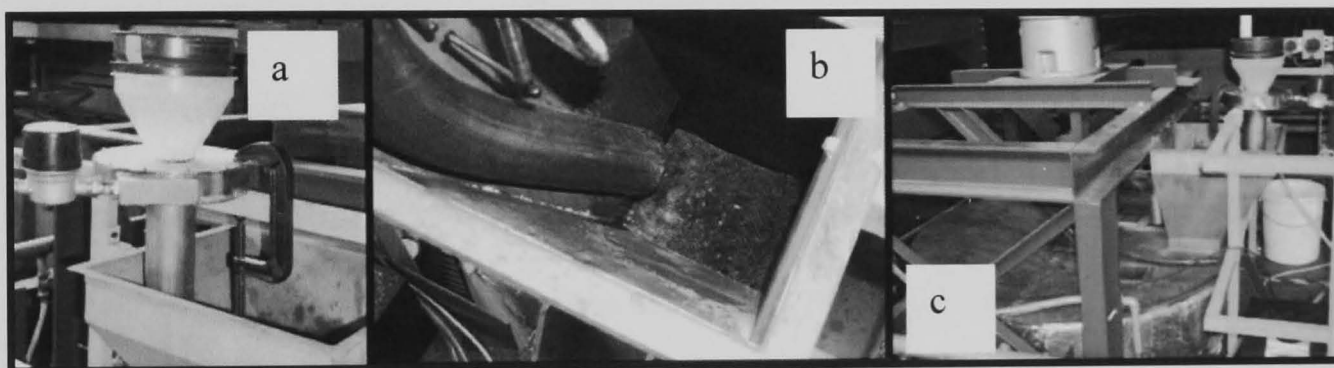


Figure 4.2: Various views of the Autex unit in position. a) view of sieve, water meter and autex unit; b) view inside hopper; c) hopper feeding into mixing tank.

An Autex unit was design by Brown (2001) to mix the CMC, water and biocide. The Autex unit created a vortex to which the CMC powder was added. The chute on the unit was directed into a hopper, through a metal grid and into a 2.5m³ cylindrical covered tank fitted with a stirrer with a maximum rotational speed of 60 rpm, supplied by Thringe-Scott, Belfast. To transfer the CMC to the steel

pipe loop a flexible pipe connection was designed to connect the outlet of the mixing tank to valve V2 (Section 4.5.6).

To add and remove solid particles from the pipe flow loop a diverter valve and flexible tank inlet pipe were incorporated into the design and a settling tank obtained. Using these components the flow could be diverted through the weigh tank, while the tank inlet pipe was relocated to feed the settling tank. Then by switching the diverter valve the solids could be pumped out of the flow loop.

4.5 Components

4.5.1 Pipework

To achieve a flexible layout, the pipe loop consisted of sections of between 0.25m and 2m in length. The pipes had a diameter of 0.055m, connected by flanges sealed by O-rings (Appendix B.1), in keeping with the diameter and flanges of the Perspex flow loop and swirl pipes already obtained. This allowed interchange of pipes between the flow loops. The pipe materials considered are given in Table 4.1. Steel is the most corrosion resistant, but Wood *et al.* (1998) found that a medium density polyethylene coating had a higher erosion resistance than steel. Despite this stainless steel (316L schedule 10) was chosen as the pipe material for the test flow loop because of its wide availability and usage in industry. All pipework was manufactured by the Pipeline Centre, Nottingham.

Table 4.1: Summary of advantages and disadvantages of main pipe materials (adapted from Bain and Bonnington, 1970).

Pipe material	Advantages	Disadvantages
Plastic	Can be resistant to virtually all corrosion. Resistance to friction abrasion satisfactory.	Not suitable for cutting/tearing erosion
Asbestos cement	Relatively light weight, easier handling than alternatives.	
Cast Iron	Quite corrosion resistant	At high velocity slurries can cause high wear at joints
Concrete	Resistant to pitting and tuberculation	Cracking due to shrinkage common with concrete linings
Stainless steel	Speed of construction and ease of handling, without risk of damage. High resistance to corrosion.	Expensive

In order to assess the effects of bend radius, three different radii were purchased, 110mm, 220mm and 330mm. These radii correspond to radius to diameter ratios (R/d) of 2, 4 and 6 respectively. The bends were designed to have no integral straight section so the induced swirl could be applied directly to the radius of curvature. This was in keeping with the approach used by Ganeshalingam (2002). The bends were to be substituted at the end of the bottom horizontal leg. Spacer sections of various lengths were designed to compensate for the differences in horizontal and vertical lengths of the bends (Figure 4.3).

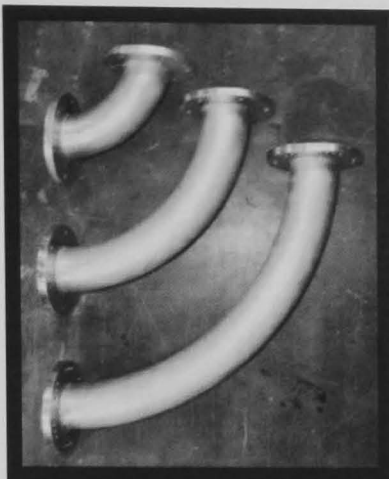
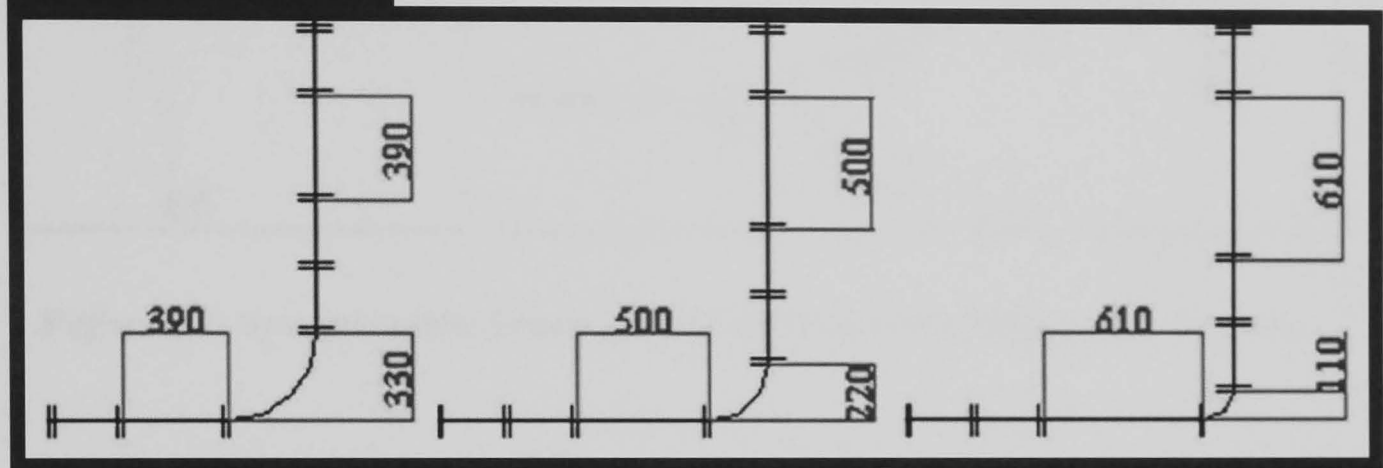


Figure 4.3, The three radii bends; diagram illustrating the spacer sections used to insert each bend (dimensions in mm).



It was recognised that inclination could be produced by removing pipe sections from the vertical leg and sloping a horizontal section to meet the new elevation. It was calculated that if 0.5m and 1m vertical sections of pipe were removed and a 3m length of pipe inclined, a slope of 9.46° and 18.43° would be produced. These angles fall within the range tested by Diniz and Coiado (1999: 5.5° , 11° , 22.5° , 34° , 45°). Special radius bends (Figure 4.4) were designed to insert between the inclined and vertical pipe flanges.

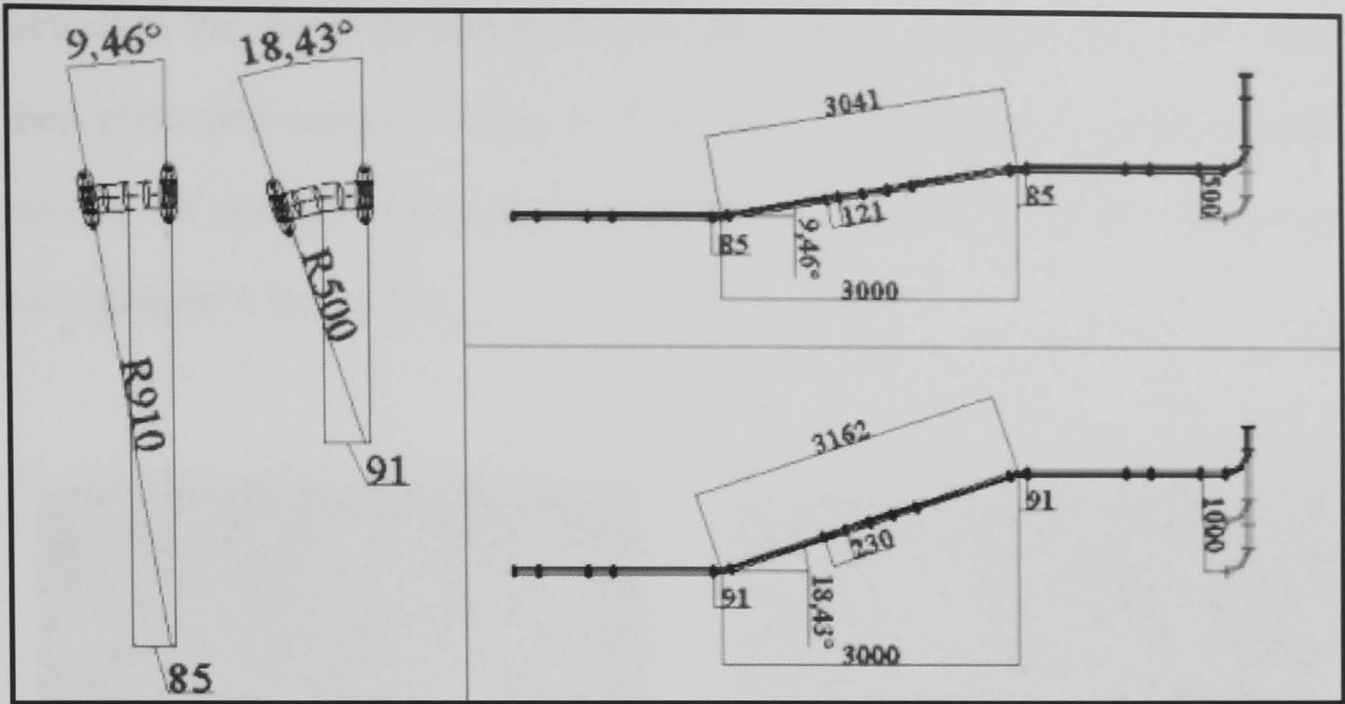


Figure 4.4: Special radius bends and inclined sections (dimensions in mm).

4.5.2 Swirl pipe

Ganeshalingam (2002) performed experimental tests using a 3-lobe pipe and used CFD modelling to optimise the design of a swirl-inducing pipe. He considered triangular, square, pentagonal, hexagonal and 2, 3, 4, 5, and 6 lobe cross-sections and found that pipes with a 4-lobe cross-section had a small advantage over the others. He also found that the total amount by which the cross-section twisted was an important factor and determined an optimum pitch-to-diameter ratio of 6 for the 3-lobe pipe and 8 for the 4-lobe pipe. Furthermore, he found that the optimum lengths for the 3 and 4-lobe pipes were 0.6m and 0.4m respectively at the optimum pitch-to-diameter ratios.

Ariyaratne (2002) produced 0.2m lengths of 3 and 4-lobe pipe from an Epoxy Photopolymer using stereolithography (Figure 4.5). The lengths of the pipes were

limited by the size of the tank in the stereolithography machine. Some tests were then performed using the Perspex flow loop in an attempt to experimentally confirm the findings of Ganeshalingam (2002) and determine which pipe should be employed in further tests.

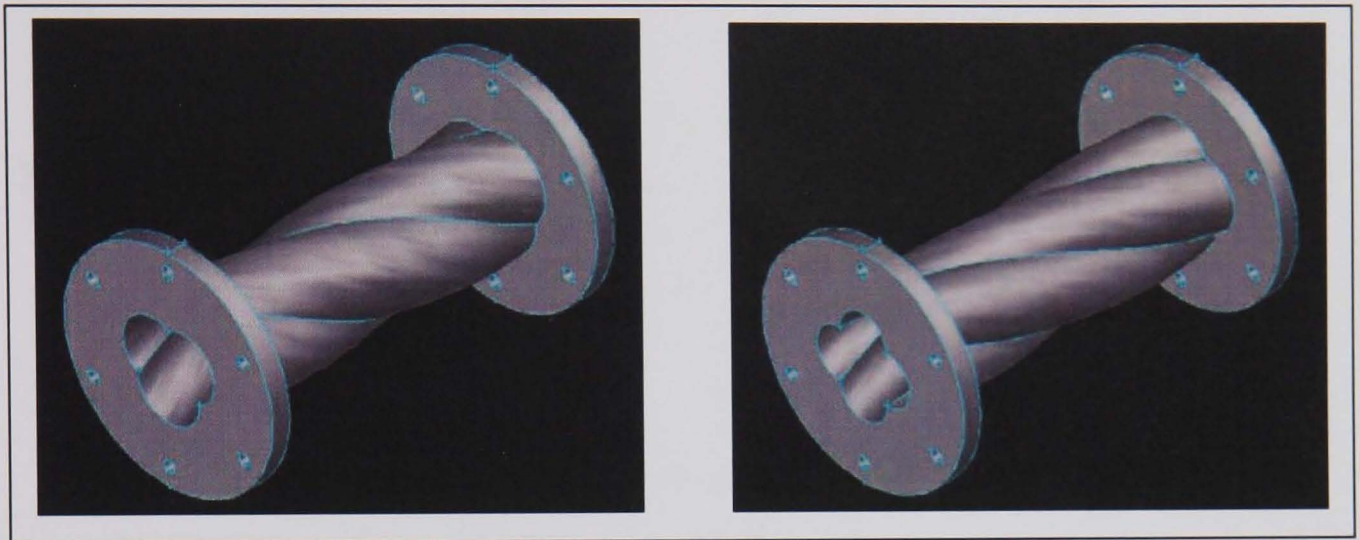


Figure 4.5: 3 and 4-lobe swirl pipes (drawn by Ariyaratne, 2002)

The tests were conducted on the Perspex flow loop as described by Ganeshalingam (2002) and shown in Figure 4.6. The flow loop had a volume of 0.21m^3 and comprised a header tank (Figure 4.6, item 1), a Mono pump (2) controlled by a frequency inverter, a de-aerator (3), interchangeable flanged Perspex pipe sections, pressure transducers (P1 - P8) and an electromagnetic flowmeter (5). The pipes were mounted on a black backboard.

Tests were performed at approximately 0.5, 1.0, 1.5, 2.0 and 2.5m/s for each concentration. For these tests white plastic beads were pumped at concentrations of 0.7%, 1.4%, 2.0% and 2.7% v/v using water as a carrier fluid. Temperature

measurements, using a mercury thermometer placed in the tank, were taken intermittently.

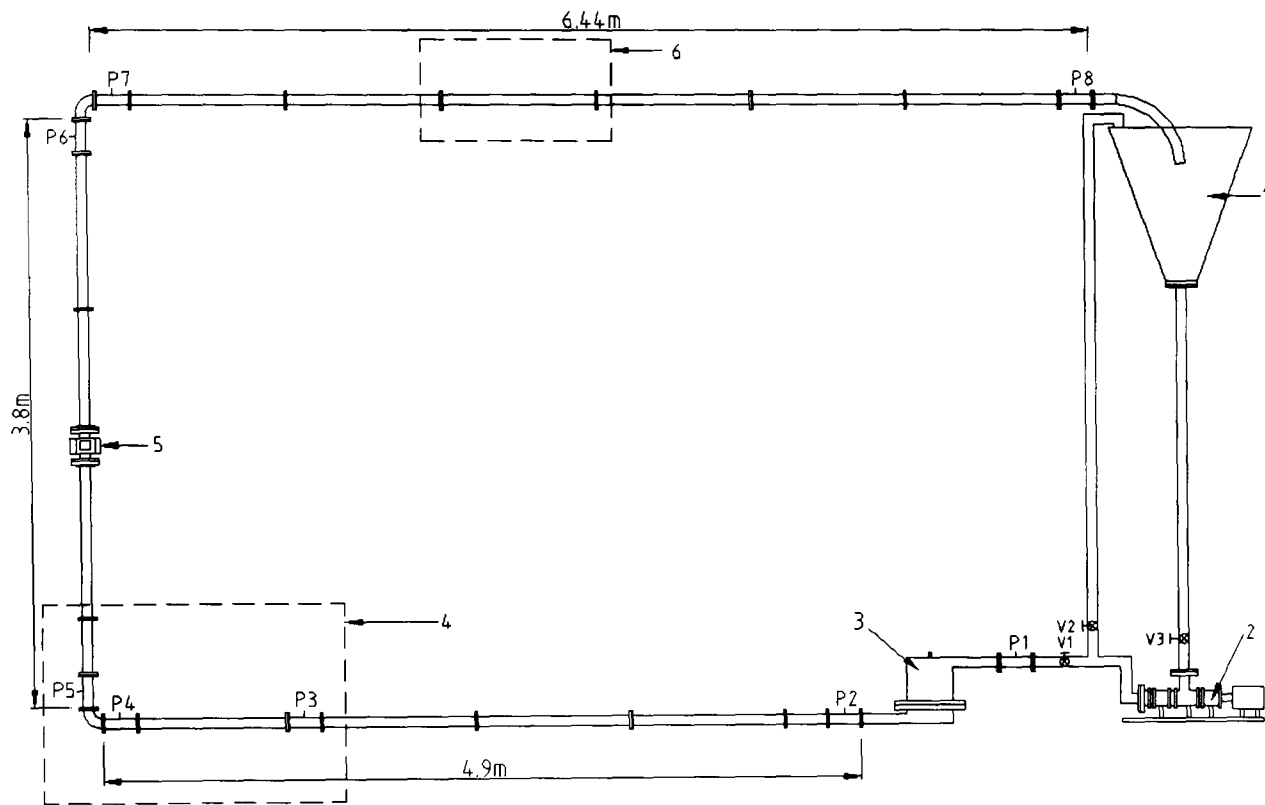


Figure 4.6: Perspex flow loop (taken from Ganeshalingam, 2002)

Tests were performed which measured the pressure drop for each concentration and velocity over the following pipe configurations:

- Top leg (measurement section 104D long, positioned 22D from bend) and horizontal to vertical bend ($H \rightarrow V$, $R/D=3$) (pressure transducer directly before bend, 94D from de-aerator) with no swirl induction present
- 3-lobe or 4-lobe pipe in the top leg (measurement section 86D long, positioned 42D from bend)
- 3-lobe or 4-lobe pipe immediately preceding $H \rightarrow V$ bend (swirl pipe and pressure transducer directly before bend, 90D from de-aerator).

Using the known lengths between the transducers on the upper leg the pressure drop per meter, with no swirl-induction present, was calculated. The pressure drop curves produced (Appendix B.12) showed the trend established in the literature for slurries of different concentrations. The results compare well to corresponding tests performed by Ganeshalingam (Appendix B.13). The pressure drop across the 3 and 4-lobe swirl pipes in the top leg was also calculated. These results do not show the classic increase in pressure drop with concentration (Durand, 1953; Worster and Denny, 1955) (Appendix B.14 and B.15) but confirmed the results of Ganeshalingam (2002) that the pressure drop over a swirl pipe is independent of concentration.



Figure 4.7: Pressure drop over bend for water only

Figure 4.7 shows the pressure drop over the bend for water. The results for all concentrations follow the same trend and are shown in Appendix B.16. Although both the 3 and 4-lobe pipes produced a reduced pressure over the bend when

compared to cylindrical pipe, little difference was noted between the 3 and 4 lobe designs. This appeared to contradict Ganeshalingam's (2002) CFD predictions, which showed a significant difference between the 3 and 4 lobe pipes, but was accounted for by the fact that the optimal lengths of pipe were not used. It is suggested that if the test were repeated using the optimised pipe lengths and perhaps a higher density solid such as sand, a difference may be evident between the two pipes.

Therefore, in the absence of strong evidence to contradict Ganeshalingam's optimised design (2002, 4-lobe 0.4m pipe with pitch to diameter ratio of 8), it was decided to employ it for the steel flow loop tests. Due to the restrictive size of the stereolithography machine tank, two 0.2m 4-lobe swirl pipes were produced and bolted together to form the specified 0.4m length.

4.5.3 Pump

Many types of pumps are available with different motive mechanisms, which transport slurry directly or indirectly. Direct displacement pumps are categorised as roto-dynamic and positive displacement pumps. Roto-dynamic pumps accelerate the fluid using a rotor whereas positive displacement pumps transport isolated volumes of the slurry in moving parts within the pump. Indirect displacement pumps generally use a liquid to transport the slurry and can be classified by the type of liquid used (Heywood *et al.* 1998). The performance of these pumps in terms of pressure head, flow rate and the particle size, abrasivity

and viscosity tolerated varies widely. Appendix B.17 gives a useful overview of the main pump types.

Selection of a suitable pump is an important design step. Poor pump selection can lead to high capital, operation and maintenance costs, downtime, vibration, noise and poor performance (Heywood *et al.* 1998). Odrowaz–Pieniazek (1979) states that the main parameters effecting pump choice are discharge pressure and abrasivity and Bain and Bonnington (1970) highlight the following considerations:

- Size of solids to be pumped.
- Stability
- Use of pump combinations
- Limitations imposed by installation
- Running cost

The most important of these considerations for this application was the size of solids to be pumped. Ideally a pump that could cope with both solids (up to 4mm) and viscosity (approx 1500mPas) was required. Several of the pumps described in Appendix B.17 were immediately seen to be inappropriate for these requirements. The co-rotating disc, lobe and flexible impeller pumps only pass fine particles, and the axial flow and piston pump cannot tolerate highly abrasive slurries. Therefore the sand water mixture would have caused a problem for these pumps. For several of the pumps no information was found on viscosity tolerance.

The School of Chemical, Environmental and Mining Engineering already owned two Mono pumps so use of one of these was considered. From Appendix B.17 it can be seen that progressive cavity pumps are suitable for solids up to 10mm, so should be suitable for 4mm solids. According to Heywood *et al.* (1998) this type of pump causes 'little damage to shear sensitive material' and Béréiziat *et al.* (1995), working with CMC, used a volumetric pump in order to avoid shear degradation. Therefore a progressive cavity pump should be suitable for the requirements of this process.

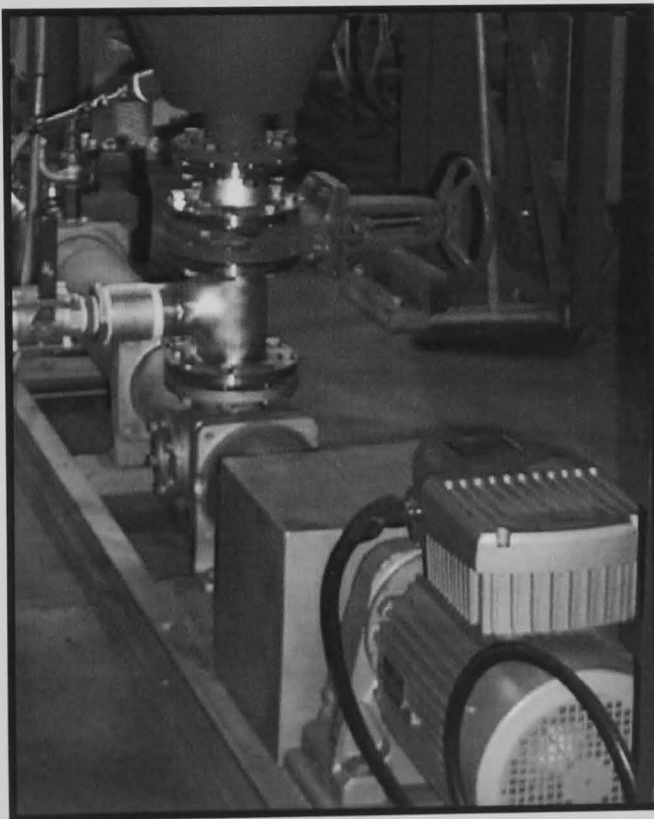
In the progressive cavity pump a single helix screw rotates eccentrically within a double helix stator (or sleeve). A continuous seal is maintained which moves along the length of the stator (Odrowaz –Pieniazek, 1979).



Figure 4.8: Helix and Stator in a progressive cavity pump, adapted from Mono Pumps Ltd (2002).

The pump was selected based on the requirements of CMC pumping. The results of the rheology tests (Chapter 3) on a 0.6% w/w CMC solution containing 100ppm of Nalco biocide showed the mean apparent viscosity over 15 days to be 1234mPas and 68.20mPas at 2.91s^{-1} and 1160s^{-1} respectively. These values were read off the pump characteristics at a pressure of 1 bar to estimate the maximum speeds that could be obtained from the pumps. For the first pump a range of 0.7-

1.4m/s was calculated, which was considered too low. The second pump (type CLN213R3) gave estimated maximum speeds of 4.3-6.3m/s. However this pump was lacking a motor. Appendix B.19 shows the pump characteristic for the second pump. Reading from the graph at a velocity of 5 m/s indicated that a 2.5 kW motor was required. However, the supplier, Mono Pumps Ltd recommended a minimum motor size of 5.5kW but after further consultation, a 7.5kW motor was purchased to accommodate the high apparent viscosity at start-up. A reduction gearbox to bring the motor to the right speed for the pump and an integrated inverter with a 7:1 turn down ratio were also purchased and installed. For the CMC, Mono Pumps Ltd estimated that a maximum speed of 4.6m/s could be achieved.



**Figure 4.9, Photograph
of the Mono pump,
gearbox and motor.**

4.5.4 Tank design

4.5.4.1 Shape

Most test flow loops require a tank to feed the pipeline. In other pipe flow loops in the School problems have been encountered with dead zones and solid fallout within the tanks. This changes the concentration of particles in the flow loop, so the input concentration is not an accurate representation of the in situ concentration. In many industrial applications the concentration of particles is critical to the process. Concentration is also an important factor in pressure drop correlations, so it was vital to have confidence in the value used. In industry, stirrers are often used to increase the residence time of solids in tanks, with a view to increasing the concentration of solids in the tank, to gain a more homogenous concentration distribution across the system. This has been utilised in one flow loop at Nottingham, however, a difference in delivered and input concentration was still observed (Jones, 2001).

Govier and Aziz (1972) have analysed the differences between in situ and input concentration in pipelines. In their work they define a phenomenon called holdup. Holdup occurred when there was a significant density difference in two materials flowing in a pipe. In solid-liquid pipe flow the less dense phase tended to have a higher in situ velocity than the denser phase. This meant that the solids were held up relative to the liquid, i.e., the concentration changed. Govier and Aziz (1972) define S as the average slip velocity ($V_l - V_s$), H as the holdup ratio (V_l/V_s) and derive:

$$H = \frac{C_l E_s}{C_s E_l} \quad (1)$$

Where: Subscripts l and s refer to liquids and solids respectively

$$S = \frac{V_{sl}}{E_l} - \frac{V_{ss}}{E_s} \quad (2)$$

C = input volume fraction

E = *in situ* volume fraction

V_{sl}, V_{ss} = superficial velocity of the phase indicated by the second subscript.

H can vary from 1 (no slip) to 100 or more.

These definitions were applicable only to pipe flow. The hydraulic environment of a tank is very different to that of a pipeline. A tank is a fluid reservoir with a large area and therefore low liquid velocity. In the reservoir, dense particles slip past the near stationary fluid and their velocity, V_s (the particle settling velocity) may exceed V_l . Therefore, the solids, with the exception of those held in dead zones, tend to settle out quickly resulting in the liquid being held up with respect to the solids.

In a test flow loop the effects of solid holdup in the pipes and liquid holdup in the tank compound resulting in a higher concentration of solids in the pipe than expected by the input concentration. An attempt was made to find further ways of mitigating against the difference between the *in situ* and input concentration.

It has been explained above that stirrers are often used to increase the residence time of solids in tanks and hence the concentration to gain a more homogenous concentration distribution across the system. An alternative to this would be to

reduce the residence time of particles in the tank to negligible and eliminate the volume of water in the tank from concentration calculations. There would still be holdup in the pipes, but this could be calculated using the Govier and Aziz (1972) relationship and would not be increased by liquid holdup.

A possible method to achieve this on the Perspex flow loop (details in Section 4.5.2) was to have a flexible inlet pipe extended to within a few centimetres of the tank outlet. Thus the tank could be modelled as vertical section of pipe, with the liquid in the tank to provide head.

A qualitative investigation into the effect of 'liquid holdup' in the Perspex flow loop was undertaken, using a standard and long inlet pipe. The particle distribution was recorded photographically, over increasing mixture velocities. The results are shown in Figure 4.10.

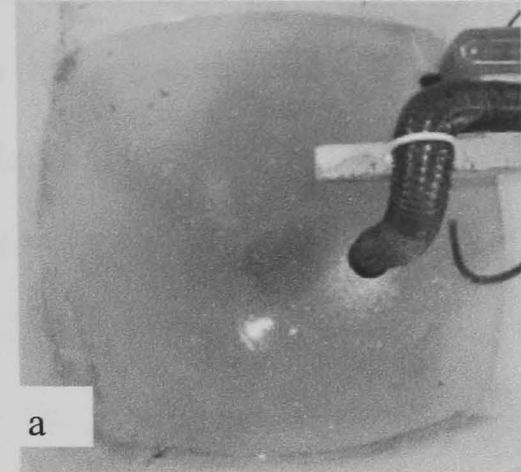
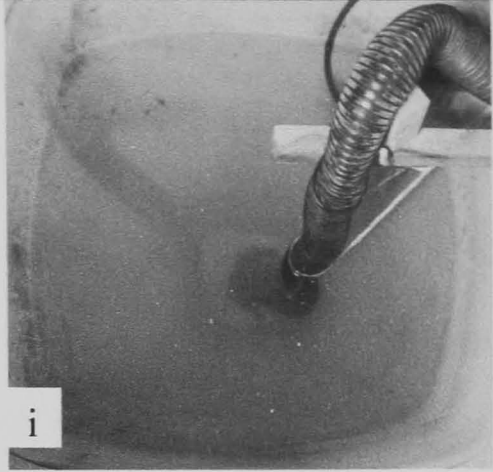
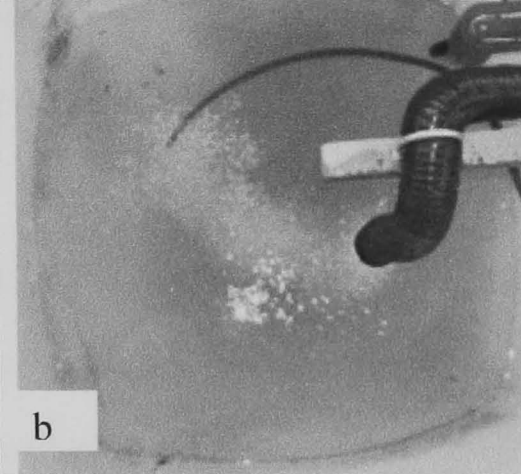
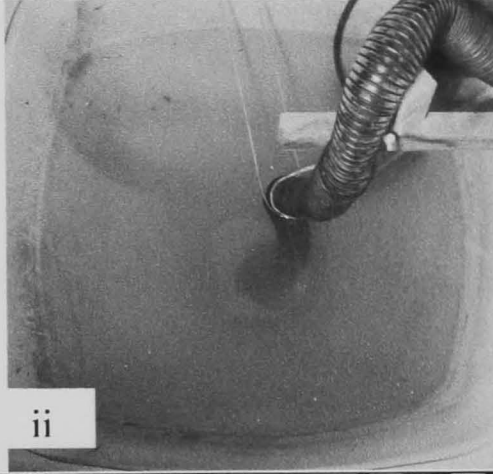
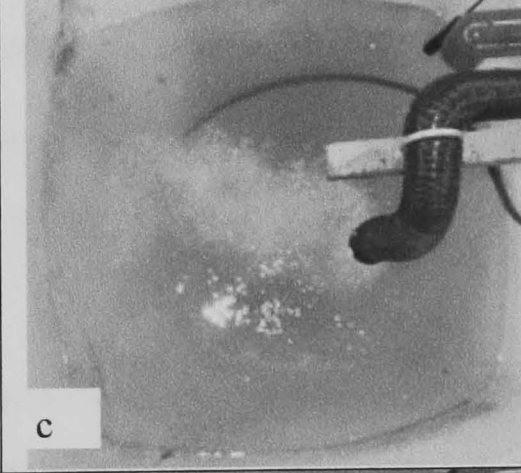

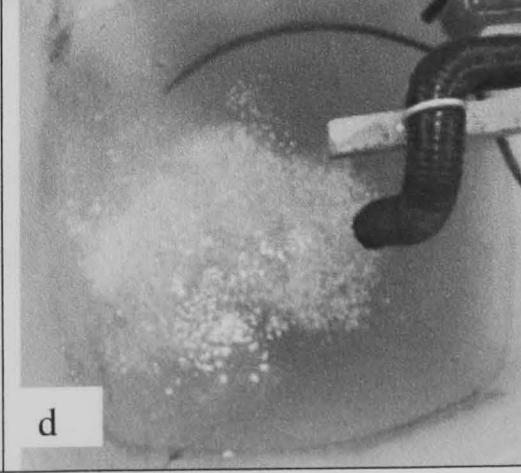
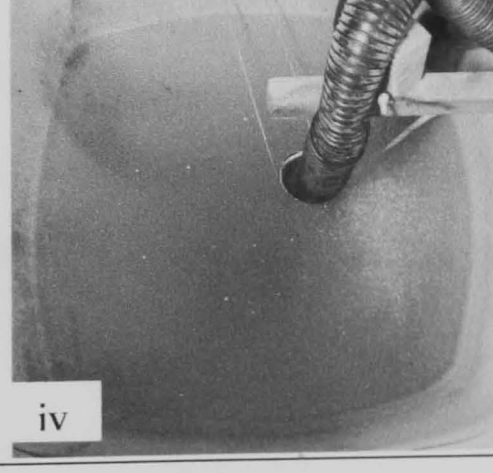
Velocity	Short inlet pipe	Long inlet pipe
1.0m/s	 a	 i
1.5m/s	 b	 ii
2.0m/s	 c	 iii
2.5m/s	 d	 iv

Figure 4.10: Photographs of the tank on the Perspex flow loop, operating with 0.7% v/v beads at varying speeds, with a long and short inlet pipe

In Figure 4.10a the fluid in the tank was relatively still and a column of particles descends to the tank outlet in a manner not dissimilar from vertical pipe flow. In this test a large liquid holdup was not expected, because the density difference between the water and the particles was not great. However, at higher speeds (b, c and d) the number of particles seen in the tank increased. The asymmetric position of the tank inlet pipe had a similar effect to the industrial stirrer, disturbing the near stationary nature of the reservoir, producing eddies and secondary flows that increased the residence times of the particles.

When a long inlet pipe was used instead of the standard length, a reduction in the number of particles in the tank was observed. In Figure 4.10i-iii few particles were observed in the tank. Only at 2.5m/s do particles begin to enter the tank. One explanation for this may be that the difference between the velocity of liquid in the pipe and the tank caused eddies to form at the base of the cone, leading to some of the particles exiting the flexible pipe being caught in these eddies.

Table 4.2 shows that some negative pressures were obtained over the top leg when using the long inlet pipe. When the standard inlet pipe, which was open to the atmosphere, was used this problem was eliminated. Therefore despite the reduction in solids concentration in the tank, a long inlet pipe was not adopted in the design of the steel flow loop, in an attempt to avoid negative pressures.

Table 4.2: Comparison of the pressures measured in the top leg of the Perspex flow loop with a long or standard inlet pipe

	Velocity / m/s	Upstream transducer / Pa	Downstream transducer / Pa	Pressure drop / Pa
Standard inlet pipe	0.99	3100	1631	1469
	1.55	3577	1102	2475
	2.02	5639	2026	3613
	2.50	7273	2312	4962
Long inlet pipe	0.98	-1503	-3301	1798
	1.52	290	-2469	2759
	2.02	2840	-1036	3877
	2.51	5781	553	5229

Instead, with the aim of eliminating dead zones, a tank with a purely conical shape was decided upon. It was intended that the shape would prevent solids becoming trapped and ensure they moved quickly through the tank, as through a virtual pipe. Concentrations could then be calculated omitting the volume of the tank and replacing it with the volume of a pipe of the tank length.

4.5.4.2 Size

The tank was sized by considering the volume of the rest of the flow loop. The tank must be large enough to hold the flow loop volume plus an additional volume to maintain a suitable head above the pump. The total flow loop volume was found to be 0.89m^3 , so an operational volume of 1m^3 was set to allow 0.11m^3 of water to remain in the tank (Appendix B.20). An iterative procedure was used to calculate a range of possible dimensions. From these possibilities, a cone with the dimensions shown in Figure 4.11 was chosen for the tank. This had a volume of

1m³, so a cylinder 0.25m high was added to the top of the cone to prevent overflow. A calculation was then performed to confirm that minimum head was sufficient to avoid cavitation (Appendix B.20).

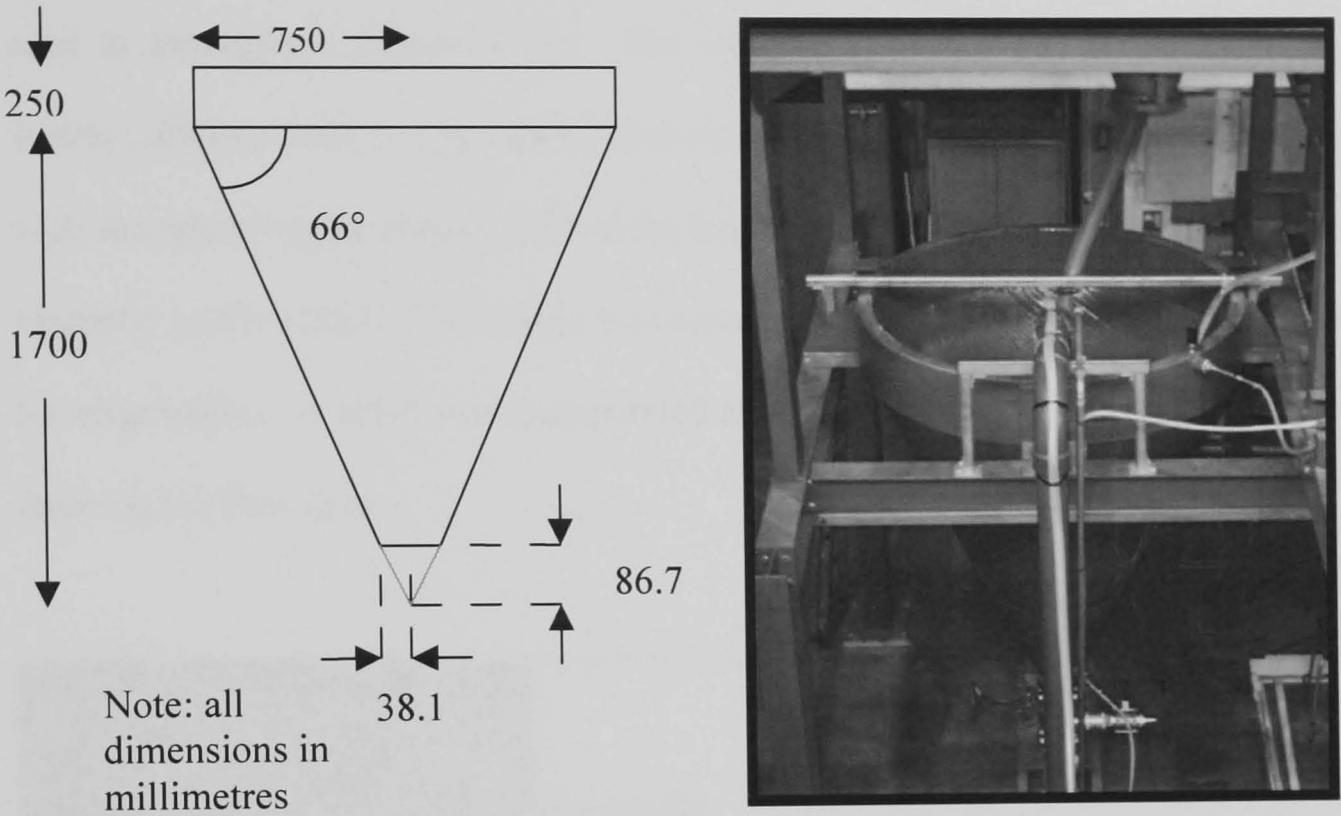


Figure 4.11: Dimensions and photograph of the conical tank

The design comprised a single skin slurry tank with a water jacket (50mm gap) to accommodate a cooling circuit. To increase durability a 6mm polyurethane lining was chosen. The tank was constructed and installed by Birtley Process Equipment Limited, Chesterfield.

4.5.5 De-aerator

The design of the de-aerator was based on an operational de-aerator on the Perspex flow loop. It consisted of a cylinder with an inlet at the top and outlet at the bottom. A vortex produced on a stand allowed any trapped bubbles to escape via a tube to atmosphere (Figure 4.12). The required diameter was estimated to be 0.30m (Abbott, 2001). The other dimensions were then calculated using ratios with the operating de-aerator, with extra length added to account for the apparent viscosity of the CMC. The design was constructed from steel with a Perspex top for observation. A valve was incorporated at the base of the de-aerator to assist in draining the flow loop.

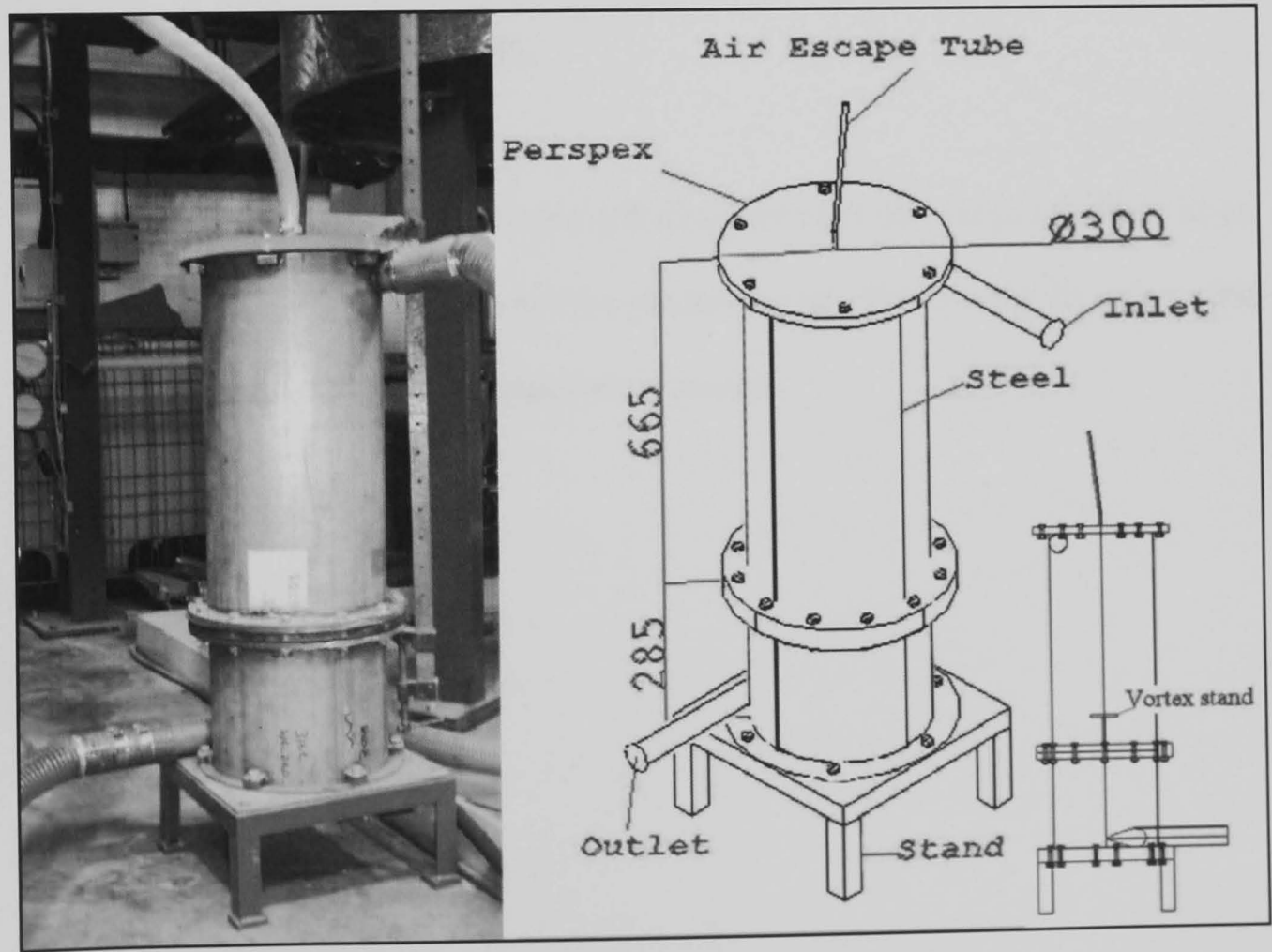


Figure 4.12: Photograph and drawings showing the de-aerator.

4.5.6 Valves

In the selection of valves for the flow loop the following were considered:

- Operating variables
- Slurry variables
- Space restrictions
- Mode of operation
- Torque required
- Time required.

If a valve was chosen that was inappropriate for a system this could lead to poor operation, leakage, vibration, noise, excessive capital and maintenance cost, downtime (Heywood *et al.*, 1998).

Appendix B.18 highlights advantages and disadvantages of a range of valves as an aid to selection. Figure 4.13 shows the positioning of valves in the flow loop and Table 4.3 explains which valve types were chosen.

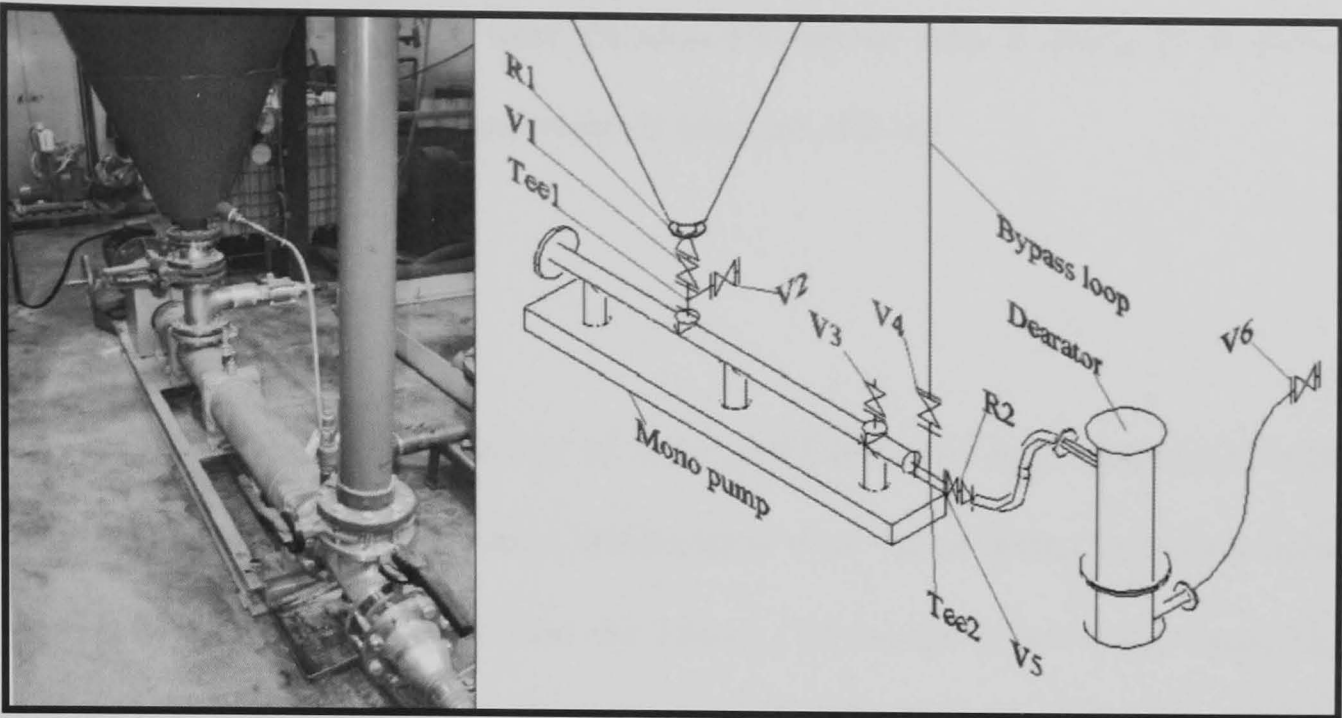


Figure 4.13: Photograph and drawing of the valves used in the flow loop.
Prefix V refers to valves, R to reducers.

Table 4.3: Valves used in the flow loop.

Part Number	Location	Valve type	Reasons for choice
V1	Under conical tank	Gate	Slim, will fit in small space
V2	Off t-piece under conical tank	Ball	Space not as restricted, easy to fit flanges.
V3	Off pump	Pressure relief	
V4	Bypass loop	Butterfly	Low ΔP , cheap, slim
V5	Dearator inlet	Butterfly	Low ΔP , cheap, slim
V6	Dearator outlet	Ball	To minimise flow disruption, easy to fit flanges.

4.5.7 Weigh tank

Modifications were made to the steel structure (Appendix B.10, B.11) so that an existing weigh tank could be positioned at a height to allow the inclination to function (Appendix B.6, B.7). An existing diverter valve system was utilised in the design to transfer flow from the main loop to the weigh tank for concentration

measurements. The valves were Paladon PV valves with a diameter of three inches, which operated at a maximum air pressure of 6 bar.

4.5.8 Cooler

It is well known that the viscosity of water and CMC vary with temperature and experience has shown that large temperature rises occur when pumping sand slurries on sister flow loops within the School. Given this information it was felt that the inclusion of a cooler in the flow loop would be advantageous. The conical tank was constructed with a double skin and a beer cooler was adapted and installed to circulate cold water through the tank jacket by A F Goose Services Ltd, Nottingham. (For heat removal calculations see Appendix B.21).

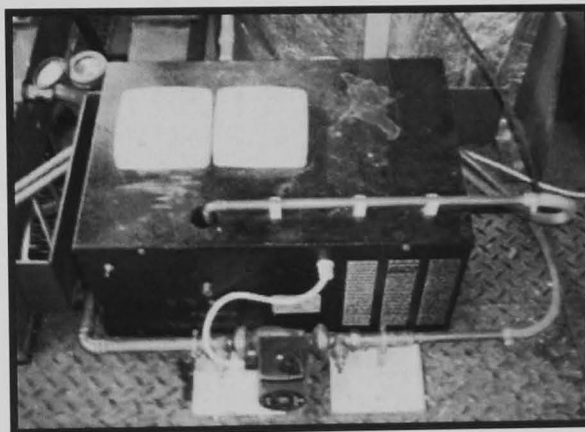


Figure 4.14: Photograph of the Cooler

4.5.9 Measurement of flow parameters

The parameters to be measured were temperature, flowrate and pressure. A K-type thermocouple temperature probe and an Endress and Hauser Promag 33 were used successfully on other pipe flow loops in the School so these were also considered for this flow loop. The Promag 33 is an electromagnetic flow meter

suitable for liquids with a conductivity $\geq 5\mu\text{Scm}^{-1}$. As each test fluid is anticipated to have a conductivity greater than $5\mu\text{Scm}^{-1}$, the Promag 33 was appropriate in this respect. The operation of the flowmeter is based on Faradays law, with the magnitude of the voltage induced being proportional to the speed of the conductor. The advantages of this type of flow meter are: linear response, clear bore, signal down to zero flow, no moving parts and can be installed at any orientation (Bain and Bonnington, 1970). A clear bore is of particular importance for the measurement of abrasive particulate flows. Literature (Béreiziat *et al.*, 1995) and experience within the School indicated that this flowmeter should be suitable for both non-Newtonian and Newtonian applications in the flow loop. The flowmeter was installed in the vertical leg, which was the manufacturer's recommended position. Adequate distance from the inlet and outlet bends was allowed to minimise flow disturbance, as shown in Table 4.4. A remote readout from the flowmeter was installed next to the pump inverter, to allow the velocity to be easily controlled easily.

Table 4.4: Flowmeter positioning

	Minimum distance from fitting /mm:	
	Inlet	Outlet
Required	250	100
Actual	1608	3750

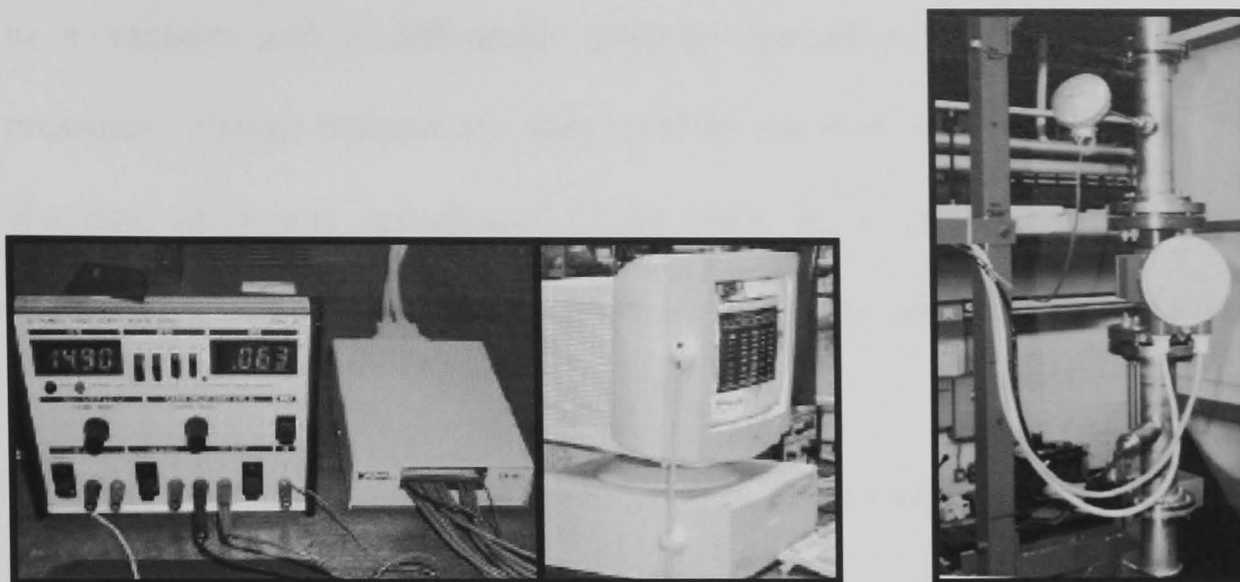


Figure 4.15: Flow measurement equipment.

Left to right: power pack, data logger and PC. Top to bottom: temperature probe, flowmeter, pressure transducer;

A data logger was purchased and installed by Ganeshalingam (2002) for use on the Perspex flow loop. The new instruments for the steel flow loop were added as additional channels on this system. The current induced in the sensors was returned to a PC fitted with a NI-DAQ 16E Series plug and play data acquisition card from National Instruments Ltd. The output signal from each sensor was recorded at a frequency of 10Hz. Ganeshalingam (2002) used LabVIEW version 6.0 to create a user interface and perform signal analysis. The data could be extracted as Microsoft Excel files.

The selection and purchasing of the pressure transducers was not so straightforward. The three main types of pressure transducer are gauge, absolute and differential. A gauge transducer compares the pipeline pressure to atmospheric pressure, while an absolute transducer compares the pipeline pressure

to a vacuum and a differential pressure transducer compares two pipeline pressures. Gauge transducers were used on the Perspex flow loop, but a lot of electrical noise was experienced which led to negative pressure drop readings. Therefore, it was felt that differential transducers may eliminate these problems.

To select a pressure transducer, an estimation of the line pressure and the pressure drop range to be measured was required. The line pressure was taken to be 1 bar and an estimate of the pressure drop range was made, based on the flow of CMC in the flow loop, using the following equation given in Govier and Aziz (1972) and rearranged from Table 2.3.

$$\frac{\Delta P}{L} = 4V^n k \left(\frac{2 + 6n}{n} \right)^n \frac{1}{D^{1+n}} \quad \text{Equation 3.1}$$

The equation is appropriate for non-Newtonian fluids flowing in the laminar regime. The fluid consistency index (k) and the flow behaviour index (n) were derived from rheology experiments and were taken to be 2.96 and 0.47 respectively (Chapter 3). This gave a minimum pressure drop (at 0.5m/s) of 0.018bar over 1m.

To determine the maximum pressure drop, a maximum velocity was required. This was decided by estimating the upper limit of the laminar regime using the experimentally determined rheological parameters and the Metzner and Reed

generalised approach as documented by Govier and Aziz (1972) and described in Section 2.2.2.

The Reynolds number is defined as:

$$\text{Re}_{MR} = \frac{D^{n'} V^{2-n'} \rho}{\gamma} \quad \text{Equation 3.2}$$

where for a power law fluid: $n' = n$ and $\gamma = k \left(\frac{1+3n}{4n} \right)^n 8^{n-1}$

Taking Re_{MR} to be 2000, the laminar regime was estimated to end at 4.06m/s. Since this was less than the estimated maximum velocity delivered by the pump (4.6m/s), a maximum velocity of 4.0m/s was substituted into Equation 3.1. This gave a pressure drop of 0.048bar/m, which was multiplied by 10, to accommodate for long lengths and increased to take account of the extra pressure loss introduced by bends and swirl pipe.

Therefore the transducers should be able to measure a differential pressure of approximately 0.018bar to 0.7bar at a line pressure of 1 bar. A list of additional requirements was drawn up for the pressure transducers. The transducers should:

- Have a high over pressure tolerance to reduce the likelihood of damage
- Be able to cope with abrasive liquids (sand and water)
- Be formed with Stainless Steel
- Be compatible with Labview, the data acquisition system.
- Have a 4-20mA output to avoid voltage drop between the transducer and the control equipment.

- Measure the differential pressure in the pipeline normally over a length of about 2 metres but have the ability to measure over 10m (cable length).

Many companies were approached, those that responded reported they had no suitable products or suggested the use of a conventional differential pressure transducer with pressure tapings through plastic pipes. This was considered unsuitable because of the possibility of CMC becoming trapped in the plastic pipes between different runs and becoming semisolid. Further consultation with several companies led to the realisation that two high accuracy gauge / absolute transducers may be a better option.

Two Model TJE Precision Gauge Pressure Transducers were purchased from RDP Electronics Ltd. They were calibrated for a line pressure of 15psig (approx. 1 bar) and had an output of 4-20mA. Each transducer had 10m of cable, 3m of which was underwater cable. The transducer was particularly designed for “*rugged industrial applications*” and had an accuracy of 0.1% full scale. It had a safe static overload of 22.5psi and a static burst pressure of 45psi. The transducer was made from stainless steel and was compatible with Labview. It therefore fitted all the requirements specified except differential. Each pressure transducers was mounted in a threaded boss that was welded to a 0.25m pipe section (see Appendix B.22 further detail of the transducer properties).

4.6 Summary

A flow loop was designed to obtain maximum length in the space allowed. It consisted of interchangeable sections of pipe of between 0.25m and 2m in length.

The design included:

- An uninterrupted straight of 12.75m (232D)
- Flexibility of swirl position
- Ability to change vertical bend radius
- Provision for the inclusion of inclined sections
- Provision for the inclusion of horizontal bends of different radius

The main components of the flow loop were a Mono pump, a de-aerator, a weigh tank (not operational), a flow meter, pressure transducers, a temperature probe and a conical tank.

After an investigation on the Perspex flow loop (Section 4.5.2), little difference was found between the performance of 0.2m lengths of 3 and 4-lobe swirl pipe. Therefore it was decided to follow the optimum swirl pipe design proposed by Ganshalingam (2002), for use on the steel flow loop. Following further tests on the Perspex flow loop a conical tank was specified for the steel flow loop with the aim of reducing dead zones and liquid holdup.

Chapter 5 OPERATIONAL PROCEDURE AND EVALUATION OF THE PIPE FLOW LOOP

This chapter outlines the general methodology used in operating the pipe flow loop, evaluates the flow loop design and highlights some problems with the performance of the system.

5.1 Summary of major changes to pipe flow loop design

In initial tests the pipe loop struggled to pump water, despite the fact that the pump motor was sized to cope with the viscous solution (Section 4.5.3). To solve the problem the motor was upgraded to 15KW and an ABB constant torque inverter drive and control panel purchased from Inverter Drive Systems, Nottingham, to control the new motor. This set-up (Figure 5.1) was found to pump water, CMC and CMC-bead mixture adequately, but stalled when pumping sand at the process conditions required. Given claims in literature that progressive cavity pumps can handle solids up to 10mm (Odrowaz-Pieniazek, 1979) and 30mm (Nesbitt, 2000), the motor required for the pump was sized based on the specifications of the viscous liquid, and the assumption made that to pump low concentrations of 4mm solids would not be a problem. However, the high settling velocity of solids in the slurries meant that the solids settled out in the pump and pipes causing blockages, (see Section 5.3.6).

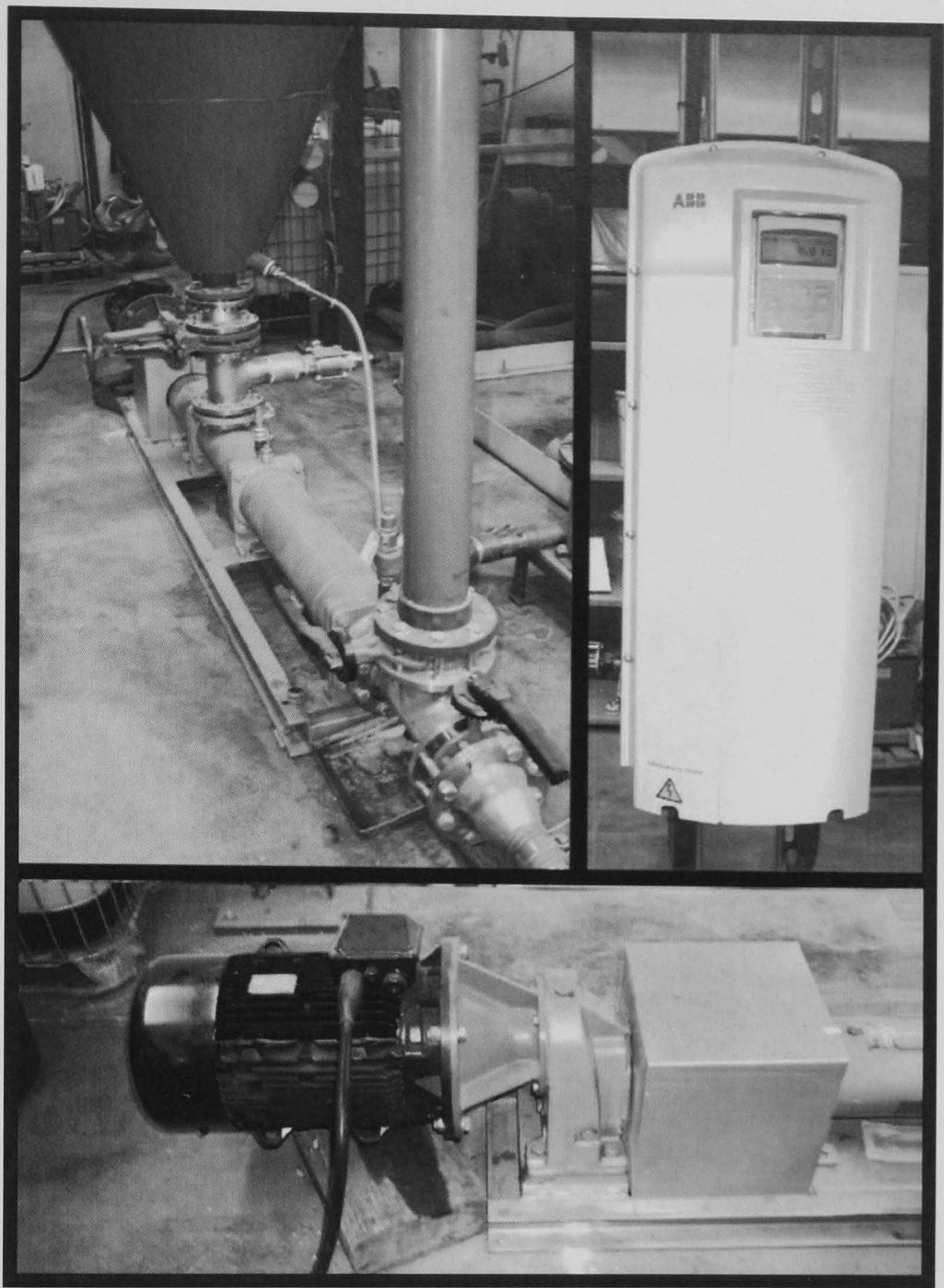


Figure 5.1: Photographs of the Mono pump, the inverter and motor.

Unblocking the system regularly was costly in terms of time, therefore it was decided to utilise a centrifugal pump adjacent to the Mono pump when conveying solids. The pump, manufactured by Warman International Ltd England (Type AH, referred to in the text as Warman pump), was controlled by a frequency inverter manufactured by PIV Electronics, and fed from a 2.5m³ covered, steel cylindrical tank (also used as the mixing tank for CMC dissolution). The tank contained a

stirrer unit manufactured by Thring-Scott, Belfast. A large ball valve and additional pipe were used to construct a link (approximately 2.5m) from the Warman pump outlet to a position close to the de-aerator. This allowed easy conversion from the Warman pump to the Mono pump and back, by reconnecting the flexible de-aerator inlet pipe and moving the flexible tank inlet pipe from the conical to cylindrical tank.

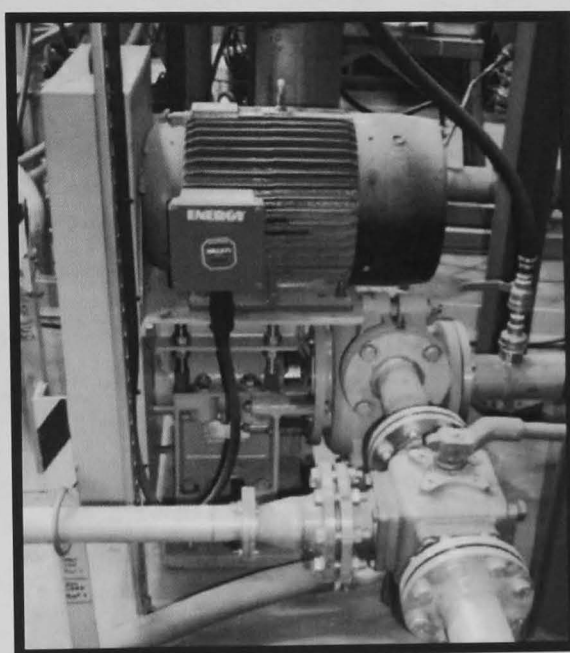


Figure 5.2: Photograph of the Warman pump.

These problems were time consuming and resulted in the construction of the flow loop running behind schedule. As a result, the weigh tank control system and the diverter valve were not commissioned. The weigh tank was by-passed, but a diverter system was essential for operation of the flow loop. Therefore, a splitter box to enable the flow to be diverted from the conical tank for sampling and shut down, was designed and installed as shown in Figure 5.3 (Gospel, 2003). Design

and construction of the splitter box was considered quicker and easier than setting up the diverter valve system.

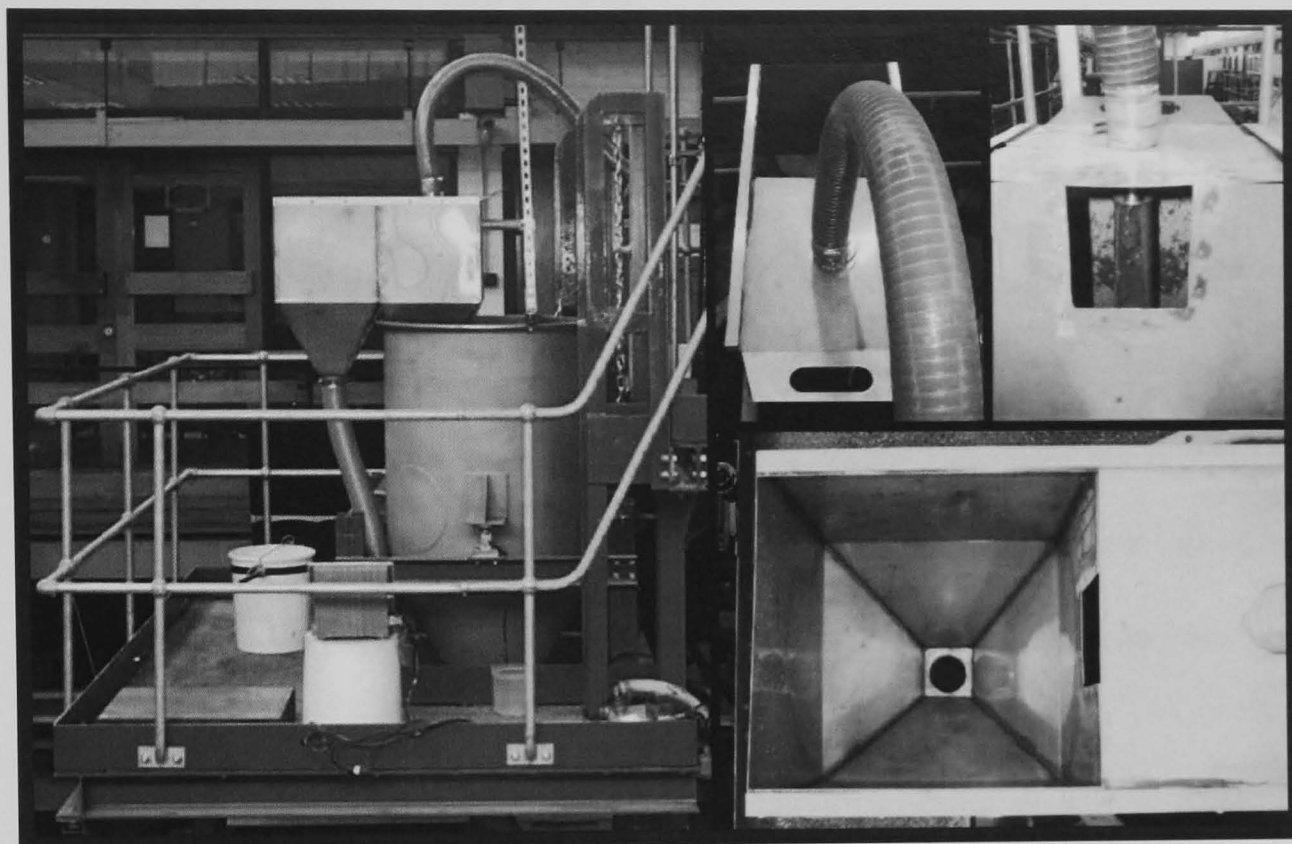


Figure 5.3: Views of the side, top and inside the splitter box

5.2 General operational procedure

1m³ of tap water was used for the all the water and water-particle tests. Firstly the flow loop was filled using the water supply valve and meter and then the pump, controlled by a frequency inverter, started at low velocity. The velocity was gradually increased to the maximum, at which point particles were added where appropriate. The above procedure applied when using either the Mono or the Warman pumps. A pre-weighed mass of particles was slowly added to the flow loop either via the weight tank (because there was no platform access to the conical tank) or via the hopper on the cylindrical tank (Figure 4.2). The slurry (or

water alone) was then circulated for 10 minutes to allow the flow to stabilise and the particles to become distributed throughout the flow loop. The appropriate tests were then performed. To shut down when testing water alone, the pump was stopped and the drain valves opened. When solids were present the splitter box was switched, to pump the solids to the settling tank and the water inlet valve was opened. When the majority of the solids were in the settling tank the pump was stopped and the remains of the slurry drained from the flow loop. All equipment was then turned off. After a test, the solids were dried in an oven at approximately 100°C and reused because of the large masses required. The dried solids were reweighed for the next test. During the water-solid tests the stirrer was set to rotate at approximately 18rpm when pumping.

To examine the effect of swirl on non-Newtonian fluids, solutions of carboxymethyl cellulose (CMC) were made. The CMC used for each test was Walocel CRTY10000 GA, supplied by Univar Ltd, Warwickshire. The dissolution methodology was designed with the aim of producing batches of CMC solution of consistent concentration and behaviour. However, small deviations from the target concentration were tolerated, as the rheological behaviour of each batch was measured before and after testing, using a Brookfield R/S Rheometer, with temperature control device FTK-CC and the CC25 measurement system (Photographs displayed in Appendix C.1).

As recommended in Chapter 3, deionised water was used to make the CMC solution. Water was prepared using a Reverse Osmosis Plant (RO-51, HOH Water Technology) belonging to the Environmental Technology Centre at the University of Nottingham. The plant removes 95-98% of all salts (HOH, 2001). The water was transported via a flexible hose to the flow loop and temporarily stored in a 1m³ sealed tank before being pumped to the autex unit, through a water meter, using a submersible pump. The conductivity of the water tested in the sealed tank varied between 8 and 16µScm⁻¹. 10kg of CMC powder was slowly fed into the top of the autex unit through a sieve and 1 litre of biocide added to the cylindrical tank. The solution was mixed overnight at 18rpm.

An implication of the use of the Warman pump for water-solid tests (Section 5.1) was that the envisaged link between the mixing tank and valve V2 (Section 4.4) could not be implemented. Therefore, after overnight mixing the CMC was transferred to the conical tank on the steel flow loop using a submersible pump (Sub 2001 Mk2, SIP Industrial Products Ltd, Loughborough). The flow loop then operated as normal with the CMC solution stored in the pipe loop overnight, between runs. As a result of the CMC characterisation tests (Chapter 3), which highlighted the need for covered storage, Polyester laser sheeting was used to seal the tank. When the CMC expired, the solution was diluted and then disposed of, with the flow loop being cleaned by opening the water inlet and drainage valves while pumping. When the solution was very dilute, the water inlet was closed,

pumping stopped and the flow loop drained. The flow loop was then refilled with water and rinsed thoroughly.

The standard method used for testing slurries in the flow loop was to set the required speed, wait for 10 minutes for the flow to settle and then record the flow rate, temperature and pressure. This was repeated as required.

Initially, following on from Ganshalingam (2002), 5000 data points were collected for each test. However, this approach was questioned because it was anticipated that over this time scale, flow conditions such as the temperature might change. The influence of the sample size on the standard deviation of the means of repeats was considered using the following formula.

σ_m = true standard error of mean

$$\sigma_m = \frac{\sigma}{\sqrt{N}}$$

σ = standard deviation of a random variable

N = total number of trials

A typical result using a sample size of 5000 gave a standard deviation of approximately 700 for a mean of 45000. This gives σ_m to be 9.90. However, when only 1600 data points were recorded for the same conditions, this gave a standard deviation of approximately the same size and hence a σ_m of 17.5. The small difference between these values and their small magnitude in comparison to

the magnitude of the mean, indicated that a sample size of 1600 would be adequate for this application. Therefore, 1600 data point were collected for all the tests.

The fact that the weigh tank was not commissioned meant that concentration measurements had to be performed by measuring the volume and mass of samples of the flow. The slurry was sampled using the splitter box, by disconnecting the flexible pipe used to empty the flow loop and replacing it with a shorter flexible pipe, from which samples could be taken. Measurement of the slurry concentration at each velocity and solids loading was laborious and took an entire day to perform. This meant that concentration measurements could not be run in conjunction with flow visualisation and it was necessary to perform them on a different day. Therefore, the concentration results indicate the approximate concentration of slurries pumped. The concentration was measured after the pressure, temperature and flow rate was logged.

To perform the tests efficiently it was necessary to change the pipe configurations without shutting down the flow loop. To do this the majority of the flow was diverted to the bypass loop by operating valves V4 and V5 (Figure 4.13). Valve V6 was then closed to trap the slurry in the de-aerator. The remaining slurry in the pipeline was then drained into buckets by removing the plug from a threaded boss, which was welded to a 0.25m pipe section. The appropriate pipe sections could then be changed, before returning the slurry that was collected in the buckets to the flow loop, via the weigh tank. The flow was then diverted back to the test loop.

5.3 Component evaluation

5.3.1 Pipework

Images of the upper and lower pipe sections are presented in Appendix C.2. During the construction of the flow loop a problem with the alignment of the flanges on the pipes arose, in which the flange at one end of each pipe was offset by a few degrees with respect to the flange at the other end. This meant that the position of the bolts twisted along a length of pipe, so that the outlet of the bends and special radius bends (for the inclined sections) were at the wrong angle. The problem was overcome by performing in-house adaptations to the pipes, including drilling new holes and slotting existing holes for the bolts.

Performing these alterations allowed the inclined section to be installed successfully in the upper leg, as shown in Figure 5.4. However, some problems were experienced because of the extra height added to the weigh tank by the splitter box (Section 5.3.6). Due to time restrictions, it was decided to perform tests on the downward inclination alone.

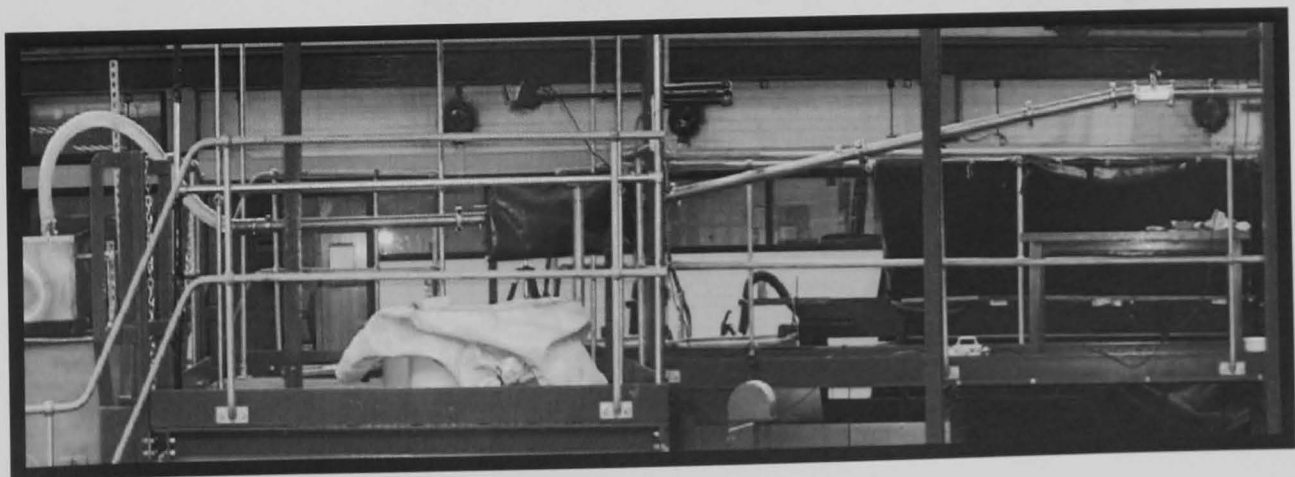



Figure 5.4: Photograph of the inclined pipe section

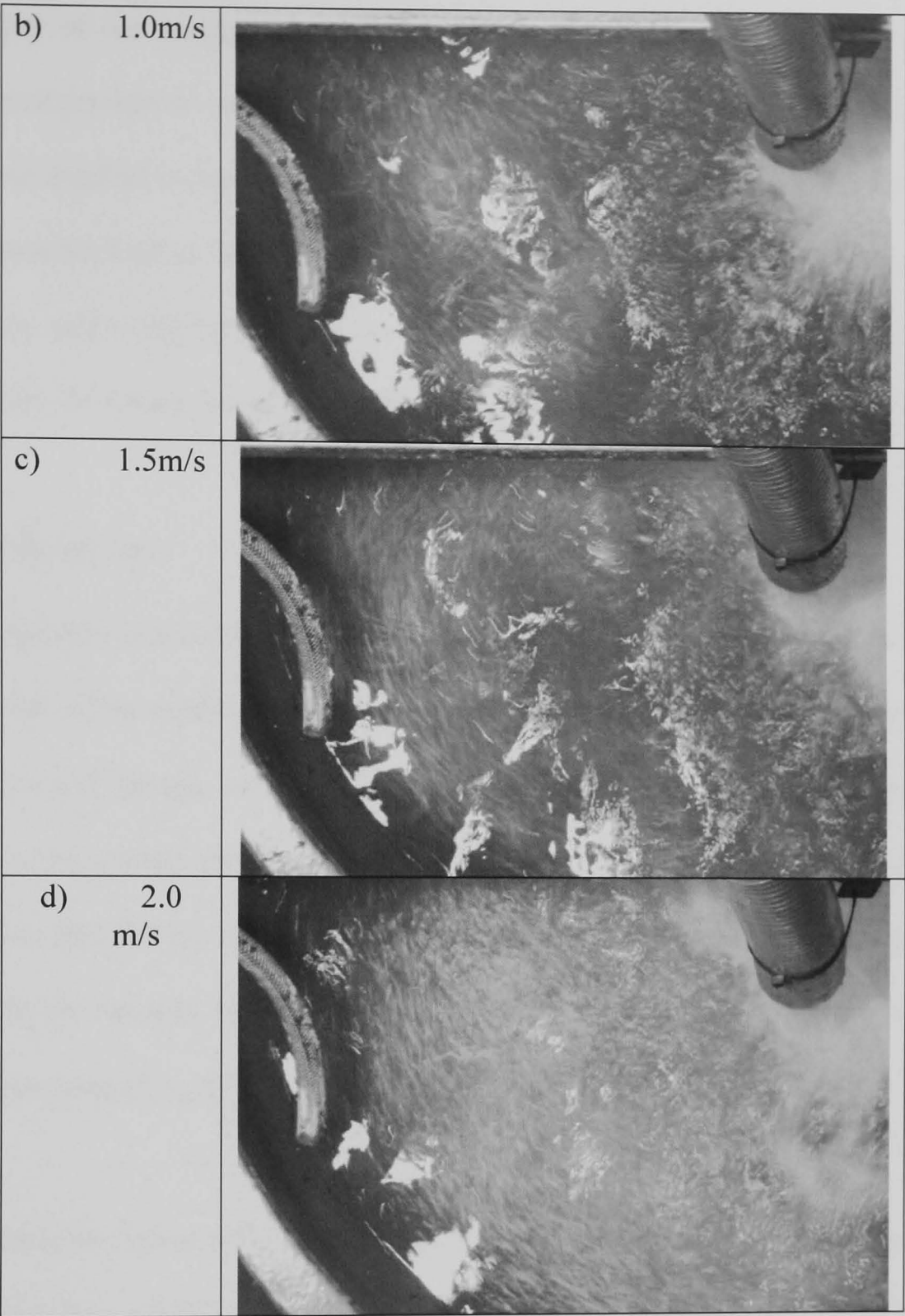
5.3.2 Tank

5.3.2.1 Shape

Figure 5.5 illustrates the distribution of particles in the conical tank. As with the results from the Perspex flow loop (Section 4.5.4), the inlet disturbed the still nature of the tank, promoting circulation of the particles. Although the idea of solids passing rapidly through the tank did not work, the tank was still superior to conventional tanks in that dead zones were eliminated. The circulation of particles in the tank had a similar effect to a mixed tank, so concentrations were monitored during testing. However, the majority of solid-liquid tests were performed using the cylindrical tank and Warman pump.

Figure 5.5: Photographs of the tank on the steel flow loop while running with 1.4% v/v beads at varying speeds.

Velocity	Short inlet pipe
a) 0.5m/s	



5.3.2.2 Size

The calculations to size the tank included the volume required to fill the weigh tank (0.725m^3), but as the weigh tank was never operational, this volume was not utilised. This meant that the tank was oversized for use without the weigh tank. Preliminary tests were performed with the design volume of 1m^3 , whilst the

possibility of the weigh tank being brought online remained. Therefore, it was considered prudent to continue with the same test volume, especially in light of the problems detailed in Section 5.5. This meant that greater quantities of CMC and solid particles had to be prepared, with the associated monetary and time costs. However, this could not have been predicted at the outset of the project and the possibility for future use of the weigh tank in the flow loop was advantageous.

5.3.3 De-aerator

Due to the size of the de-aerator, its inlet and outlet were not at the same elevation as the rest of the pipework, therefore flexible pipes, connected using worm drive hose clips and clamps, were used to link the de-aerator and pipework. These links proved to be a weak point within the flow loop. At velocities just below 3.0m/s for water and 2.0m/s for CMC, the flexible pipe became disconnected. This restricted the velocity to which the fluid could be pumped. Hence, the maximum velocities pumped in the tests were below the design velocity of 4.0m/s.

Particularly at higher velocities some leaks were experienced around the joints of the de-aerator. These were minimised by applying sash clamps to the structure and tightening nuts where possible.

5.3.4 Autex unit

To make a 1% w/w solution of CMC solution, 10kg of CMC powder had to be added in the time taken for 1m³ of water to be pumped through the autex unit.

Some problems were experienced in achieving suitable solid and liquid flow rates through the autex unit. The maximum flow from the submersible pump was not sufficient to produce a fan of water at the outlet of the autex unit and CMC powder was sometimes seen coming out of the outlet, indicating that the solid flow rate was too high. However, the solids flow rate could not be reduced because the flow rate of the water was such that the solid could barely be added before all the water had passed through the autex unit. The water flow rate could not be reduced because this rendered the vortex in the autex unit even more ineffective. A smaller autex unit would have worked more efficiently – producing a tighter vortex with less water, however, despite these problems, the use of the autex unit was more effective than simply adding the CMC powder slowly and mixing.

The metal grid over the tank inlet served to remove some of the bigger lumps of CMC produced when powder was not sufficiently wetted in the vortex. The removal of these lumps altered the concentration of the solution a little, however, a compromise in inter-batch consistency was viewed as better than having lumps of powder present in the solution.

5.3.5 Cooler

The cooler was installed and used for the tests described in Section 5.5, the axial and tangential PIV tests and the tests to assess the effect of bend radius. Following this it developed a leak and stopped working. The manufacturer was contacted and suggested that there may be air trapped in the system. However, an air release

valve had been fitted to the highest point in the circuit, so it was assumed that the problem was with the cooler itself. The cooler was not repaired because the remaining tests were to be performed on the Warman pump and thus the cooler circuit would not be utilised.

The temperature rises recorded by the temperature probe even when pumping 2.7% v/v slurries with the Warman pump were not excessive (approximately 0.5°C/hr). The reduction in operational velocity and concentration reduced the need for the cooler.

5.3.6 Splitter box

Operation of the splitter box was successful for the standard configuration (Figure 5.6). A flexible pipe allowed the top of the splitter box to be slid through the two positions. However, when the configuration was changed to include a downward inclination in the top leg, the final level of the top leg dropped. This meant that the flexible pipe curved up before dropping again to the splitter box, as shown in Figure 5.4. When pumping solids, this sudden upward inclination was prone to blockage. The problem was first experienced attempting to pump 5.4% v/v sand at 1.5m/s when the entire flow loop became blocked with sand. Further tests were then performed incorporating a 1m long 3-lobe steel swirl pipe before the flexible pipe in an attempt to minimise the problem. This did not allow the initial target concentrations to be pumped successfully, but a maximum concentration of 2.7% v/v could be pumped at 0.5m/s. Therefore the planned test concentrations were

changed from 1.4%, 2.7% and 5.4% v/v to 1.4%, 2.0% and 2.7% v/v. These remain in keeping with the concentrations tested by Ganeshalingam (2002).

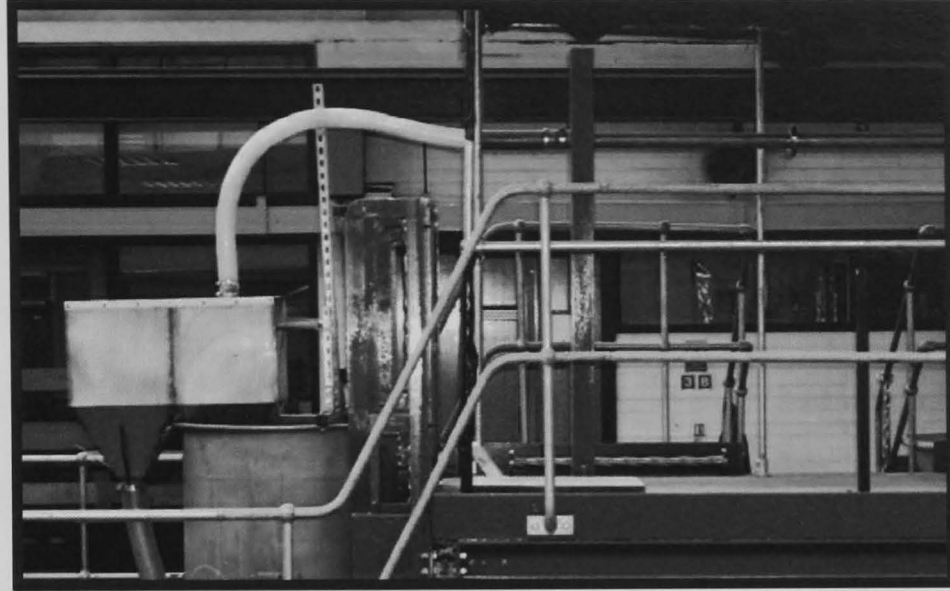


Figure 5.6: View of the top leg of the flow loop in the standard configuration.

5.4 Calibration

Calibration of the sensors, particularly the pressure transducers, was very important because the components were subject to variation due to ambient temperature changes, component aging and electrical noise.

A calibration certificate was received with the pressure transducers, which displayed the capacity of the transducers and the calibration factor. These were used to calculate the relationship between the current received and the pressure indicated. This data was input into Labview and the pressure transducers calibrated by recording the pressure at known heights of water. When the recorded values and the pressure calculated from the head of water did not match,

as shown in Appendix C.3a, a correction was made to the pressure-current equation. This procedure is the same as that used by Ganeshalingam (2001) for the Perspex flow loop, with the exception that Ganeshalingam simply read the head of water from a scale placed next to the vertical leg. To calibrate the pressure transducers on the steel flow loop a depth meter was needed. A weighted 2-core wire was connected to a multi-meter and the free ends lowered down the vertical leg. The free ends were separated so the circuit would only be complete when they touched the water surface. At this point the reading on the multi-meter changed and the depth of the wires was measured.

The temperature probe was calibrated at four different temperatures using a mercury thermometer as standard. As can be seen from Appendix C.3b, the results showed that the temperature probe was reading low by 2.5°C over the range tested. To resolve this, 2.5 was added to the 'user value' that fixed the calibration performed by Labview. The temperature probe was then tested again, in the same way, to check the calibration. A difference of 0.2°C over the temperature range assessed was recorded and considered acceptable.

The flowmeter was calibrated by comparing the readout to a velocity calculated by taking a timed sample of the flow. The sample was taken by diverting the flow from the loop into a bucket using the splitter box. The bucket was calibrated so that the volume of the sample could be calculated and an up and down sweep was performed. The flowmeter routinely gave a higher value than the calculated value

with a maximum difference of 16%. However, the majority of the results gave a difference close to 10% (Appendix C.3c and d). Given the human error involved in the timed flow sample, these results were considered satisfactory.

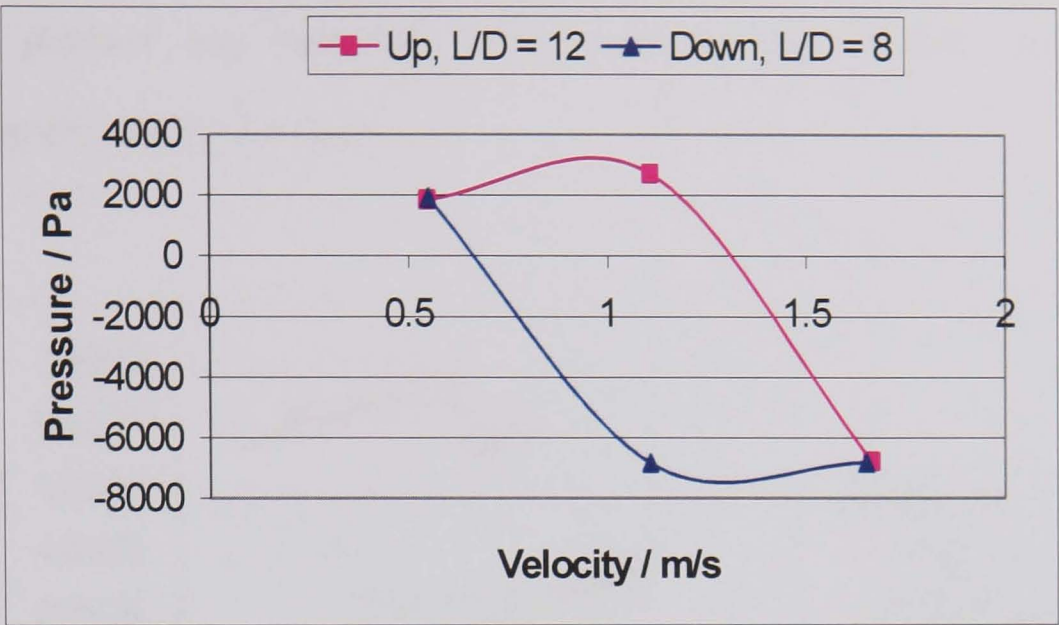
5.5 Hysteresis

After calibration, a series of tests were conducted to look at the decay of swirl in water and CMC using particle image velocimetry. The velocity was increased from 0.5m/s to 1.0m/s and 1.5m/s then decreased to 1.0m/s and 0.5m/s (approximately $Re = 27\,500 - 82\,500$ for water and $Re_{MR} = 150 - 650$ for CMC). During the axial PIV tests unexplained pressure patterns were observed for the water results (see Figure 5.7a), so further tests, consultation with manufacturers and a literature search were conducted in parallel to investigate this phenomenon. However, as shown in Figure 5.7b the effect was minimal when pumping CMC and later results using a different batch of CMC and transducers taken from the Perspex flow loop, shown even less hysteresis (Figure 5.7c).

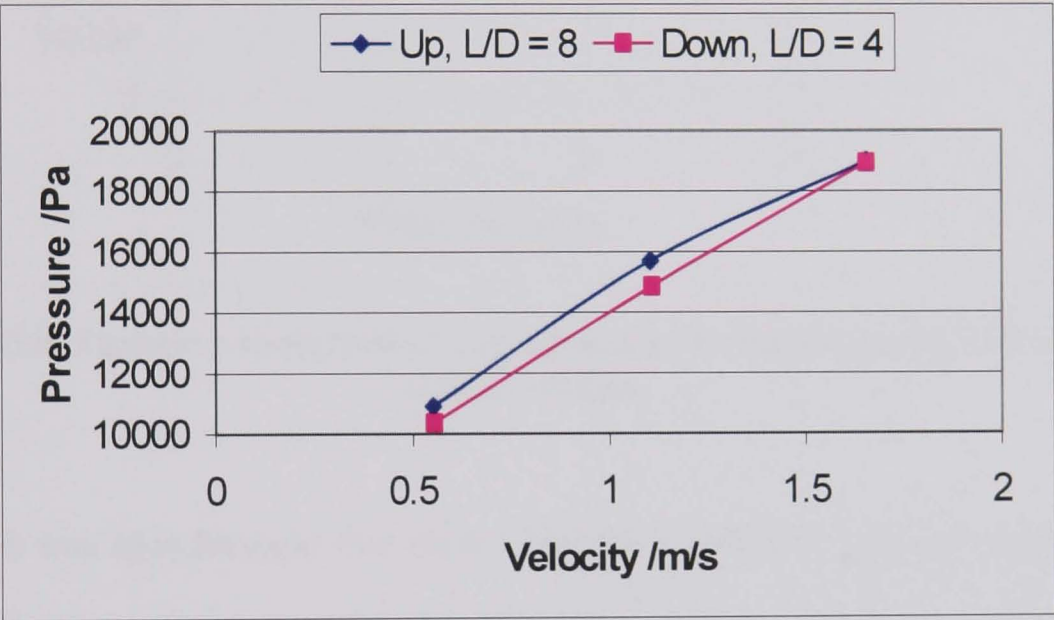
Figure 5.7: Graphs showing the pressures recorded during PIV experiments.

The L/D values refer to the position at which PIV results were taken.

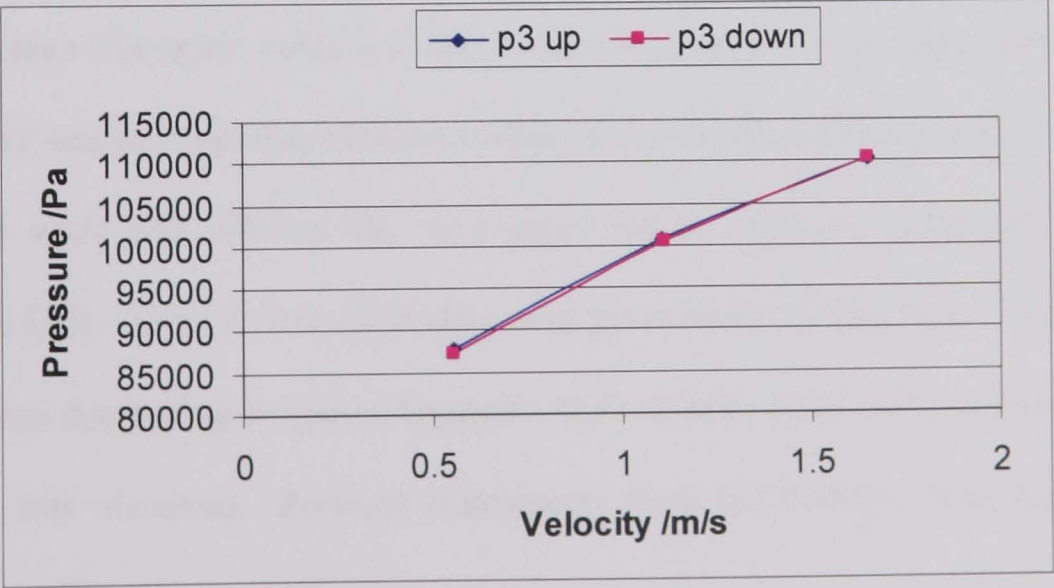
a) Pressure over top leg with swirl, water and steel transducer, PT30



b) Pressure over top leg with swirl, CMC and steel transducer, PT30



c) Pressure over 220mm bend with swirl, CMC and Perspex transducer, p3



A series of tests were performed in which the velocity was increased and decreased incrementally while measuring pressure. Figure 5.8 illustrates that a different pressure was measured when increasing the velocity than when decreasing the velocity for water.

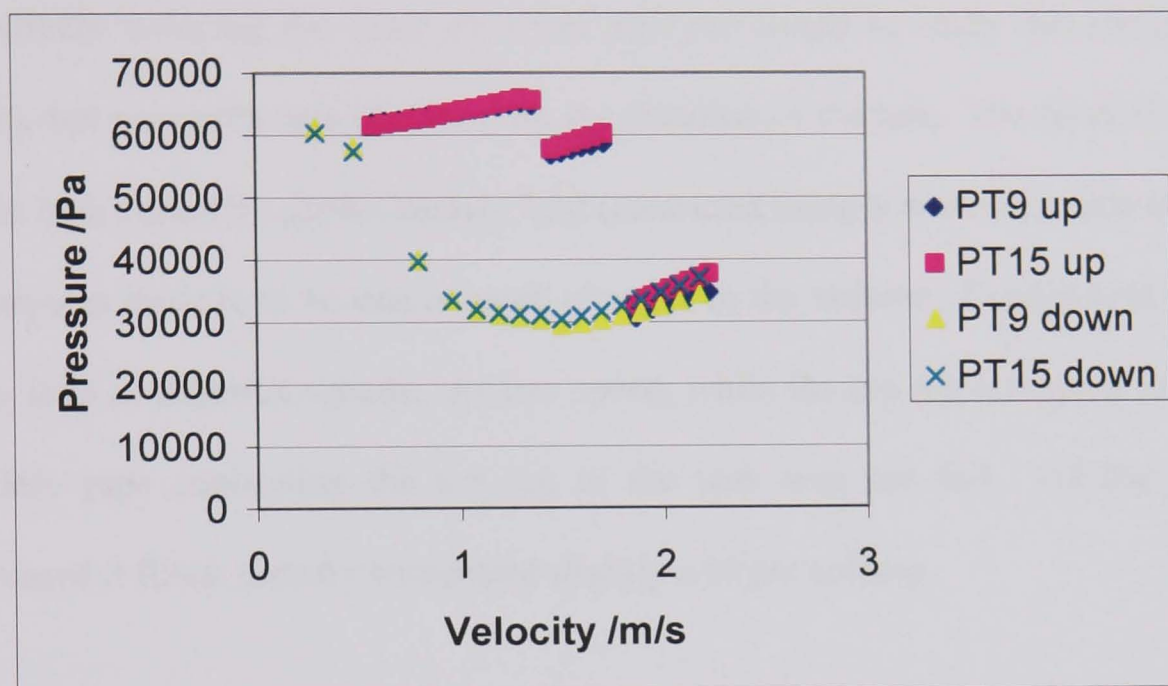


Figure 5.8: Pressure hysteresis observed using the Mono pump with the de-aerator online.

Initially it was hypothesised that there could be a problem with the pump so the Warman pump was connected to the flow loop and the test performed again. A hysteresis area was again evident in the results (Appendix C.4c), although the area was slightly smaller than that observed when using the Mono pump and tests were performed with and without the de-aerator online with no noticeable effect (Appendix C.4). Next, a new calibration was performed, increasing the head over 6 points then decreasing it again (Appendix C.5). Under these static conditions no hysteresis was observed. Pressure transducers from the Perspex flow loop were

added to the steel flow loop to try to identify whether there was a problem with the pressure transducers, but there was little change from previous results (Appendix C.6a).

It was hypothesised that a vortex may be forming in the tank at high speed effectively reducing the head, so a test was performed to study this (Appendix C.6b), but no vortex was observed for the duration of the test. The level of water in the tank varied by approximately 2cm (measured using a mark on a plumb line), which was thought to be due to small changes in the volume of water held in the flow loop at different speeds. At low speed, while the top leg remained full, the flexible pipe connecting the top leg to the tank was not full. As the speed increased it filled, thereby containing slightly a larger volume.

Small air bubbles were observed trapped in the recess between the Perspex pressure transducers and the pipe, although they did not cover the whole transducer. These were present at low velocity but disappeared by 1.2m/s. This approximately corresponded to the first drop in pressure. However, bubbles were not present for second drop (Appendix C.6b). For the remainder of the tests the flow loop was run for a few minutes at $>1.5\text{m/s}$ before testing, which removed any bubbles from the Perspex pressure transducers. The presence of bubbles was then monitored throughout the tests and bubbles were never observed; yet the hysteresis remained.

Therefore it was proven that neither the Mono pump, the presence of the de-aerator, the pressure transducers, the production of a vortex or air trapped in the pressure transducers were the sole cause of the hysteresis observed. In addition it was confirmed that measuring the pressure drop over the swirl pipe or bend ($R/D = 4$), and moving the pressure transducers further away from the bend, had no effect on the hysteresis pattern (Appendix C.6c and d). Lastly a similar test was performed on the Perspex flow loop, which yielded a smaller area of hysteresis with a different pattern (Appendix C.6e). The fact that the Perspex pressure transducers produced a different hysteresis pattern when installed on the Perspex loop, compared to the steel loop, suggested that the origin of the problem was not the transducers.

Throughout this testing regime, consultation with outside companies was undertaken. The pressure transducer manufacture, RDP, stated that the TJE transducers have approximately a 20 Pa hysteresis and cited the pump as a possible problem. Mono Pumps Ltd suggested the following:

Table 5.1: Result of consultation with Mono Pumps Ltd

Mono suggestions	Comment, Action taken
Probably a system problem	-
The output could be unstable because the pump is running slow – check the speed is not varying on the inverter.	Another up down sweep was performed recording the pump speed at each velocity. Appendix C.6f shows that the up and down lines coincide.
Flowmeters are slow acting and pressure transducers fast acting, wait longer between setting flow and taking reading.	A stabilisation time of ten minutes has always been used. To extend this would risk the flow conditions changing, e.g. Temperature.
Pressure transducers can be effected by pulsations	Consultation with RDP confirmed that if the calibration lines (in static conditions) for the up and down direction coincide the transducers are unlikely to be the cause of the hysteresis. Pulsing could bring forward the date of fatigue. However, signs of damage are not yet evident.
Air can effect flow meter	The flowmeter was calibrated by comparing the readout to a velocity calculated by taking a timed sample of the flow. An up and down sweep was performed. The flowmeter routinely gave a higher value than the calculated value with a maximum difference of 16%. The difference between results on the up sweep and down sweep was insignificant (Appendix C.3c and d).
Install pressure dampening	Wasp (1977) highlights that pulsations can be a problem with positive displacement pumps, however the test indicate the same phenomena occurs with the Warman pump, so this solution was disregarded.
Recommend 4-point pressure tapings.	No action was taken because of time constraints
Recommend snubbing, electronic damping.	
Is it operating in transitional regime?	Calculations (Appendix C.7) showed that the flow of water in the loop was not completely turbulent.

A literature search yielded little results except a paper by Kaupert and Staubli, (1999). They performed experiments to determine the position, size and strength of impeller re-circulation for a centrifugal pump and stated:

'Hysteresis in a pump characteristic results from instability phenomena involving complex three dimensional flow with re-circulation'

The graphs they presented had a different shape and a small hysteresis height (approximately 4027Pa) in comparison to the current results (hysteresis height of approximately 30000Pa). Therefore, the results were on a different scale to the current results. Hence the hysteresis in the steel flow loop when using the Warman pump was probably not due to impeller re-circulation.

The information leads to the conclusion that the hysteresis may have occurred because the flow in the loop was not completely turbulent. This theory is supported by the fact that when pumping CMC in the laminar flow regime little hysteresis was observed. Given the particularly high velocity required to achieve complete turbulence when pumping water (Appendix C.7), little could be done to avoid operating below this threshold. Ideally, more research into this phenomenon should be performed. However, the current work was primarily concerned with pressure drop results and those did not show hysteresis (Section 5.6), so to avoid further delay it was decided to perform all tests on the down curve.

5.6 Negative pressure drop

When performing the investigation into hysteresis negative pressure differences were observed at low velocities in the lower leg, as shown in Figure 5.9. In addition, the portion of the curve that was negative increased with time (Results shown in Appendix C.8, in chronological order). A recalibration then reduced the negative portion of the curve to its initial level, before it increased again.

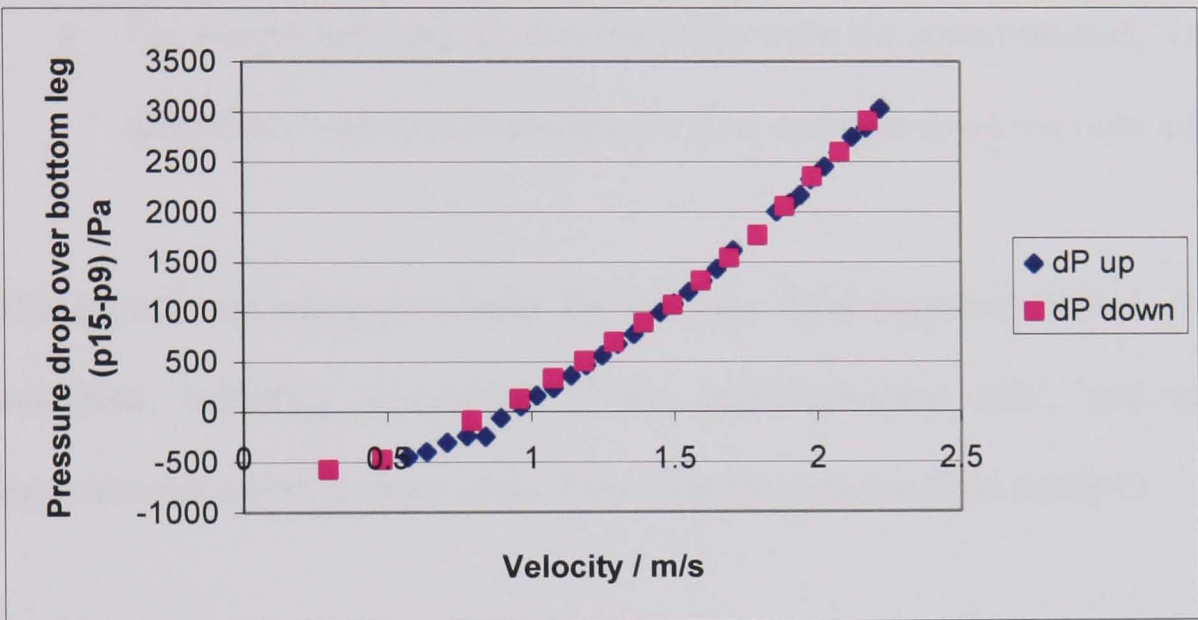


Figure 5.9: Pressure drop over the lower pipe section when pumping water with the Mono pump, with the de-aerator online.

Despite the manufacturers claim that the transducers were suitable for “*rugged industrial applications*”, they rapidly drifted from the calibration. A possible reason for this was the high regularity with which the transducers were moved, made necessary since only two were purchased. The Perspex transducers remained faithful to the calibration longer and since a greater number were available they could be moved less frequently. It was therefore decided to use the Perspex pressure transducers for the remainder of the experiments.

5.7 Summary

This chapter describes the differences between the commissioned flow loop and the design, explains the reasons for these differences and evaluates the performance of key components. The most significant changes were as follows:

- The purchase of a larger motor for the Mono pump
- Construction of a link between a Warman pump and the pipeline to allow the pump to be used for particle slurries.
- The weight tank and the diverter valve were not commissioned. Instead a splitter box was used to sample the flow and shut down the flow loop.

The general operating procedure for the pipe loop experiments has also been described, including dissolution of the non-Newtonian fluid, and start up, measurement and shut down of the flow loop for each test fluid category.

Some unusual pressure results, which show hysteresis, are presented and discussed. The effect was attributed to operating in the transitional turbulent zone and since the pressure loss results appeared normal, the test programme was continued without further delay. The steel pressure transducers showed an unacceptable level of drift, therefore the Perspex transducers were employed for the remainder of the tests.

Chapter 6 VISUALISATION OF SWIRLING FLOWS

Particle image velocimetry (PIV) was employed to examine the distribution of axial and tangential velocity downstream of the swirl-inducing pipe. The experiments were undertaken in a similar way to those of Ganeshalingam (2002) to maintain some constancy with his work while advancing knowledge about the application of swirling pipe flows to industrial use. In addition the application of a novel electrical resistance tomography (ERT) technique to pipeline transport was investigated.

6.1 Visualisation of swirling flows using particle image velocimetry

6.1.1 Introduction

To evaluate the intensity and decay of swirling flows and consequently the performance of swirl flow pipes and their successful application to industrial use, an accurate appreciation of the distribution of axial and tangential velocities was required. Ganeshalingam (2002) initiated the determination of these parameters for swirl flow pipes by performing extensive CFD analyses and validating his results with experiments on the Perspex flow loop using particle image velocimetry (PIV) and by comparisons with published data. He found good agreement between his CFD predictions and experimental results in terms of pressure drop and axial velocity downstream of a swirl flow pipe and also found

that decay rates obtained from CFD showed good agreement with the exponential formula of Steenbergen and Voskamp (1998). In addition, he noted that the radial distribution of the tangential velocities determined by CFD, fitted a pattern described by Steenbergen and Voskamp (1998). They classified swirl flows as: the “*concentrated-vortex (CV)*” pattern in which the rotation is concentrated near the pipe centre, the “*solid-body (SB)*” pattern with an almost uniform rotation and the “*wall-jet (WJ)*” with angular momentum distributed near the wall, as shown in Figure 6.1. Ganeshalingam’s results closely matched the wall-jet classification. To extend Ganeshalingam’s work, a set of experiments similar to his validation tests were performed on the steel flow loop in an attempt to assess the impact of pipe roughness on the decay of swirling flows and obtain experimental confirmation that the swirl flow pipe produced a wall-jet swirl pattern. These experiments were also performed using a carboxymethyl cellulose solution to investigate the use of swirl-inducing pipe when pumping viscous liquids.

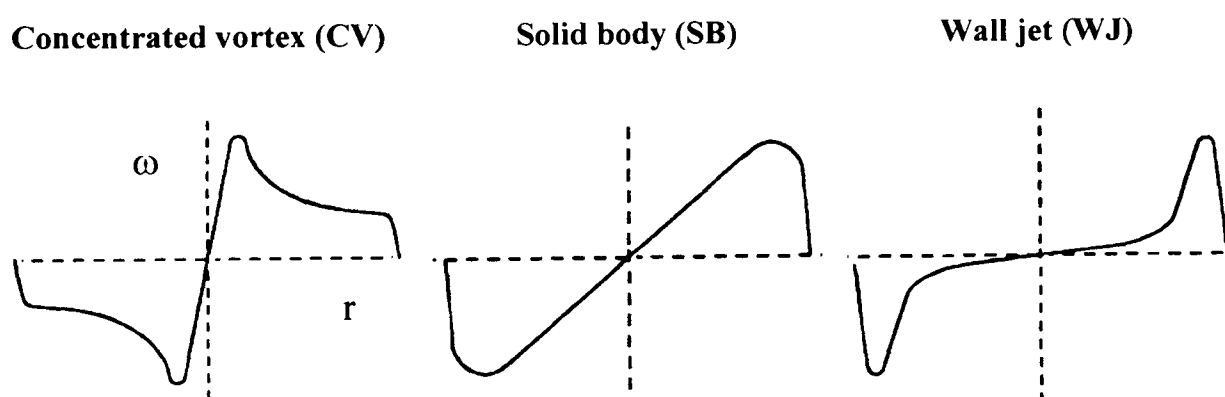


Figure 6.1: Classification of swirl types (redrawn from Steenbergen and Voskamp, 1998)

6.1.2 General methodology

A PIV system is a non-intrusive technique that can be used to measure the instantaneous velocity field inside a pipe. It is an optical technique, which measures the velocity of micron-sized tracer particles within the flow, through a transparent test section. The flow is illuminated in most cases, by a thin laser sheet, which can produce pulses of light of specified duration. This light is scattered by the tracer particles and recorded by a camera, positioned perpendicular to the light sheet. The camera is used to capture multiple images of the position of particles within the flow so that the particle displacement can be determined by cross-correlation of consecutive images. By combining this information with the knowledge of the time interval between the images and the camera magnification, the velocity of the particles can be calculated. A PC equipped with acquisition and analysis software is used to control this process. Adrian (1991) and Grant (1997) provide detailed descriptions of the theory and application of PIV systems.

The Dantec FlowMap® particle image velocimetry system (Dantec Measurement Technology Inc., Skovlunde, Denmark) used by Ganeshalingam was utilised again for the current experimental work, which was performed with assistance from the School of Mechanical, Materials and Manufacturing Engineering, University of Nottingham.

Dantec Dynamics (2003) recommend the use of seeding particles with a specific gravity close to 1 g/cm^3 and a size in the range $5 \text{ }\mu\text{m}$ to $100 \text{ }\mu\text{m}$, but state that any particles that follow the flow satisfactorily and scatter enough light can be used. For this application the flow was seeded with talc with a specific gravity of 2.79 g/cm^3 (determined using a 50ml density bottle with water) and a 50% passing size of $26\text{ }\mu\text{m}$ (Appendix D.1, determined using a Malvern Mastersizer S). The light source, a twin pulsed Nd:YAG laser produced light at a wavelength of 532 nm . Beam transmission optics were used to produce a laser light sheet with a thickness of $1\text{-}2\text{mm}$.

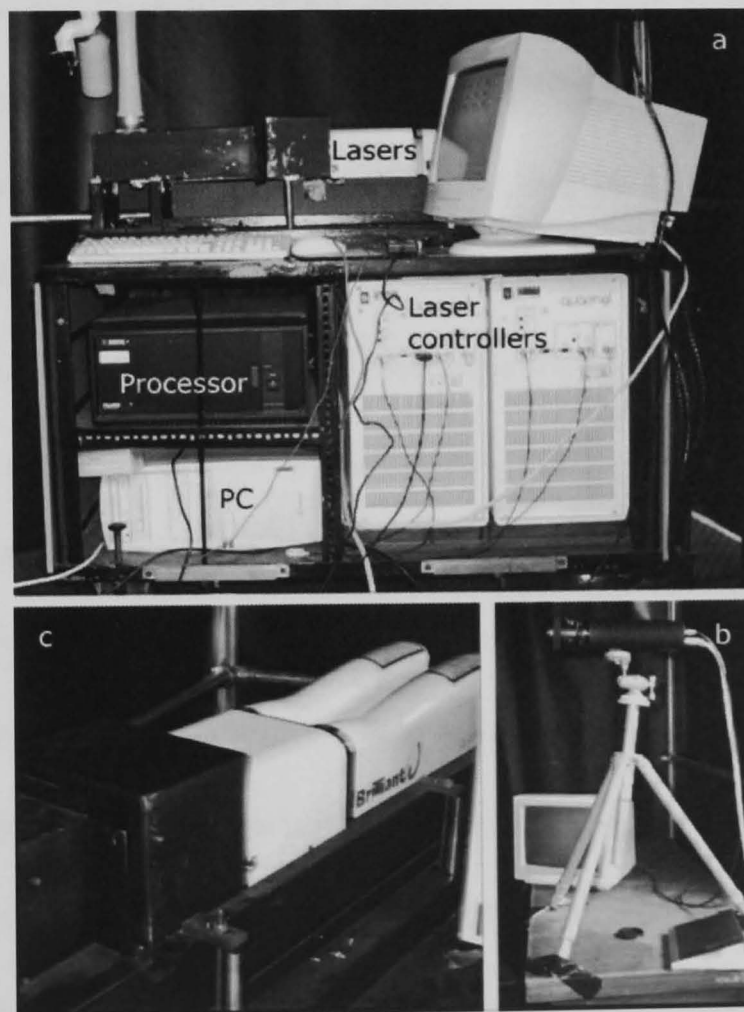


Figure 6.2: a: Laser trolley containing the lasers and controllers, processor and PC, b: lasers, c: camera and viewing screen.

A Dantec CCD camera, model 80C42 Double Image 700/type 8, with a resolution of 768 x 498 pixels, was used to capture images of the flow field in the area lit by the laser sheet. For each process condition two bursts of light were fired from the lasers, each consisting of two pulses and the camera was set to capture 8 images: 2 pictures for every laser pulse. The frame rate of the camera was synchronized to the laser by the Dantec PIV 2000 processor and software.

6.1.3 Measurement of axial velocity

6.1.3.1 Additional methodology

The axial velocity was measured in the upper leg, for both water and CMC, when preceded by a swirl pipe or a standard pipe. When using the swirl pipe measurements were taken at 4 positions: 4, 8, 12, and 16 diameters downstream of the swirl pipe. When using the standard pipe, measurements were taken at one position only ($L/D = 16$, a distance of $189D$ from the bend), under the assumption that the flow was stable. For each test condition measurements were taken at three nominal velocities of 0.5, 1.0 and 1.5m/s (approximately $Re = 27\,500 - 82\,500$ for water and $Re_{MR} = 150 - 650$ for CMC). The equipment was set up as shown in Figure 6.3 and for each new position the light source and camera were moved. The positions required were determined by referring to graduated adhesive tape placed along the viewing box. The time between laser bursts was arbitrarily fixed at 1000ms, while the time between pulses was set according to the velocity as shown in Table 6.1, to ensure the same particles were captured in consecutive images.

Table 6.1: Time between laser pulses

Axial velocity / m/s	Time between pulses/ μ s	Estimated distance travelled by particle /mm
0.5	2000	1.0
1.0	1000	1.0
1.5	500	0.75

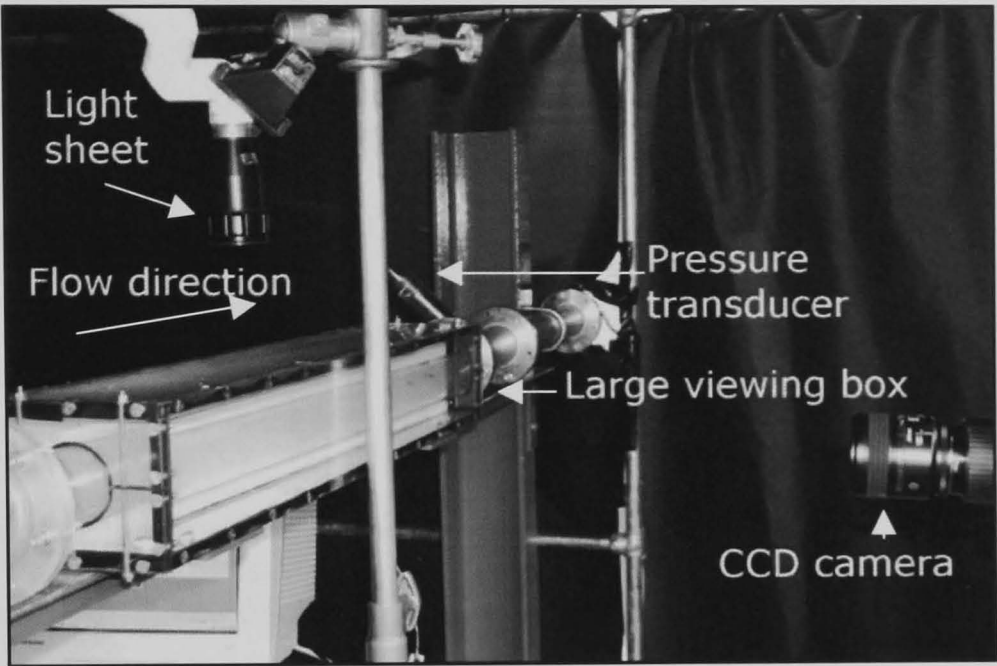


Figure 6.3: Experimental set up for axial PIV tests.

6.1.3.2 Biological and Rheology test results and discussion

The CMC solution was made on the 2nd of May 2003. Photographs of the biological test strips are shown in Appendix D.2. They show that significant amounts of bacteria were detected in the CMC from the 6th to the 9th of May. This indicated that the biocide concentration used in the desktop experiments (Chapter 3) was not sufficient to keep the solution free of bacteria in the large-scale tests. This may be due to a lower level of cleanliness in the pipe loop laboratory than in the rheology laboratory. A bacteria check was made every day, however the test strips had to be incubated for 48 hours, so there was a 48 hour delay in detection. Therefore it was not until after testing on the 9th of May that more biocide was added. Following this the bacteria strips showed that $<10^2$ bacteria were present.

Although in the desktop tests the presence of bacteria was not conclusively proven to affect the rheology of the samples, the presence of bacteria in the large-scale test could be traced in the apparent viscosity measurements. Figure 6.4 shows a trend of decreasing apparent viscosity over the 6th to the 9th of May after which the measurements become more stable. However over the 7th and 8th of May, when the Axial PIV tests were performed a plateau was observed and the rheology was relatively constant.

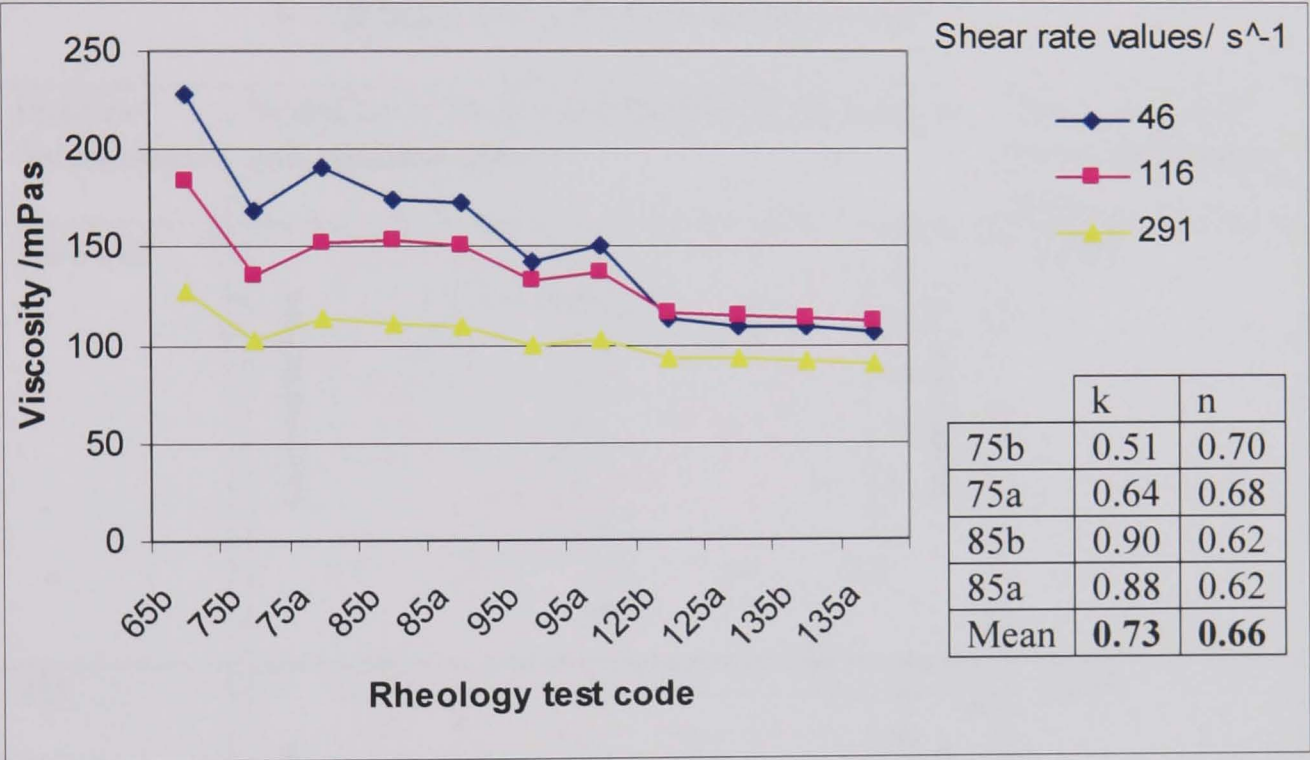


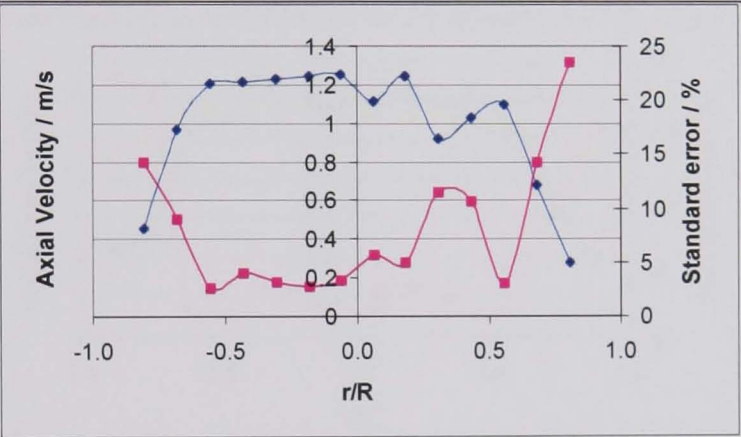
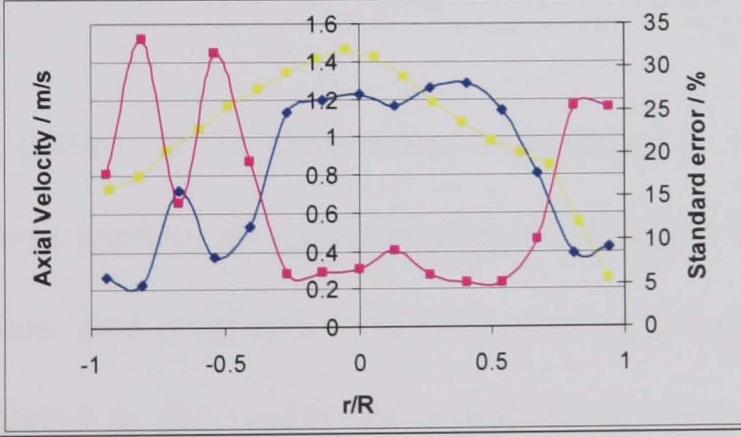
Figure 6.4: Rheological parameters and graph to show the change in apparent viscosity with age for axial PIV tests
(code: day, month, before or after testing in pipe loop)

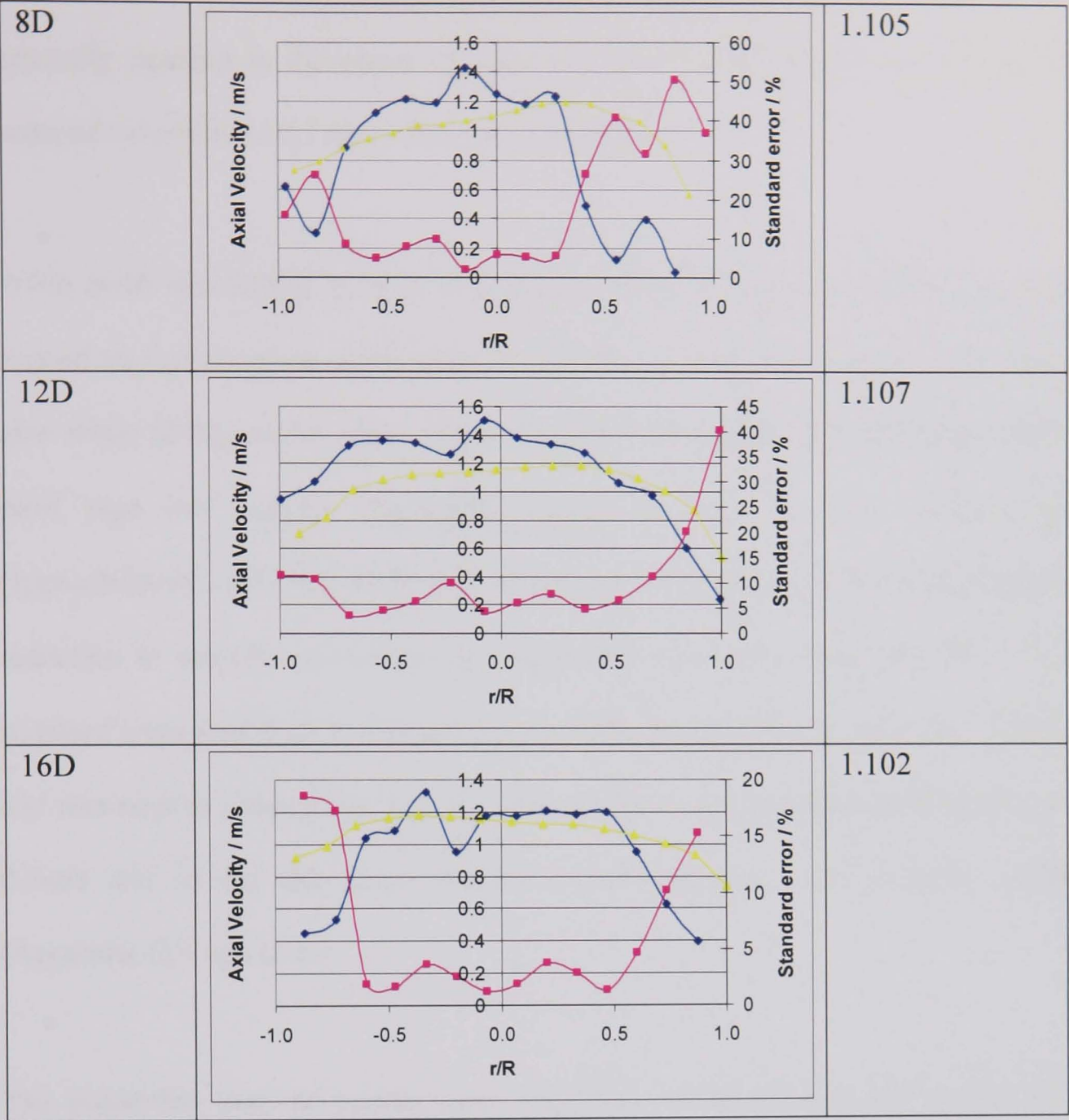
6.1.3.3 Flow test results and discussion

Figure 6.5 shows the results for the axial PIV test performed on water at 1.0m/s. The procedure used to process the data and the remaining results are presented in Appendix D.3-D.6.

Figure 6.5: Variation in axial velocity with cross section for water at a nominal velocity of 1.0m/s (Re = 55 000)

- Key: —◆— Mean x-sectional velocity: current results
 —■— Mean x-sectional velocity: Ganeshalingam (2002)
 —■— Standard error (16 points: current results)

Position downstream	Variation in axial velocity with cross-section and standard error	Mean velocity from flowmeter/ m/s
No swirl		1.062
4D		1.111



Referring to the curves for the current results displayed in Figure 6.5, when no swirl-induction was applied, the graph implied the standard curve for cylindrical pipe flow. The low data point at 0.4 r/R is matched by a higher error. A similar pattern was repeated in the results for a nominal velocity of 0.5 and 1.5m/s (Appendix D.4 and D.6), although the 1.5m/s curve was slightly flatter than the others. The results shown in Figure 6.5 have a centreline velocity between 1.2 - 1.5m/s, a range a little higher than the mean velocities recorded by the flow meter,

as expected. The results for all velocities demonstrate this, with data points generally peaking in the centre at velocities of 0.5 - 0.6m/s and 2 - 2.2m/s for nominal velocities of 0.5 and 1.5m/s respectively.

When swirl was added, at short distance downstream the axial velocity profiles formed an asymmetrical shape with the velocity staying higher at one wall of the pipe while falling at the other. At a distance of 4 diameters downstream of the swirl pipe the velocity diminished rapidly towards the base of the pipe (approximately $-0.4 r/R$), while at a distance of 8 diameters downstream a similar reduction in velocity was observed towards the top of the pipe ($0.4 r/R$). The standard error was high in these positions, however the change was very distinct and was seen to a lesser extent in the same positions at a nominal axial velocity of 0.5m/s and in the 8D graph for the 1.5m/s nominal axial velocity results (Appendix D.4 and D.6).

The possibility that the results were indicative of pulsation in the system was considered. Mizushima *et al.* (1975) discussed the effect of pulsation on turbulent flows with particular reference to the velocity profile. They found that the velocity profiles were similar to those of steady flow except that near the wall the profiles were contorted. The shapes they recorded displayed some similarity to the results obtained here, although the contortions appeared much smaller.

Miller (1989) described a threshold pulsation index as part of a method to estimate bias errors for flowmeters and stated that a threshold pulsation index of 0.03 was a

reasonable definition of steady flow. Therefore the following equation was applied to determine whether pulsation was present in the current results.

$$\text{Pulsation Index} = \frac{V_{\max} - V_{\min}}{(2 \times V_{\text{mean}})} \quad \text{Where } V = \text{Velocity} / \text{m/s}$$

Typical pulsation indices calculated were 0.029, 0.014, and 0.009 for nominal velocities of 0.5, 1.0, and 1.5m/s respectively. Therefore it was concluded that pulsation was not a significant problem. It is worthy of note that the Pulsation Index increased in value as nominal flow velocity was reduced. It reached a near-critical value when the velocity was reduced to 0.5m/s. The conclusion that pulsation was not significant for the pipe flows tested was supported by the observation that low values occurred at opposing sides of the cross-section as the swirl progressed down the pipe and that downstream the results became more symmetrical and appeared to be returning to the original velocity profile. In addition, it was found that measurement of an asymmetrical pattern downstream of a swirl inducing pipe was not unprecedented, since Wang *et al.* (2003) detected crescent shaped zones of high concentration to the top right of the pipe, using electrical resistance tomography.

Therefore, the asymmetry in the results was considered to be a symptom of swirling flow. This was logical, since at the outside of the pipe the swirling fluid travelled at an angle through the illuminated region. The laser sheet was thin and

therefore only a fraction of the x-component of the velocity was captured, resulting in the low values observed.

This theory was further supported by CFD results obtained by Ariyaratne (2004), which predicted that for a 4-lobe swirl pipe, high tangential velocities occurred in the lobes with lower tangential velocities occurring in a core of circular cross-section (Figure 6.6b). From this, it was reasonable to conclude that the asymmetry measured by PIV was a result of the distinct demarcation between the core and lobe zones with low axial velocities recorded in the lobe zones for the reason explained above. It was also noted that the core of the pipe had a diameter of 39mm, which constituted 78% of the pipe diameter, and that the central core appeared approximately circular to about 50% of the pipe diameter from the centre. Comparing these values to Figure 6.5, it can be seen that the distortions occur predominantly outside this zone. Furthermore, the outer layers of the core displayed a rounded 4-sided shape, which is suggested to have contributed to the increased standard deviation observed in this area.

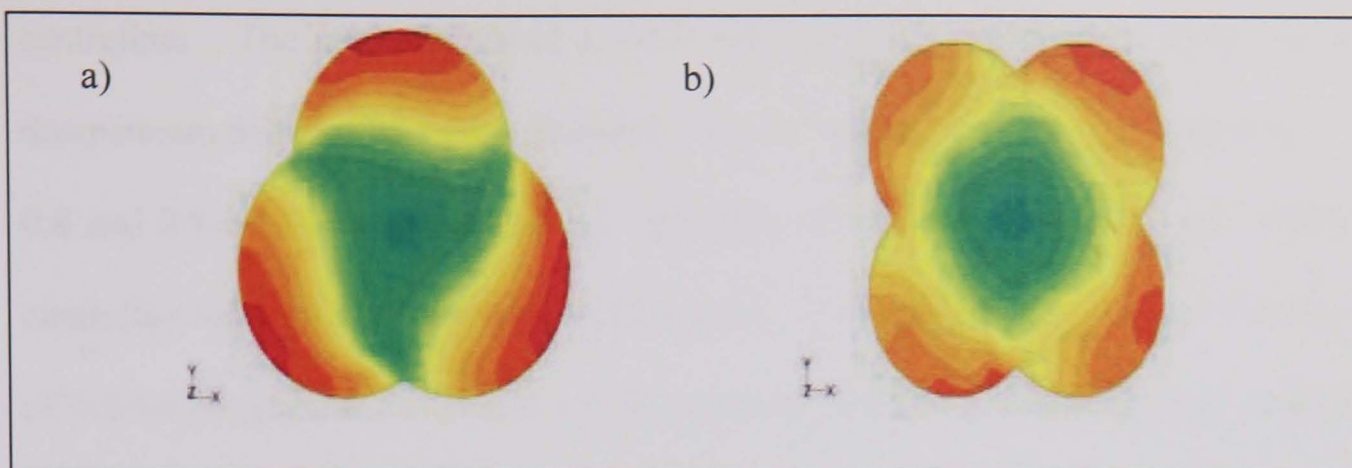


Figure 6.6: CFD predictions for the tangential velocity contours at exit of swirl pipe (Ariyaratne, 2004)

Red represents regions of maximum velocity, green and blue represent regions of minimum and zero velocity respectively.

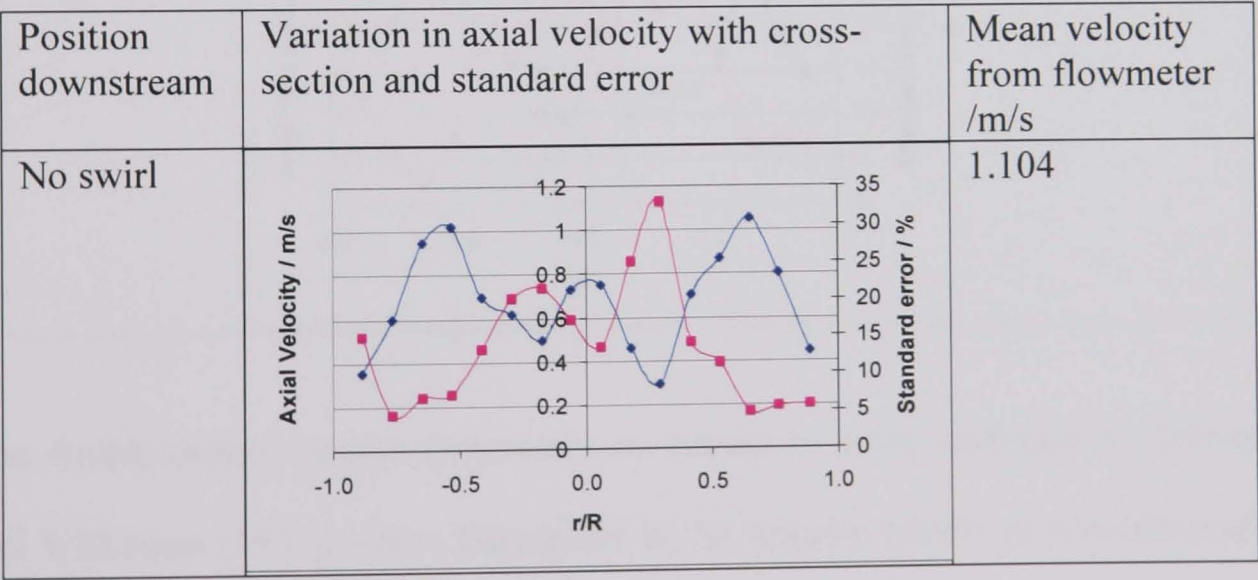
The PIV results obtained by Ganeshalingam (2002), using the Perspex pipe loop and a non-optimal 3-lobe pipe, were plotted in Figure 6.5 for ease of comparison with the current results. They did not show as much asymmetry as the current results, but this was explained with reference to Figure 6.6a. It was suggested that as the triangular core flow progressed downstream it rotated, leading to a variation in the tangential velocity at any given position. This variation would be translated into the axial velocity distribution as x-components and averaged (as described in Appendix D.3), producing the curved axial distribution recorded by Ganeshalingam (2002). However, since the core produced by the 4-lobe pipe was circular, the x-component of the tangential velocity at any given position would remain relatively constant, allowing the formation and measurement of the distinct annular and core regions.

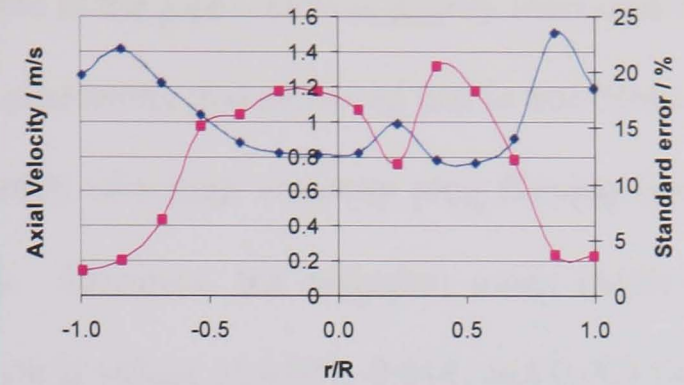
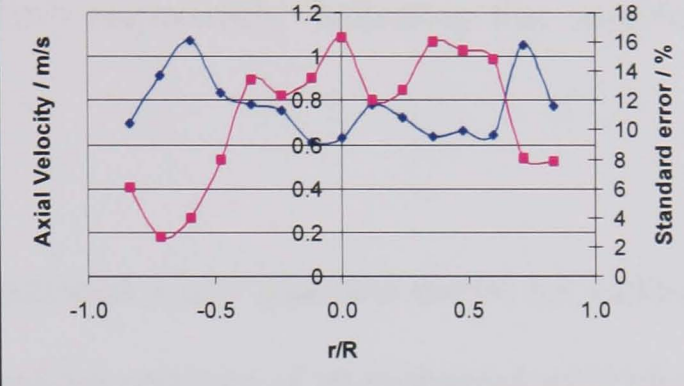
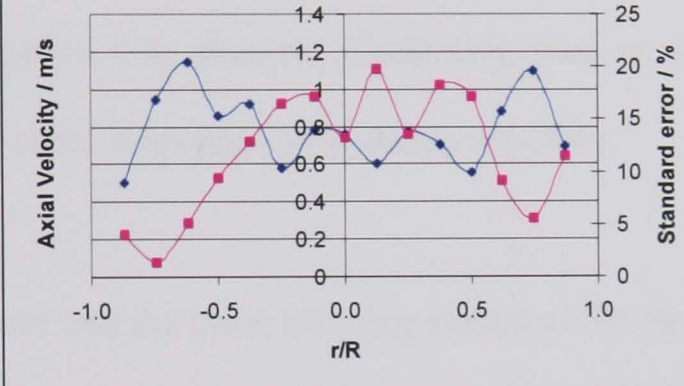
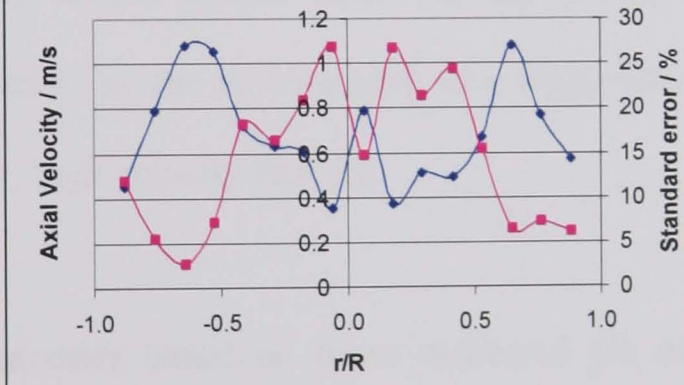
The axial PIV results for CMC, at a nominal velocity of 1.0m/s (Figure 6.7) were dominated by a pattern consisting of two peaks with a lower velocity at the

centreline. The peaks occurred at -0.6 and 0.6 r/R for all graphs except for a downstream distance of 4 pipe diameters, where they occurred at approximately -0.8 and 0.8 r/R . The peaks attained velocities of between 1.0 and 1.5m/s , with a centreline velocity of between 0.6 and 0.8m/s . The graphs for a nominal velocity of 0.5m/s (Appendix D.7) were a little more confused, but a double peak pattern was discernable when no swirl induction was applied and at a downstream distance of 8 and 16 diameters from the swirl pipe. When pumping at a nominal velocity of 1.5m/s (Appendix D.9), without swirl-induction, a standard velocity profile with no trace of the double peak was obtained. However, the pattern was present in the remaining measurements for this velocity, with the peak velocities drawing closer to the pipe centre and higher standard error recorded in the pipe centre, as distance from the swirl pipe increased.

Figure 6.7: Variation in axial velocity with cross section for CMC at a nominal velocity of 1.0m/s ($Re_{MR} = 380$)

Key: —●— Mean x-sectional velocity —■— Standard error (16 points)



4D		1.108
8D		1.104
12D		1.113
16D		1.107

The double-peaked pattern observed was similar to work reviewed by Edwards and Wilkinson (1971), where distortions in the velocity profile of non-Newtonian fluids were produced by oscillation. At high frequencies, it was found that flow close to the wall was dominant. Furthermore, they showed that as a result of

pulsation, shear rate at the pipe wall was greatly increased, but remained relatively unaffected at the pipe centre and proposed that in non-Newtonian fluids this would lead to the formation of a high viscosity plug flowing through a lubricating low viscosity annulus. However, the pulsation index (Miller, 1989) for the CMC results yielded typical values of 0.027, 0.014, and 0.009 for nominal velocities of 0.5, 1.0, and 1.5m/s respectively, indicating that significant pulsation was not present.

Slatter (1999) developed a new pipeflow model for yield-pseudoplastic fluids, in which he described the presence of an unsheared solid plug (Section 2.3). In this situation no pulsation was present, illustrating that an unsheared plug can be developed by the shear rates present in steady pipeflow.

Given this evidence and the shear thinning nature of the fluid, it was reasonable to conclude that the double-peaked axial velocity profile was produced, in the absence of pulsation, by the development of a high-viscosity, low velocity core and low viscosity, high velocity annulus.

Rheological parameters based on those measured for the CMC were recently incorporated into CFD predictions (Ariyaratne, 2004). The results confirmed the existence of a high viscosity core, in fully developed cylindrical pipe flow (Figure 6.8, left). The impact of swirl-induction on the core flow is difficult to determine from the PIV results. The 0.5m/s results show less definition in the two-peak pattern for 4, 8 and 12, diameters downstream of the swirl-inducing pipe,

indicating a possible breakdown of the low shear core. This is not discernable in the 1.0 and 1.5m/s results, however was indicated by the CFD predictions, as demonstrated by Figure 6.8.

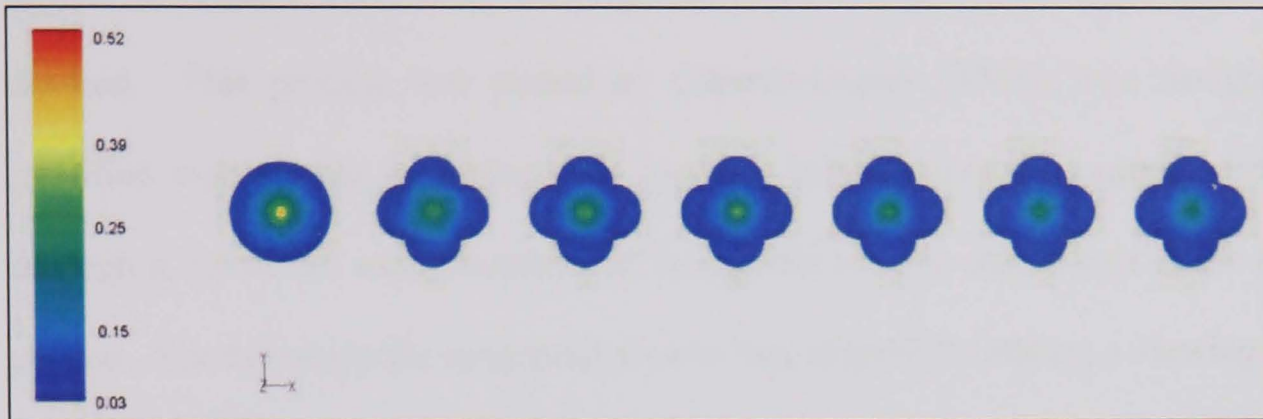


Figure 6.8: Viscosity patterns in pipe cross-sections ($P/D = 4$), Ariyaratne (2004).

Direction of flow is from left to right. Red represents regions of maximum viscosity, green and blue represent regions of minimum viscosity respectively.

In view of the suitability of the core region for transporting solids (Section 2.3), a pipe optimised for non-Newtonian fluids, may be of use to settle out particles, by breaking down the core region. This could possibly be applied in particle separation, for example inserting a swirl pipe at a cyclone inlet to deliver particles from the outside edge of the pipe, rather than from the central core.

A number of irregularities in the CMC results remain unaccounted for such as a secondary peak on the centreline of some graphs, occasional instances where a conventional laminar curve was recorded rather than the double peak pattern and the variation in the position of the peaks. The explanation of these results is impossible without more data should be considered for future work.

6.1.4 Measurement of tangential velocity

6.1.4.1 Additional methodology

Before a measurement of the tangential velocity could be made using a PIV system a suitable method of viewing the cross section of the pipe had to be devised. This process was started by Ganeshalingam (2001), who designed a modified pipe for use as a tangential viewer. Initial attempts to capture images through it, however, were unsuccessful being able to view only a part of the cross section. For this study the tangential viewer was adapted by adding a viewing box, shown in Figure 6.9. This was filled with water to prevent total internal reflection, so the whole pipe cross section could be viewed. The tangential viewing pipe was installed in the test loop in the position shown in Figure 6.9.

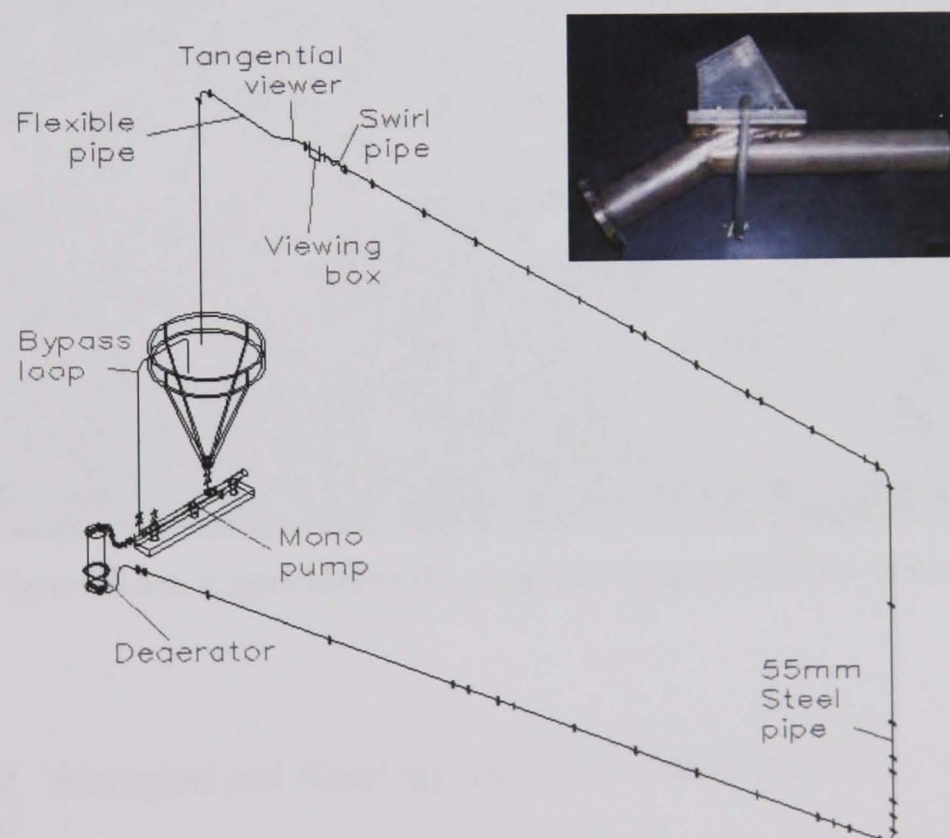


Figure 6.9: Photograph of the tangential viewer and diagram of the pipe loop configuration used for these tests

The pipe flow loop and PIV equipment were set up as shown in Figure 6.10 and tests performed using two fluids, water and CMC. For each fluid, PIV measurements were taken at a distance approximately 5 pipe diameters downstream of the swirl/standard pipe by careful positioning of the light sheet. Measurements were taken under two conditions for each fluid - when preceded by swirl and when preceded by a standard pipe. For the water tests, measurements were taken at five nominal axial velocities of 0.5, 1.0, 1.5, 2.0 and 2.5m/s ($Re = 27\,500 - 137\,500$), while CMC measurements were taken at nominally 0.5, 1.0 and 1.5m/s ($Re_{MR} = 140 - 670$). The time between laser bursts and laser pulses was set to 1000ms and 200 μ s respectively.

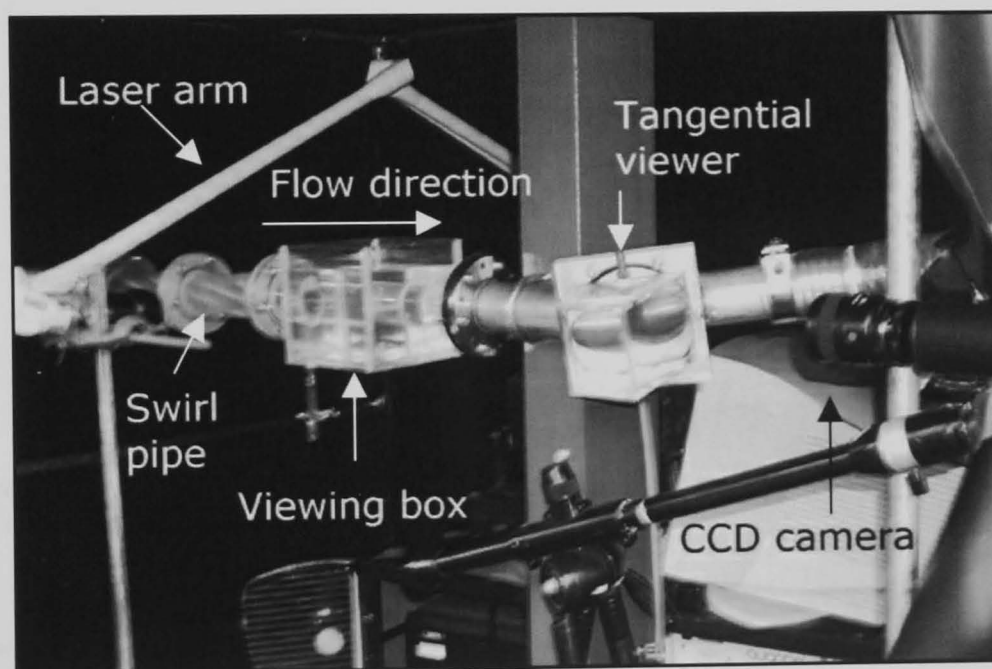


Figure 6.10: Experimental set up for tangential PIV tests.

6.1.4.2 Biological and Rheology test results and discussion

It was deduced from the biological presence in the CMC used for the PIV tests to measure axial velocity, that the biocide concentration in the desktop experiments

was not sufficient to keep the solution free of bacteria in the large-scale tests. Therefore, during this test biocide was added periodically. The biological tests strips indicated low levels of bacteria for the duration of testing (Appendix D.10) and the apparent viscosity remained relatively stable (Figure 6.11), with the exception of the initial result. This batch of CMC solution was made on the 22nd of July and tangential PIV tests performed on the 23rd of July. A significant increase was detected in the rheology results before and after the pipe flow experiment, contrary to the degradation that may be expected. This increase was attributed to allowing insufficient time for the solution to hydrate.

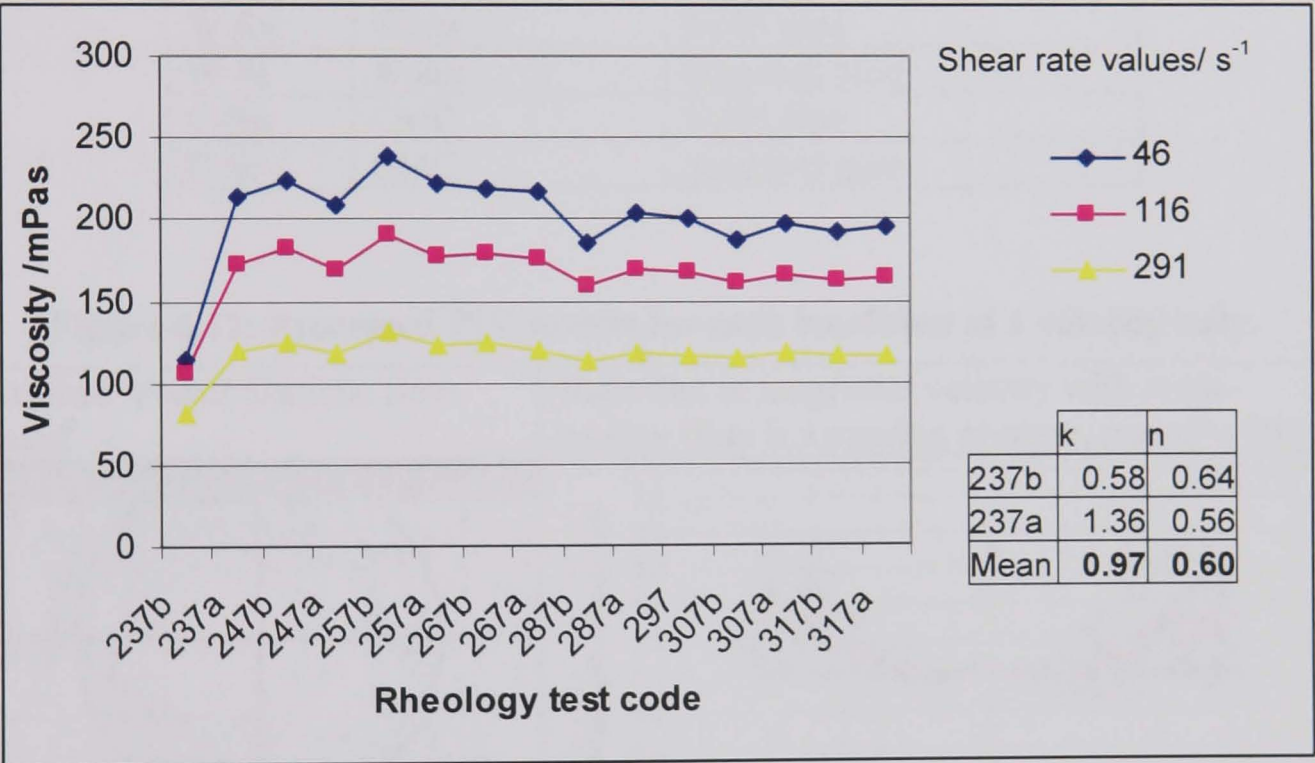


Figure 6.11: Rheological parameters and graph to show the change in apparent viscosity with age for tangential PIV tests
(code: day, month, before or after testing in pipe loop)

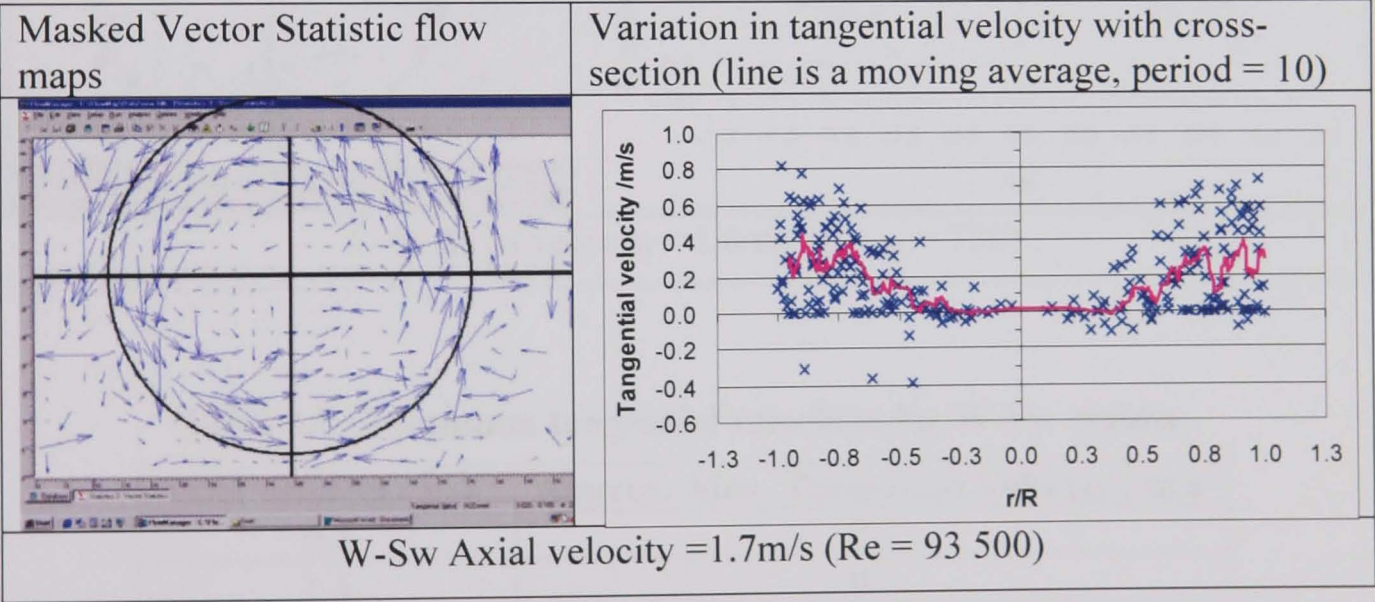
6.1.4.3 Flow test results and discussion

In the discussion the codes shown in Table 6.2 were used to refer to the experimental conditions of interest. The raw data was processed as described in Appendix D.11 and a selection of the results are presented in Figure 6.12. For each condition one velocity only is presented, as the rest are similar (Appendix D.12-15), except for W-Sw where the maximum magnitude changes. These changes are noted in Table 6.3.

Table 6.2: Reference codes for the tests performed.

Code	Fluid under test	Viewing box preceded by:
W-Sw	Water	Swirl pipe
W-St	Water	Standard pipe
C-Sw	CMC	Swirl pipe
C-St	CMC	Standard pipe

Figure 6.12: Processed PIV results for each condition at 1 velocity only.



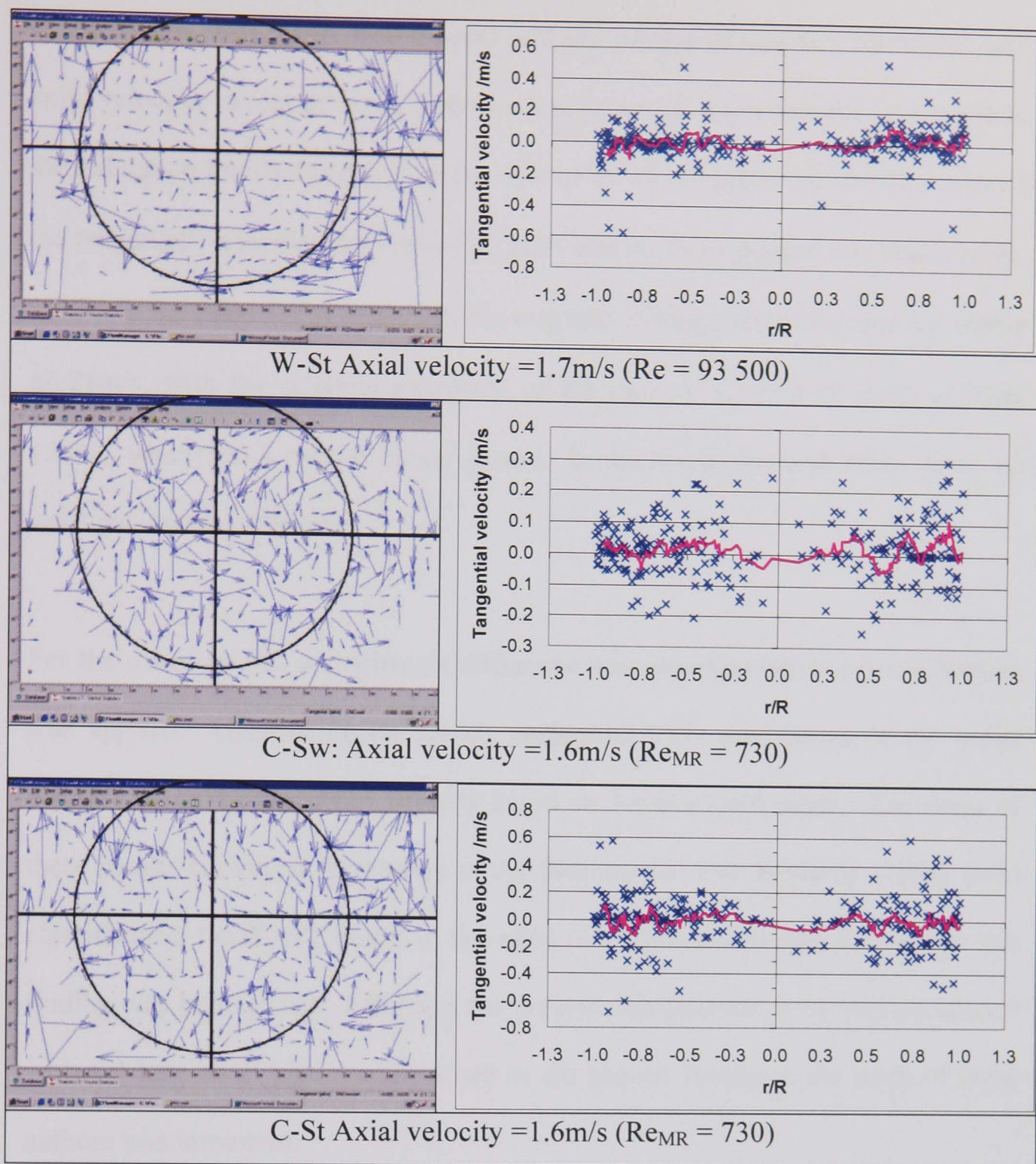


Table 6.3: Maximum tangential velocities for W-Sw results.

Axial velocity / m/s	Approx. Max. Tangential Velocity / m/s
0.5	0.1
1.1	0.3
1.7	0.4
2.2	0.2
2.8	0.7

In the W-Sw tests, swirl was evident and the tangential velocity increased with axial velocity, except at 2m/s, where it was assumed that a mistake was made in the validation threshold input. In the case of W-St, at each axial velocity most of the tangential velocities lay within ± 0.2 m/s and no swirl pattern was discernable. Similarly for cases C-Sw and C-St, the majority of tangential velocities lay within ± 0.25 m/s, with the possible exception of the case of C-St at an axial velocity 1.5m/s, which has a slightly larger spread. In the results for both these cases, no swirl pattern was detected.

For the water results, a significant difference was observed when swirl indication was applied. Ganeshalingam (2002) performed CFD predictions of the radial distribution of the tangential velocity based on 3-lobed swirl pipes. The shape of these results compared favourably to the Steenbergen and Voskamp (1998) swirl classification “*wall-jet*”, however the need for experimental data to confirm this finding was highlighted. Although the present experimental work was conducted with a 4-lobe swirl pipe a comparison of the present results to the work of these authors was important.

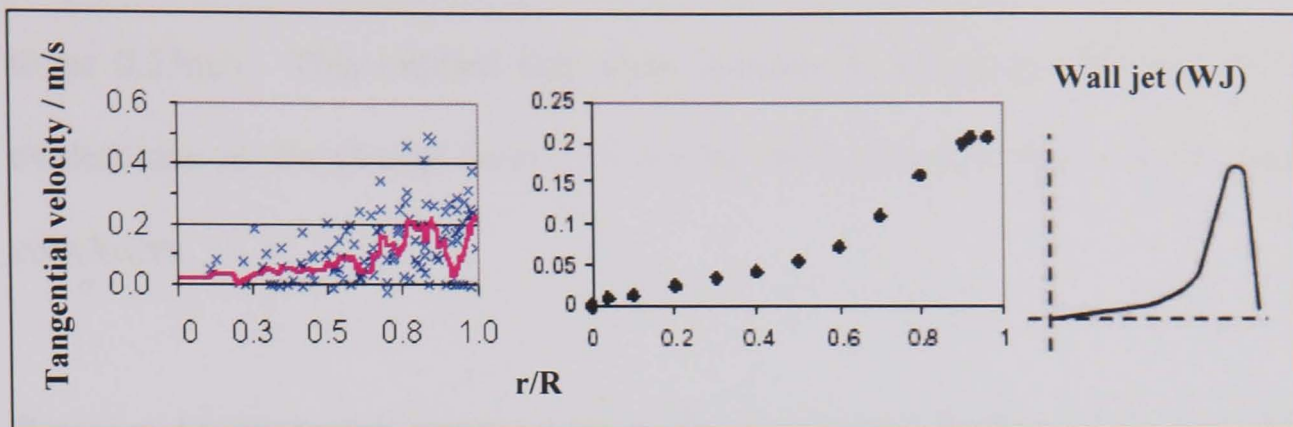


Figure 6.13: Radial distribution of tangential velocity.

From left to right, PIV results (nominal velocity 1.0m/s), CFD predictions (velocity 1.0m/s, Ganeshalingam, 2002), wall jet swirl type (Steenbergen and Voskamp 1998)

Figure 6.13 illustrates that the shape of the PIV results obtained conforms closely to the Steenbergen and Voskamp (1998) swirl classification of wall-jet and the CFD predictions performed by Ganeshalingam (2002). There is a tendency for the high velocity wall region to be wider than expected from the wall-jet model, but part of this may be due to the uncertainties over the position of the pipe wall in this method. This was an important result, which proved that high tangential velocities were generated by the swirl-inducing pipe in the wall region. This enabled the particles to be effectively redistributed leading to the benefits found by Raylor *et al.* (1999).

Ganeshalingam's CFD predictions (2002), gave maximum tangential velocities of approximately 0.21m/s for 1m/s and 0.44m/s for 2m/s. These results were compared to the current ones at the lower velocity, but unfortunately the 2.2m/s PIV result was anomalous. At 1.1m/s the maximum mean tangential velocity was approximately 0.3m/s. If a linear increase in tangential velocity was assumed, by

interpolating, the tangential velocity at 1.1m/s predicted by the CFD was estimated to be 0.23m/s. This implied that some increase in the tangential velocity was evident due to the change from 3 to 4-lobe swirl pipe, but this is by no means conclusive.

Figure 6.14 illustrates more recent CFD predictions performed by Ariyaratne (2003) for the 4-lobe pipe. The magnitude of the PIV results compared very well to the CFD predictions at all velocities (Figure 6.14, Appendix D.16, Table 6.4), however the shapes were quite different, with Ariyaratne’s results resembling the solid-body pattern described by Steenbergen and Voskamp (1998). It was thought that this may be due to differences in the turbulence model used. Ariyaratne (2003) used the k-epsilon model whereas Ganeshalingam (2002) used the Reynolds stress model recommended by Raylor (1998).

**Table 6.4: Maximum tangential velocities for W-Sw and CFD results
Ariyaratne (2003).**

Nominal Axial velocity / m/s	Approx. Max. Tangential Velocity / m/s	
	PIV results	CFD predictions (Ariyaratne, 2003)
0.5	0.1	0.11
1.1	0.3	0.25
1.7	0.4	0.38
2.2	0.2	0.51
2.8	0.7	-

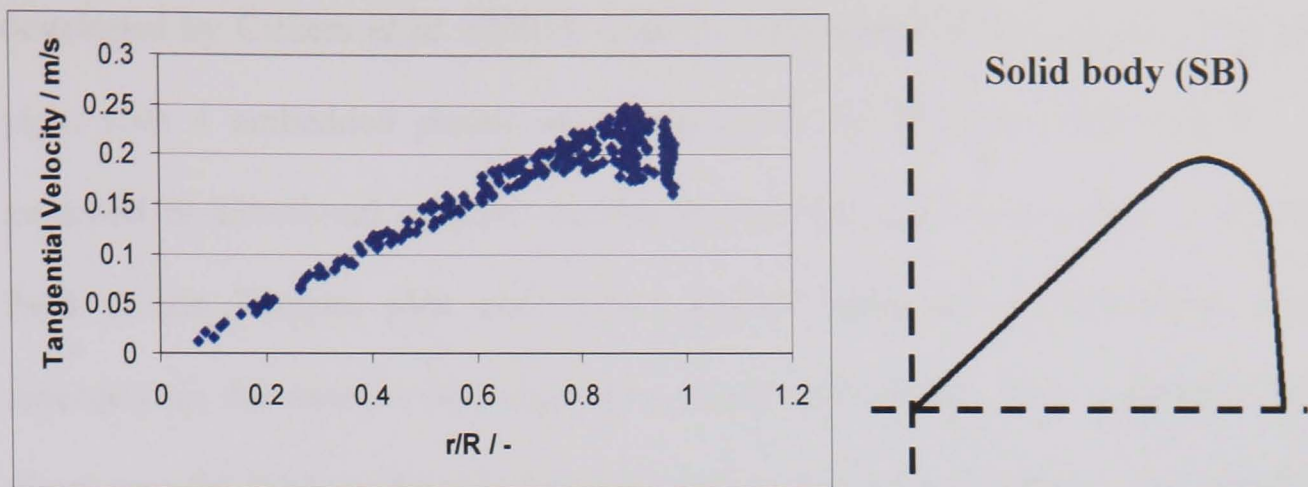


Figure 6.14: Recent CFD predictions of the radial distribution of tangential velocity.

From left to right: CFD predictions (axial velocity 1.0m/s, Ariyaratne, 2003), solid body swirl type (redrawn from Steenbergen and Voskamp 1998)

6.2 Visualisation of swirling flows using a novel electrical resistance tomography system

6.2.1 Introduction and methodology

An electrical resistance tomography (ERT) system operates by injecting current into a conducting medium, such as a water-based slurry, from various electrode pairs, then measuring the potential difference produced on the remaining electrode pairs. A sequence of current inputs is used to generate a matrix of data, which can be processed with a reconstruction algorithm and viewed as an image.

The opportunity arose to conduct an investigation into the use of a novel ERT system on the Perspex and Steel flow loops, in collaboration with Department of Chemical Engineering, UMIST and Department of Chemical Engineering, University of Capetown, South Africa. The ERT system utilised was a prototype

developed by Cilliers *et al.* (2001), used in conjunction with an adapted Perspex pipe, with 4 embedded planes of 16 electrodes, as shown in Figure 6.15. A switched bi-directional constant current source was used to produce an electric field in the Perspex pipe and then potential difference measurements were recorded on the positive and negative current half cycles. This technique used direct current pulses, which meant that unlike conventional systems, the potential difference measurements did not require demodulation. This simplified the system considerably and created the potential for high-speed operation. The system operated at approximately 3 kHz, which eliminated the need for electrical screening to prevent noise. The reconstruction program used the Newton-Raphson algorithm and depicted the image using 616 elements with a resolution in the order of 5%.

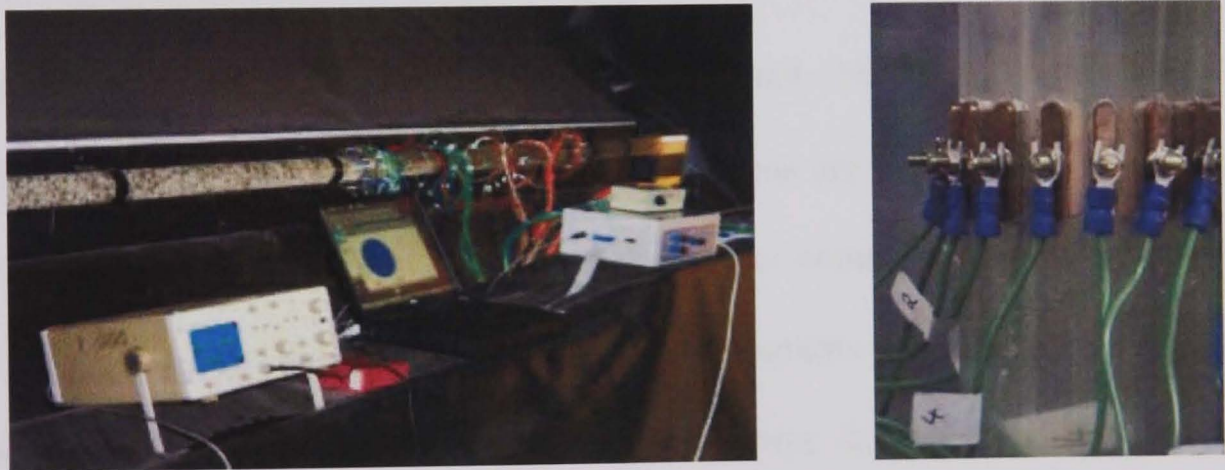
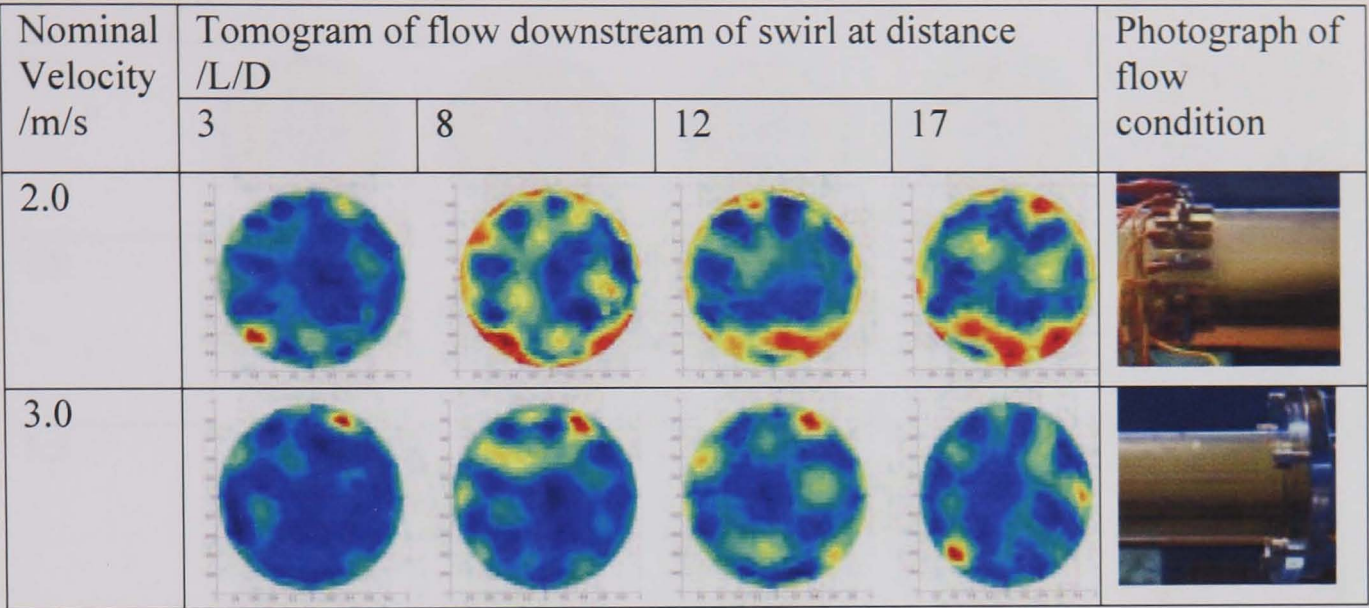


Figure 6.15a: ERT operating on the Perspex flow loop; b: Electrodes

6.2.2 Results and discussion

6.2.2.1 Sand



Conductive (water)  Non-conductive (sand)

Figure 6.16: Tomograms and photographs of the flow condition at various velocities and downstream distances from the swirl pipe with a sand concentration of 0.7% v/v

Tomography results for a sand-water mixture (particle density: 2640 kg/m³, particle size: 2000-1000μm), with 50mg/l of salt (NaCl) added to serve as an electrolyte, are shown in Figure 6.16. Red areas are areas of non-conductance; blue indicates conductive areas and the vertical columns represent downstream distance from the swirl pipe. The 2.0m/s tomograms indicated some deposition, which increased as distance from the swirl pipe increased, while the 3.0m/s tomograms showed a more homogenous distribution. Visual observation and the photographs presented verified both these results.

6.2.2.2 Plastic beads

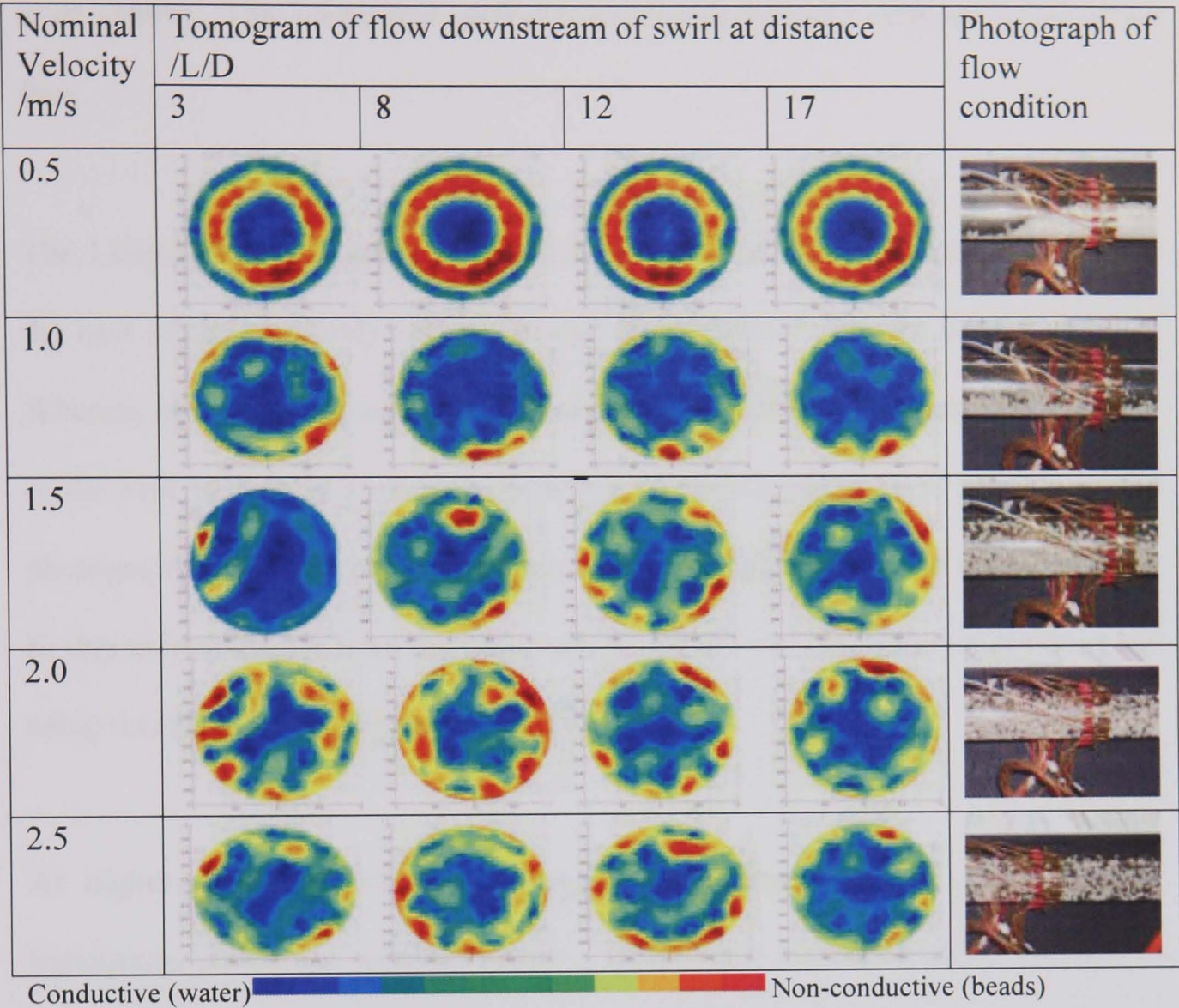


Figure 6.17: Tomograms and photographs of the flow condition at various velocities and downstream distances from the swirl pipe with a bead concentration of 1.4% v/v

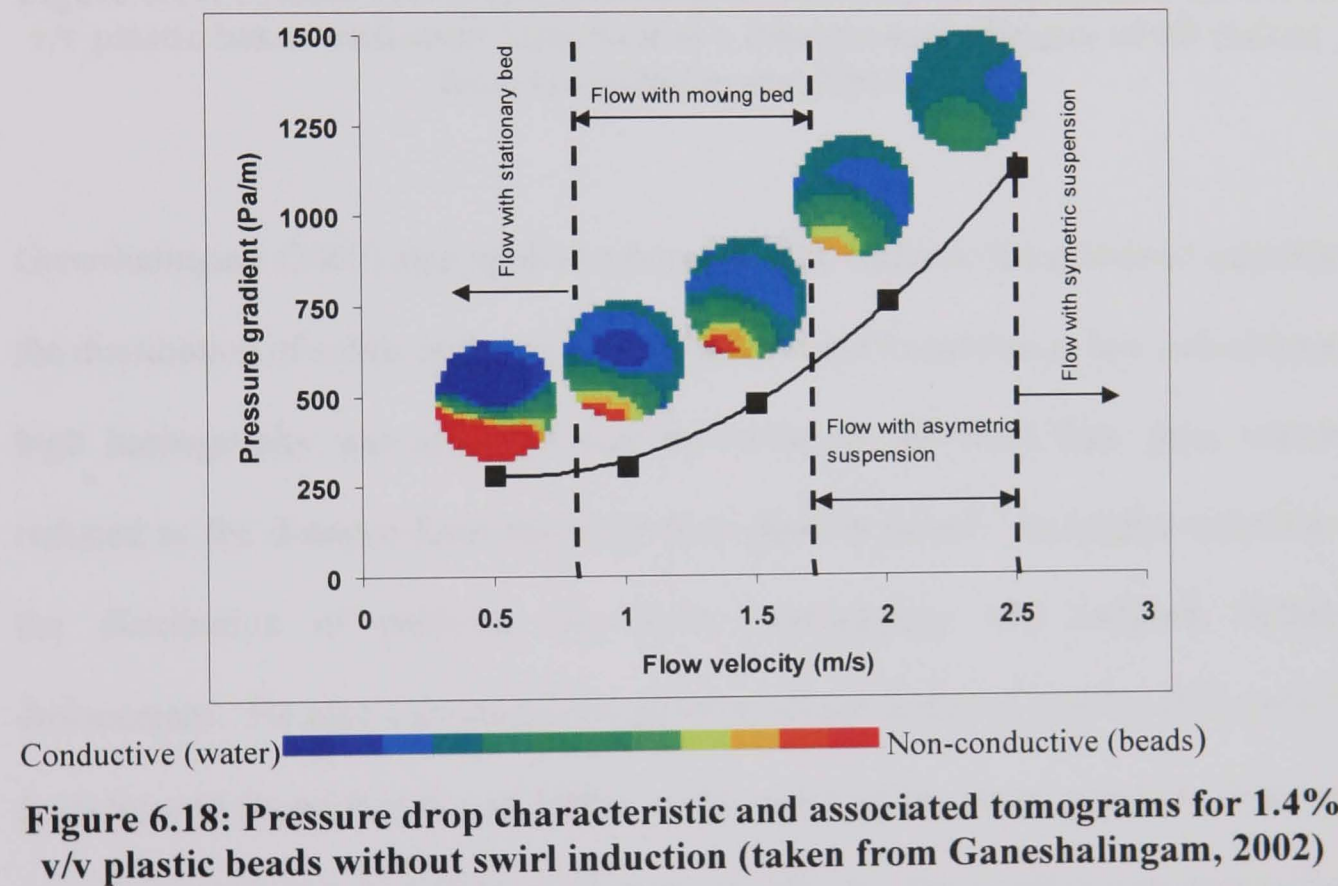
Figure 6.17 illustrates results obtained when testing plastic bead-water mixture (particle density: 1351 kg/m³, 50% passing size: 1750 μm) in the Perspex flow loop. It can be seen that the red areas in the 0.5m/s tomograms did not represent the distribution of beads in the photograph. A possible explanation proposed was that the instrument was struggling to take readings because the bed of non-conductive particles was so thick. Reliable measurements were also difficult to take at this velocity because each electrode plane recorded at a different time and

the flow of beads was intermittent, exhibiting dunes flow as described by Simkhis *et al.* (1999). This meant that each tomogram represented a different cycle of the flow.

The 1.0m/s tomograms gave an indication of a higher solids concentration toward the base of the pipe (red) with the carrier liquid (blue) in the top half of the pipe. Whereas in the 1.5, 2.0 and 2.5m/s tomograms there was more green in the centre of the pipe indicating a more uniform mix of particles and liquid verified by the photographs. The red and yellow observed at the perimeter of the tomogram may be due to interference from the pipe wall, which has been observed in previous test using this ERT system (Stevenson, 2002).

At higher solids concentrations the annular pattern observed in the 0.5m/s tomograms above was more common. While some indication of the location of the red block twisting as downstream distance increased may be drawn from the tomograms (Appendix D.18, 1.0 and 1.5m/s, Appendix D.19, 1.5m/s), a deep blue core was present, which did not correspond to visual observations. Slatter, (1999) describes the existence of a similar annular pattern, however, this occurs with laminar pipeflow of non-Newtonian liquids. In addition, coarse particles tend to concentrate in the core region, rather than the annular region as the tomograms indicate (Section 2.3). In light of these contradictions it was concluded that the results displaying the annular pattern were distorted. As described above this was likely to be because the high concentration of non-conductive material was preventing the passage of current between the correct electrodes.

Figure 6.18 and Figure 6.19 illustrate results Ganeshalingam (2002) obtained using a more conventional ERT system on the Perspex flow loop. Under essentially the same process conditions, results of much higher quality were obtained. By correlating his tomography and pressure drop results a clear demonstration of the effect of swirling flow was produced (Figure 6.18 and Figure 6.19). Comparison of Figure 6.18 and Figure 6.19 shows that, over the measurement section, swirl-induction eliminated particle settling and created an asymmetric particle suspension at lower velocities than could be obtained without swirl.



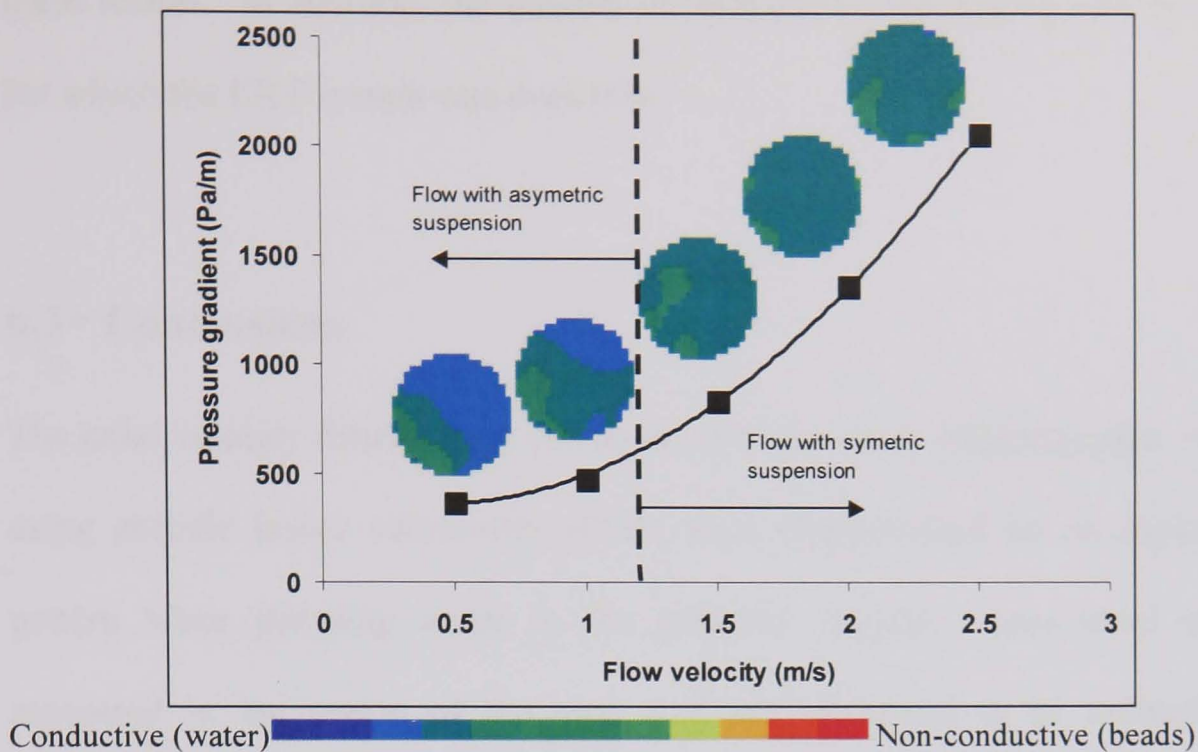


Figure 6.19: Pressure drop characteristic and associated tomograms for 1.4% v/v plastic beads with swirl induction at a downstream distance of 8D (taken from Ganeshalingam, 2002).

Ganeshalingam (2002) also applied a homogeneity factor to his results to quantify the distribution of solids in the pipe cross-section and found that at low velocities a high homogeneity was achieved near the outlet of the swirl flow pipe, which reduced as the distance from the swirl flow pipe increased. At higher velocities the distribution of particles was more homogenous and endured further downstream. He also considered the position of the centre of gravity of the solid particles and found that it was higher at the outlet of the swirl pipe than without swirl-induction and that it decayed more rapidly at higher solids concentrations and lower flow velocities.

The quality of the current results meant that the homogeneity factor and centre of gravity analysis employed by Ganeshalingam (2002) could not be repeated for

these results. In addition, the number of tests performed was limited by the time for which the ERT system was available.

6.3 Conclusions

The axial velocity distributions downstream of the swirl-inducing pipe, measured using particle image velocimetry (PIV), were characterised by an asymmetrical pattern when pumping water in the turbulent regime. Low axial velocities measured in the region of the pipe wall are suggested to be indicative of a significant tangential velocity component in that region. Ganeshlingam's PIV results (2002) showed limited asymmetry and it was suggested that this was a result of differences in the flow structures generated by the 3 and 4-lobe swirl pipe. The velocity profile for the laminar flow of carboxymethyl cellulose highlighted the presence of a low-shear core, which was then confirmed by Ariyaratne (2004) using CFD. In both cases the possibility of pulsation influencing the results was investigated but proved unlikely.

The radial distribution of tangential velocities measured using PIV when pumping water through swirl-inducing pipe was well represented by the wall-jet pattern suggested in the literature. This was an important step in further understanding these flows.

The laminar flow of carboxymethyl cellulose through the current swirl flow pipe geometry showed no swirl pattern, indicating that higher apparent viscosity

reduced the swirl induced by the current swirl pipe design. Further testing to optimise the swirl flow pipe for viscous non-Newtonian fluids is recommended.

Flow visualisation performed using electrical resistance tomography (ERT) indicated a decrease in the homogeneity of the particle distribution as distance from the swirl pipe increased and velocity decreased, when testing 1.4% v/v beads at velocities of 1.0 – 2.5m/s and 0.7% v/v sand at velocities of 2 and 3m/s. However problems were encountered when performing measurements at higher concentrations and lower velocities. To improve the measurements the ERT system should be developed to take readings on each set of electrodes simultaneously and the use of higher currents and salt concentrations investigated.

Chapter 7 EFFECT OF SWIRL-INDUCTION BEFORE BENDS

This chapter examines the effect of bend radius and upstream swirl-induction on the pressure drop over the bend when pumping water, CMC and a sand-water slurry.

7.1 Introduction

Flow through bends is a subject of particular interest in industry. When pumping heterogeneous slurries, pipe bends wear more rapidly than other components requiring frequent replacement, which is costly in terms of parts and downtime. At the same time non-Newtonian flow through bends is of interest because of its many applications in heat exchangers and piping systems. This leads to an interest in any advantage that can be gained by inducing swirling flow prior to bends.

The effect of installing swirl-induction before bends when pumping plastic beads in a Perspex flow loop, was investigated by Raylor (1998) and Ganeshalingam (2002) and found to be beneficial in terms of pressure drop. The aim of the following tests was to determine whether a similar effect was detected on the steel flow loop using denser, more abrasive slurries and higher viscosity liquids.

The pressure drop was measured across three bends with radius of curvature to diameter ratios (R/D) of 2, 4 and 6 when preceded by either a swirl flow pipe or a cylindrical pipe. The test programme was initially run pumping water to serve as a

reference point, before repeating the tests with CMC only and 2.7% v/v coarse sand–water slurry.

7.2 Methodology specifics

The general methodology for the operation of the flow loop, dissolution and rheological testing of the CMC described in Chapter 4 was followed for these tests. They were performed at nominal velocities of 0.5, 1.0, 1.5, 2.0 and 2.5m/s ($Re = 27\,500 - 137\,500$) for water only, 0.5, 1.0 and 1.5m/s ($Re_{MR} = 130 - 600$) for the CMC only and 0.5, 1.0, 1.5 and 2m/s for the coarse sand-water slurry at a concentration of 2.7% v/v. The pressure drop for each test material and velocity was measured over the following pipe configurations:

- Lower leg and horizontal to vertical bend (H→V), for each radius bend, with no swirl induction present
- 4-lobe pipe in the lower leg
- 4-lobe pipe immediately preceding H→V bend, for each radius bend

It was initially considered that the pressure drop directly over the bend could be calculated by subtracting the pressure drop over the swirl pipe and the pressure drop in the vertical pipe from the measured pressure drop. However, since a satisfactory evaluation of the pressure drop over the swirl pipe (for all slurries) or the vertical pipe (for the sand-water slurry) could not be obtained, as explained in Section 8.3.3, the total measured values of pressure drop over the bend with and without swirl were compared.

7.3 Results and discussion

7.3.1 Biological and rheology tests results

The batch of CMC used for these tests was the same as for the PIV tests to measure tangential velocity. Biocide was added periodically throughout the test and biological tests strips indicated low levels of bacteria for the duration of testing (Appendix D.10). The tests were performed on the 30th and 31st of July when the apparent viscosity remained relatively stable (Figure 7.1), which meant the results could be considered unaffected by changes in rheology.

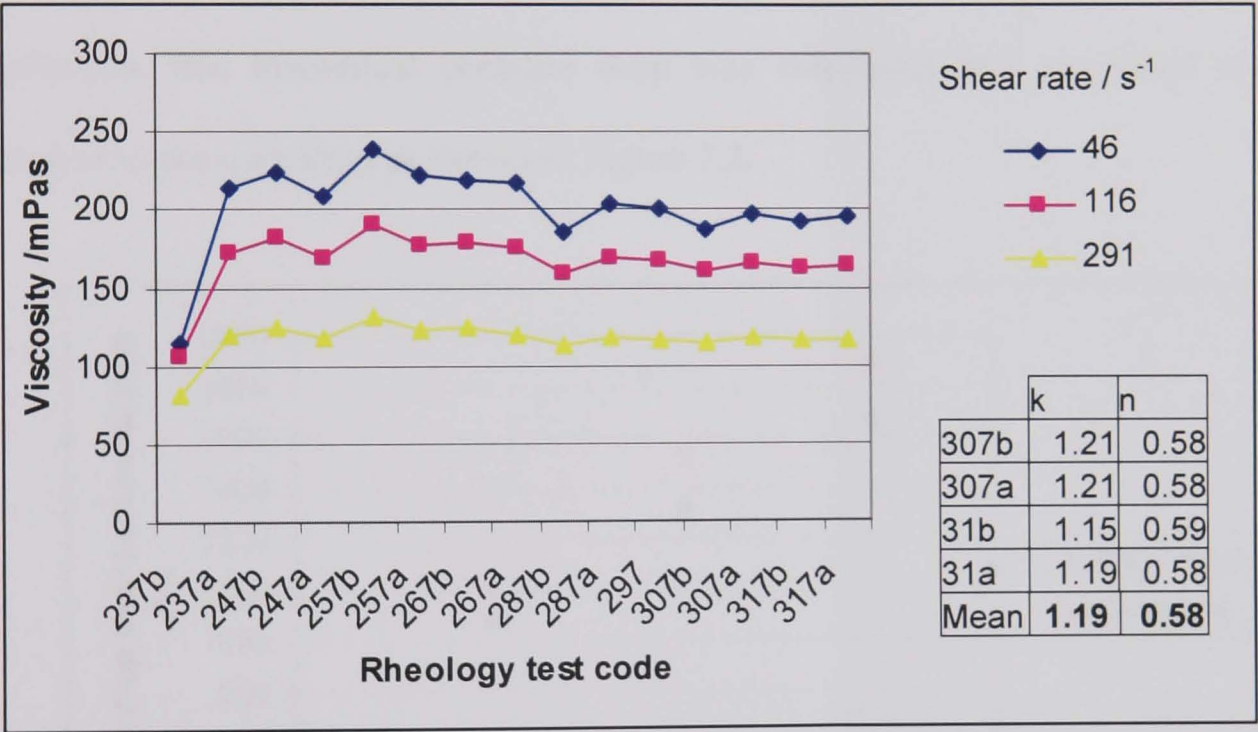


Figure 7.1: Rheological parameters and graph to show the change in apparent viscosity with age for CMC bend tests
(code: day, month, before or after testing in pipe loop)

7.3.2 Pressure drop over cylindrical pipe

The relationship between the volumetric flow rate and the pressure drop over a horizontal pipe when pumping non-Newtonian fluids in the laminar flow regime can be theoretically derived (Govier and Aziz, 1972). The equation, a rearrangement of that shown in Table 2.3, for a power law fluid is as follows:

$$\Delta P = \frac{4V^n kL}{D^{(1+n)}} \left(\frac{2+6n}{n} \right)^n \quad \text{Equation 7.1}$$

Using the rheological parameters shown in Figure 7.1 and the experimental velocities this theoretical pressure drop was calculated and compared to the measured pressure drop as shown in Figure 7.2.

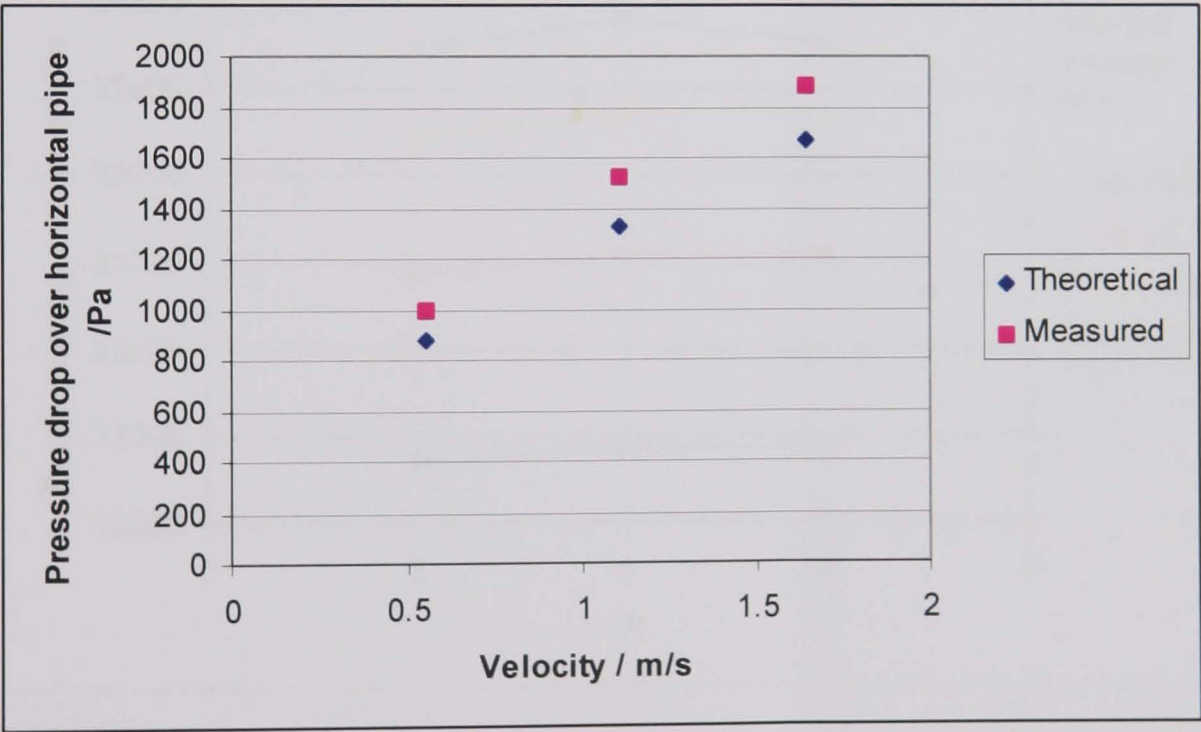


Figure 7.2: Comparison of the theoretical and measured pressure drop over horizontal pipe for CMC.

It can be seen from Figure 7.2 that the measured values were consistently higher than the theoretical values. This difference equates to approximately 14%, which was considered satisfactory in view of the flowmeter calibration and the size of rheology test sample (approximately 100ml from 1m³). It was assumed that a similar level of accuracy was associated with the measurement of the pressure drop of the water and water-sand slurry.

7.3.3 Effect of bend radius on pressure drop over bend

It can be seen from Figure 7.3 and Appendix E.1 that there was a tendency for the greatest pressure loss to occur at $R/D = 4$, with a minimum pressure drop for $R/D = 2$, however, the difference between bends of different radii was small.

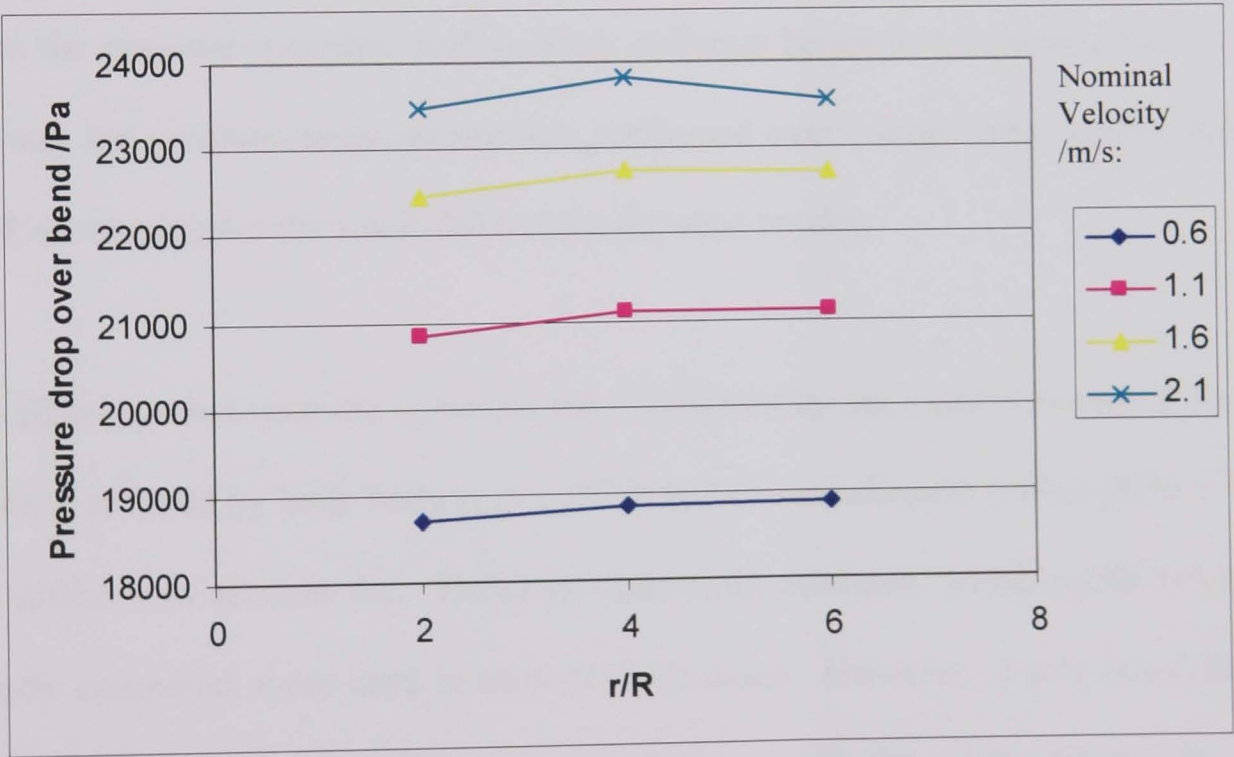


Figure 7.3: Pressure drop over various radii bends for the 2.7% v/v coarse sand–water slurry, with no swirl induction.

The size of these differences was sensible in the context of the literature. Ayukawa (1969) investigated the pressure drop over bends with bend curvature to radius ratios (R/r) of 19-39 and Toda *et al.* (1972) tested bends with an R/r range of 8-32. In comparison, the range of bends tested in the current research was small (current test bends expressed as R/r were 4, 8 and 12), although encompassed the optimum radius ratio of approximately 8 ($R/D = 4$), found by Toda *et al.* (1972). Additionally, Toda *et al.* (1972) found that as the distance of the measuring points from the bend increased, the effect of the radius of curvature decreased. The upstream pressure transducer was positioned 11 diameters before the bend because of the need to include the swirl pipe directly before it, to ensure maximum swirl intensity within the bend. The downstream transducer was located between 27 and 31 diameters after the bend so the flow disturbance produced by the bend did not affect the pressure recorded, and to allow different bends to be incorporated. In this way the pressure measurement was performed over a larger pipe section than ideal, accounting for the small differences between results.

The difference between the optimum bend indicated by the current results ($R/D = 2$) and that found by both Toda *et al.* (1972) and Ganeshalingam (2002) ($R/D = 4$) was difficult to account for. Different fluid-solid mixtures, which could not be directly compared, were used in each of these cases. However, it was noted that the optimum bend for water alone was inconsistent with the water only results of these authors, indicating that the discrepancy found was not due to differences in the fluids / slurry tested. A reasonable explanation of the unusual pattern in the current results was that there were small differences in the finish of the steel

bends, which led to a larger pressure drop in the $R/D = 4$ bend. A visual inspection of the bend did not provide any evidence for this, however a more detailed survey is required before the theory can be dismissed.

7.3.4 Effect of swirl on pressure drop over bend

Previous authors have found that incorporating a swirl-inducing pipe before a bend leads to a pressure drop advantage (Raylor, 1999; Ganeshalingam, 2002). Ganeshalingam found a crossover in the pressure drop curves for swirl and no swirl in the region of 0.75-1.5m/s. The pressure drop curves for the current result are presented in Appendix E.2. However, Figure 7.4 was plotted to aid comparison of the two conditions using the pressure cost as follows:

$$\text{Pressure cost} = \begin{array}{ccc} \text{pressure drop with} & - & \text{pressure drop without} \\ \text{swirl induction} & & \text{swirl induction} \end{array}$$

where a negative result indicates a pressure benefit and a positive result, a pressure cost associated with use of the swirl pipe. Since, by practical necessity, the velocity was reset between measurement of the pressure drop with and without swirl induction, there was a slight difference in the test velocities. The results were subtracted with no correction for velocity applied; therefore, the pressure cost graph is not entirely accurate. However as the velocities are close, it was considered a useful way to indicate the patterns in the results.

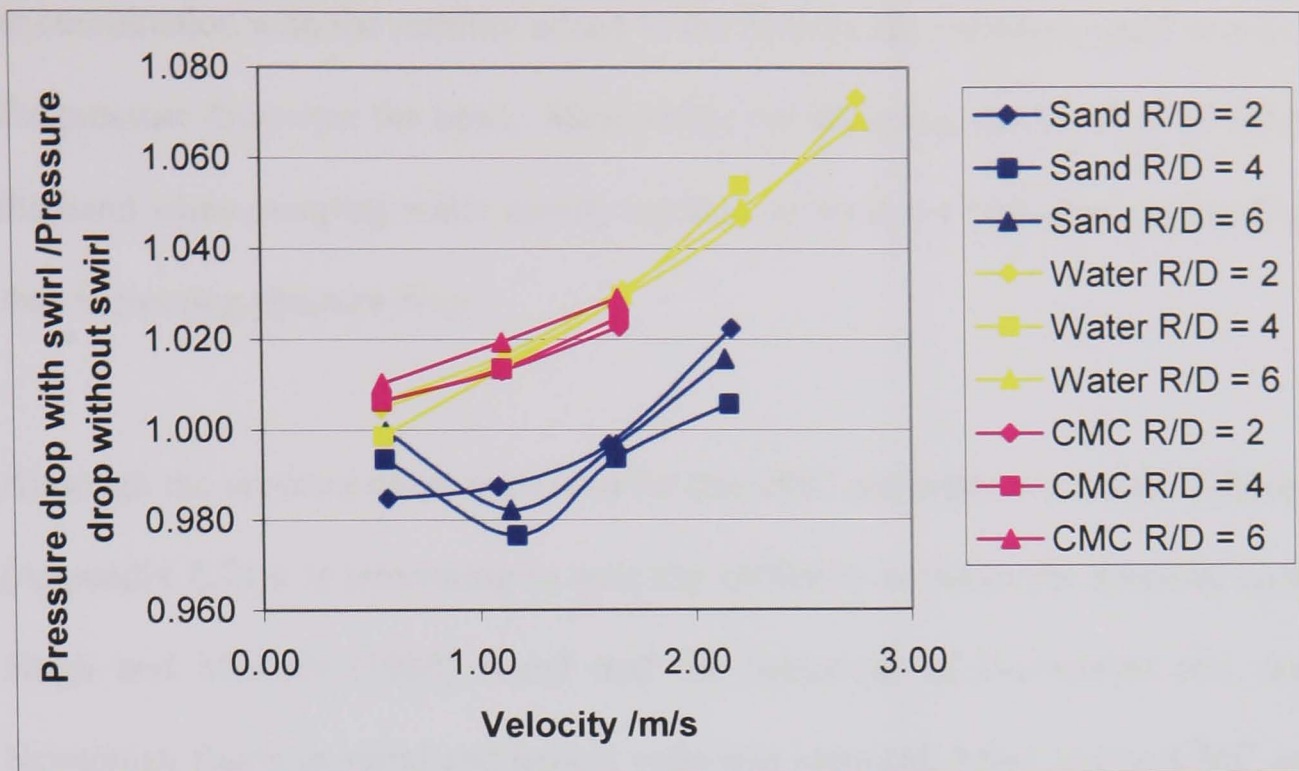


Figure 7.4: Graph to show the effect of swirl before a bend

The figure indicates that the crossover observed in Ganeshalingam's results was also present in the current results for the sand-water slurry, occurring at a slightly higher velocity of approximately 1.8m/s. A cross over was also evident in Ganeshalingam's results for water only, for lower radius bends. However this was not repeated in the steel flow loop, where water and CMC exhibited a greater pressure loss across the bends when swirl was present.

Mukhtar *et al.*, (1995) found that the relative pressure (pressure drop in bend / pressure drop in equal length straight pipeline) for slurries was lower than for water, since the presence of solid particles in the bend inhibited secondary flows. In this case, the presence of the swirl pipe before the bend acted to increase the homogeneity of the particles and reduce wall friction due to the particle bed, which

in combination with the stability added to the flow by the particles, acted to reduce the pressure drop over the bend. Meanwhile, incorporating swirl induction before the bend when pumping water merely acted to increase the turbulence of the fluid thus increasing pressure drop.

Although the pressure drops measured for the CMC and water were quite different (Appendix E.2) it is interesting to note the similarity between the pressure costs. Singh and Mishra (1980) found that the behaviour of Newtonian and non-Newtonian fluids in spiral and helical coils was identical, when testing CMC and starch solutions with pseudoplastic behaviour, and water and starch solutions with Newtonian behaviour. However they drew comparisons between these fluids flowing in the same regime, unlike the current comparison, where CMC and water flowed in the laminar and turbulent regimes respectively. The differences in the response of the fluids to the swirl-inducing pipe are highlighted in Chapter 6. It is reasonable to assume that the similarity in the results was caused by measuring the pressure drop over a large distance, rather than just the pipe bend, resulting in a minimisation of the effects. This also accounts for the small differences in the effect of swirl preceding bends of different radii. Further experimentation including the use of flow visualisation on the bend is recommended to gain greater insights into these results.

7.4 Conclusions

- Following on from previous investigations, the effect of bend radius and upstream swirl-induction on the pressure drop over the bend was investigated, with the added dimension of pumping a pseudoplastic fluid and a water based slurry with higher density solids.
- The pressure drop over cylindrical pipe for CMC was compared to a theoretical calculation of the same quantity and the results considered satisfactory.
- The pressure drop difference between bends of various radii was found to be small and this was sensible in the context of the literature. In general the pressure drops over the $R/D = 2$ bend were minimum, with the $R/D = 4$ bend giving the greatest pressure drops. This conflicted with the literature and was attributed to differences in the finish of the bends.
- The inclusion of swirl prior to the bends was found to be of benefit in terms of pressure loss for velocities of 0.5-1.8m/s, a marginally greater range than that found by Ganeshalingam when testing with plastic beads and a 3-lobe swirl pipe.
- The inclusion of swirl prior to the bends was found to result in a pressure cost when pumping water and CMC.

- In view of the small pressure drop differences between the bends of various radii, the remaining tests were performed with the 100mm radius bend ($R/D = 2$) primarily because it was easier in practical terms to incorporate into the pipe flow loop.

Chapter 8 EFFECT OF SWIRL ON SETTLING SLURRIES

The effect of swirl-induction before vertical bends and inclined pipes was studied for a range of settling slurries. The pressure drop was measured and the tangential velocity estimated using a photographic technique.

8.1 Introduction

Previous experimental work at Nottingham has examined the effect of swirl-induction on plastic beads of one size only (Raylor, 1998, Ganeshalingam, 2002). The aim of this investigation was to obtain experimental data describing the performance of the 4-lobe swirl pipe for a range of slurries and thus gain a greater appreciation of the applicability of swirl induction to industrial applications. Industrial slurry flow is complex and difficult to model, involving many variables such as the size, shape, density, size distribution and hardness of the particles. As this was the first extensive investigation into the use of the swirl flow pipe with mineral slurries the number of variables investigated was limited to specific gravity and particle size, and carrier fluid viscosity. The effect of specific gravity was investigated using coal (approximately $1.2\text{--}1.5\text{g/cm}^3$), sand (2.65g/cm^3) and magnetite (approximately $4.5\text{--}5.2\text{g/cm}^3$) each with a particle size range between $2000\text{--}1000\mu\text{m}$. A further particle size range was tested for coal and two sizes of sand. The measurements were used to assess the pressure benefits of incorporating swirl and the decay of swirl associated with these slurries.

8.2 Methodology specifics

The general methodology for the operation of the flow loop, dissolution and rheological testing of the CMC described in Chapter 5 was followed for these tests. For the reasons described in Section 5.1 the Warman pump was used. The tests were performed at nominal velocities of 0.5, 1.0, 1.5 and 2m/s when water was the carrier fluid and 0.5, 1.0, 1.5m/s when CMC was the carrier fluid. In general, the target slurry concentrations were 1.4, 2.0 and 2.7% v/v, although some slurries were tested at one concentration only, as shown in Table 8.1. The velocity, temperature and pressure drop were logged throughout the experiments, with the pressure drop measured over the following pipe configurations:

- Standard pipe on bottom leg (measurement section 64D, 127D from de-aerator).
- Swirl and standard pipe on bottom leg (measurement section 55D cylindrical and 0.4m 4-lobe swirl pipe, 127D from de-aerator).
- Horizontal to vertical ($H \rightarrow V$, $R/D = 2$) bend with no swirl induction (pressure transducer preceding 0.5m standard pipe directly before bend, 195D from de-aerator; second transducer 29D from bend outlet).
- 4-lobe pipe immediately preceding $H \rightarrow V$ bend (swirl pipe and pressure transducer directly before bend, 195D from de-aerator; second transducer 29D from bend outlet).
- Downward sloping standard pipe section (58D), horizontal standard pipe section (10D) and Perspex pipe (7D) (measurement section located 88D of standard pipe and 19D of Perspex pipe from $V \rightarrow H$ bend ($R/D = 4$))

- Downward sloping standard pipe section (51D), 0.4m 4-lobe swirl pipe, horizontal standard pipe section (10D) and Perspex pipe (7D) (measurement section located 88D standard pipe and 19D Perspex pipe from V→H bend)

To analyse the decay of the induced swirl and assess the effect of induced swirl in the inclined section, photographs were taken at three positions, as shown in Figure 8.1. Photographs were taken at positions 1 and 2 when the swirl pipe was included upstream, at positions 1 and 3 when the swirl pipe was removed and at position 3 when the swirl pipe was included in the inclined section.

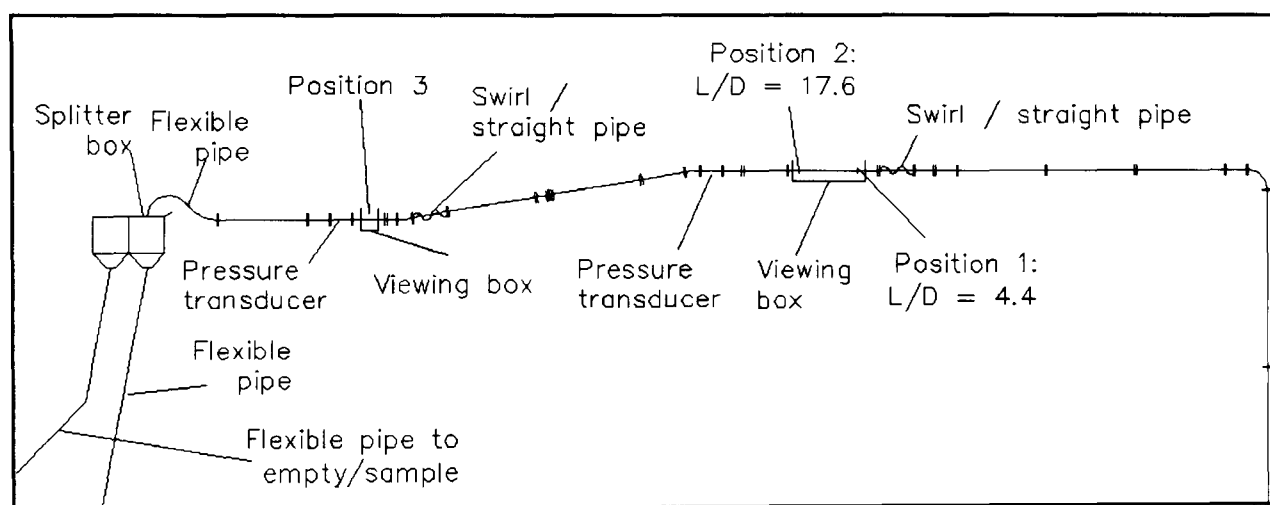


Figure 8.1: Diagram of the top leg of the flow loop for particle tests

The densities and sizes of the materials used to prepare the slurries and the concentrations tested are shown in Table 8.1. All the materials were prepared by screening to within the sizes shown using a Russell Finex high-speed separator (with 22 inch screens). The densities of two samples of each material were determined using a 50ml density bottle with water. The samples were not ground, but tested as they were used in the pipe flow loop to more closely determine the density of the material pumped.

Table 8.1: Parameters of the solids used in the tests; % v/v = $V_s/V_l \times 100$.
Reference code, used in Figures, comprises first letter of material and reference to particle size.

Material	Size μm	Reference code	Input Mass kg	Density kg/m ³	Actual Conc. % v/v	Target Conc. % v/v
Plastic beads	Nominal $d_{50}=1750$ *	-	36	1351	2.7	2.7
Coal	Ultra-course: 4000-2000	c24	18	1390	1.3	1.4
			27	1390	1.9	2.0
			36	1390	2.6	2.7
	Coarse: 2000-1000	cc	18	1530	1.2	1.4
			27	1530	1.8	2.0
			36	1530	2.4	2.7
Sand	Coarse: 2000-1000	sc	36	2640	1.4	1.4
			54	2640	2.1	2.0
			72	2640	2.7	2.7
	Medium: 1000-500	sm	36	2640	1.4	1.4
			54	2640	2.1	2.0
			72	2640	2.7	2.7
	Fine: $d_{50}=118$	sf	72	2600	2.8	2.7
Magnetite	2000-1000	mc	68	4970	1.4	1.4

* Determined by Raylor (1998), flattened after long use.

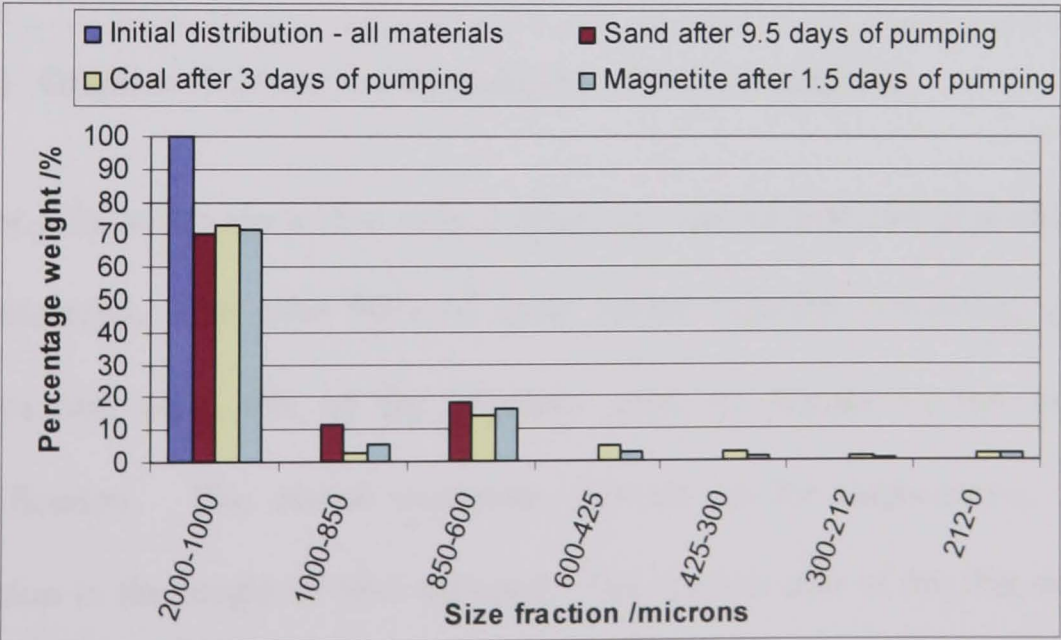
The small difference between the target input concentration and the actual input concentration in Table 8.1 occurred because testing on the flow loop began before a determination of the density of the materials was made. So the input mass was calculated from an estimation of the density and rounded up to the nearest integer.

8.3 Results and discussion

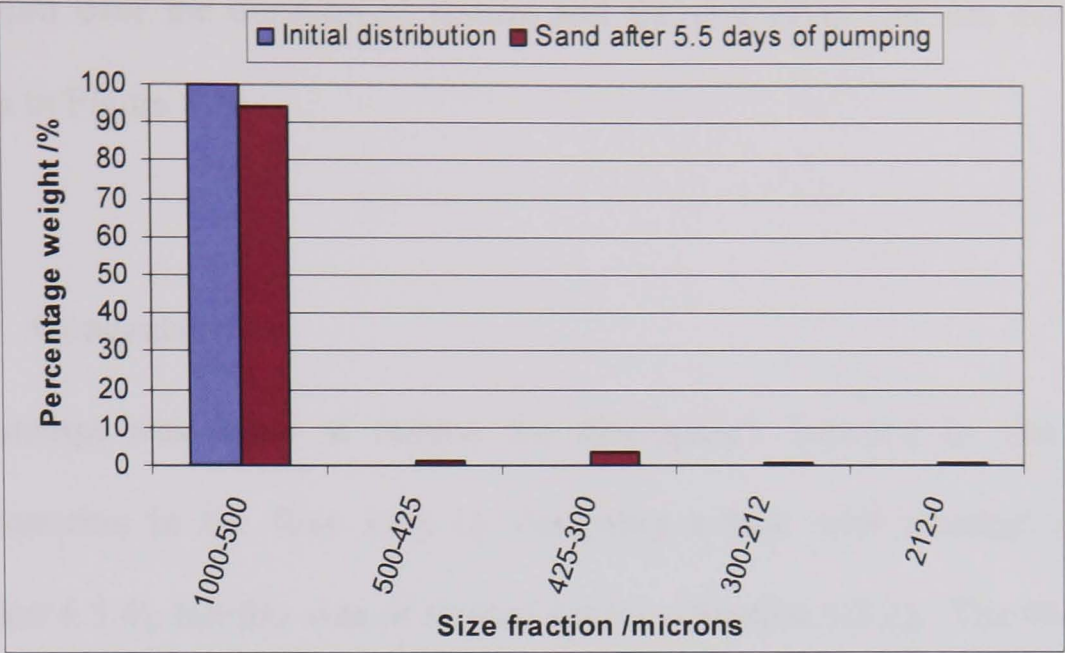
8.3.1 Particle size

After the pipeline tests, samples of the remaining particles were sized to investigate the particle degradation experienced. The size distribution of the coarse and medium particles was measured by taking a 5 kg sample and feeding this through a 1000 μ m or 500 μ m screen determined by the initial particle size. The underflow was weighed then riffled to a suitable mass for sieve analysis. A set of appropriately sized sieves were selected from the root 2 series and agitated using a Pascall Inclino Sieve Shaker. The size distribution of the fine particles was determined using a Malvern Mastersizer S. The size distribution of the large coal particles was not measured because this material was crushed using a rolls crusher to prepare the coarse coal particles. The results are presented in Figure 8.2.

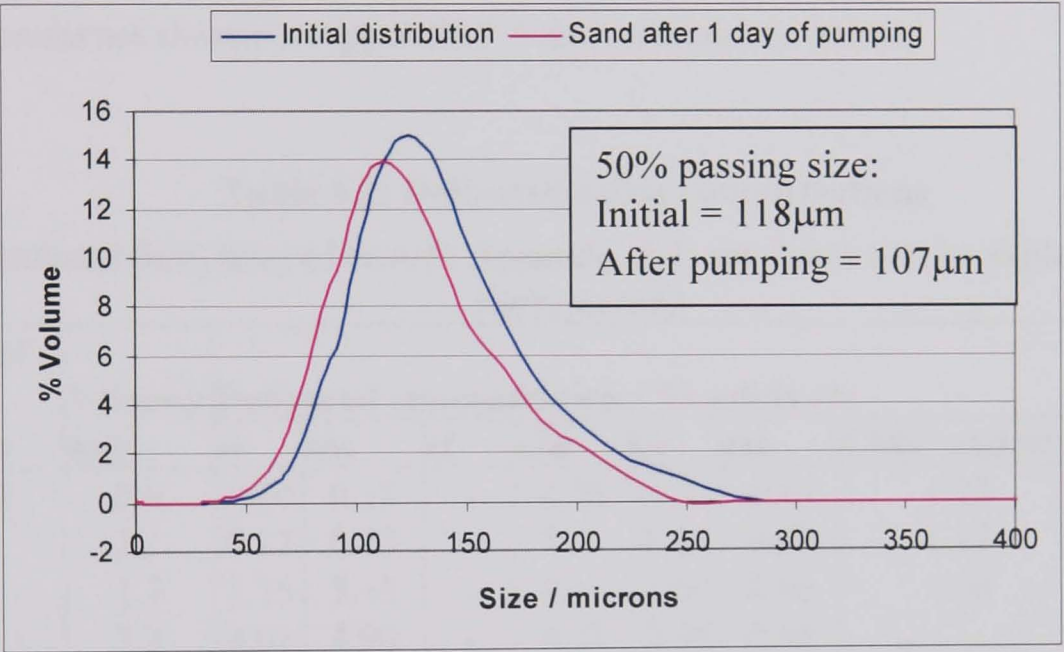
Figure 8.2: Series of graphs to illustrate the degradation of solid particles



a) Graph to illustrate the degradation of the coarse particles



b) Graph to illustrate the degradation of the medium particles



c) Graph to illustrate the degradation of the fine particles

Figure 8.2a and b show that only a small amount of material degraded to a very fine material, with over 90% of each coarse material remaining greater than 600µm and only 6% of the medium sand no longer in the original size classification. The coarse materials showed similar degradation, despite the variation in the length of time pumped. The median size of the fine sand reduced

by 11 μ m over the duration of testing and the change in the size distribution is shown in Figure 8.2c.

8.3.2 Concentration

An attempt was made to reduce the discrepancy between in situ and input concentration in the flow loop by designing a tank with minimal dead zones (Section 4.5.4), but this was of limited success (Section 5.3.2). The best available technique to evaluate concentration was to take a sample of the delivered flow. The results are shown in Appendix F.1 and summarised below.

Table 8.2: Delivered solids concentrations

(Calculated from lines of best-fit Appendix F.1, see Table 8.1 for explanation of slurry codes)

Target conc. % v/v	Velocity m/s	Delivered concentration / % solids v/v							
		sc	sm	sf	c24	cc	mc	CMC and sc	beads
1.4	0.6	-0.05	0.15	-	4.76	-1.81	-0.01	1.23	-
	1.1	0.13	0.73	-	7.19	0.36	0.40	1.12	-
	1.7	3.35	3.15	-	8.16	2.60	0.66	1.06	-
	2.3	4.01	4.90	-	9.38	2.05	0.88		-
2.0	0.6	0.47	0.38	-	5.98	0.24	-	-	-
	1.1	2.44	2.78	-	9.60	2.01	-	-	-
	1.7	5.78	5.87	-	11.40	3.67	-	-	-
	2.3	6.92	7.45	-	11.15	4.02	-	-	-
2.7	0.6	1.00	0.62	5.60	7.21	2.32	-	-	12.77
	1.1	4.79	4.87	4.92	12.04	3.68	-	-	14.17
	1.7	8.24	8.62	4.46	14.69	4.76	-	-	15.07
	2.3	9.88	10.05	4.15	12.93	6.02	-	-	15.69

Since solids holdup in a pipe, occurs in the presence of a concentration or velocity gradient (Goiver and Aziz, 1972), holdup should decrease and delivered concentration increase with velocity. This pattern was observed in most of the

results. Furthermore, higher delivered concentrations are expected for smaller particle slurries, since these exhibit more homogenous flow than larger particle slurries. This difference was evident between the medium and coarse sand, but was not the case for the ultra-coarse and coarse coal. There was also a large variation between the results and the target value and between each other. This was attributed to the many complex factors involved, such as, the relationship between delivered concentration and in situ concentration, the presence of a tank in the pipe flow loop and the shape, size, density and surface properties of the solids.

In addition to these factors the results were also influenced by the methodology employed. As explained in Chapter 4, the concentration results were calculated from the mass and volume of a sample of the flow. The results of three samples were averaged, however there was a fairly large deviation between each trial. This was attributed to an inadequate sample size, which was restricted to 20-25 l by the need to lift the sample onto a balance. For future work it is recommended that the weigh tank be commissioned. This would allow calculation of the delivered concentration from a sample that would be more representative of the flow (up to approximately 700 l). In addition it is recommended that reliable methods for measurement of the in situ concentration be investigated.

Since improving the methodology and repeating the tests was not feasible within the time-scale of the project, the results must be interpreted as they stand. Furthermore, where literature was available, the pressure drop results (Section

8.3.3) generally followed the patterns described, confirming that the large variation in the concentration results obtained was predominantly a product of inadequate sampling.

8.3.3 Pressure drop

Initially, an attempt was made to calculate the pressure loss across the 4-lobe swirl pipe measured in the bottom horizontal leg. Using the method adopted by Ganeshalingam (2002), the pressure drop over 3.0m of pipe with a circular cross section (standard pipe) was determined and subtracted from the pressure drop across the 0.4m swirl pipe followed by 3.0m of standard pipe. An alternative method was to measure the pressure drop over the swirl pipe directly, but this method was avoided because of the increased risk of damage to the pressure transducers caused by swirling particles.

The results obtained are shown in Appendix F.2-F.5. Previous results using the Perspex flow loop (Section 4.5.2) indicated that the pressure drop over a swirl pipe was independent of concentration, by the proximity and crossing of pressure drop curves. Regardless of concentration, particle size and density the results from the steel flow loop were also clustered close to one another, the only significantly different results being the CMC curves. The results for coal slurries suggested a reduction in pressure loss with increasing concentration, but because the differences between the curves were small, more evidence is required to form a reliable conclusion on this matter. However, consideration of the coarse sand and

magnetite results, which exhibit irregular curves, led to the identification of a flaw in the method. The calculation assumed that the pressure drop over the standard pipe when swirl induction was present was equal to the pressure drop over the standard pipe without swirl induction. While this approximation appeared satisfactory when pumping plastic beads in the Perspex loop, rough pipe flow of slurries with denser particles have shown more sensitivity to this assumption, perhaps indicting a greater difference between the flow in standard pipe with and without swirl.

To avoid this problem the results were presented as measured, using only the following direct comparison between the results:

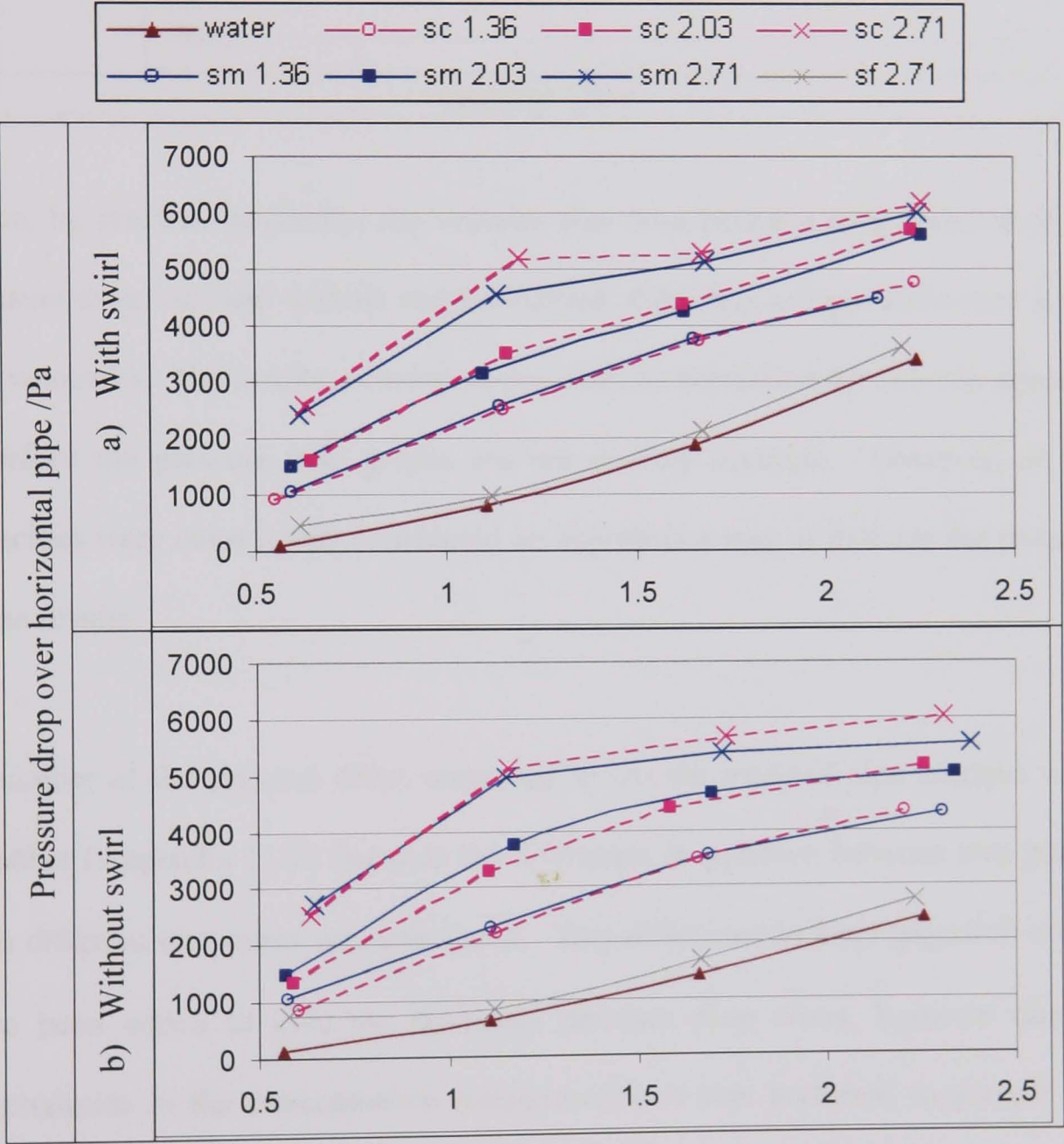
$$\text{Pressure cost} = \text{pressure drop with swirl induction} - \text{pressure drop without swirl induction}$$

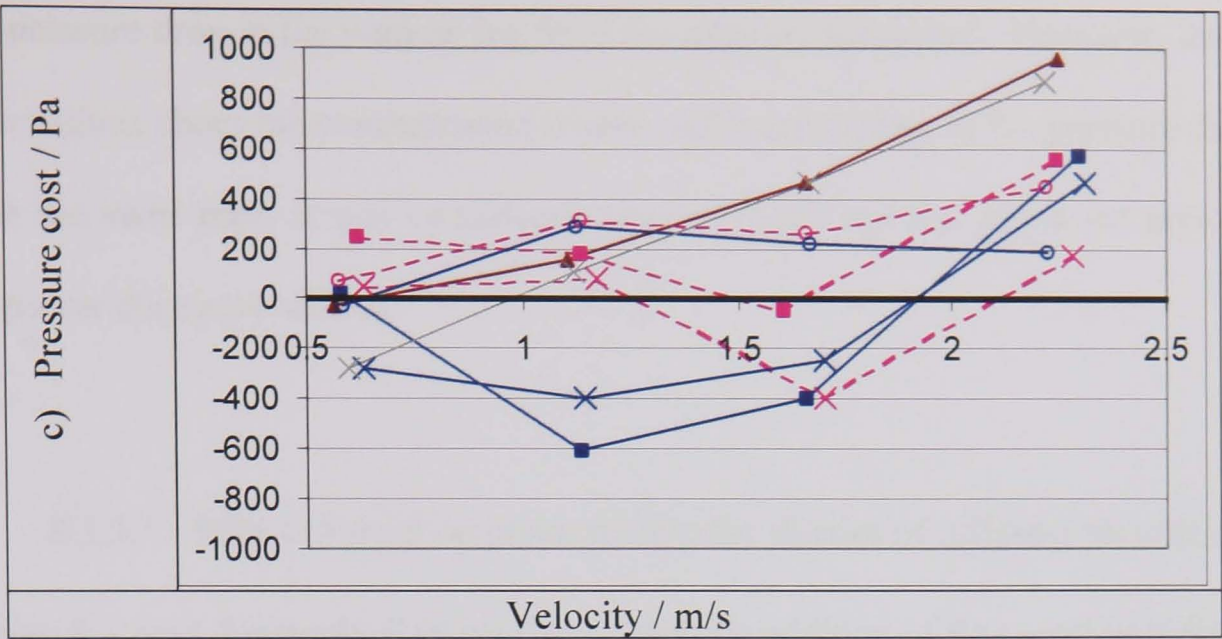
where a negative result indicates a pressure benefit and a positive result, a pressure cost. Therefore, to assess the effect of swirl induction in a horizontal pipeline the pressure drop across a 0.4m swirl pipe followed by a 3.0m standard pipe is compared with the pressure drop over a 3.5m length of standard pipe.

The results, presented in Appendix F.6-F.20, were sorted first by slurry variable (particle size, etc). then by pipe geometry (horizontal, etc). For each condition, three graphs are displayed, as shown in Figure 8.3. The first graph (a) shows the relationship between the pressure drop over the measurement section for various

slurries when swirl was included, followed by a graph to show the same when swirl was absent (b) and a graph of the pressure cost against velocity (c) for these slurries.

Figure 8.3: Pressure drop and cost over horizontal pipes for sand slurries of various particle sizes.





Since, by practical necessity, the velocity was reset between measurement of the pressure drop with and without swirl induction, there was a slight difference in the test velocities. The results were subtracted with no correction for velocity applied; therefore the pressure cost graphs are not entirely accurate. However, as the velocities were close it was considered an appropriate way to indicate the patterns in the results.

A number of the pressure drops measured across the inclined pipe sections were negative (Appendix F.10) because the difference in pressure between two points with different elevations was calculated. This difference in head ($\rho_s g \times 0.5$) could have been added to give the frictional pressure drop alone, however due to uncertainties in the concentration measurements it was preferred to present the results as collected.

Similarly, it was initially anticipated that the pressure drop over the bend could be found by subtracting the pressure drop over the swirl pipe and an approximation of

the pressure drop in the vertical leg from the pressure measured. However, due to reservations about the concentration results and irregularities in the pressure drops over the swirl pipe, it was considered prudent to present the measured pressure drop over the entire section.

8.3.3.1 Effect of swirl on pressure drop for slurries of different particle size

Figure 8.3 (and Appendix F.6) confirmed that the addition of fine sand particles to water increased the pressure drop over a standard pipe. As the particle size was increased to medium, a larger pressure drop was obtained and the additional pressure drop increased with concentration. However, little difference was observed between the pressure drop for medium and coarse sand sizes. The coarse results were slightly higher for a concentration of 2.7% v/v, but crossover with the medium sand pressure curve was still evident at the lowest velocity (Figure 8.3). Durand (1953) found similar results while studying sand and gravel slurries, showing that increasing the size of particles increased the pressure drop, up until a particle size greater than 1.5 or 2mm. Since the size of the current sand was slightly smaller at 1-2mm and 0.5-1mm, the results were plotted in the same way as Durand's results, to confirm this finding. Figure 8.4 (Appendix F.7) illustrates the similarity between the pressure drop measured over the cylindrical pipe for medium and coarse sand slurries, while highlighting the difference between this and the same quantity for the fine sand slurry. In view of the problems associated with the concentration results, it should be noted that these curves were produced using the 'actual concentration' values from Table 8.1. Therefore the spread in the

results at low velocity was attributed to differences between the in situ concentration and the ‘actual concentration’, which will be greater at low velocity. The addition of swirl did not appear to change the pattern of the slurries relative to each other.

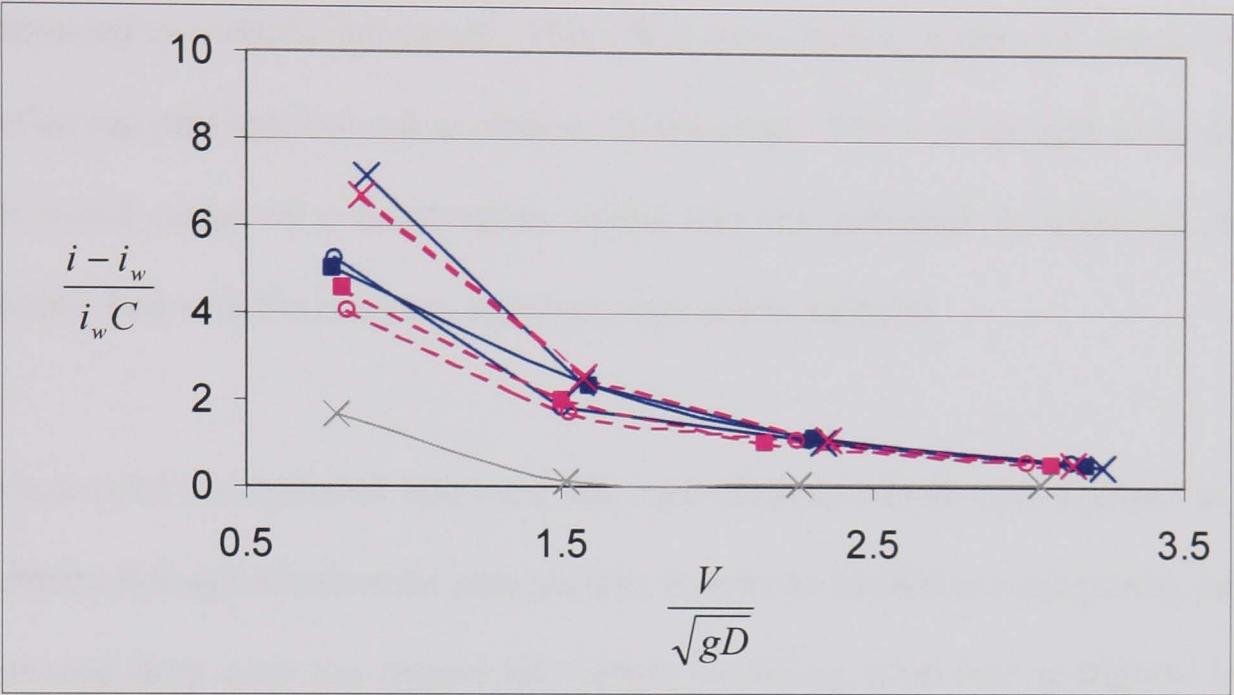
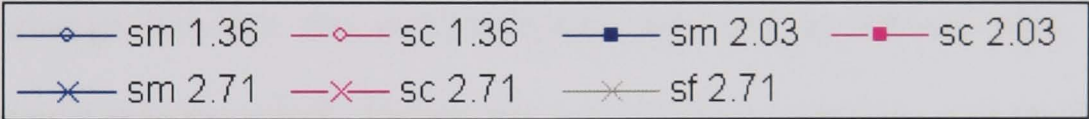


Figure 8.4: Comparison of pressure loss over horizontal pipe, for slurries of various particle sizes, with no swirl-induction present (after Durand, 1953)



From the coal results, it is clearly seen that the larger particle size gave a larger pressure drop (Appendix F.9). This conformed to the results of Worster and Denny (1955) who conducted an extensive investigation of the flow of coal in pipelines. They found pressure drop to increase with particle size up to approximately 3.2mm - 4.8mm, beyond which particle size was independent of pressure drop. The size range of coarse particles used in this investigation was below this threshold, hence an increase in pressure drop between the slurries was

observed. This was again confirmed by plotting the results in the form used by Durand (1953) (Appendix F.9).

Durand (1953) and Worster and Denny (1955) found that the pressure drop increased with solids concentration and the excess pressure drop due to particles decreased as velocity increased. This effect was clearest in the coal results in the horizontal pipeline, but not as obvious in the sand. This was thought to be due to the small range of concentrations tested and the potential interference of the particle bed with the pressure measurements at low velocity.

When swirl was induced into sand and coal slurries, which were pumped at low velocity through a horizontal pipe section, a pressure benefit was measured, i.e. the pressure drop over the horizontal section including swirl had a slightly lower pressure drop than without swirl (Appendix F.6c and F.8c). Since there was an abrupt change between the swirl-inducing pipe and cylindrical pipe, a high pressure cost was expected. Hence, the fact that some pressure cost results were negative is testament to the effectiveness and potential of the swirl pipe. The graphs tend to show a positive gradient, which confirms the findings of previous authors (Schriek *et al.*, 1974; Singh and Charles, 1976 and Ganeshalingam, 2002) that swirl is most effective at lower velocities. It is also interesting to note that greater benefit was achieved when pumping slurries with a higher target concentration and that the results for water and the fine sand slurry appear to have a different gradient to the coarse sand results. This difference in gradient may be indicative of different flow mechanisms, with the fine sand slurry and water

exhibiting viscous fluid behaviour, distinct from the remaining heterogeneous slurries.

The pressure drops over the inclined section (Appendix F.10 and F.11) follow a similar pattern to the results of the horizontal tests, with an increase in pressure drop with concentration, as expected from the results of Doron *et al.* (1997) (Section 2.6). Again, larger particles in the slurry led to larger pressure drops, with coarse and medium sand slurries giving a similar results and the addition of swirl producing no significant changes in the pattern of the slurries relative to each other. The pressure costs were also similar to that of horizontal pipe in that swirl was most effective at the lower velocities and possibly higher concentrations. The water and fine sand slurry (Appendix F.10) display a pressure drop curve of the shape typically found in the literature, in some cases crossing the straighter curves of the other sand slurries at low velocity. The shape of the straighter curves was thought to be due to the formation of a stationary bed distorting the lowest velocity result.

The results for the pressure drop over a bend differ a little from previous patterns and each other (Appendix F.12 and F.13). The fine sand slurry and water gave a higher pressure drop, relative to the other slurries, than previously recorded. This was explained with reference to Mukhtar *et al.* (1995), who found that secondary flows within a long radius, horizontal 90° bend were inhibited by the presence of solids. This could lead to a reduction in the additional pressure drop due to the

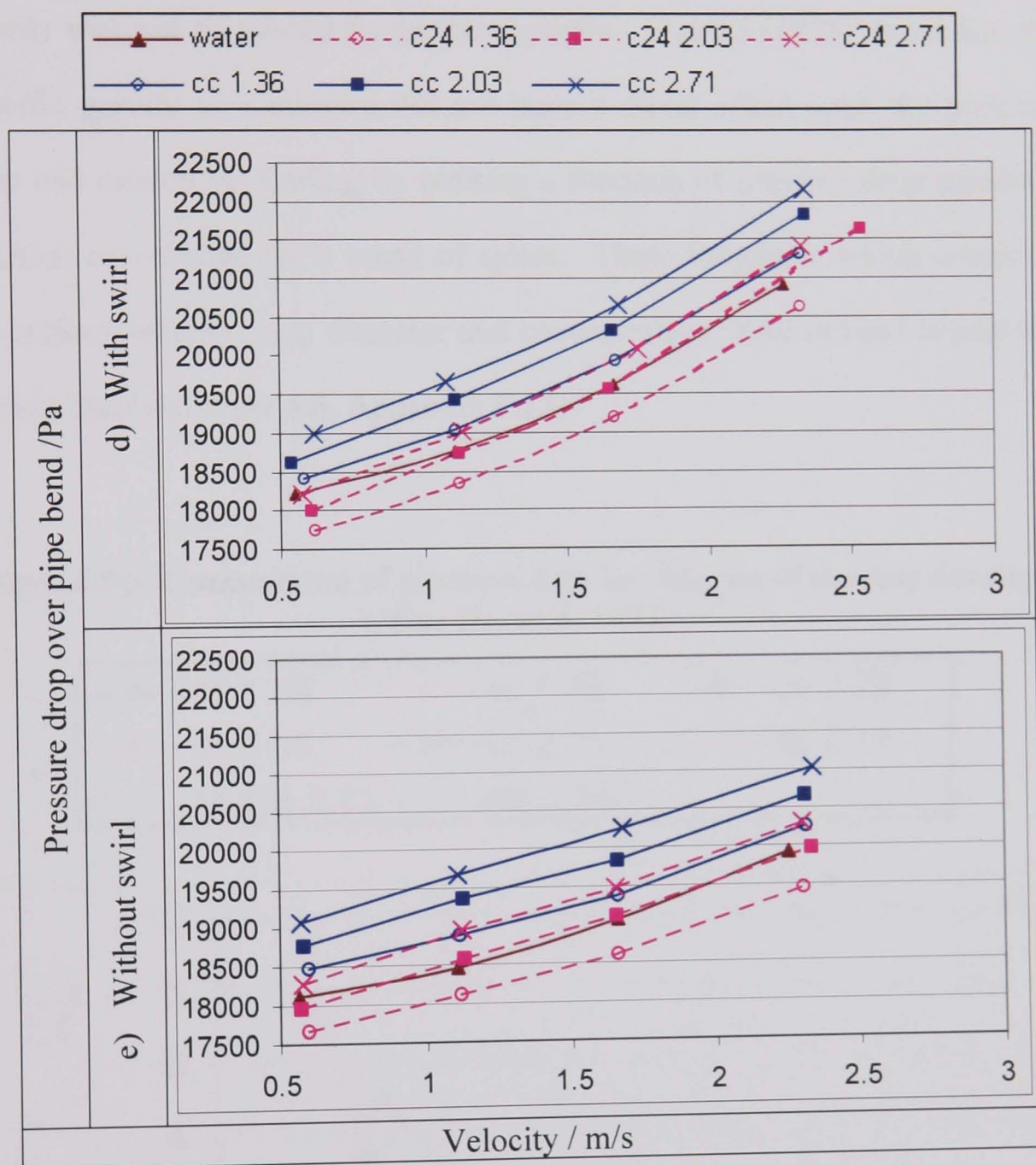
presence of particles, as observed, although the effect was likely to be smaller in vertical bends since these were also affected by gravity.

Another interesting result was that the pressure drops across the bend for the coarse coal slurries (2000-1000 μ m) were clearly greater than for the ultra-coarse coal slurries (4000-2000 μ m). A possible explanation for this effect was based on earlier research performed by Mukhtar *et al.* (1993), who found that particles within a vertical bend were more homogeneously distributed than in horizontal pipe and that this deviation was most pronounced for larger particles. Given that a more homogenous particle distribution results in a reduced pressure loss, as demonstrated by the pressure cost results for horizontal pipe, the greater homogeneity imparted to the ultra-coarse particles by the bend may have resulted in the lower pressure drops measured. However, this relative reduction in the pressure loss over the bend for coarse particles was not measured when pumping sand slurries. This was attributed to the complex interaction of unknown factors, such as the shape of the particles, and the size distribution of particles within the specified size ranges.

Toda *et al.* (1972) investigated the effect of the radius of curvature of a bend on the pressure drop across it, examining a range of velocities and concentrations for vertical and horizontal bends. One of their findings, for vertical bends, was that the additional pressure drop due to particles was constant regardless of flow rate. The results tend to support this, with and without the inclusion of swirl. Figure 8.5

illustrates the parallel curves obtained when the pressure drop over a bend was measured for coal slurries.

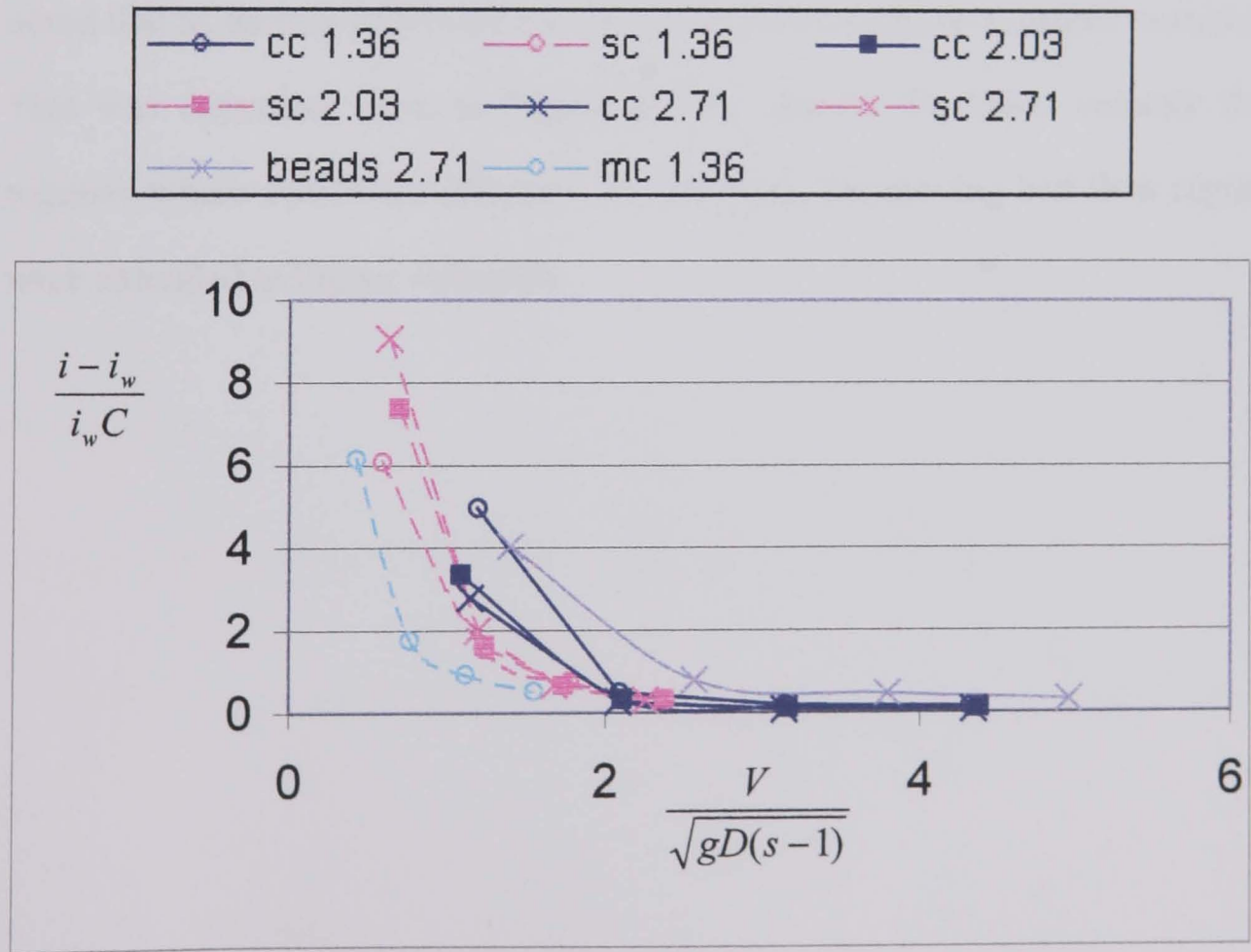
Figure 8.5: Pressure drop over horizontal pipes a bend for coal slurries of various particle sizes.



8.3.3.2 Effect of swirl on pressure drop for slurries of different densities

The data in Appendix F.14 appears to show an increase in the pressure drop with specific gravity, however the variation in critical velocity with specific gravity was not accounted for in these graphs. Durand (1953) found that the specific gravity of a mixture did not have a direct effect upon the pressure drop and proved his finding by plotting a function of pressure drop against a function of velocity, for a range of solids. These functions, which corrected for critical velocity, pipe diameter and concentration, were utilised to plot the current results (Figure 8.6, Appendix F.15).

Figure 8.6: Comparison of pressure loss for slurries of various density (after Durand, 1953)



The resulting curves were reasonably similar, with some deviation at low velocity. As explained in Section 8.3.3.1 the results were plotted using the 'actual concentration' values from Table 8.1. Therefore the deviation between the curves was attributed to differences between the in situ concentration and the 'actual concentration', which will be greater at low velocity, and variations in the size distribution of particles within the specified size ranges.

The data in Appendix F.16-F.17 serves to show the shape of individual curves, although the pressure drops for different materials cannot be directly compared since they relate to different flow regimes. The pressure costs calculated for different density slurries flowing through each pipe configuration, show the positive gradient previously observed and give an indication that the swirl pipe was more effective when pumping more concentrated slurries. It was also noted that as density increased the swirl pipe was beneficial at higher velocities. This was expected, since at higher specific gravity the lower velocity flow regimes where swirl was effective, for example, the moving bed flow regime, were extended to higher velocities.

8.3.3.3 Effect of swirl on pressure drop for slurries with different viscosity carrier fluids

Benefits documented in literature (Heywood, 1998, Section 2.3) relating to capacity of shear thinning fluids to transport coarse particles were not illustrated by these results (Appendix F.18-20). It was considered that possible benefits were not observed because the apparent viscosity of the CMC was higher than that considered by this author. As with previous results, swirl induction was more effective at lower velocities and when pumping slurries rather than pure liquids.

8.3.4 Tangential velocity

An attempt was made to determine the tangential velocities of particles downstream of a swirl-inducing pipe from photographs. It was proposed that by using an appropriate shutter speed, the track of particles could be captured and the photographs subsequently analysed to mathematically describe, in terms of xy co-ordinates, the path of the particles. Given that the mean axial flowrate (u) can be measured and assuming that the particle paths captured are at the extreme edge of the pipe (hence $R = 0.025\text{m}$), the tangential velocities can be calculated as follows:

From the theory of angular and horizontal motion:

$$\theta = \omega t$$

Equation 8.1

$$t = \frac{x}{u}$$

Equation 8.2

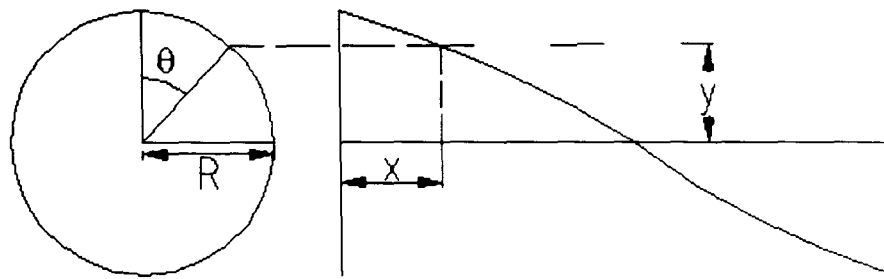


Figure 8.7: Diagram of the cross-section (LHS) and length (RHS) of pipe with particle track

From Figure 8.7:

$$y = R \cos \theta \quad \text{Equation 8.3}$$

Two methods of calculating the average angular velocity of a particle over its track emerge. Firstly, θ and t can be calculated (for a number of co-ordinates that describe the particle path) from Equation 8.3 and 8.2 respectively. Then the angular velocity over the particle track (ω) is the gradient of the graph of θ against t (Equation 8.1).

Alternatively:

Combining Equations 8.1 and 8.2 for θ and substituting this into Equation 8.3 gives:

$$y = R \cos \frac{\omega x}{u}$$

or

$$y = R \cos Ax \quad \text{where} \quad A = \frac{\omega}{u}$$

So if $\cos^{-1} \frac{y}{R}$ is plotted against x for a number of co-ordinates then the gradient of the line produced will be A , from which ω can be found. In both calculation

methods Equation 8.4 is used to convert the angular velocity to the tangential velocity.

$$v = r\omega \quad \text{Equation 8.4}$$

The second calculation method was used as a check to reduce the possibility of numerical mistakes being made. An example analysis is shown in Figure 8.8. Where possible, three lines tracing the particle tracks were drawn onto the photographs, using Paint Shop Pro (Jasc Software Inc.) version 6.00. The central lines corresponded to approximate distances of 4.4D (position 1) and 17.6D (position 2) downstream of the swirl pipe. Coordinates on the lines were then determined (at the points shown) using rulers in Paint Shop Pro. The coordinates were calibrated to the scale in the photograph and adjusted to place the x-axis along the pipe centreline (also drawn on the photographs). Thus several coordinate sets were determined for each condition enabling the above calculations to be performed.

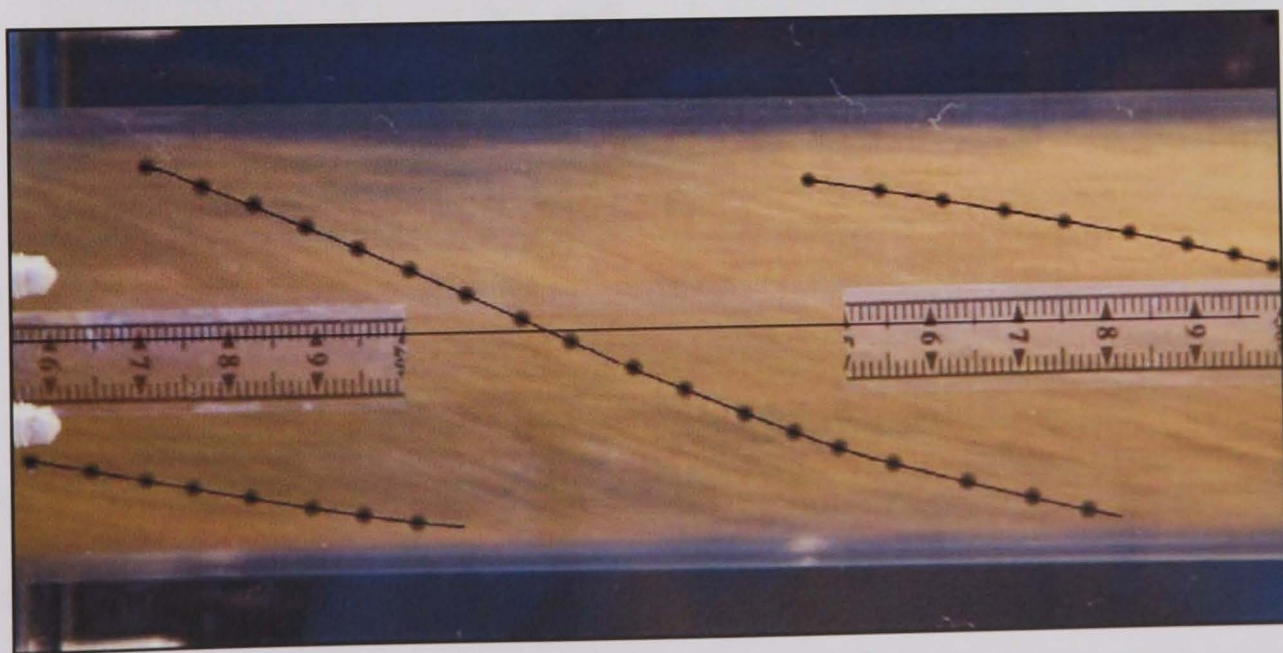


Figure 8.8: Example analysis (1.4% v/v coarse sand, 1.7m/s)

A number of problems were encountered with the method, such as the subjectivity associated with drawing the particle paths. Co-ordinates to describe the paths were determined manually and so were subject to human error, despite repeated checking. The analysis was also extremely time consuming, which limited the number of determinations that could be performed – only 1 picture was analysed for each condition. Furthermore, during the tests the amount of solids passing a particular pipe position was observed to vary with time, as illustrated in Figure 8.9. The colour of the sand appeared darker and lighter at the maximum and minimum flow rates and a variation was detected in the sound at all velocities tested. To mitigate against this problem an attempt was made to capture photographs at the peak flow rate to obtain some constancy between measurements. Despite these problems, the results were assumed to provide a good overview of the behaviour of the flow and an interesting analysis of the results has been made.

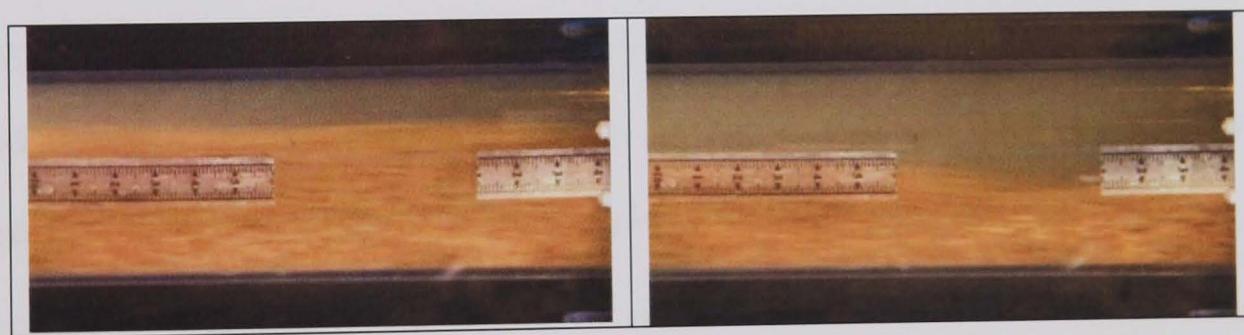


Figure 8.9: Two photographs taken under the same conditions to illustrate the unsteady flow observed (2.7% v/v coarse sand, 1.1m/s).

A series of photographs were taken at position one (Figure 8.1), when preceded by standard pipe to illustrate flow under test conditions without swirl induction. These photographs also provided an indication of the flow conditions at the inlet to

the swirl pipe when it was used. The photographs are therefore presented alongside the swirl decay photographs in Appendix F.21-F.30, an example is shown in Figure 8.10. It was observed that the particles formed either a moving bed or underwent some saltation and remained in the bottom section of the pipe in all cases except for 2.7% v/v at 1.7 and 2.3m/s. In these cases the particles encroached a little farther up the pipe, but this may be due to the fact that these conditions were conducted at the end of the day when the fines content of the mixture was probably higher due to the degradation that had taken place during the day.

The swirl flow induced by the swirl pipe can clearly be seen in Figure 8.10b and c. The decay between positions 1 and 2 (Figure 8.1) was also clear. The velocities determined from the central line show fairly well defined patterns, with the top RHS and bottom LHS lines showing more variation. An example of the centreline tangential velocity results is plotted in Figure 8.11, with the remaining graphs in Appendix F.31, F.34 and F.37. Tangential velocities obtained from the top RHS and bottom LHS lines (Figure 8.10) are presented in Appendix F.32-33, F.35-36 and F.38-39. These results showed more irregularity than the centreline results because of the difficulty of fixing the position of these lines in the photographs. It was difficult to distinguish patterns in these results so they are not discussed further.

Figure 8.10: An example of the results for 1.4% v/v coarse sand at an axial velocity of 1.7m/s.

Note: Each tangential velocity corresponded to a line drawn on the photograph. Velocities are listed from top RHS to bottom LHS.

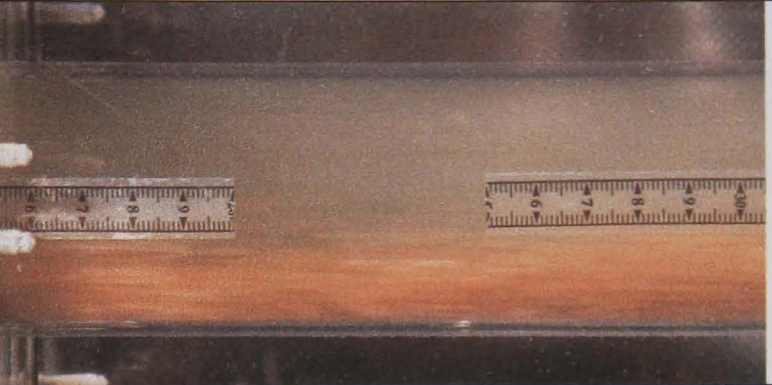
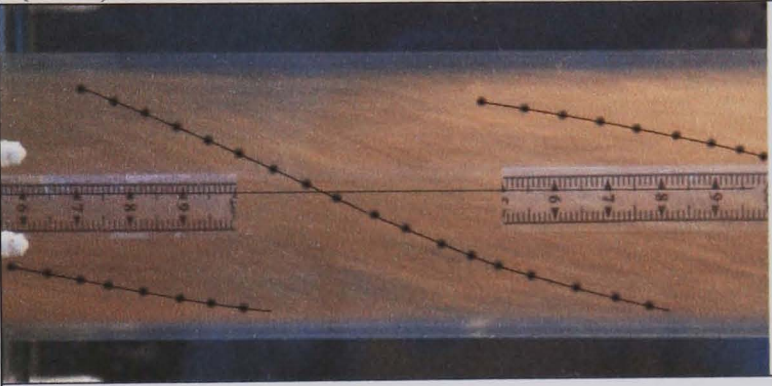
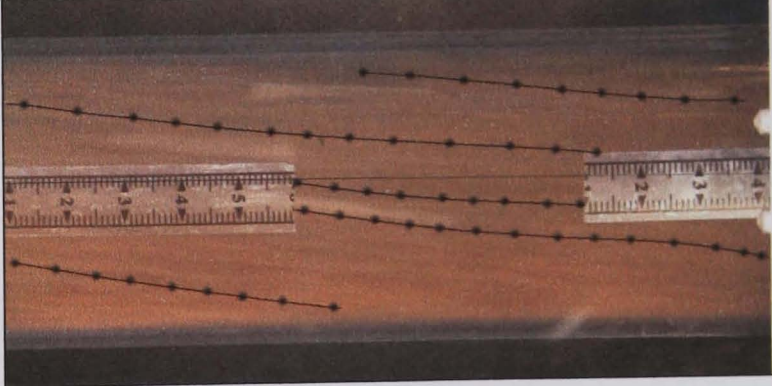
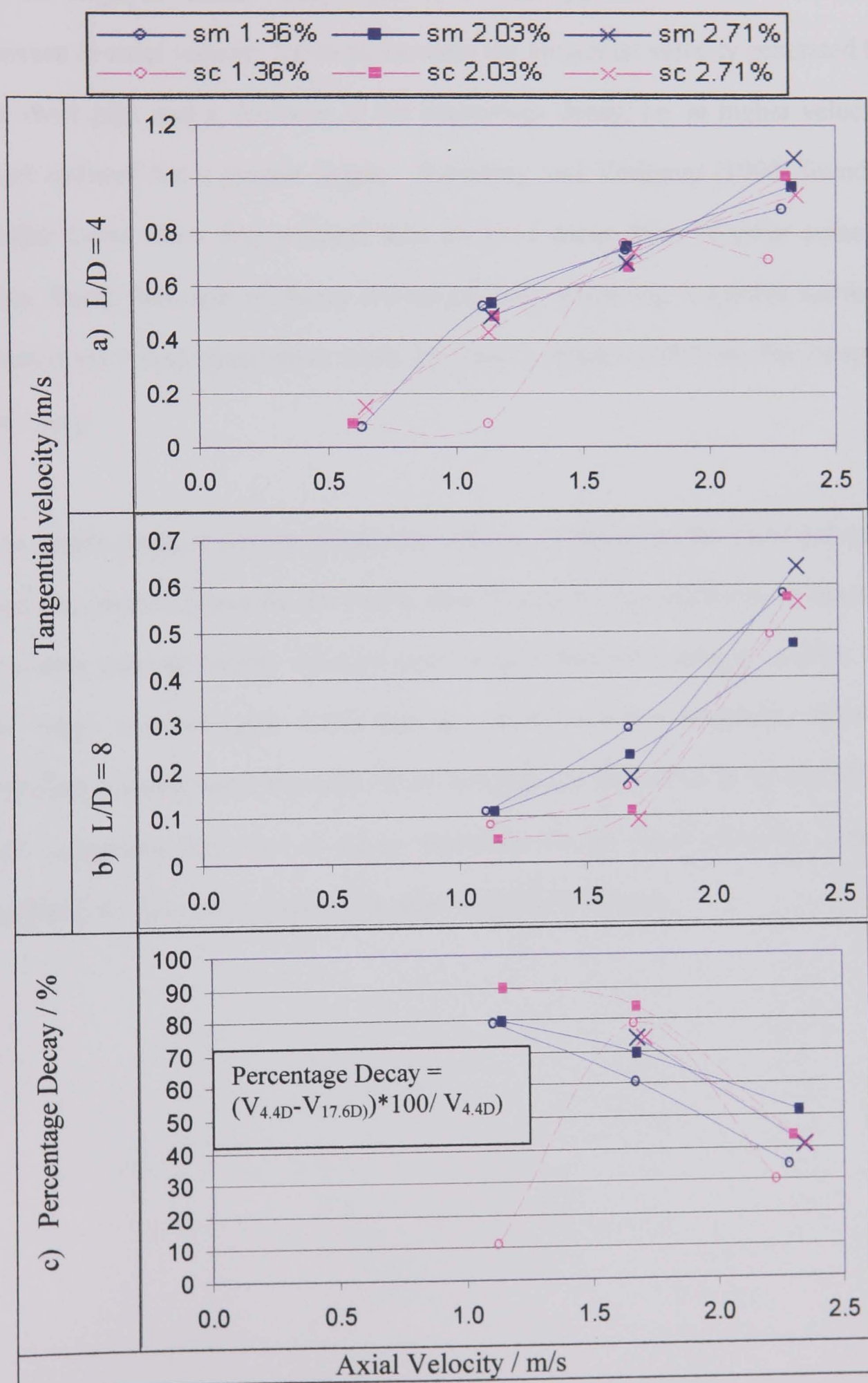
Photograph	Position	Images (shutter speeds /s) and tangential velocities /m/s
(a)	1 (no swirl)	 (1/60)
(b)	1 (4.4D downstream)	 0.39; 0.76; 0.43 (1/60)
(c)	2 (17.6D downstream)	 0.20; 0.16; 0.15; 0.18; 0.39 (1/50)

Figure 8.11: Series of graphs showing the tangential velocity and percentage decay verses the axial velocity, for sand slurries of various particle sizes, determined from the central lines.



8.3.4.1 Decay of swirling flows for slurries of different particle size

For the range of values tested, Figure 8.11 (and Appendix F.31) shows that an increase in axial velocity led to an increase the tangential velocity generated by the swirl pipe and a decrease in the percentage decay, i.e. at higher velocity swirl endured for a greater length. Steenberg and Voskamp (1998) found a similar trend when they collated data on swirl decay from 16 other authors. They found that rate of decay decreased with increasing Reynolds number, reinforcing visual observation made by Ganeshalingam (2002) on the Perspex flow loop.

The graphs suggest that the tangential velocity produced by the swirl-inducing pipe was slightly lower for the coarse sand (Figure 8.11a) and the swirl induced in coarse particle slurries decayed more rapidly than finer particle slurries, for the range tested (Figure 8.11b and c). Since a lower tangential velocity indicates a lower swirl intensity, these findings are supported by Kitoh (1991) who suggested that rate of decay depended on the swirl intensity, with a tendency for low swirl numbers to give high rates of decay.

An attempt was made to take photographs for the coal slurries using a white background, however the tendency of coal to colour the water made the photographs particularly unclear.

8.3.4.2 Decay of swirling flows for slurries of different densities

Appendix F.34 also shows the increase in induced tangential velocity and reduction in percentage decay with velocity previously observed. Appendix F.34a indicates that, for the range of particle densities tested, a similar tangential velocity was initially induced in each slurry. However at $L/D = 17.6$ (b) the tangential velocities for different particle densities have separated, thus a larger rate of decay was detected for denser particle slurries.

8.3.4.3 Decay of swirling flows for slurries with different viscosity carrier fluids

Again, the increase in induced tangential velocity and reduction in percentage decay with velocity was observed (Appendix F.37). The graphs indicated that less tangential velocity was induced into the CMC-sand slurry than the water-sand slurry. The photographs for the CMC-sand slurry (Appendix F.30) indicated that although some swirl was observed a sliding bed was present at all velocities tested, with and without swirl. This confirms the conclusions of the PIV experiments (Section 6.1.4), that little swirl was induced into the CMC by the 4-lobe swirl pipe.

8.3.4.4 Inclination

Photographs at the exit of the inclined section (position 3) with and without swirl induction for each of the slurries are displayed in Appendix F.40-F.49 with an example shown in Figure 8.12.

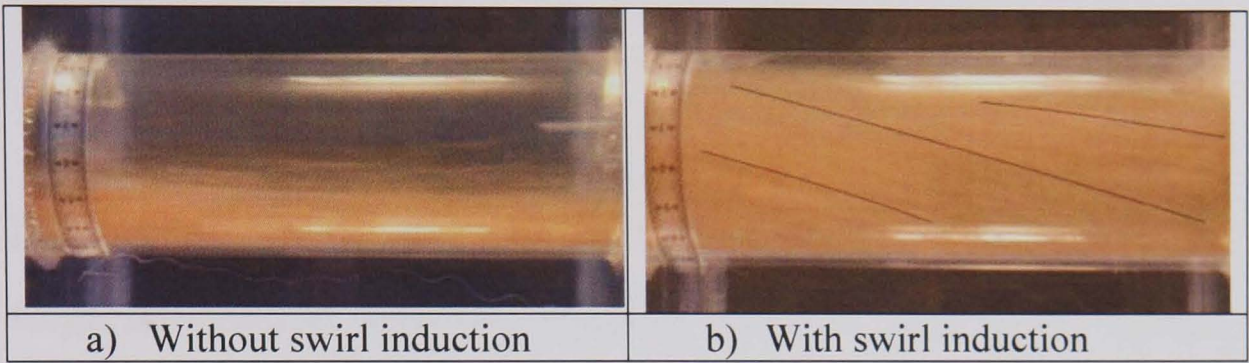


Figure 8.12: Flow downstream of an inclined section of pipe with and without swirl induction (1.4% v/v coarse sand, 1.7m/s).

Alike to the flow developed in position 1 when no swirl induction was present, a sliding bed or saltation is observed in these photographs and the particles remain predominantly in the lower half of the pipe. It is seen that the addition of swirl distributed the particles more evenly, with the exception of the lowest velocity, when the particle bed sometimes remained. This conclusion applies to each slurry except the fine sand-water slurry, for which the quality of photographs was too poor to allow observation of the swirl pattern and the CMC slurry to which little swirl was induced.

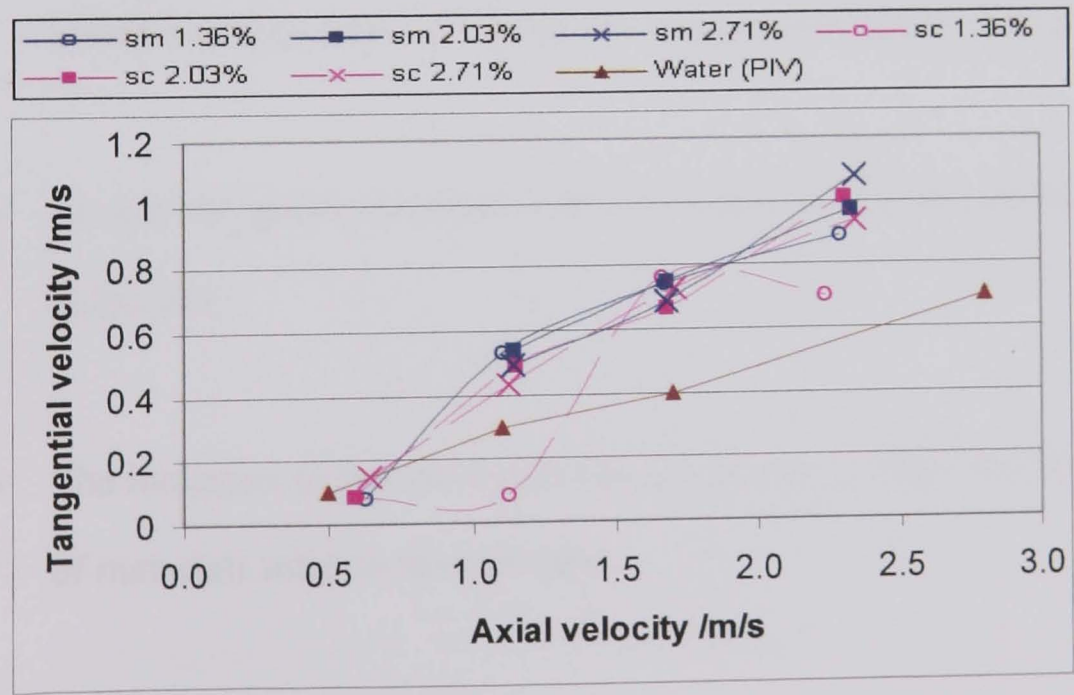
It was anticipated that the inclusion of swirl induction in a downward sloping pipe section might reduce the likelihood of pipeline blockage, by virtue of the improved particle distribution. During the commissioning of the pipe flow loop blockage of

the loop was a problem. However this was not due to the inclined section but rather the steep inclination of the flexible hose connecting the pipes to the splitter box (Section 5.3.6). To solve this problem the use of swirl pipe to mitigate against blockage was utilised. It was evident that swirl induction could increase the allowable slurry concentration and the severity of the pipe geometries that could be accommodated, but only up until a limit, dependent upon the pipe system.

8.3.4.5 Comparison to PIV data

Although the data was determined by different methods, a comparison of the PIV tangential velocities measured and the tangential velocities obtained from the photographs may be beneficial. Figure 8.13 shows that the tangential velocities from water only (PIV) were lower than those determined from the photographs. It was expected that a larger tangential velocity be induced in an unloaded fluid, therefore this difference was attributed to problems with optical scaling. However the method was useful as a comparative technique and provided interesting results.

Figure 8.13: Comparison of PIV and photographic data



8.4 Conclusions

- The effect of particle size and specific gravity on the pressure drop across a 3.5m section of pipe with circular cross section in the bottom leg was in fairly good agreement with that expected from the literature.
- The increase in pressure drop with particle size observed for horizontal pipe was also evident in inclined pipe flow.
- At low velocities, inclusion of the 4-lobe swirl pipe had a positive, if small, effect on the pressure drop across a length of horizontal or downward sloping pipe.
- Results confirm findings that swirl was most effective at lower velocities and indicate that, within the experimental range, swirl induction holds most advantage for slurries with higher concentrations.
- As specific gravity increased the swirl pipe became beneficial for higher velocities.
- The inclusion of the swirl pipe did not appear to affect the pressure drop of materials relative to each other.

The interpretation and accuracy of the results was limited by the following

- Uncertainty over the interference of a particle bed with pressure measurements at 0.5m/s. An alternative method to monitor pressure drop should be investigated.
- Uncertainty over the accuracy of concentration measurements / effect of holdup within the pipe flow loop.

A novel photographic technique that involved tracking particles at the outside of the bore of the pipe was used to estimate the tangential velocity of swirling particles and led to the following conclusions:

- The rate of decay of induced swirl, vital information when swirl is applied to working pipelines, has been shown to conform to observations in the literature.
- The tangential velocity induced was observed to increase with axial velocity also conforming to observations in literature.
- Results from the photographic technique have enabled valuable comparisons on the effect of the swirl inducing pipe on the flow of different slurries to be made.

- Experimental evidence illustrated, within the ranges tested, that swirl induced into slurries containing larger and denser particles decayed more rapidly.
- The results suggested that the initial tangential velocities induced were less for coarse-particle slurries, however appeared to be independent of density.
- This technique confirmed particle image velocimetry results, which indicated that little swirl was induced into the CMC by the 4-lobe swirl pipe.
- Photographic evidence of an improvement in particle distribution downstream of an inclined pipe section with the inclusion of swirl was provided.
- The slurry tangential velocities were compared to data obtained from particle image velocimetry for water. The PIV values were found to be consistently lower due to problems with optical scaling.

Chapter 9 CONCLUSIONS AND RECOMMENDATIONS

9.1 Design of a steel pipe flow loop

Use of 0.2m lengths of 3 and 4-lobe swirl pipe prior to the bend on the Perspex flow loop led to a reduction in pressure drop over the bend but little difference was detected between the performance of the pipes. Therefore, the optimum swirl pipe design proposed by Ganshalingam (2002), was used for the steel flow loop experiments.

9.2 Velocity distribution downstream of swirl inducing pipes

The axial velocity distribution downstream of the swirl-inducing pipe was measured using particle image velocimetry (PIV). When pumping water in the turbulent regime, the results were characterised by an asymmetrical pattern, which was attributed to a core flow structure generated by the 4-lobe swirl pipe. The radial distribution of tangential velocities downstream of the swirl-inducing pipe was well represented by the wall-jet pattern suggested in literature.

The axial velocity profile for carboxymethyl cellulose highlighted the presence of a low-shear core, which was confirmed by Ariyaratne (2004) using CFD. When pumping carboxymethyl cellulose through the current swirl flow pipe geometry in the laminar flow regime, no significant tangential velocity was detected, indicating that higher viscosity reduced the swirl induced by the current swirl pipe design.

9.3 Electrical resistance tomography (ERT)

Initial tests, using a novel electrical resistance tomography (ERT) technique, indicated a decrease in the homogeneity of the particle distribution as distance from the swirl pipe increased and velocity decreased. This result was supported by Ganeshalingam's results (2002), however problems were encountered when performing measurements at high concentrations and low velocities.

9.4 Effect of swirl induction before bends

Following on from previous investigations, the effect of bend radius and upstream swirl-induction on the pressure drop over the bend was investigated. This study extended previous work by investigating the application of swirl when pumping a pseudoplastic fluid and a sand-water slurry.

- The pressure drop over horizontal cylindrical pipe for CMC was compared to a theoretical calculation of the same quantity and the results considered satisfactory.
- The pressure drop difference between bends of various radii was found to be small and this was sensible in the context of the literature.
- When testing sand-water slurries using a 4-lobe swirl pipe, the inclusion of swirl prior to the bends was found to be of benefit in terms of pressure loss for velocities of 0.5-1.8m/s. This range was marginally greater than that

found by Ganeshalingam (2002) when testing plastic beads using a 3-lobe swirl pipe.

- The inclusion of swirl prior to the bends was found to result in a pressure cost when pumping water and CMC.

9.5 Effect of swirl on settling slurries

- The effect of particle size and specific gravity on the pressure drop across a 3.5m section of pipe with circular cross section in the bottom leg was in fairly good agreement with that expected from literature.
- The increase in pressure drop with particle size observed for horizontal pipe was also evident in inclined pipeflow.
- At low velocities, inclusion of the 4-lobe swirl pipe had a positive, if small, effect on the pressure drop across a length of horizontal or downward sloping pipe or bend.
- Results confirm findings that swirl induction was most effective at lower velocities and indicate that, within the experimental range, swirl induction holds most advantage for slurries with higher concentrations.

- As specific gravity increased the swirl pipe became beneficial at higher velocities.
- The inclusion of swirl did not appear to affect the pressure drop of materials relative to each other.

A novel photographic technique, that involved tracking particles at the outside of the bore of the pipe, was used to estimate the tangential velocity of swirling particles. The technique enabled valuable comparisons of the effect of the swirl inducing pipe on the flow of different slurries to be made, leading to the following conclusions:

- The rate of decay of induced swirl, vital information when swirl is applied to working pipelines, has been shown to conform to observations in the literature.
- The tangential velocity induced was observed to increase with axial velocity also conforming to observations in the literature.
- The improvement in particle distribution downstream of swirl induction, documented by previous researchers, was demonstrated to occur when pumping higher density solids.

- Experimental evidence illustrated, within the ranges tested, that swirl induced into slurries containing larger and denser particles decayed more rapidly.
- The results suggested that the initial tangential velocities induced were less for coarse-particle slurries, however appeared to be independent of density.
- This technique confirmed particle image velocimetry results, which indicated that little swirl was induced into the CMC by the 4-lobe swirl pipe.
- Photographic evidence of an improvement in particle distribution downstream of an inclined pipe section with the inclusion of swirl was provided.
- The slurry tangential velocities were compared to data obtained from particle image velocimetry for water. The PIV values were found to be consistently lower, perhaps due to problems with optical scaling.

9.6 Thesis contribution

This section explicitly highlights the original contribution made by this thesis to knowledge about the swirling pipeflow of non-Newtonian and particle-laden fluids.

- Experimental data was obtained on the effect of a 4-lobe near-optimal swirl pipe on coal-water, sand-water and magnetite-water slurries of various particle size.
- Experimental data on the tangential velocity of swirling flows downstream of a near-optimal swirl-inducing pipe was provided.
- At low velocity, experimental data highlighted a reduction in the total pressure drop experienced across a 3.0m horizontal pipe section, a downward sloping section and vertical pipe bends, when the swirl-inducing pipe was present.
- A novel photographic technique was used to produce a comparative analysis of the tangential velocity induced into slurries.
- It was confirmed that a higher viscosity reduced the swirl induced by the current swirl pipe design.

9.7 Recommendations

Results indicated that the use of upstream swirl induction reduced the pressure loss over a pipe bend and a 3.0m horizontal and downward sloping pipe section. It is recommended that these results be verified for horizontal bends and upward sloping pipes.

Experiments showed that the current swirl pipe design did not effectively induce swirling flow into higher viscosity fluids. Therefore, it is recommended that an optimised swirl pipe design for application to viscous / homogenous fluids be developed.

When testing sand-water slurries using a 4-lobe swirl pipe, the inclusion of swirl prior to bends was found to be beneficial in terms of pressure loss, for a greater range of velocities than when testing with plastic beads and a 3-lobe swirl pipe. It is anticipated that at greater concentrations, this beneficial velocity range will be increased even further and recommended that a range of higher concentrations be tested to determine whether there is a limit to this effect.

To apply the novel ERT system to pipeflow measurements, the system should be developed to take readings on each set of electrodes simultaneously and the use of higher currents and salt concentrations investigated.

The following points outline ways in which the interpretation and accuracy of the results was limited and recommend solutions to these problems.

- Difficulties were experienced in obtaining a suitable measure of the pressure drop over the bend since the transducers could not be placed directly over the bend because of the swirl pipe prior to, and the flow disturbance after the bend. Since the upstream and downstream pipe sections on the steel flow loop are long enough to ensure fully developed flow, it is recommended that the pressure drop over a geometry be measured using at a number of points along these pipe sections as described by Toda *et al.* (1972) and Turian *et al.* (1998).
- There was some uncertainty over the interference of a particle bed with pressure measurements at low velocity. An alternative method to monitor pressure drop should be investigated, such as 4-point pressure tapings.
- The accuracy of concentration measurements was uncertain and the effect of holdup within the pipe flow loop was not defined. It is recommended that the weigh tank be commissioned for future tests to allow better measurements of the delivered concentration to be made. In addition, methods to measure the in situ concentration, such as reliable tomography systems should be investigated. A correlation between the in situ and delivered concentration could then be made, avoiding the need for measurement of in situ concentration for all tests.

REFERENCES

Abbot, J. 2001, Personal Communication.

Adrian, R. J. 1991, "Particle-Imaging Techniques for Experimental Fluid Mechanics", *Annual Review of Fluid Mechanics*, vol. 23, pp. 261-304.

Arena, U., Langeli, C. B., & Cammarota, A. 1998, "L-valve Behaviour with Solids of Different Size and Density", *Powder Technology*, vol. 98, pp. 231-240.

Ariyaratne, C. 2002, Personal Communication.

Ariyaratne, C. 2003, Personal Communication.

Ariyaratne, C. 2004, Personal Communication.

Ayukawa, K. 1969, "Pressure Drop in the Hydraulic Conveyance of Solid Materials through a Bend in a Vertical Plane", *Bulletin of Japan Society of Mechanical Engineering*, vol. 12, no. 54, pp. 1388-1396.

Azko Nobel Chemicals Ltd. 2001, Flexibility on CMC [Pamphlet].

Bain, A. G. & Bonnington, S. T. 1970, *The Hydraulic Transport of Solids by Pipeline*. Oxford, Pergamon Press Ltd.

Baker, P. J., Jacobs B.E.A., Jacobs. & Bonnington, S. T. c. e. 1979, *A Guide to Slurry Pipeline Systems*. Cranfield, BHRA Fluid Engineering.

Béreiziat, D., Devienne, R., & Lebouché, M. 1995, "Local Flow Structure for Non-Newtonian Fluids in a Periodically Corrugated Wall Channel", *Journal of Enhanced Heat Transfer*, vol. 2, no. 1-2, pp. 71-77.

Blecher, L., Lorenz, D. H., Lowd, H. L., Wood, A. S., & Wyman, D. P. 1980, "Polyvinylpyrrolidone", In *Handbook of Water-soluble Gums and Resins.*, R. L. Davidson, ed., McGraw-Hill, London.

Brown, D. 2001, Personal Communication.

✓ Butler, R. W. & Klug E.D. 1980, "Hydroxypropyl cellulose", In *Handbook of Water soluble Gums and Resins*, R. L. Davidson, ed., McGraw-Hill, London.

Carlson, J. & Ing, R. K. 2003, "Ultrasonic Speckle Correlation Imaging of 2D Particle Velocity Profiles in Multiphase Flows", *Flow Measurement and Instrumentation*, vol. 14, no. 4-5, pp. 193-200.

Charles, M. E., Cheh, C. H. S., & Chu, L. H. L. 1971, "The Flow of Settling Slurries in Tubes with Internal Spiral Ribs", *The Canadian Journal Chemical Engineering.*, vol. 49, pp. 737-741.

Chhabra, R. P. & Richardson, J. F. 1999, *Non-Newtonian Flow in the Process Industries, Fundamentals and Engineering Applications* Butterworth-Heinmann. Oxford.

CIBSE 1988. *Chartered Institute of Building Service Engineers Guide* Staples Printers Ltd, St Albans.

Cilliers, J. J., Xie, W., Neethling, S. J., Randall, E. W., & Wilkinson, A. J. 2001.

"Electrical Resistance Tomography Using a Bi-directional Current Pulse Technique", *Measurement Science and Technology*, vol. 12, pp. 997-1001.

Condron, A. 2002, Personal Communication.

Cottrell, I. W., Kang, K. S., & Kovacs, P. 1980, "Xanthan Gum" In *Handbook of Water-soluble Gums and Resins*, R. L. Davidson, ed., McGraw-Hill, London.

Coulson, J. M., Richardson, J. F., Backhurst, J. R., & Harker, J. H. 1990, *Chemical Engineering (Fluid Flow, Heat Transfer and Mass Transfer)*, Forth edn, Pergamon Press, Oxford.

Dantec Dynamic. Principals of Particle Image Velocimetry [online]. Available at: <<http://www.dantecdynamics.com/>> [2nd May 2003]

Das, S. K., Biswas, N., & Mitra, A. K. 1991, "Non-Newtonian Liquid Flow in Bends", *The Chemical Engineering Journal*, vol. 45, pp. 165-171.

Diniz, V. E. M. G. & Coiado, E. M. 1999, "Two-phase (Solid -liquid) Flow in Inclined Pipes", In *Proceedings of the 14th International Conference on Hydrotransport*, BHR Group, Cranfield, pp. 555-566.

Dodge, D. W. & Metzner, A. B. 1959, "Turbulent Flow of Non-Newtonian Systems", *A.I.Ch.E. Journal*, vol. 5, no. 2, pp. 189-204.

Doron, P., Simkhis, M., & Barnea, D. 1997, "Flow of Solid-liquid Mixtures in Inclined Pipes", *International Journal of Multiphase Flow*, vol. 23, no. 2, pp. 313-323.

Durand, R. 1953, "Basic Relationships in the Transportation of Solids in Pipes - Experimental Research", *Proceedings Minnesota International Hydraulics Convention*, pp. 89-103.

Edwards, M. F., Jadallah, M. S. M. & Smith, R. 1985, "Head Losses in Pipe Fittings at Low Reynolds Numbers ", *Chemical Engineering Research and Design*, vol. 63, pp. 43-50.

Edwards, M. F. & Wilkinson, W. L. 1971, "Review of Potential Applications of Pulsating Flow in Pipes", *Transactions of Institution of Chemical Engineers*, vol. 49, pp. 85-94.

Escudier, M. P. & Presti, F. 1996, "Pipe Flow of a Thixotropic Liquid", *Journal of Non-Newtonian Fluid Mechanics*, vol. 62, pp. 291-306.

Escudier, M. P., Presti, F., & Smith, S. 1999, "Drag Reduction in the Turbulent Pipe Flow of Polymers", *Journal of Non-Newtonian Fluid Mechanics*, vol. 81, pp. 197-213.

Escudier, M. P., Gouldson, I. W., Pereira, A. S., Pinho, F. T., & Poole, R. J. 2001. "On the Reproducibility of the Rheology of Shear-thinning Liquids", *Journal of Non-Newtonian Fluid Mechanics*, vol. 97, pp. 99-124.

Feddersen, R. L. & Thorp, S. N. 1993, "Sodium Carboxymethyl Cellulose". In *Industrial Gums, Polysaccharides and their Derivatives*, Third edn, R. L. Whistler & BeMiller J.N., eds., Academic Press Inc, London.

Ganeshalingam, J. 2002, *Swirl-Induction for Improved Solid-Liquid Flow in Pipes*. PhD thesis, School of Chemical, Environmental and Mining Engineering, University of Nottingham.

Ganeshalingam, J. 2001, Personal Communication.

Geldard, R. 2000, "Investigation of the Response of Sewage Sludge Following the Injection of a Pulse of Air at Varying Solids Concentration". Unpublished Work.

Ghannam, M. T. & Esmail, M. N. 1997, "Rheological Properties of CMC", *Journal of Applied Polymer Science*, vol. 64, no. 2, pp. 289-301.

Gillies, R. G., Shook, C. A., & Wilson, K. C. 1991, "An Improved Two Layer Model for Horizontal Slurry Pipeline Flow", *The Canadian Journal Chemical Engineering*, vol. 69, pp. 173-178.

Glicksman, M. 1969, "Synthetic Hydrocolloids", In *Gum Technology in the Food Industry*, Academic Press Inc, New York, pp. 472-505.

Gordon, H. M. & Gordon, H. A. 1899, *Conduit or Pipe*, 630,605 (patent).

Gospel, A. 2003, Personal Communication.

Govier, G. W. & Aziz, K. 1972, *The Flow of Complex Mixtures in Pipes*. Van Nostrand Reinhold Co.. London.

- Grant, I. 1997, "Particle Image Velocimetry: a Review", *Proceedings of the Institution of Mechanical Engineers*, vol. 211, no. C, pp. 55-76.
- Greminger, G. K. Jr. & Krumel, K. L. 1980, "Alkyl and Hydroxyalkylalkylcellulose", In *Handbook of Water-soluble Gums and Resins*, R. L. Davidson, ed., McGraw-Hill, London.
- Gupta, A. K., Lilley, D. G., & Syred, N. 1984, *Swirl flows* Abacus Press, Tunbridge Wells.
- Heywood, N. I., Alderman, N. J., & Cursley, C. J. 1998, *In Plant Slurry Pumping Systems* Unpublished, copyright AEA Technology PLC.
- HOH Water Technology. 2001, "Mounting and Operational Instruction for HOH RO-51 Reverse Osmosis Plant". Unpublished Work
- Horii, K., Matsumae, Y., Cheng, X. M., Takei, M., Yasukawa, E., & Hashimoto, B. 1991, "An Erosion Resistant Pipe Bend", *Journal of Fluids Engineering*, vol. 113, no. March, pp. 149-151.
- Howard, G. W. 1939, "Transportation of Sand Gravel in a Four-inch Pipe", *Trans ACSE*, vol. 104, pp. 1334-1380.
- Howard, G. W. 1941, "Effect of Riffling on Four-inch Pipe Transporting Solids", *Trans ACSE*, vol. 106, pp. 135-157.
- Hughmark, G. A. 1961, "Aqueous Transport of Settling Slurries". *Engineering Approaches*, vol. 53, no. 5, pp. 389-390.

Ilicali, C. & Engez, S. T. 1996, "Laminar Flow of Power Law Fluids in Concentric Annuli", *Journal of Food Engineering*, vol. 30, pp. 255-262.

Jeremic, M. L. 1982, *Elements of Hydraulic Coal Mine Design*, First edn, Trans Tech Publications, Germany.

Jinescu, V. V. 1974, "The Rheology of Suspensions", *International Chemical Engineering*, vol. 14, no. 3, pp. 397-420.

Joergens, G. 2002, Personal Communication.

Johnson, S. B., Franks, G. V., Scales, P. J., Boger, D. V., & Healy, T. W. 1999, "Surface Chemistry-rheology Relationships in Concentrated Mineral Suspensions", *International Journal of Mineral Processing*, vol. 58, pp. 267-304.

Jones, G. 2000, Personal Communication.

Jones, T. F. 1997, *Pipe Design for Improved Particle Distribution and Reduced Wear*. ECSC Final Report 7220-EA/841

Jones, T. F. 2001, Internal Report on BNFL Project. Unpublished Work

Kaupert, K. A. & Staubli, T. 1999, "The Unsteady Pressure Field in a High Specific Speed Centrifugal Pump Impeller-Part II: Transient Hysteresis in the Characteristic", *Journal of Fluids Engineering*, vol. 121, pp. 627-632.

Kawatra, S. K. & Bakshi, A. K. 1995, "Determination of Changes in Rheological Properties of Coal Slurries in Process Streams", *Coal Preparation*, vol. 15, pp. 165-175.

Kitoh, O. 1991, "Experimental Study of Turbulent Swirling Flow in a Straight Pipe", *Journal of Fluid Mechanics*, vol. 225, pp. 445-479.

Kittredge, C. P. & Rowley, D. S. 1957, "Resistance Coefficients for Laminar and Turbulent Flow Through One-Half Inch Valves and Fittings", *Trans of the ASME*, vol. 79, pp. 1759-1766.

Kokpinar, M. A. & Gogus, M. 2001, "Critical Flow Velocity in Slurry Transporting Horizontal Pipelines", *Journal of Hydraulic Engineering*, vol. 127, no. 9, pp. 763-771.

Krieth, F. & Sonju, O. K. 1965, "The Decay of a Turbulent Swirl in a Pipe", *Journal of Fluid Mechanics*, vol. 22, no. 2, pp. 257-271.

Kulicke, W.-M., Kull, A. H., Kull, W., & Thielking, H. 1996, "Characterization of Aqueous Carboxymethyl Cellulose Solutions in terms of their Molecular Structure and its Influence on Rheological Behaviour", *Polymer*, vol. 37, no. 13, pp. 2723-2731.

Logos, C. & Nguyen, Q. D. 1996, "Effect of Particle Size on the Flow Properties of a South Australian Coal-water Slurry", *Powder Technology*, vol. 88, pp. 55-58.

Maier, H., Anderson, M., Karl, C., Magnuson, K., & Whistler, R. L. 1993, "Guar, Locust Bean, Tara and Fenugreek gums", In *Industrial Gums, Polysaccharides and their Derivatives*, Third edn, R. L. Whistler & BeMiller J.N., eds., Academic Press Inc, London.

Maruyama, T., Ando, J.-I., & Mizushina, T. 1980, "Flow of Settling Slurries in Horizontal Pipes", *Journal of Chemical Engineering of Japan*, vol. 13, no. 4. pp. 269-274.

Mashelkar, R. A. & Devarajan, G. V. 1976, "Secondary Flow of Non-Newtonian Fluids: Part 2 - Frictional Losses in Laminar Flow of Purely Viscous and Viscoelastic Fluids through Coiled Tubes", *Transactions of the Institution of Chemical Engineers*, vol. 54, pp. 108-114.

Metzner, A. B. & Reed, J. C. 1955, "Flow of Non-Newtonian Fluids - Correlation of the Laminar, Transition and Turbulent-flow Regions", *A.I.Ch.E. Journal*, vol. 1, no. 4, pp. 434-440.

Miller, R. W. 1989, *Flow Measurement Engineering Handbook*, Second edn, McGraw-Hill, London.

Mishra, R., Singh, S. N., & Seshadri, V. 1998, "Study of Wear Characteristics and Solid Distribution in Constant Area and Erosion-resistant Long-radius Pipe Bends for the Flow of Multisized Particulate Slurries", *Wear*, vol. 217, no. 2, pp. 297-306.

Mizushina, T., Maruyama, T., & Hirasawa, H. 1975, "Structure of the Turbulence in Pulsating Pipe Flows", *Journal of Chemical Engineering of Japan*, vol. 8, no. 3, pp. 210-216.

Mono Pumps Ltd. [online] Available at: <<http://www.mono-pumps.com/>> [1st Oct 2002]

Mukhtar, A., Singh, S. N., & Seshadri, V. 1995, "Pressure Drop in a Long Radius 90° Horizontal Bend for the Flow of Multisized Heterogeneous Slurries", *International Journal of Multiphase Flow*, vol. 21, no. 2, pp. 329-334.

Mukhtar, A., Singh, S. N., & Seshadri, V. 1993, "Distribution of Solid Particles in Multisized Particulate Slurry Flow Through a 90° Pipe Bend in Horizontal Plane", *Bulk Solids Handling*, vol. 13, no. 2, pp. 379-385.

Murakami, M., Kitoh, O., Katayama, Y., & Iida, Y. 1976, "An Experimental Study of Swirling Flow in Pipes", *Bulletin of Japan Society of Mechanical Engineering*, vol. 19, no. 128, pp. 118-126.

Nasr-El-Din, H. & Shook, C. A. 1987, "Effect of a 90 Degree Bend on Slurry Velocity and Concentration Distributions", *Journal of Pipelines*, vol. 6, pp. 239-252.

Nesbitt 2000, *Guide to European Pumps and Pumping*, Second edn, Professional Engineering Publishing, London.

Newitt, M. C., Richardson, J. F., Abbott, M., & Turtle, R. B. 1955, "Hydraulic Conveying of Solids in Horizontal Pipes", *Transactions of the Institution of Chemical Engineers*, vol. 33, no. 2, pp. 92-110.

Ni, F. & Matousek, V. 1999, "Flow of Aqueous Mixture of Sand Composed of Fractions of Different Particle Size", In *Proceedings of the 14th International Conference on Hydrotransport*, BHR Group, Cranfield, pp. 31-43.

- Nouri, J. M. & Whitelaw, J. H. 1997, "Flow of Newtonian and Non-Newtonian Fluids in an Eccentric Annulus with Rotation of the Inner Cylinder", *International Journal of Heat and Fluid Flow*, vol. 18, no. 2, pp. 236-237.
- Odrowaz Pieniazek, S. 1979, "Solids Handling Pumps, a Guide to Selection", *The Chemical Engineer* pp. 94-101.
- Park, N. A. & Irvine, T. F. 1997, "Anomalous Viscosity-temperature Behaviour of Aqueous Carbopol Solutions", *Journal of Rheology*, v41 pp167-173, vol. 41, pp. 167-173.
- Perona, P. 2003, "An Experimental Investigation of Laminar-Turbulent Transition in Complex Fluids", *Journal of Food Engineering*, vol. 60, pp. 137-145.
- Pinho, F. T., Oliveira, P. J., & Miranda, J. P. 2003, "Pressure Losses in the Laminar Flow of Shear-thinning Power-law Fluids across a Sudden Axisymmetric Expansion", *International Journal of Heat and Fluid Flow*, vol. 24, pp. 747-761.
- Pinho, F. T. & Whitelaw, J. H. 1990, "Flow of Non-Newtonian Fluids in a Pipe", *Journal of Non-Newtonian Fluid Mechanics*, vol. 34, pp. 129-144.
- Primavera, A. 2001, "Minimising Wear in Pipe Bends by Swirl Dispersion of Particles". Unpublished Work.
- Pugh, F. J. & Wilson, K. C. 1999. "Role of the Interface in Stratified Slurry Flow", *Powder Technology*, vol. 104, pp. 221-226.
- R.T.Vanderbilt Company, 2001, "Vanzan" Product brochure.

- Raylor, B. 1998, *Pipe Design for Improved Particle Distribution and Improved Wear*, PhD thesis, School of Chemical, Environmental and Mining Engineering, University of Nottingham.
- Raylor, B., Jones, T. F., & Miles, N. J. 1999, "Helically Formed Pipes Improve the Efficient Transportation of Particle-laden Liquids", In *Proceedings of the 14th International Conference on Hydrotransport*, BHR Gorup, Cranfield, pp20-29.
- Recknagle, K. P. & Shekarriz A. 1998, "Laminar Impeller Mixing of Newtonian and Non-Newtonian Fluids: Experimental and Computational Results", *Proceedings of FEDSM 98*.
- Richardson, J. F., Chhabra, R. P., & Khan, A. R. 1999, "Multiphase Flow of non-Newtonian Fluids in Horizontal Pipes", In *Proceedings of the 14th International Conference on Hydrotransport*, BHR Gorup, Cranfield, pp. 283-303.
- Robinson, A. W. 1923, *Delivery Pipe for Hydraulic Dredging Machines*, 1,451,272 (patent).
- Rockwood Specialties. [online] Available at: <<http://www.laponite.com/>> [2001].
- Roco, M. C. & Shook, C. A. 1985, "Critical Deposit Velocity in Slurry Flow", *AIChE Journal*, vol. 31, no. 8, pp. 1401-1404.
- Roh, N.-S., Shin, D.-H., Kim, D.-C., & Kim, J.-D. 1995, "Rheological Behaviour of Coal-water Mixtures". *Fuel*, vol. 74, no. 8, pp. 1220-1225.

- Rosenberg, A. 1997, *Level Swell in Reactors During Emergency Relief Venting*, Department of Chemical Engineering, University of Nottingham.
- Rutgers, R. 1962, "Relative Viscosity and Concentration", *Rheologica Acta*, vol. 2, no. 4, pp. 305-348.
- Sa Pereira, A. & Pinho, F. T. 1994, "Turbulent Pipe Flow Characteristics of Low Molecular Weight Polymer Solutions", *Journal of Non-Newtonian Fluid Mechanics*, vol. 55, pp. 321-344.
- Schriek, W., Smith, L. G., Haas, D. B., & Husband, W. H. W. 1974, "The Potential of Helically Ribbed Pipes for Solids Transport", *CIM Bulletin*, vol. October, pp. 84-91.
- Seaman, J. K. 1980, "Locust Bean Gum" In *Handbook of Water-soluble Gums and Resins*, R. L. Davidson, ed., McGraw-Hill, London.
- Severn Trent Water. [online] Available at: <<http://www.stwater.co.uk/>> [2004].
- Shi, F. N. & Napier-Munn, T. J. 1996, "A Model for Slurry Rheology", *International Journal of Mineral Processing*, vol. 47, pp. 103-123.
- Simkhis, M., Barnea, D., & Taitel, Y. 1999, "Dunes in Solid-liquid Flow in Pipes", In *Proceedings of the 14th International Conference on Hydrotransport*. BHR Group, Cranfield, pp. 51-61.

Singh, R. P. & Mishra, P. 1980, "Friction Factor for Newtonian and Non-Newtonian Fluid Flow in Curved Pipes", *Journal of Chemical Engineering of Japan*, vol. 13, no. 4, pp. 275-280.

Singh, V. P. & Charles, M. E. 1976, "The Flow of Sand/Water Slurries in Horizontal Pipes with Internal Spiral Ribs - Effect of Rib Height", *The Canadian Journal Chemical Engineering*, vol. 54, pp. 249-254.

Skelland, A. H. P. 1967, *Non-Newtonian Flow and Heat Transfer* John Wiley and Sons, Inc., New York.

Slatter, P. T. 1999, "The Role of Rheology in the Pipelining of Mineral Slurries", *Mineral Processing and Extractive Metallurgical Review*, vol. 20, no. 1, pp. 281-300.

Slatter, P. T. & Pienaar, V. G. 1999, "Establishing Dynamic Similarity for Non-Newtonian Fittings Loss", In *Proceedings of the 14th International Conference on Hydrotransport*, BHR Group, Cranfield, pp. 245-253.

Slatter, P. T. & Van Sittert, F. P. 1999, "Analysis of Rough Wall Non-Newtonian Turbulent Flow", In *Proceedings of the 14th International Conference on Hydrotransport*, BHR Group, Cranfield, pp. 209-222.

Smith, R. A. 1955, "Experiments on the Flow of Sand-water Slurries in Horizontal Pipes", *Transactions of the Institution of Chemical Engineers*, vol. 33, pp. 85-92.

Spells, K. E. 1955, "Correlations for Use in Transport of Aqueous Suspensions of Fine Solids Through Pipes", *Transactions of Institution of Chemical Engineers*, vol. 33, pp. 79-84.

Steenbergen W. & Voskamp J. 1998, "The Rate of Decay of Swirl in Turbulent Pipe Flow", *Flow Measurement Instrumentation*, vol. 9, no. 2, pp. 67-78.

Stelzer, G. I. & Klug, E. D. 1980, "Carboxymethylcellulose" In *Handbook of Water-soluble Gums and Resins*, R. L. Davidson, ed., McGraw-Hill, London.

Stepanoff, A. J. 1969, *Gravity Flow of Bulk Solids and Transportation of Solids in Suspension*, Wiley, Chichester.

Stevenson, R. 2002, "Developing ERT and Exploring Applications". Unpublished Work

Sundqvist, A., Sellgren, A., & Addie, G. 1996a, "Pipeline Friction Losses of Coarse Sand Slurries - Comparison with a Design Model", *Powder Technology*, vol. 89, pp. 9-18.

Sundqvist, A., Sellgren, A., & Addie, G. 1996b, "Slurry Pipeline Friction Losses for Coarse and High Density Industrial Products", *Powder Technology*, vol. 89, pp. 19-28.

Sutherland, I. W. 1984, "Hydrolysis of Unordered Xanthan in Solutions by Fungal Cellulases", *Carbohydrate Research*, vol. 131, no. 1, pp. 93-104.

Tam, K. C. & Tiu, C. 1989, "Steady and Dynamic Shear Properties of Aqueous Polymer Solutions", *Journal of Rheology*, vol. 33, no. 2, pp. 257-280.

Tanner, R. 1985, *Engineering Rheology* Clarendon Press, Oxford.

Tchobanoglous, G., Burton, F. L., & . 1991, *Wastewater Engineering, Treatment, Disposal and Reuse.*, Third edn, McGraw-Hill Inc., London.

Toda, M., Komori, N., Saito, S., & Maeda, S. 1972, "Hydraulic Conveying of Solids through Bends", *Journal of Chemical Engineering of Japan*, vol. 5, no. 1, pp. 4-13.

Turian, R. M., Yuan, T.-F., & Mauri, G. 1971, "Pressure-drop Correlation for Pipe Flow of Solid-liquid Suspensions", *AIChE Journal*, vol. 17, no. 4, pp. 809-817.

Turian, R. M. & Yuan, T.-F. 1977, "Flow of Slurries in Pipelines", *AIChE Journal*, vol. 23, no. 3, pp. 232-243.

Turian, R. M., Ma, T.-W., Hsu, F.-L. G., & Sung, D.-J. 1998, "Flow of Concentrated Non-Newtonian Slurries: 2 Friction Losses in Bends, Fittings, Valves and Venturi Meters", *International Journal of Multiphase Flow*, vol. 24, no. 2, pp. 243-269.

Walters, K. 1980, *Rheometry: Industrial Applications* Research Studies Press.

Wang, M., Jones, T. F., & Williams, R. A. 2003, "Visualization of Asymmetric Solids Distribution in Horizontal Swirling Flows Using Electrical Resistance

Tomography", *Transactions of Institution of Chemical Engineers*, vol. 81, no. A, pp. 854-861.

Wang, Y. & Chukwu, G. A. 1996, "Unsteady Axial Laminar Couette Flow of Power-Law Fluids in a Concentric Annulus", *Industrial Engineering and Chemical Research*, vol. 35, pp. 2039-2047.

Wasp, E. J., Kenny, J. P., & Gandhi, R. L. 1977, *Solid-liquid Flow Slurry Pipeline Transport* Trans Tech Publications, Rockport.

Wilson, K. C. & Thomas, A. D. 1985, "A New Analysis of the Turbulent Flow of Non-Newtonian Fluids", *The Canadian Journal Chemical Engineering*, vol. 63, August, pp. 539-546.

Wolfe, S. E. 1967, "The Transport of Solids in Helically Ribbed Pipes", *The Canadian Mining and Metallurgical Bulletin* February, pp. 221-223.

Wood R.J.K., Puget, Y., Tretheway, K. R., & Stokes, K. 1998, "The Performance of Marine Coatings and Pipe Materials Under Fluid-borne Sand Erosion", *Wear*, vol. 219, pp. 46-59.

Worster, R. C. & Denny, D. F. 1955, "Hydraulic Transport of Solid Material in Pipes", *Proceedings of the Institution of Mechanical Engineers*, vol. 169, pp. 563-586.

Yuille, N. A. 1928. *Dredger Pipe Line*. 1,662,178 (patent).

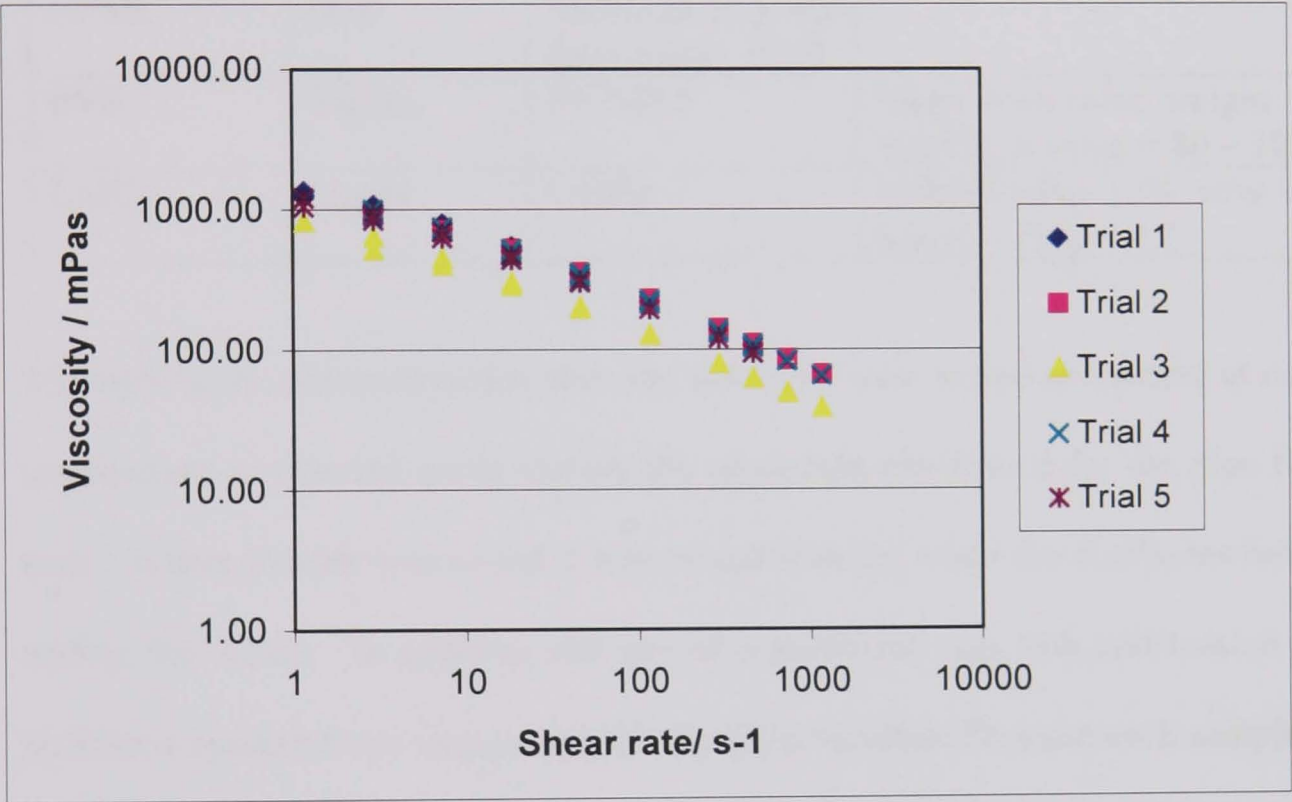
Appendix A. SELECTION OF TEST MATERIALS

- A.1 Results of tests to assess the concentration of 32,306-3 required
- A.2 Results of a series of tests to assess the apparent viscosity of 32,306-3 at 0.6%
- A.3 Additional Methodology
- A.4 Recommended dissolution methods
- A.5 – A.10 Photographs of VOR rheometer
- A.11 The change in apparent viscosity with shear rate for solutions tested
- A.12 – A.14 Biological indicator strips for the series 1 samples
- A.15 Results of series 2 biological tests
- A.16 Homogenous groups indicated by the Scheffe test
- A.17 – A.18 Variation in overnight weight loss with time compared to ambient temperature and outside humidity
- A.19 – A.20 Apparent viscosity variation with temperature for open Nalco sample and open control sample (series 2)
- A.21 – A.23 The variation in thixotropy of the open Nalco sample and open control sample and with temperature on Day 2, Day 8 and Day 15

A.1 Results of tests to assess the concentration of 32,306-3 required.

Product No.	Concentration/ % w/w	Apparent viscosity range measured / mPas
323063	0.10	5.22 – 12.80
323063	0.50	41.50 – 655
323063	0.60	65-1360
323063	0.75	89-3150
323063	0.90	115-5440
C-4888	2.50	125 – 527

A.2 Results of a series of tests to assess the apparent viscosity of 32,306-3 at 0.6% w/w.



A.3 Additional Methodology

Table 1A gives details of the fluids used in the selection tests. No biocide was used, so the solutions were mixed and stored overnight in a refrigeration room held at 6°C to discourage micro-bacterial action. In a further attempt to mitigate against degradation the rheological measurements were taken within 24 hours of

making the solution. The solutions were stored in open beakers to simulate the open tank on the flow loop. At least three analyses were performed for each solution, often more until a suitable geometry or range of results was attained.

Table 1A: Fluids used in the selection tests.

Fluid	Supplier	Product number	Further Details
Xanthan Gum	Sigma	G-1253	800-1200mPas (1% w/w in water)
MC	Dow	Food grade	-
HPC	Hercules	type MF	-
HPMC	Dow	Methocel E grade food gums. E4M	-
PVP	Sigma	PVP-360	Mean molecular weight = 360000, k value = 80 – 100
CMC	Sigma	C4888	400-800mPas (2% w/w in water) – D.S. = 0.7

Throughout the characterisation tests the solutions were mixed and stored at room temperature to simulate more closely the procedure envisioned for the pipe flow tests. Where biocide was added it was mixed with the water for 5 minutes before adding the solute. In addition, the use of a particular cup, bob and torsion bar stabilised because there was comparatively little variation between each sample so the majority of measurements were within the torsion range. The 14mm diameter cup and bob, and the 10.890gcm torsion bar were used for most rheological tests. Three trials were performed for each sample, each day. The details of the tests performed are outlined in Table 2A.

Table 2A: Outline of the aims and details of the each characterisation test series

Test series and Aim	Samples					
	CMC	Water	Conc./ % w/w	Biocide concentration /ppm and type		Storage
1. Biocide selection, age and temperature characterisation	Sigma 3,23063	Tap	0.60	-	None	Open
					None	Pipe
			0.61	400	Proxel	Open
			0.60	400	Busan	Open
					Busan	Pipe
2. Biocide selection, age and temperature characterisation	Sigma 3,23063	Tap	0.61	-	None	Open
				-	None	Pipe
			0.61	100	Nalco 2593	Open
					Nalco 2593	Sealed
					Nalco 2593	Pipe
3. To compare CMC types, assess the effect of salt; conduct transient time tests and assess change in rheology over days 1-2.	Sigma 3,23063	Tap	0.65	103	Nalco 2593	Sealed
		De-ionised	0.6	100		
	Walocel	Tap	0.79	102		
		De-ionised	0.82	107		
		Tap	1.02	101		
		Tap	1.51	108		
		Tap	1.74	102		
		De-ionised	1.72	114		
4. To assess the effect of biocide concentration, and the repeatability of sample preparation.	Walocel	De-ionised	1.00	100	Nalco 2593	Sealed
			1.00	101		
			1.01	999		
			1.40	100		
			1.39	101		
			1.39	1001		
			1.84	100		
			1.81	100		
			1.79	1016		

Note: Proxel GXL: (aqueous dipropylene glycol solution of 1,2-benzisothiazolin-3-one), Acecia, Manchester.
Busan 1060: (Hexahydro-1,3,5,tris(2-hydroxyethyl)-s-triazine in solution). Buckman Laboratories, Manchester
Nalco 2593 (5-chloro-2-methyl-4-isothiazolin-3-one, 2-methyl-4-isothiazolin-3-one in aqueous solution), Nalco, The Netherlands

For series 1 and 2, each solution was made on Day 1, using tap water taken from the rheology lab. The samples were made from 0.6% w/w Sigma 3.23063 CMC

and were stored in open glassware for the first night, before being split as appropriate. To the series 1 samples no biocide, 400ppm Proxel biocide or 400ppm Busan biocide were added and to the series 2 samples no biocide or 100ppm Nalco biocide was added. During series 2, two samples containing Nalco biocide were tested, one being stored in open glassware and the other in sealed glassware in an attempt to simulate an open / sealed tank on the flow loop. Rheological tests were performed on the samples from Day 2 to 15 inclusive.

In series 2, tests were performed to assess the temperature dependence of CMC. On Days 2, 8 and 15 rheological measurements for the control and open Nalco sample were performed over a range of temperatures. On day 2 and 8, the rheological tests were undertaken at 15, 20, 30, 35 and 40°C by changing the manual temperature adjustment in the instrument control programme. Only two trials could be performed because of time constraints. In addition, the daily measurement at 25°C (three trials), taken out of sequence, made up the 6th point. On Day 15 the instrument was set to automatically perform one trial of the usual up/down sweep at each of the temperatures above in sequence. The thermal equilibrium time was set at 300s. This was performed twice over for the Nalco sample and once for the control, again due to time constraints.

During series 3 and 4 rheological tests were performed on Day 2, except for the 1.5, 1.7 and 2.0% w/w tap water solutions that were tested on Days 1 and 2. All the solutions were stored overnight in sealed glassware at room temperature. The

temperature was not logged, the overnight weight loss not recorded and biological tests not performed. The tap water used was taken from the pipe loop laboratory and de-ionised water from the Reverse Osmosis Plant, used for pipe flow tests (Chapter 5). The repeat samples in series 4 were mixed separately and not split from one solution.

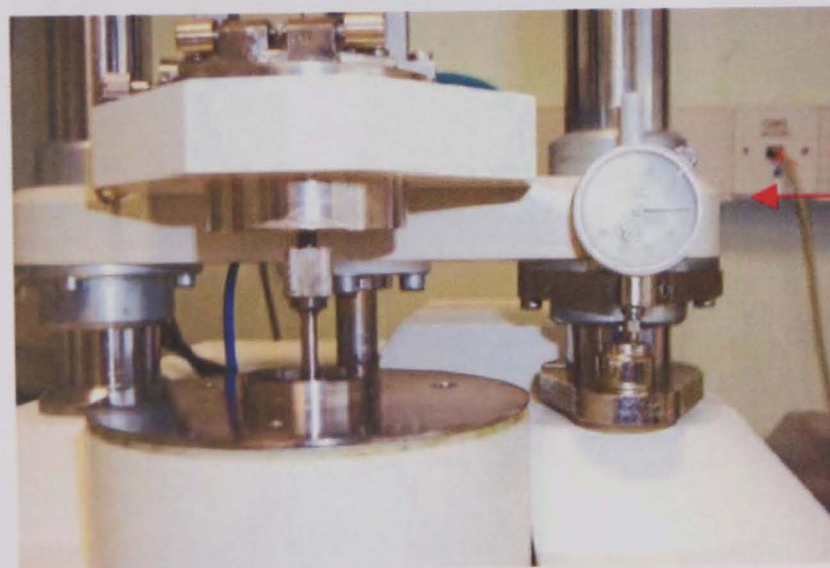
A.4 Recommended dissolution methods.

Fluid	Method	Reference
Carboxy-methyl cellulose	'Gradual controlled addition of the CMC powder – preferably in the <i>vortex of a rapidly stirred volume of water</i> – is recommended.' Or 'wet the dry powder with a small amount of polar liquid (e.g. ethanol) and add this to the water'	Azko Nobel (2001)
	More soluble in hot water. Higher degree of substitution gave more rapid dissolution; higher molecular weight was less soluble. <i>Add to a vortex</i>	Feddersen and Thorpe (1993)
	Mixed for more than 4 hrs, settled for > 8hrs for complete hydration. Circulated for 2/3 periods of 3min to remove trapped air then settle 8hrs to allow bubbles to come out.	Pinho and Whitelaw (1990)
	Put a mass in to 1 litre and allowed sufficient time for the dissolution using no external heat or power, kept at 23°C.	Ghannam and Esmail (1997)
	Only good common solvent is water. Degree of dispersion varies with degree of substitution and molecular weight. Wetting with ethanol may be easier on large scale than adding slowly to vortex.	Stelzer and Klug (1980)
	Agitated at 700rpm while added, then mixed at 200rpm for 90 min in a closed vessel, condensed water then returned, stood for 24 hours to hydrate or mixed 560-1000rpm until visibly homogenous then left for 24 hours.	Escudier <i>et al.</i> (2001)
Polyvinyl-pyrrolidone	Readily soluble in cold water, with an unusual solubility in organic solvents.	Glicksman (1969)
Xanthan Gum	Xanthan gum was added slowly to distilled water while <i>stirring at ~800rpm</i> . Stirred for 2hrs and brought to 25°	Cottrell <i>et al.</i> (1980)
	<i>A mixer used to develop a deep vortex</i> – with the gum slowly sifted to the upper wall of the vortex. Propeller mixers were preferred, mixed until the solution was smooth and uniform, ~30mins or longer for larger batches.	R.T.Vanderbilt Company, Inc. (2000)
	As for CMC	Escudier <i>et al.</i> (2001)
Guar gum	Rate of dissolution and viscosity development increased with decreasing particle size	Maier <i>et al.</i> (1993)
Hydroxy-propyl-cellulose	Soluble in water. Complete solubility at ambient or elevated temperatures.	Butler and Klug (1980)
Hydroxy-propyl-methyl-cellulose	Soluble in cold water and insoluble in hot water. If degree of substitution was lower than 1.4 solubility decreased. Use one of following techniques: Disperse in water heated to above gel point then cool and stir. <i>Disperse in cold water with a high shear mixer</i> – periods of several minutes should not lead to appreciable degradation Disperse in small amount of solvent than add to water. Solubility improved by <i>chilling to below 10° in makeup</i> .	Greminger and krumel (1980)



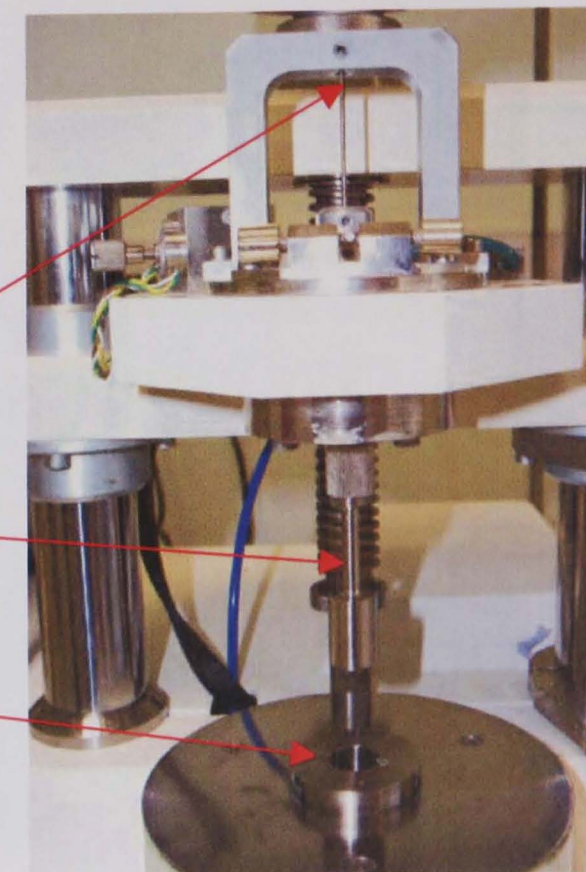
A.5 VOR rheometer and computer

Handle to raise and lower bob



A.6 Bob position for measurement

Micrometer to set gap size



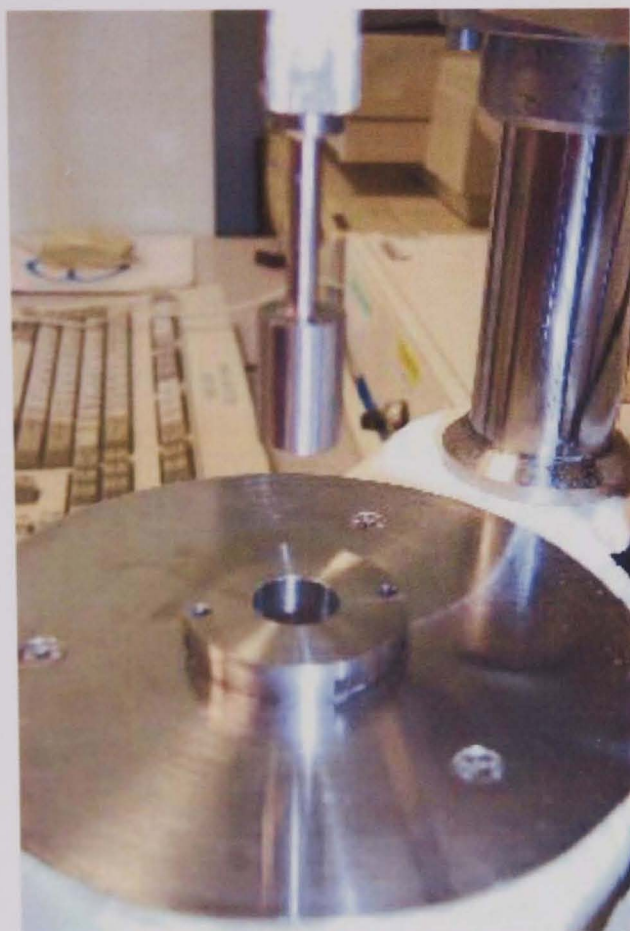
Torsion bar

Bob

Cup

A.7 Torsion bar and raised 14mm bob

A.5-A.7



A.8 14mm bob and cup



A.9 25mm bob and cup

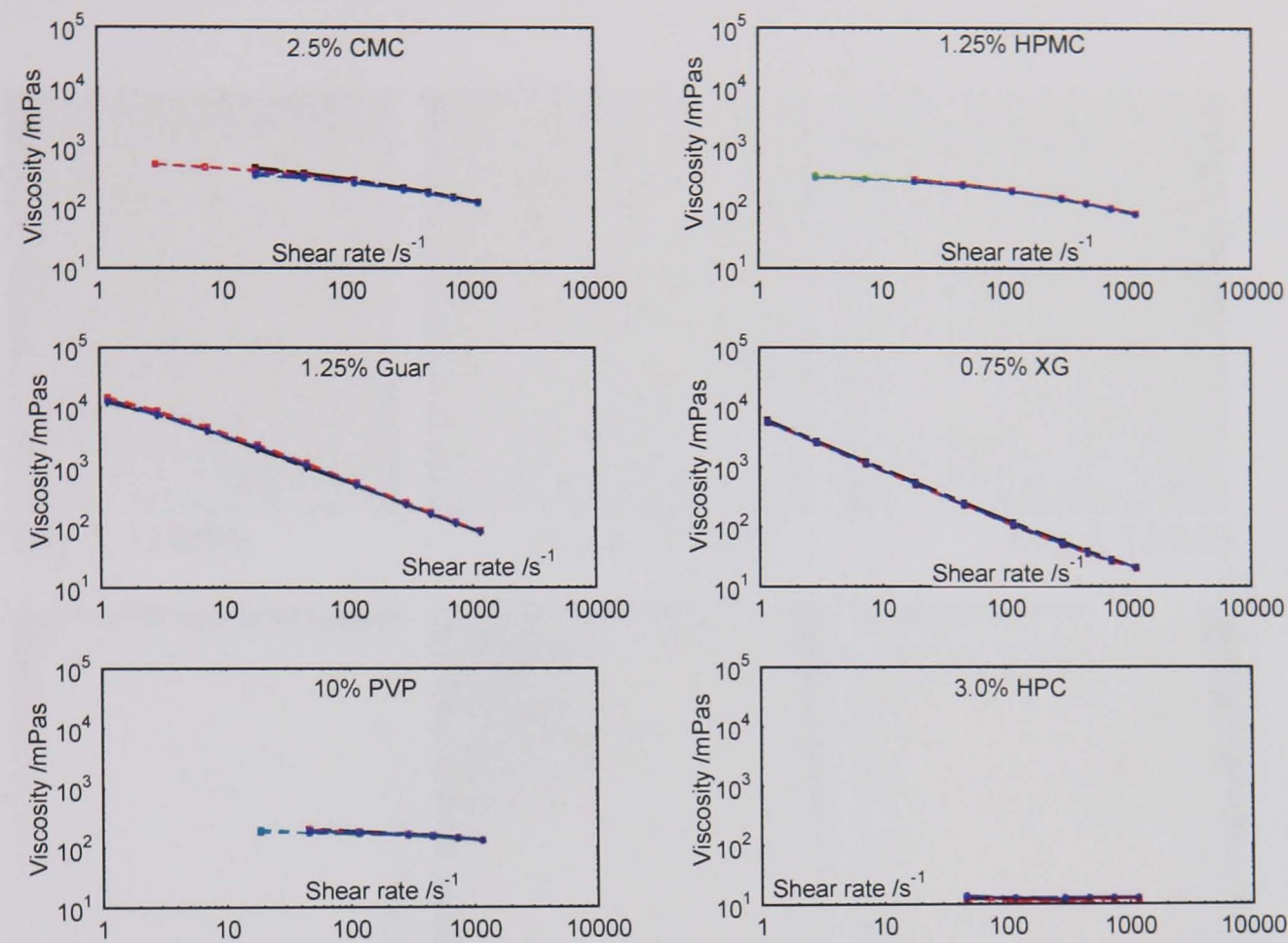


A.10 High shear mixer: Janke and Kunkel, Ultra-turrax T25

A.8-A.10

A.11 The change in apparent viscosity with shear rate for solutions tested.

Full names of solutions are given in Nomenclature. The up and down curves are plotted and each trial is shown as a different colour.

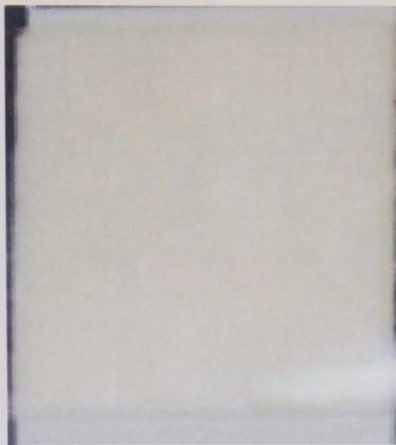


A.12 Biological indicator strips for Busan samples, series 1, open and stored in a length of pipe

Red/pink colour on the pad indicates the presence of bacteria. The greater the area/intensity of red the more bacteria are present.



Day 2, 11/8/01;



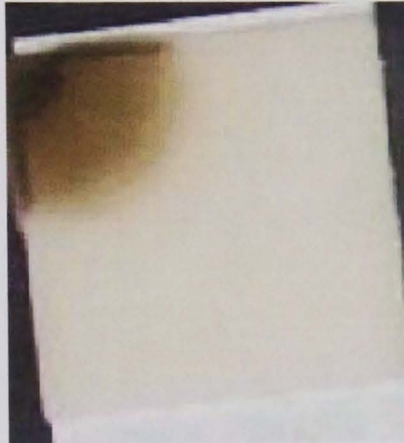
Day 3, 12/8/01;



Day 4, 13/8/01



Day 5, 14/8/01;



Day 7, 16/8/01;



Day 9, 18/8/01



Day 11, 20/8/01



Day 13, 22/8/01



Day 15, 24/8/01

Pipe test

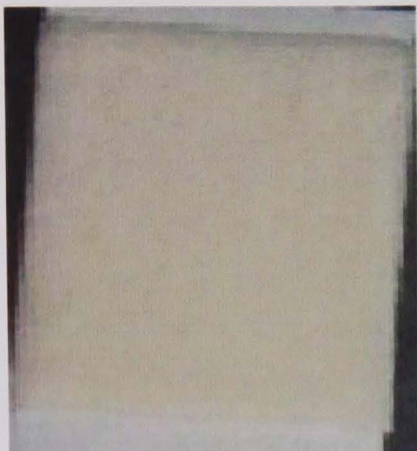


Day 2, 11/8/01, sealed pipe input



Day 15, 24/8/01, pipe output

A.13 Biological indicator strips for Proxel open sample, series 1



Day 2, 11/8/01;



Day 3, 12/8/01;



Day 4, 13/8/01



Day 5, 14/8/01;



Day 7, 16/8/01;



Day 9, 18/8/01



Day 11, 20/8/01



Day 13, 22/8/01



Day 15, 24/8/01

A.14 Biological indicator strips for control samples, series 1, open and stored in a length of pipe



Day 2, 11/8/01, pipe input



Day 3, 12/8/01;



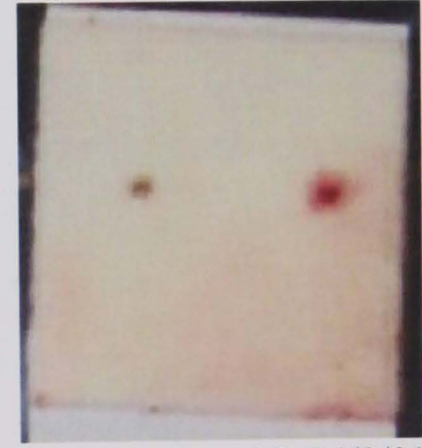
Day 4, 13/8/01



Day 5, 14/8/01;



Day 15, 24/8/01



Day 15, 24/8/01
pipe output

A.15 Results of series 2 biological tests

Sample/Day	2	4	6	8	10	12	14	15	Pipe
CO2, CP2	Growth	Growth	Growth	Growth	Growth	None	Growth	Growth	Growth
NO, NP	None	None	Ltd	Ltd	Ltd	None	Ltd	None	None
NS	None	Ltd	Ltd	None	Ltd	None	Ltd	None	-

Key:
Growth – majority of plate is covered in growth
None – no growth evident
Ltd – small growth covering limited area of the plate
CO2 – series 2 control sample, open
CP2 – series 2 control sample, stored in pipe length
NO – Nalco biocide, open
NP – Nalco biocide, stored in pipe length
NS – Nalco biocide, sealed overnight

A.16 Homogenous groups indicated by the Scheffe test.

Sample	Day	Shear rate ls^{-1}								
		2.91	7.31	18.5	46	116	291	461	731	1160
Busan open	2	xxxx	xxxx	xxxx	xxxx	xxxx	xxxx	xxxx	xxxx	xxxx
	3	xxxx	xxxx	xxxx	xxxx	xxxx	xxxx	xxxx	xxxx	xxxx
	4	xxxx	xxxx	xxxx	xxxx	xxxx	xxxx	xxxx	??xxxx??	xxxx
	5	xxxx	xxxx	xxxx	xxxx	xxxx	xxxx	xxxx	xxxx	xxxx
	6	xxxx	xxxx	xxxx	xxxx	xxxx	xxxx	xxxx	xxxx	xxxx
	7	xxxx	xxxx	xxxx	xxxx	xxxx	xxxx	xxxx	xxxx	xxxx
	8	xxxx	xxxx	xxxx	xxxx	xxxx	xxxx	xxxx	xxxx	xxxx
	9	xxxx	xxxx	xxxx	xxxx	xxxx	xxxx	xxxx	xxxx	xxxx
	10	xxxx	xxxx	xxxx	xxxx	xxxx	xxxx	xxxx	xxxx	xxxx
	11	xxxx	xxxx	xxxx	xxxx	xxxx	xxxx	xxxx	xxxx	xxxx
	12	xxxx	xxxx	xxxx	xxxx	xxxx	xxxx	xxxx	xxxx	xxxx
	13	xxxx	xxxx	xxxx	xxxx	xxxx	xxxx	xxxx	xxxx	xxxx
	14	xxxx	xxxx	xxxx	xxxx	xxxx	xxxx	xxxx	xxxx	xxxx
	15	xxxx	xxxx	????	xxxx	????				xxxx
Series 1 control open	2	xxxx	xxxx	xxxx	xxxx	xxxx	xxxx	xxxx	xxxx	xxxx
	3	xxxx	xxxx	xxxx	xxxx	xxxx	xxxx	xxxx	xxxx	xxxx
	4	xxxx	xxxx	xxxx	xxxx	xxxx	xxxx	xxxx	xxxx	xxxx
	5	xxxx	xxxx	xxxx	xxxx	xxxx	xxxx	xxxx	xxxx	xxxx
	6	xxxx	xxxx	xxxx	xxxx	xxxx	xxxx	xxxx	xxxx	xxxx
	7	xxxx	xxxx	xxxx	xxxx	xxxx	xxxx	xxxx	xxxx	xxxx
	8	xxxx	xxxx	xxxx	xxxx	xxxx	xxxx	xxxx	xxxx	xxxx
	9	xxxx	xxxx	xxxx	xxxx	xxxx	xxxx	xxxx	xxxx	xxxx
	10	xxxx	xxxx	xxxx	xxxx	xxxx	xxxx	xxxx	xxxx	xxxx
	11	xxxx	xxxx	xxxx	xxxx	xxxx	xxxx	xxxx	xxxx	xxxx
	12	xxxx	xxxx	xxxx	xxxx	xxxx	xxxx	xxxx	xxxx	xxxx
	13	xxxx	xxxx	xxxx	xxxx	xxxx	xxxx	xxxx	xxxx	xxxx
	14	xxxx	xxxx	xxxx	xxxx	xxxx	xxxx	xxxx	xxxx	xxxx
	15	xxxx	xxxx	xxxx	xxxx	xxxx	xxxx	xxxx	??xxxx??	xxxx
Proxel open	2	xxxx	xxxx	xxxx	xxxx	xxxx	xxxx	xxxx	xxxx	xxxx
	3	xxxx	xxxx	xxxx	xxxx	xxxx	xxxx	xxxx	xxxx	xxxx
	4	xxxx	xxxx	xxxx	xxxx	xxxx	xxxx	xxxx	xxxx	xxxx
	5	xxxx	xxxx	xxxx	xxxx	xxxx	xxxx	xxxx	xxxx	xxxx
	6	xxxx	xxxx	xxxx	xxxx	xxxx	xxxx	xxxx	xxxx	xxxx
	7	xxxx	xxxx	xxxx	xxxx	xxxx	xxxx	xxxx	xxxx	xxxx
	8	xxxx	xxxx	xxxx	xxxx	xxxx	xxxx	xxxx	xxxx	xxxx
	9	xxxx	xxxx	xxxx	xxxx	xxxx	xxxx	xxxx	xxxx	xxxx
	10	xxxx	xxxx	xxxx	xxxx	xxxx	xxxx	xxxx	xxxx	xxxx
	11	xxxx	xxxx	xxxx	xxxx	xxxx	xxxx	xxxx	xxxx	xxxx
	12	xxxx	xxxx	xxxx	xxxx	xxxx	xxxx	xxxx	xxxx	xxxx
	13	xxxx	xxxx	xxxx	xxxx	xxxx	xxxx	xxxx	xxxx	xxxx
	14	xxxx	xxxx	xxxx	xxxx	xxxx	xxxx	xxxx	xxxx	xxxx
	15	xxxx	xxxx	xxxx	xxxx	xxxx	xxxx	xxxx	xxxx	xxxx

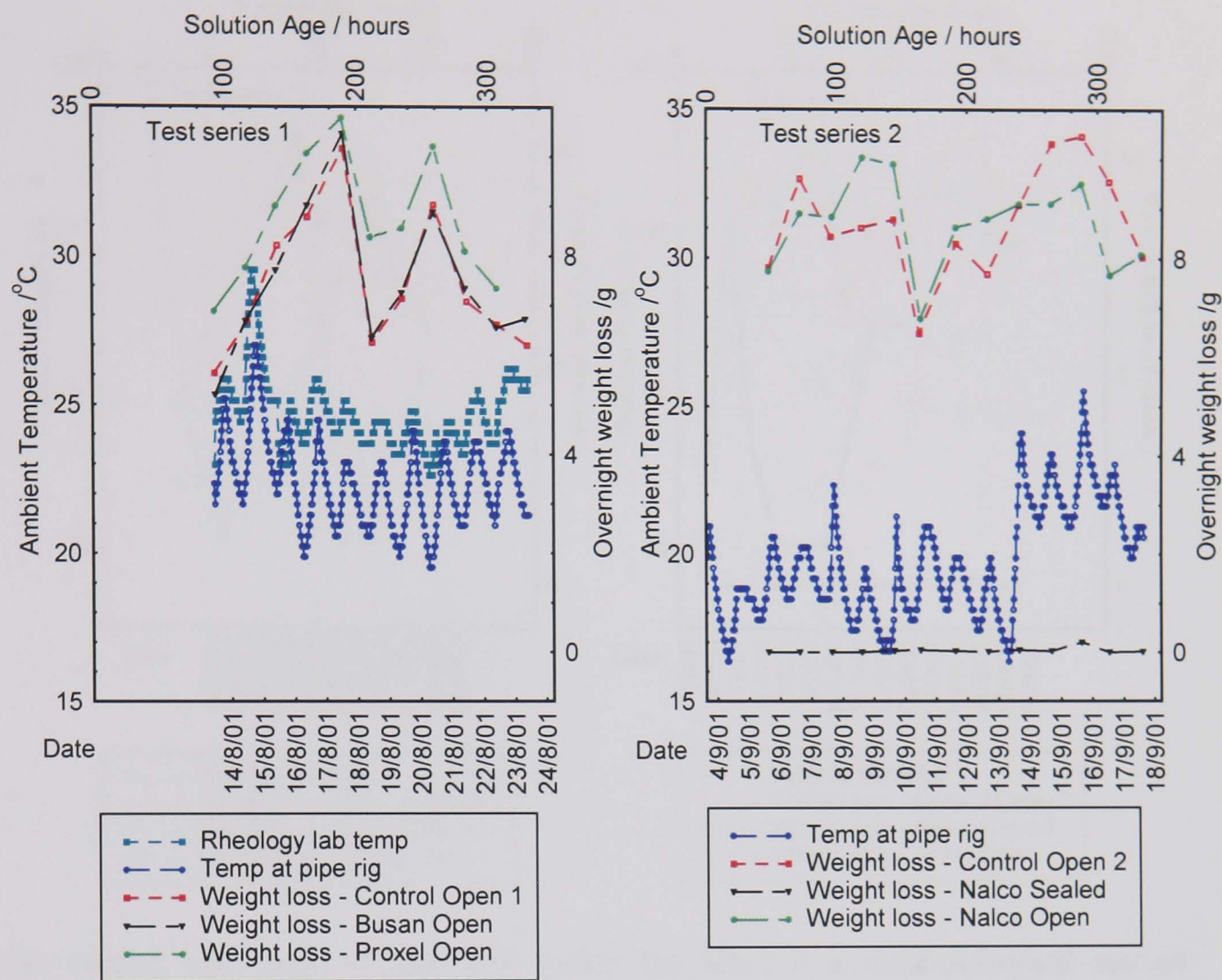
Key:
xxxx – part of homogenous group
??xxxx?? – uncertain part of homogenous group
Blank square – significantly different result
???? – uncertain significantly different result

Sample	Day	Shear rate \s ⁻¹								
		2.91	7.31	18.5	46	116	291	461	731	1160
Nalco sealed	2	xxxx	xxxx	xxxx	xxxx	xxxx	xxxx	xxxx	xxxx	xxxx
	3	xxxx	xxxx	xxxx	xxxx	xxxx	xxxx	xxxx	xxxx	xxxx
	4	xxxx	xxxx	xxxx	xxxx	xxxx	xxxx	xxxx	xxxx	xxxx
	5	xxxx	xxxx	xxxx	xxxx	xxxx	xxxx	xxxx	xxxx	xxxx
	6	xxxx	xxxx	xxxx	xxxx	xxxx	xxxx	xxxx	xxxx	xxxx
	7	xxxx	xxxx	xxxx	xxxx	xxxx	xxxx	xxxx	xxxx	xxxx
	8	xxxx	xxxx	xxxx	xxxx	xxxx	xxxx	xxxx	xxxx	xxxx
	9	xxxx	xxxx	xxxx	xxxx	xxxx	xxxx	xxxx	xxxx	xxxx
	10	xxxx	xxxx	xxxx	xxxx	xxxx	xxxx	xxxx	xxxx	xxxx
	11	xxxx	xxxx	xxxx	xxxx	xxxx	xxxx	xxxx	xxxx	xxxx
	12	xxxx	xxxx	xxxx	xxxx	xxxx	xxxx	xxxx	xxxx	xxxx
	13	xxxx	xxxx	xxxx	xxxx	xxxx	xxxx	xxxx	xxxx	xxxx
	14	xxxx	xxxx	xxxx	xxxx	xxxx	xxxx	xxxx	xxxx	xxxx
	15	xxxx	xxxx	xxxx	xxxx	xxxx	xxxx	xxxx	xxxx	xxxx
Nalco open	2	xxxx	xxxx	xxxx	xxxx	xxxx	xxxx	xxxx	xxxx	xxxx
	3	xxxx	xxxx	xxxx	xxxx	xxxx	xxxx	xxxx	xxxx	xxxx
	4	xxxx	xxxx	xxxx	xxxx	xxxx	xxxx	xxxx	xxxx	xxxx
	5	xxxx	xxxx	xxxx	xxxx	xxxx	xxxx	xxxx	xxxx	xxxx
	6	xxxx	xxxx	xxxx	xxxx	xxxx	xxxx	xxxx	xxxx	xxxx
	7	xxxx	xxxx	????	xxxx	xxxx	xxxx	??xxxx??	????	xxxx
	8	xxxx								xxxx
	9	xxxx	xxxx	xxxx	xxxx	xxxx	xxxx	xxxx	xxxx	xxxx
	10	??xxxx??								??xxxx??
	11									
	12									
	13									
	14									
	15									
Series 2 control open	2				xxxx	xxxx	xxxx	xxxx	xxxx	xxxx
	3				xxxx	xxxx	xxxx	xxxx	xxxx	xxxx
	4				xxxx	xxxx	xxxx	xxxx	xxxx	xxxx
	5				xxxx	xxxx	xxxx	xxxx	xxxx	xxxx
	6				xxxx	xxxx	xxxx	xxxx	xxxx	xxxx
	7				xxxx	xxxx	xxxx	xxxx	xxxx	xxxx
	8				xxxx	xxxx	xxxx	xxxx	xxxx	xxxx
	9									xxxx
	10							????		
	11									????
	12									
	13									
	14									
	15									

Key:
xxxx – part of homogenous group
??xxxx?? – uncertain part of homogenous group
Blank square – significantly different result
???? – uncertain significantly different result

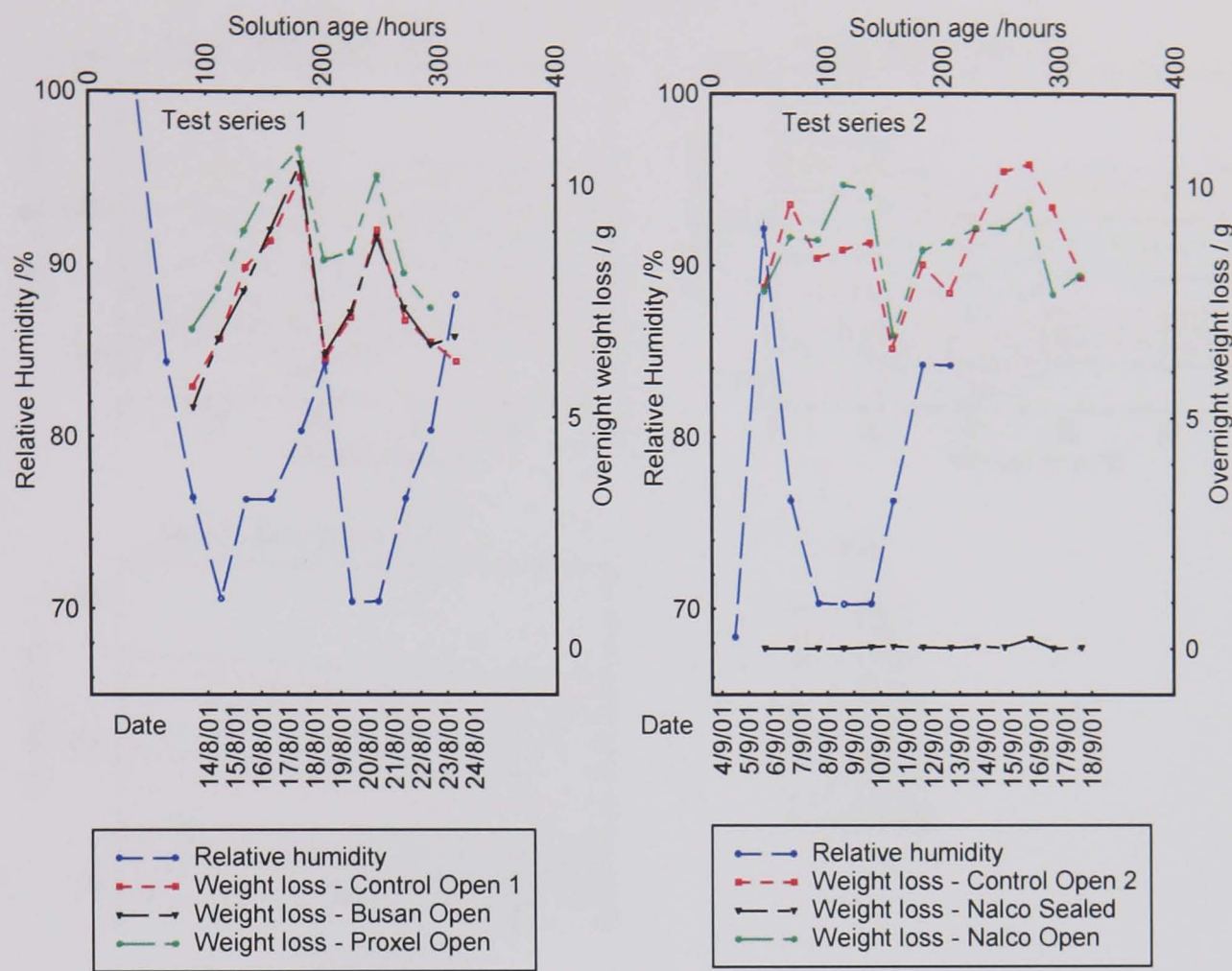
..... This data could not be included in the analysis because of missing data points, due to the apparent viscosity being out of the torque range of the instrument.

A.17 Variation in ambient temperature and overnight weight loss with time.



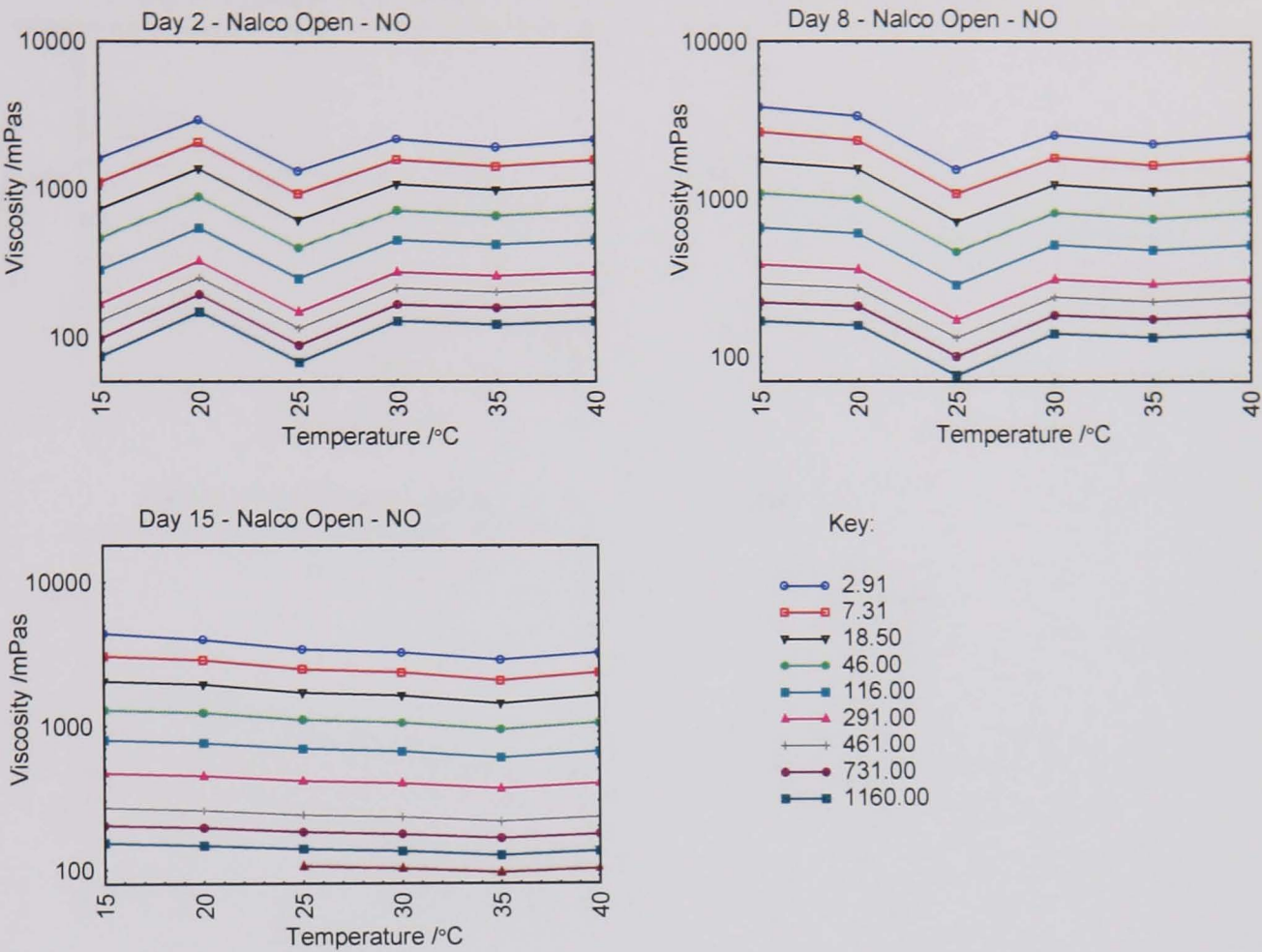
No obvious correlation can be seen between the temperature and the weight loss. The weight losses for each sample followed the same pattern, with Proxel slightly higher than the others because it had a larger volume. In test series two the weight losses of the two Nalco samples do not follow the same pattern as would be expected due to identical storage conditions. Sealing a Nalco sample overnight virtually eliminated overnight weight loss.

A.18 Variation in outside humidity and overnight weight loss with time.

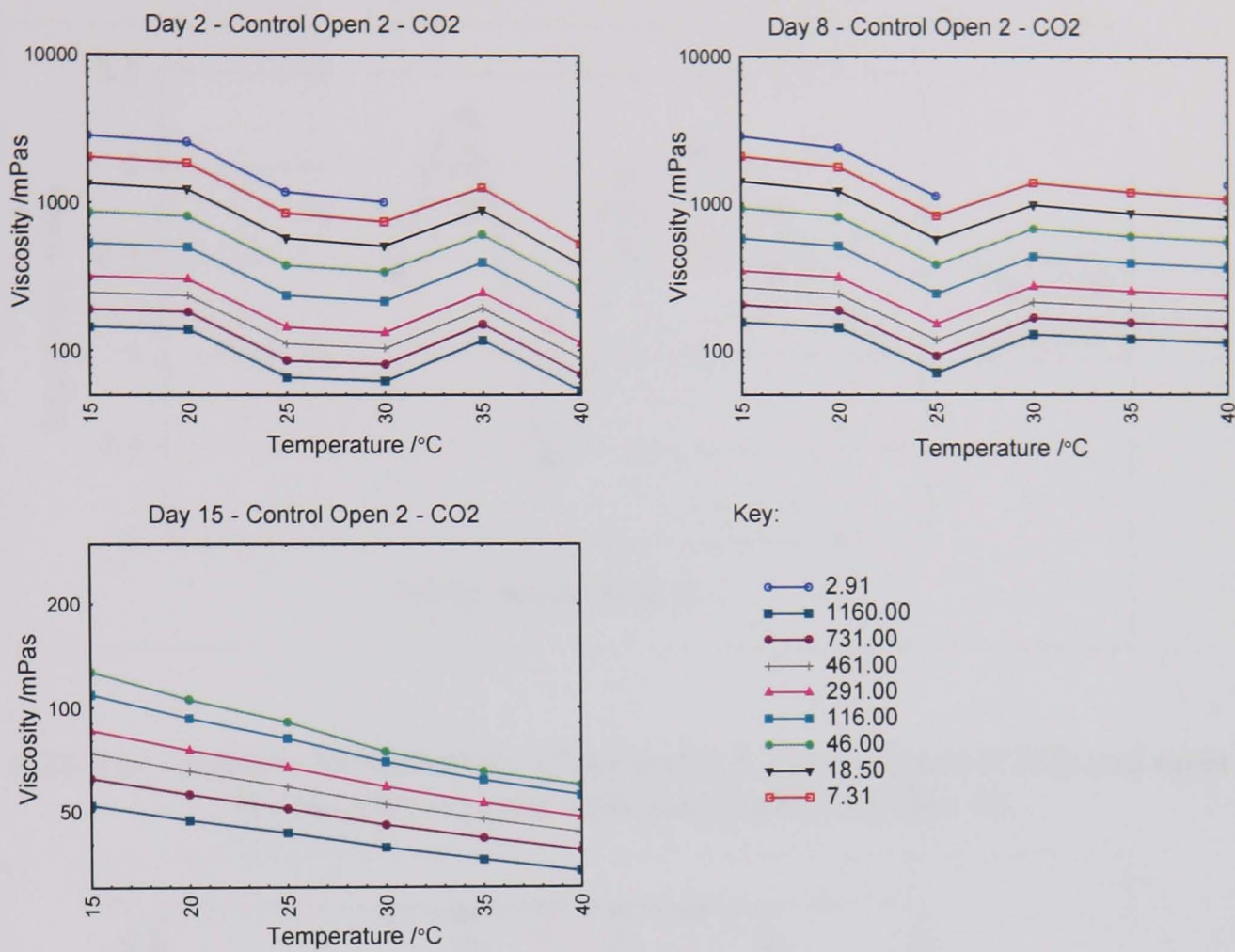


No record was kept of humidity inside the lab but a meteorological station measured the wet and dry bulb temperatures outside every day on the site of the rheology lab. The average temperatures were calculated over each 24 hours and the relative humidity was obtained from the mean temperatures using tables (CIBSE, 1988). The nearest tabulated value to the means were used. This rough estimation of the humidity was performed as an initial check to determine whether any pattern was seen. No obvious correlation is observed.

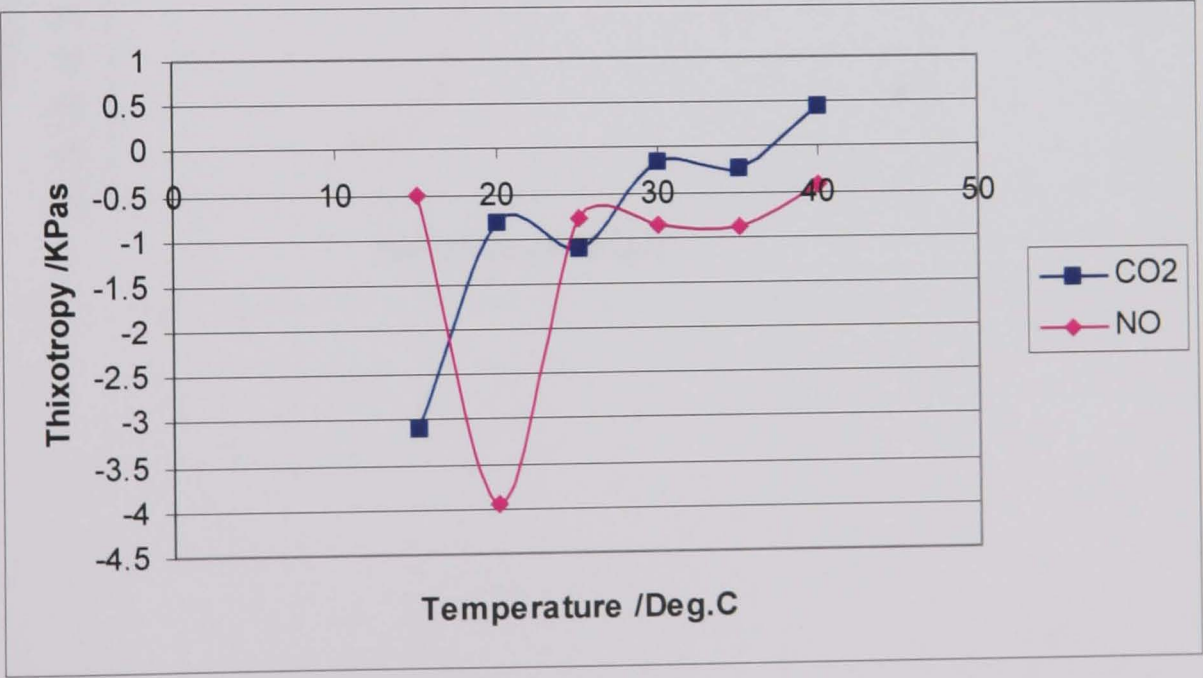
A.19 Apparent viscosity variation with temperature for open Nalco sample (series 2)



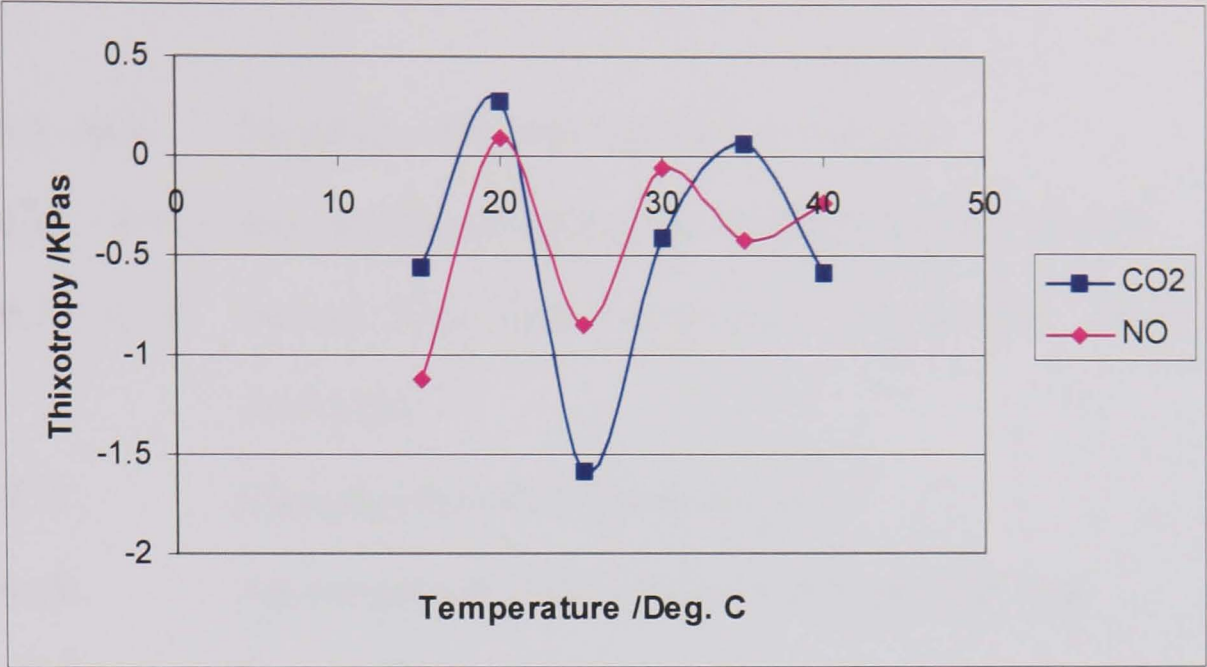
A.20 Apparent viscosity variation with temperature for open control sample (series 2)



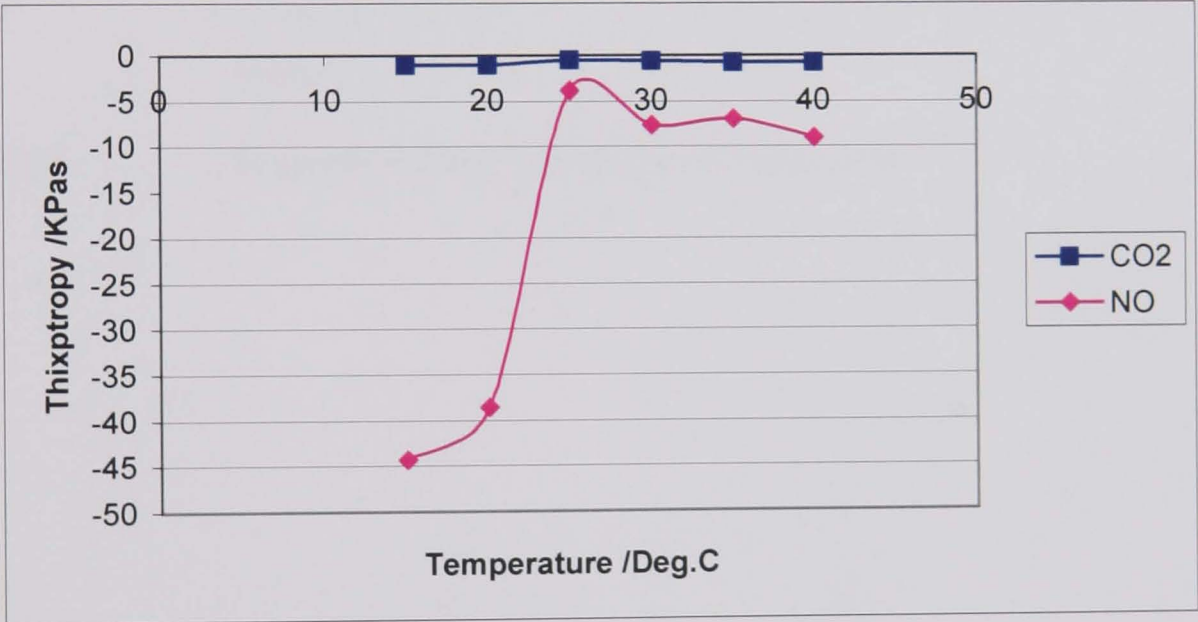
A.21 The variation in thixotropy of the series 2, open control (CO2) and open Nalco (NO) samples with temperature on Day 2



A.22 The variation in thixotropy of the series 2, open control (CO2) and open Nalco (NO) samples with temperature on Day 8



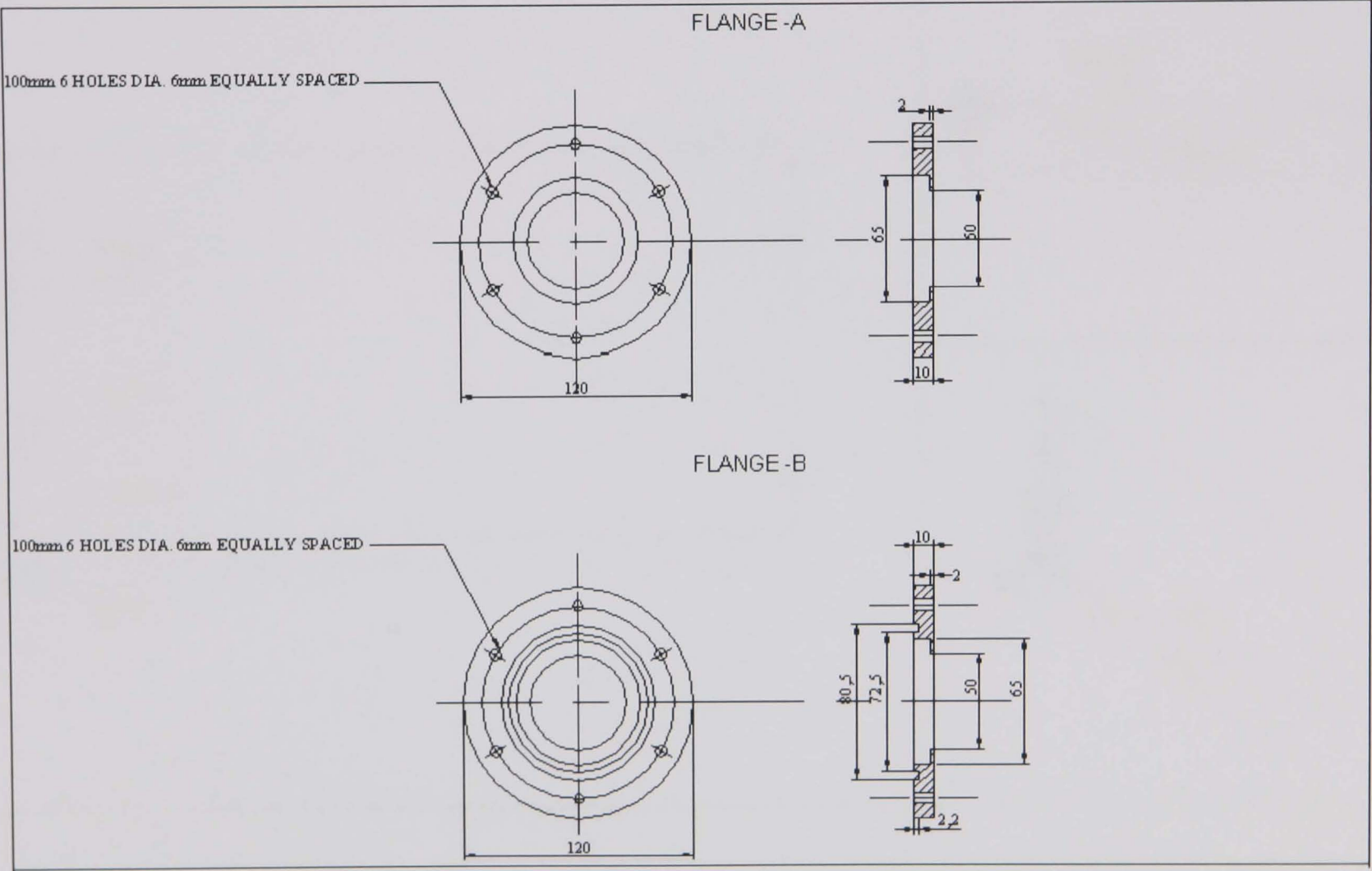
A.23 The variation in thixotropy of the series 2, open control (CO2) and open Nalco (NO) samples with temperature on Day 15



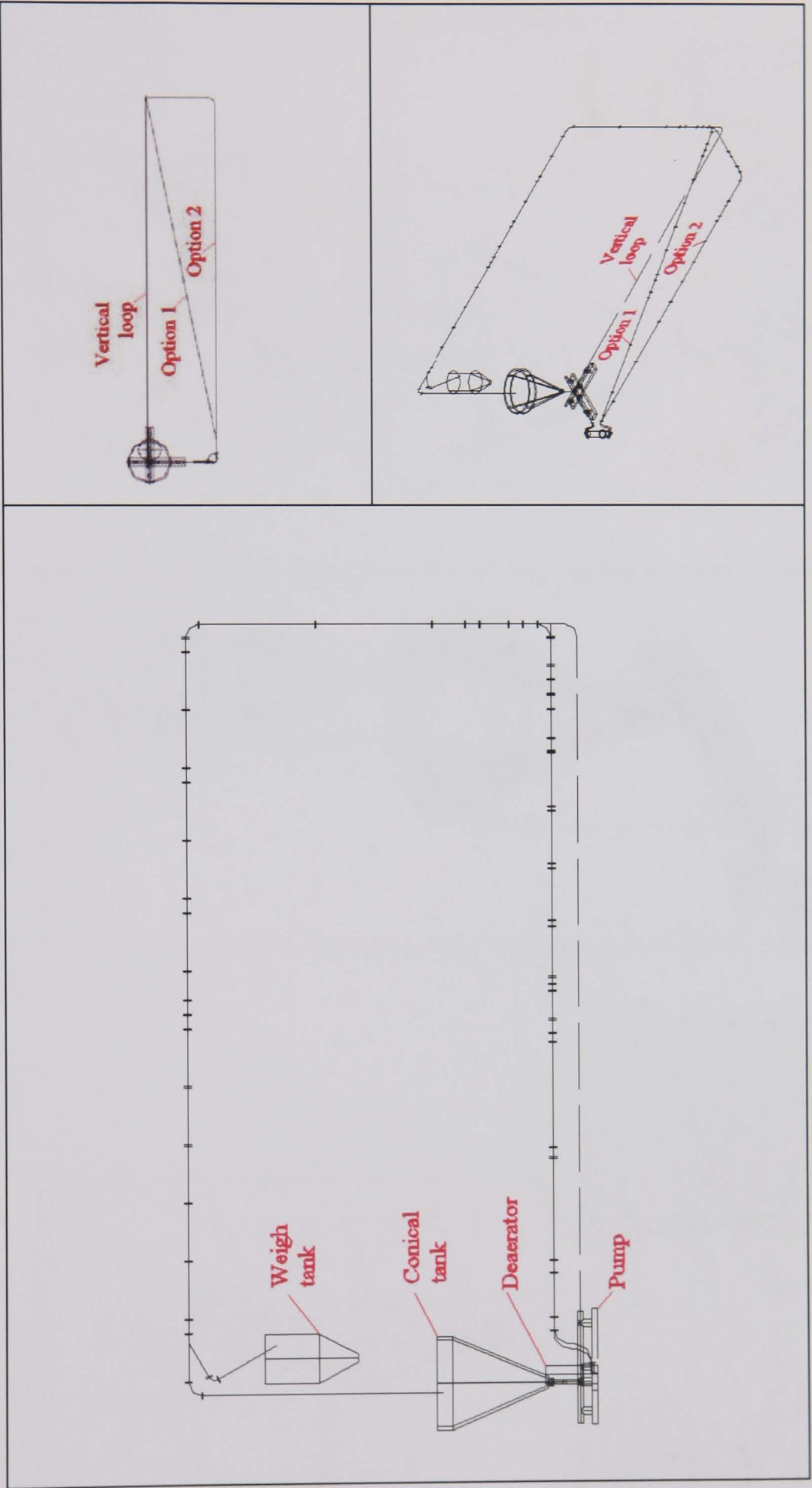
Appendix B. DESIGN OF A STEEL PIPE FLOW LOOP

B.1 – B.9	Diagrams of the steel pipe flow loop design
B.10 – B.11	Plan and side elevation of the flow loop support structure
B.12– B.16	Pressure drop results from the tests to compare the 3 and 4-lobe swirl pipes
B.17	Characteristics of various pump types
B.18	Advantages and disadvantages of various valve types
B.19	Pump characteristic
B.20	Calculations to size conical tank
B.21	Calculations to determine the heat removal requirement of the cooler
B.22	Properties of the TJE pressure transducers

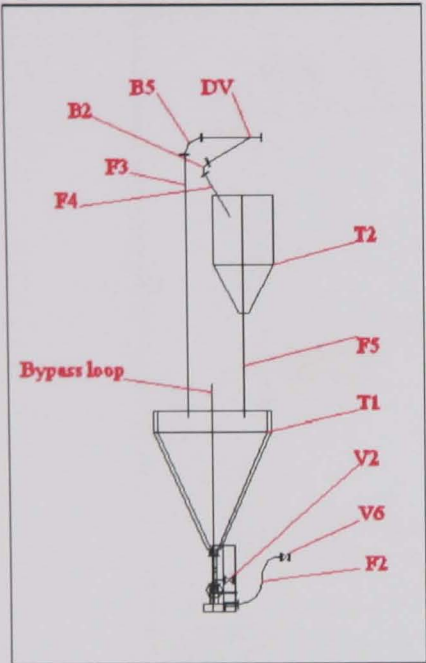
B.1 Flanges (Drawn by Ganeshalingam, 2001)



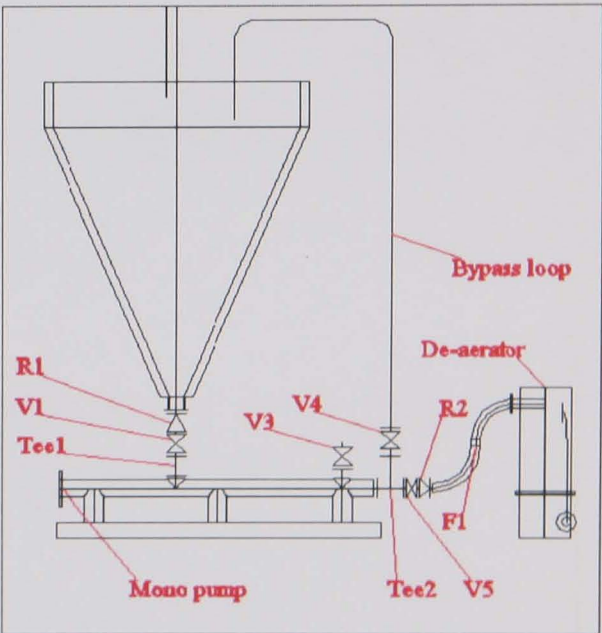
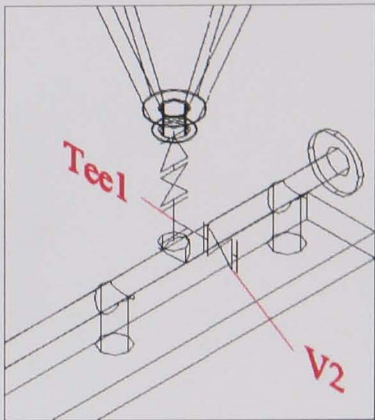
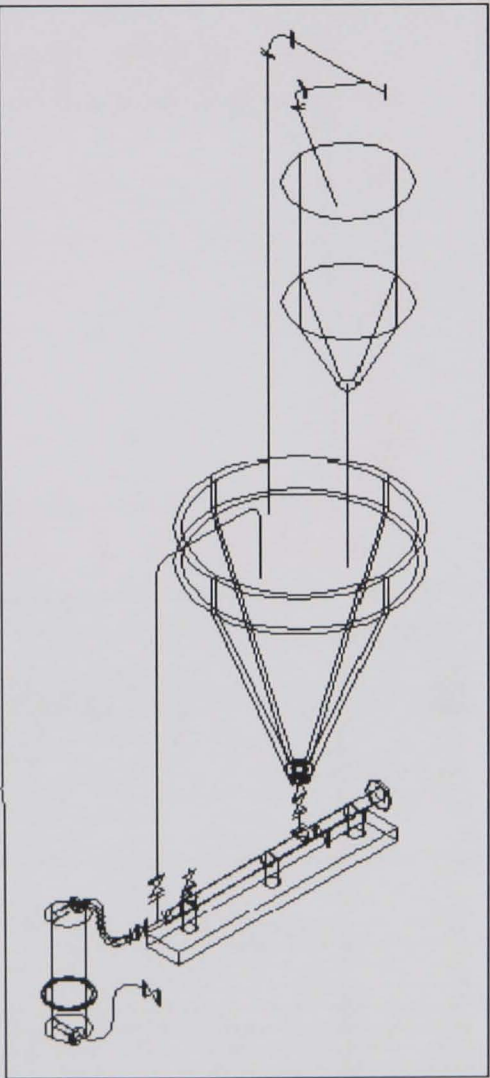
B.2 Design options



B.3 Phase 1 of commissioning

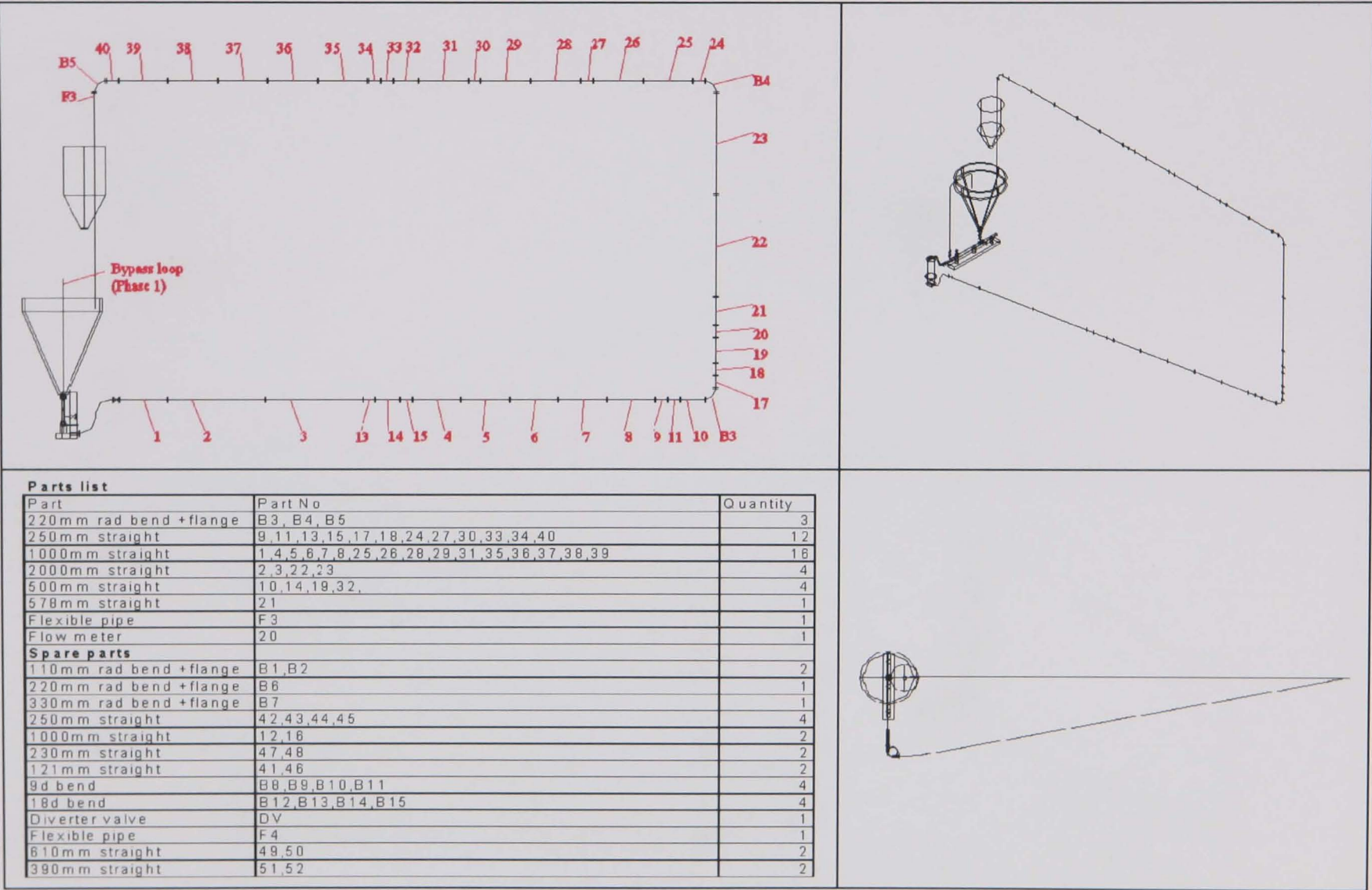


Parts list	
Part	Part No
Conical tank	T 1
W eigh tank	T 2
Bypass loop	-
Mono pump	-
Deaerator	-
Reducer	R 1,R 2
T piece	Tee1,Tee2
Gate valve	V 1
Ball valve	V 2,V 6
Pressure release valve	V 3
Butterfly valve	V 4,V 5
Flexible pipe	F 1,F 2,F 3,F 4,F 5
110mm rad bend + flange	B 2
220mm rad bend + flange	B 5
D iverter valve	D V



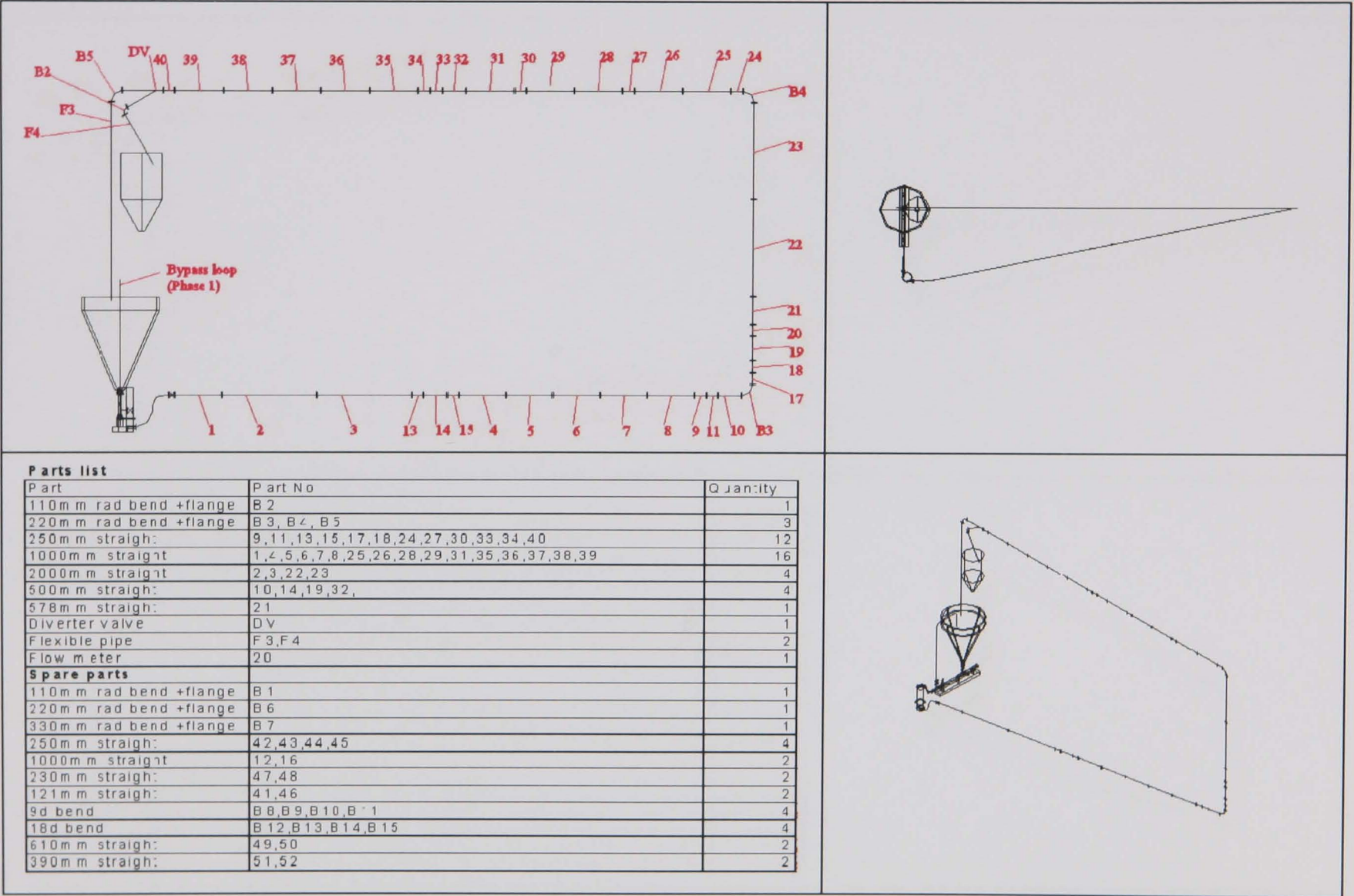
B.4 Phase 2 of commissioning

B.4

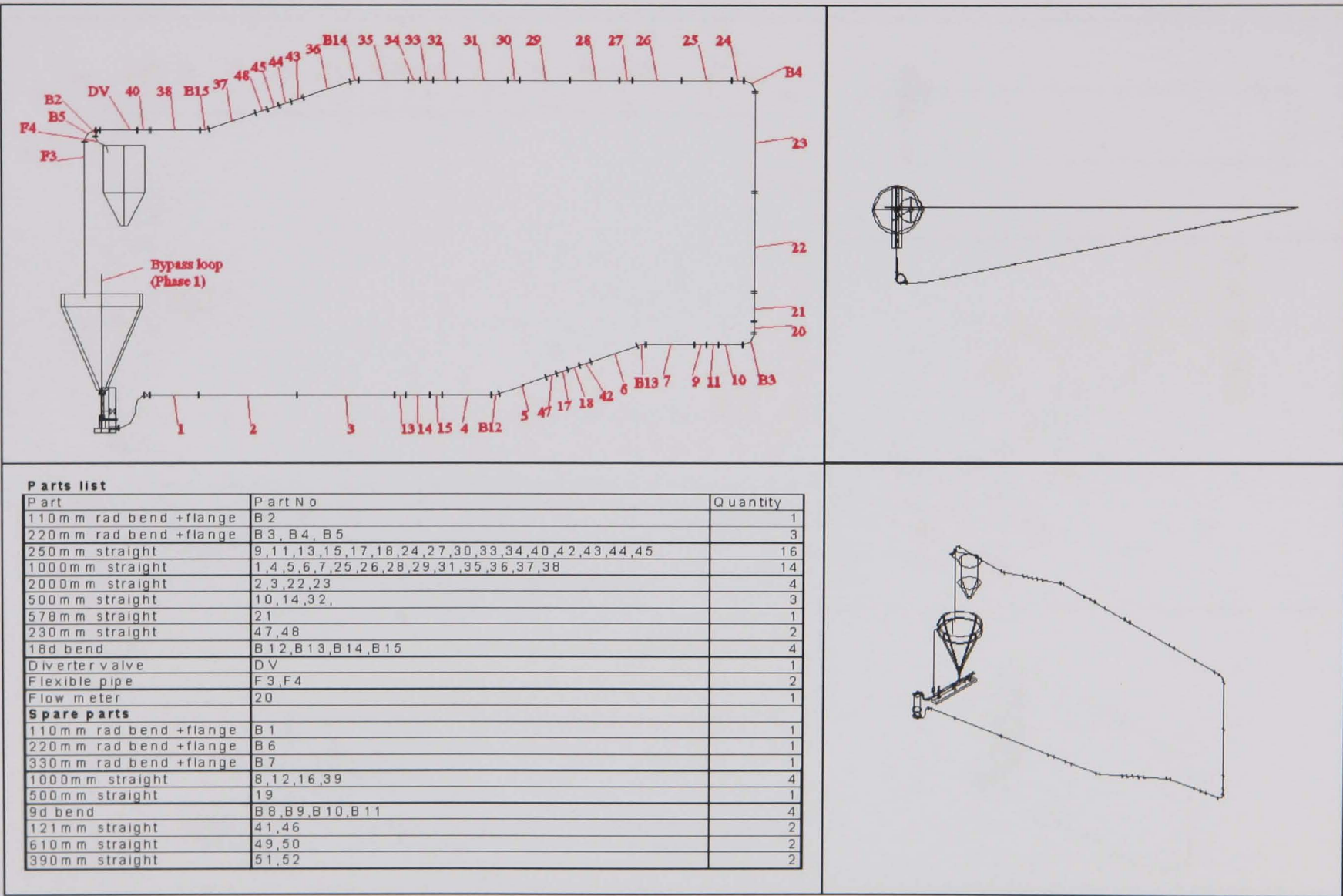


B.5 Diagonal configuration

B.5

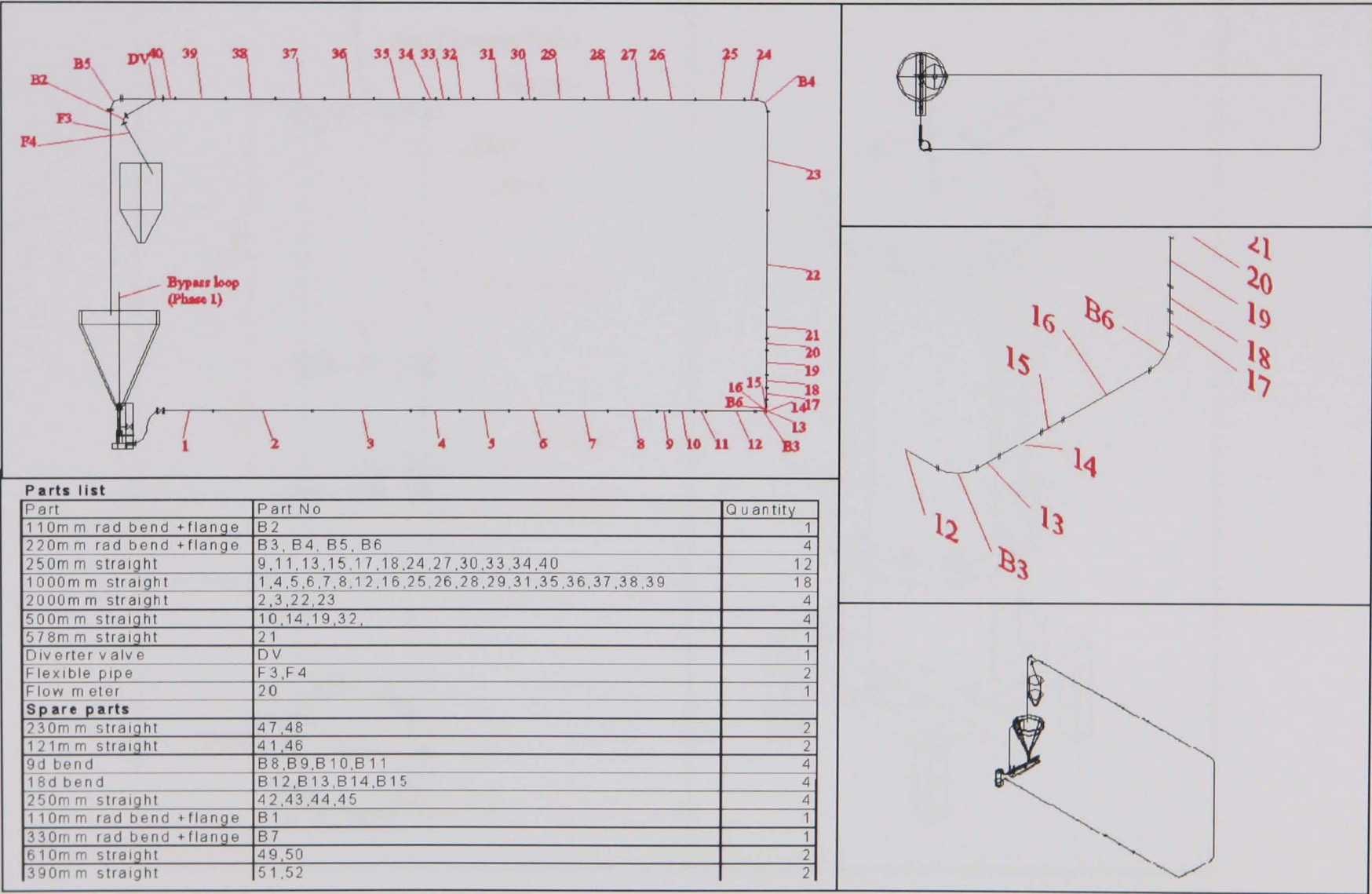


B.7 Diagonal configuration with 18° inclined section

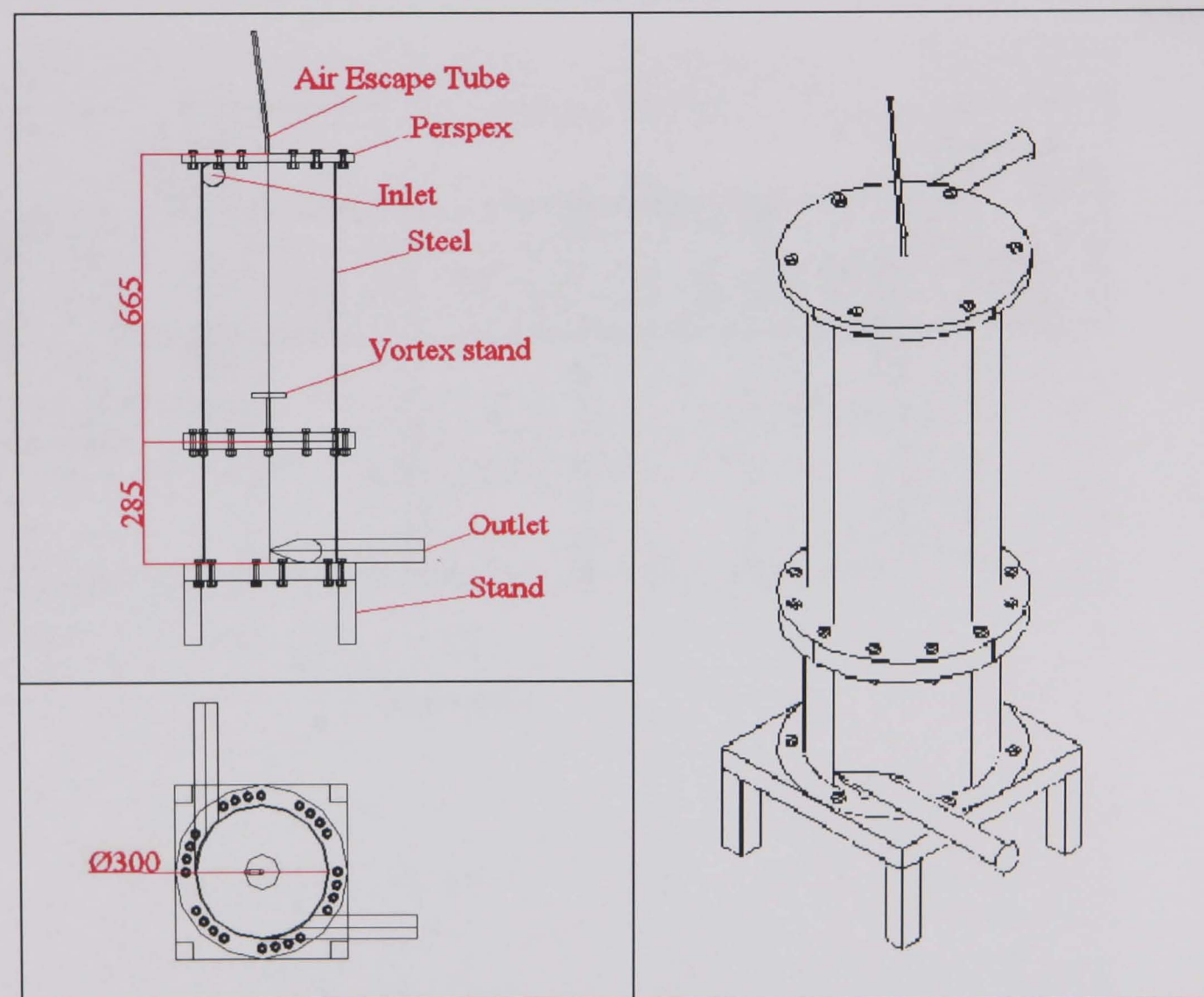


B.7

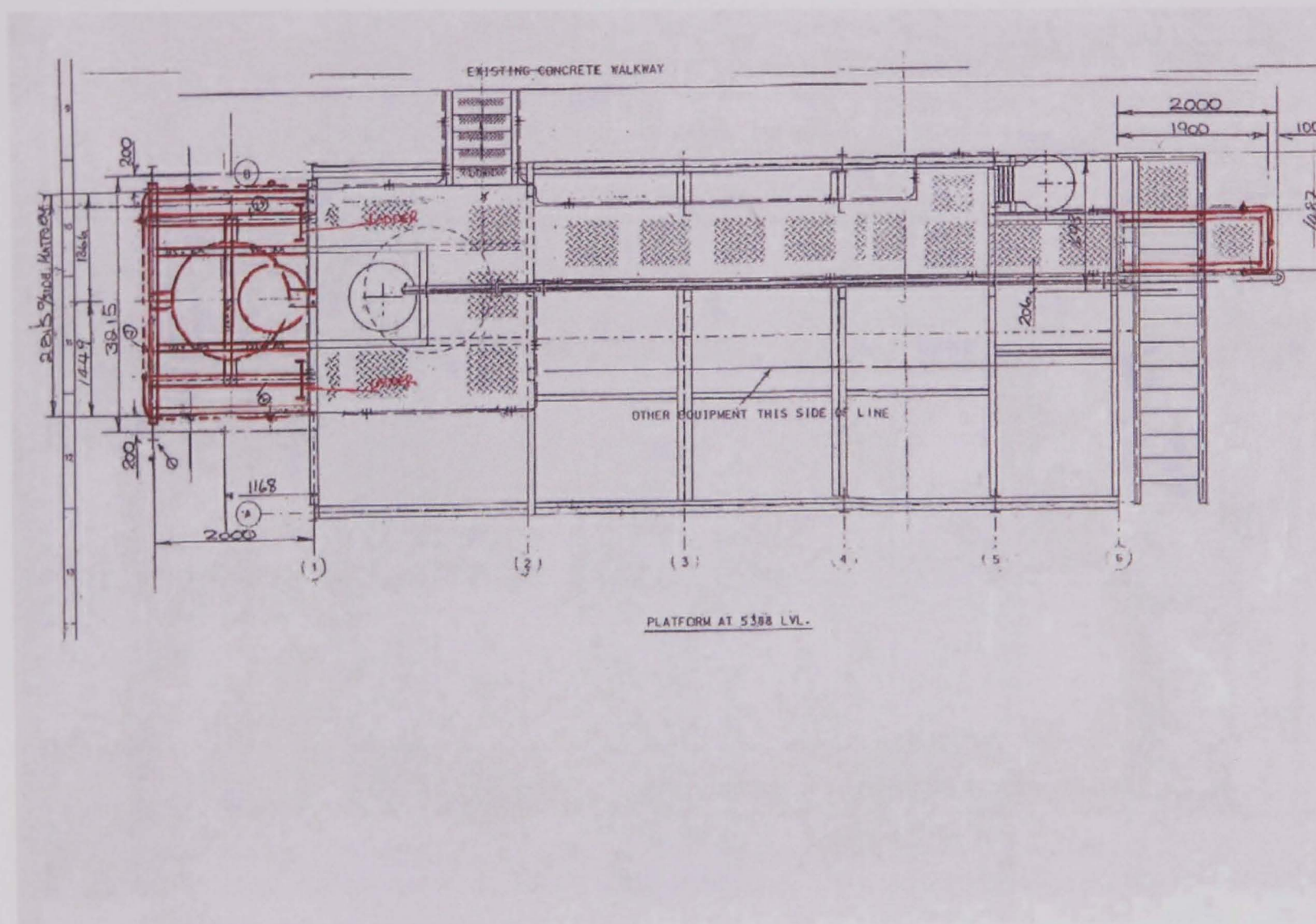
B.8 Horizontal bend configuration



B.9 De-aerator

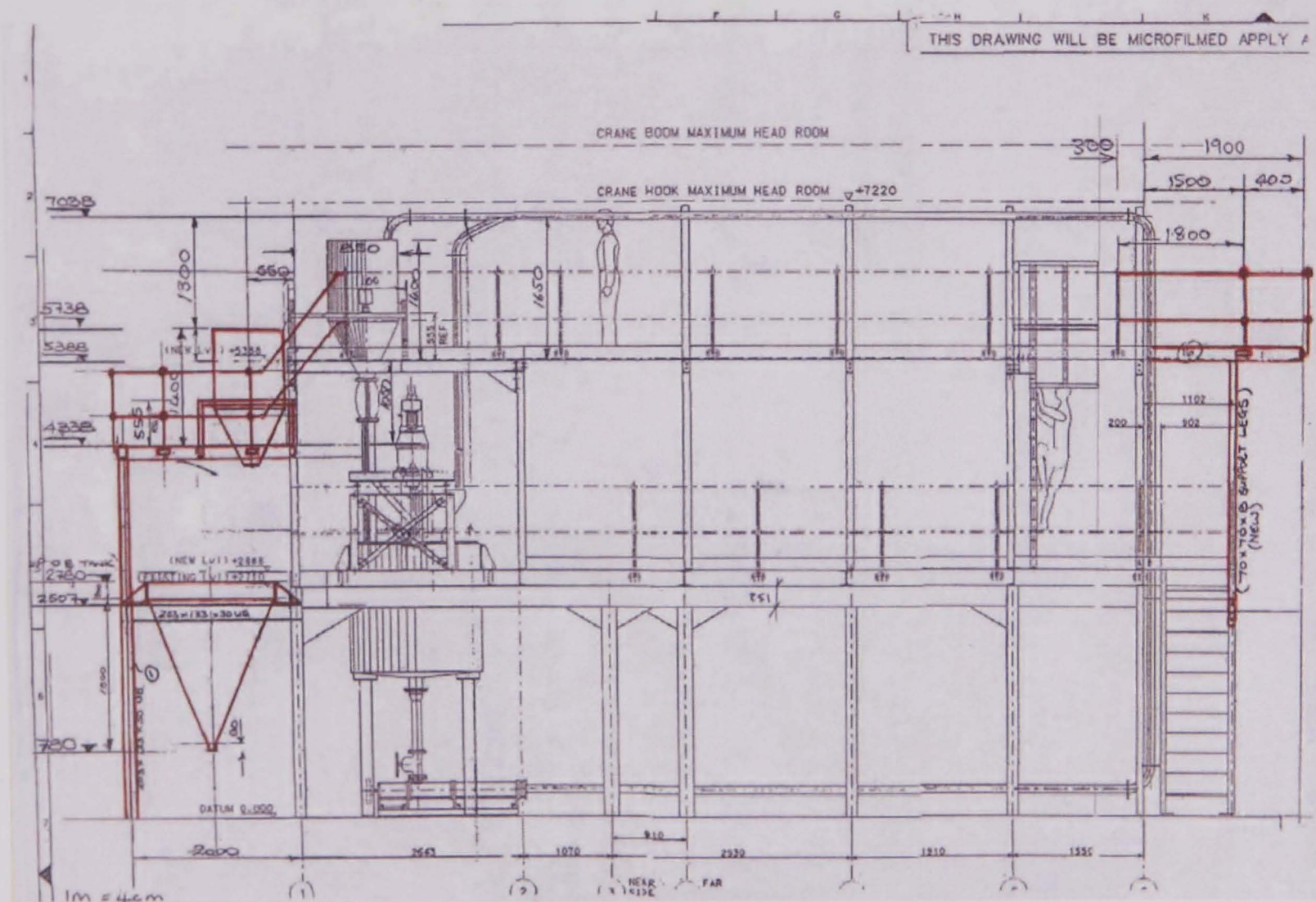


B.10 Plan of the existing flow loop support structure with modifications in red. (Original plans by Birtley Process Equipment Ltd, Chesterfield).

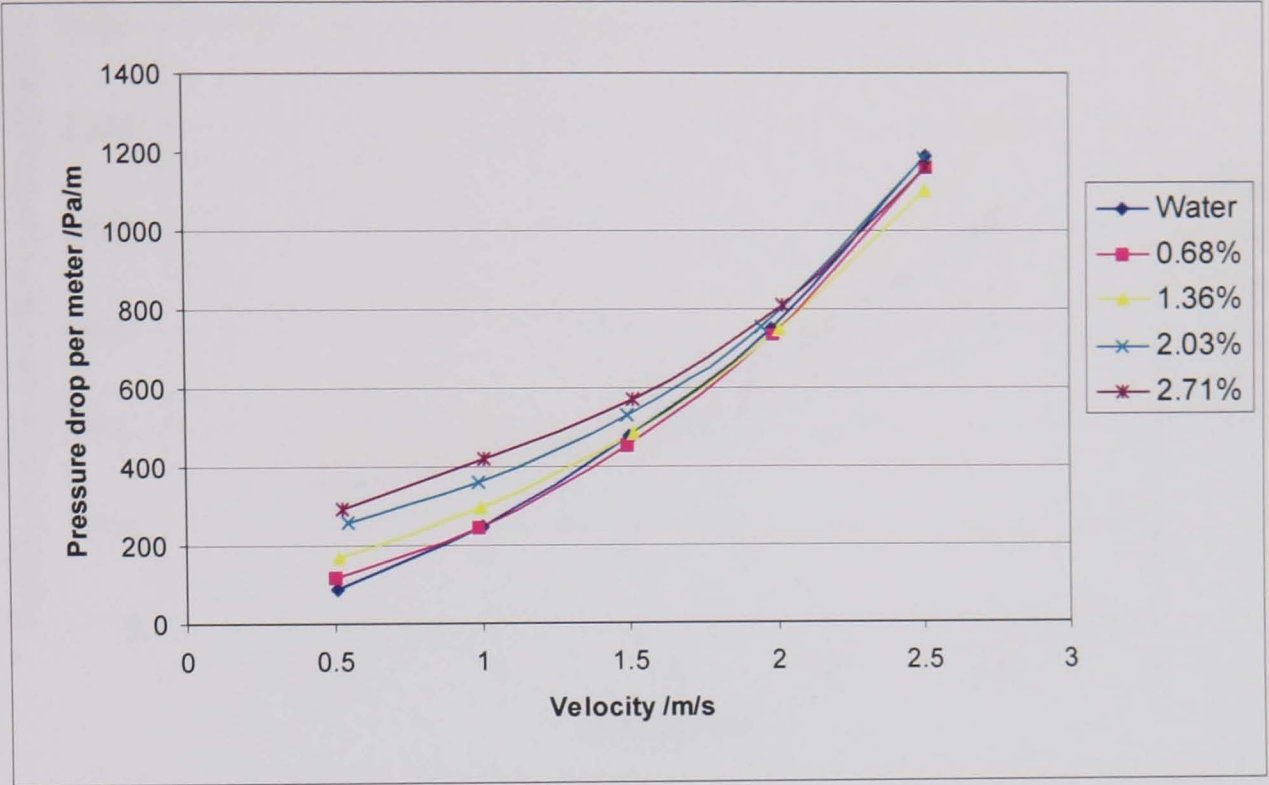


B.10

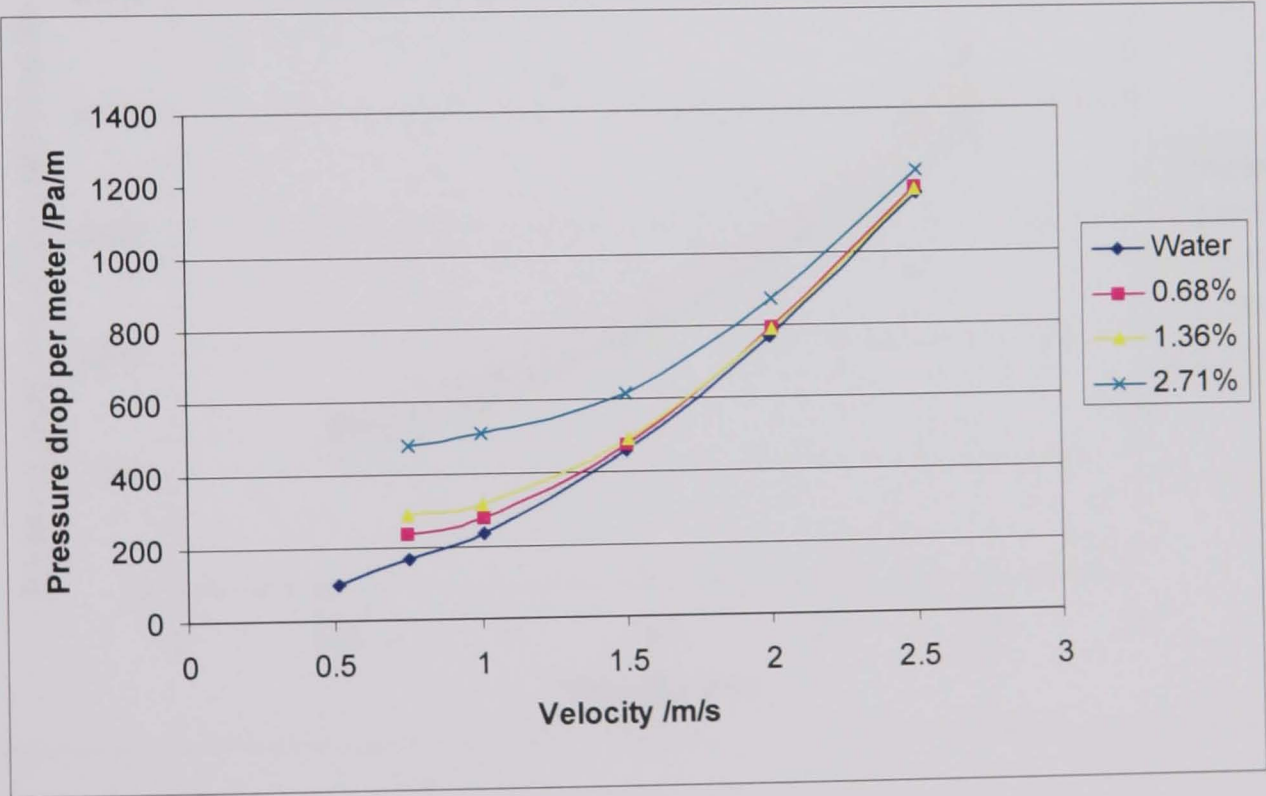
B.11 Side elevation of the existing flow loop support structure with modifications in red (Original plans by Birtley Process Equipment Ltd, Chesterfield).



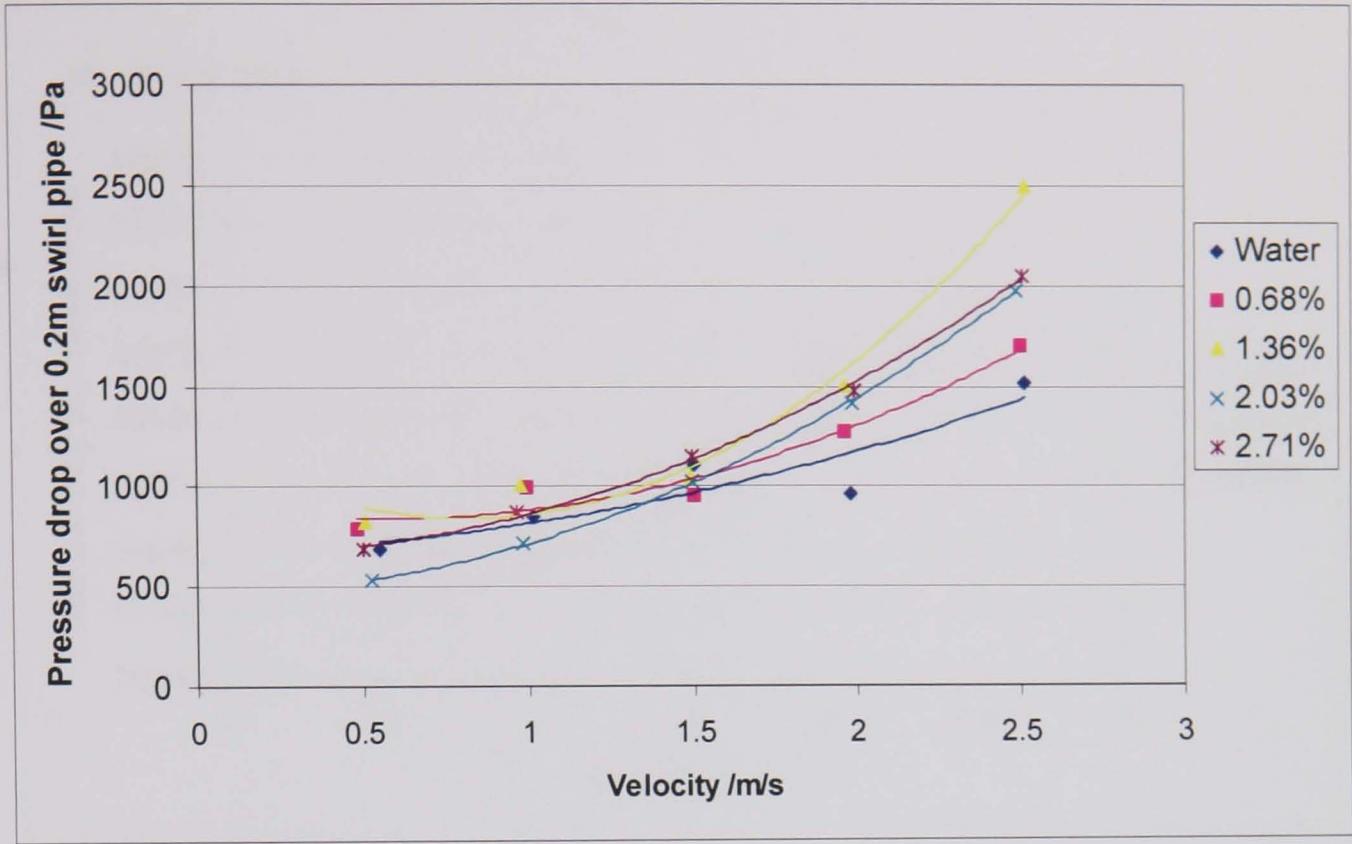
B.12 Pressure drop characteristic for various solids concentrations, top leg



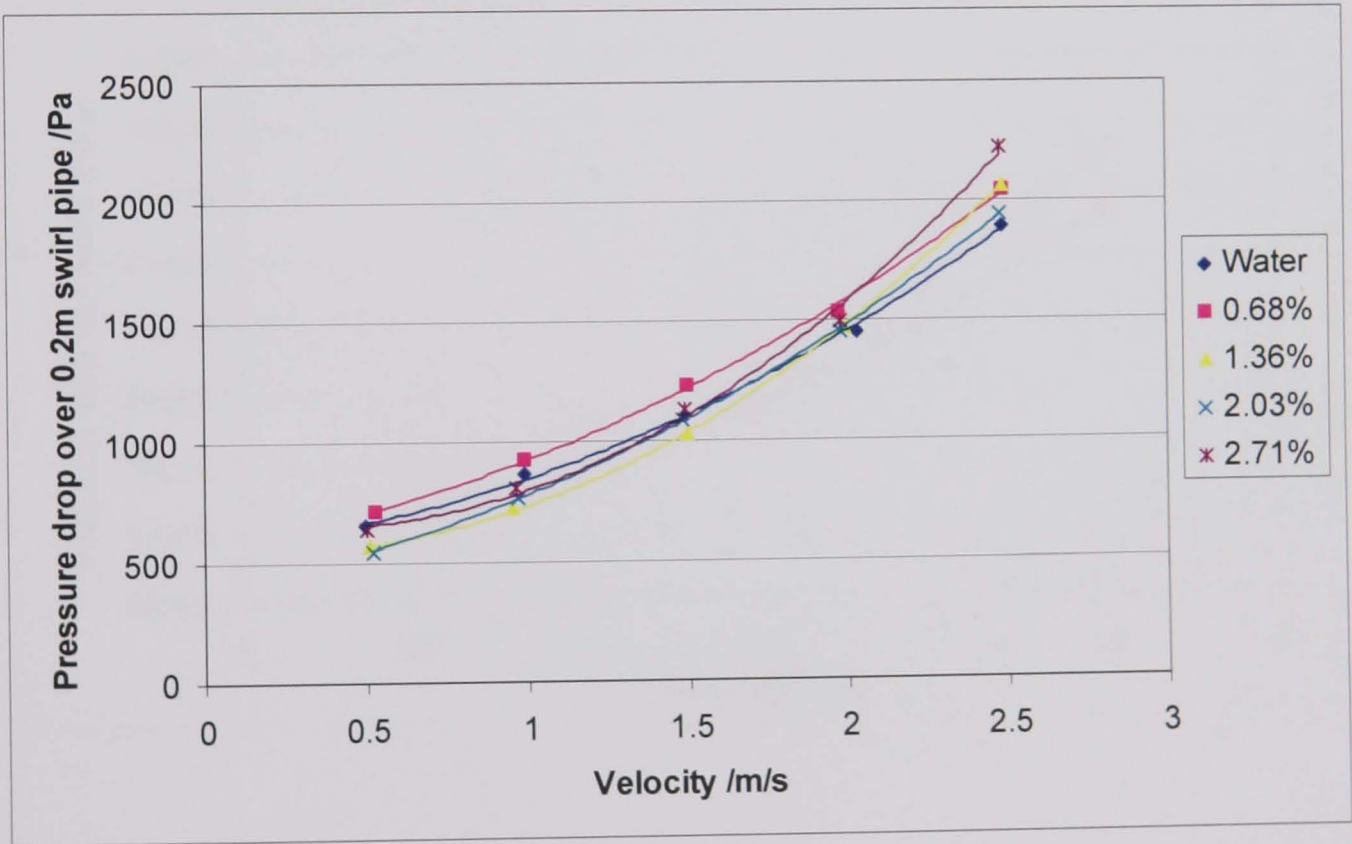
B.13 Ganeshalingam's (2002) corresponding data: Pressure drop characteristics for various solids concentrations, top leg



B.14 Pressure drop characteristic over 3-lobe swirl pipe

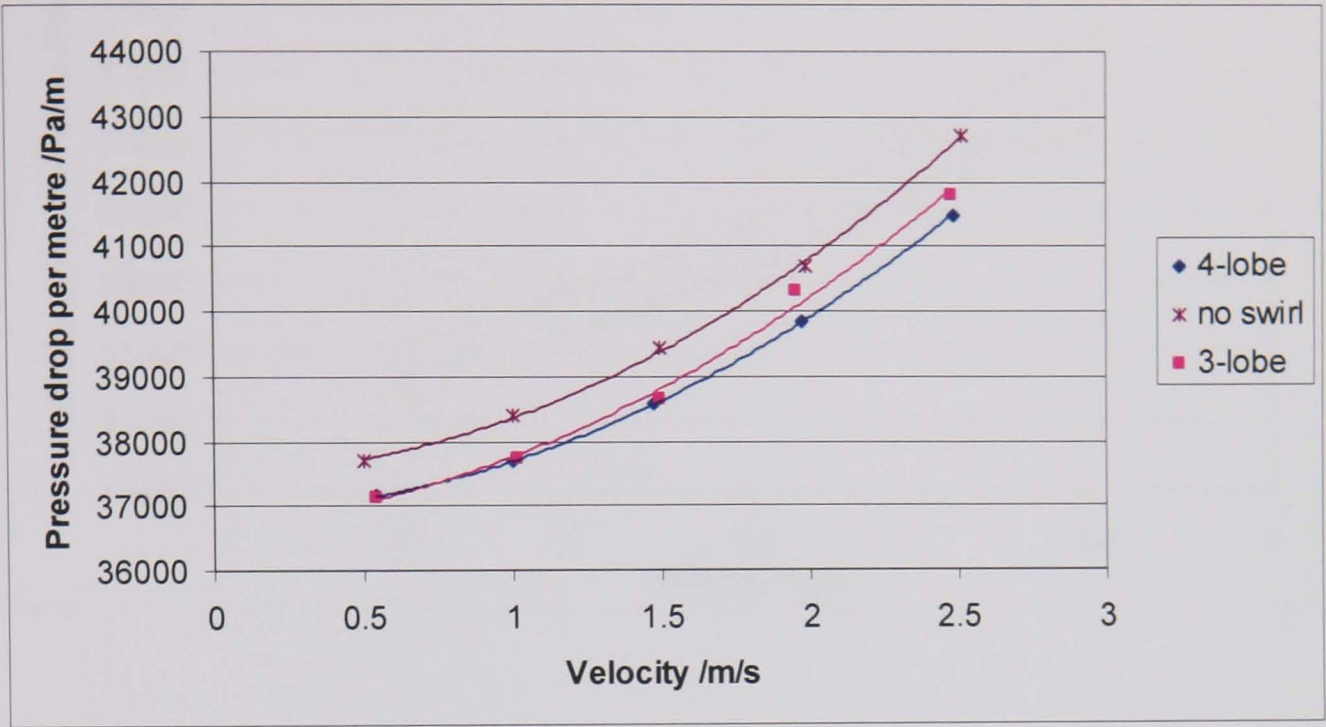


B.15 Pressure drop characteristic over 4-lobe swirl pipe

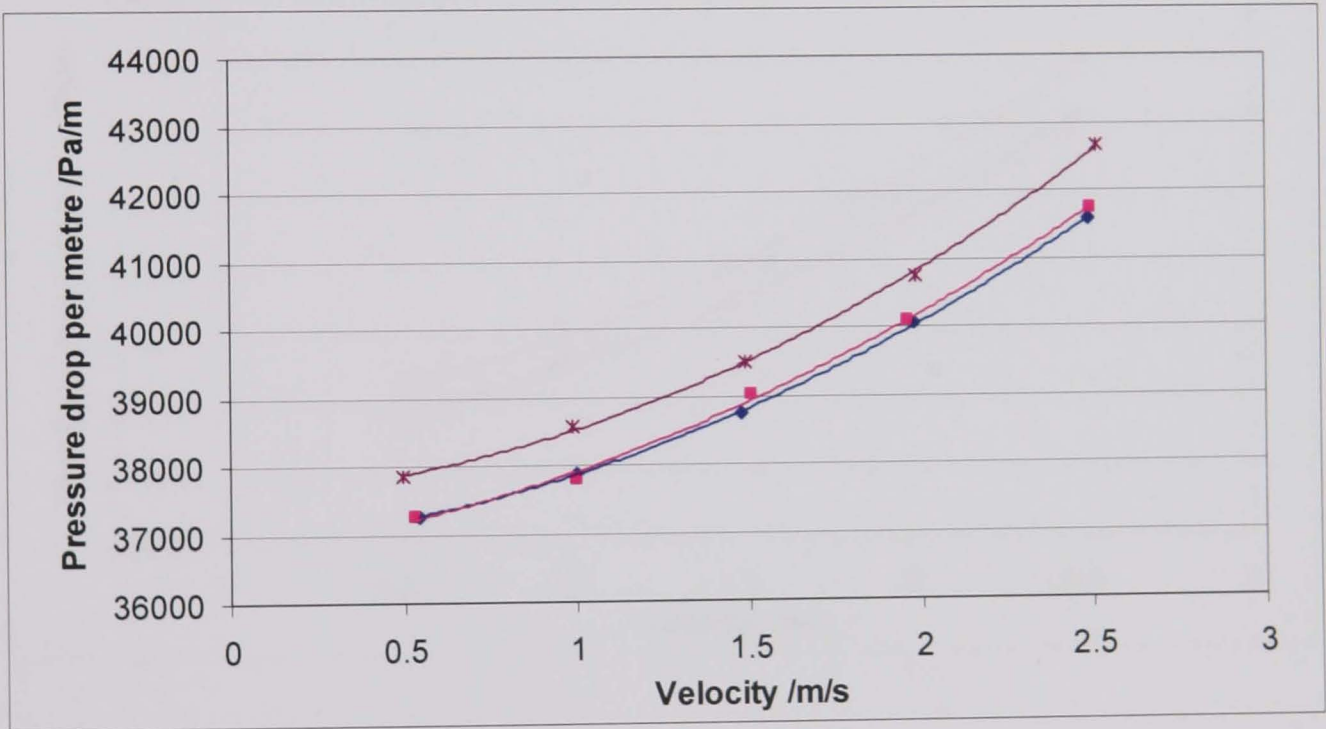


B.16 Pressure drop characteristics over bend for various concentrations

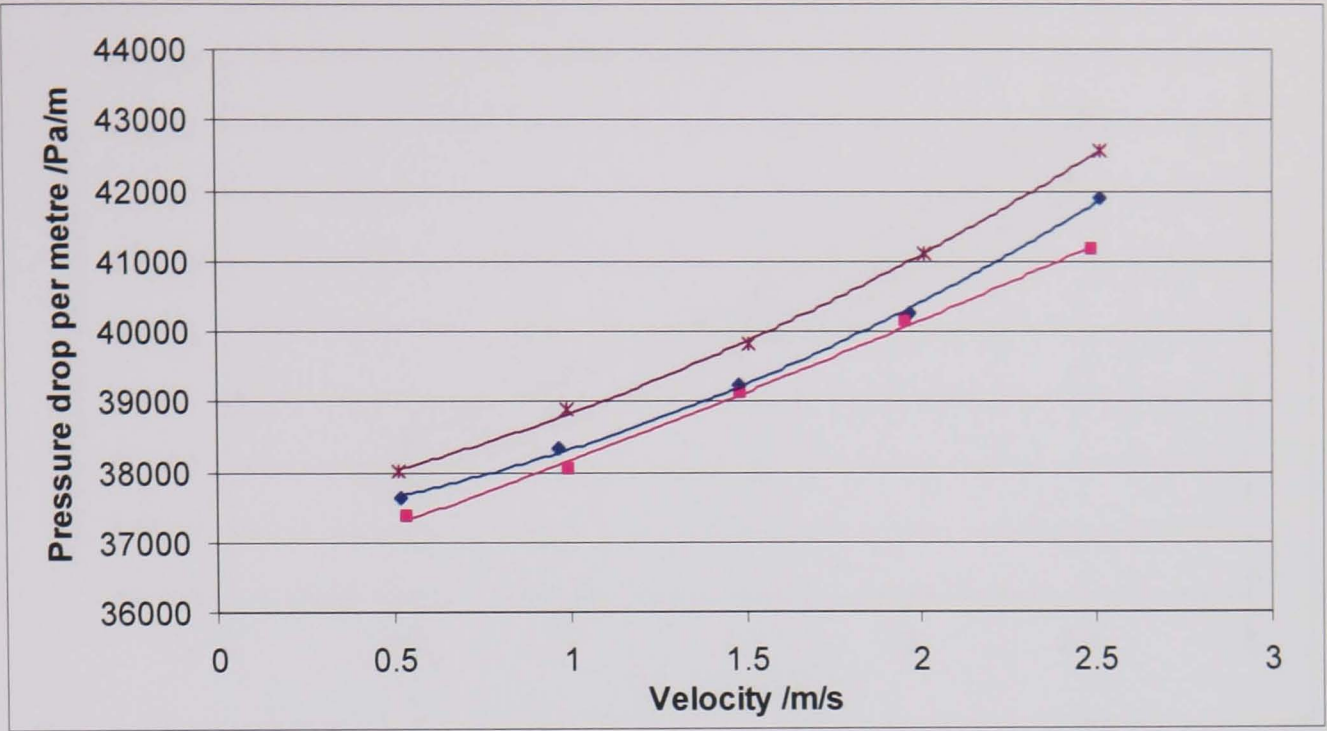
a) Water only



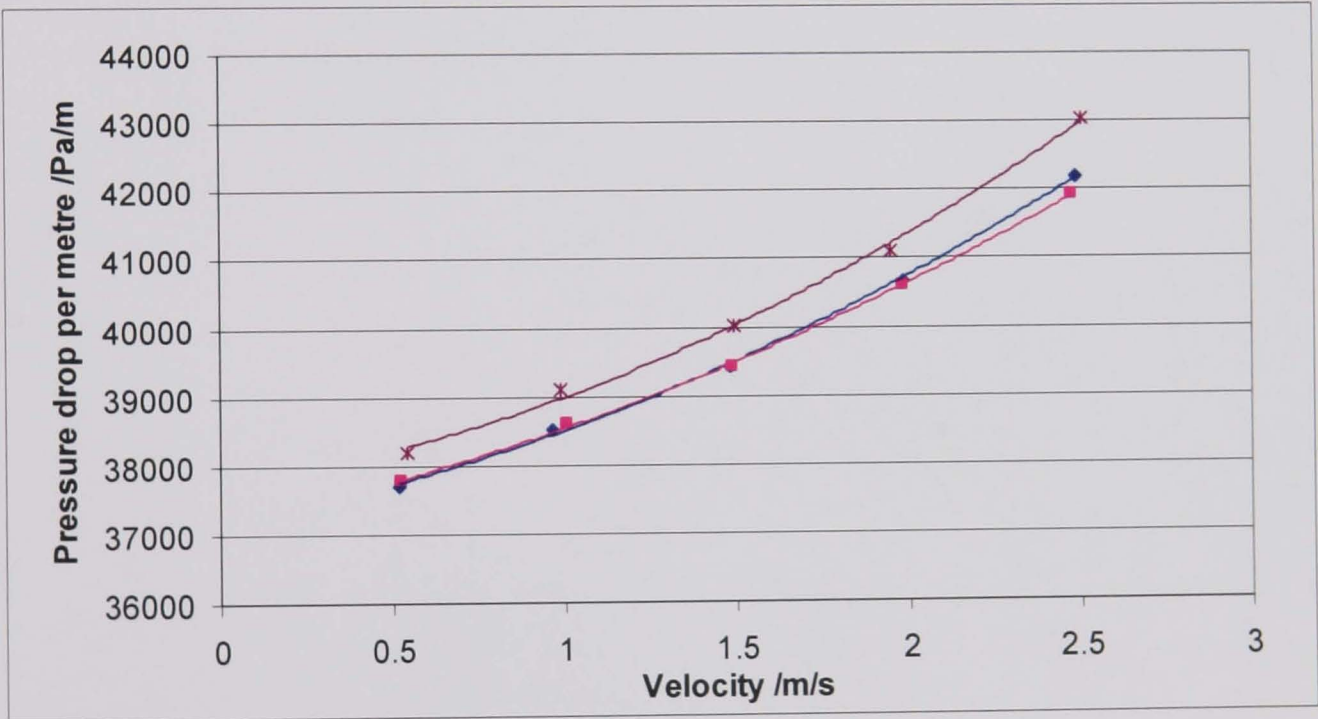
b) 0.7% v/v beads (key as above)



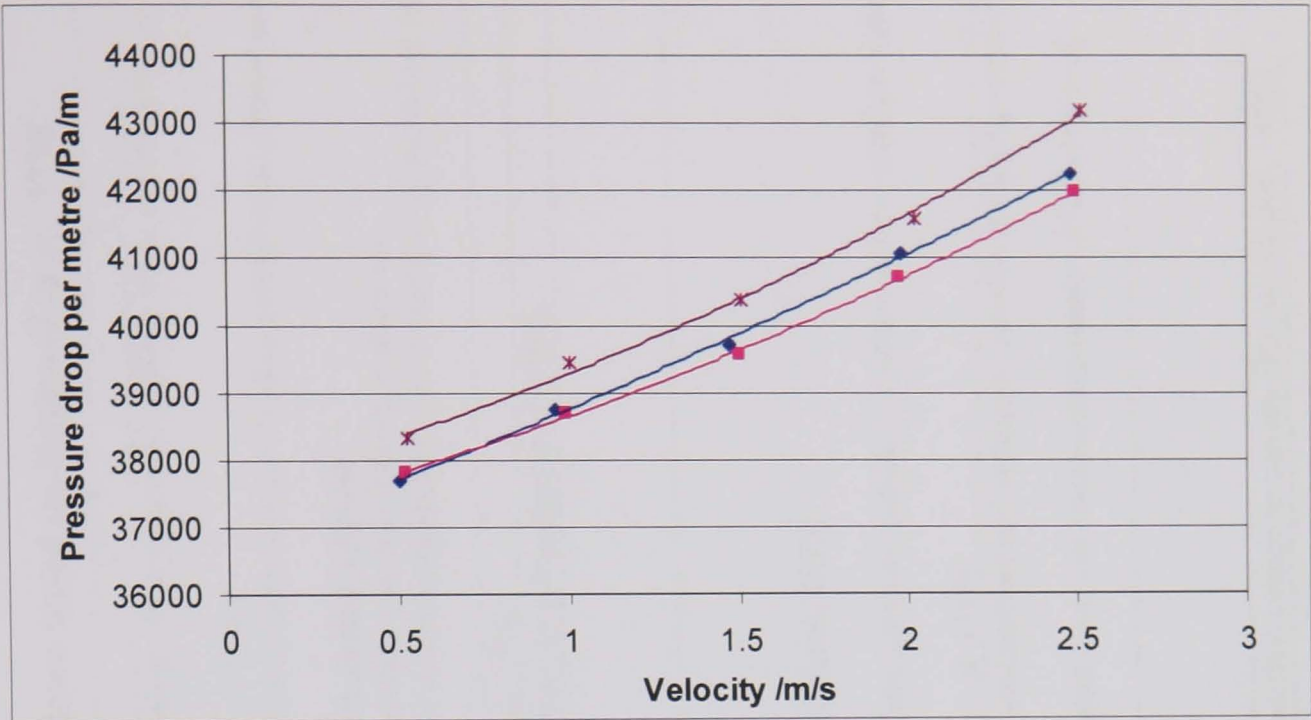
c) 1.4% v/v beads (key as above)



d) 2.0% v/v beads (key as above)



e) 2.7% v/v beads (key as above)



B.17 Characteristics of various pump types. Types and sub type breakdown based on Heywood *et al.* 1998

Type and sub types		Characteristics
Direct displacement	Roto-dynamic	Centrifugal
		Low capital, low head, low efficiency, high capacity, mechanically simple. Problems: shaft sealing, wear, can be prone to blockage. Can be very large, often lined. Flow up to 17000m ³ /hr (Heywood <i>et al.</i> 1998) Better for large particles over short distances, to get large pressure requires large diameter leading to high wear. (Baker <i>et al.</i> 1979) Usually cheapest and lowest maintenance cost, continuous flow but moderately efficient. Large capacity pumps have an average efficiency of 65% and handle solids less than 200mm in diameter. Impeller and liner wear can be server. Difficult to keep pump volume constant, flexibility must be built in by providing tall sumps or speed alteration. (Odrowaz-Pieniazek, 1979)
		Axial flow
		Not suitable for high concentrations or abrasive fluids (Heywood <i>et al.</i> 1998)
	Positive displacement	Co-rotating disc
		Good for high viscosities. Max particle size 400µm. Flow up to 6800 m ³ /hr (Heywood <i>et al.</i> 1998).
		Archimedean screw
		<ul style="list-style-type: none"> - Very high flow rate, up to 22000m³/hr - Can pump large (>100mm) and abrasive solids - Simple, low maintenance (Heywood <i>et al.</i> 1998)
	Rotary	Progressive cavity / Mono
		<ul style="list-style-type: none"> - Speed governed by abraisvity - Efficiency ~60%. - Solids up to 10mm diameter - Manufacturers claim no degradation. (Odrowaz-Pieniazek, 1979) - Largest up to 1200m³/hr, <p>Adv. Self-priming; uniform discharge; reversible; little damage to shear sensitive material. Continuous flow constant value and speed characteristics Dis. Damaged if run dry, requires pressure relief valve. (Heywood <i>et al.</i> 1998)</p>
		Peristaltic
		Advantages: self-priming; can be ran dry; reversible; copes with air entrainment and abrasives; suitable for highly corrosive materials. Disadvantages: hose life is variable and can fail unexpectedly; Pulsatile flow; can cause contamination (Heywood <i>et al.</i> 1998).
		Lobe
		Can pump viscous flows but only fine particles. Flow rate up to 680m ³ /hr (Heywood <i>et al.</i> 1998). Little degradation (Odrowaz-Pieniazek, 1979).
		Flexible impeller
		Can cope with very low viscosity and low concentrations of fine particles; cannot be run dry (Heywood <i>et al.</i> 1998).

Fluid displacement		Reciprocating	Piston	<ul style="list-style-type: none"> - Usually confined to slurries with low abrasivity - High efficiency ~95% - Life of parts relatively short depending upon application - Pulsatile (Odrowaz-Pieniazek, 1979). - Generally relatively high flow but pressure limited (Baker <i>et al.</i> 1979)
			Plunger	<ul style="list-style-type: none"> - Can handle very abrasive slurries - Viscosity ~20Pas, solids normally <25mm - Up to 1140m³/hr (Heywood <i>et al.</i> 1998) - Self priming, may pump high solids concentrations (Tchobanglous and Burton, 1991), - Efficiency > 90 % (Odrowaz-Pieniazek, 1979). - Generally capable of high pressure but flow restricted (Baker <i>et al.</i> 1979).
			Diaphragm	<ul style="list-style-type: none"> - Limited to low discharge pressure - Solids handled limited to ~6mm diameter - Life ~1000 hrs or less on arduous duties - Less prone to wear than other reciprocating. (Odrowaz-Pieniazek, 1979) - Max discharge ~40m³/hr unless hydraulically coupled - Mechanically simple - Good for abrasive slurries - Low shear - Pulsatile (Heywood <i>et al.</i> 1998).
	Water		Lock hopper	<p>Advantages: virtually no wearing parts; can pass large solids at high pressures; reduced solids attrition; high efficiency; range of capacities.</p> <p>Disadvantages: needs sophisticated control system and skilled labour (Heywood <i>et al.</i> 1998).</p>
			Jet pumps/ eductor	<p>No moving parts. Slurry diluted (typically 1:5), flow rate up to 6000m³/hr, can pass stringy material 500mm long, reasonable for high viscosities (Heywood <i>et al.</i> 1998).</p> <p>Typical efficiency ~20% (Odrowaz-Pieniazek, 1979).</p> <p>Driving fluid injected at right angles to the slurry, dilution of slurry, jet pump feeding suction of centrifugal has many attractions (Baker <i>et al.</i> 1979).</p>
	Oil		Mars oil Barrier piston	<p>Suited to very abrasive slurries. (Odrowaz-Pieniazek, 1979).</p> <p>Pump is limited to slow speed (Baker <i>et al.</i> 1979)</p> <p>Advantages: no moving parts in contact with slurry; efficiency relatively unaffected by concentration (Heywood <i>et al.</i> 1998); long parts life (Odrowaz-Pieniazek, 1979).</p> <p>Disadvantages: high cost (Heywood <i>et al.</i> 1998); problems with settling of slurry in low points; requires a full time operator (Odrowaz-Pieniazek, 1979).</p>

		Hydraulic exchange	Advantages: slurry contacts no moving parts; low capital and spares cost; efficiency unaffected by solids concentration; Disadvantages: very expensive (Heywood <i>et al.</i> 1998).
	Air	Air operated diaphragm	<ul style="list-style-type: none">- Simple operation and maintenance- Solids 5mm to 10mm- Concentrations up to 90% solids by weight- Discharge 55 m³/hr- Head up to 75m- Relatively low efficiency- Self-priming (Odrowaz-Pieniazek, 1979).
		Peuma pump	<ul style="list-style-type: none">- No rotating/ moving parts in contact with slurry- Relatively inefficient- Up to 80% solids by weight- Discharge ~ 3000m³/hr (Odrowaz-Pieniazek, 1979).

NB: When duplicate information was found in the sources it was referenced to one author only. Values for the capacity of the pumps quoted by Heywood *et al.* (1998) were consistently higher than the other authors. When different capacities are given in different sources Heywood *et al.* (1998) values are reproduced here since this was the most recent work consulted.

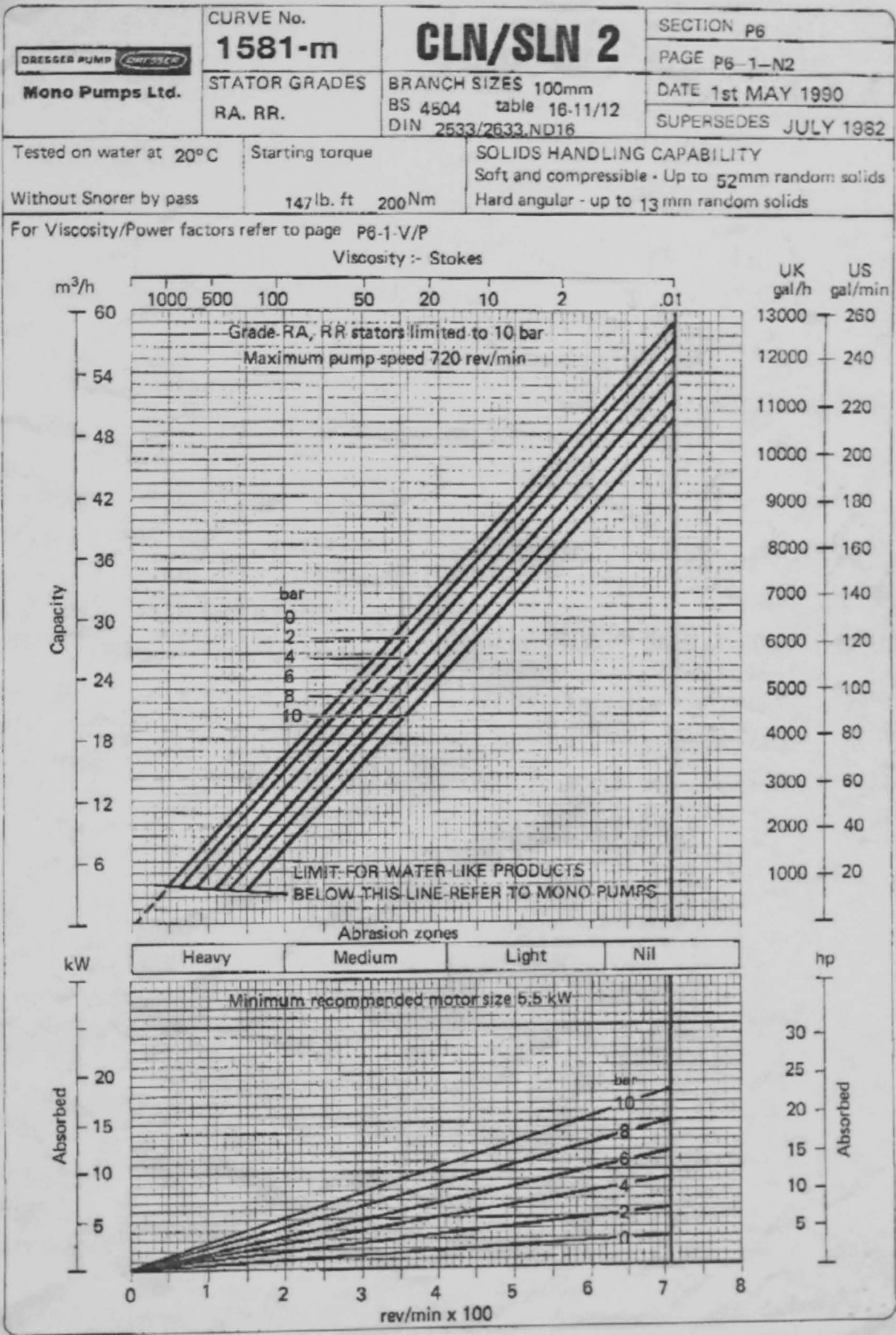
B.18

B.18 Advantages and Disadvantages of various valve types.

Type and sub types		Operation	Advantages	Disadvantages
Gate	Knife	Knife edge passing through a packing box.	Simple, cheap, avoids dead space, thus avoids solids accumulation, slim.	Box prone to leak, easy to damage by applying pressure in wrong direction.
	Parallel / Conduit	Cuts through slurry	High capacity, fast actuation	May leak for fine narrow size particles.
	Penstock		Can cope with large volumes	Manual operation
Globe	Straight, angle, oblique, needle.	High temperature and pressure fine slurry applications	Durable, wear-resistant	Very expensive

Diaphragm	General points	-	Operating mechanism out of contact with slurry, less expensive, easily cleaned.	Larger sizes more difficult/ expensive, leaks upon diaphragm failure.
	Weir	Screw contacts diaphragm to weir.	Tight shutoff, long life, low maintenance, suitable for throttling.	Passage constriction may be undesirable, subject to erosive wear.
	Straight-through	Closure by wedge-shaped diaphragm	Parallel or tapered bore, minimum resistance in open position.	Shorter life, limited material choice.
Pinch	E.g. Iris	Elastomer tube that clamp pinches.	Tube replacement straightforward, mechanism isolated from flow, tight closure when entrained solids present, minimal risk of clogging.	Size, pressure, temperature, life limited by elastomer, elastomer must be compatible with process material, not drainable, expensive.
Plug	E.g. Lifting tapered plug, Eccentric plug	Standard plug, rotate 90°, one way allows passage	Operation simple, fast response, little flow disruption, pressure drop low	Need to lubricate every operation.
Ball	Floating / trunnion	Central ball with circular hole is rotated.	Smooth flow passage, pressure drop low.	Leakage may occur, fine particles may come between ball and seat leading to wear.
Butterfly		Circular disc rotated 90°.	Economical, high flow capacity, minimum space for installation, pressure drop low.	Not piggable, disc always in contact with slurry, sensitive to sludge/ sticky solids. Solids lodge between sealing ring and disc.
Swinging transfer tube		Short tube swung between adjacent pipes	No dead legs to block or harden. Rugged construction, fast-acting	Relatively high cost
Rotating disc		Disc slides across aperture	Low leakage, suitable for abrasive high temperature and pressure.	
Segmented ball		Rotate hollowed out spherical segment (partial ball)	Compact, good control, high range.	Lower capacity than full bore valve, seats wear quicker than butterfly.

B.19 Pump characteristic



B.20 Calculations to size conical tank

The tank must be large enough to hold a volume enough to fill the entire flow loop and maintain a suitable head above the pump. Therefore, the tank volume required was the sum of pipe volume, the weigh tank volume, the de-aerator volume and the volume remaining in the tank.

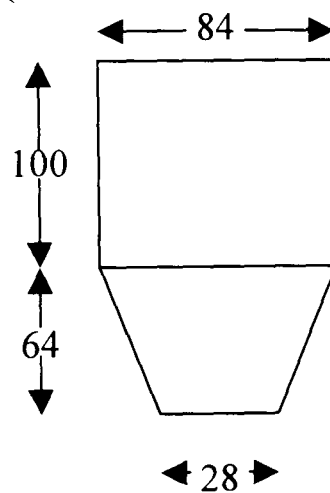
- Flow loop volume

- Pipe volume

Pipe length approximately 40m, pipe radius = 0.0275

$$\text{Pipe volume} = \pi \times 0.0275^2 \times 40 = \mathbf{0.095\text{m}^3}$$

- Weigh tank volume (all dimensions in cm)



$$\text{Volume of a cone} = \pi/3 \times r^2 \times h$$

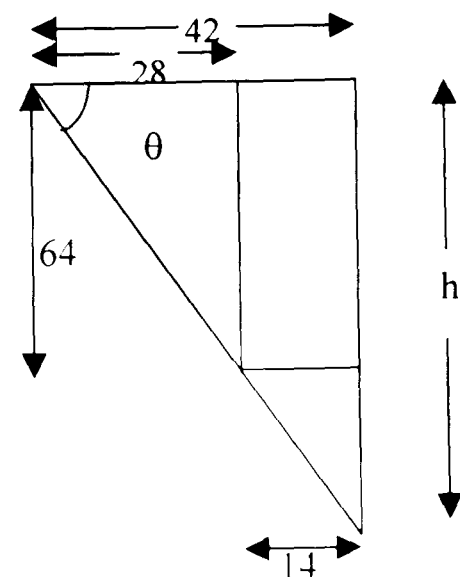
$$\theta = \tan^{-1}(64/28) = 66^\circ$$

$$h = 42 \tan 66 = 96\text{cm}$$

$$\therefore V = \pi/3 \times 0.42^2 \times 0.96 -$$

$$\pi/3 \times 0.14^2 \times 0.32 + \pi \times 0.42^2 \times 1$$

$$= \mathbf{0.725\text{m}^3}$$

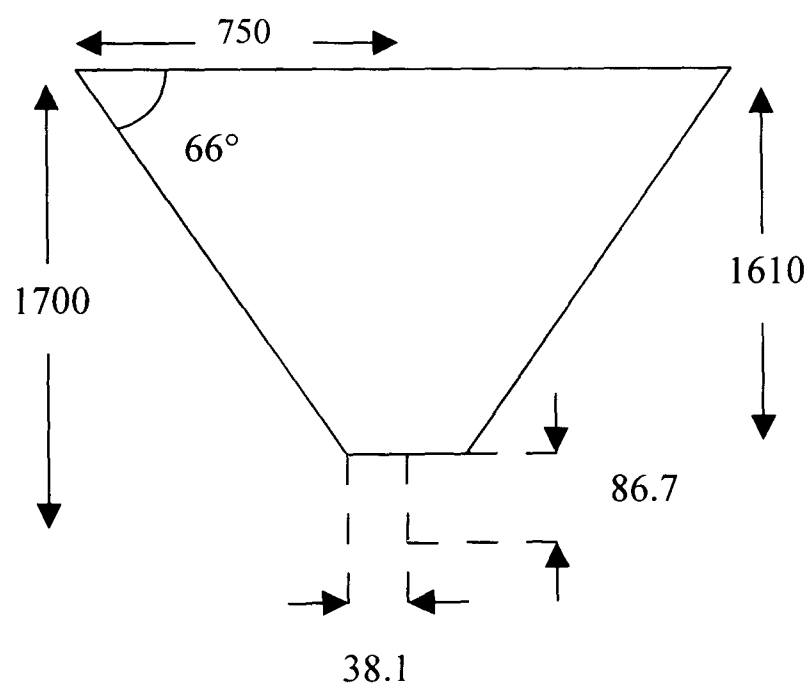


iii. De-aerator volume
 $\pi \times 0.312^2 / 4 \times 0.915 = \mathbf{0.070\text{m}^3}$

Volume of entire flow loop = $0.095 + 0.725 + 0.070 = \mathbf{0.89\text{m}^3}$

- Tank dimensions

An operational volume of 1m^3 was set to allow 0.11m^3 of water to remain in the tank when the flow loop was full. An iterative procedure was used to calculate a range of possible dimensions, using trigonometry and the equation for the volume of a cone above. From these possibilities, the following dimensions were chosen for the tank.



Volume of tank = 1.0 m^3

A cylinder 0.25m high was added to the top of the tank to prevent overflow.

- Net positive suction head (NPSH) calculation

The following calculations were performed to check that the minimum head was sufficient to avoid cavitation in the pump. To avoid cavitation: NPSH available < NPSH required.

- Liquid height at minimum volume

Using the previous results and diagrams:

Volume of liquid in tank + volume of cone point = total volume of cone

$$0.11 + (1/3\pi 0.0381^2 \times 0.0867) = \pi r^2 h / 3$$

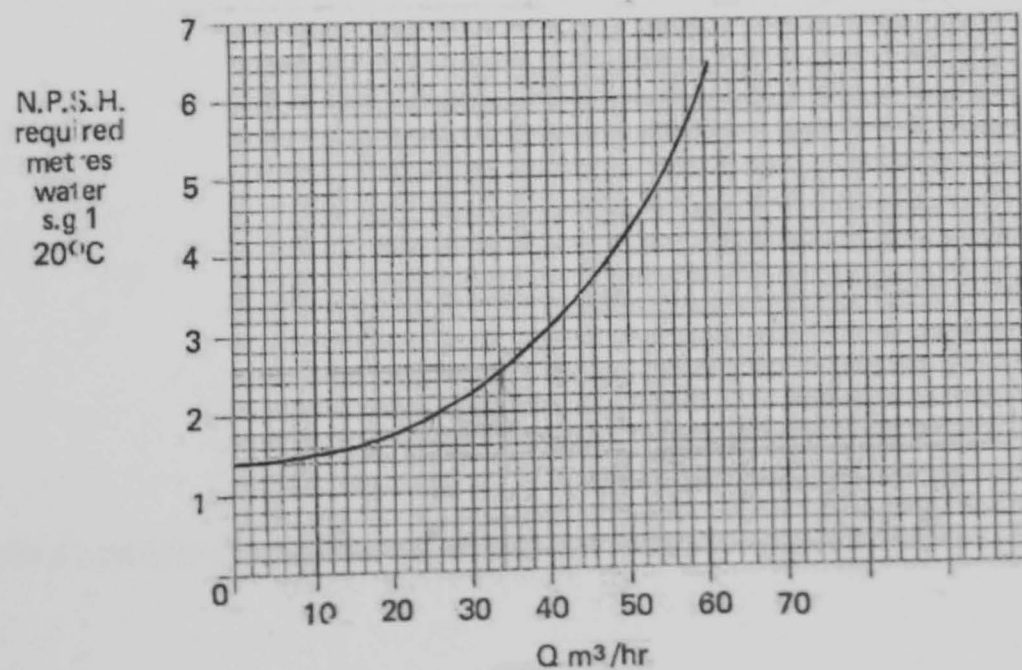
Substitute in $h = r \tan 66$ gives

$$r = \sqrt[3]{\frac{3(0.11 + 1.3 \times 10^{-4})}{\pi \tan 66}} = 0.36\text{m}$$

$$\therefore h = 0.36 \tan 66 = \mathbf{0.81\text{m}}$$

- NPSH required

The NPSH required can be obtained from the manufacturers curve:



The curve shows that for the maximum flow rate of 4m/s (34.2m³/hr) the **NPSH required** is approximately **2.5m**.

iii. NPSH available – water

The NPSH available can be calculated from the following equation (Coulson *et al.*, 1990):

$$NPSH_{available} = \frac{P_0}{\rho g} + H - h_f - \frac{P_v}{\rho g}$$

Where:

P_v = vapour pressure of liquid

P_0 = pressure in tank

In this case:

At 18°, $P_v = 2059\text{Pa}$; P_0 = atmospheric pressure = 101,325Pa; $H = 0.81\text{m}$

Frictional head losses through the t-piece and gate valve that will connect the tank and pump were estimated using the formula and k values below taken from Nesbitt (2000).

$k = 0.1$ for the t-piece (straight – through)

$$h_f = \frac{kv^2}{2g}$$

$k = 0.2$ for the gate valve (fully open)

$v = 4\text{m/s}$

This gave a combined frictional head loss of **0.24m**

Substituting these values into the formula above gives:

$$\begin{aligned} NPSH_{available} &= \frac{101325}{9810} + 0.81 - 0.24 - \frac{2059}{9810} \\ &= \mathbf{10.7m} \end{aligned}$$

Therefore NPSH available is greater than the NPSH required and thus the size of the tank ensures sufficient head is maintained above the pump when the pipe-loop is full.

iv. NPSH available – CMC

The liquid height at minimum volume and NPSH required that were calculated for water also apply to the case of CMC.

The NPSH available can be calculated from the following equation (Condron, 2002)

$$NPSH_{available} = H + \frac{10.2}{(\rho[P_0 - P_v])} - h_f$$

Where:

P_v = vapour pressure of liquid

P_0 = pressure in tank

In this case:

At 18°, $P = 0.02059$ bar (Joergens, 2002); P_0 = atmospheric pressure = 1.01325 bar; $H = 0.81$ m; $\rho = 1.0028$ gcm⁻³

Frictional head losses can be estimated using the same formula as for water. The k values were estimated from the correlations of Kittredge and Rowley (1957) by calculating the generalised Reynolds number for the process conditions ($v = 4\text{m/s}$, $K = 2.96$, $n = 0.46$, $\rho = 1002.8\text{kgm}^{-3}$).

$k = 0.6$ for the t-piece (straight – through)

$$h_f = \frac{kv^2}{2g}$$

$k = 2.0$ for the gate valve (fully open)

$v = 4\text{m/s}$

This gave a combined frictional head loss of **2.12m**

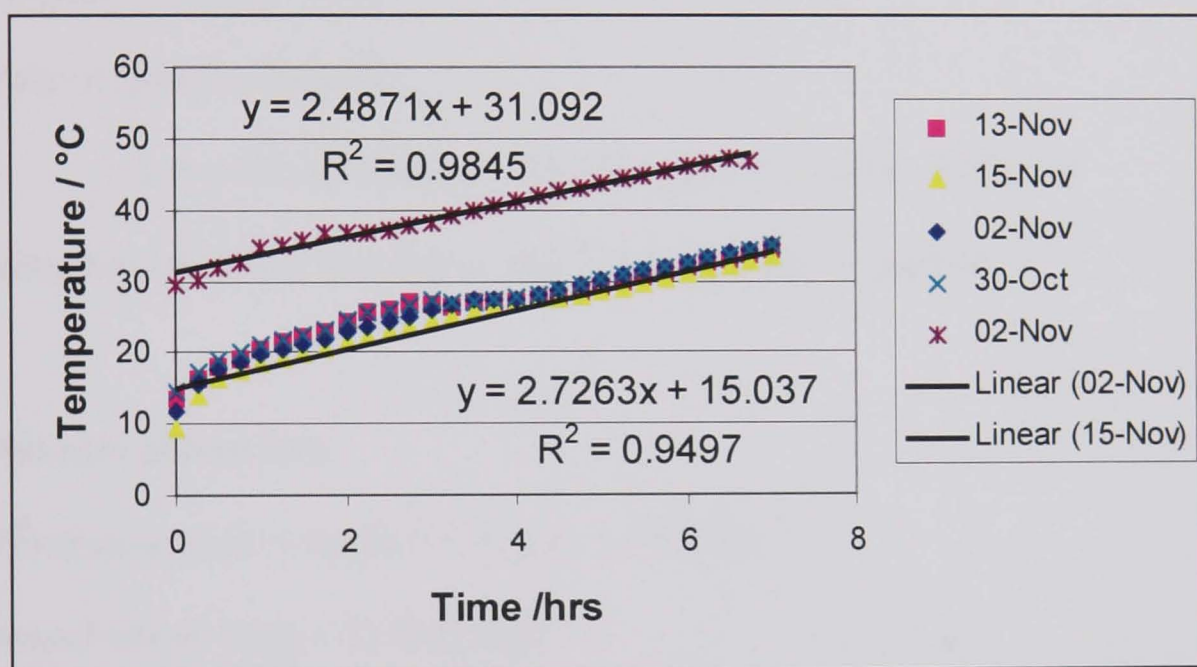
Substituting these values into the formula above gives:

$$\begin{aligned} NPSH_{available} &= 0.81 + \frac{10.2}{(1.0028[1.01325 - 0.02059])} - 2.12 \\ &= \mathbf{8.9m} \end{aligned}$$

Again the NPSH available is greater than the NPSH required, which implies that the size of the tank is sufficient.

B.21 Calculations to determine the heat removal requirement of the cooler.

The calculations presented below were based on data obtained from another flow loop within the School. The loop had a lagged tank, an effective pipe length of 6m and was used to pump a sand water mixture. These calculations were used to estimate the heat input expected when pumping in the new steel flow loop. As can be seen from the graph below, with an initial water temperature of 13.6°C the temperature rose to 34.6°C in 7 hours. This equates to a rate of temperature increase of 3°C per hour.



Natural cooling through the pipe wall

i. Conduction

At maximum temperature, heat lost through the pipe walls = $kA(34.6 - 13.6)/t$

Length of exposed pipe (80 mm N.B.) = 6m

Area of pipe wall, $A = \pi \times (0.08)^2 \times 6 = 1.51 \text{ m}^2$

Thermal conductivity (stainless), $k = 16$

Thickness, $t = 5\text{mm}$

$$\therefore \text{Heat lost by conduction in 7 hours} = 16 \times 1.51 \times 21 / 0.005 = 101472 \text{ J}$$

$$\text{i.e. Rate of loss by conduction} = 101472 / (7 \times 3600) = 4.03 \text{ W}$$

ii. Convection

$$1.65(34.6 - 13.6)^{0.25} = 3.532 \text{ W}$$

iii. Radiation

Assume emissivity = 0.9

Rate of radiation heat loss

$$= 0.9 \times 5.67 \times 10^{-8} (307.6^4 - 286.6^4) \times 1.51 / (7 \times 3600) = 0.0067 \text{ W}$$

$$\text{Total rate of natural heat loss} = 4.03 + 3.53 + 0.007 = \mathbf{7.567 \text{ W}}$$

Net rate of heat loss

$$\text{Flowrate at } 7\text{m/s} = \pi(0.04)^2 \times 7 \times 3600 = 127 \text{ m}^3\text{hr}^{-1}$$

$$\text{Mass Flow at } 7 \text{ m/s} = 127000 \text{ kg hr}^{-1}$$

$$\text{Total heat gained in one hour} = 127000 \times \text{sp.ht} \times \text{temp rise}$$

$$= 127000 \times 4.18 \times 3 = 1.59\text{MJ}$$

$$\therefore \text{Net rate of heat loss} = 1592580 / 3600 = 442 \text{ W}$$

Estimated heat input from pumping

$$= 442 - 7.6 \text{ W} = \mathbf{414.4 \text{ W}}$$
 (pipe heat losses $\approx 1.7\%$)

Based on the above case an estimation of the heat loss in the current flow loop design (approx. 40m of pipe, unlagged tank) can be made based on the following assumptions:

- loss by conduction, convection, radiation through pipes is minor
- pump heating is similar to the case described above

\therefore Need cooling coil to remove approx **500 W**.

B.22 Properties of the TJE pressure transducers (RDP Electronics Ltd)

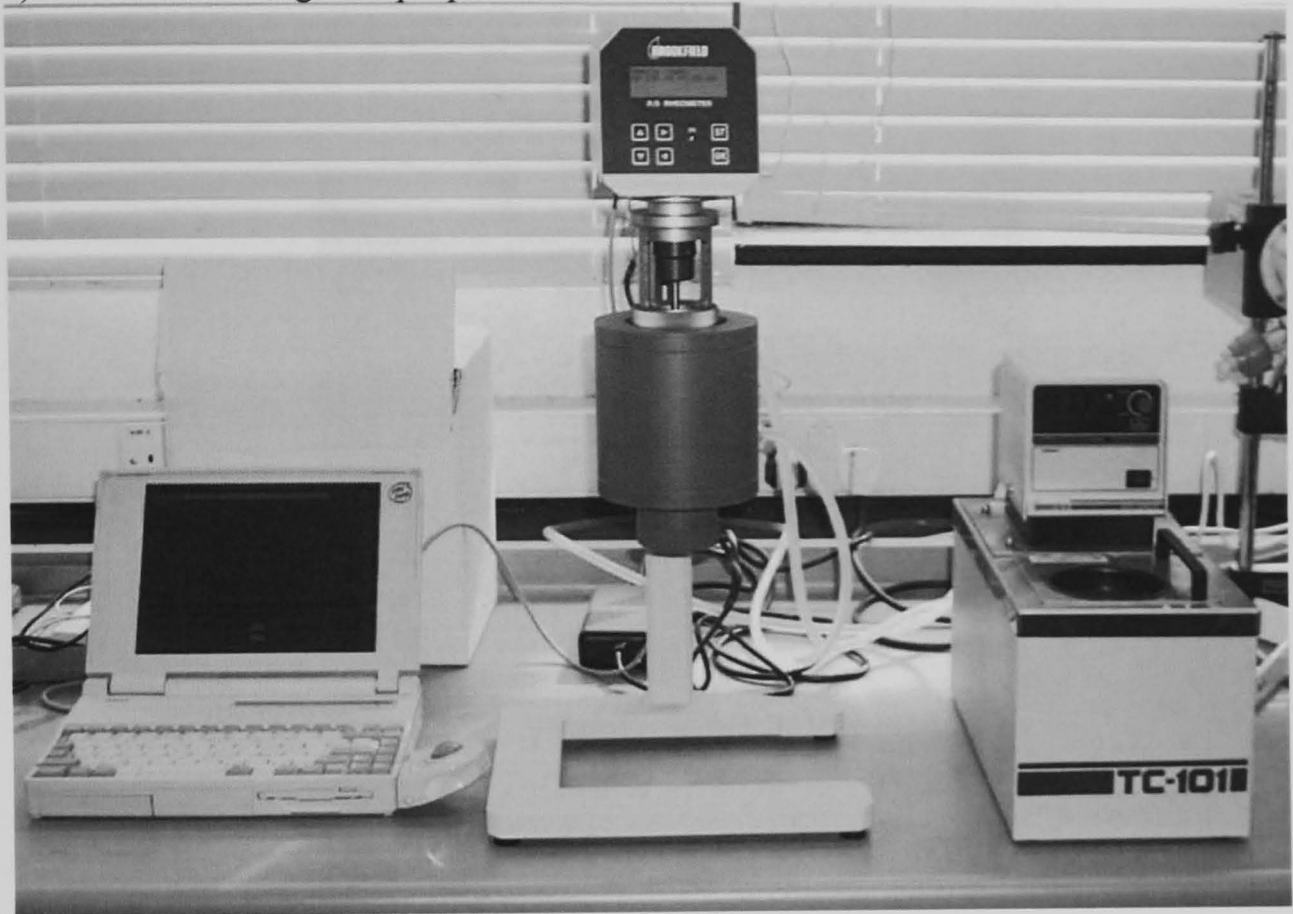
Property	Description
Pressure range	0-15psi gauge.
Length	60mm
Diameter	38mm
Supply voltage	9-32VDC
Port threads	¼” – 18NPT Male with ¾” HEX
Accuracy	±0.1% F.S
Amplification	Internal amplifier, 4-20mA, 2 wire.
Safe static overload pressure	22.5psi
Static burst pressure	45psi
Cable per transducer	PVC four-core screened cable, 7m Underwater cable, 3m, to reduce the possibility of damage during cleaning connected by DIN plugs
Case material	17-4 PH Stainless
Wetted parts material	17-4 PH and 15-5 PH stainless

Appendix C. OPERATIONAL PROCEDURE AND EVALUATION OF THE PIPE FLOW LOOP

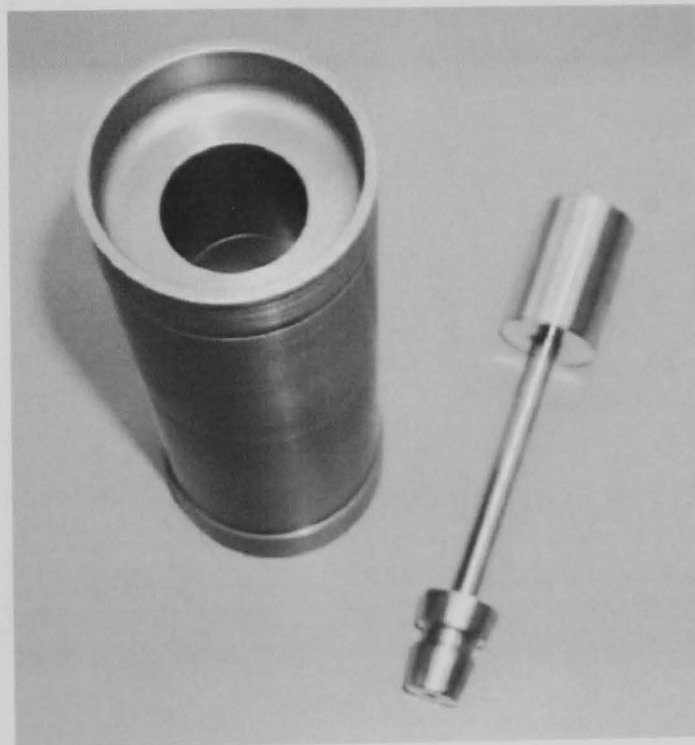
- C.1 Photographs of the Brookfield rheometer
- C.2 Photographs of the steel pipe loop
- C.3 Calibration of instrumentation
- C.4 A series of graphs to show the pressure recorded with the incremental increase and decrease of pumping frequency, under various test conditions.
- C.5 Calibration graphs for all four pressure transducers
- C.6 A second series of graphs to show the pressure recorded with the incremental increase and decrease of pumping frequency, under various test conditions
- C.7 Calculation of the Reynolds number for water pumped in the flow loop
- C.8 Series of graphs to show the pressure drop over the bottom leg, associated with the results displayed in C.4 and C.6

C.1 Photographs of the Brookfield rheometer

a) From left to right: laptop, rheometer and water bath



b) CC25 cup and bob

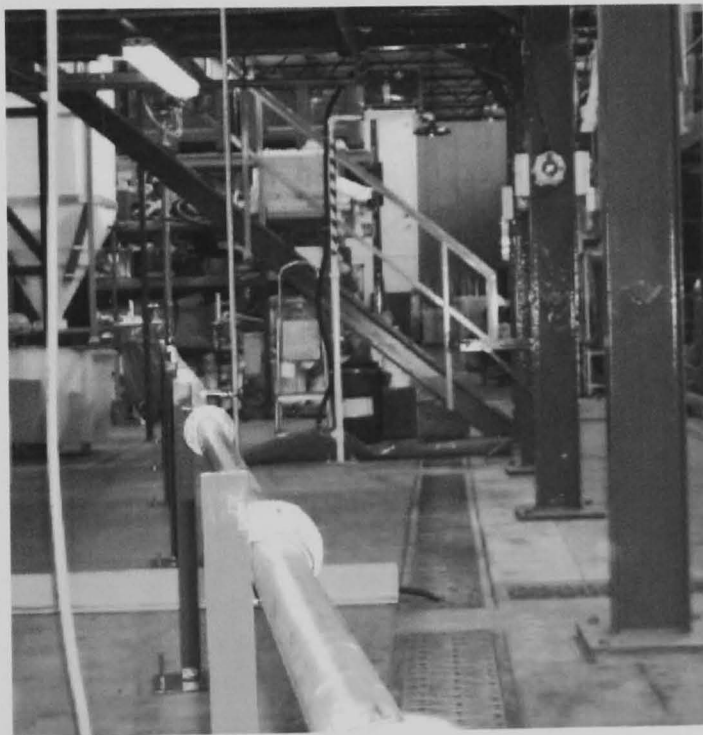


C.2 Photographs of the steel pipe loop

a) Upper leg

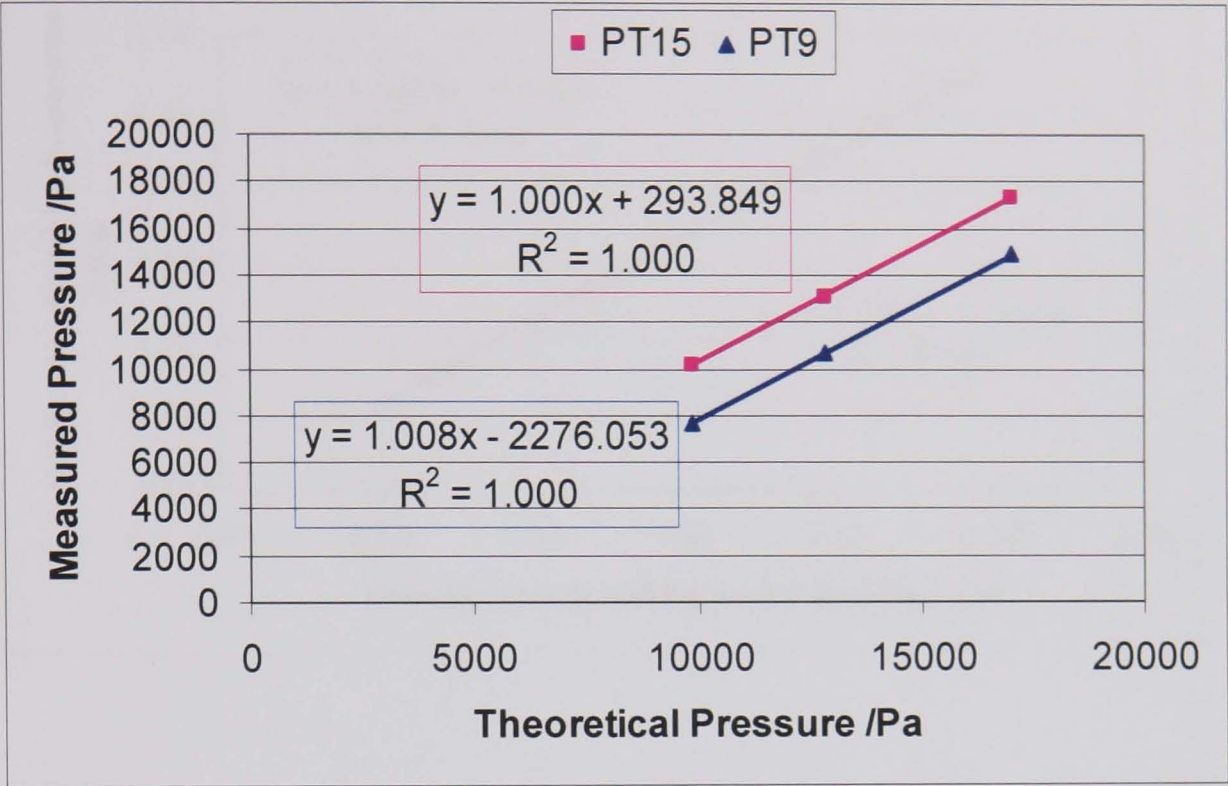


b) Lower leg

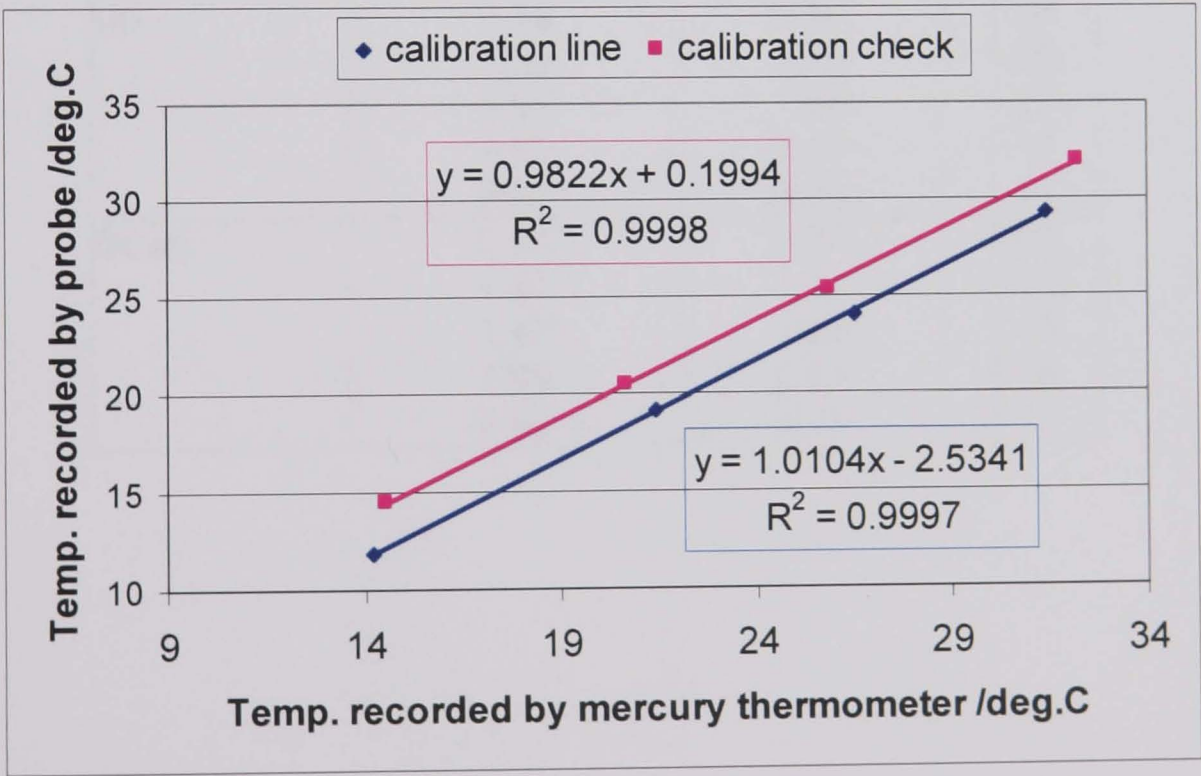


C.3 Calibration of instrumentation

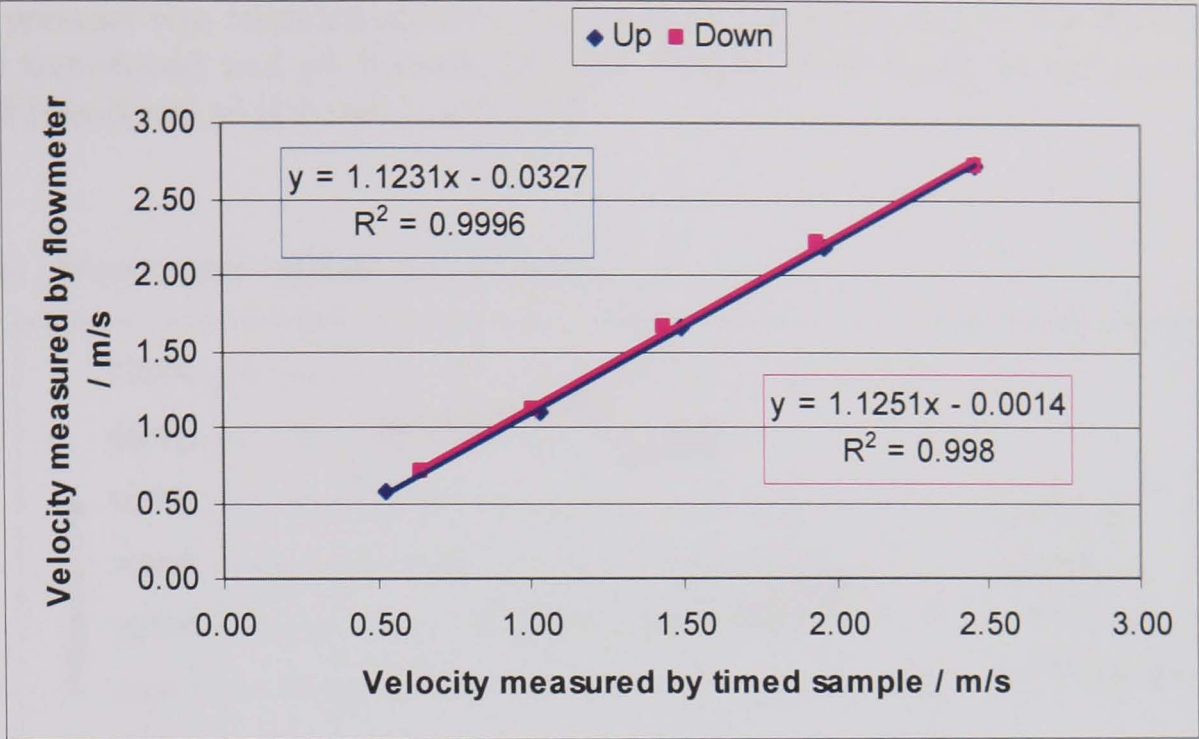
a) Pressure transducer calibration graph



b) Temperature probe calibration and check



c) Flowmeter calibration graph



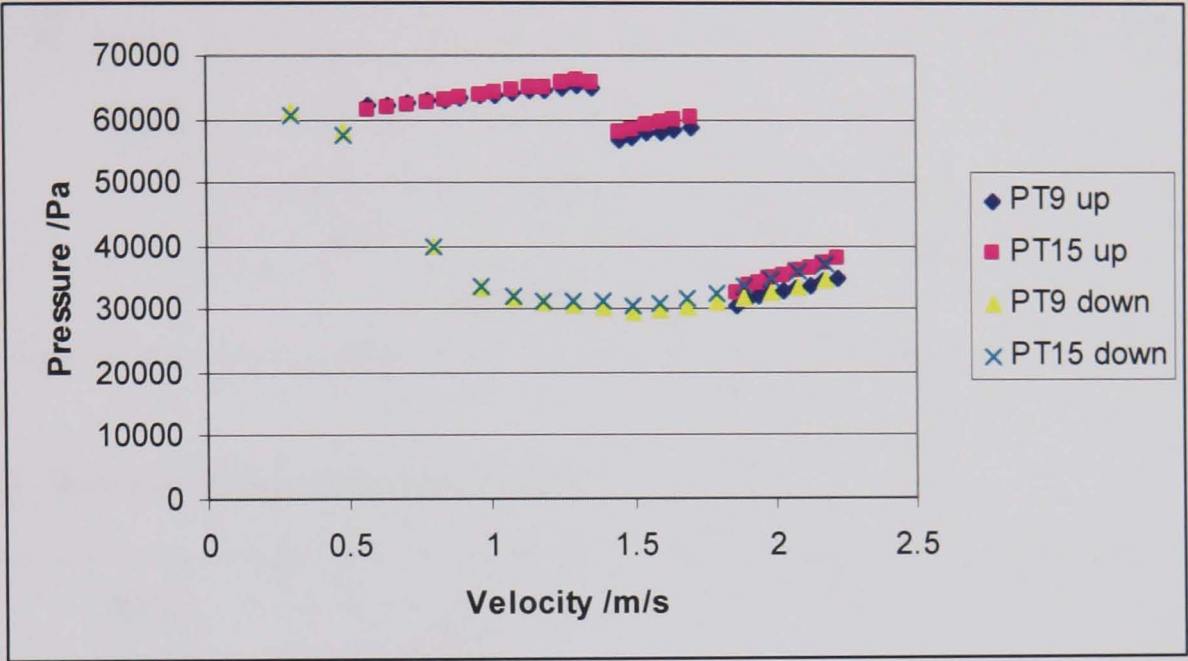
d) Flowmeter calibration data

Measurement Direction	Velocity measured by:		Ratio of S/F
	Timed sample (S)	Flowmeter (F)	
Up	0.53	0.58	1.09
	1.03	1.10	1.06
	1.49	1.65	1.10
	1.97	2.18	1.11
	2.46	2.73	1.11
Down	0.64	0.70	1.09
	1.01	1.11	1.11
	1.43	1.66	1.16
	1.94	2.21	1.14
	2.46	2.73	1.11

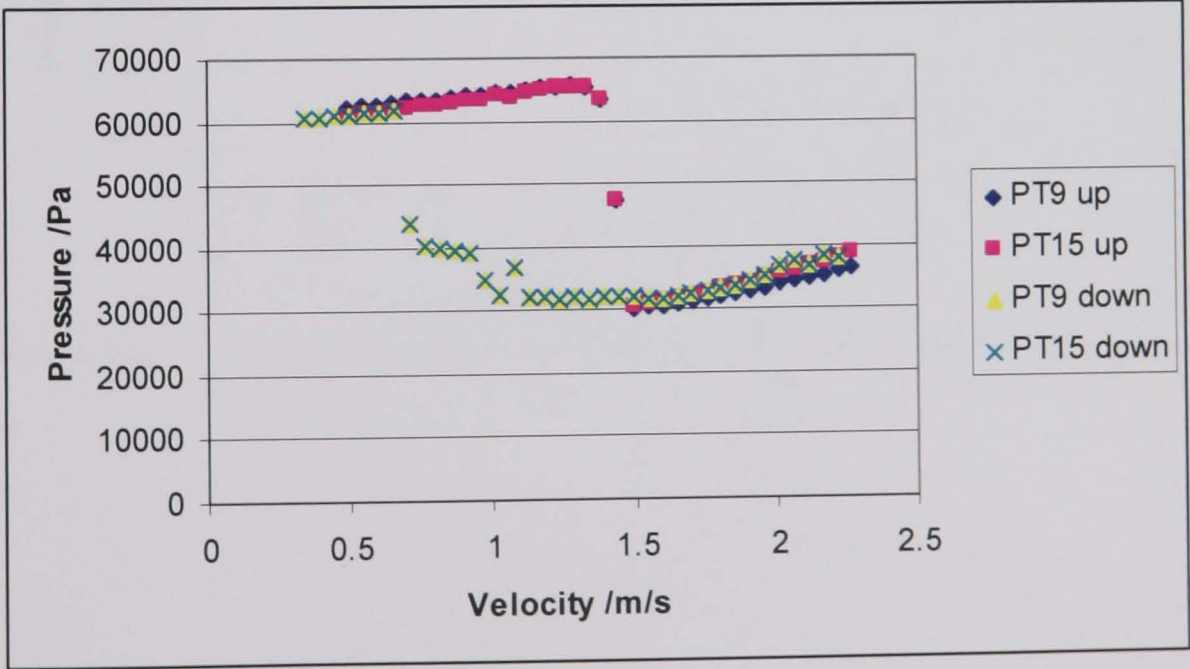
C.4 A series of graphs to show the pressure recorded with the incremental increase and decrease of pumping frequency, under various test conditions.

The pressure was recorded on two / four transducers on the bottom leg (PT9 [new steel transducer] and p4 [transducer from Perspex flow loop] downstream and PT15 [steel] and p3 [Perspex] upstream)

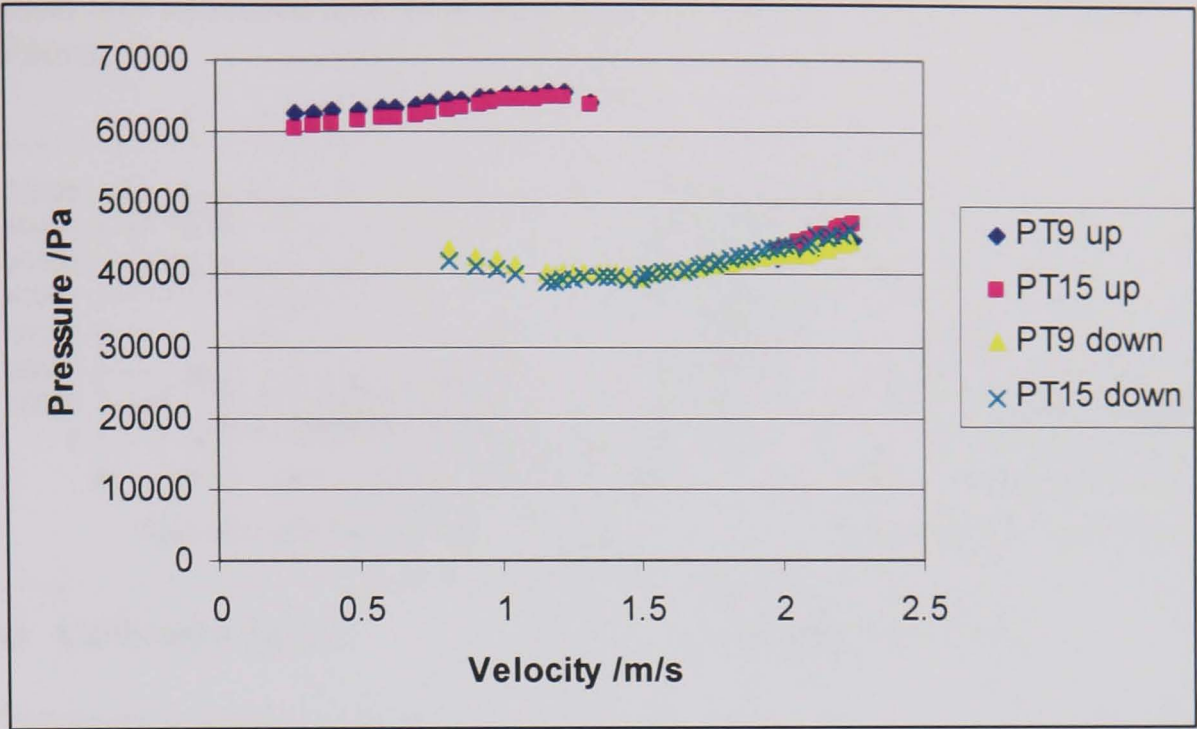
a) Mono pump with de-aerator online



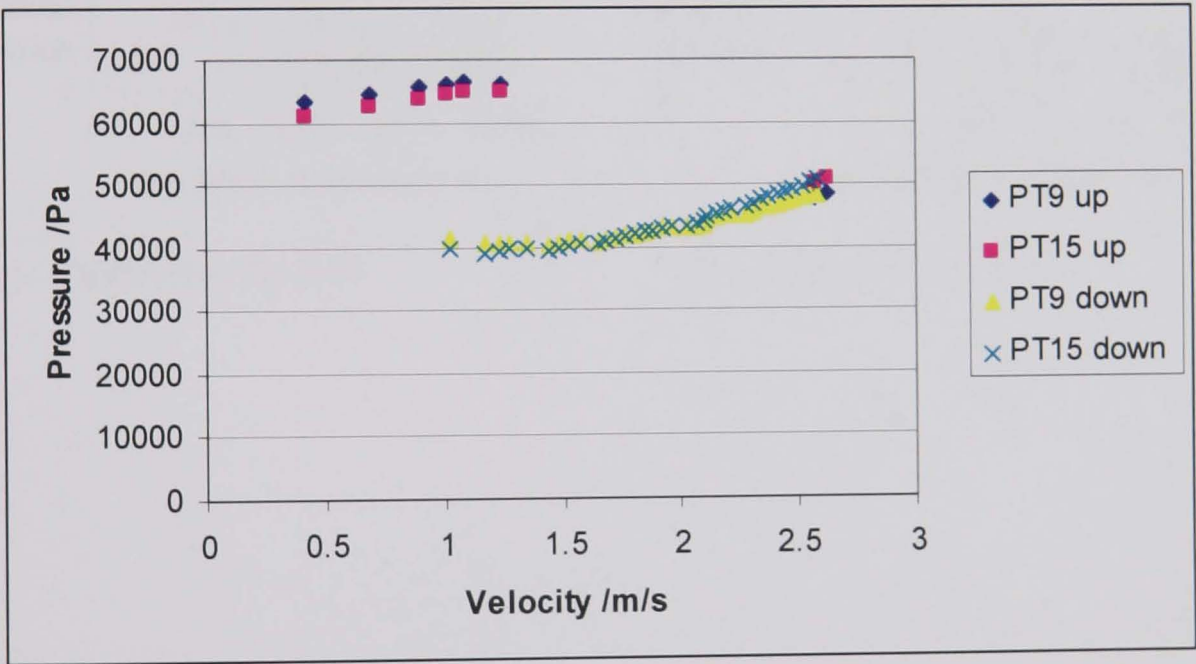
b) Mono pump without de-aerator



c) Warman pump with de-aerator online

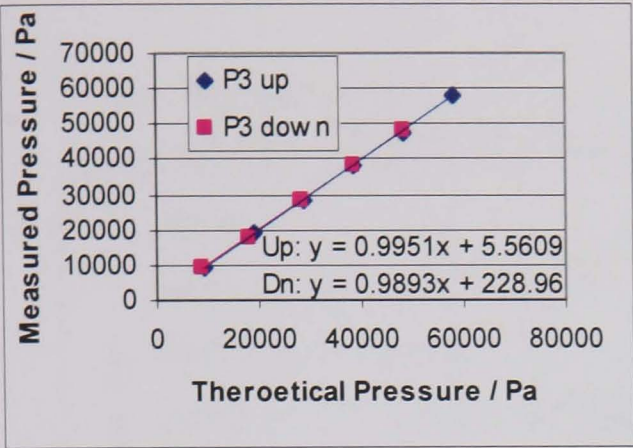


d) Warman pump without de-aerator

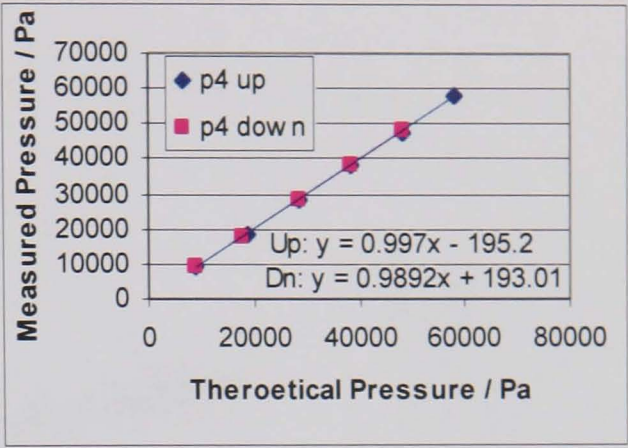


C.5 Calibration graphs for all four pressure transducers.

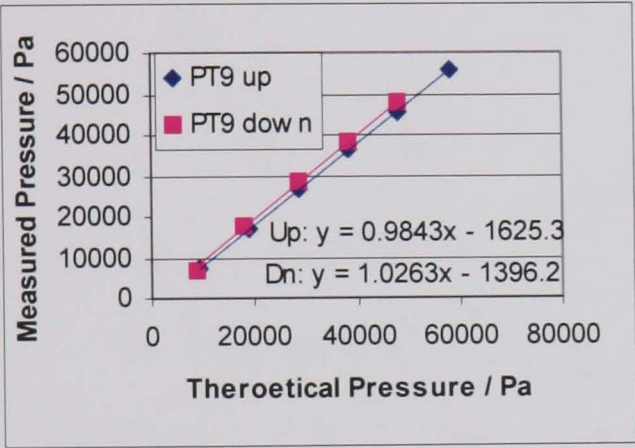
The head was increased and decreased; no hysteresis was found in these static conditions.



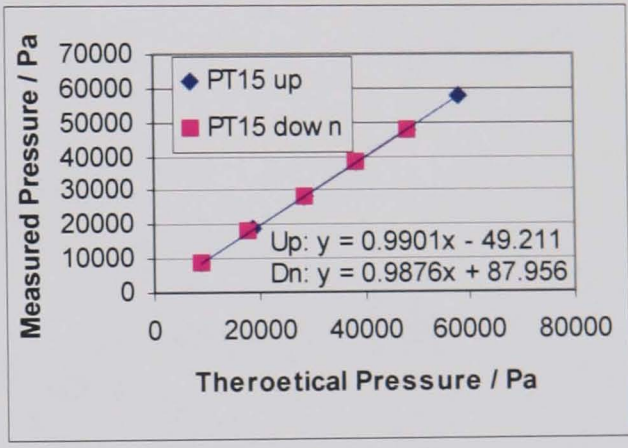
a) Calibration for p3



b) Calibration for p4



c) Calibration for PT9

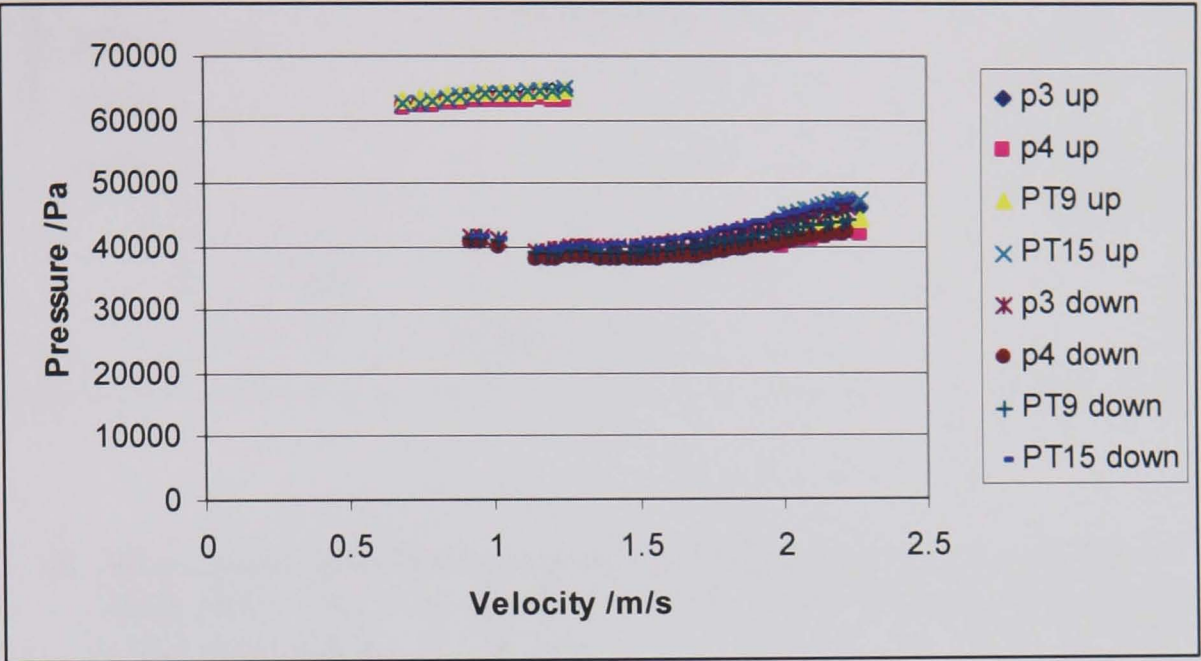


d) Calibration for PT15

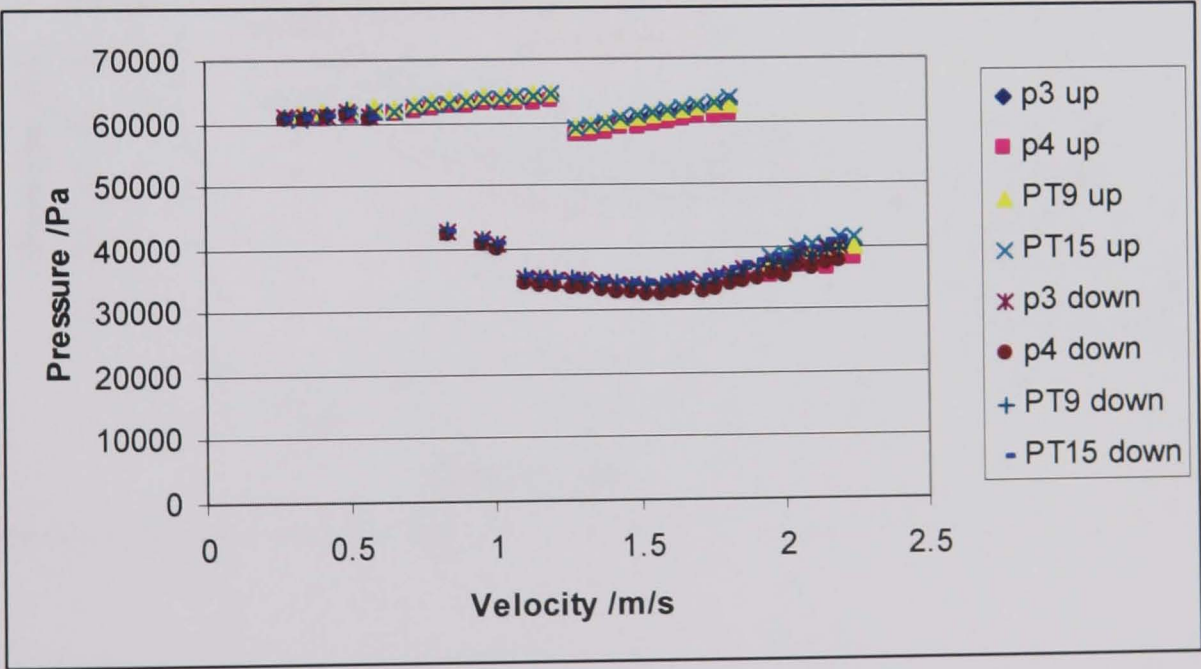
C.6 A second series of graphs to show the pressure recorded with the incremental increase and decrease of pumping frequency, under various test conditions.

This series was performed after re-calibration.

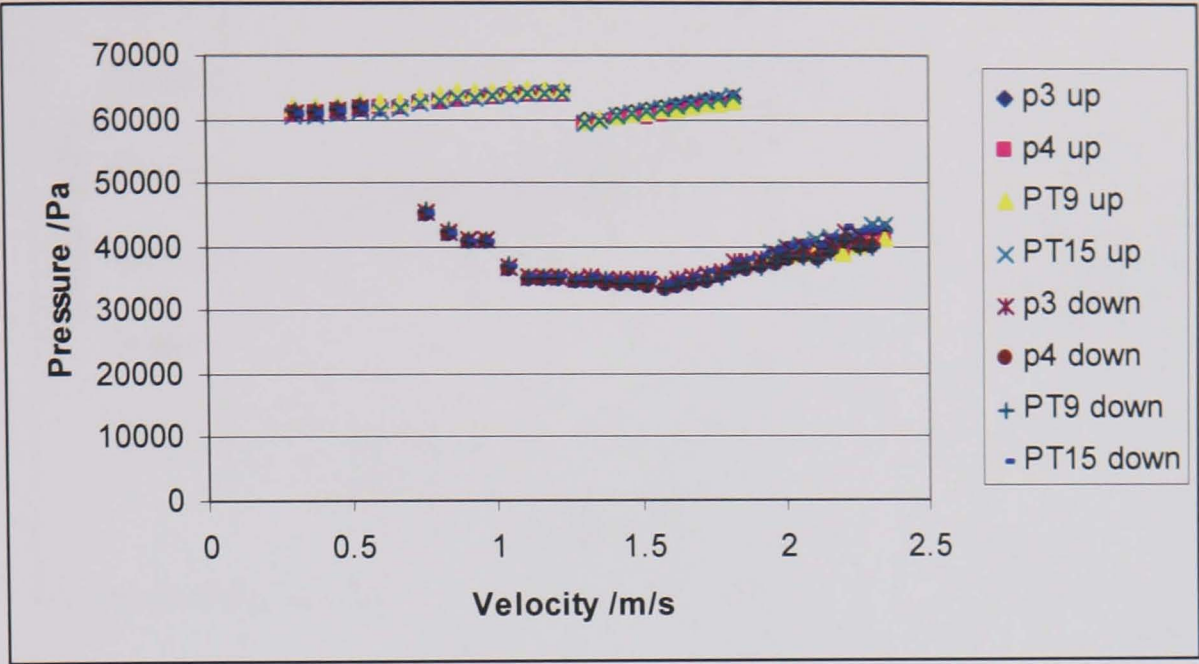
a) Warman pump and de-aerator with 2 extra pressure transducers (p3, p4, from Perspex flow loop)



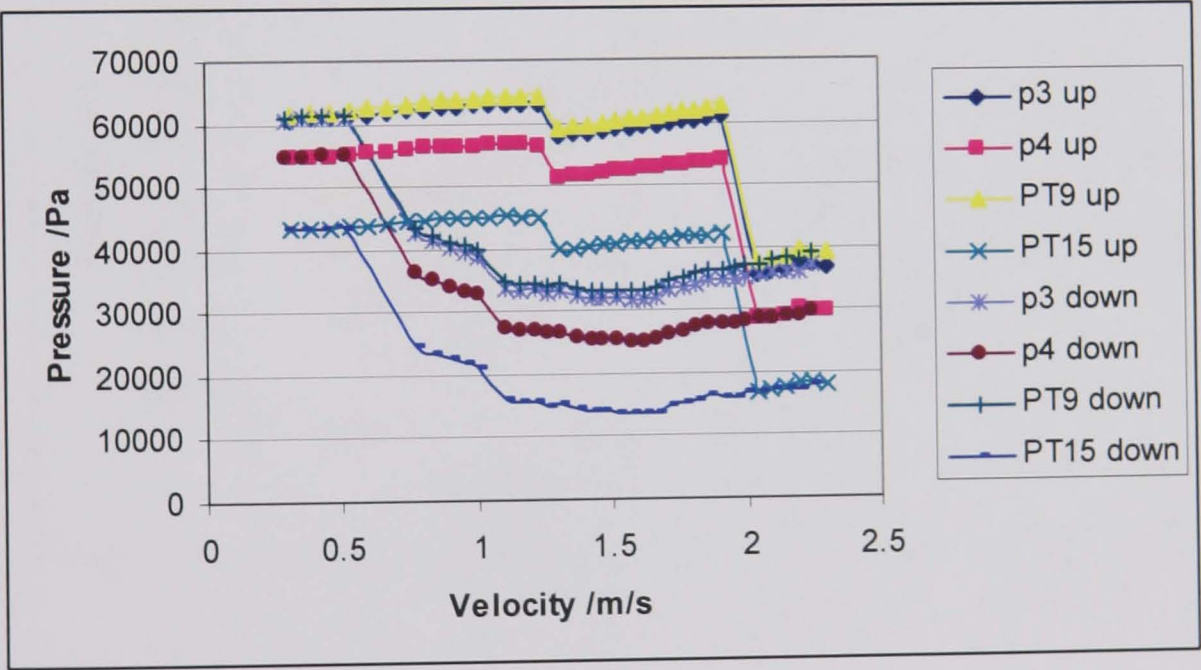
b) Mono pump and de-aerator with 2 extra pressure transducers, observing vortex, tank level and bubbles.



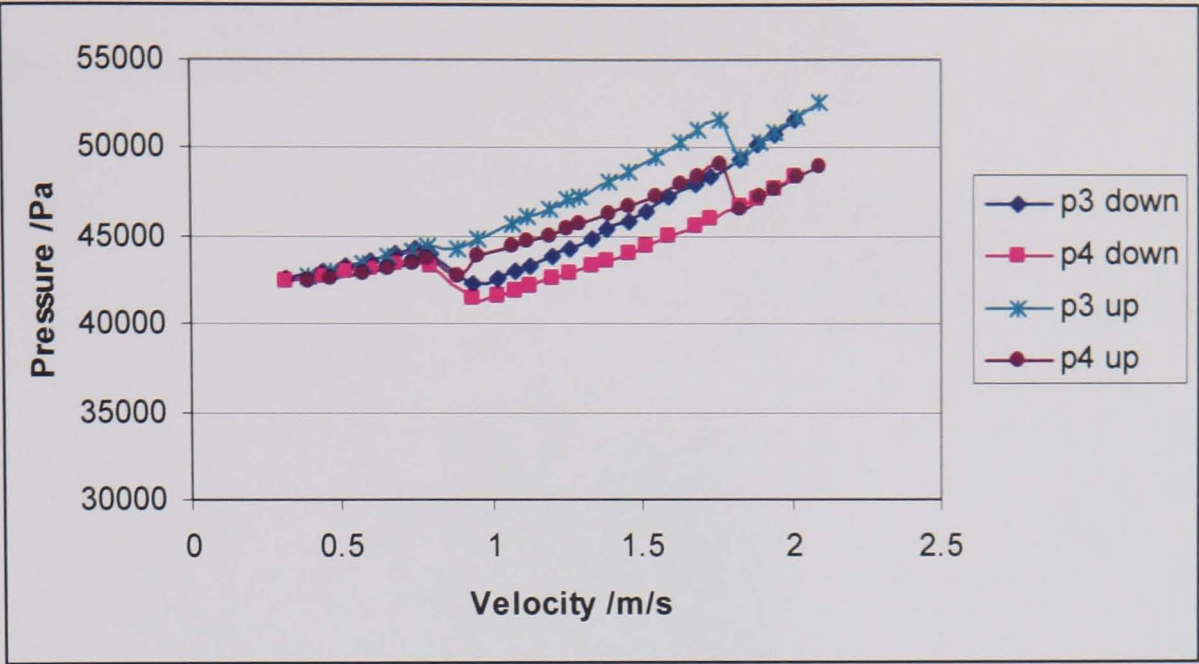
c) Mono pump and de-aerator with 2 extra pressure transducers and swirl pipe in bottom leg



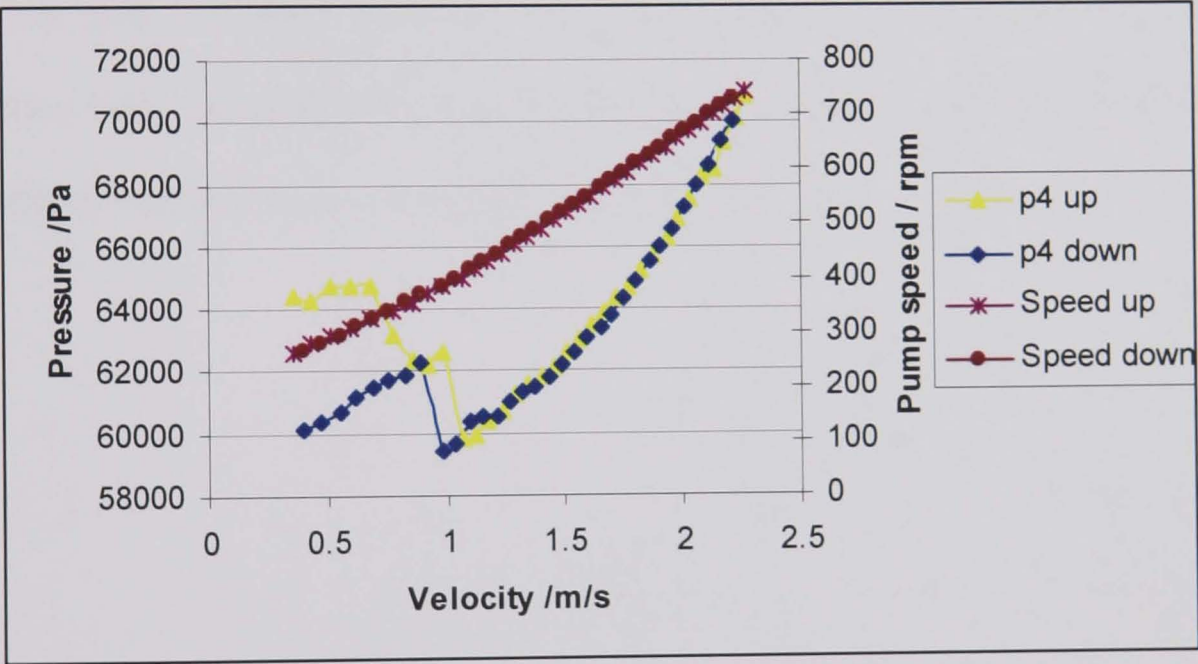
d) Mono pump and de-aerator with 2 extra pressure transducers over bend (R/D = 4). Note: p4 and PT15 are in the vertical leg, 0.583m and 1.787m above p3 and PT9.



e) Perspex flow loop, pressure measured on bottom leg



f) Mono pump and de-aerator, pressure measured on the bottom leg observing the pump speed.



C.7 Calculation of the Reynolds number for water pumped in the flow loop

The Reynolds numbers were calculated for water using the following equation and data.

$$Re = \frac{VD}{\nu}$$

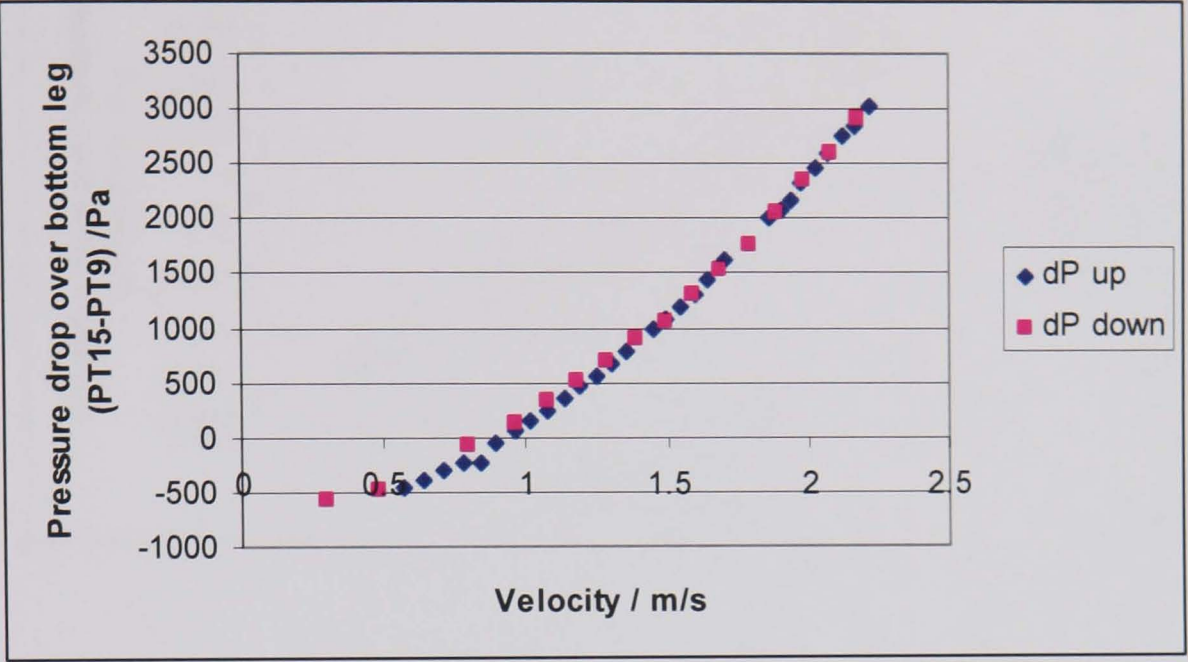
Where: D = pipe diameter = 0.055m
V = flow velocity / m/s
 ν = dynamic viscosity = $1 \times 10^{-6} \text{ m}^2\text{s}^{-1}$

Velocity / m/s	Reynolds Number
0.5	27500
1.0	55000
1.5	82500
2.0	110000
23.6	1300000

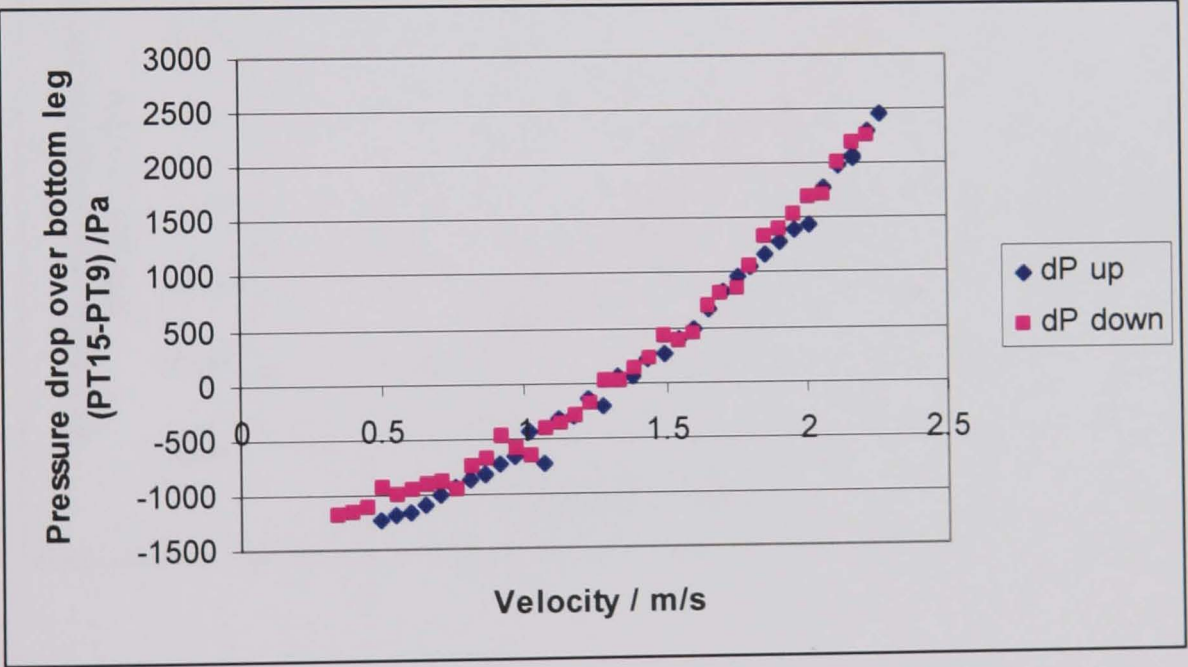
Using the moody chart and taking the absolute relative roughness of steel to be 0.05mm ($k/d = 0.0009$) gives a lower limit of transition of 2000. The flow becomes fully turbulent at a Reynolds number of approximately 1300000. The velocity would have to be 23.6m/s for complete turbulence.

C.8 Series of graphs to show the pressure drop over the bottom leg (PT15 – PT9) associated with the results displayed in C.4 and C.6

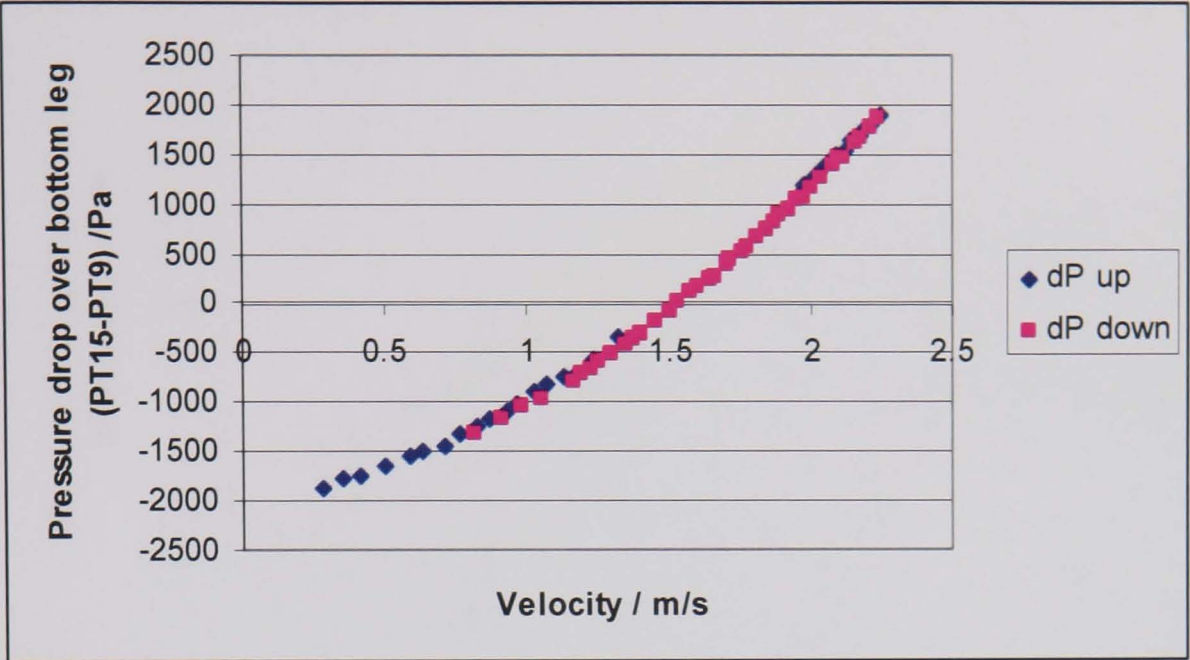
a) Mono pump with de-aerator online



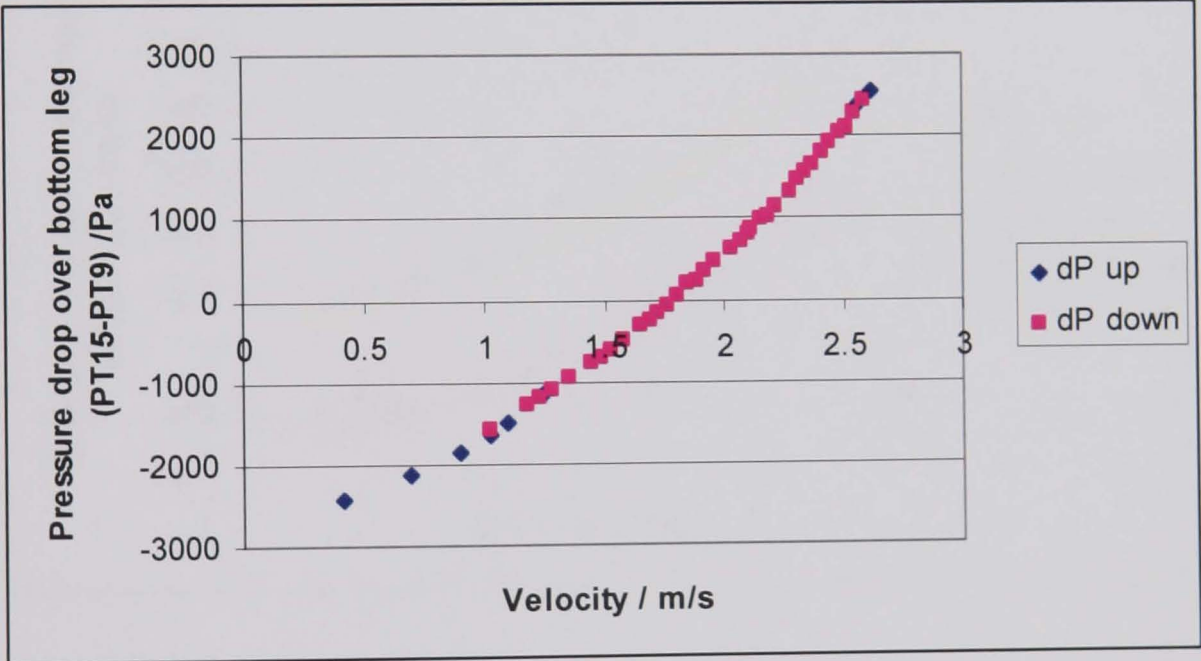
b) Mono pump without de-aerator



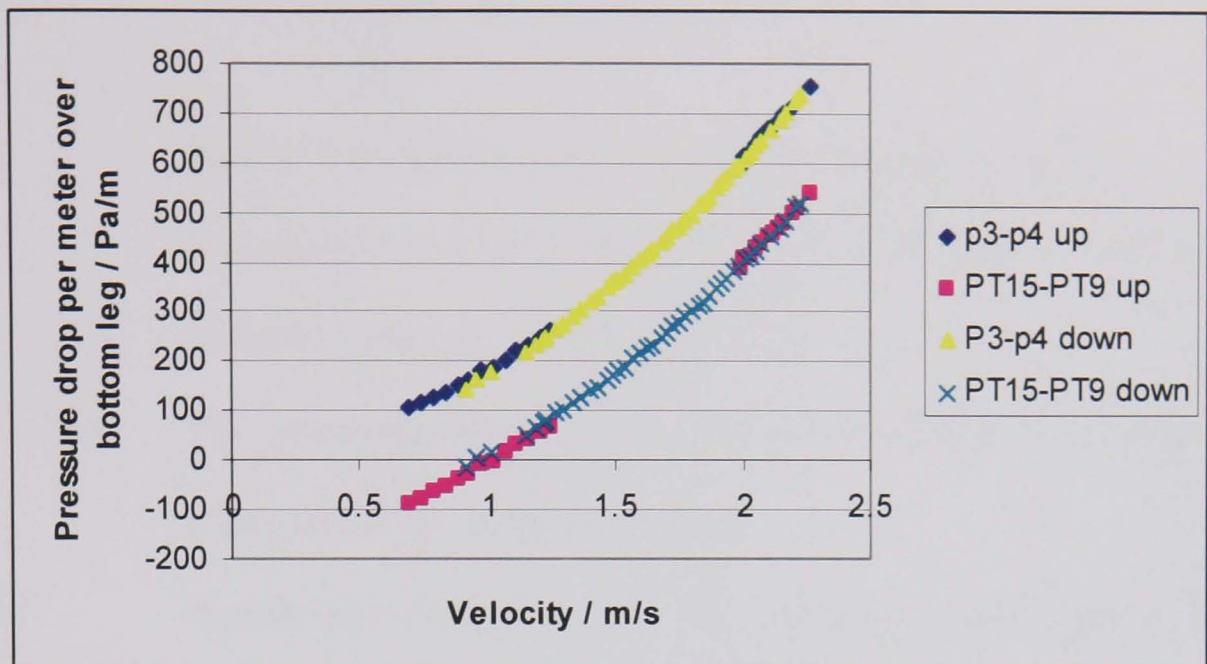
c) Warman pump with de-aerator online



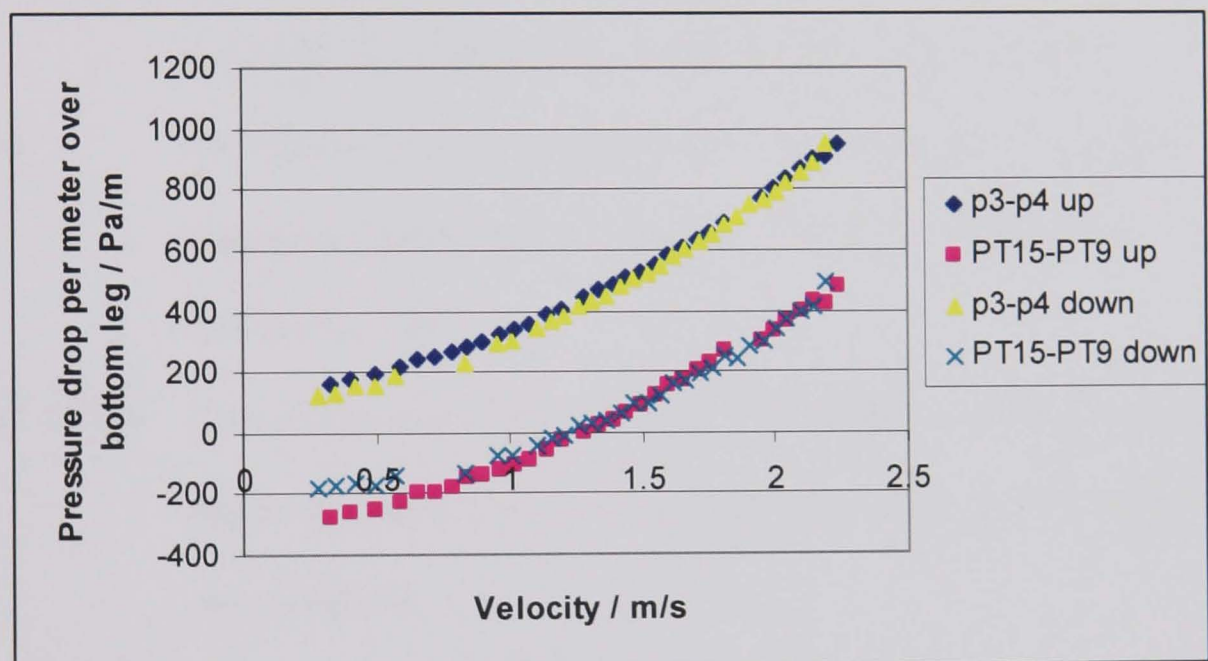
d) Warman pump without de-aerator



- e) Warman pump and de-aerator with Perspex (p3, p4) pressure transducers



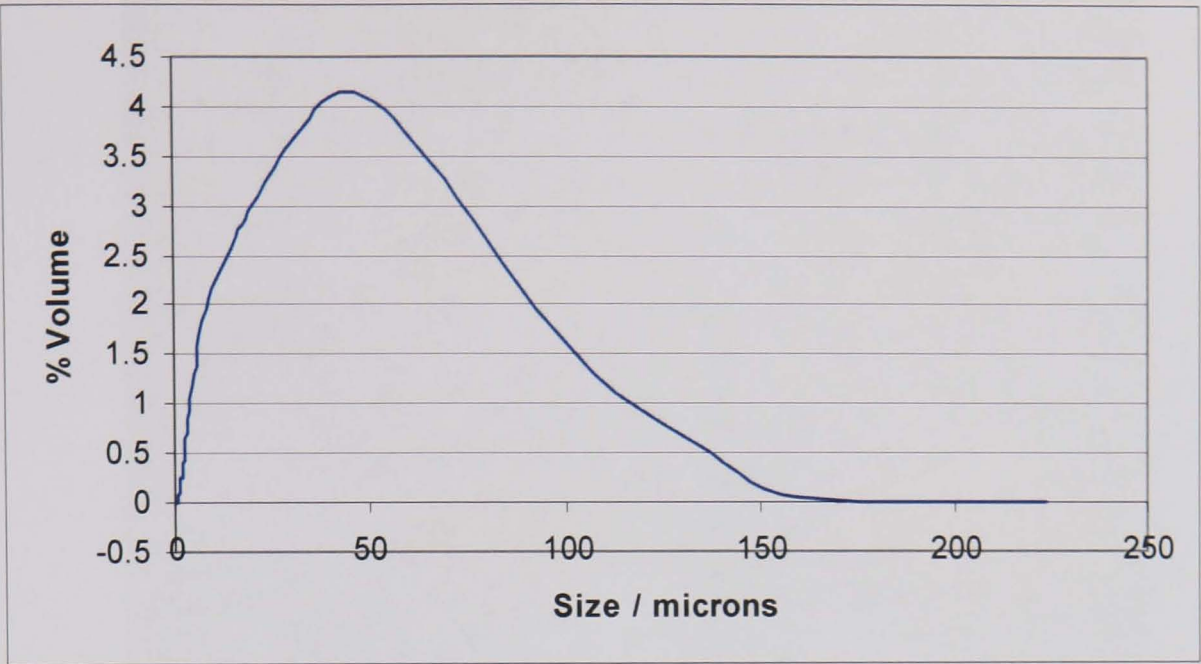
- f) Mono and deaerator with 2 extra pressure transducers, observing vortex, tank level and bubbles.



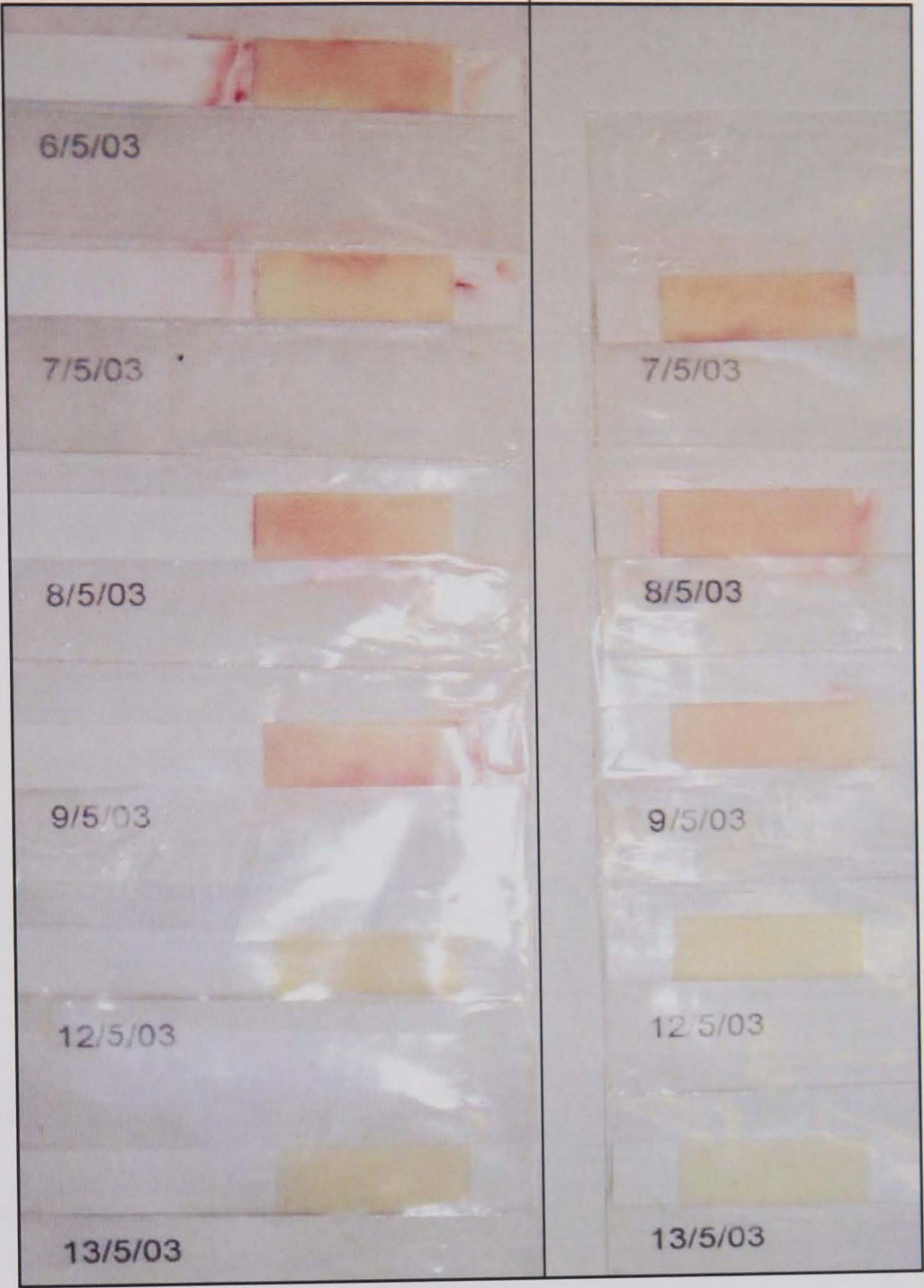
Appendix D. VISUALISATION OF SWIRLING FLOWS

- D.1 Particle size distribution of the talc used as a tracer particle
- D.2 Biological test results for the CMC used in the axial velocity tests
- D.3 Data Processing for the axial PIV results
- D.4 – D.9 PIV measurements of the axial velocity distribution of water and CMC at various nominal velocities
- D.10 Biological test results for the CMC used in tangential velocity tests
- D.11 Data Processing for the tangential PIV results
- D.12 – D.15 PIV measurements of the tangential velocity distribution in water and CMC downstream of a swirl-inducing / standard pipe
- D.16 CFD predictions for tangential velocity distribution of water 4 diameters downstream of a 4-lobe swirl pipe (performed by Ariyaratne, 2003)
- D.17 – D.20 Tomograms and photos of the flow condition at various velocities and downstream distances from swirl pipe, with various bead concentrations

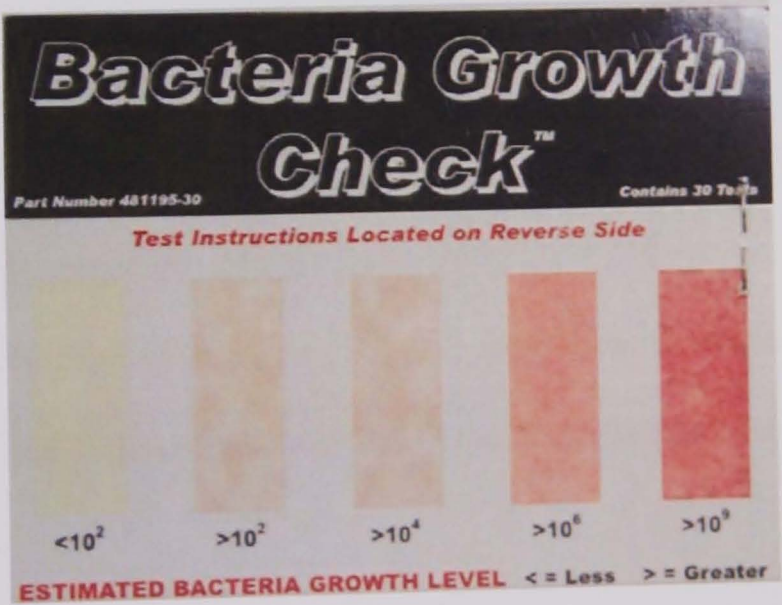
D.1 Particle size distribution of the talc used as a tracer particle



D.2 Biological test results for the CMC used in the axial velocity tests



LHS column shows the test strips taken before testing the fluid in the flow loop and RHS column shows the test strips taken after testing the fluid, for the days shown.



D.3 Data Processing for the axial PIV results

The images were processed using Dantec software and stored on the computer. The CCD camera was set to capture eight images (4 image pairs) for each process condition, an example of which is shown in Figure 1Da. A mask was then drawn and applied to each image to exclude the area outside the pipe from the correlation (Figure 1Db). The particles in an image pair were then cross-correlated to produce vectors describing the particle motion (Figure 2Da). Thus, for each process condition 4 raw vector maps were obtained. A range validation was then performed, according to the scheme shown in Table 1D, to exclude unlikely vectors. Such vectors occur by the erroneous correlation of two individual particles. Particularly high values, or unlikely directions were excluded as shown in Figure 2Db. Finally the mean of the 4 validated data sets was taken to produce the single 'vector statistics' map (Figure 2Dc).

Table 1D: Validation thresholds used for the range validation of both fluids for the axial PIV tests

Nominal axial velocity / m/s	Validation threshold /m/s	
	Minimum	Maximum
0.5	0.00	0.75
1.0	0.00	1.50
1.5	0.00	2.25

In addition to the images and vector maps, a data file containing the vector statistics can also be obtained from the Dantec software. This was used to produce the graph shown in Figure 2Dd. The graph shows the change in the axial velocity

values with pipe cross-section. The axial velocity value displayed was the mean over 16 data points, along the pipe length.



Figure 1D: Example of images captured by the CCD camera

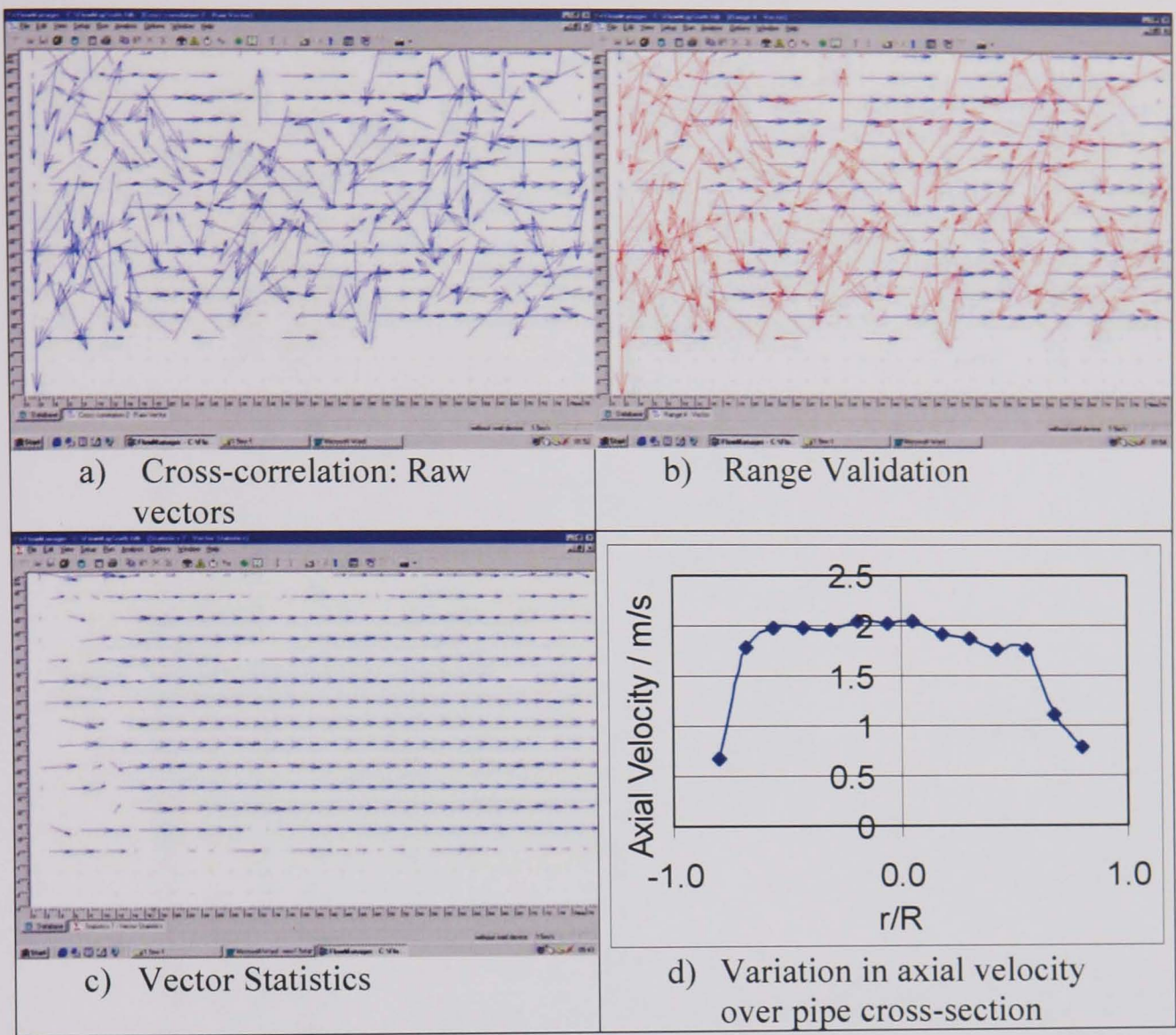
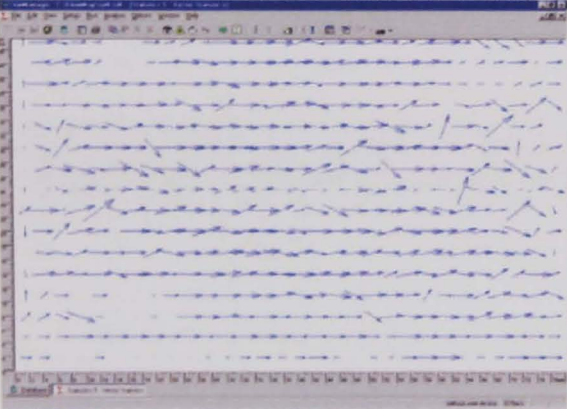
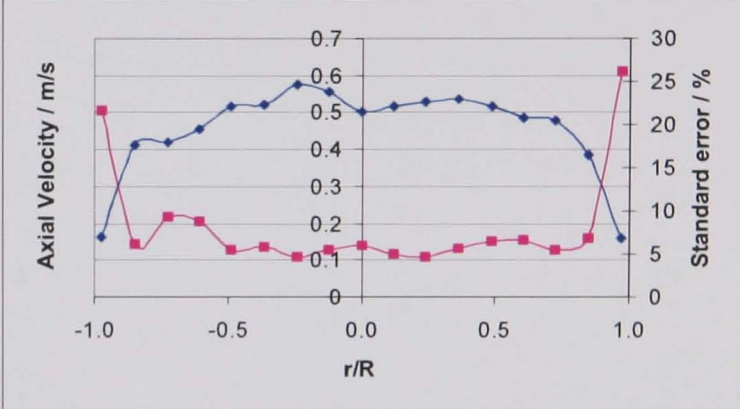
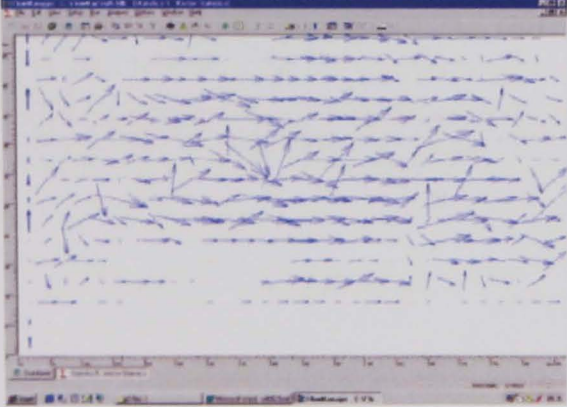
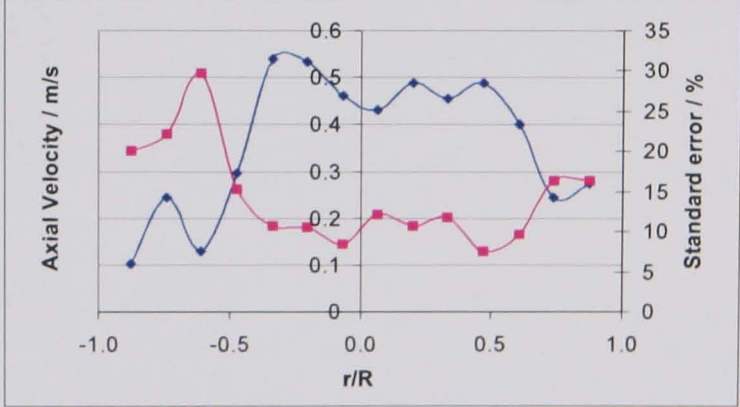

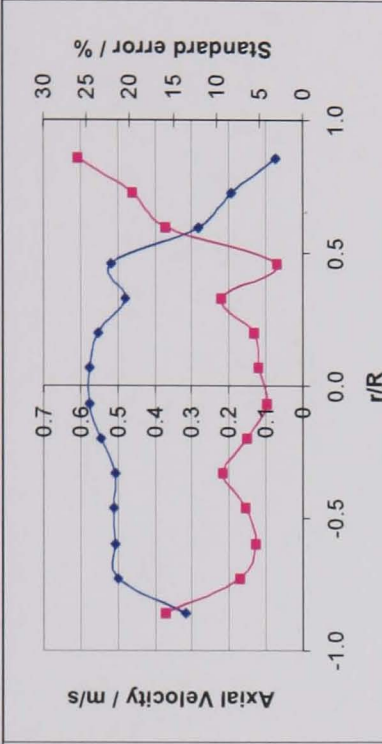
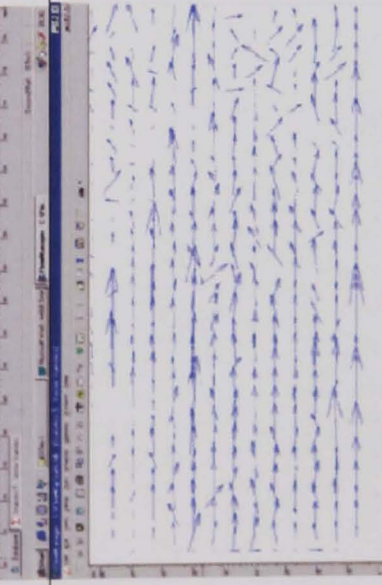
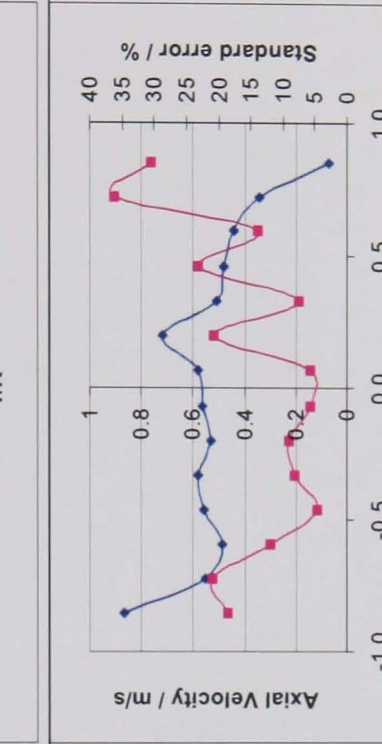


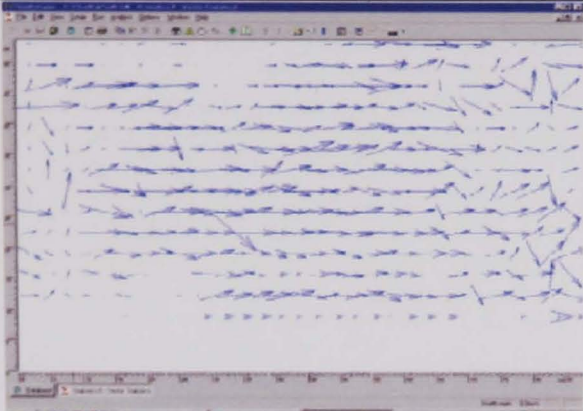
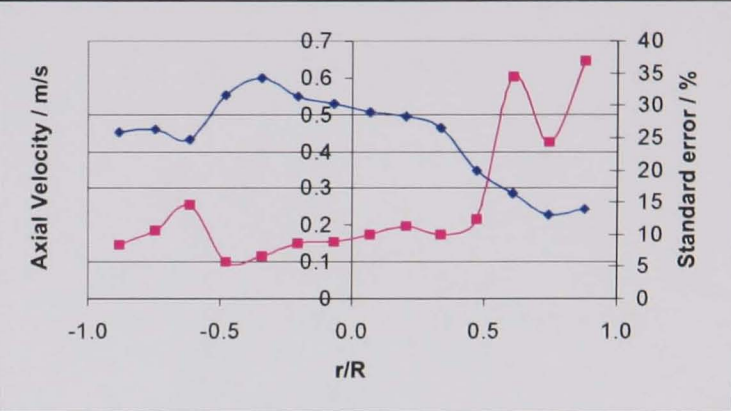
Figure 2D: Illustration of the processing of the axial PIV data (Water, no swirl, nominal axial velocity: 1.5m/s).

D.4 PIV measurements of the axial velocity distribution in water at 0.5m/s

Key: —◆— Mean x-sectional velocity —■— Standard error (16 points)

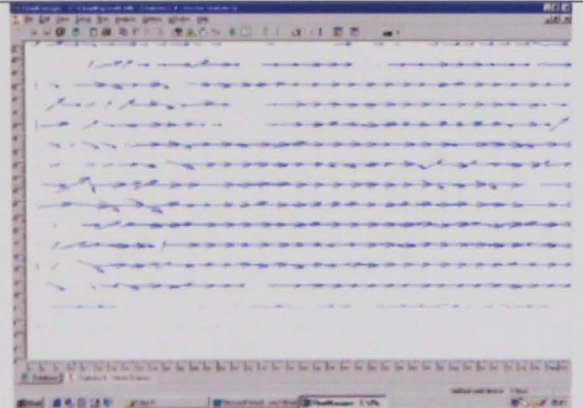
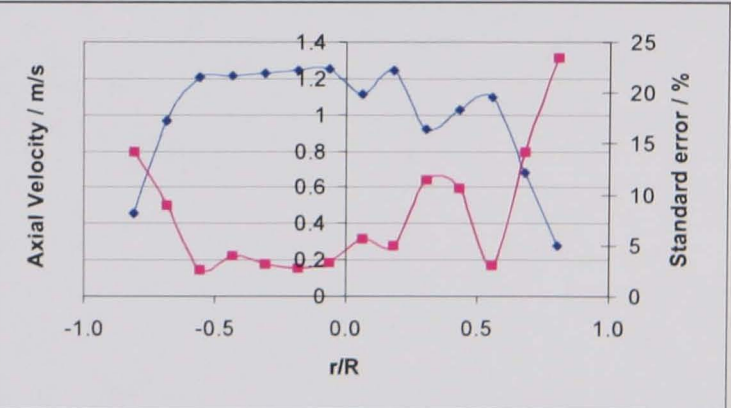
Position	Vector statistics flow map	Variation in axial velocity with cross-section and standard error	Mean velocity from flowmeter/ m/s
No swirl			0.559
4D			0.564

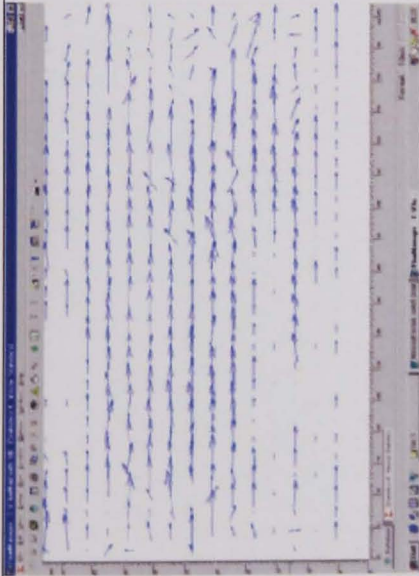
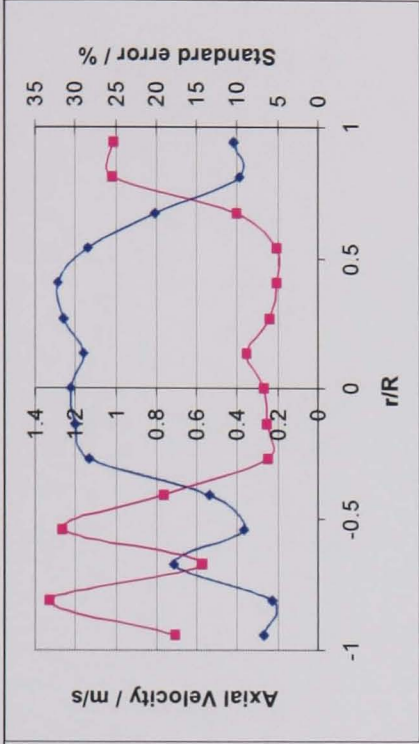
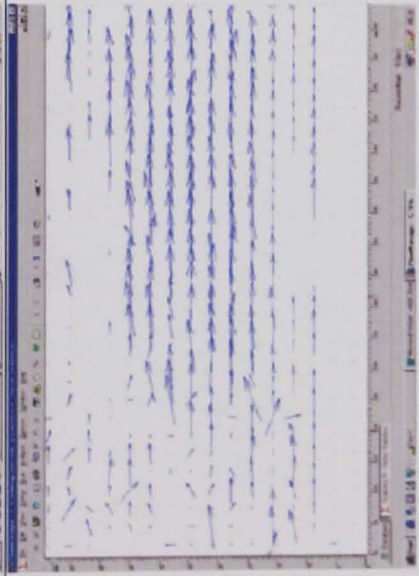
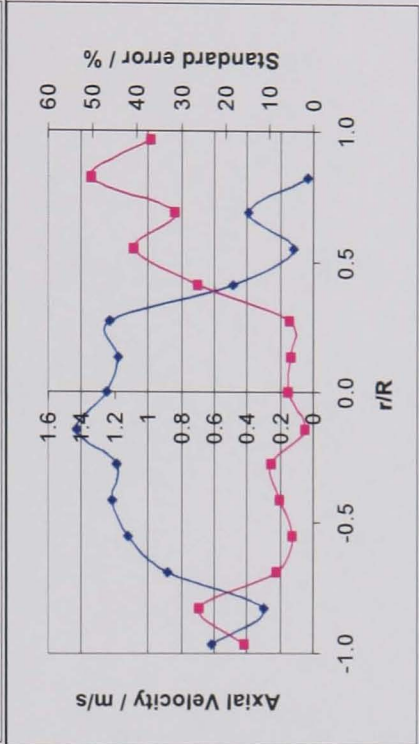
8D			0.549
12D			0.546

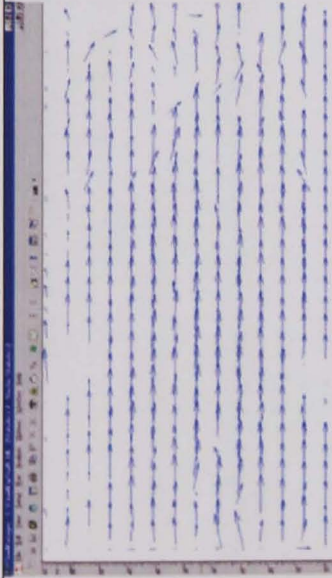
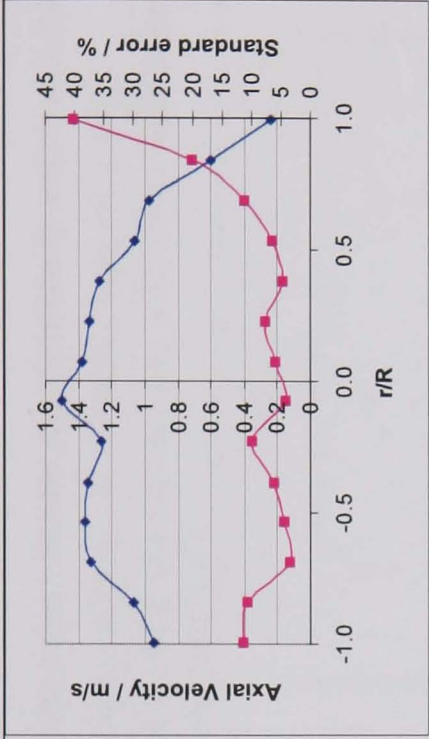
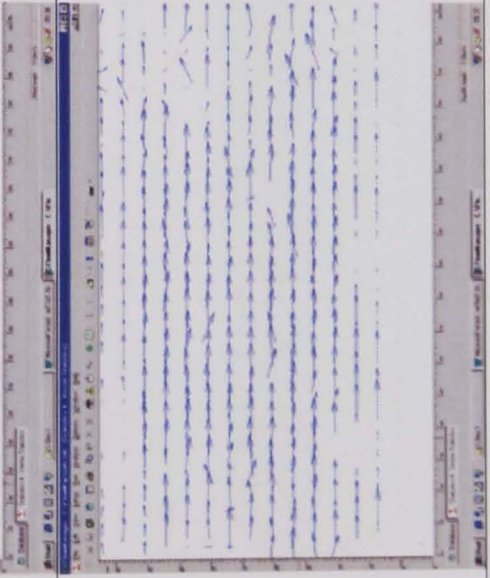
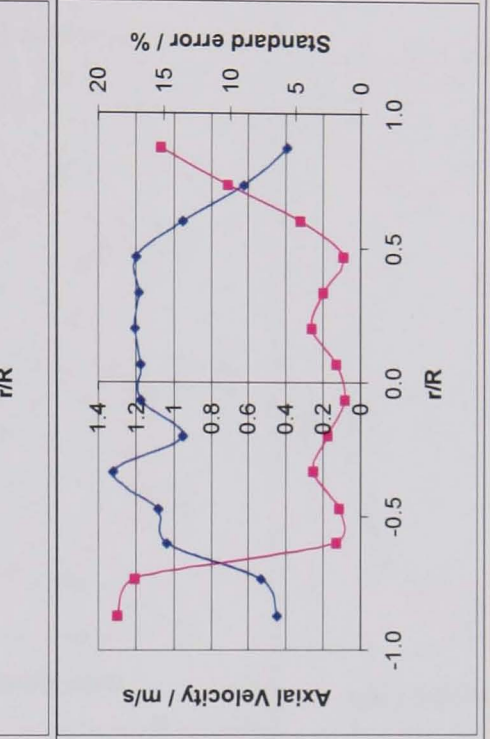
16D			0.556
-----	--	---	-------

D.5 PIV measurements of the axial velocity distribution in water at 1.0m/s

Key: —●— Mean x-sectional velocity —■— Standard error (16 points)

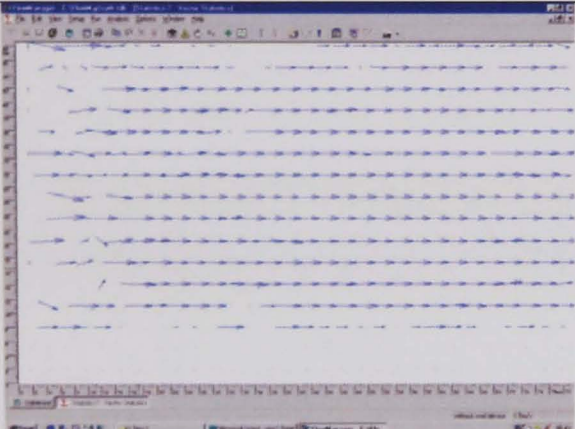
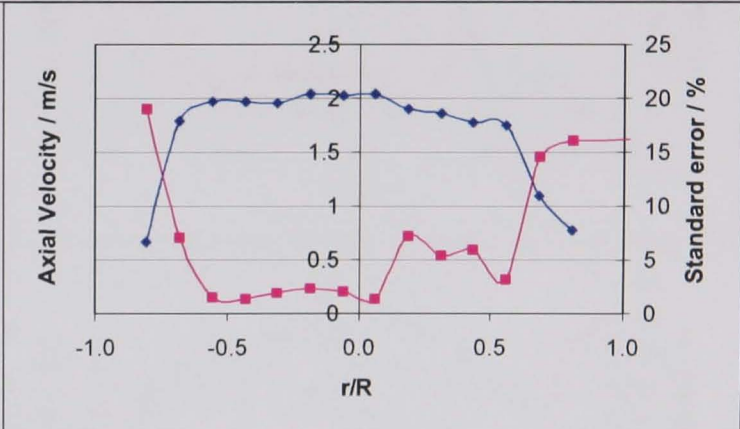
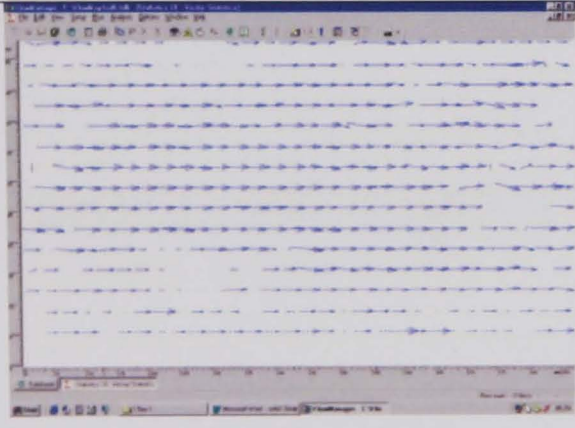

Position	Vector statistics flow map	Variation in axial velocity with cross-section and standard error	Mean velocity from flowmeter/ m/s
No swirl			1.062

4D			1.111
8D			1.105

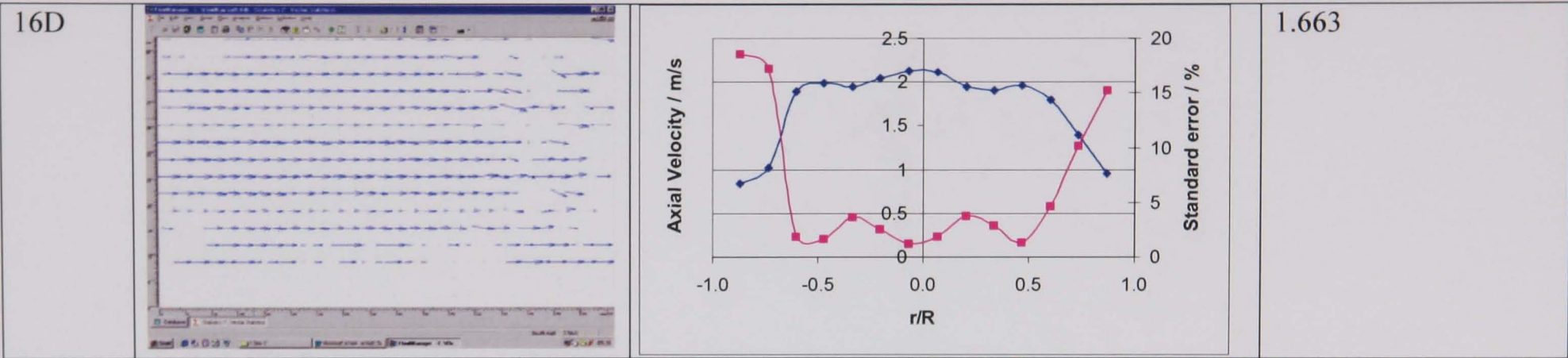
12D			1.107
16D			1.102

D.6 PIV measurements of the axial velocity distribution in water at 1.5m/s

Key: —◆— Mean x-sectional velocity —■— Standard error (16 points)

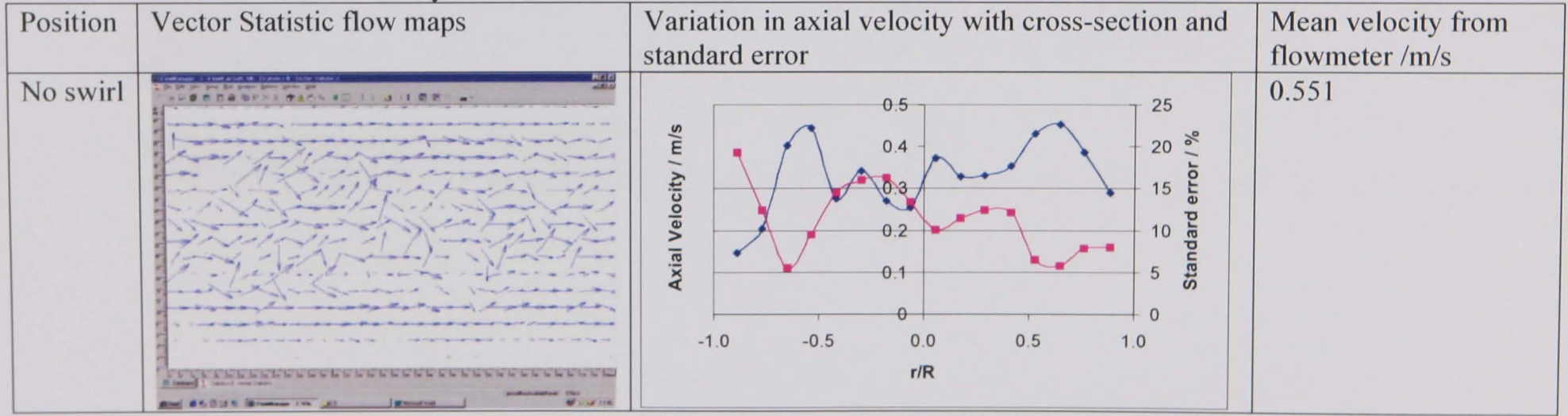
Position	Vector statistics flow map	Variation in axial velocity with cross-section and standard error	Mean velocity from flowmeter/ m/s
No swirl			1.668
4D			1.699

8D			1.651
12D			1.663

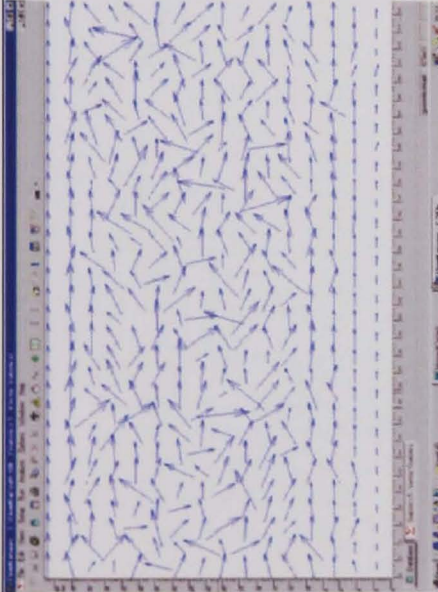
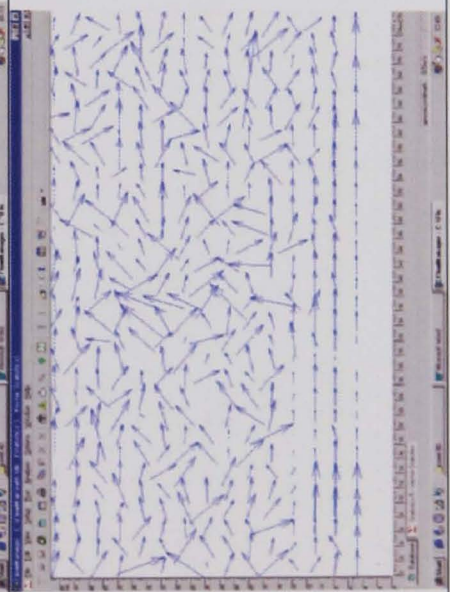
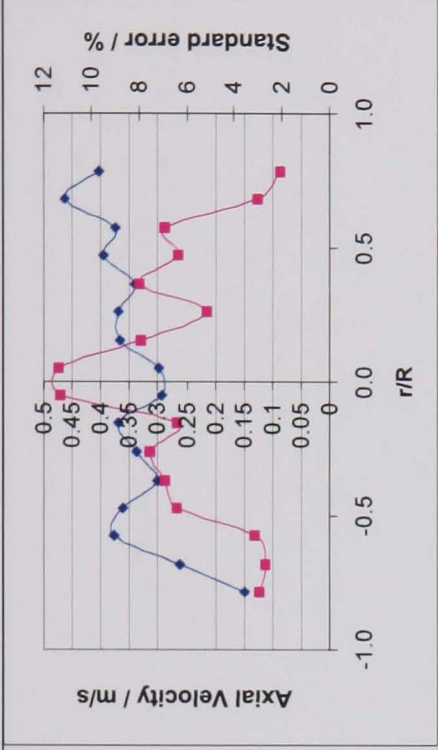
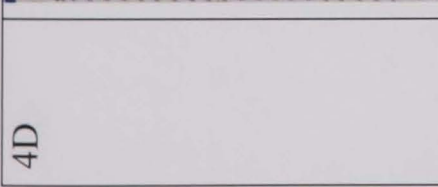
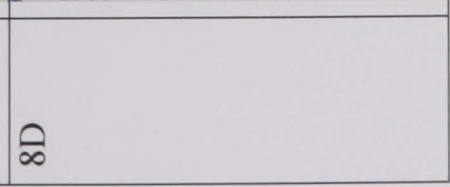
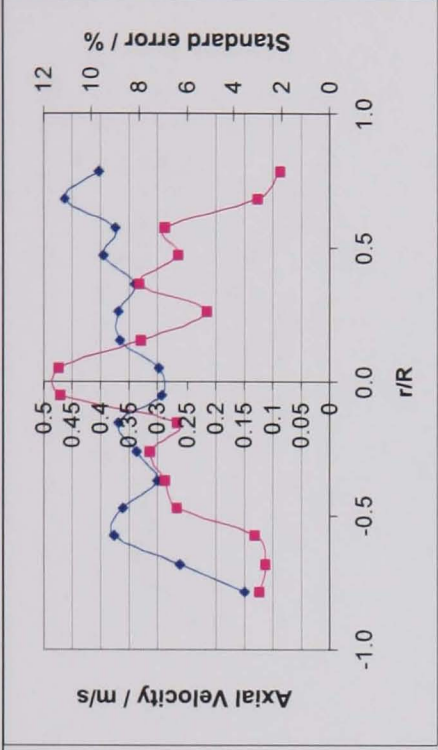


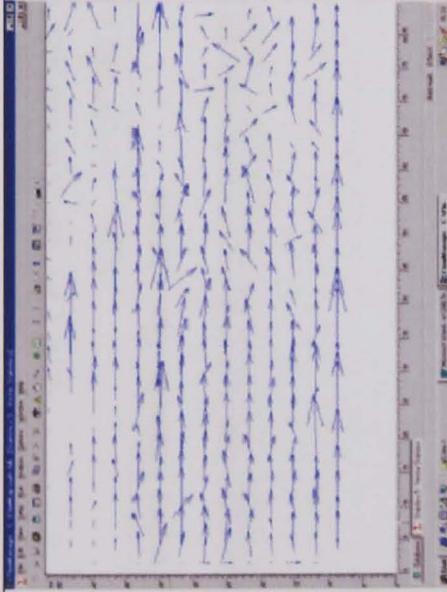
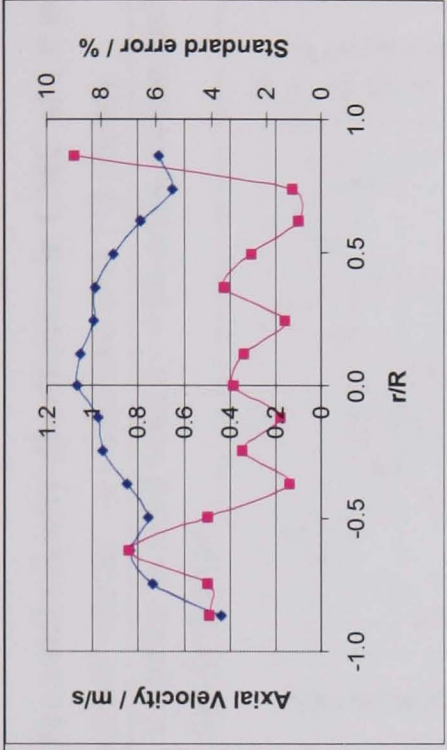
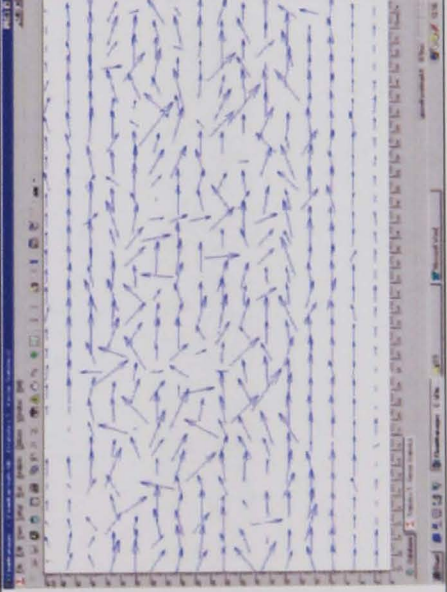
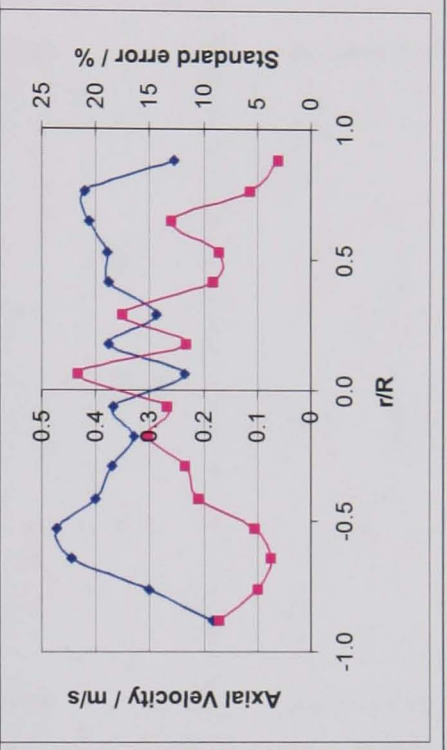
D.7 PIV measurements of the axial velocity distribution in CMC at 0.5 m/s.

Key: —●— Mean x-sectional velocity —■— Standard error (16 points)



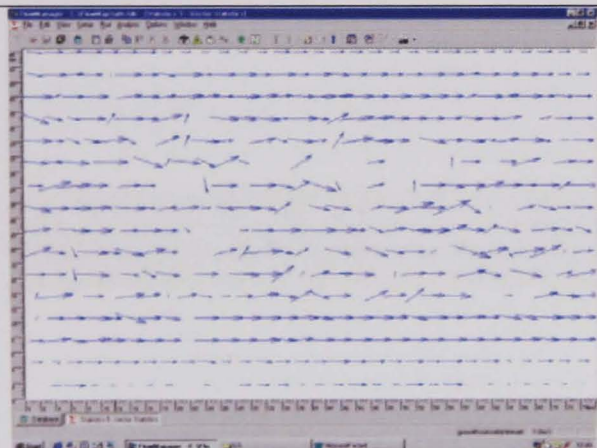
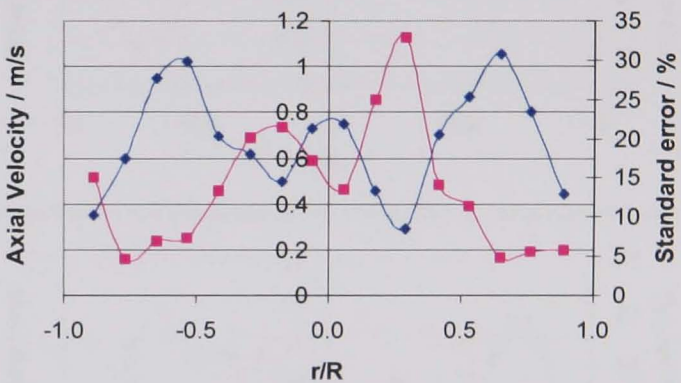
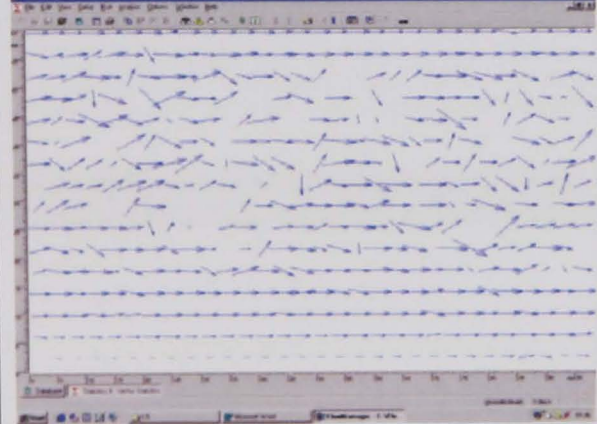
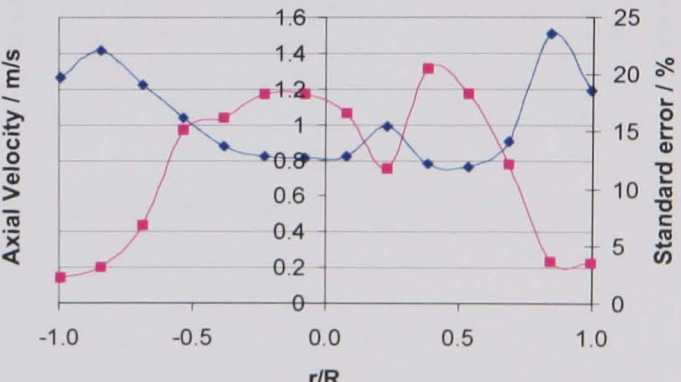
D.7

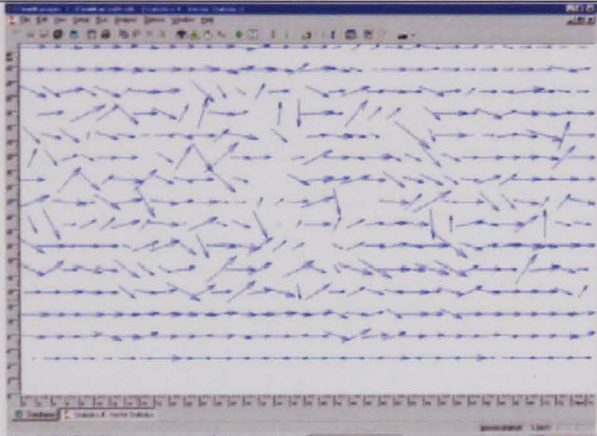
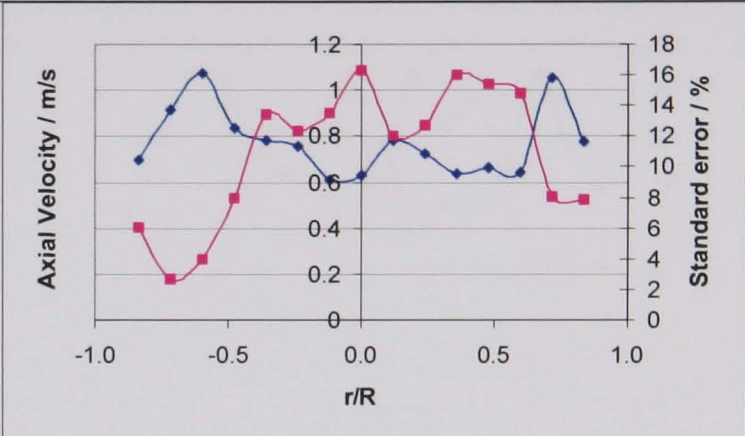
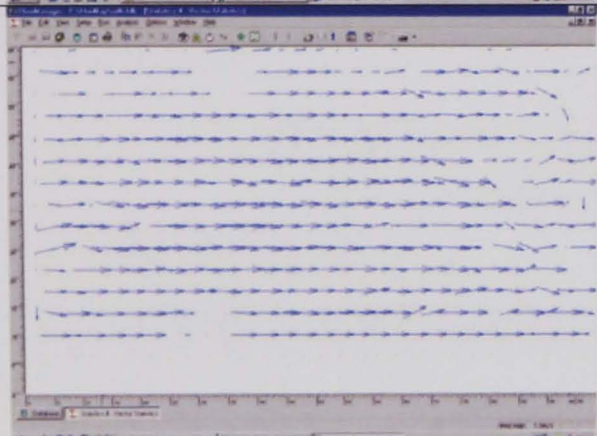
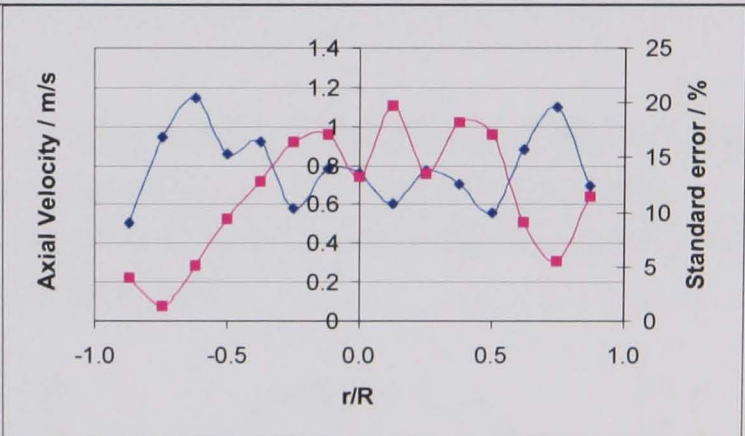
4D			 <p>Axial Velocity / m/s</p> <p>Standard error / %</p> <p>r/R</p>	0.553
8D			 <p>Axial Velocity / m/s</p> <p>Standard error / %</p> <p>r/R</p>	0.551

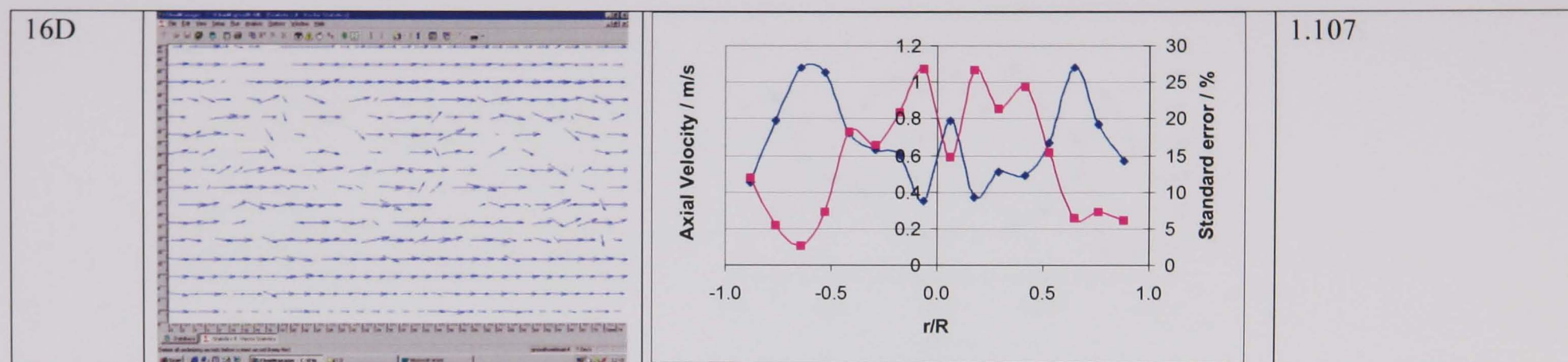
12D			0.551
16D			0.548

D.8 PIV measurements of the axial velocity distribution in CMC at 1.0 m/s.

Key: —◆— Mean x-sectional velocity —■— Standard error (16 points)

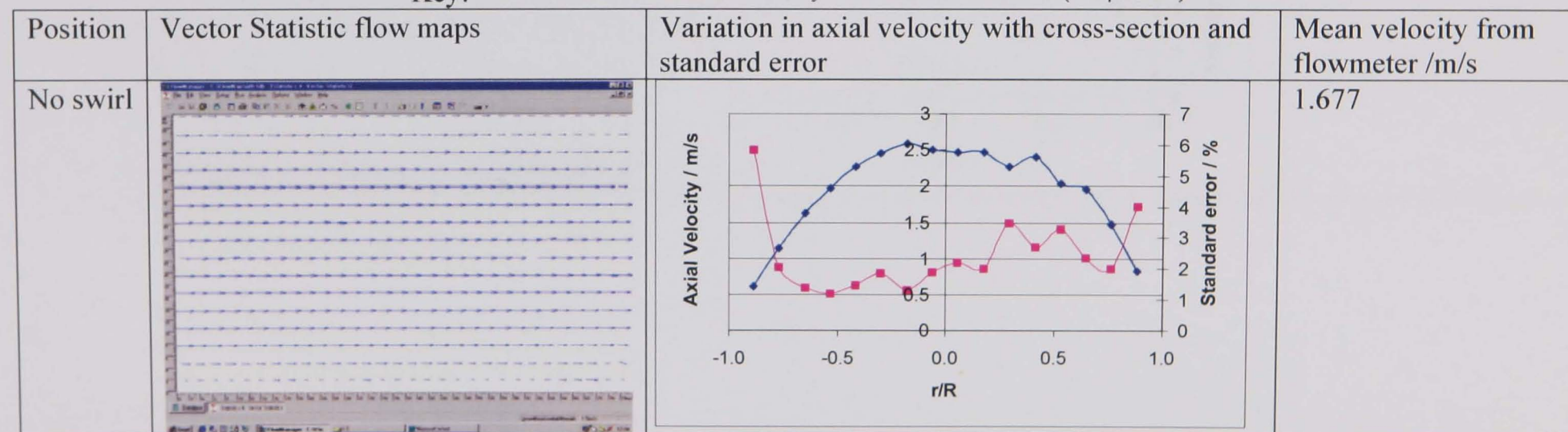
Position	Vector Statistic flow maps	Variation in axial velocity with cross-section and standard error	Mean velocity from flowmeter /m/s
No swirl			1.104
4D			1.108

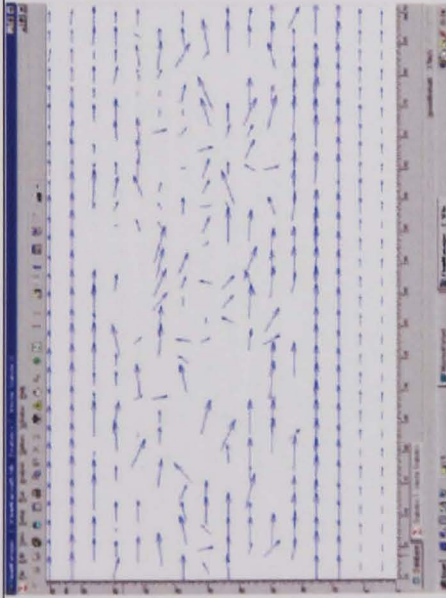
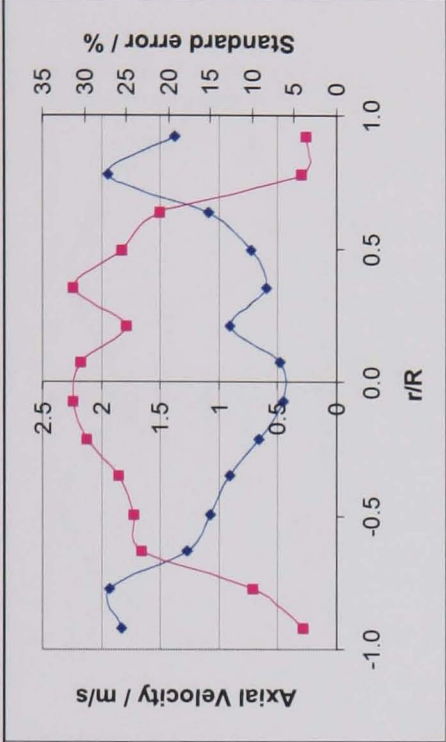
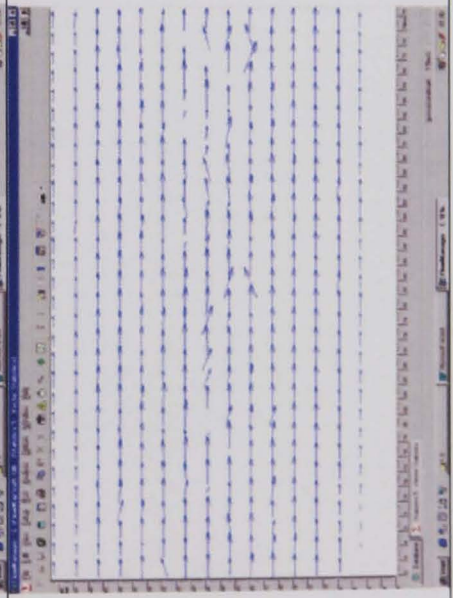
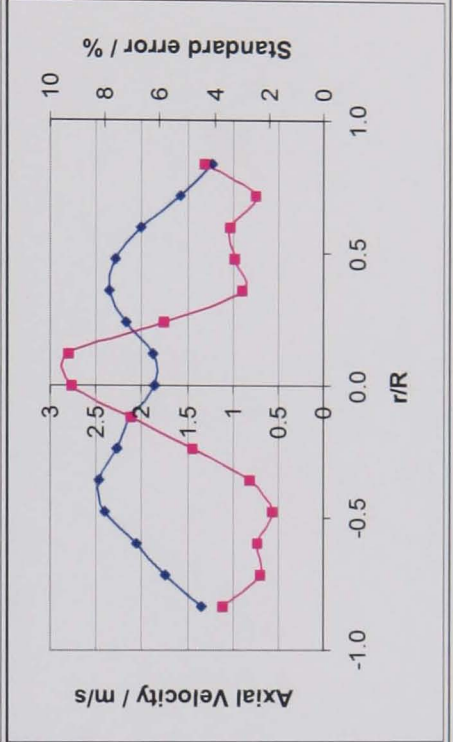
8D			1.104
12D			1.113

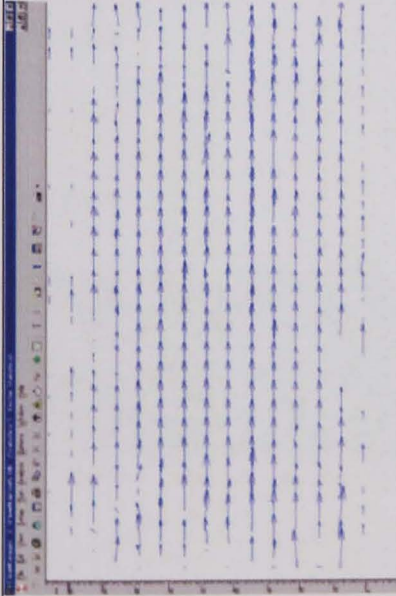
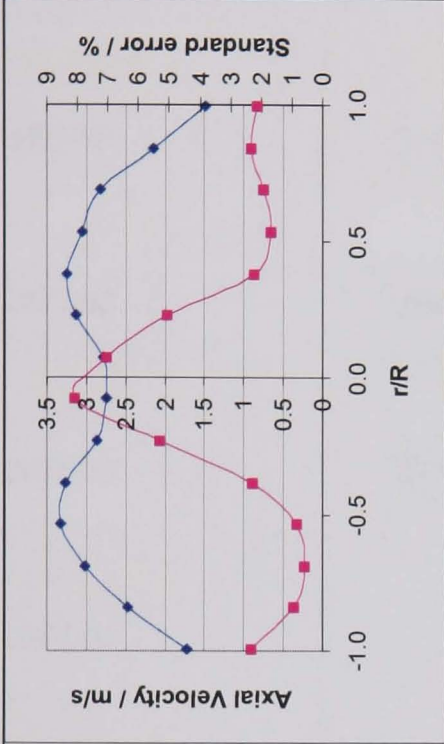
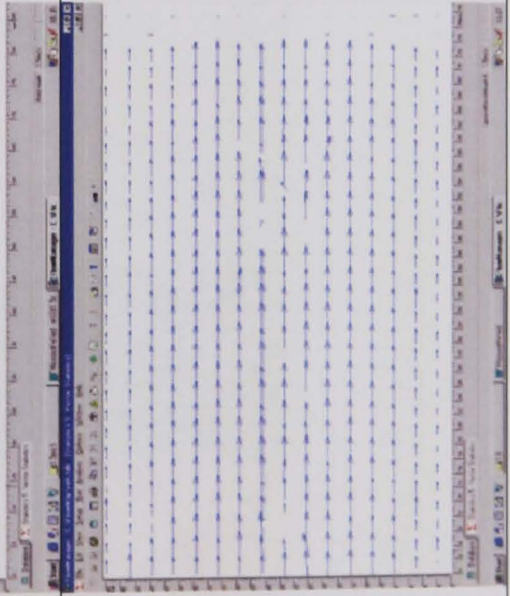
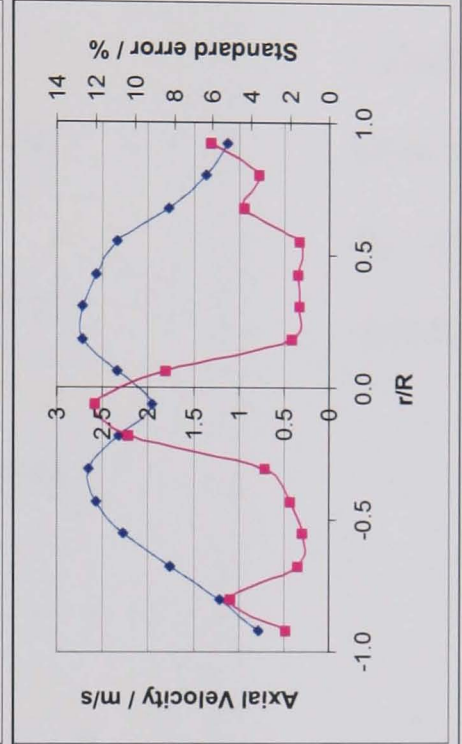


D.9 PIV measurements of the axial velocity distribution in CMC at 1.5 m/s.

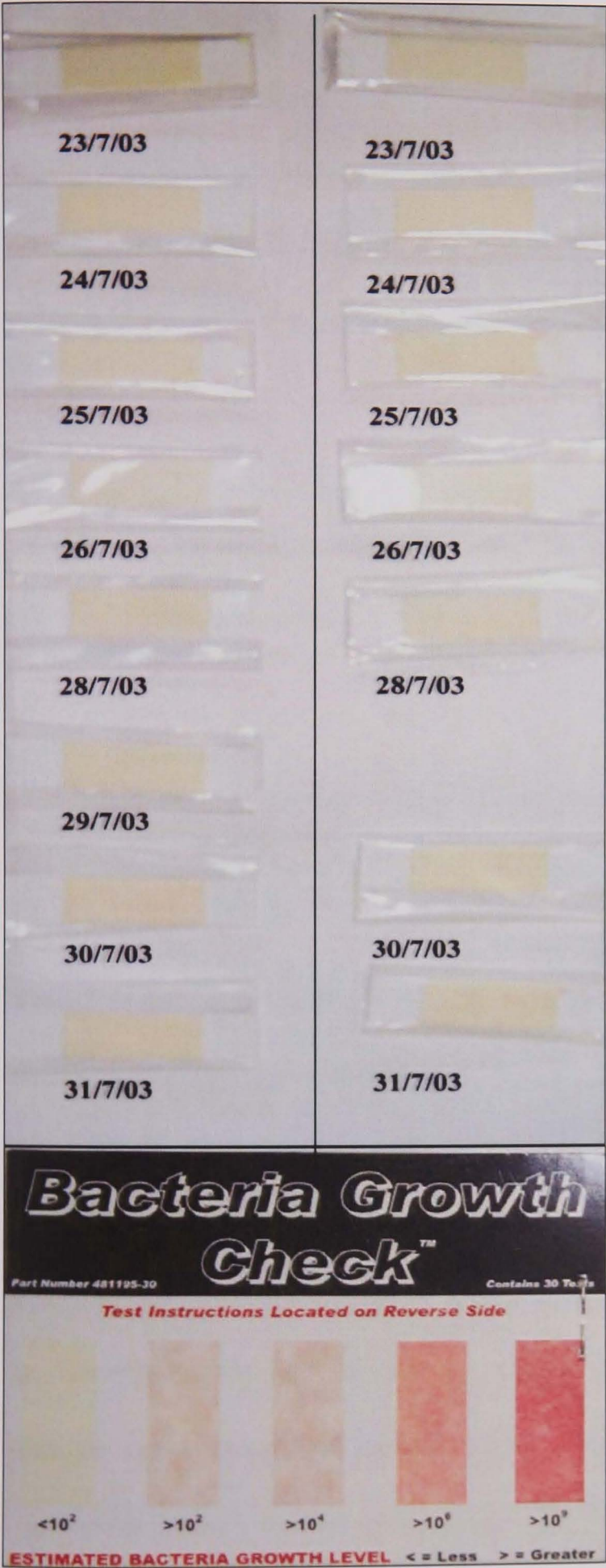
Key: —◆— Mean x-sectional velocity —■— Standard error (16 points)



4D			1.655
8D			1.656

12D			1.659
16D			1.660

D.10 Biological test results for the CMC used in tangential velocity tests



LHS column shows the test strips taken before testing the fluid in the flow loop and RHS column shows the test strips taken after testing the fluid for the days shown.

D.11 Data Processing for the tangential PIV results

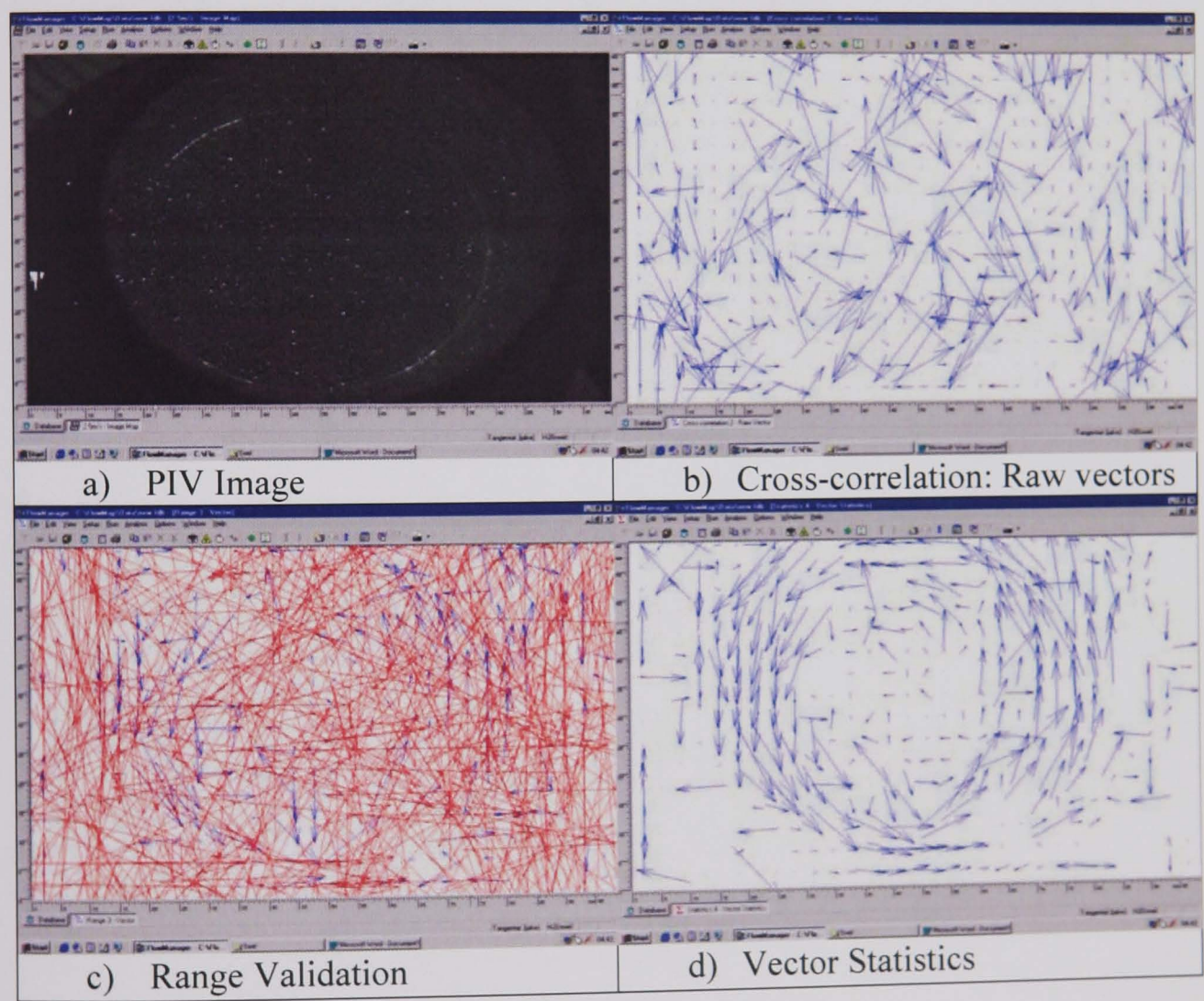
The data was processed in a similar way to the axial results, however a circular mask proved difficult to draw in the Dantec software, so no mask was applied during that stage of the processing of the tangential PIV results. The raw images were cross-correlated (Figure 3Db) and validated (Figure 3Dc) according to the scheme show in Table 2D, resulting in a single vector statistics image (Figure 3Dd).

Table 2D: Validation thresholds used for the range validation of both fluids for the tangential PIV tests.

Nominal axial velocity / m/s	Validation threshold /m/s	
	Minimum	Maximum
2.5	-1.0	1.0
2.0	-1.0	1.0
1.5	-0.8	0.8
1.0	-0.5	0.5
0.5	-0.3	0.3

As before the vector statistics data file was used to perform further analysis on the results. The Dantec software uses an x-y co-ordinate system with the origin located in the bottom left-hand corner of the image. Before any calculations were performed the co-ordinates were adjusted to move the origin to the centre of the pipe (the central cross in Figure 3Dg) to coincide with the CFD convention used by Ganeshalingam (2002) and Ariyaratne (2003). To calculate the tangential velocity, α was calculated for each vector, then a logic formula was applied, which utilised the x and y co-ordinates to calculate which quadrant the vector was located in and applied the appropriate formula for θ (see Figure 3De). Given θ , the

tangential velocity could be calculated. The calculations were initially performed on the full dataset. However, it was evident that many of the data points plotted lay outside the pipe (see Figure 3Df), so a circular mask of known radius was applied to the vector statistics diagram (Figure 3Dg). (Note that the dataset extends beyond the vector statistics diagram and contains data corresponding to the entire area of the circle). The results were then plotted as shown in Figure 3Dh.



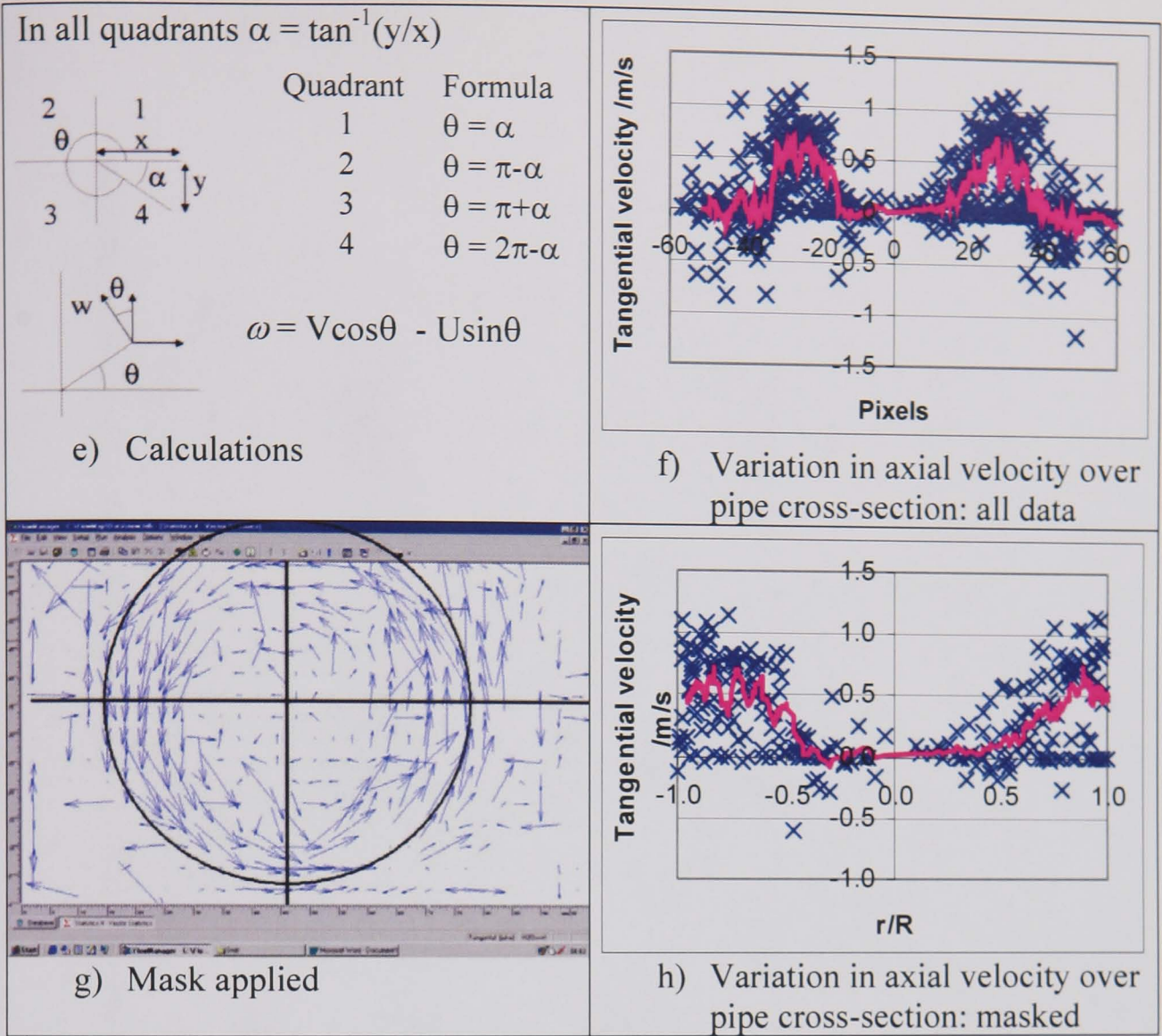
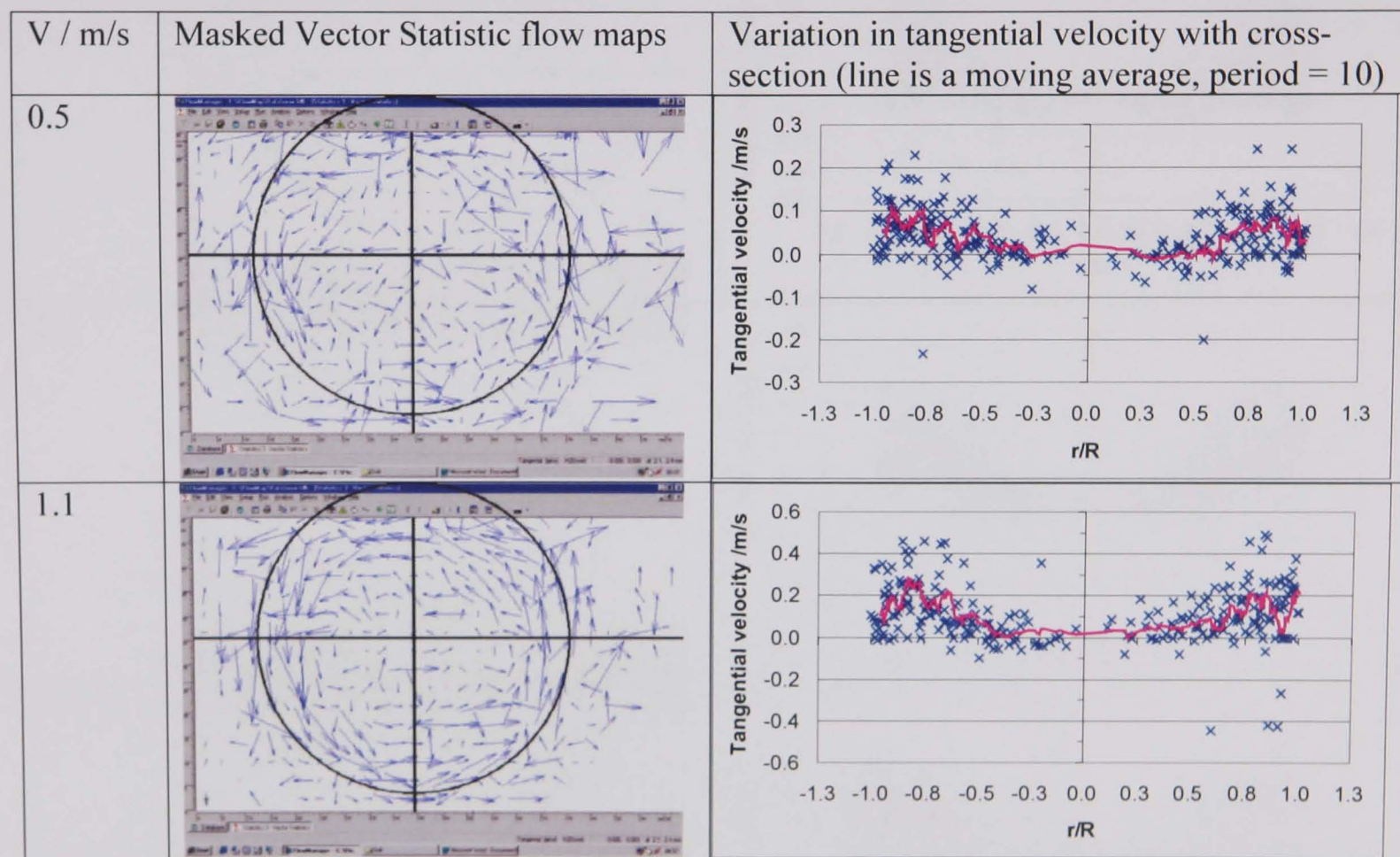
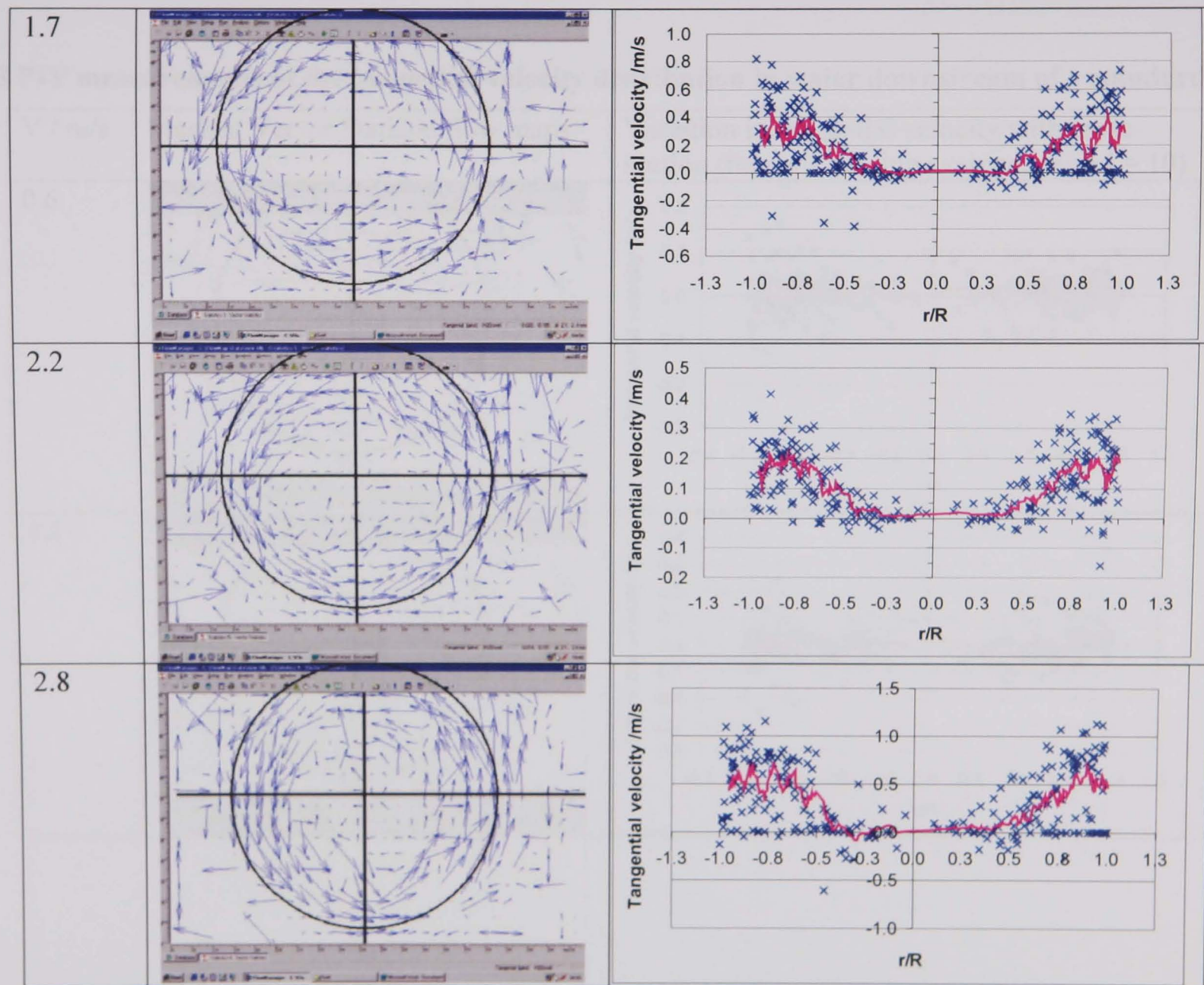


Figure 3D: Illustration of the processing of the tangential PIV data (Water, nominal axial velocity: 2.5m/s, with swirl upstream).

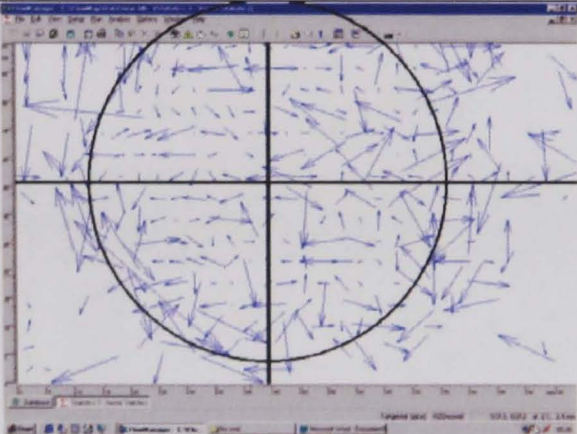
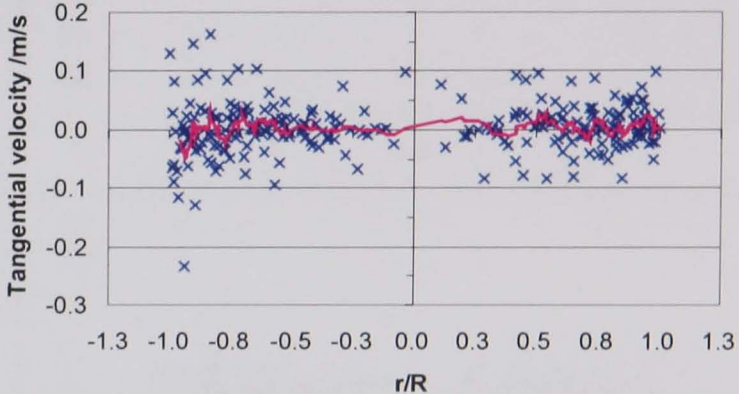
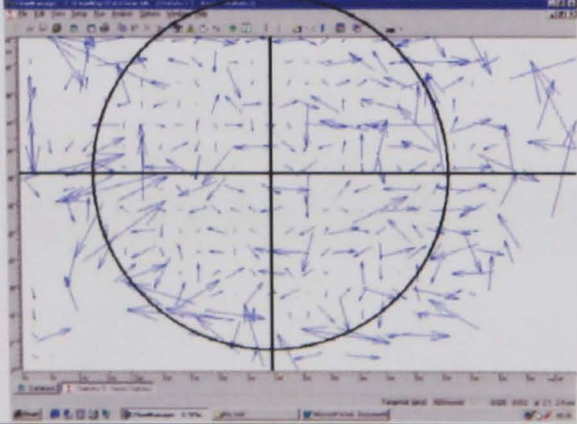
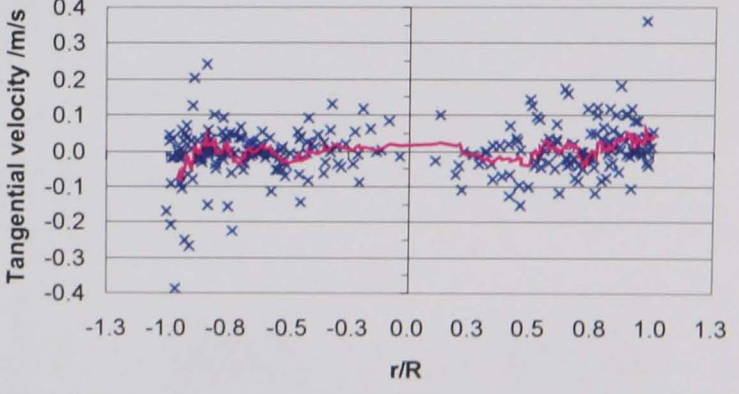
D.12 PIV measurements of the tangential velocity distribution in water downstream of a swirl-inducing pipe.



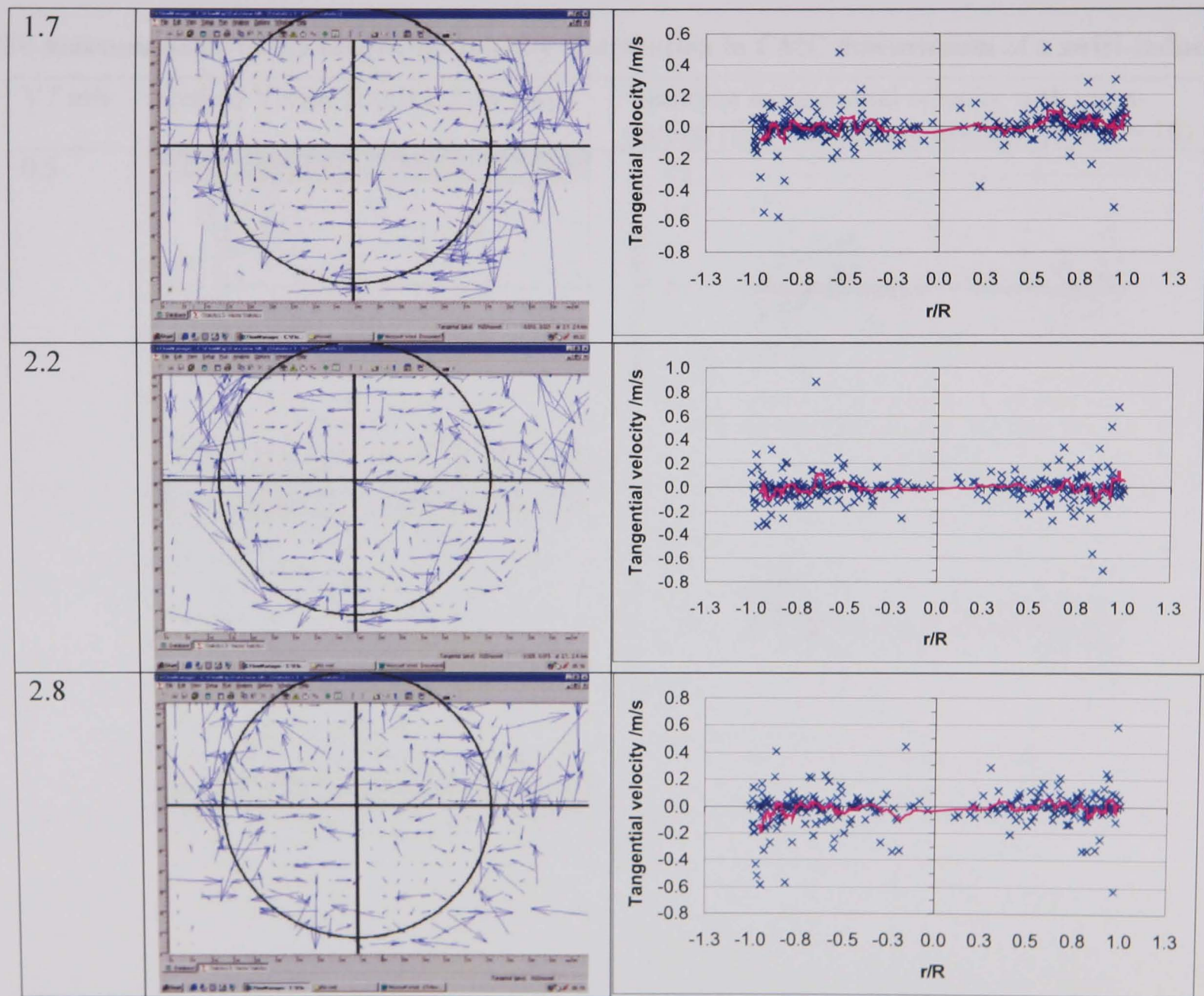
D.12

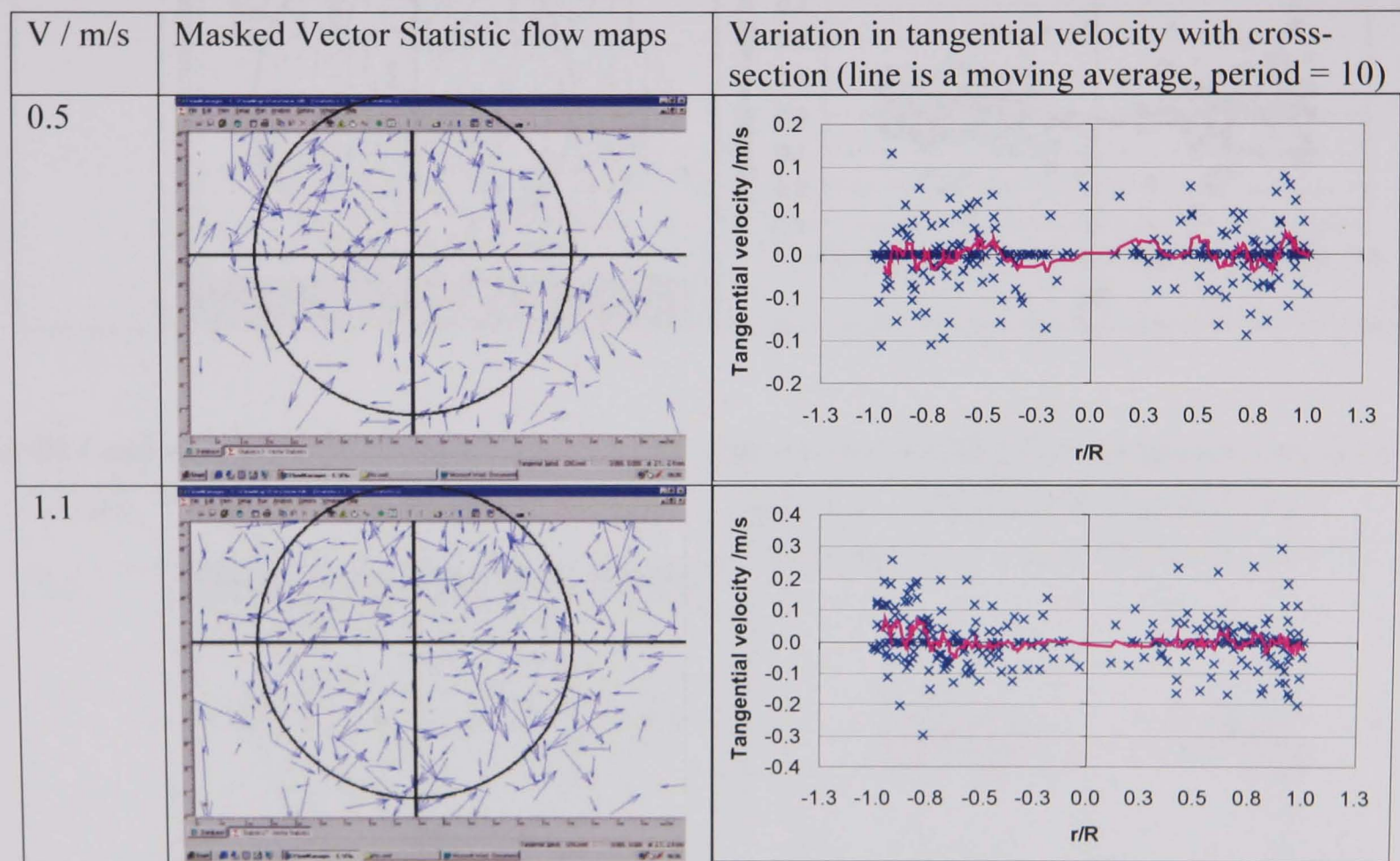


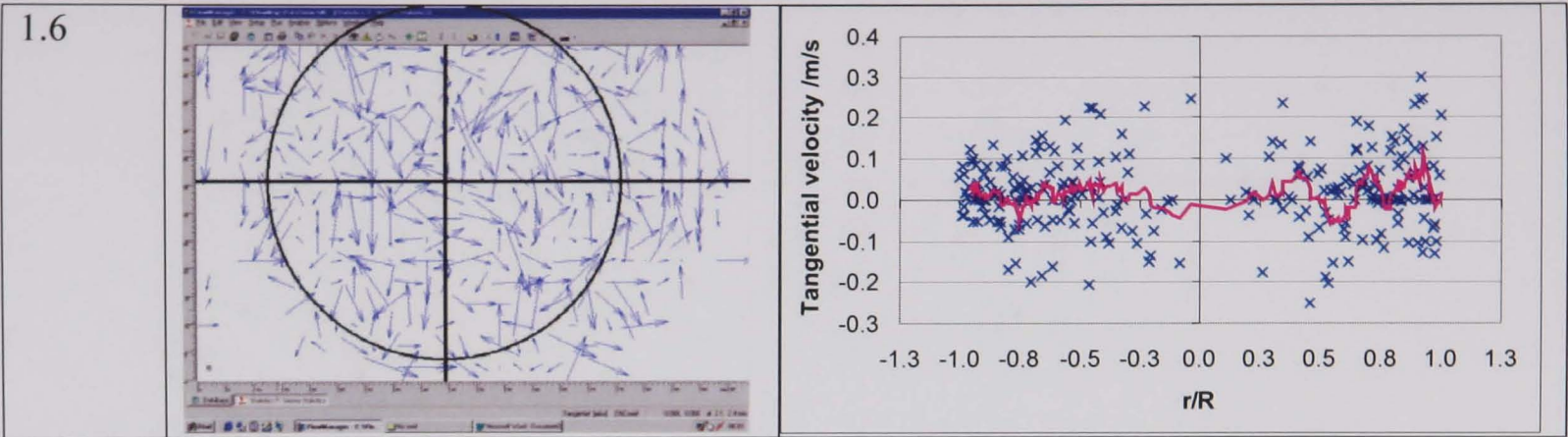
D.13 PIV measurements of the tangential velocity distribution in water downstream of a standard pipe.

V / m/s	Masked Vector Statistic flow maps	Variation in tangential velocity with cross-section (line is a moving average, period = 10)
0.6		
1.1		

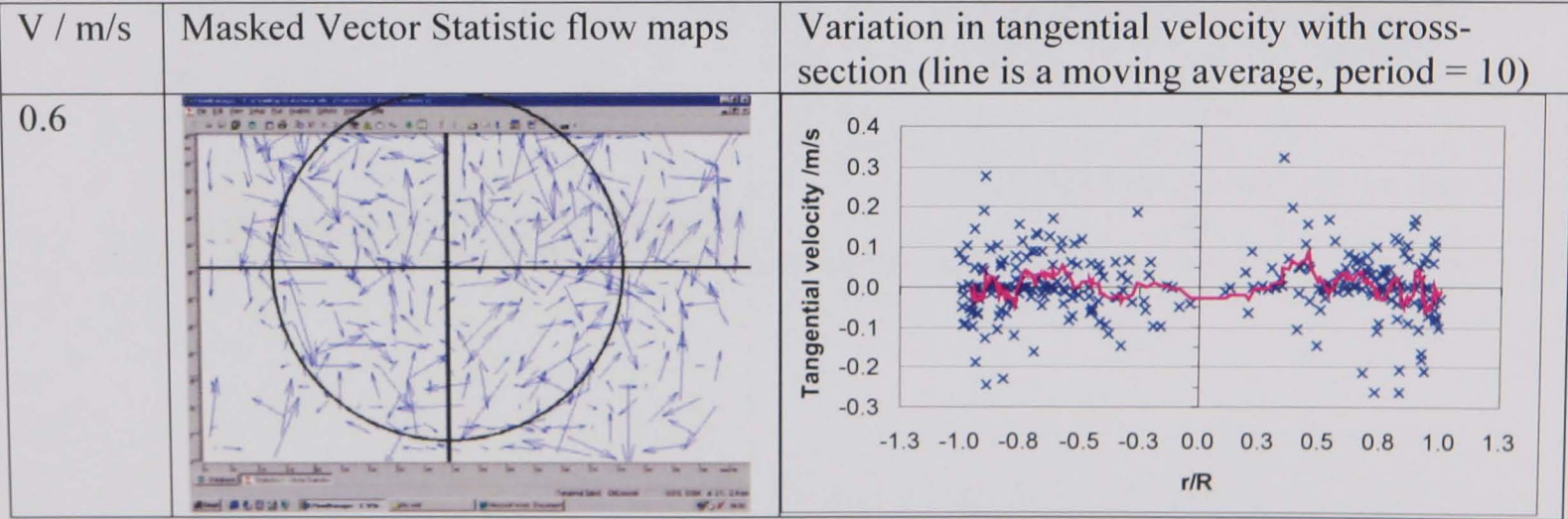
D.13

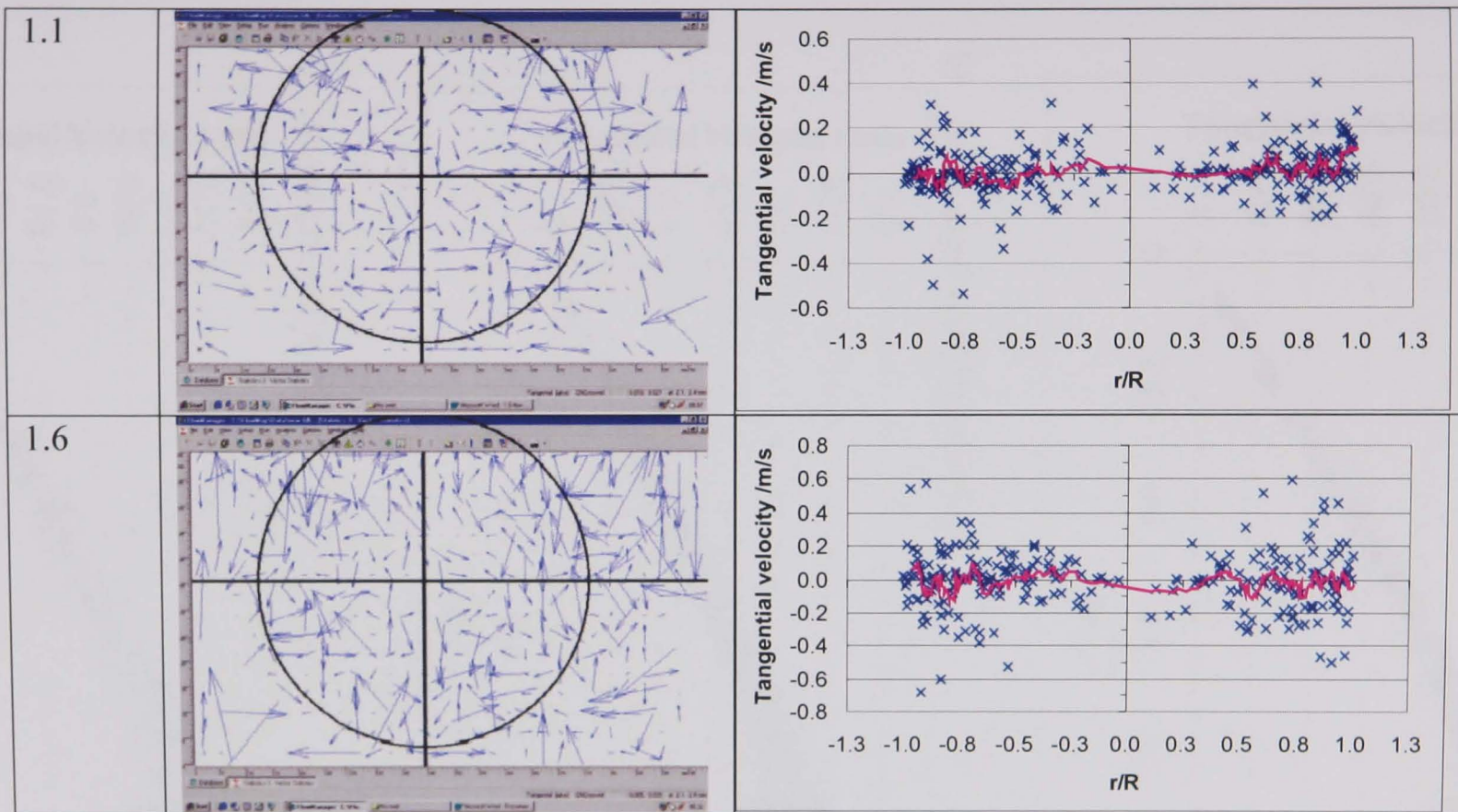


D.14 PIV measurements of the tangential velocity distribution in CMC downstream of a swirl-inducing pipe.



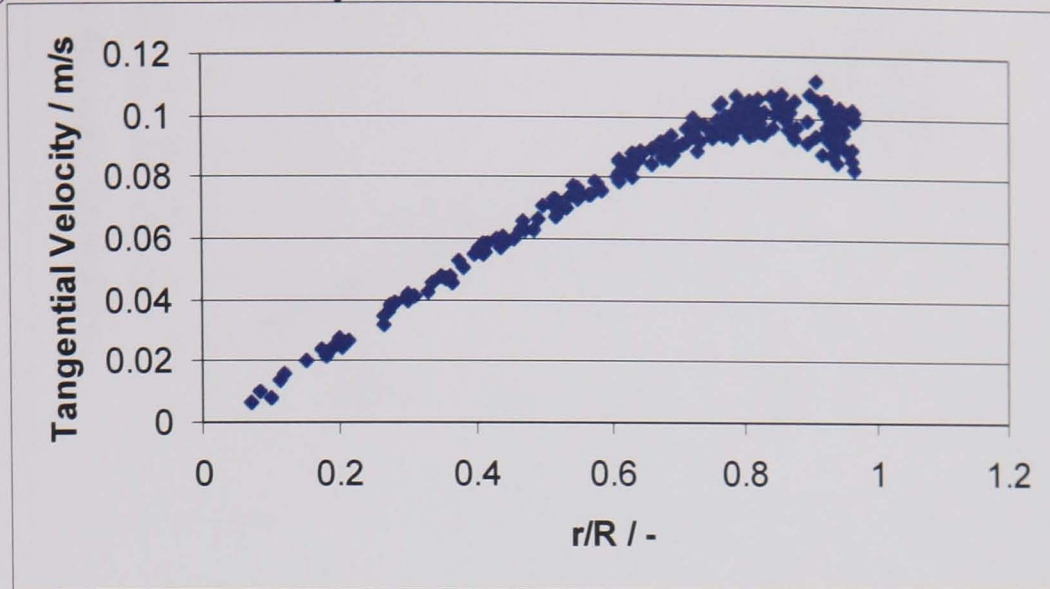
D.15 PIV measurements of the tangential velocity distribution in CMC downstream of a standard pipe.



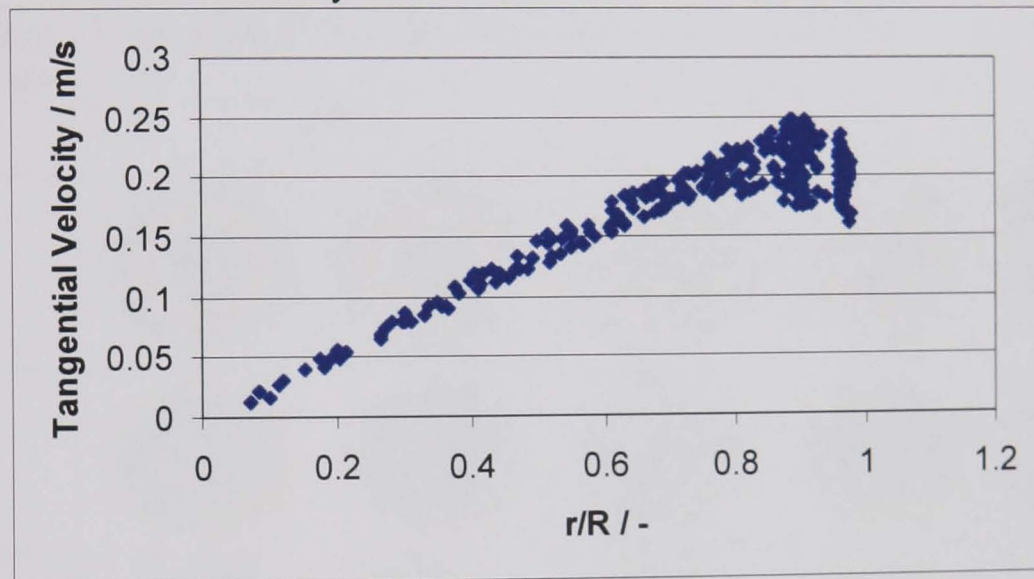


D.16 CFD predictions for the tangential velocity distribution of water 5 diameters downstream of a 4-lobe swirl pipe (performed by Ariyaratne, 2003)

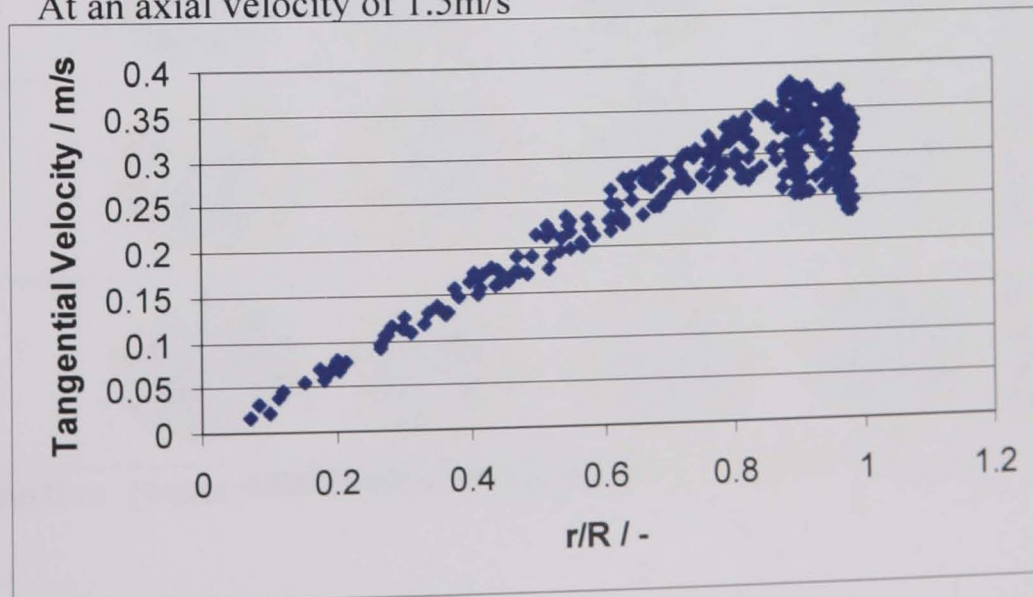
a) At an axial velocity of 0.5m/s



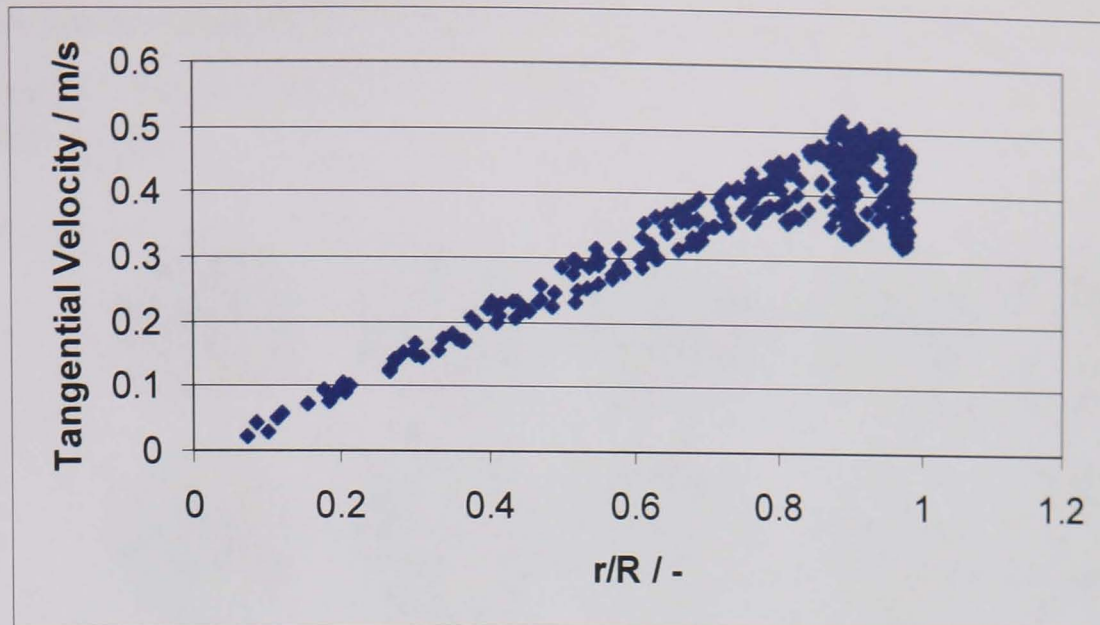
b) At an axial velocity of 1.0m/s



c) At an axial velocity of 1.5m/s



d) At an axial velocity of 2.0m/s

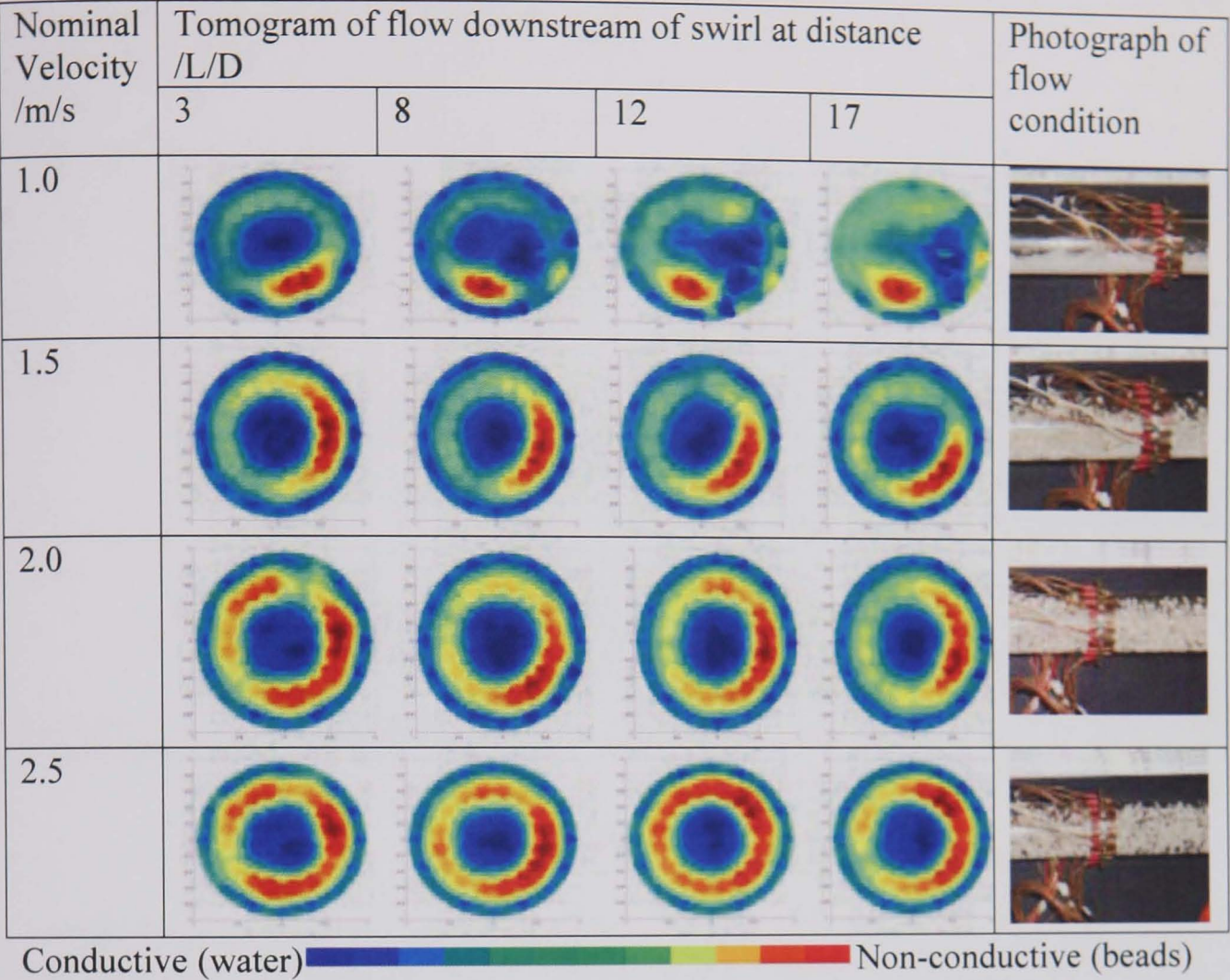


D.17 Tomograms and photos of the flow condition at various velocities and downstream distances from swirl pipe, with a bead concentration of 1.4% v/v

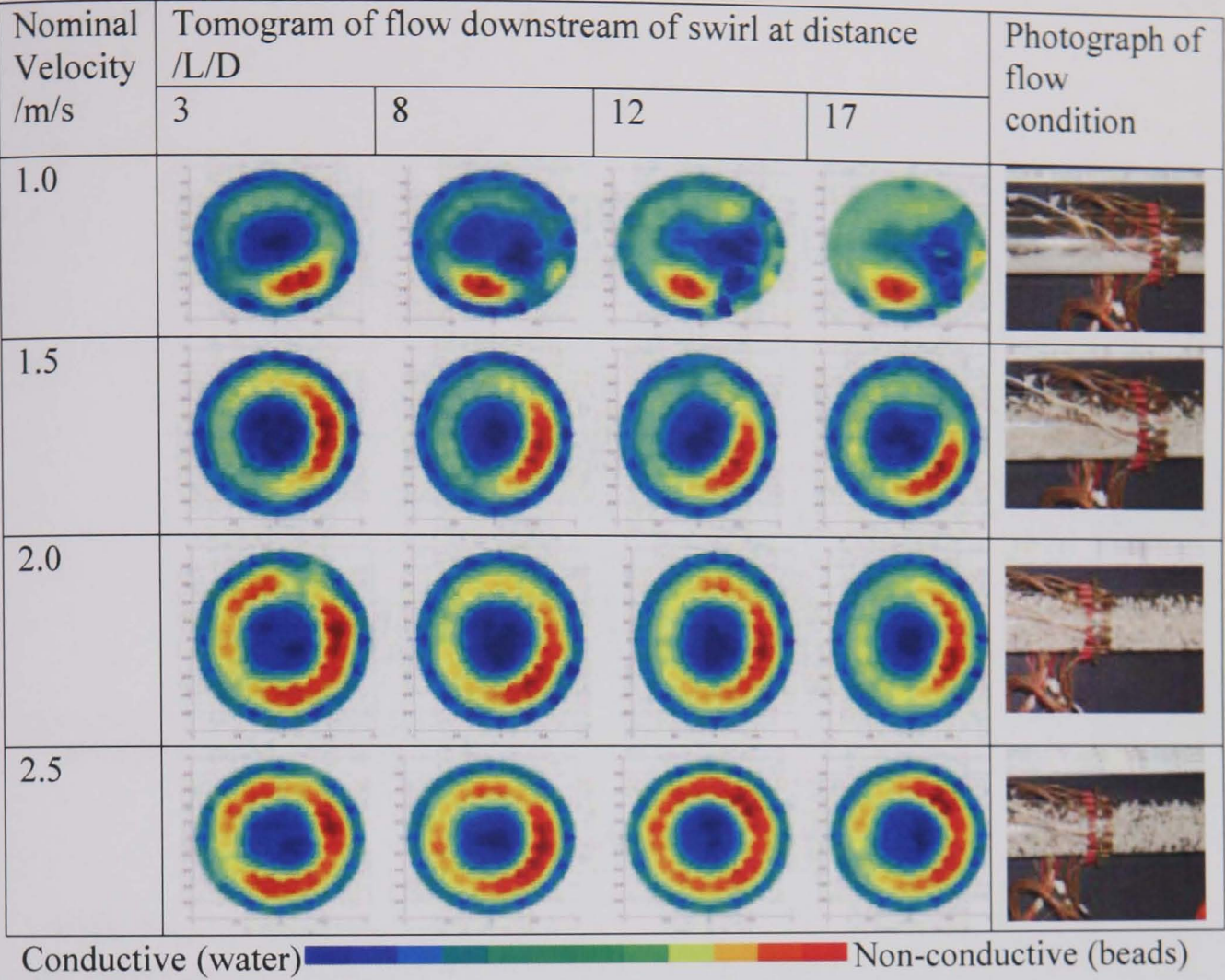
Nominal Velocity /m/s	Tomogram of flow downstream of swirl at distance /L/D				Photograph of flow condition
	3	8	12	17	
0.5					
1.0					
1.5					
2.0					
2.5					

Conductive (water) Non-conductive (beads)

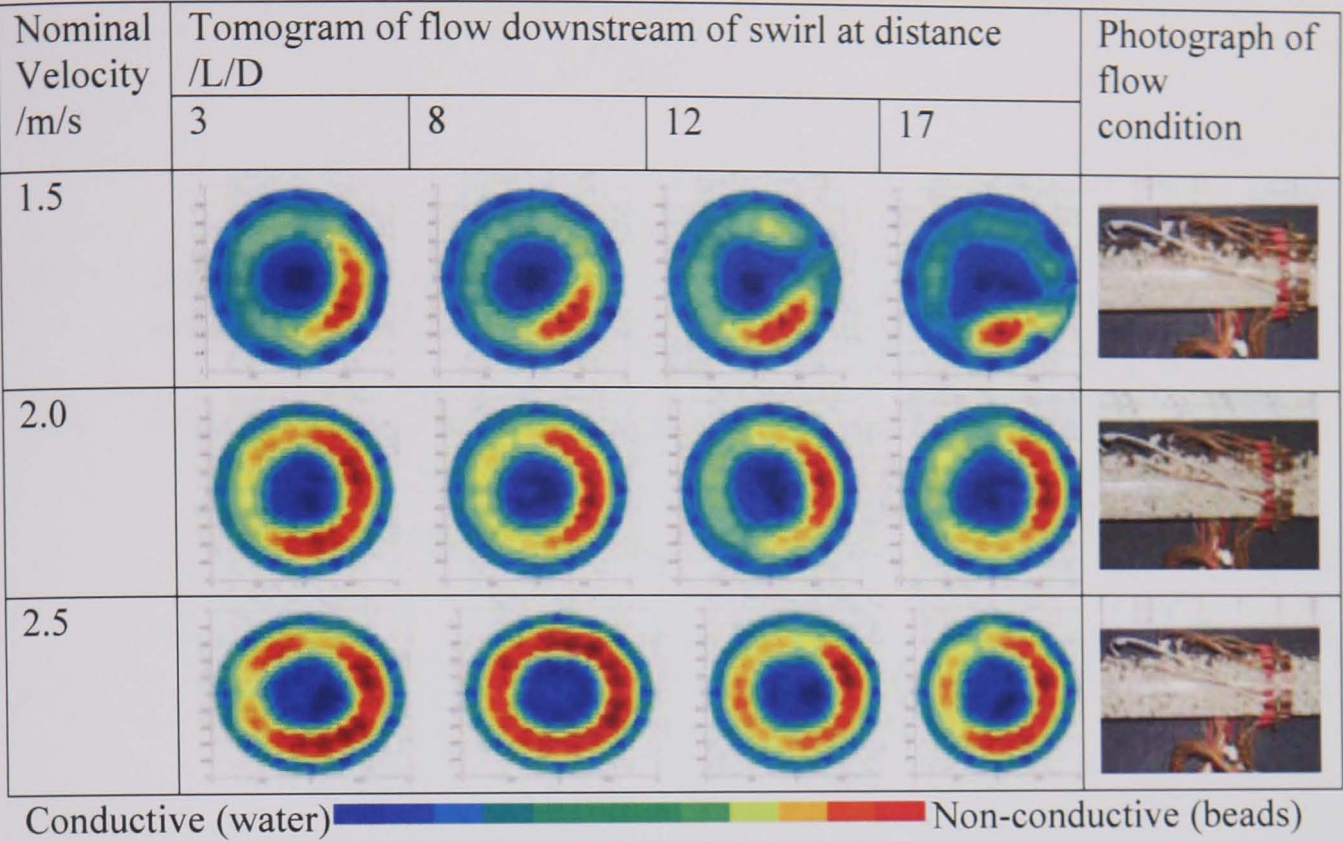
D.18 Tomograms and photos of the flow condition at various velocities and downstream distances from swirl pipe, with a bead concentration of 2.0% v/v



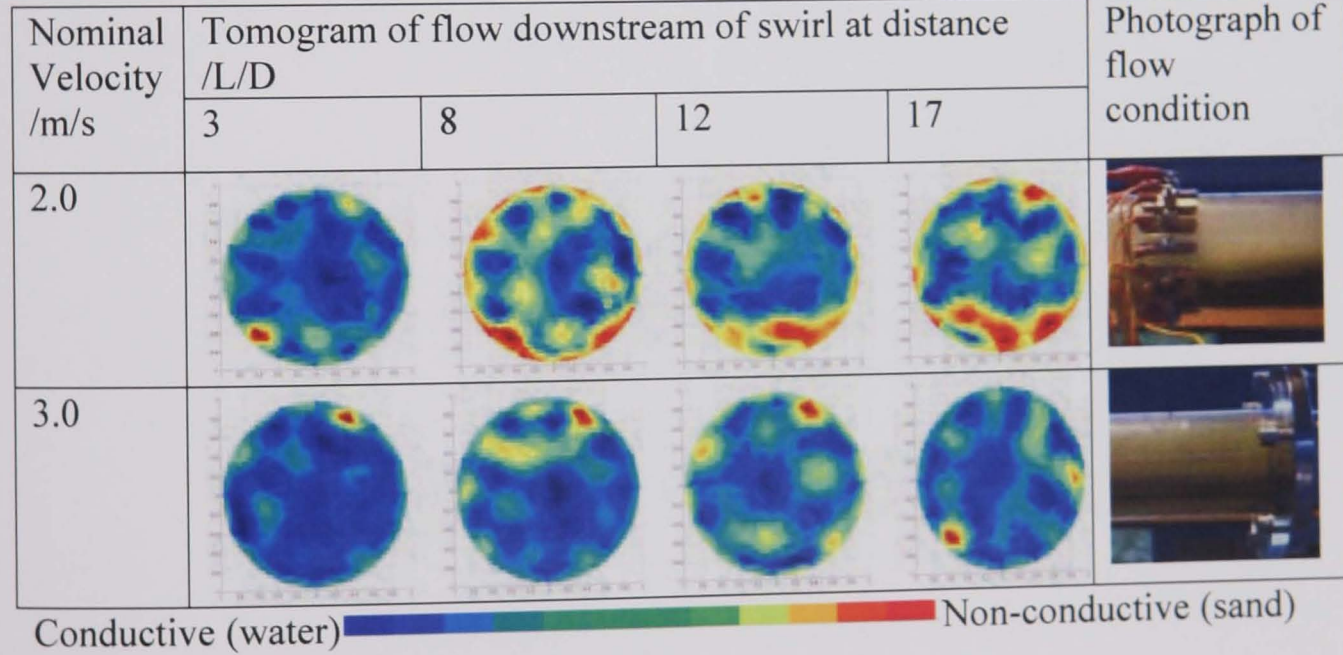
D.18 Tomograms and photos of the flow condition at various velocities and downstream distances from swirl pipe, with a bead concentration of 2.0% v/v



D.19 Tomograms and photos of the flow condition at various velocities and downstream distances from swirl pipe, with a bead concentration of 2.7% v/v



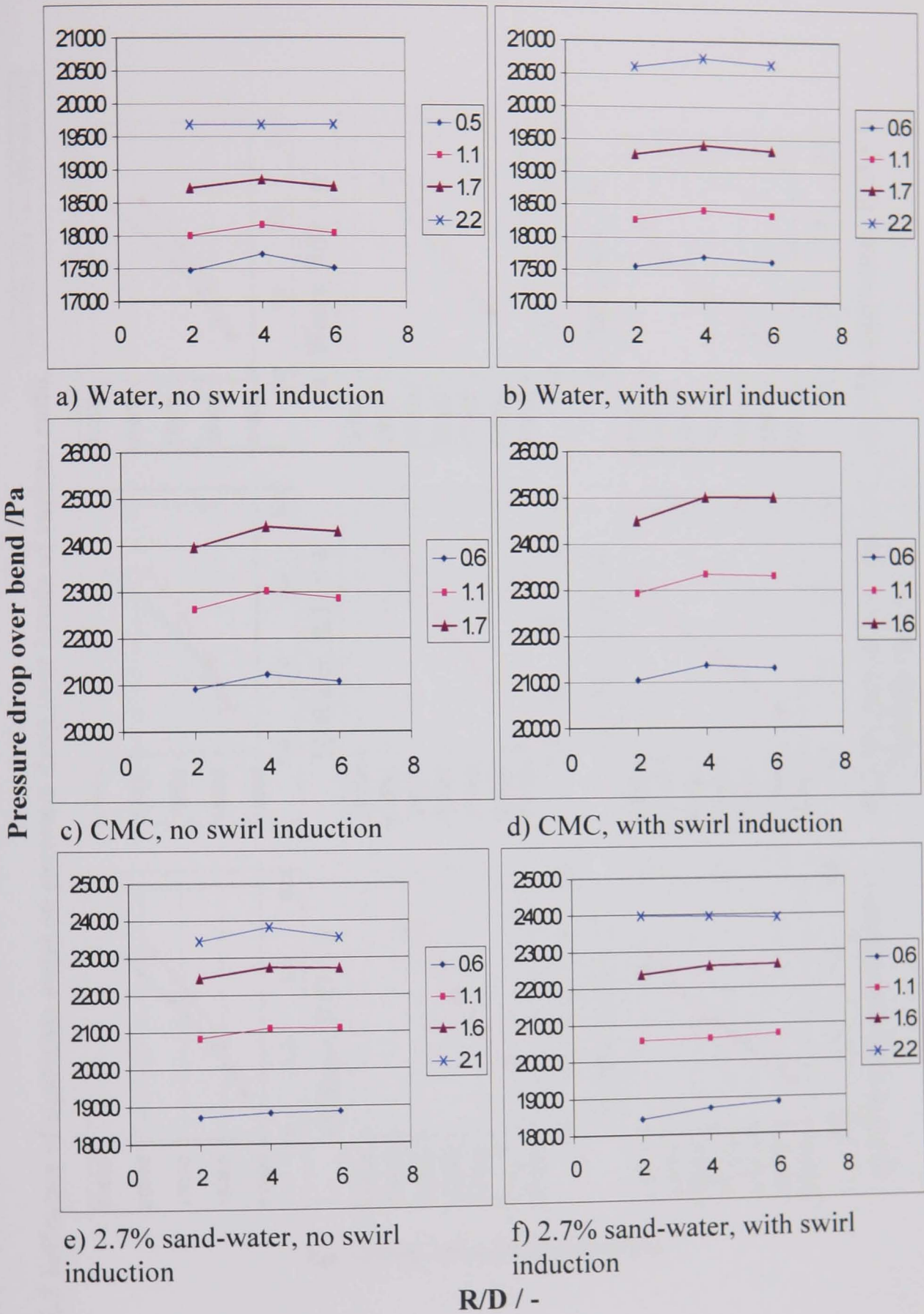
D.20 Tomograms and photos of the flow condition at various velocities and downstream distances from swirl pipe, with a bead concentration of 0.7% v/v



Appendix E. EFFECT OF SWIRL INDUCTION BEFORE BENDS

- E.1 Influence of radius of curvature of a bend on pressure drop over the bend with and without upstream swirl induction
- E.2 Influence of upstream swirl on pressure drop over bends of various radii

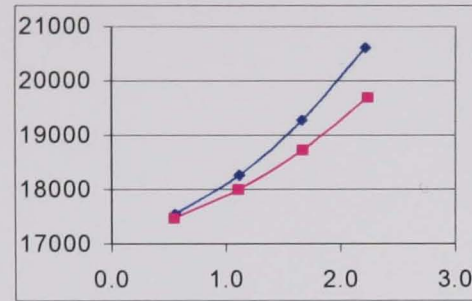
E.1 Influence of radius of curvature of a bend on pressure drop over the bend with and without upstream swirl induction at various velocities.



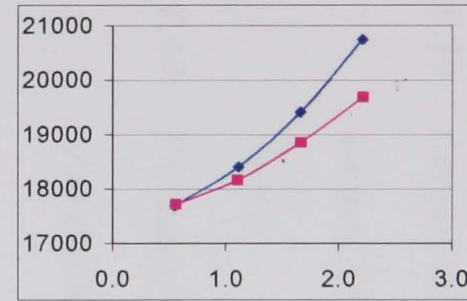
E.2 Influence of upstream swirl on pressure drop over bends of various radii.

—●— With swirl —■— Without swirl

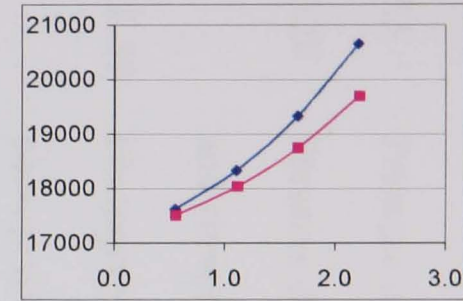
Pressure drop over bend / Pa



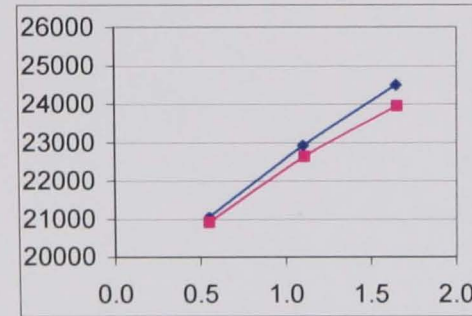
a) Water, R/D = 2



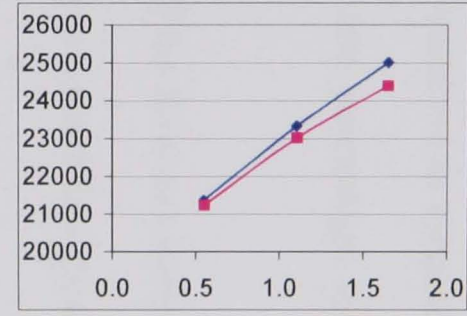
b) Water, R/D = 4



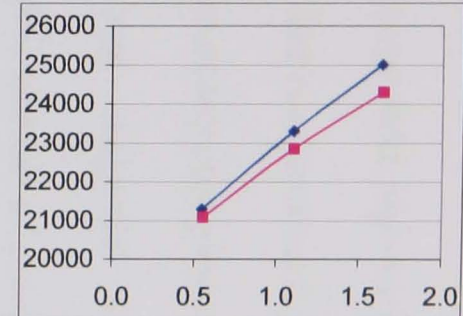
c) Water, R/D = 6



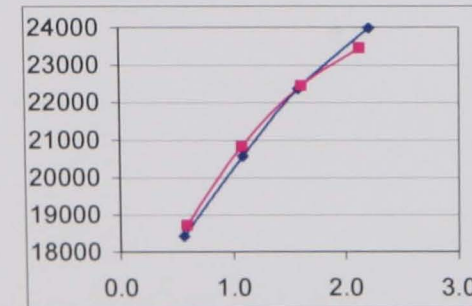
d) CMC, R/D = 2



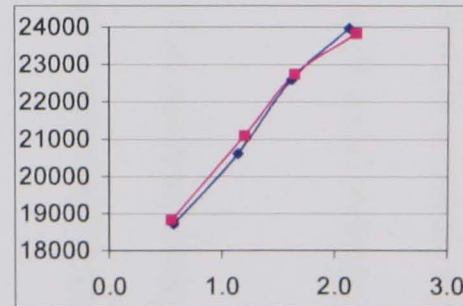
e) CMC, R/D = 4



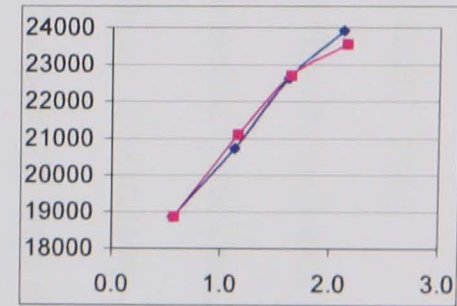
f) CMC, R/D = 6



g) 2.7% sand-water, R/D = 2



h) 2.7% sand-water, R/D = 4



i) 2.7% sand-water, R/D = 6

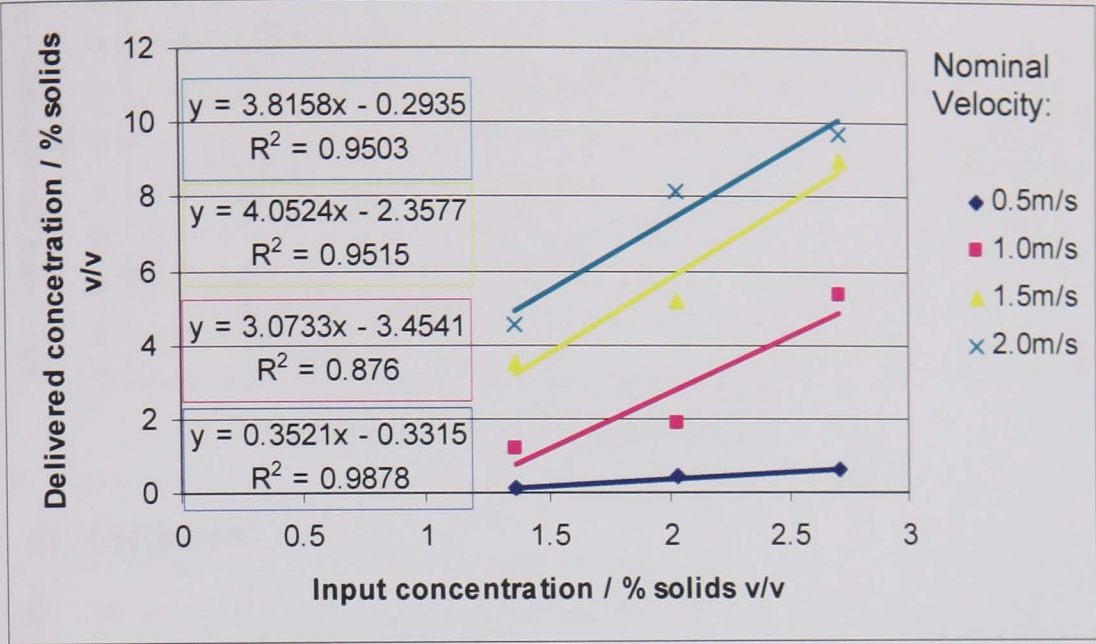
Velocity / m/s

Appendix F. EFFECT OF SWIRL ON SETTLING SLURRIES

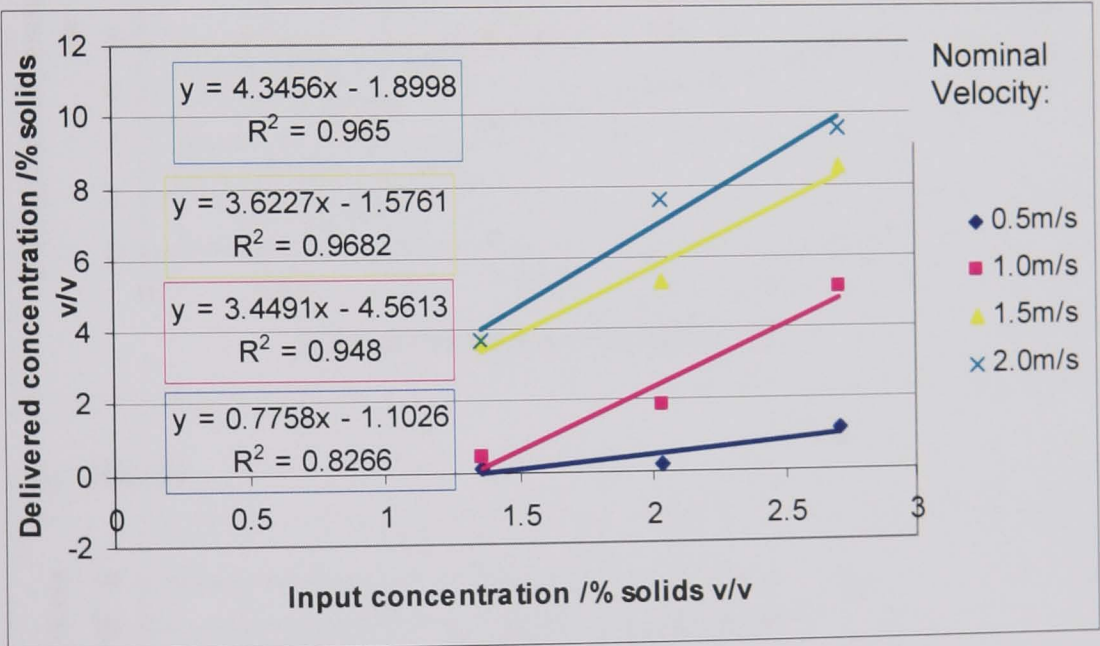
- F.1 Results of the concentration measurements
- F.2 – F.5 Pressure drop over swirl pipe for each slurry / fluid
- F.6 – F.20 Pressure drop and cost over each geometry for each slurry / fluid
and comparison of selected pressure loss data (after Durand, 1953)
- F.21 – F.30 Photographs and tangential velocities determined from the
photographs, downstream of a swirl flow pipe, for each slurry
- F.31 – F.39 Graphs of the variation in tangential velocity (central, top RHS and
bottom LHS) and percentage decay with axial velocity, for each
slurry
- F.40 – F.49 Photographs of the flow downstream of an inclined section of pipe
with and without a swirl flow pipe section included for each slurry

F.1 Results of the concentration measurements

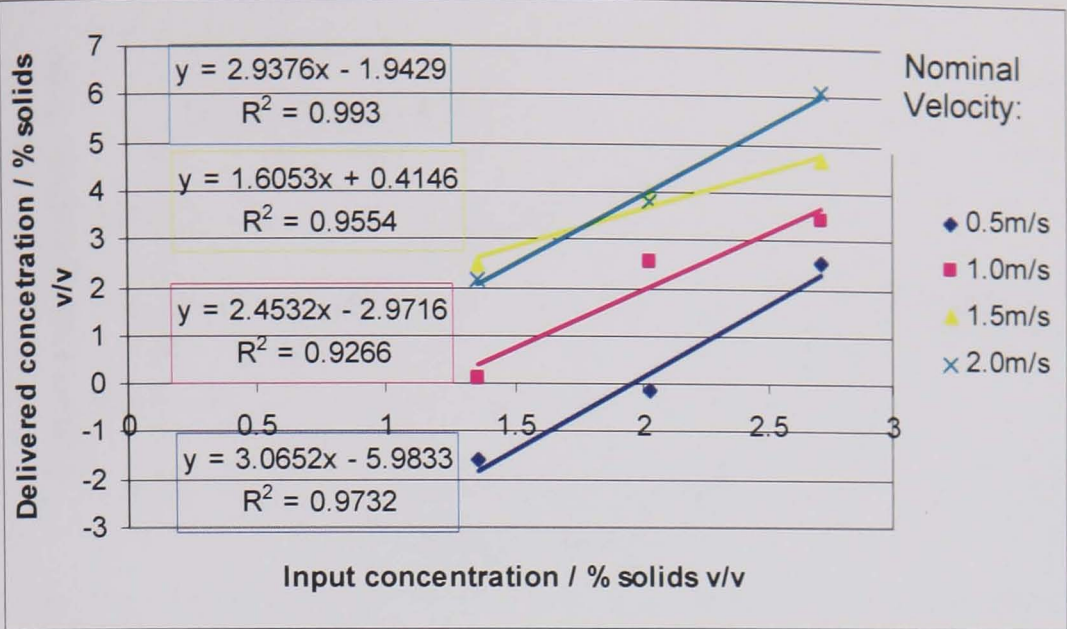
a) Medium sand



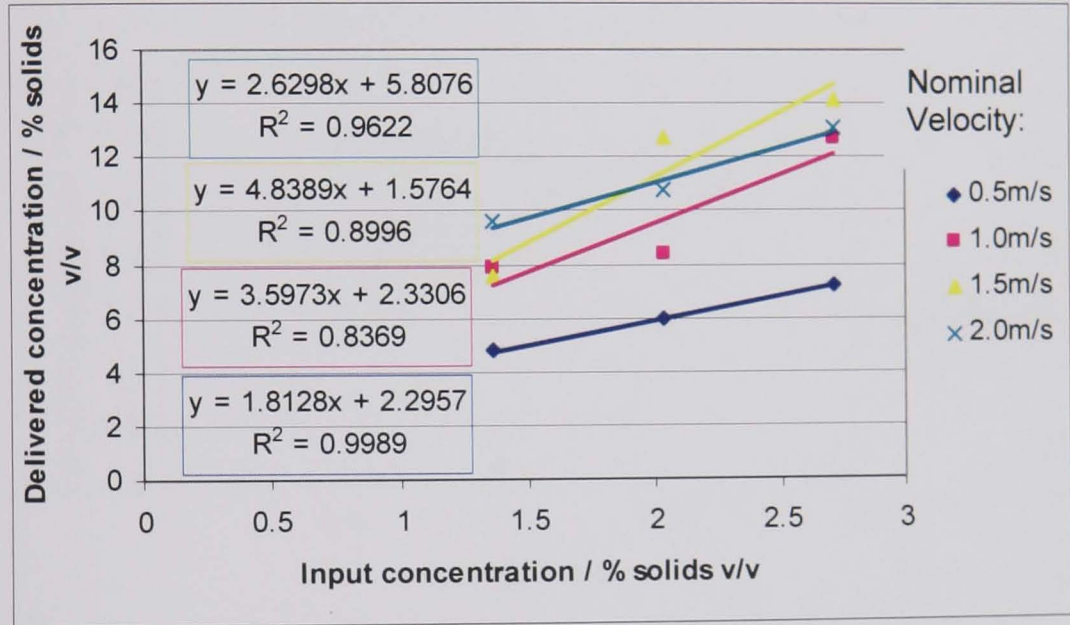
b) Coarse sand



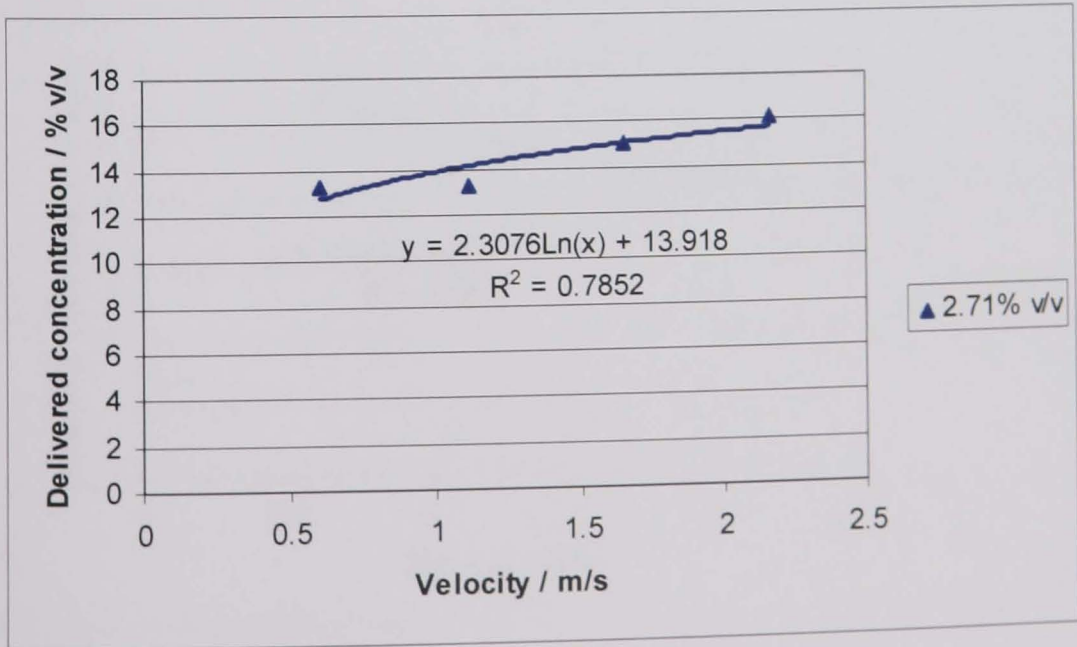
c) Coarse coal



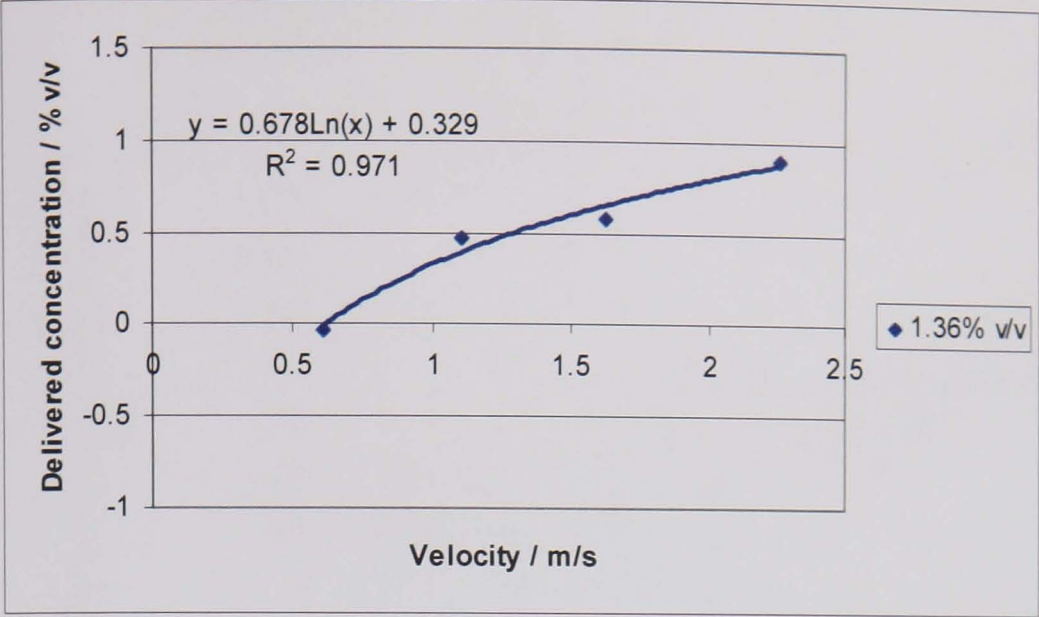
d) Large coal



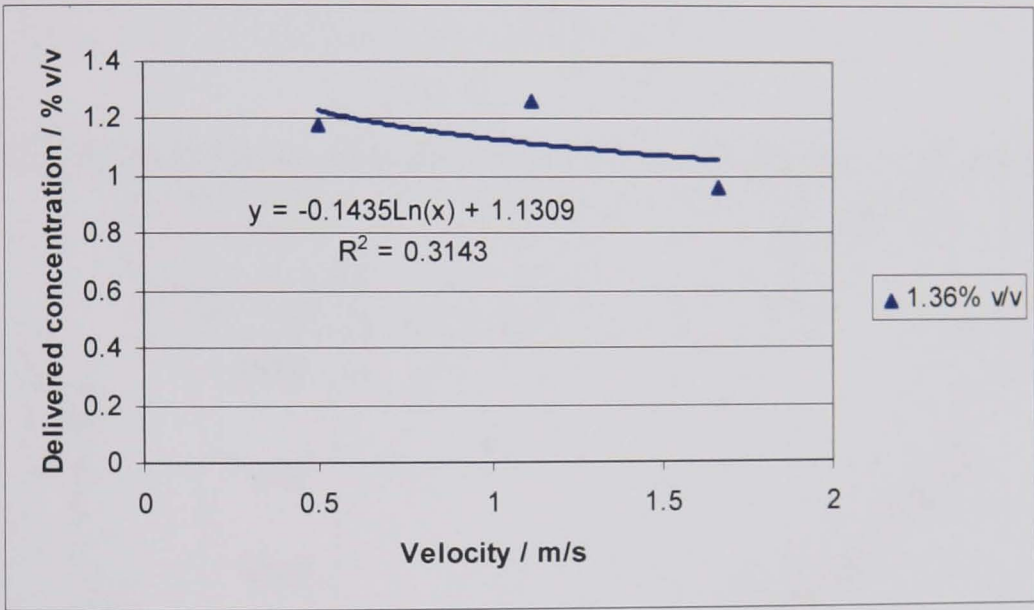
e) Beads



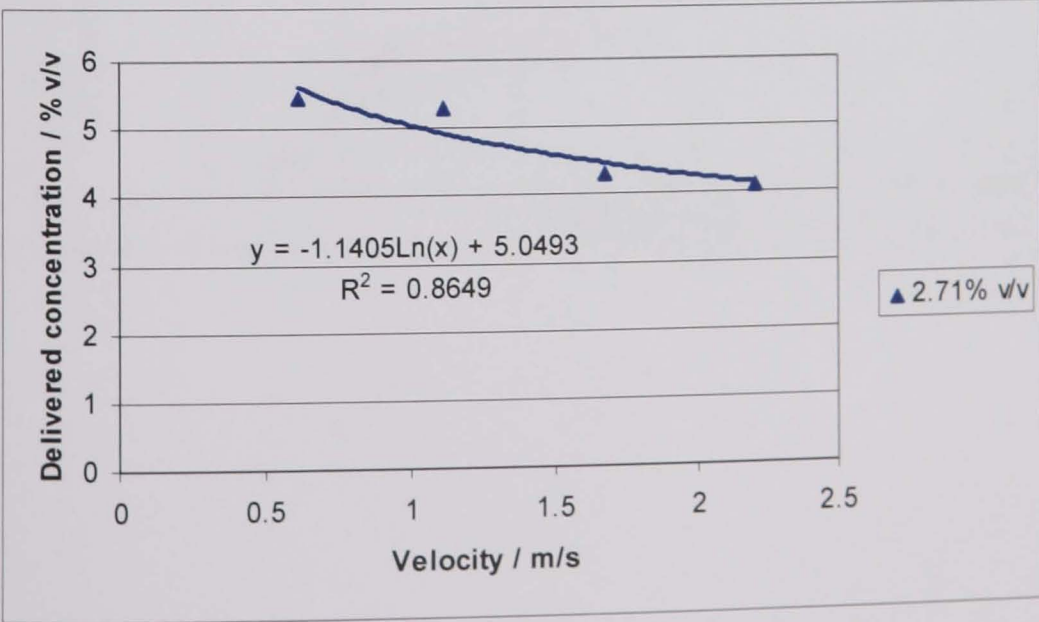
f) Coarse magnetite



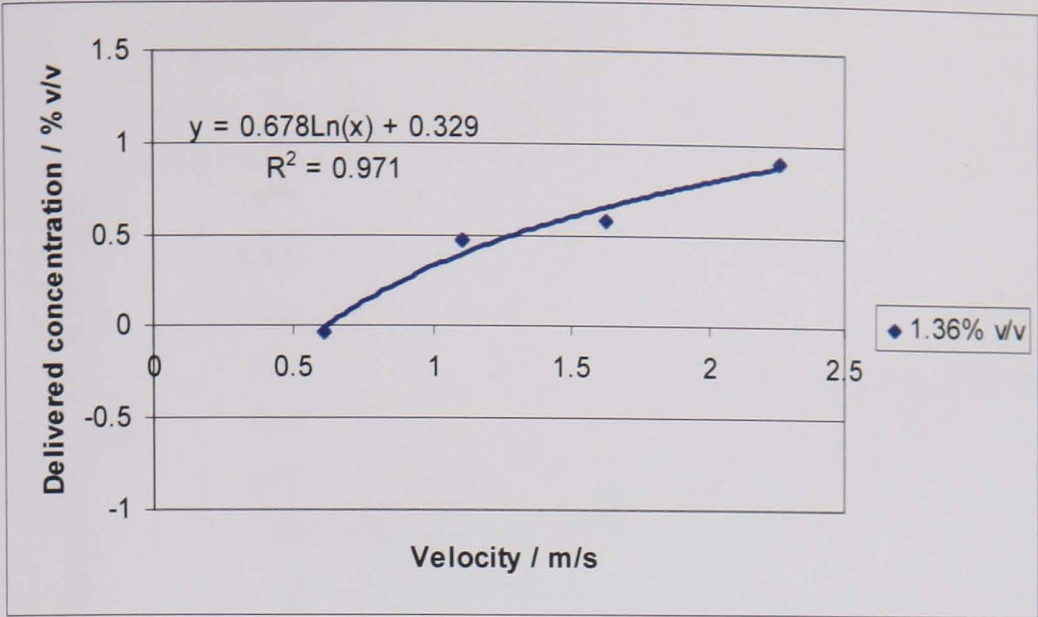
g) CMC and coarse sand



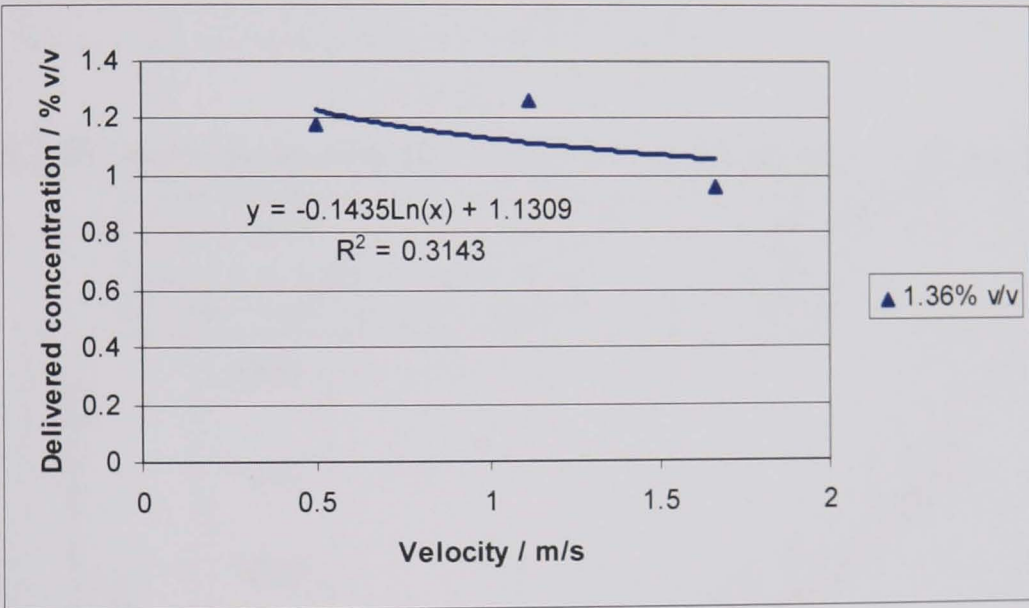
h) Fine sand



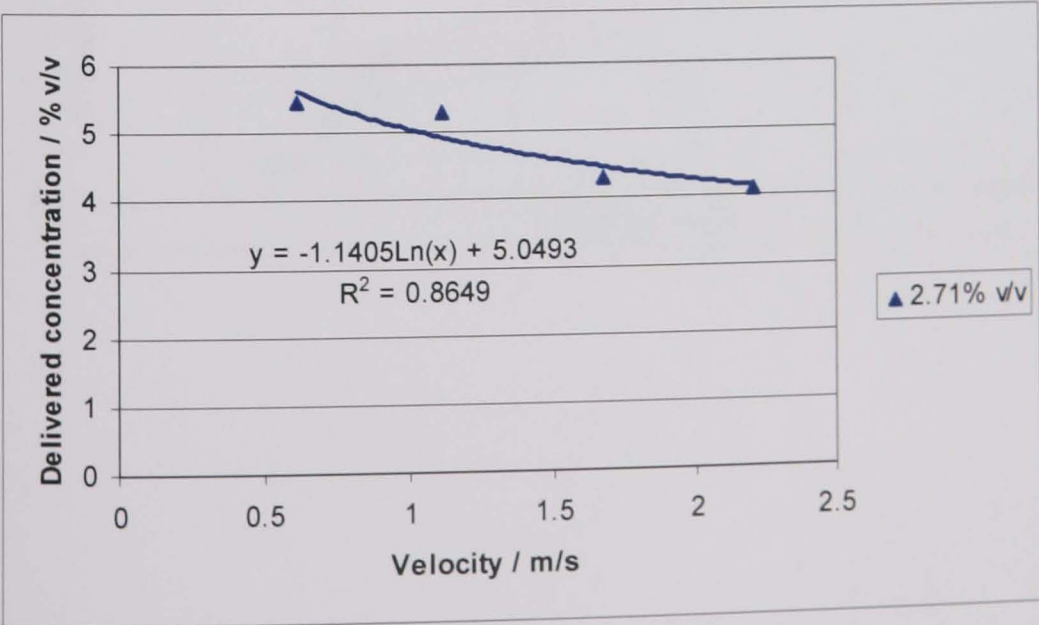
f) Coarse magnetite



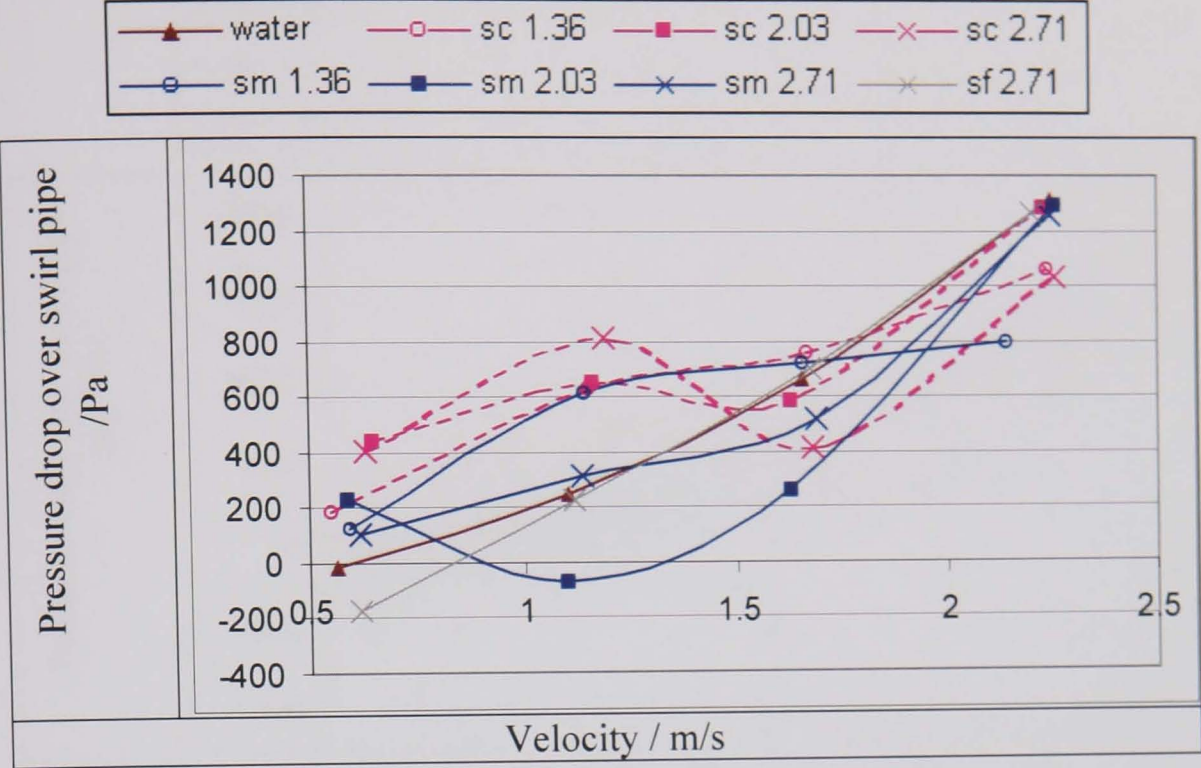
g) CMC and coarse sand



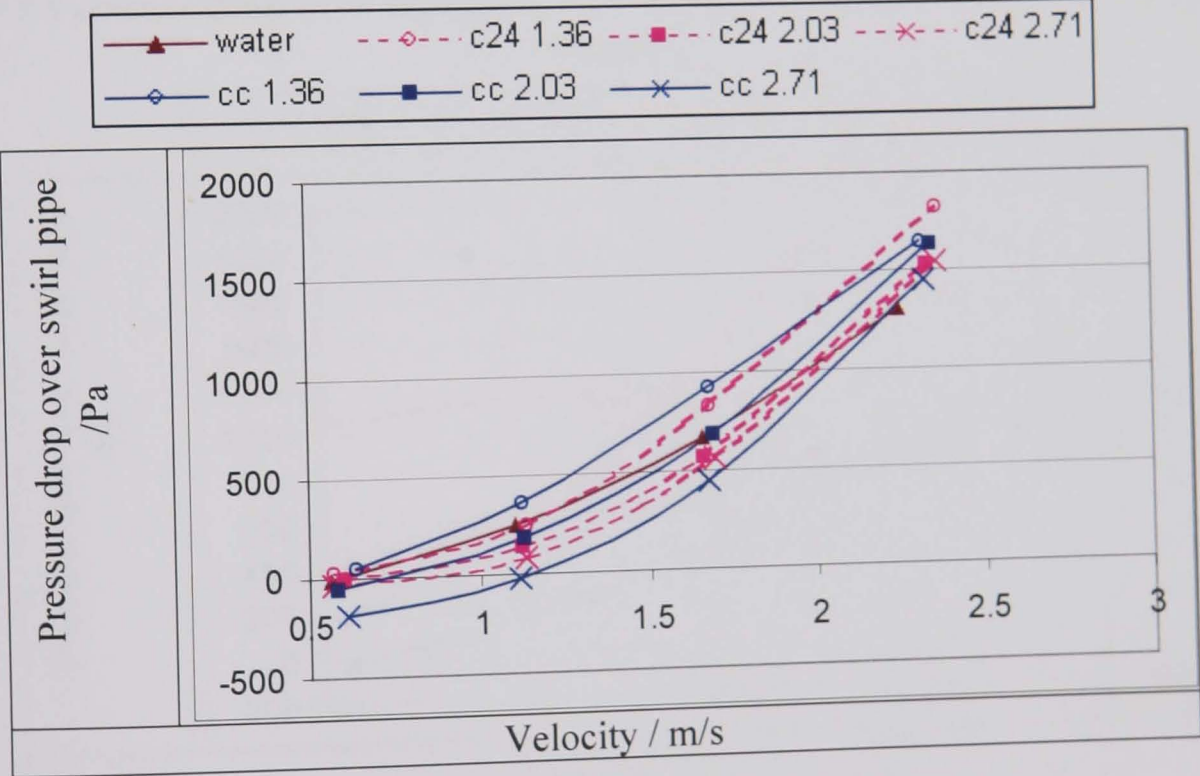
h) Fine sand



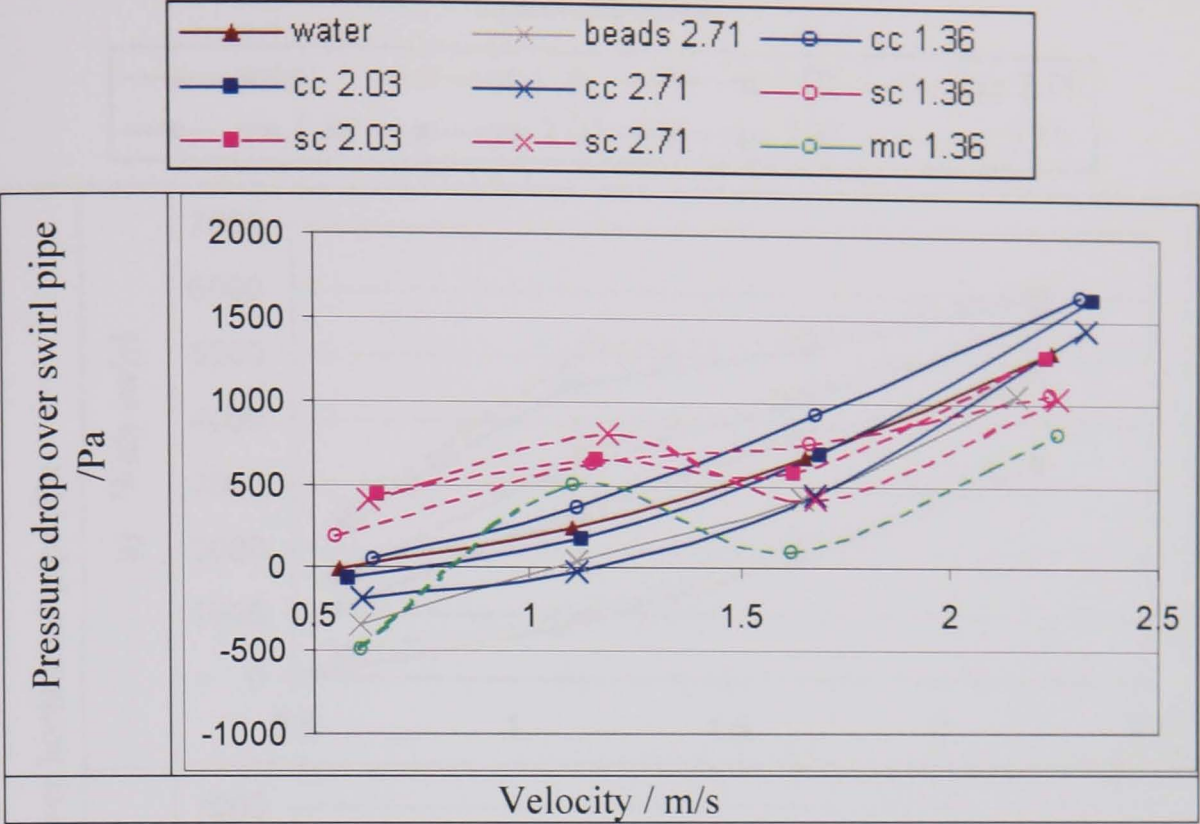
F.2 Pressure drop over swirl pipe for sand slurries of various particle sizes.



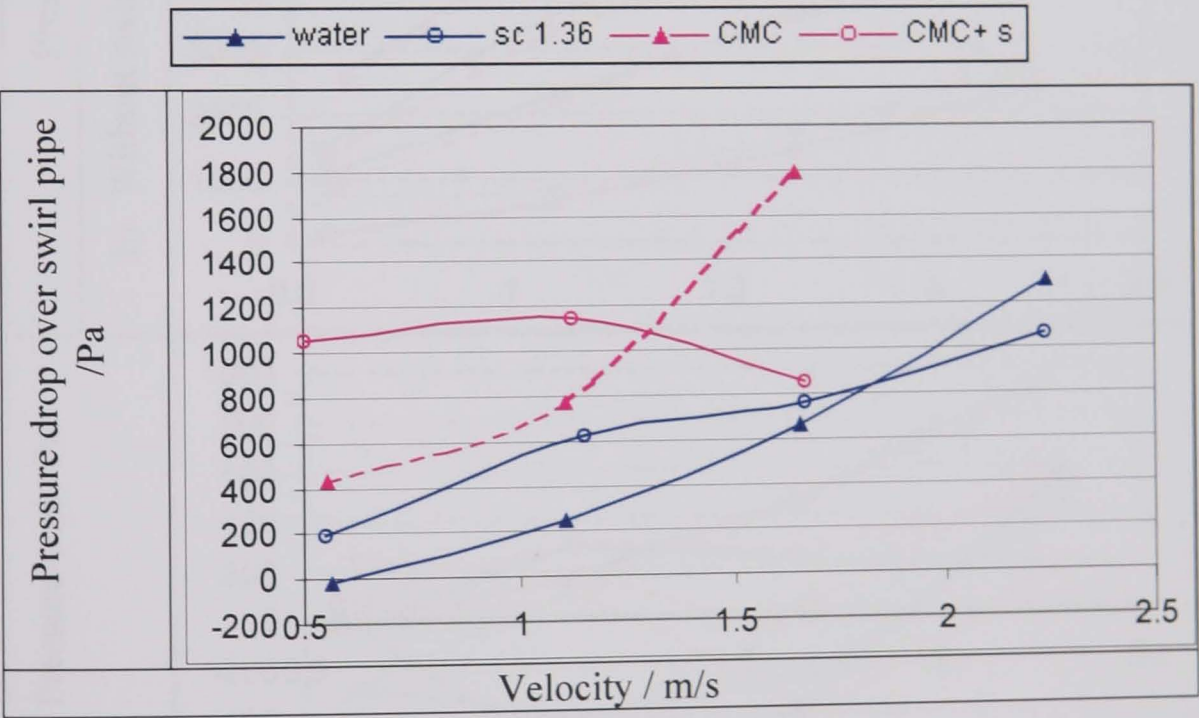
F.3 Pressure drop over swirl pipe for coal slurries of various particle sizes.



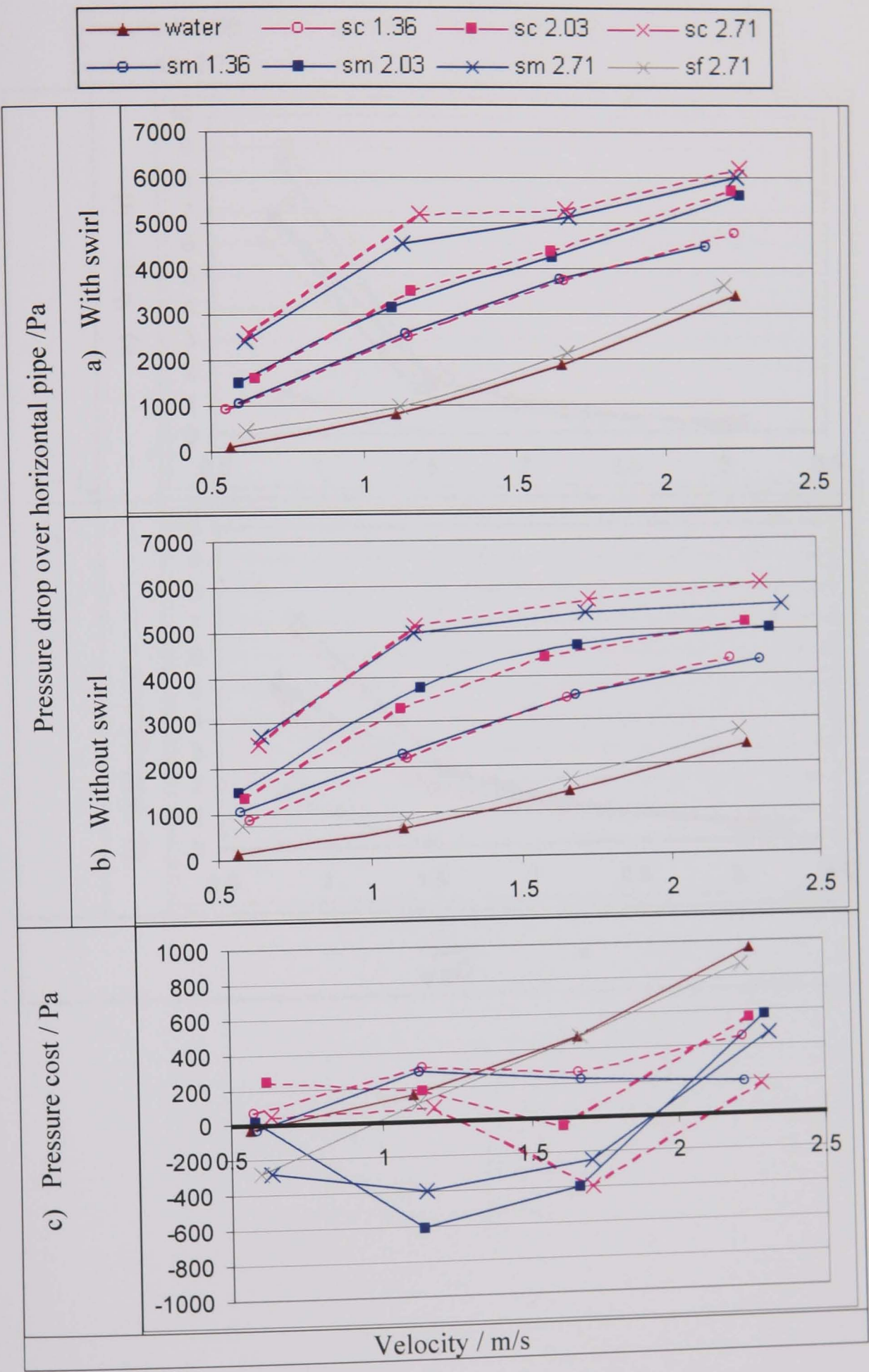
F.4 Pressure drop over swirl pipe for slurries of various densities.



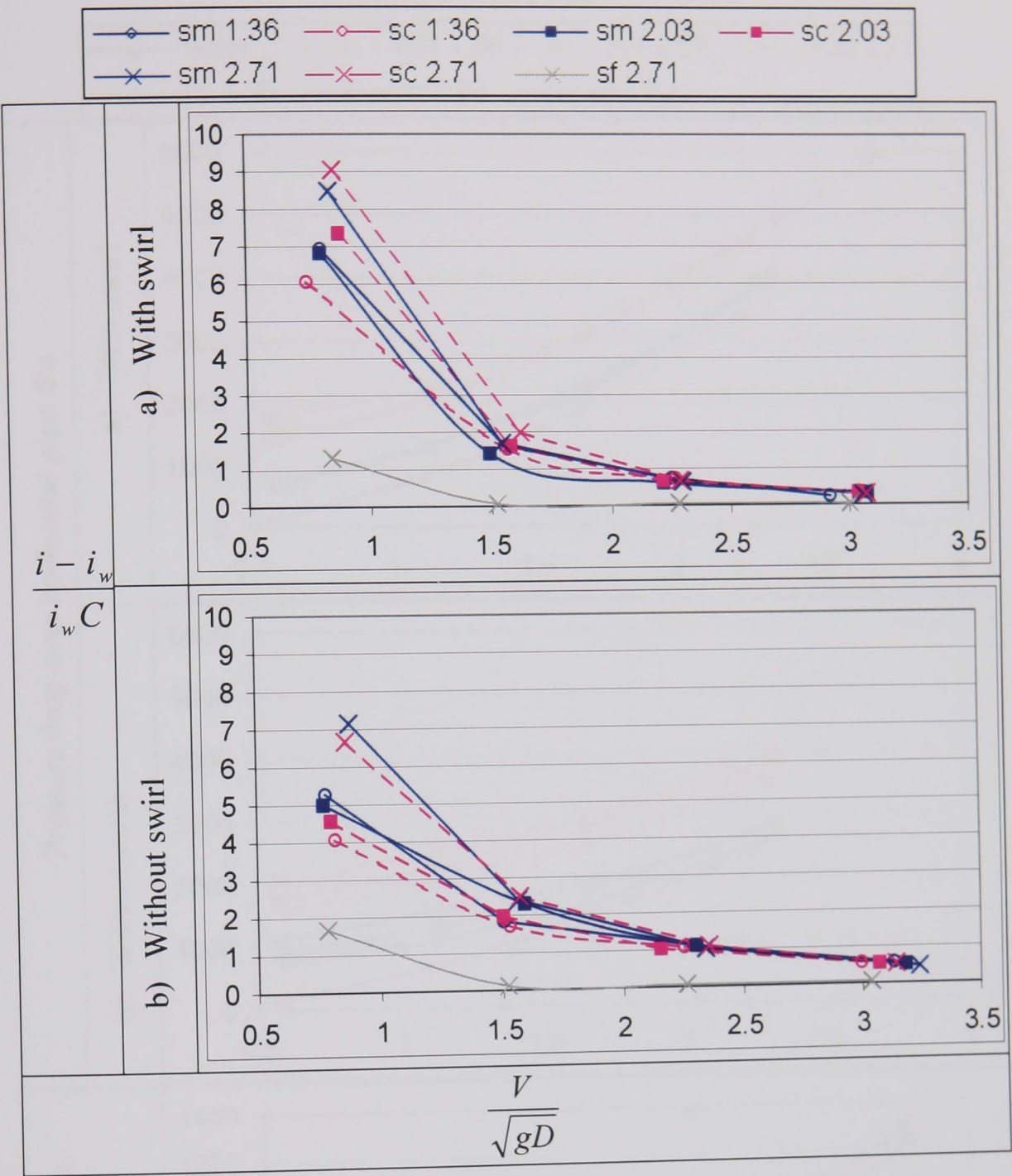
F.5 Pressure drop over swirl pipe for slurries with carrier fluids of various viscosity.



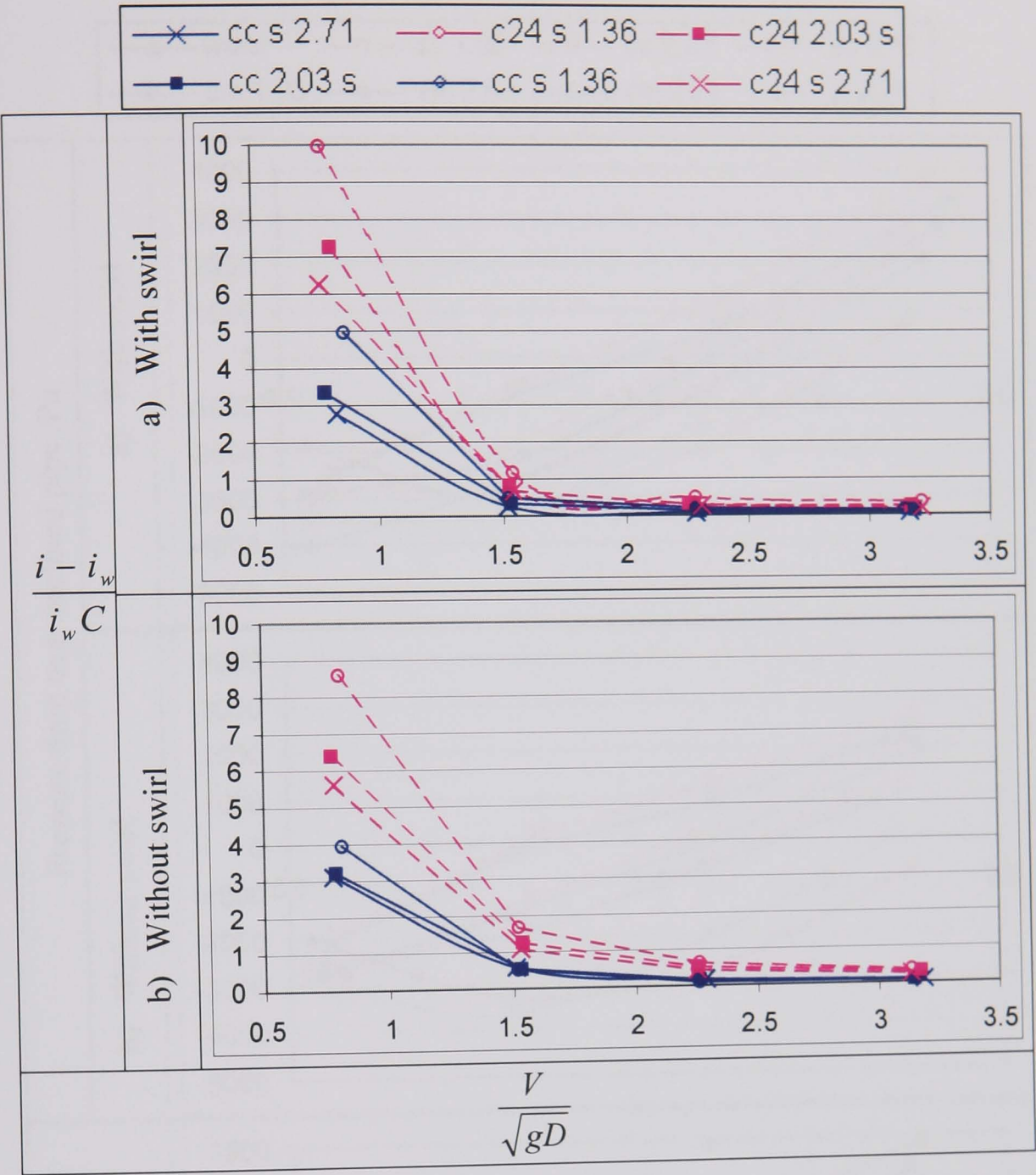
F.6 Pressure drop and cost over horizontal pipes for sand slurries of various particle sizes.



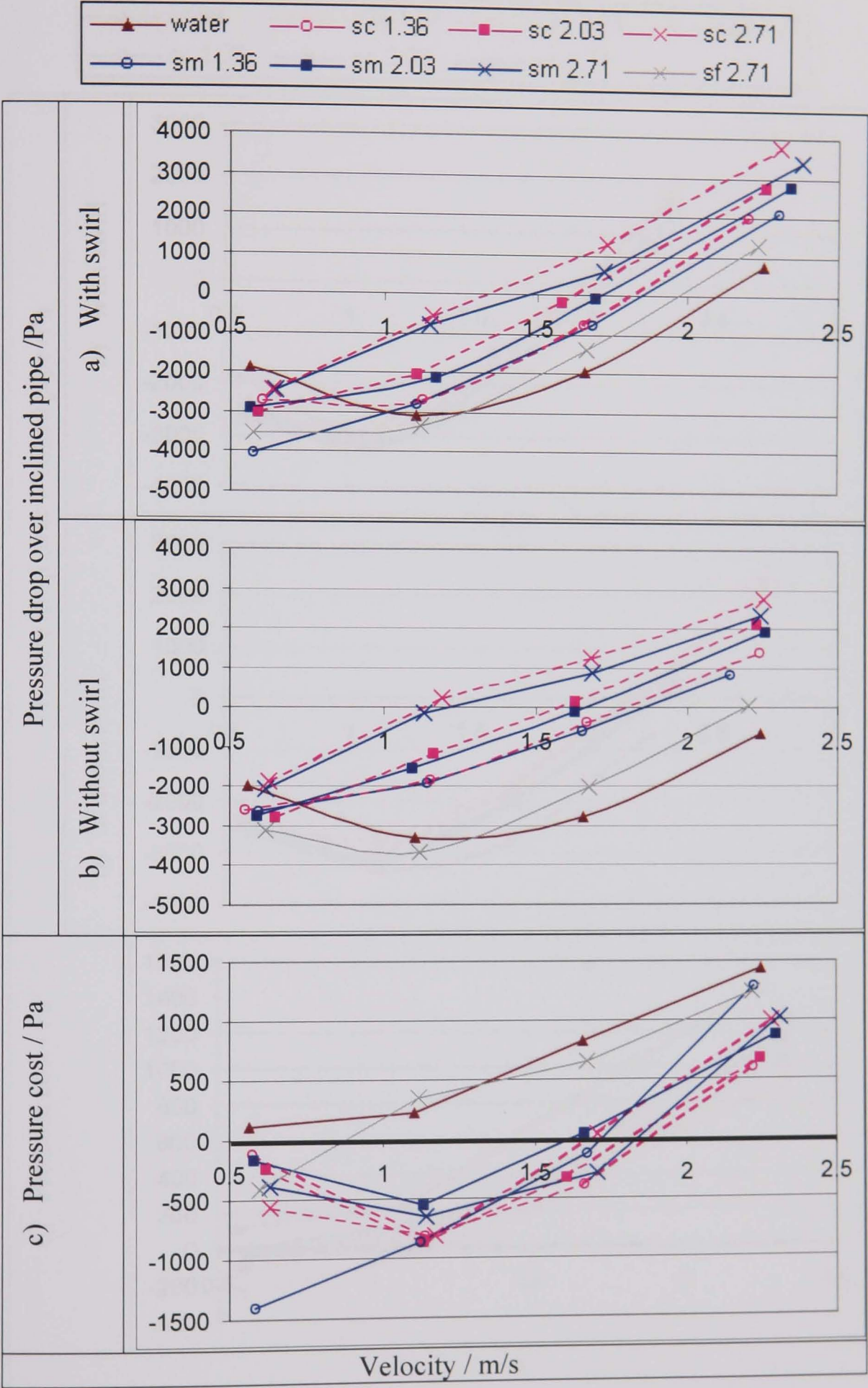
F.7 Comparison of pressure loss over horizontal pipes, for sand slurries of various particle size (after Durand, 1953)



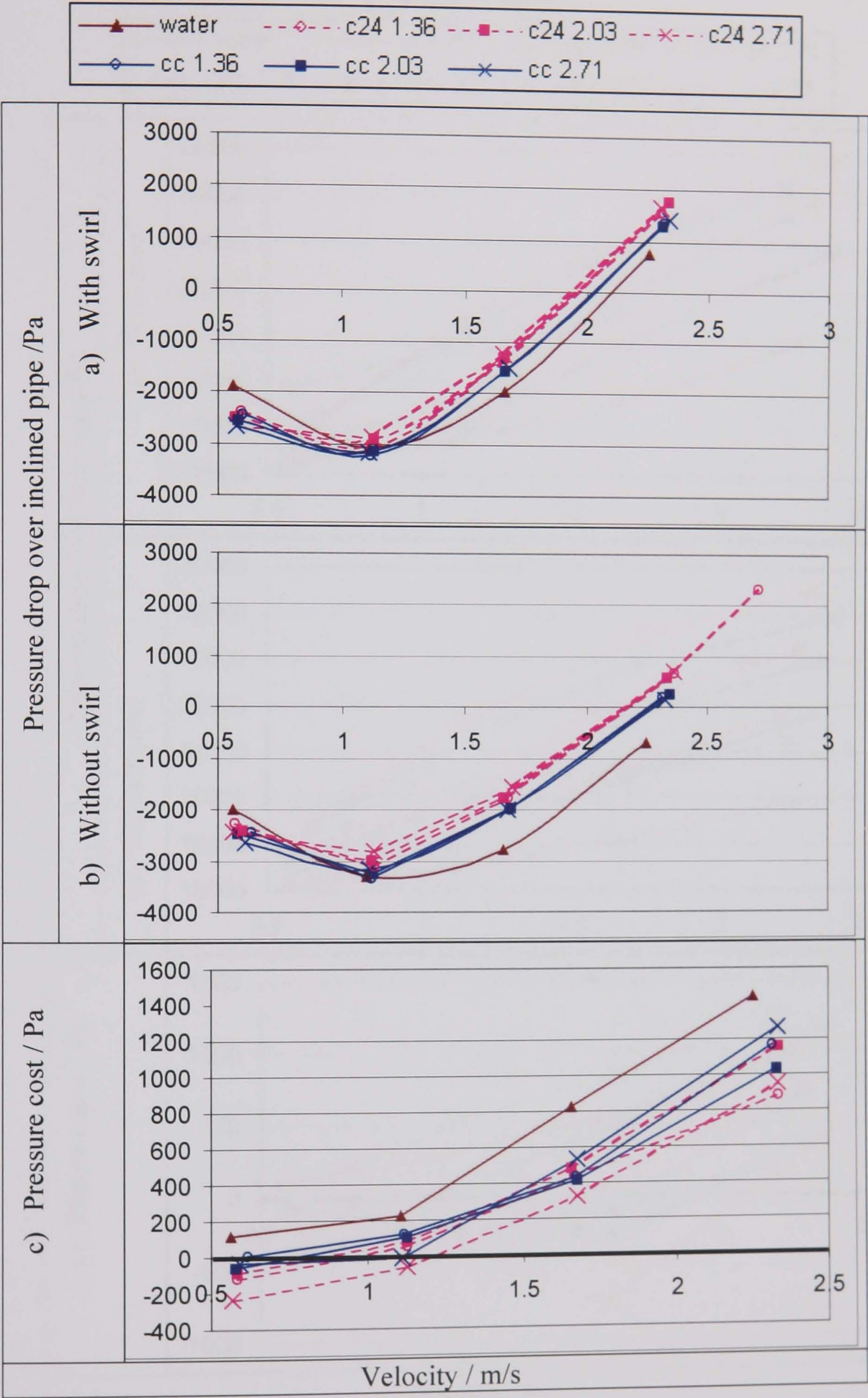
F.9 Comparison of pressure loss over horizontal pipes, for coal slurries of various particle size (after Durand, 1953)



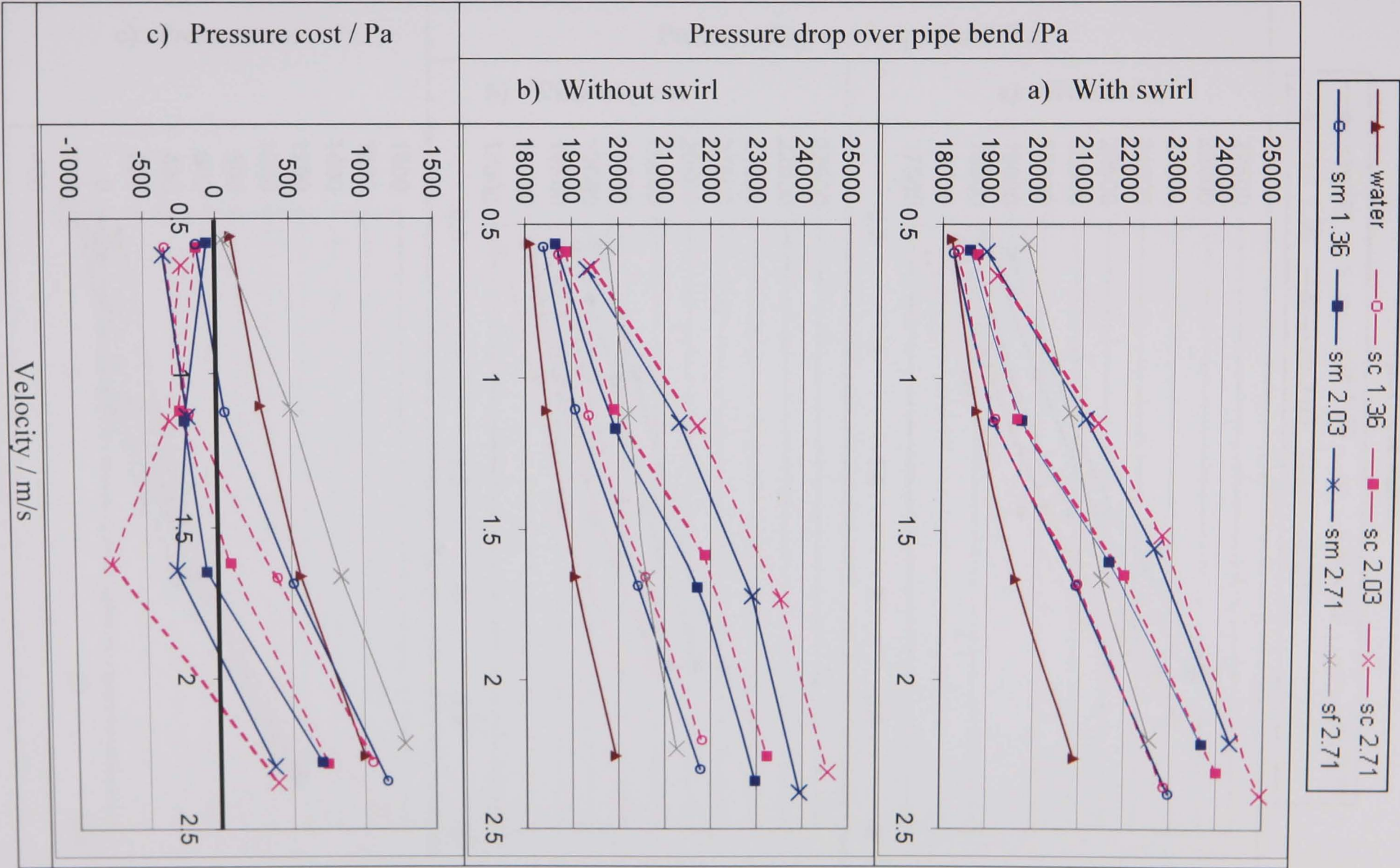
F.10 Pressure drop and cost over inclined pipes for sand slurries of various particle sizes.



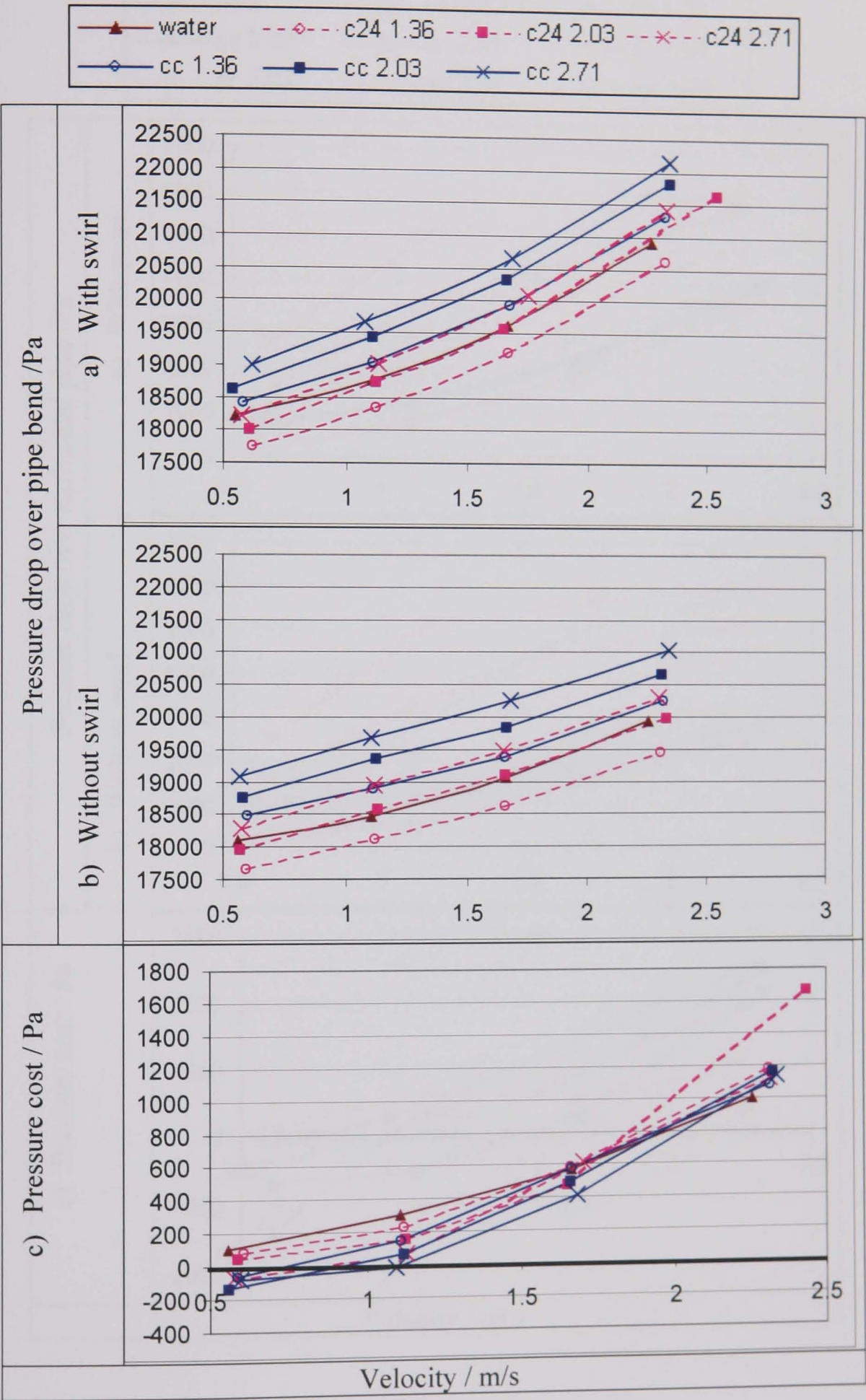
F.11 Pressure drop and cost over inclined pipes for coal slurries of various particle sizes.



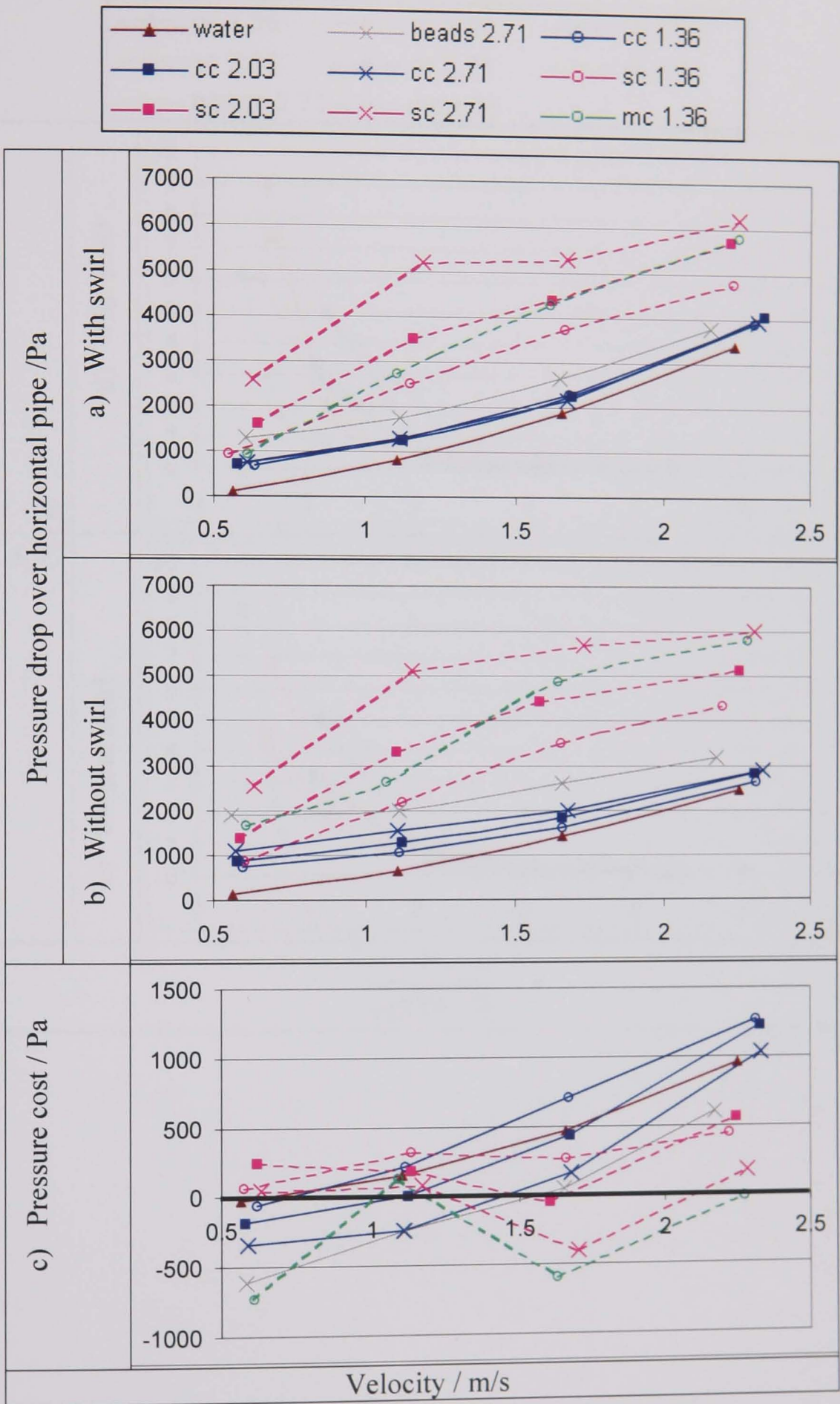
F.12 Pressure drop and cost over a pipe bend for sand slurries of various particle sizes.



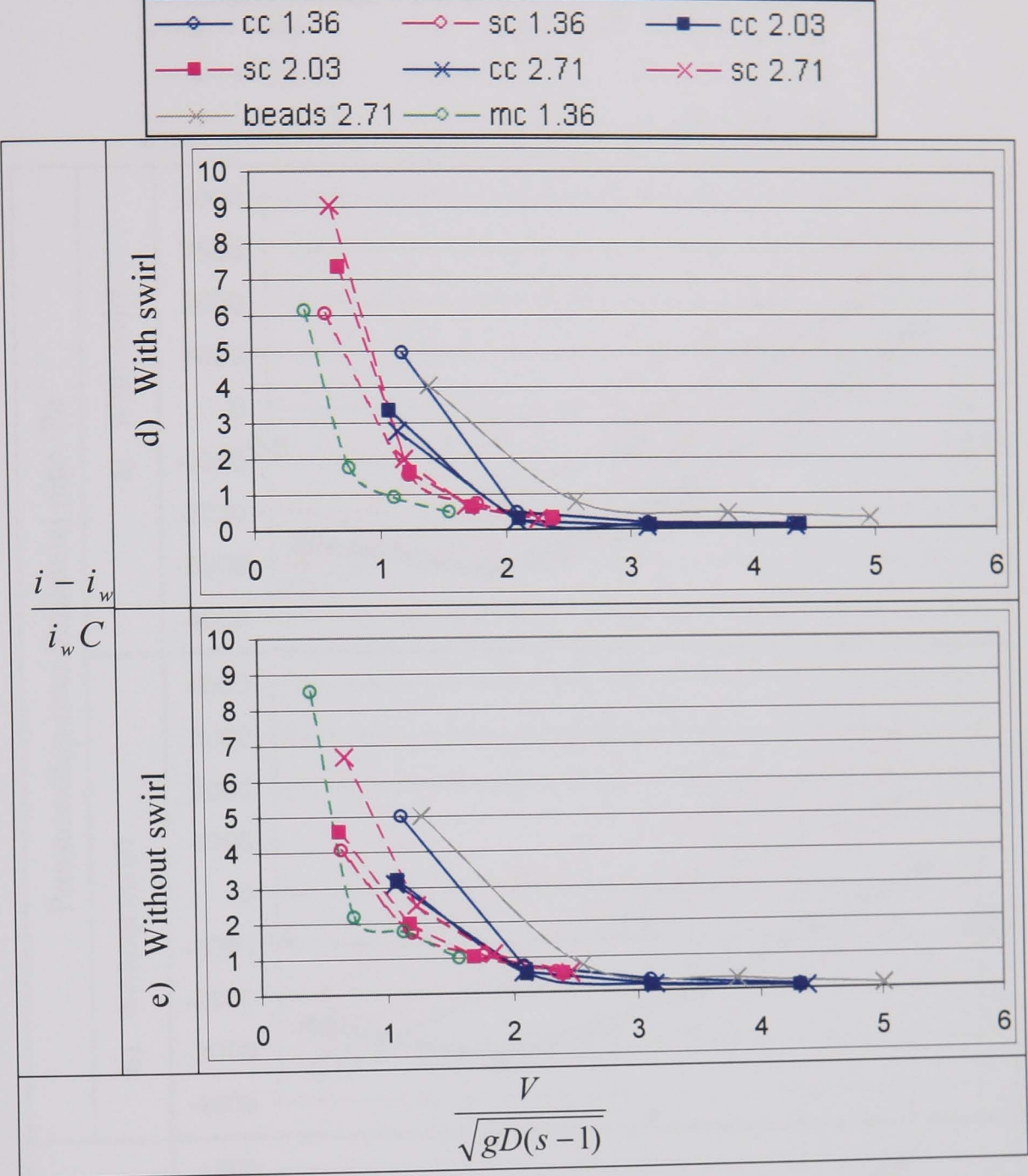
F.13 Pressure drop and cost over a pipe bend for coal slurries of various particle sizes.



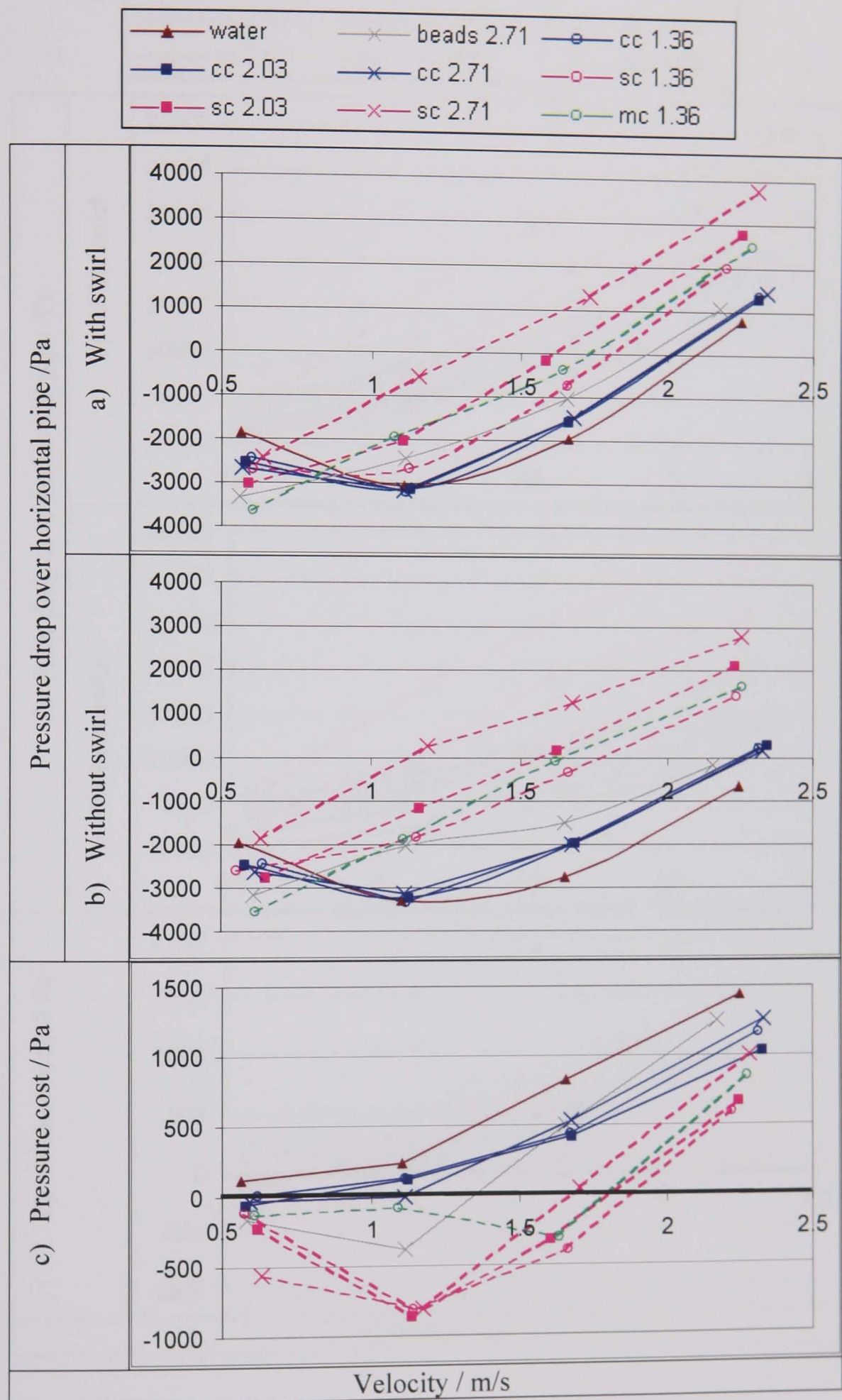
F.14 Pressure drop and cost over horizontal pipes for slurries of various densities.



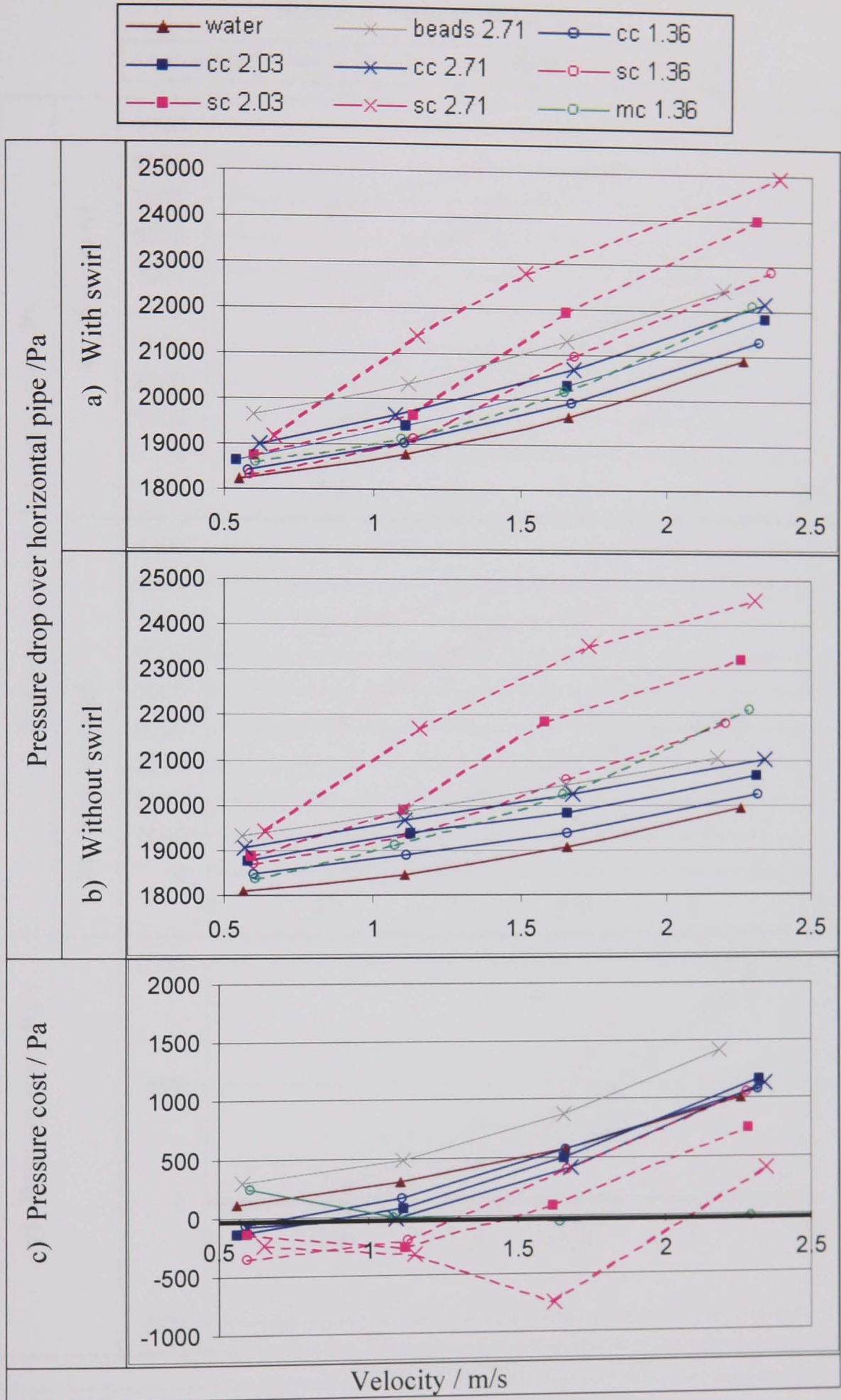
F.15 Comparison of pressure loss for slurries of various density (after Durand, 1953)



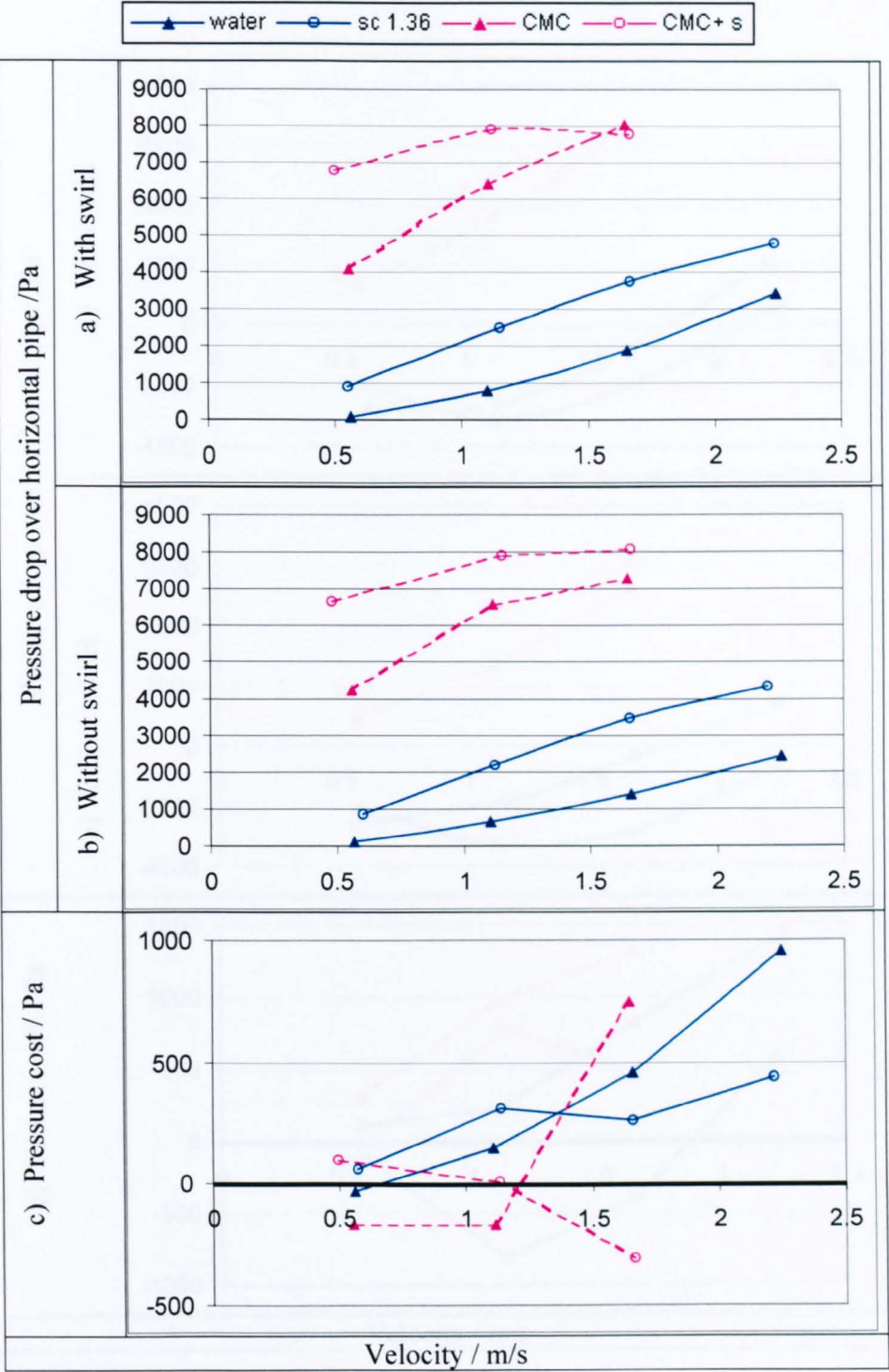
F.16 Pressure drop and cost over inclined pipe for slurries of various densities.



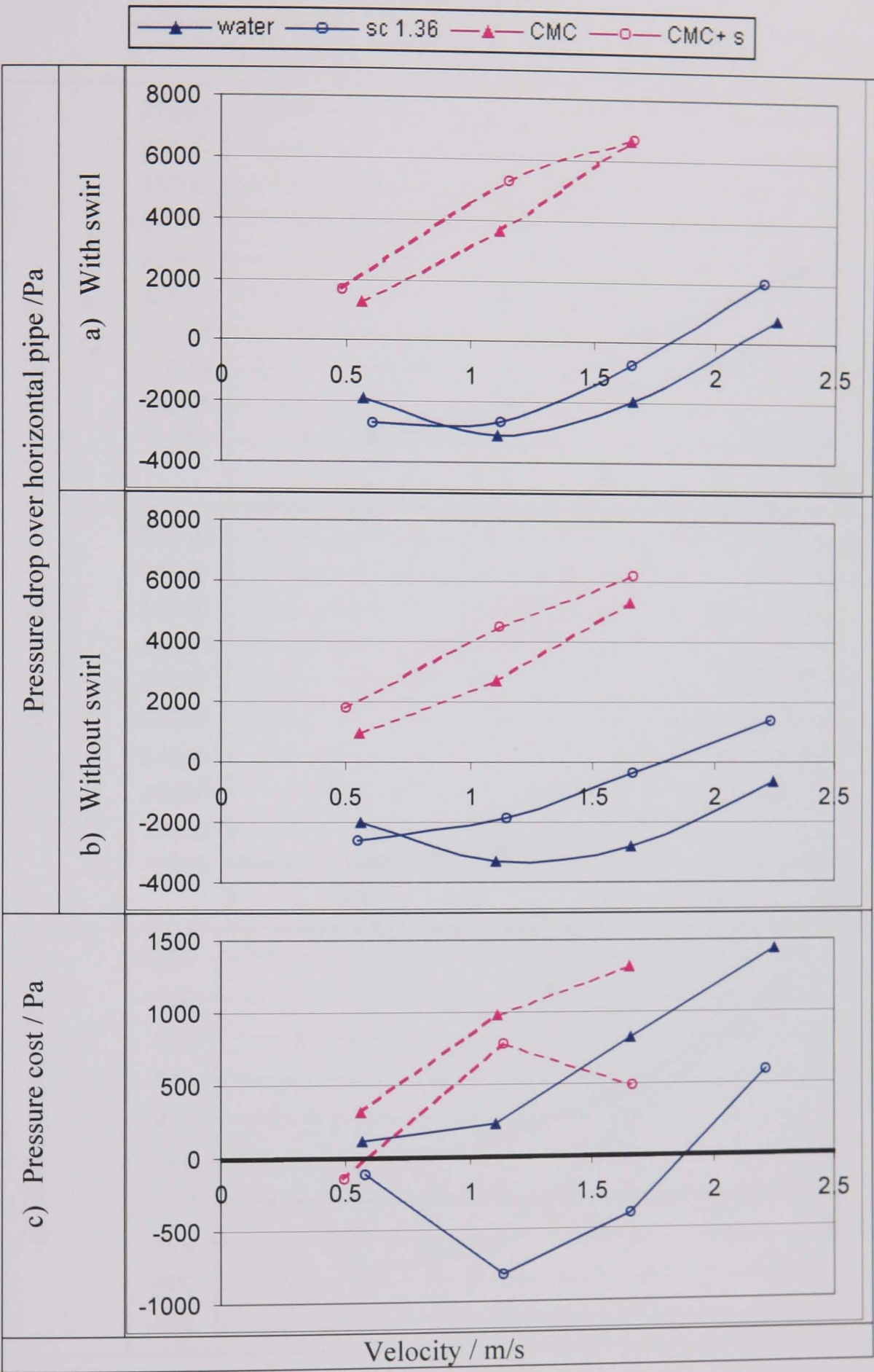
F.17 Pressure drop and cost over a pipe bend for slurries of various densities.



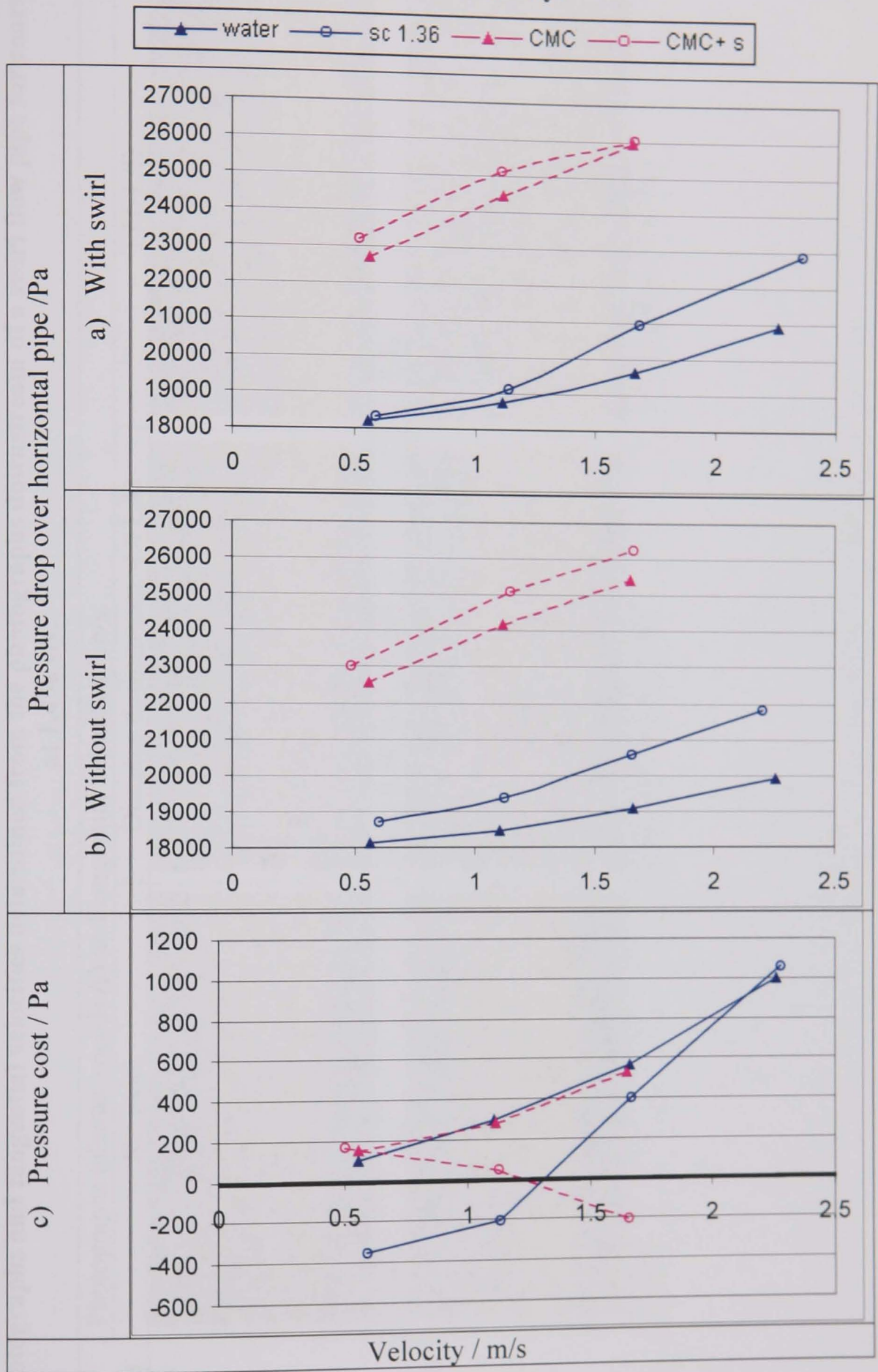
F.18 Pressure drop and cost over horizontal pipe for slurries with carrier fluids of various viscosity.




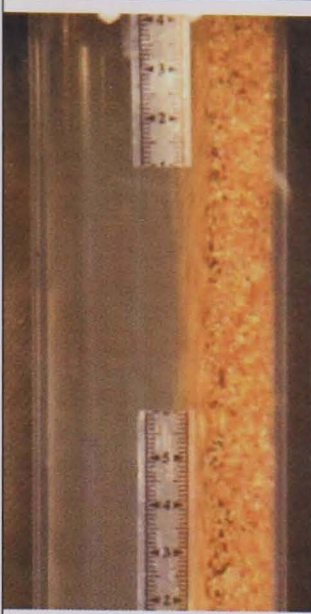
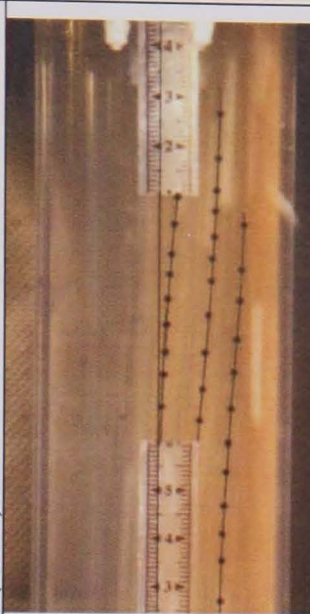
F.19 Pressure drop and cost over inclined pipe for slurries with carrier fluids of various viscosity.

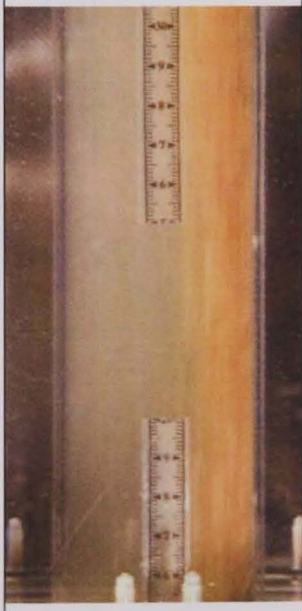
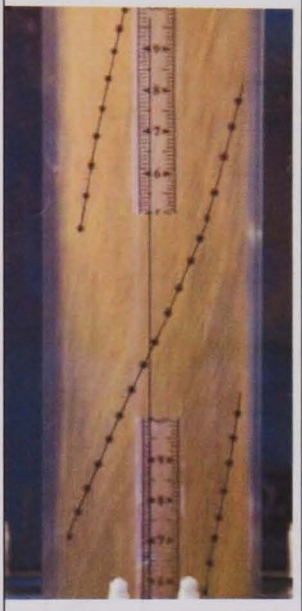

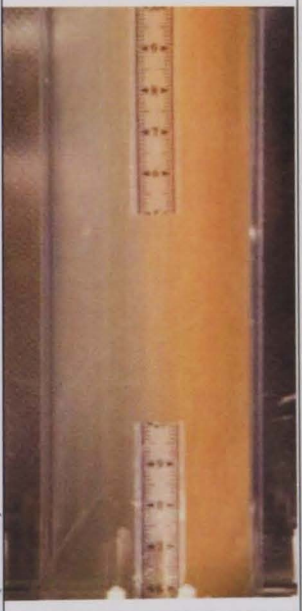
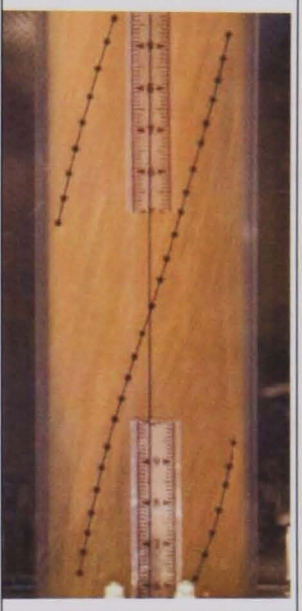
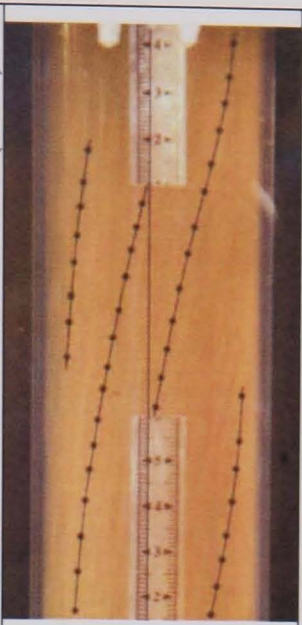


F.20 Pressure drop and cost over a pipe bend for slurries with carrier fluids of various viscosity.



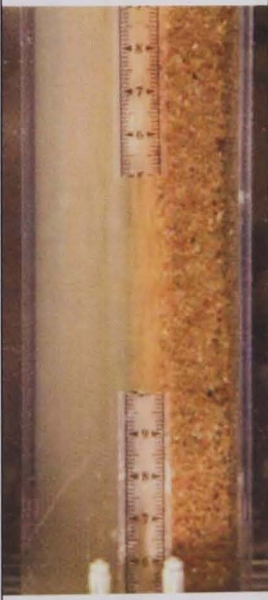
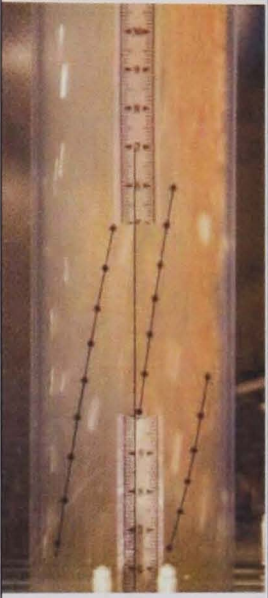


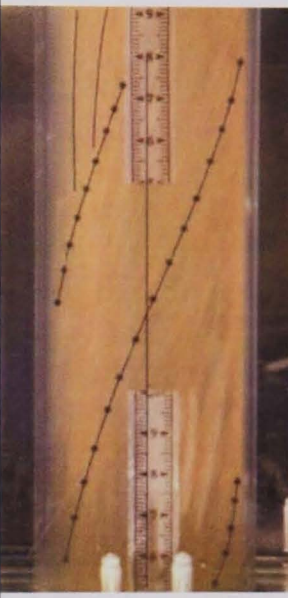
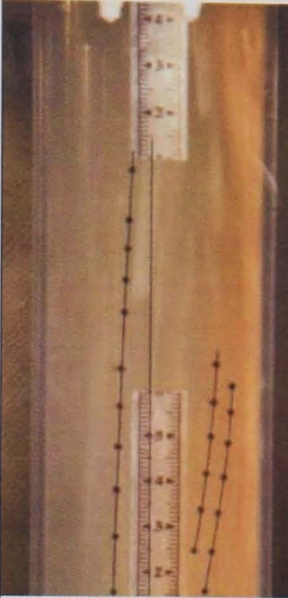
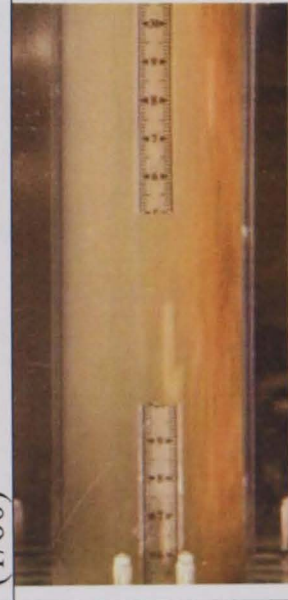


F.21 Photographs and tangential velocities determined from the photographs downstream of a swirl flow pipe for coarse sand at 1.4% v/v.


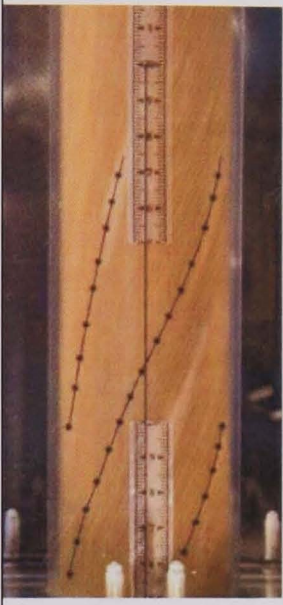
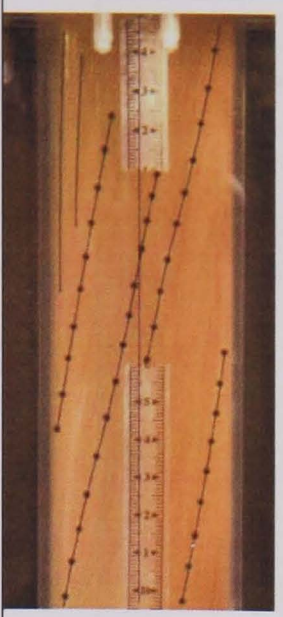
V / m/s	Photographs (shutter speeds /s) and tangential velocities / m/s:		
	No swirl	Distance downstream, 4.4 L/D	17.6 L/D
0.6			
	(1/60)	0.07; 0.09; 0.11 (1/30)	(1/60)
1.1			
	(1/60)	0.07; 0.09; 0.27 (1/30)	0.07; 0.08; 0.09 (1/40)

1.7			
	(1/60)	0.39; 0.76; 0.43 (1/60)	0.20; 0.16; 0.15; 0.18; 0.39 (1/50)
2.2			
		0.81; 0.70; 0.86 (1/60)	0.29; 0.42; 0.56; 0.45 (1/50)

Note: Each tangential velocity corresponds to a line drawn on the photograph. Velocities are listed from top RHS to bottom LHS.


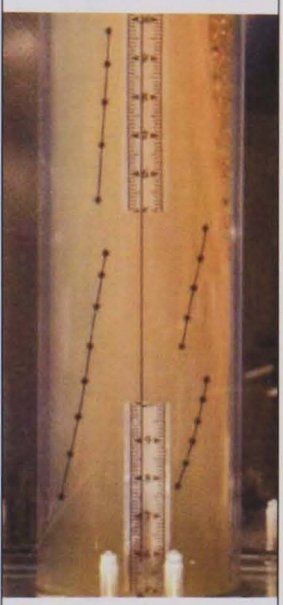




F.22 Photographs and tangential velocities determined from the photographs downstream of a swirl flow pipe for coarse sand at 2.0% v/v.


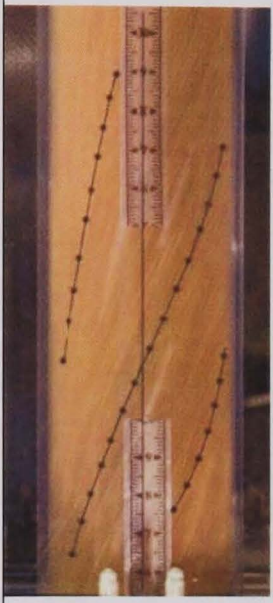
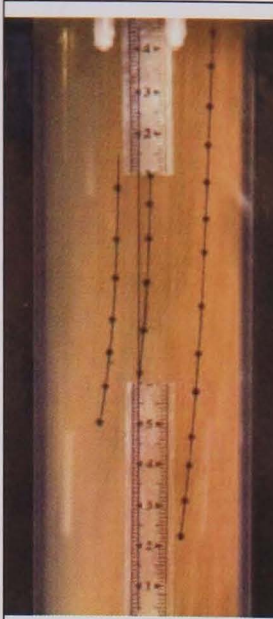

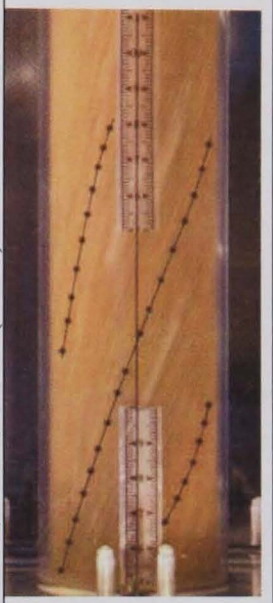
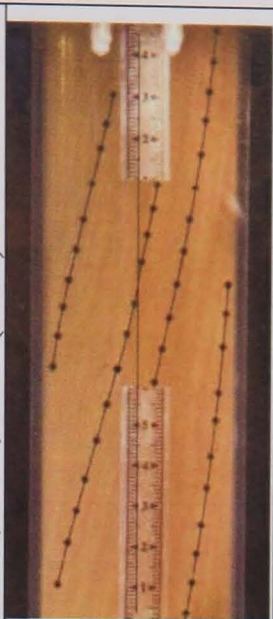
V / m/s	Photographs (shutter speeds /s) and tangential velocities / m/s:		
	No swirl	Distance downstream, 4.4 L/D	17.6 L/D
0.6			
	(1/60)	0.13; 0.09; 0.16 (1/60)	(1/60)
1.1			
	(1/60)	0.46; 0.49; 0.39 (1/40)	0.05; 0.15; 0.20 (1/30)
1.7			
	(1/60)	0.59; 0.67; 0.48 (1/60)	0.11; 0.06 (1/30)

2.3			
	(1/60)	0.57; 1.01; 0.96 (1/60)	0.50; 0.54; 0.6; 0.55 (1/50)

Note: Each tangential velocity corresponds to a line drawn on the photograph. Velocities are listed from top RHS to bottom LHS.

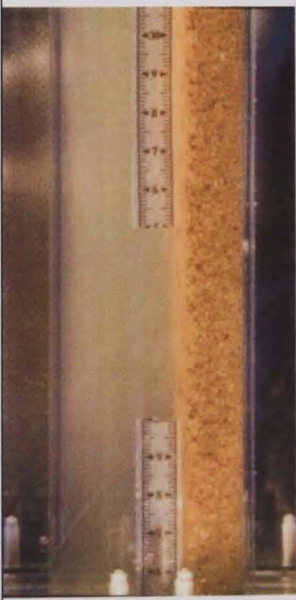
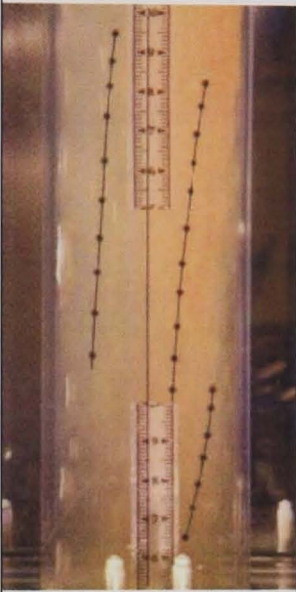
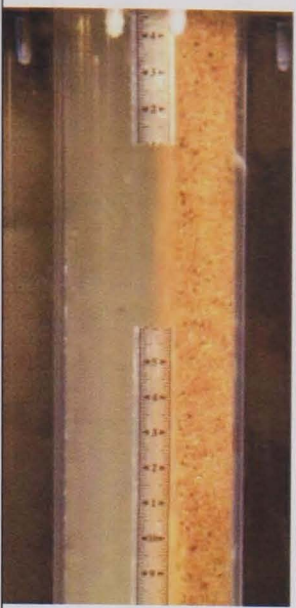
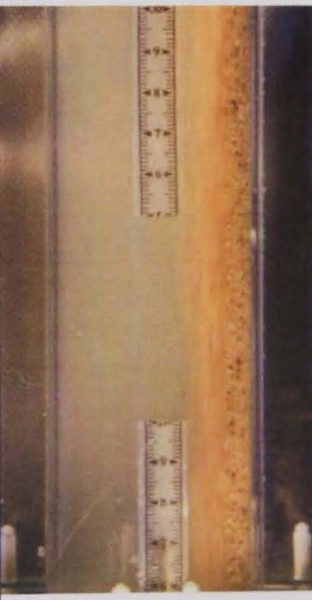
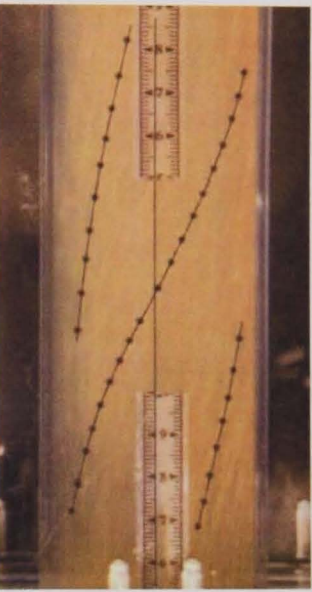
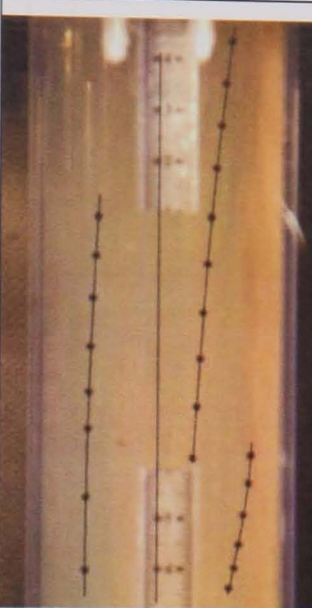

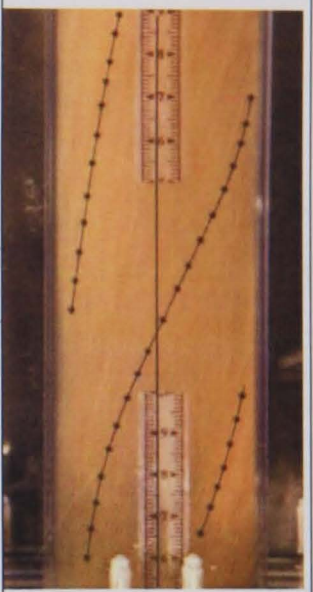
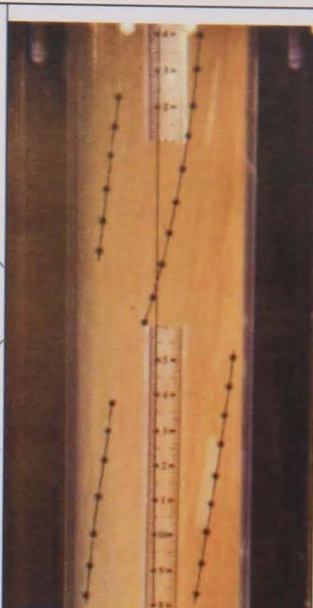
F.23 Photographs and tangential velocities determined from the photographs downstream of a swirl flow pipe for coarse sand at 2.7% v/v.

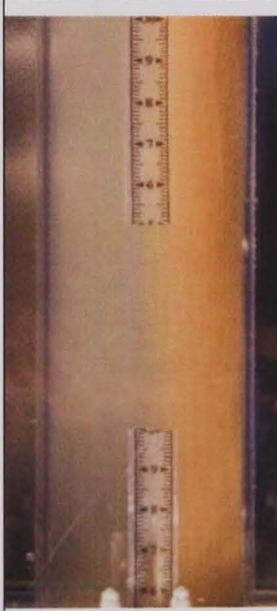
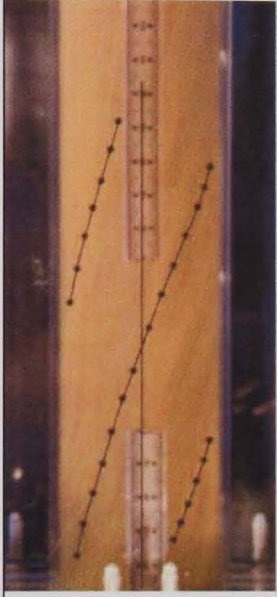
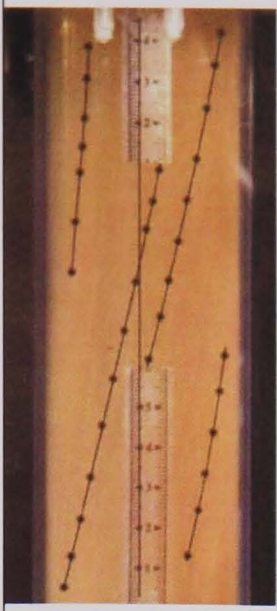
V / m/s	Photographs (shutter speeds /s) and tangential velocities / m/s:		
	No swirl	Distance downstream, 4.4 L/D	17.6 L/D
0.6			
	(1/60)	0.04; 0.15; 0.21; 0.16 (1/30)	(1/60)
1.1			
	(1/60)	0.34; 0.43; 0.29 (1/60)	(1/30)

1.7			
	(1/40)	0.39; 0.73; 0.72 (1/60)	0.13; 0.09; 0.12 (1/60)
2.3			
	(1/60)	0.61; 0.94; 1.11 (1/60)	0.65; 0.63; 0.49; 0.44 (1/60)

Note: Each tangential velocity corresponds to a line drawn on the photograph. Velocities are listed from top RHS to bottom LHS


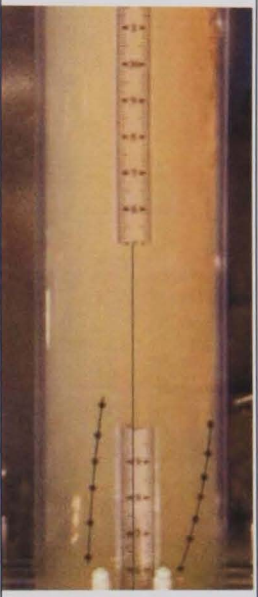
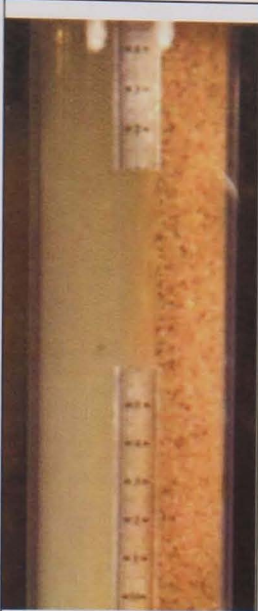

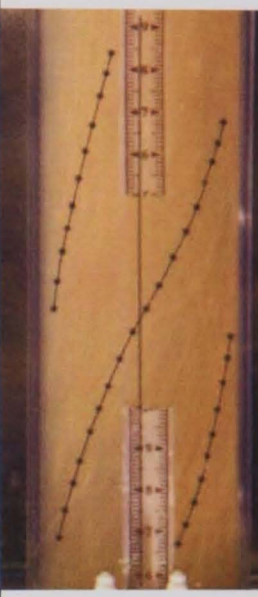
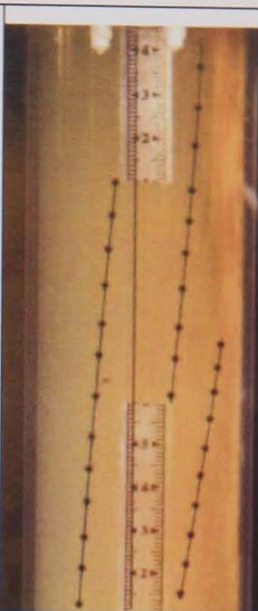
F.24 Photographs and tangential velocities determined from the photographs downstream of a swirl flow pipe for medium sand at 1.4% v/v.

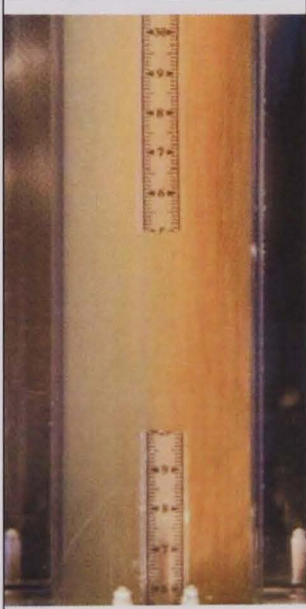
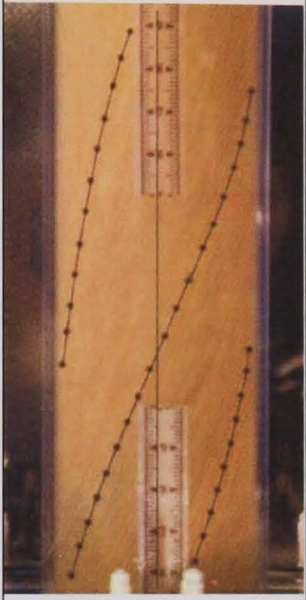
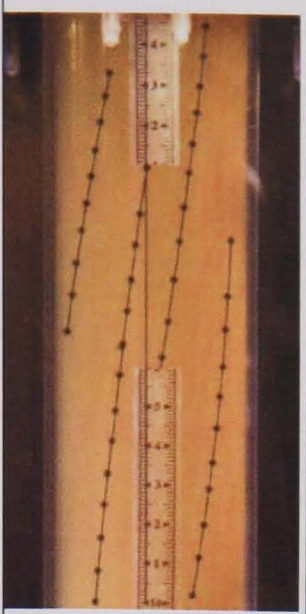
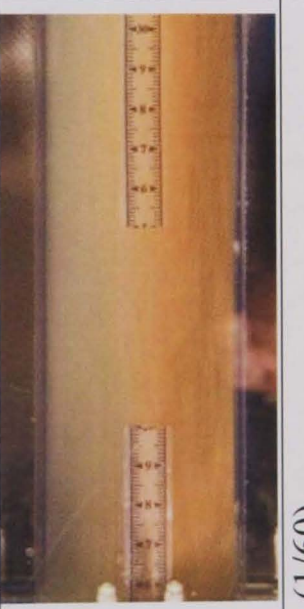
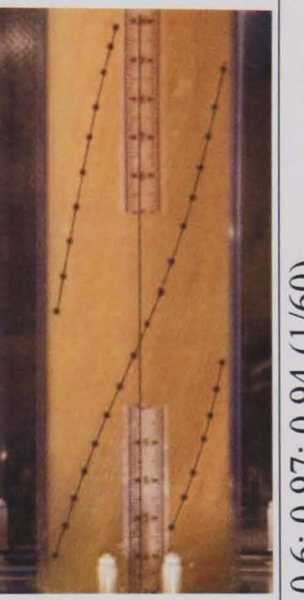
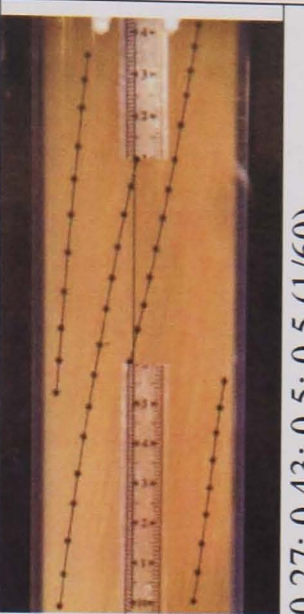
V / m/s	Photographs (shutter speeds /s) and tangential velocities / m/s:		
	No swirl	Distance downstream, 4.4 L/D	17.6 L/D
0.6			
	(1/60)	0.05; 0.08; 0.15 (1/60)	(1/50)
1.1			
	(1/60)	0.22; 0.53; 0.32 (1/60)	0.04; 0.11; 0.23 (1/50)
1.7			
	(1/60)	0.33; 0.74; 0.67 (1/60)	0.29; 0.26; 0.32; 0.35 (1/60)

2.3			
	(1/60)	0.77; 0.89; 1.06 (1/60)	0.22; 0.56; 0.60; 0.59 (1/60)

Note: Each tangential velocity corresponds to a line drawn on the photograph. Velocities are listed from top RHS to bottom LHS.


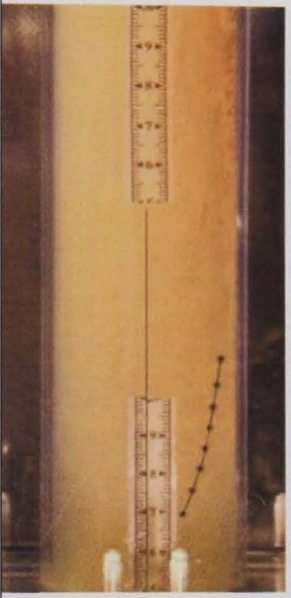


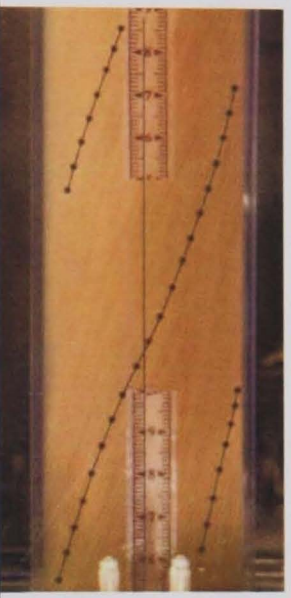

F.25 Photographs and tangential velocities determined from the photographs downstream of a swirl flow pipe for medium sand at 2.0% v/v.


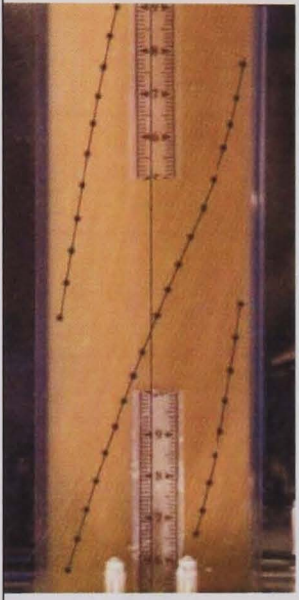
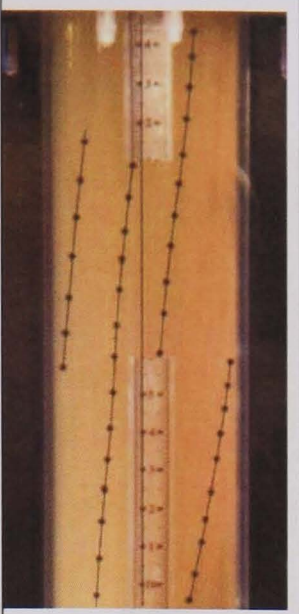

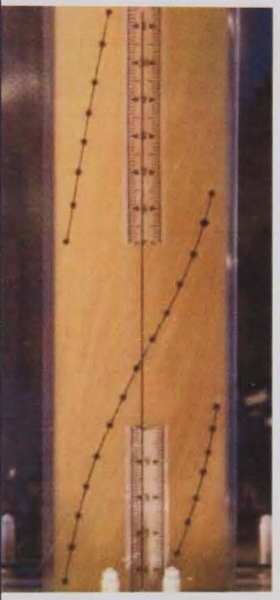
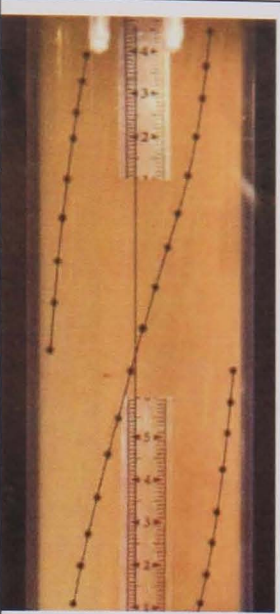
V / m/s	Photographs (shutter speeds /s) and tangential velocities / m/s:		
	No swirl	Distance downstream, 4.4 L/D	17.6 L/D
0.6			
	(1/60)	0.06; 0.18 (1/40)	(1/60)
1.1			
	(1/60)	0.33; 0.54; 0.40 (1/60)	0.09; 0.11; 0.23 (1/60)

1.7			
	(1/60)	0.44; 0.75; 0.59 (1/60)	0.35; 0.21; 0.24; 0.26 (1/60)
2.3			
	(1/60)	0.6; 0.97; 0.94 (1/60)	0.27; 0.43; 0.5; 0.5 (1/60)

Note: Each tangential velocity corresponds to a line drawn on the photograph. Velocities are listed from top RHS to bottom LHS.

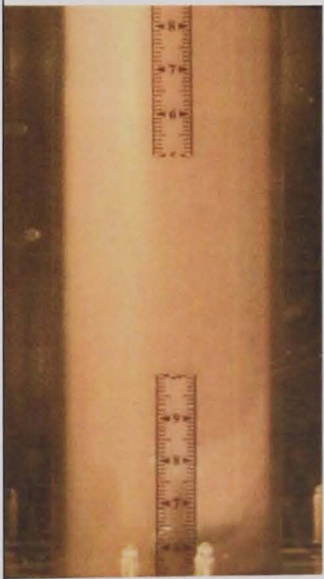
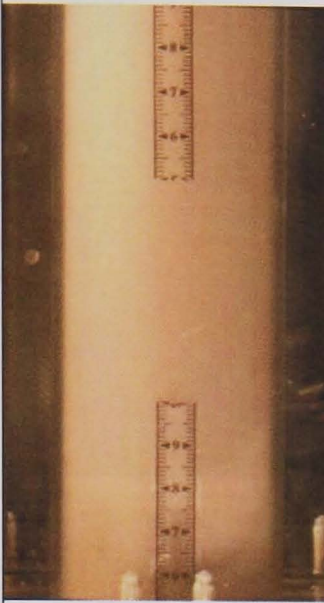
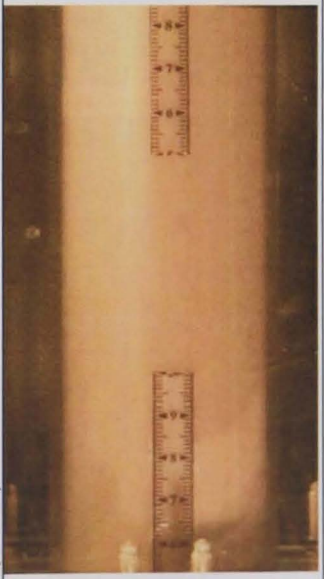
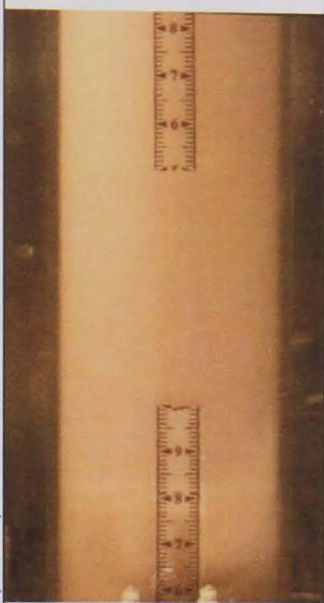
F.26 Photographs and tangential velocities determined from the photographs downstream of a swirl flow pipe for medium sand at 2.7% v/v.

V / m/s	Photographs (shutter speeds /s) and tangential velocities / m/s:		
	No swirl	Distance downstream, 4.4 L/D	17.6 L/D
0.6	 (1/60)	 0.18 (1/60)	 (1/60)
1.1	 (1/60)	 0.44; 0.49; 0.41 (1/50)	 (1/60)

1.7			
	(1/60)	0.38; 0.69; 0.46 (1/40)	0.24; 0.15; 0.21; 0.45 (1/60)
2.3			
	(1/60)	0.51; 1.08; 0.96 (1/60)	0.39; 0.64; 0.57 (1/60)

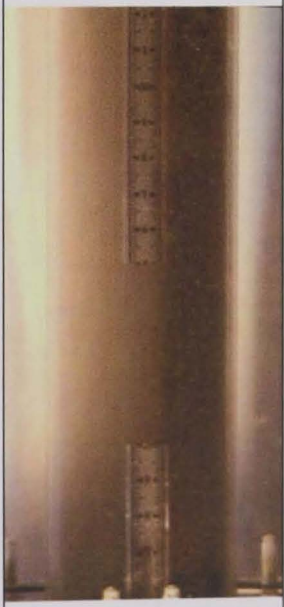

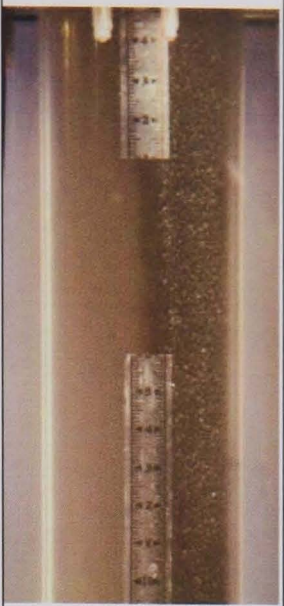

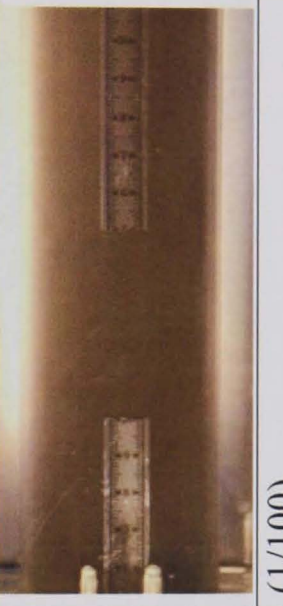
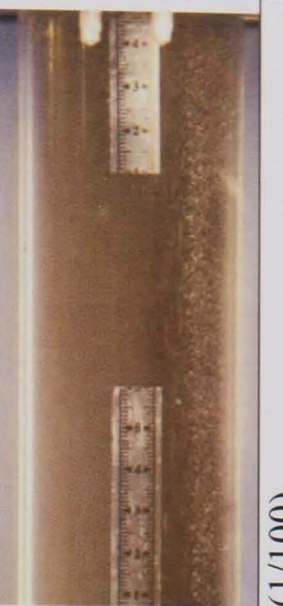
Note: Each tangential velocity corresponds to a line drawn on the photograph. Velocities are listed from top RHS to bottom LHS



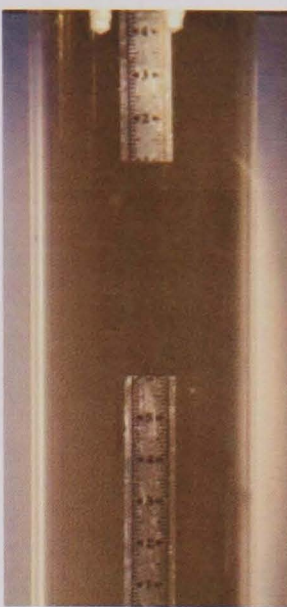

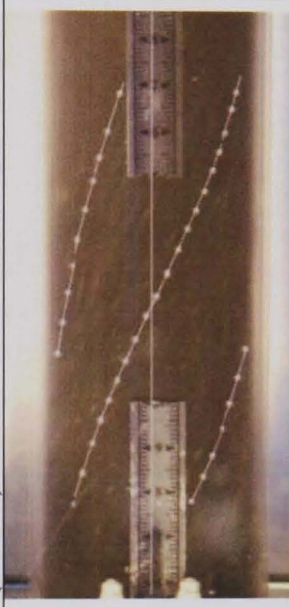
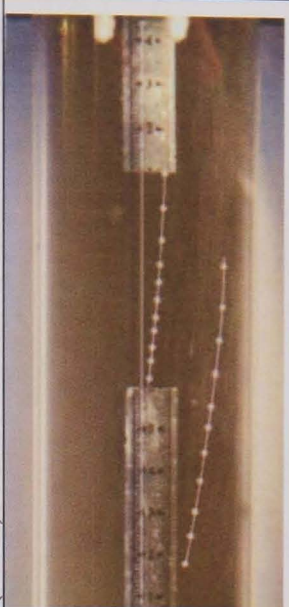
F.27 Photographs of fine sand at 2.7% v/v with no swirl induction.

V / m/s	Photographs (shutter speeds /s)	V / m/s	Photographs (shutter speeds /s)
	No swirl		No swirl
0.6	 (1/60)	1.7	 (1/60)
1.1	 (1/60)	2.2	 (1/60)

After the quality of these photographs were examined it was considered futile to take photographs for the $L/D = 4$ and $L/D = 8$ conditions.


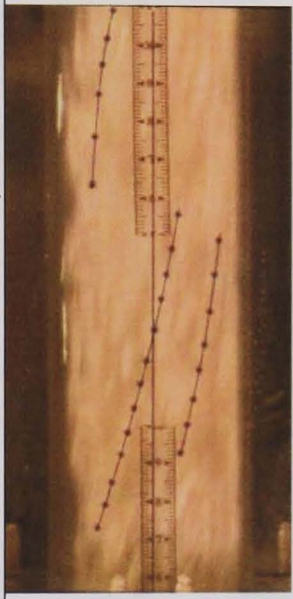
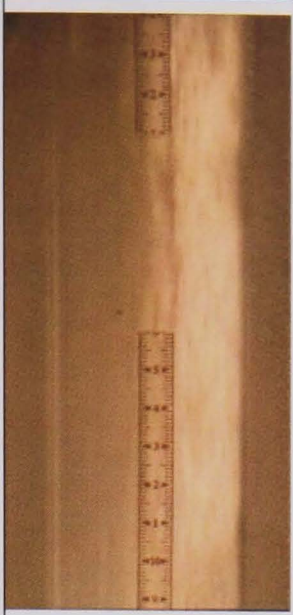
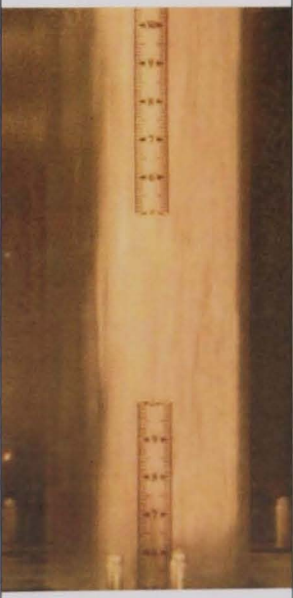
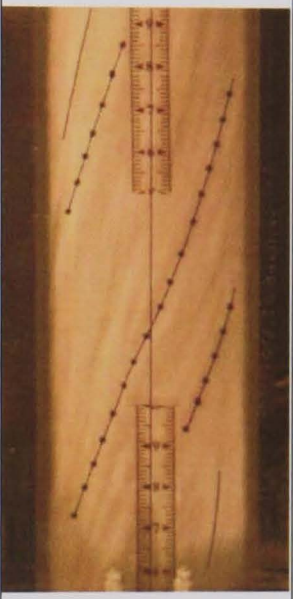
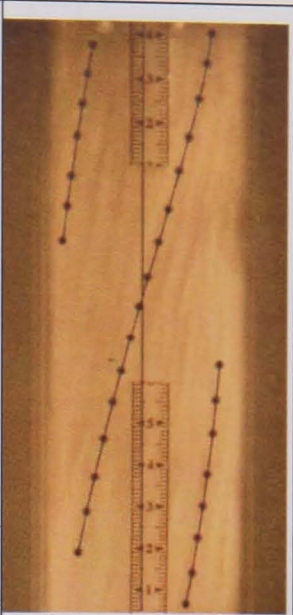
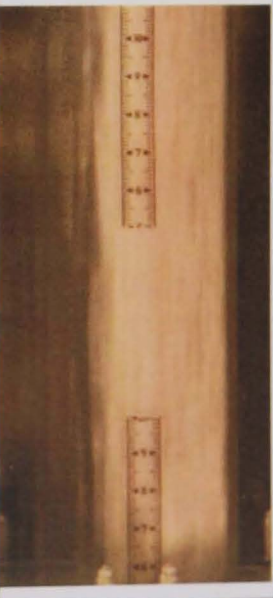
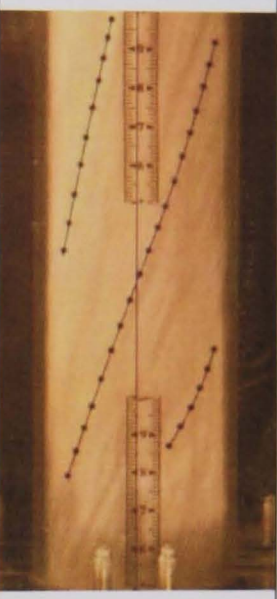
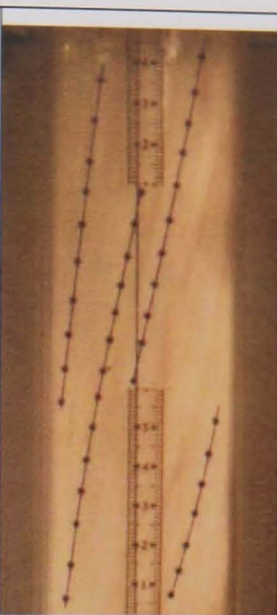
F.28 Photographs and tangential velocities determined from the photographs downstream of a swirl flow pipe for coarse magnetite at 1.4% v/v.

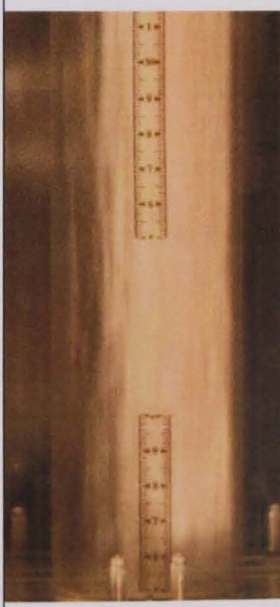
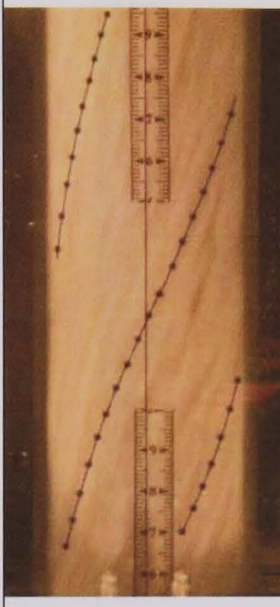
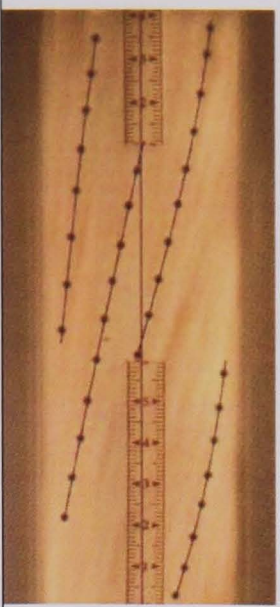
V / m/s	Photographs (shutter speeds /s) and tangential velocities / m/s:		
	No swirl	Distance downstream, 4.4 L/D	17.6 L/D
0.6			
	(1/100)	(1/50)	(1/100)
1.1			
	(1/100)	(1/100)	(1/100)

1.7		(1/100)		(1/100)		(1/60)	
	2.4		(1/50)		0.74; 1.03; 1.12 (1/60)		0.20; 0.40 (1/60)

Note: Each tangential velocity corresponds to a line drawn on the photograph. Velocities are listed from top RHS to bottom LHS.



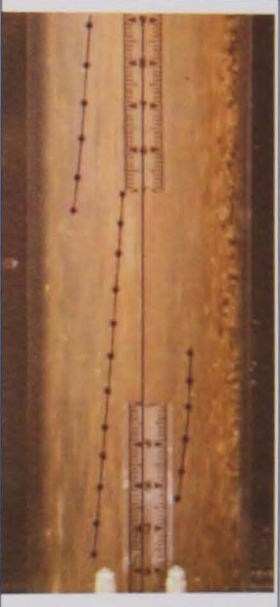
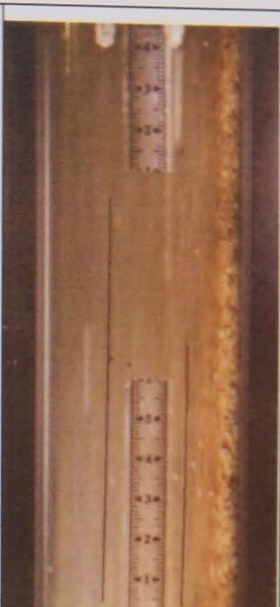
F.29 Photographs and tangential velocities determined from the photographs downstream of a swirl flow pipe for plastic beads at 2.7% v/v.

V / m/s	Photographs (shutter speeds /s) and tangential velocities / m/s:		
	No swirl	Distance downstream, 4.4 L/D	17.6 L/D
0.6			
	(1/60)	0.08; 0.14; 0.11(1/50)	(1/30)
1.1			
	(1/50)	0.45; 0.46; 0.50 (1/40)	0.22; 0.32; 0.20 (1/30)
1.7			
	(1/60)	0.41; 0.64; 1.00 (1/50)	0.25; 0.34; 0.38; 0.54 (1/30)

2.2			
	(1/60)	0.62; 0.96; 1.09 (1/60)	0.33; 0.52; 0.55; 0.61 (1/60)

Note: Each tangential velocity corresponds to a line drawn on the photograph. Velocities are listed from top RHS to bottom LHS.

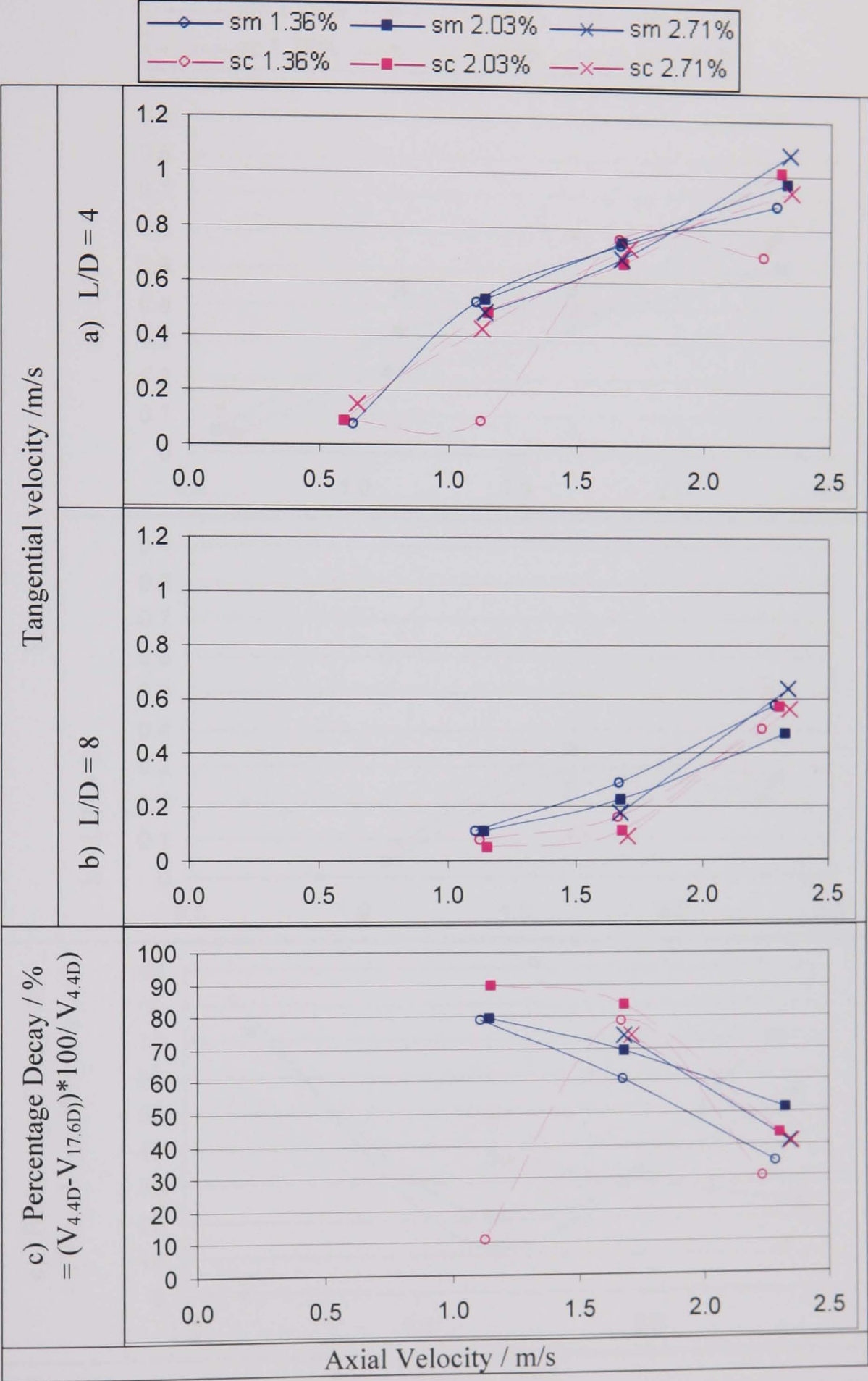
F.30 Photographs and tangential velocities determined from the photographs downstream of a swirl flow pipe for CMC and coarse sand at 1.4% v/v.

V / m/s	Photographs (shutter speeds /s) and tangential velocities / m/s:		
	No swirl	Distance downstream, 4.4 L/D	17.6 L/D
0.5			
	(1/40)	(1/30)	(1/30)
1.1			
	(1/40)	0.12; 0.09; 0.10 (1/60)	(1/30)

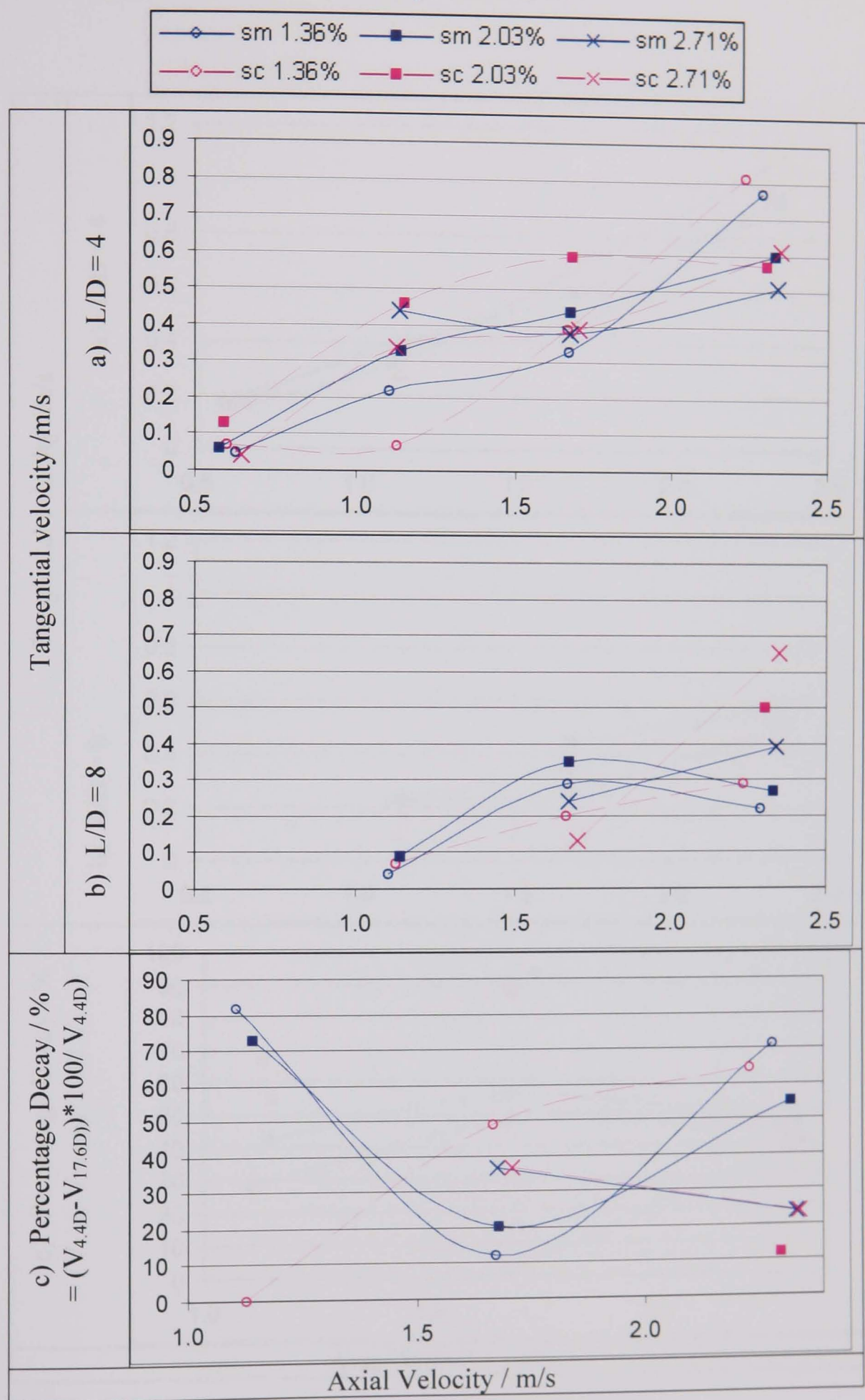
1.7			
	(1/50)	0.09; 0.17; 0.11 (1/50)	0.07; 0.11 (1/50)

Note: Each tangential velocity corresponds to a line drawn on the photograph. Velocities are listed from top RHS to bottom LHS.

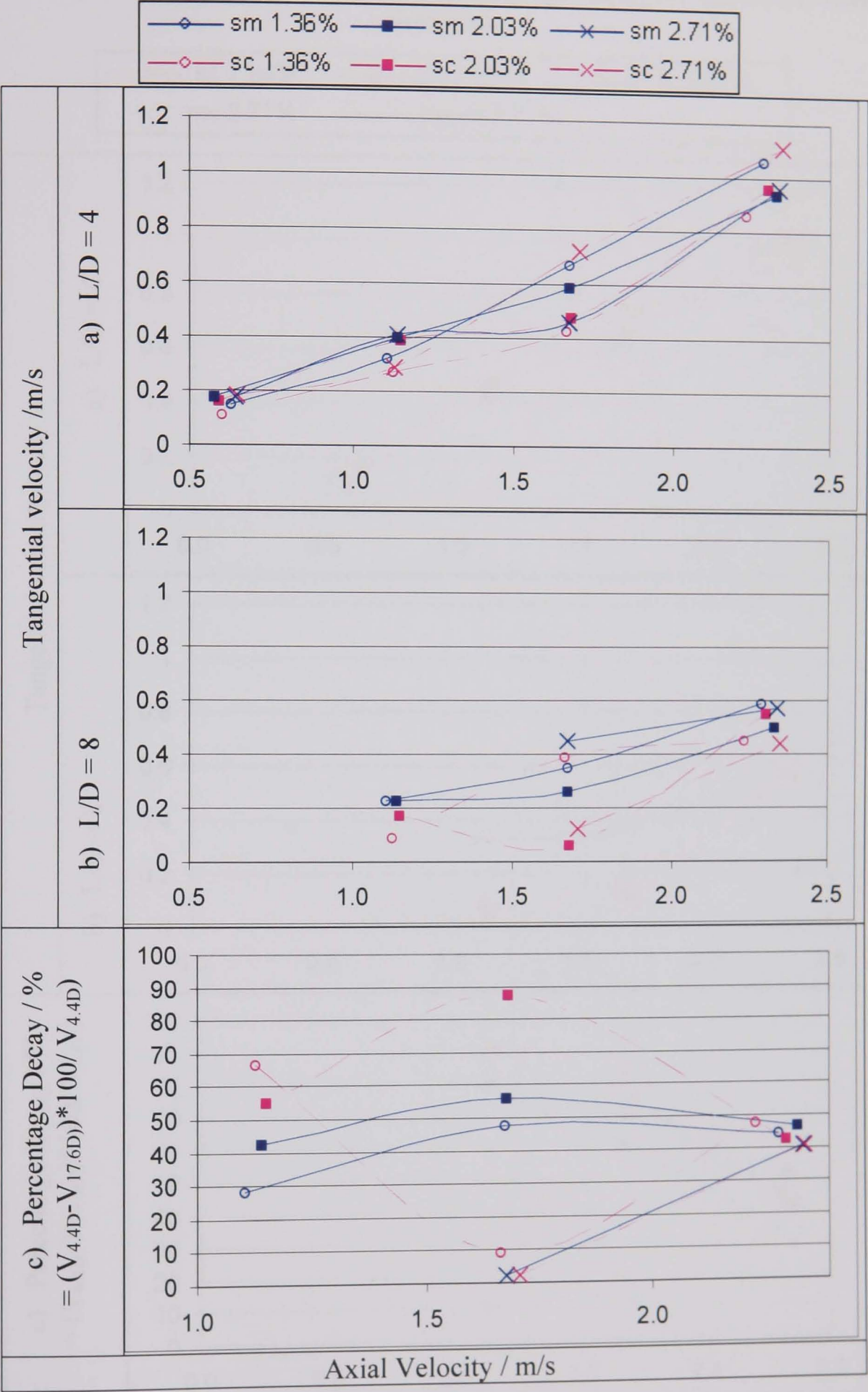
F.31 Tangential velocity (central) and percentage decay for sand slurries of various particle sizes.



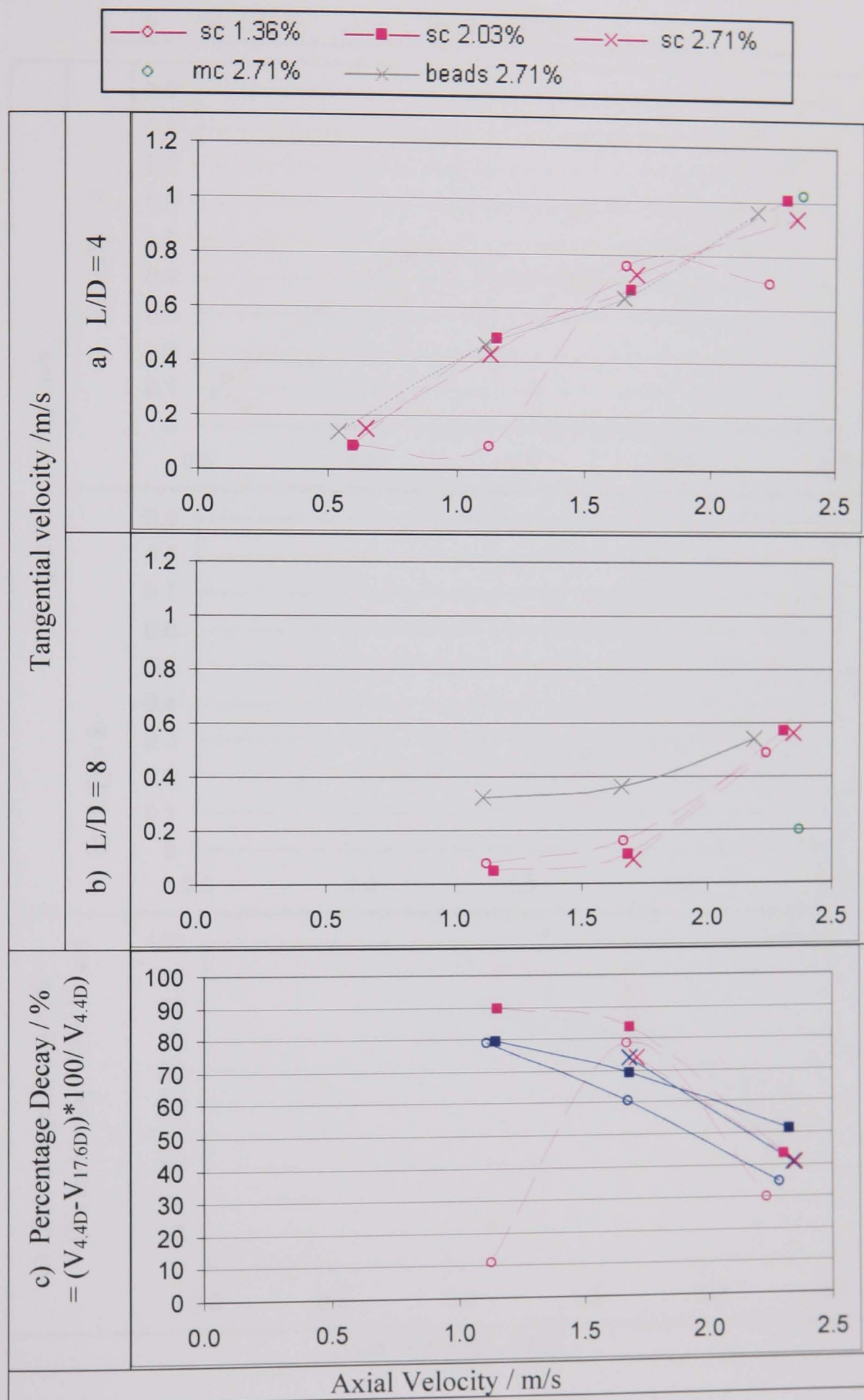
F.32 Tangential velocity (top RHS) and percentage decay for sand slurries of various particle sizes.



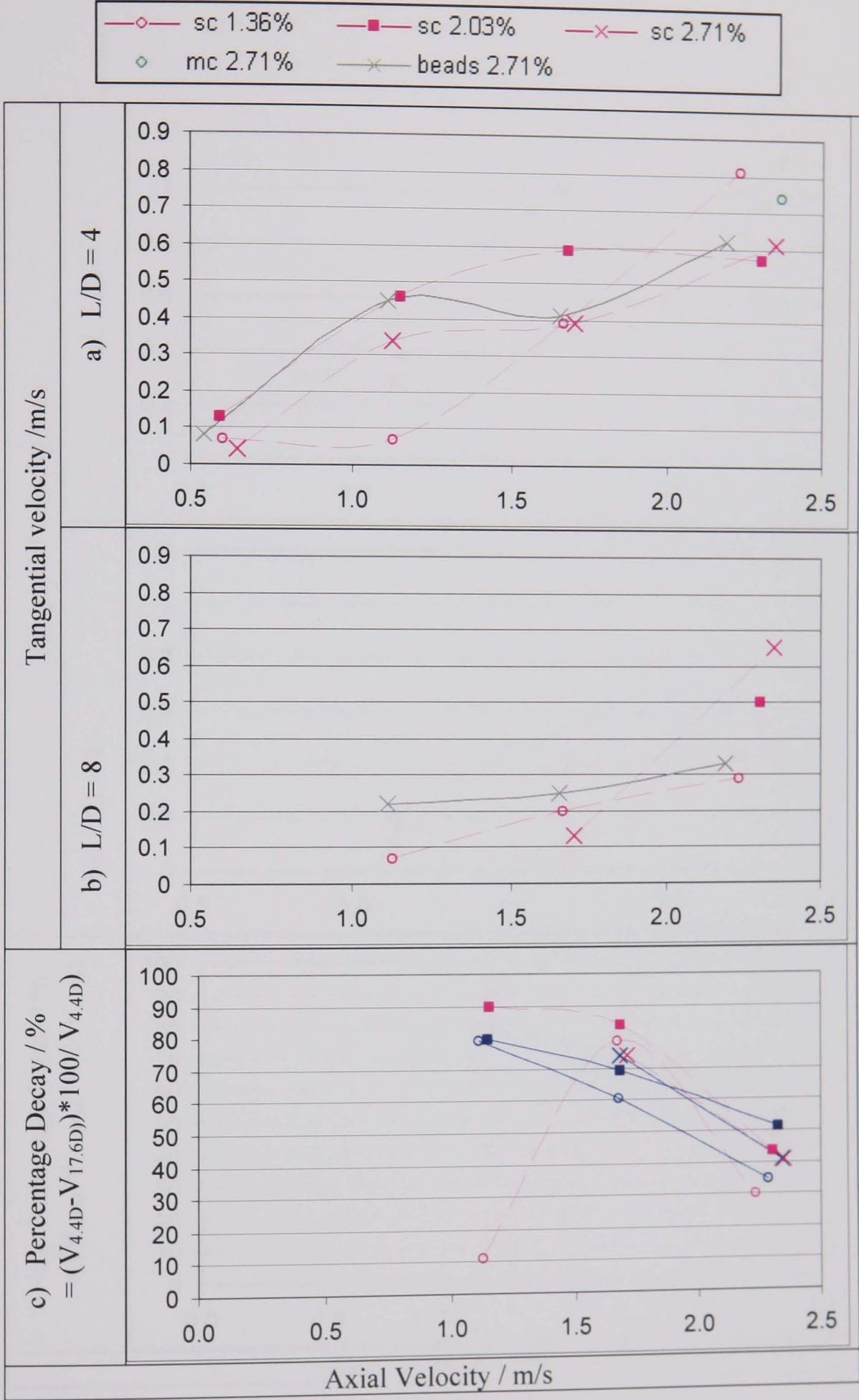
F.33 Tangential velocity (bottom LHS) and percentage decay for sand slurries of various particle sizes.



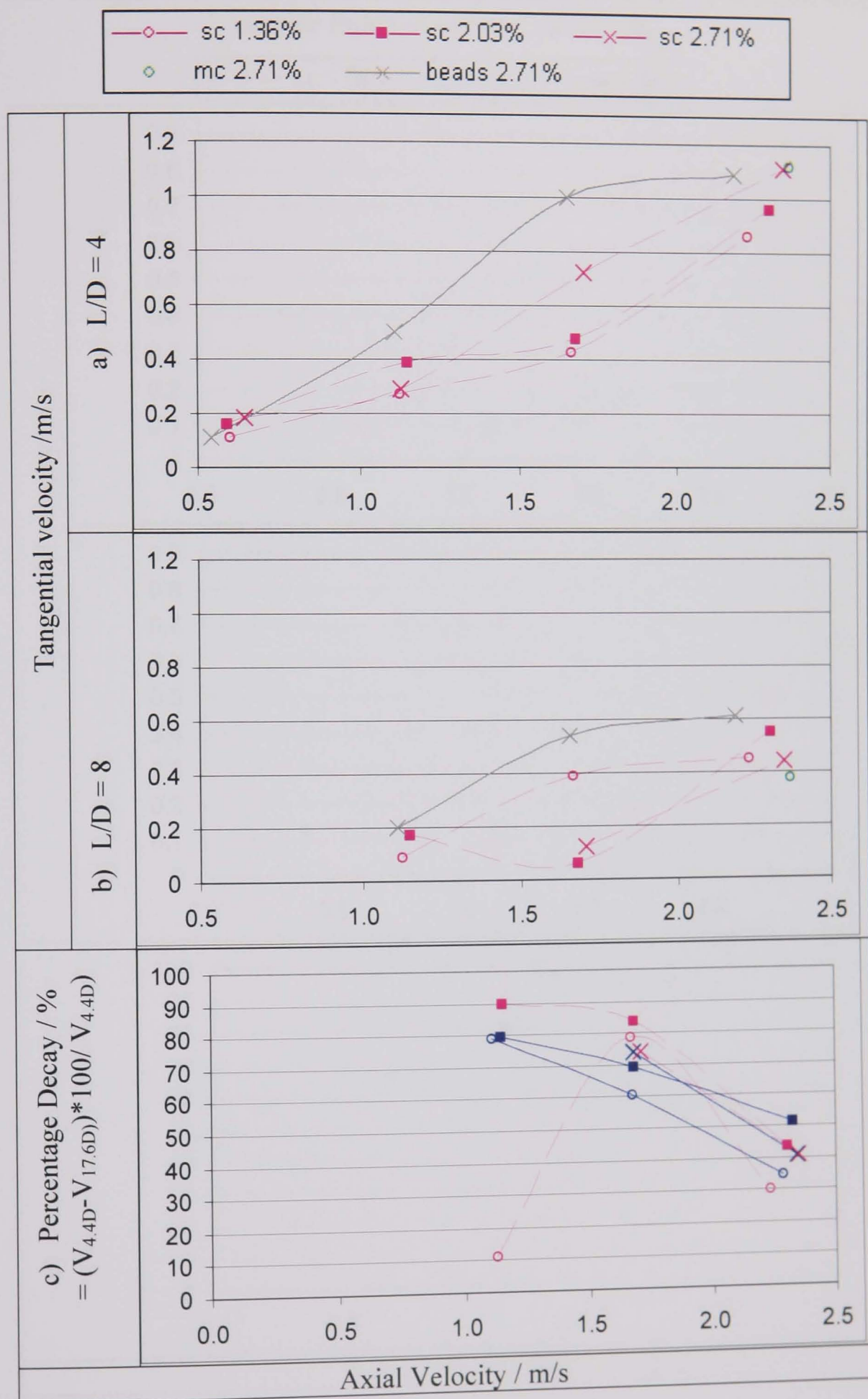
F.34 Tangential velocity (central) and percentage decay for slurries of various densities.



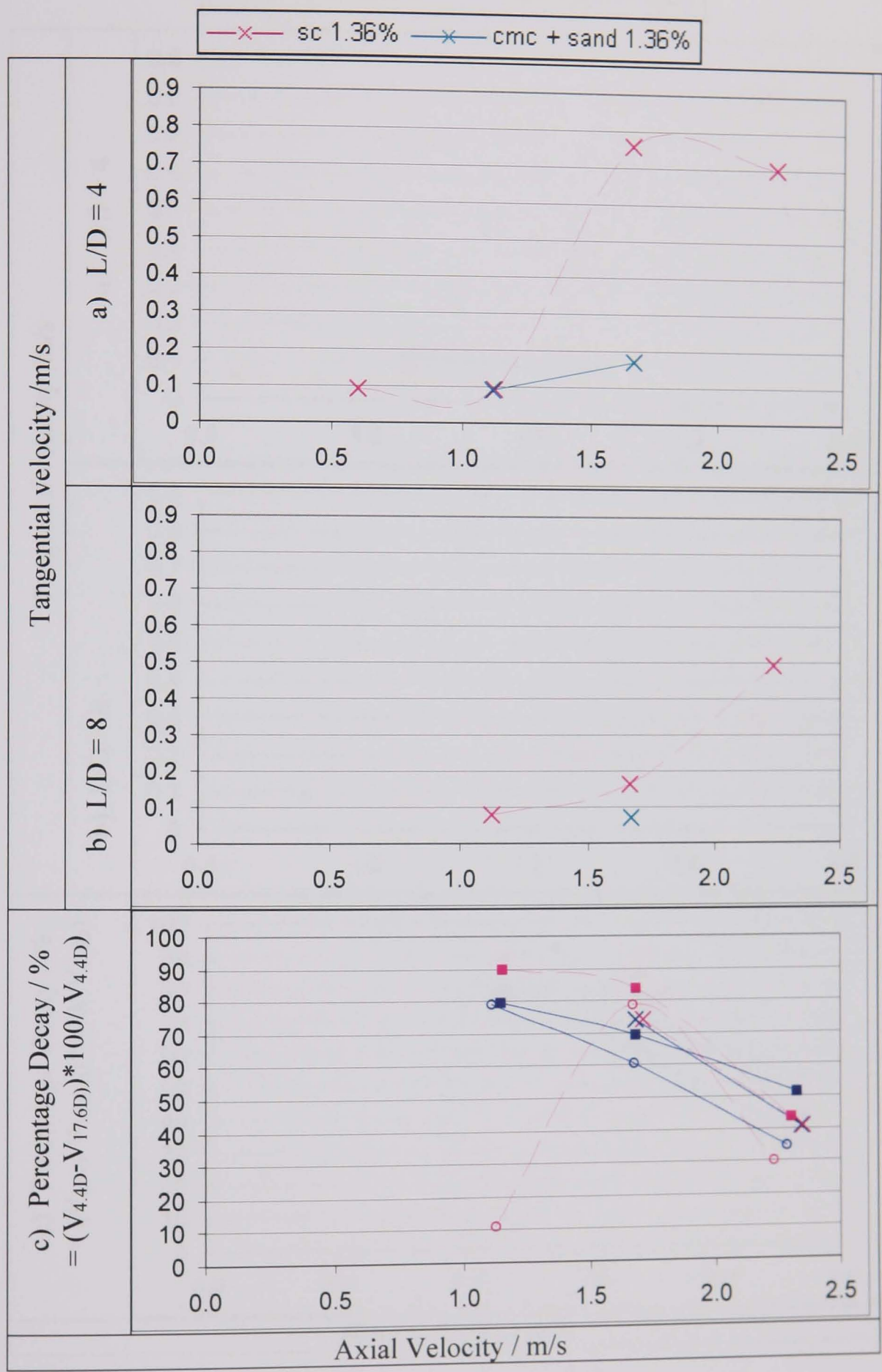
F.35 Tangential velocity (top RHS) and percentage decay for slurries of various densities.



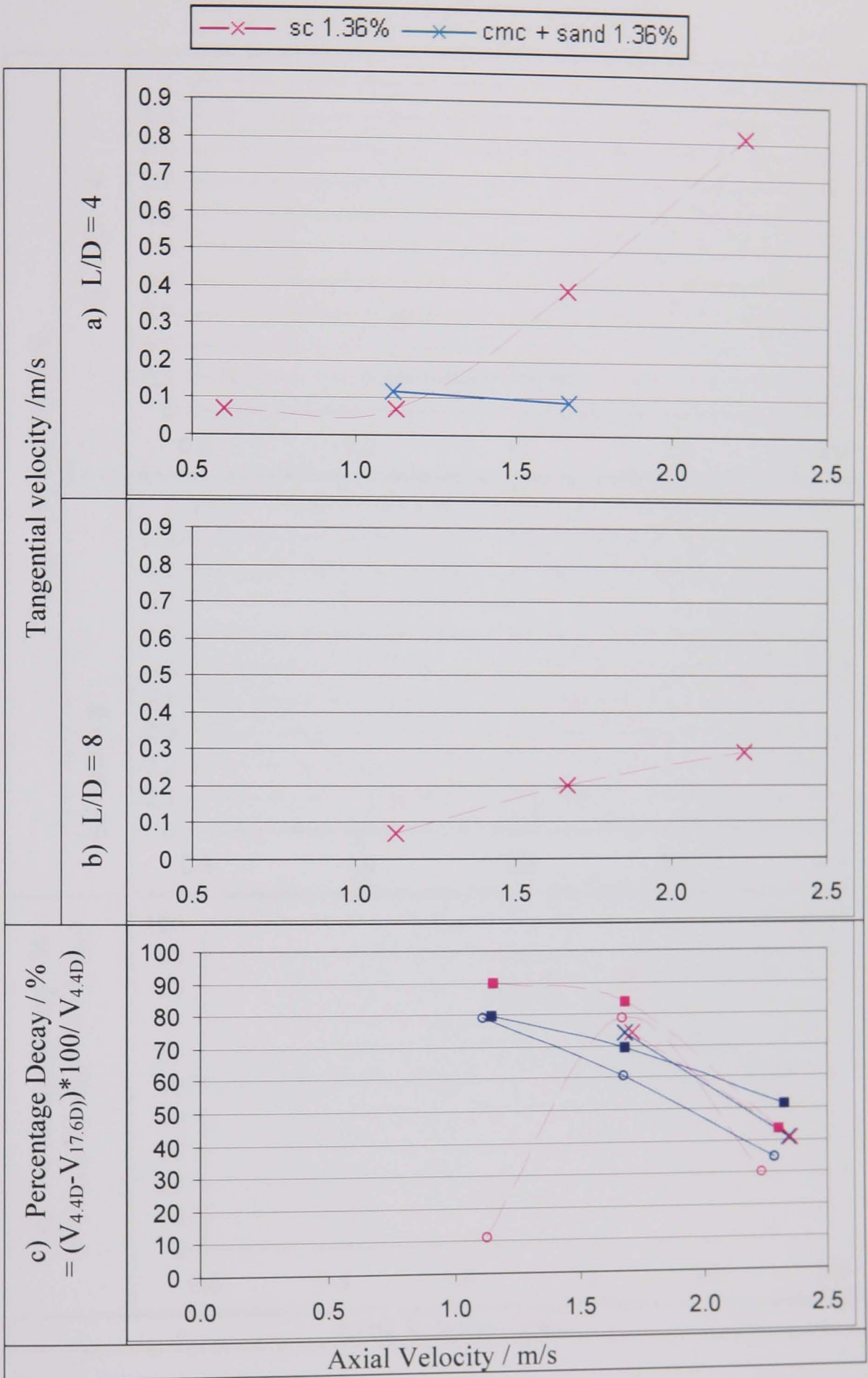
F.36 Tangential velocity (bottom LHS) and percentage decay for slurries of various densities.



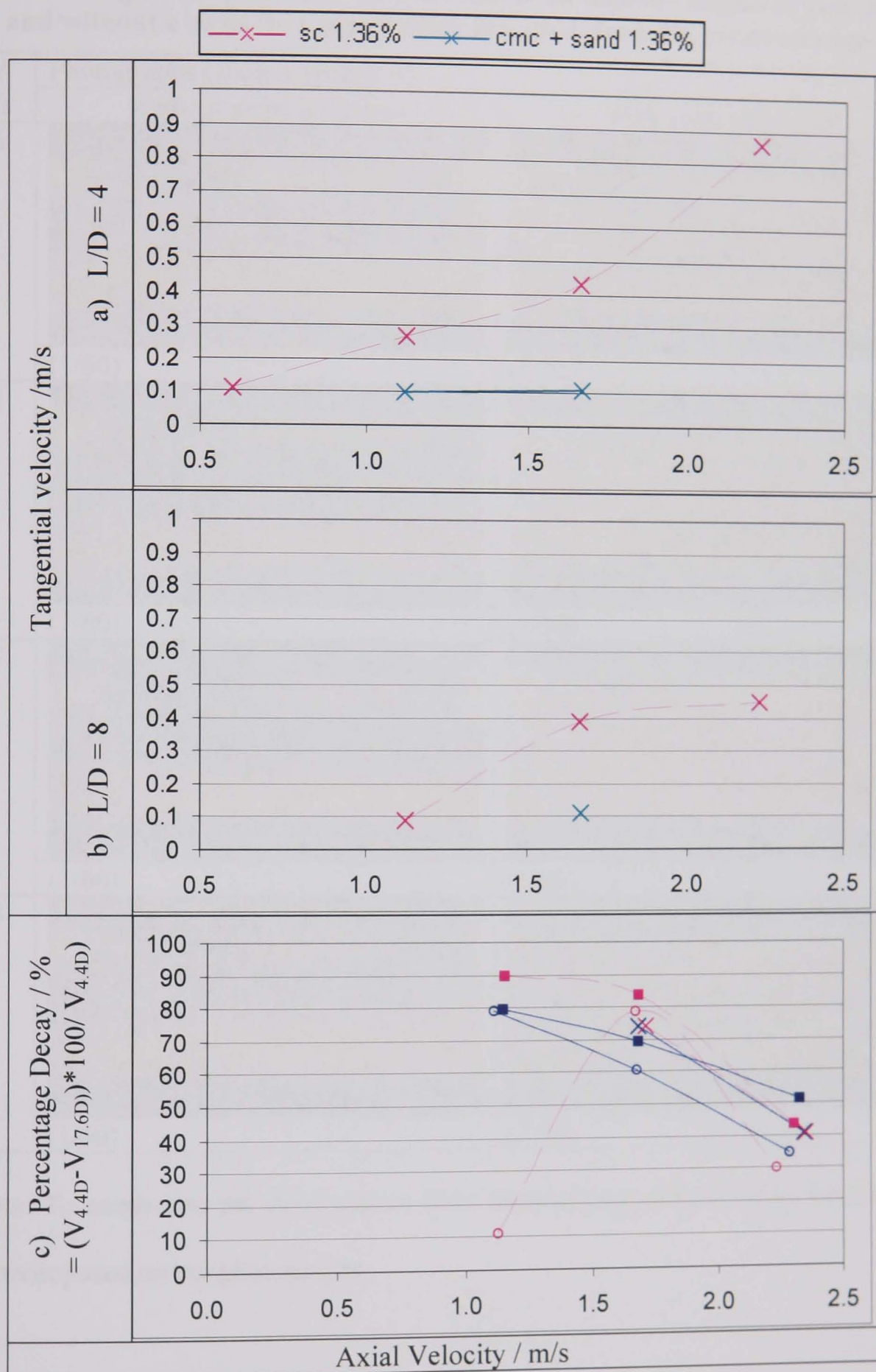
F.37 Tangential velocity (central) and percentage decay for slurries with carrier fluids of various viscosities.



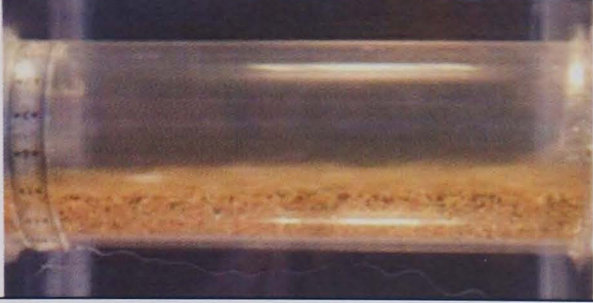

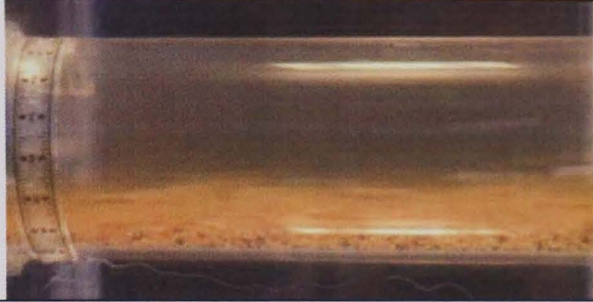
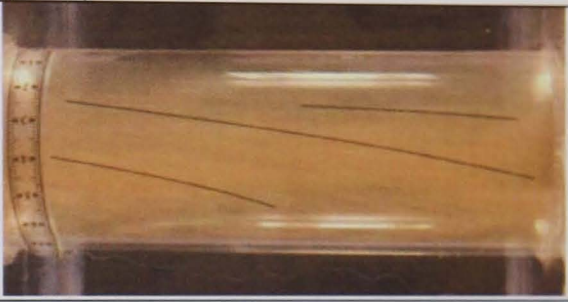
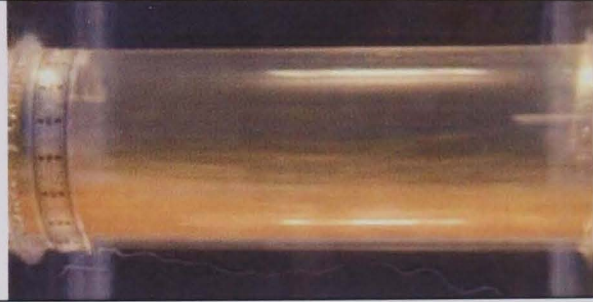



F.38 Tangential velocity (top RHS) and percentage decay for slurries with carrier fluids of various viscosities.



F.39 Tangential velocity (bottom LHS) and percentage decay for slurries with carrier fluids of various viscosities.

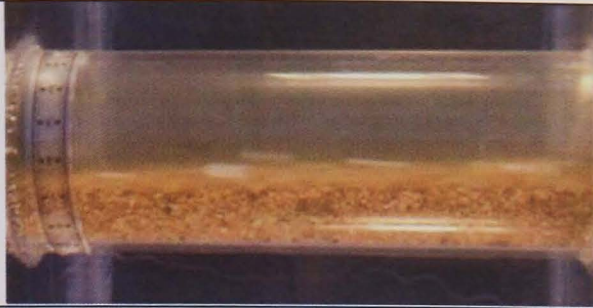









F.40 Photographs of the flow downstream of an inclined section of pipe with and without a swirl flow pipe section included, for 1.4% v/v coarse sand.

V / m/s	Photographs (shutter speeds /s)	
	Without swirl induction	With swirl induction
0.6		
	(1/60)	(1/40)
1.1		
	(1/60)	(1/50)
1.7		
	(1/60)	(1/60)
2.3		
	(1/60)	(1/60)









Note: To emphasise the swirl pattern lines representing particle tracks have been superimposed on the photographs.

F.41 Photographs of the flow downstream of an inclined section of pipe with and without a swirl flow pipe section included for 2.0% v/v coarse sand.

V / m/s	Photographs (shutter speeds /s)	
	Without swirl induction	With swirl induction
0.6		
	(1/60)	(1/50)
1.1		
	(1/60)	(1/50)
1.7		
	(1/60)	(1/50)
2.3		
	(1/60)	(1/60)

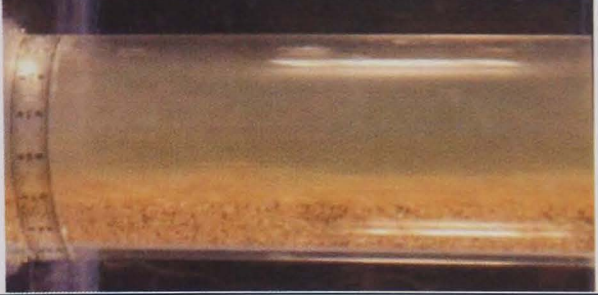
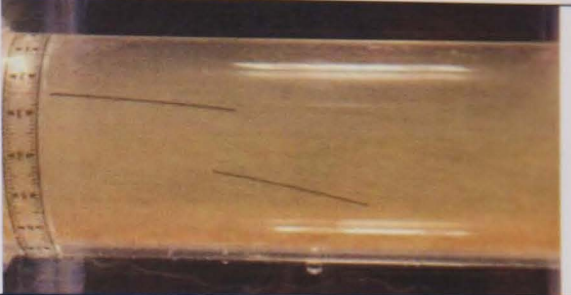
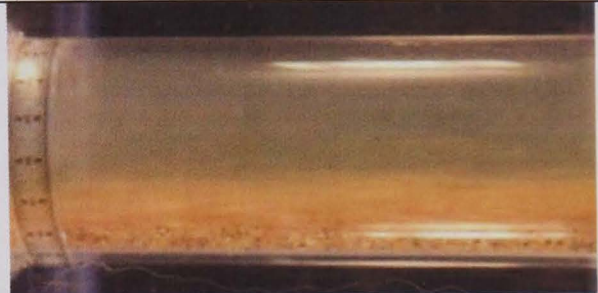





Note: To emphasise the swirl pattern lines representing particle tracks have been superimposed on the photographs.

F.42 Photographs of the flow downstream of an inclined section of pipe with and without a swirl flow pipe section included for 2.7% v/v coarse sand.

V / m/s	Photographs (shutter speeds /s)	
	Without swirl induction	With swirl induction
0.6		
	(1/60)	(1/60)
1.1		
	(1/60)	(1/40)
1.7		
	(1/30)	(1/50)
2.3		
	(1/60)	(1/60)

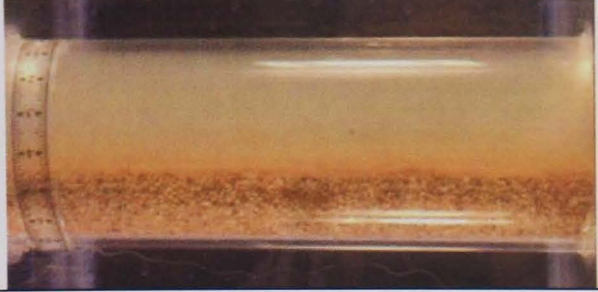

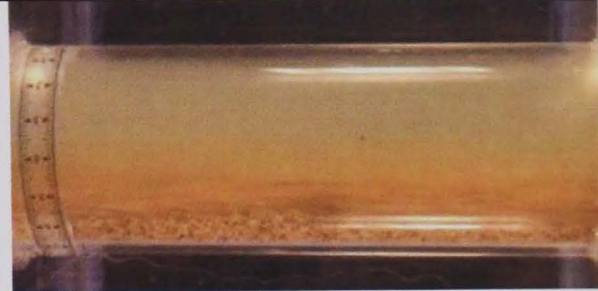





Note: To emphasise the swirl pattern lines representing particle tracks have been superimposed on the photographs.

F.43 Photographs of the flow downstream of an inclined section of pipe with and without a swirl flow pipe section included for 1.4% v/v medium sand.

V / m/s	Photographs (shutter speeds /s)	
	Without swirl induction	With swirl induction
0.6		
	(1/60)	(1/60)
1.1		
	(1/60)	(1/50)
1.7		
	(1/60)	(1/60)
2.3		
	(1/60)	(1/60)

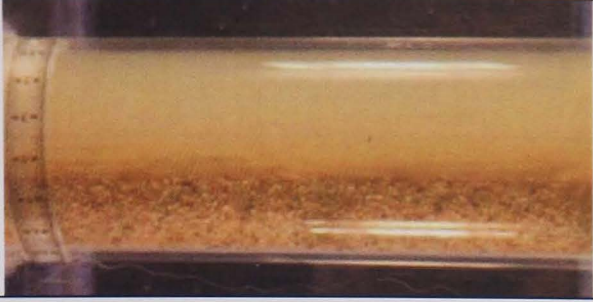


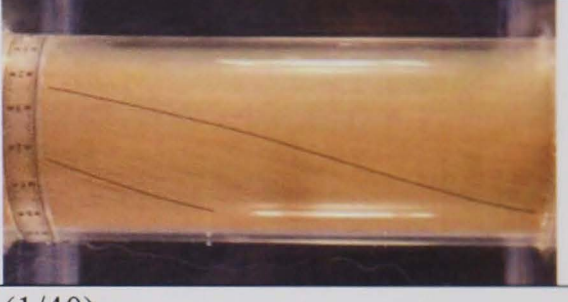




Note: To emphasise the swirl pattern lines representing particle tracks have been superimposed on the photographs.

F.44 Photographs of the flow downstream of an inclined section of pipe with and without a swirl flow pipe section included 2.0% v/v medium sand.

V / m/s	Photographs (shutter speeds /s)	
	Without swirl induction	With swirl induction
0.6		
	(1/60)	(1/60)
1.1		
	(1/50)	(1/60)
1.7		
	(1/60)	(1/60)
2.3		
	(1/60)	(1/60)


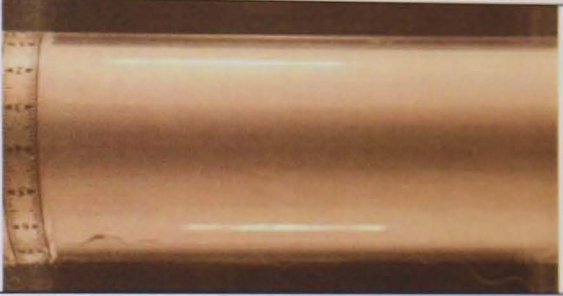


Note: To emphasise the swirl pattern lines representing particle tracks have been superimposed on the photographs.

F.45 Photographs of the flow downstream of an inclined section of pipe with and without a swirl flow pipe section included for 2.7% v/v medium sand.

V / m/s	Photographs (shutter speeds /s)	
	Without swirl induction	With swirl induction
0.6		
	(1/60)	(1/60)
1.1		
	(1/60)	(1/40)
1.7		
	(1/30)	(1/60)
2.3		
	(1/60)	(1/60)

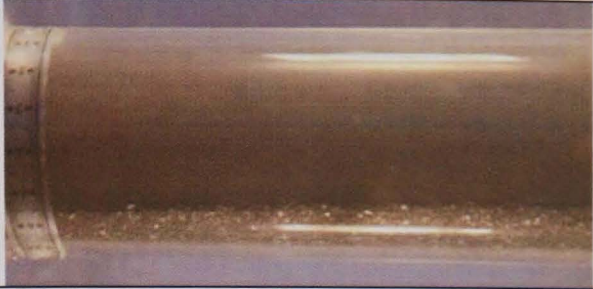

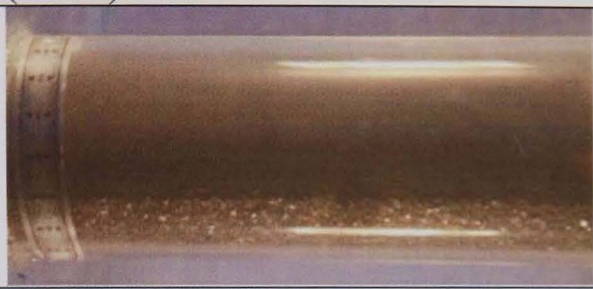
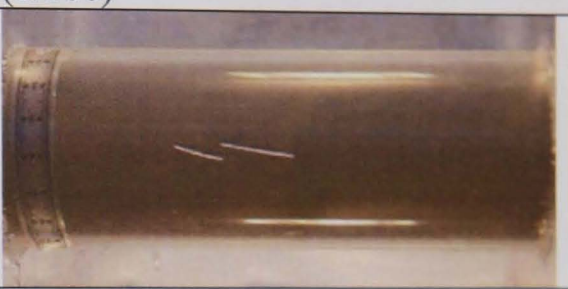
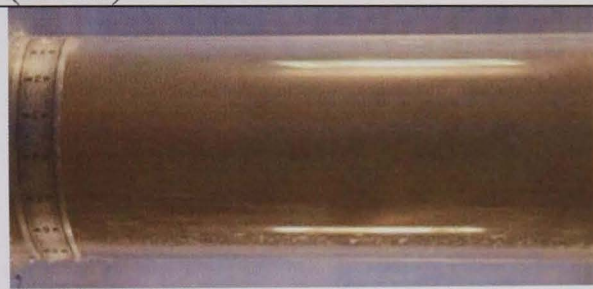



Note: To emphasise the swirl pattern lines representing particle tracks have been superimposed on the photographs.

F.46 Photographs of the flow downstream of an inclined section of pipe with and without a swirl flow pipe section included for 2.7% v/v fine sand.

V / m/s	Photographs (shutter speeds /s)	
	Without swirl induction	With swirl induction
0.6		
		(1/60)
1.1		
		(1/40)
1.7		
		(1/40)
2.2		
		(1/50)



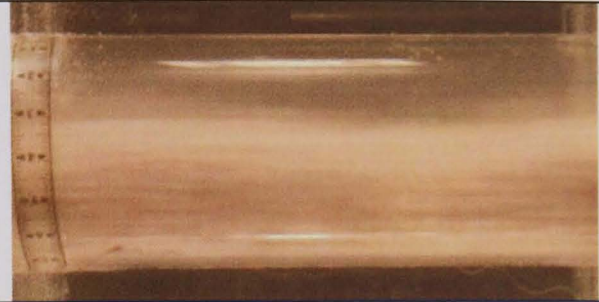
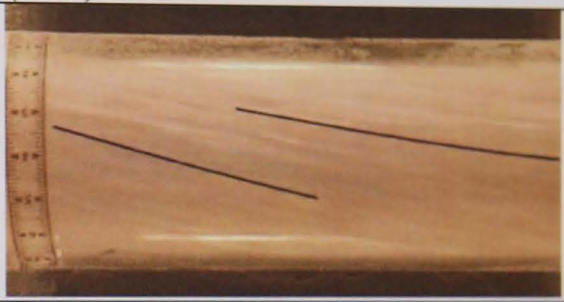
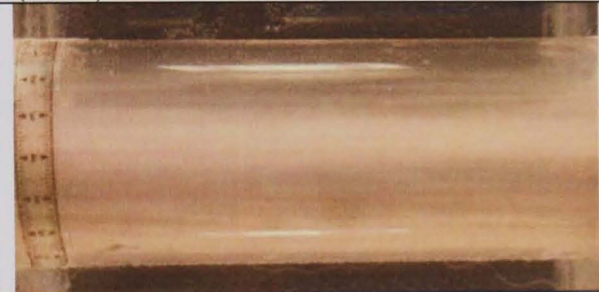
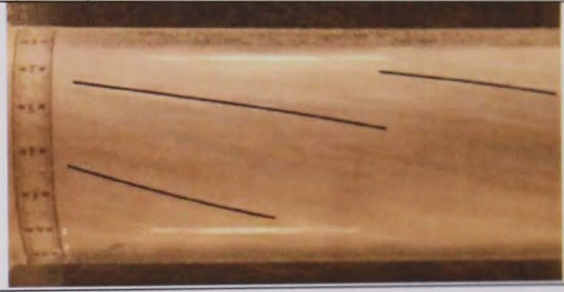
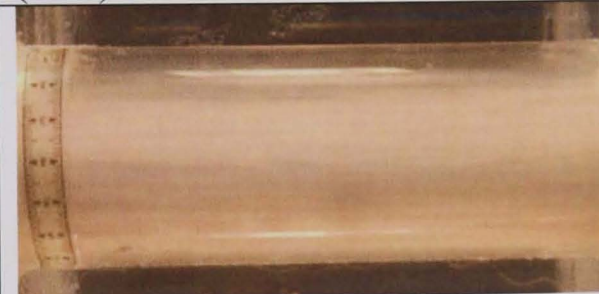

After the quality of these photographs were examined it was considered futile to take photographs for the inclined section without swirl induction.

F.47 Photographs of the flow downstream of an inclined section of pipe with and without a swirl flow pipe section included for 1.4% v/v coarse magnetite.

V / m/s	Photographs (shutter speeds /s) and tangential velocities / m/s:	
	Without swirl induction	With swirl induction
0.6		
	(1/100)	(1/100)
1.1		
	(1/100)	(1/80)
1.7		
	(1/100)	(1/40)
2.3		
	(1/60)	(1/100)



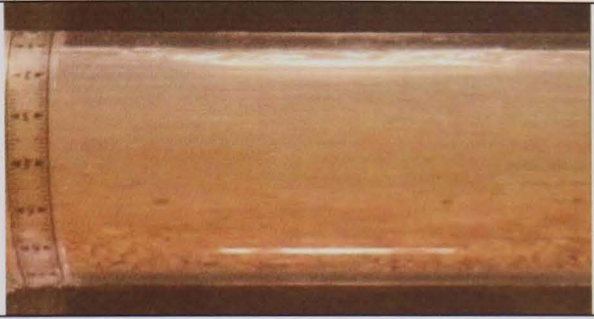
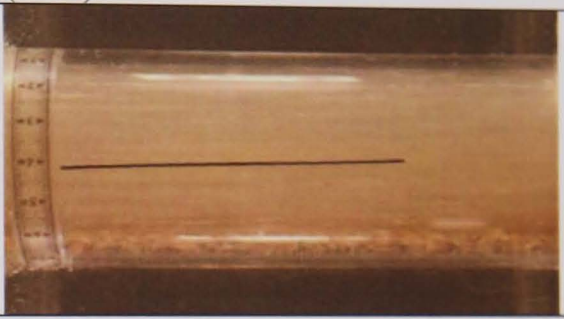
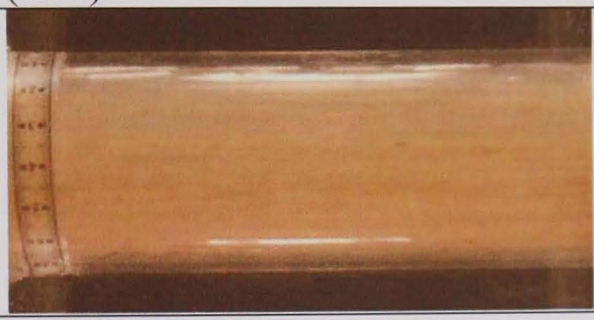

Note: To emphasise the swirl pattern lines representing particle tracks have been superimposed on the photographs.

F.48 Photographs of the flow downstream of an inclined section of pipe with and without a swirl flow pipe section included for 2.7% v/v plastic beads.

V / m/s	Photographs (shutter speeds /s)	
	Without swirl induction	With swirl induction
0.6		
	(1/30)	(1/30)
1.1		
	(1/30)	(1/40)
1.7		
	(1/30)	(1/60)
2.2		
	(1/40)	(1/60)

Note: To emphasise the swirl pattern lines representing particle tracks have been superimposed on the photographs.

F.49 Photographs of the flow downstream of an inclined section of pipe with and without a swirl flow pipe section included for CMC and 1.4% v/v coarse sand.

V / m/s	Photographs (shutter speeds /s)	
	Without swirl induction	With swirl induction
0.5		
	(1/40)	(1/40)
1.1		
	(1/30)	(1/30)
1.7		
	(1/50)	(1/30)

Note: To emphasise the swirl pattern lines representing particle tracks have been superimposed on the photographs.